frontiers | Research Topics

Tracing earth surface processes using novel isotopic approaches

Edited by
Kang-Jun Huang, Heng Chen, Wang Zheng and Mao-Yong He

Published in
Frontiers in Earth Science

ISSN 1664-8714
ISBN 978-2-83251-533-4
DOI 10.3389/978-2-83251-533-4

About Frontiers

Frontiers is more than just an open access publisher of scholarly articles: it is a pioneering approach to the world of academia, radically improving the way scholarly research is managed. The grand vision of Frontiers is a world where all people have an equal opportunity to seek, share and generate knowledge. Frontiers provides immediate and permanent online open access to all its publications, but this alone is not enough to realize our grand goals.

Frontiers journal series

The Frontiers journal series is a multi-tier and interdisciplinary set of open-access, online journals, promising a paradigm shift from the current review, selection and dissemination processes in academic publishing. All Frontiers journals are driven by researchers for researchers; therefore, they constitute a service to the scholarly community. At the same time, the *Frontiers journal series* operates on a revolutionary invention, the tiered publishing system, initially addressing specific communities of scholars, and gradually climbing up to broader public understanding, thus serving the interests of the lay society, too.

Dedication to quality

Each Frontiers article is a landmark of the highest quality, thanks to genuinely collaborative interactions between authors and review editors, who include some of the world's best academicians. Research must be certified by peers before entering a stream of knowledge that may eventually reach the public - and shape society; therefore, Frontiers only applies the most rigorous and unbiased reviews. Frontiers revolutionizes research publishing by freely delivering the most outstanding research, evaluated with no bias from both the academic and social point of view. By applying the most advanced information technologies, Frontiers is catapulting scholarly publishing into a new generation.

What are Frontiers Research Topics?

Frontiers Research Topics are very popular trademarks of the *Frontiers journals series*: they are collections of at least ten articles, all centered on a particular subject. With their unique mix of varied contributions from Original Research to Review Articles, Frontiers Research Topics unify the most influential researchers, the latest key findings and historical advances in a hot research area.

Find out more on how to host your own Frontiers Research Topic or contribute to one as an author by contacting the Frontiers editorial office: frontiersin.org/about/contact

Tracing earth surface processes using novel isotopic approaches

Topic editors

Kang-Jun Huang — Northwest University, China
Heng Chen — Columbia University, United States
Wang Zheng — Tianjin University, China
Mao-Yong He — Institute of Earth Environment, Chinese Academy of Sciences (CAS), China

Citation

Huang, K.-J., Chen, H., Zheng, W., He, M.-Y., eds. (2023). *Tracing earth surface processes using novel isotopic approaches*. Lausanne: Frontiers Media SA. doi: 10.3389/978-2-83251-533-4

This Research Topic has been realized in collaboration with Dr. Ximing Chen, Postdoc Researcher at Florida State University.

Table of contents

frontiers in Earth Science

ORIGINAL RESEARCH
published: 10 November 2021
doi: 10.3389/feart.2021.757094

Spatiotemporal Variation of Hydrogen and Oxygen Stable Isotopes in the Yarlung Tsangpo River Basin, Southern Tibetan Plateau

Ya-Ni Yan[1], Jun-Wen Zhang[1], Wei Zhang[1], Gui-Shan Zhang[1], Jian-Yang Guo[2], Dong Zhang[3], Jie Wu[4] and Zhi-Qi Zhao[1]**

[1]School of Earth Science and Resources, Chang'an University, Xi'an, China, [2]State Key Laboratory of Environmental Geochemistry, Institute of Geochemistry, Chinese Academy of Sciences, Guiyang, China, [3]School of Resource and Environment, Henan Polytechnic University, Jiaozuo, China, [4]School of Chemistry and Materials Science, Guizhou Education University, Guiyang, China

OPEN ACCESS

Edited by:
Mao-Yong He,
Institute of Earth Environment (CAS), China

Reviewed by:
Si-Liang Li,
Tianjin University, China
Buli Cui,
Ludong University, China

***Correspondence:**
Jun-Wen Zhang
zhangjunwen@tju.edu.cn
Zhi-Qi Zhao
zhaozhiqi@chd.edu.cn

Specialty section:
This article was submitted to Hydrosphere, a section of the journal Frontiers in Earth Science

Received: 11 August 2021
Accepted: 08 October 2021
Published: 10 November 2021

Citation:
Yan Y-N, Zhang J-W, Zhang W, Zhang G-S, Guo J-Y, Zhang D, Wu J and Zhao Z-Q (2021) Spatiotemporal Variation of Hydrogen and Oxygen Stable Isotopes in the Yarlung Tsangpo River Basin, Southern Tibetan Plateau. Front. Earth Sci. 9:757094. doi: 10.3389/feart.2021.757094

Characterization of spatiotemporal variation of the stable isotopes $\delta^{18}O$ and δD in surface water is essential to trace the water cycle, indicate moisture sources, and reconstruct paleoaltimetry. In this study, river water, rainwater, and groundwater samples were collected in the Yarlung Tsangpo River (YTR) Basin before (BM) and after the monsoon precipitation (AM) to investigate the $\delta^{18}O$ and δD spatiotemporal variation of natural water. Most of the river waters are distributed along GMWL and the line of d-excess = 10‰, indicating that they are mainly originated from precipitation. Temporally, the $\delta^{18}O$ and δD of river water are higher in BM series (SWL: $\delta D = 10.26\delta^{18}O+43.01$, $R^2 = 0.98$) than AM series (SWL: $\delta D = 9.10\delta^{18}O + 26.73$, $R^2 = 0.82$). Spatially, the isotopic compositions of tributaries increase gradually from west to east (BM: $\delta^{18}O = 0.65$Lon (°)-73.89, $R^2 = 0.79$; AM: $\delta^{18}O = 0.45$Lon (°)-57.81, $R^2 = 0.70$) and from high altitude to low (BM: $\delta^{18}O = -0.0025$Alt(m)-73.89, $R^2 = 0.66$; AM: $\delta^{18}O = -0.0018$Alt(m)-10.57, $R^2 = 0.58$), which conforms to the "continent effect" and "altitude effect" of precipitation. In the lower reaches of the mainstream, rainwater is the main source, so the variations of $\delta^{18}O$ and δD are normally elevated with the flow direction. Anomalously, in the middle reaches, the $\delta^{18}O_{mainstream}$ and $\delta D_{mainstream}$ values firstly increase and then decrease. From the Saga to Lhaze section, the higher positive values of $\delta^{18}O_{mainstream}$ are mainly caused by groundwater afflux, which has high $\delta^{18}O$ and low d-excess values. The $\delta^{18}O_{mainstream}$ decrease from the Lhaze to Qushui section is attributed to the combined action of the import of depleted ^{18}O and D groundwater and tributaries. Therefore, because of the recharge of groundwater with markedly different $\delta^{18}O$ and δD values, the mainstream no longer simply inherits the isotopic composition from precipitation. These results suggest that in the YTR Basin, if the $\delta^{18}O$ value of surface water is used to trace moisture sources or reconstruct the paleoaltimetry, it is necessary to rule out the influence from groundwater.

Keywords: stable isotopes, Yarlung Tsangpo River, mainstream, tributaries, groundwater recharge

INTRODUCTION

The stable isotopes, $\delta^{18}O$ and δD, in precipitation are widely used as a fingerprint for the hydrological processes and atmospheric circulation (Fette et al., 2005; Zhu et al., 2007; Singh et al., 2013; Guo et al., 2017; Wu et al., 2019). The Tibetan Plateau (TP) is the highest and widest high-altitude region on Earth, and the uplift history and terrain atmosphere of the region are of scientific interest (Garzione et al., 2000; Rowley et al., 2001; Spicer et al., 2003; Quade et al., 2011). Because of the so-called "continent effect" and "altitude effect" of isotope composition in precipitation (i.e., the negative relationship between $\Delta\delta^{18}O$ or $\Delta\delta D$ in precipitation and transport distance and elevation) producing heavier monsoonal rainfall first with transported distance, and then with orographic lifting, stable isotopes have also been used to trace moisture sources and to reconstruct paleoelevation of the TP (Garzione et al., 2000; Poage and Chamberlain, 2001; Rowley et al., 2001; Hren et al., 2009; Li and Garzione, 2017). A global network for isotopes in precipitation (GNIP) has been established by the International Atomic Energy Agency to monitor the long-term changes in $\delta^{18}O$ and δD in global precipitation. However, because of the few isotope-monitoring stations in the TP, the study of precipitation isotopic variability and hydrological processes in this region is usually hampered.

Based on the consideration that stream water can provide a time-integrated record of the isotopic composition of precipitation (Gat, 1996; Kendall and Coplen, 2001), a number of studies have used the isotopes in river water as a substitute for modern precipitation to further reconstruct paleoelevation or to trace moisture sources (Garzione et al., 2000; Hren et al., 2009; Yang et al., 2012a; Bershaw et al., 2012; Kong and Pang, 2016; Li and Garzione, 2017). At present, significant negative isotope–altitude relationships have been reported: for example, the lapse rate of $\delta^{18}O$ in river water is about −0.21‰ per 100 m in the northeastern TP (Bershaw et al., 2012), −0.24‰ per 100 m in the southern TP (Ding et al., 2009), −0.28‰ per 100 m in the high Himalayas of Nepal and −0.31‰ per 100 m in the Niyang River watershed (Florea et al., 2017), while it is as low as −0.36‰ per 100 m in the southern Himalaya (Wen et al., 2012) and about −0.19‰ per 100 m in the Hengduan Mountains (Hoke et al., 2014).

The Yarlung Tsangpo River (YTR) Basin was thought to be influenced by two climatic systems: a monsoonal system in the east and a westerly system in the west (Tian et al., 2001a; Tian et al., 2007; Hren et al., 2009; Gao et al., 2013; Yu et al., 2016; Ren et al., 2016, 2018). Monsoon-derived precipitation was found to have low $\delta^{18}O$ and d-excess (d-excess = δD-$8\delta^{18}O$) values (Dansgaard, 1964), and westerlies-derived precipitation had high values of both $\delta^{18}O$ and d-excess values (Tian et al., 2001a; Tian et al., 2005; Tian et al., 2007; Xu et al., 2011; Yang et al., 2012b; Yu et al., 2016). Hren et al. (2009) reported that the westernmost monsoon influence reached almost to 86°E, recording a minimum $\delta^{18}O$ value of approximately minus 20‰ for the YTR.

In addition to precipitation, groundwater recharge and ice/glacier melt water entering the YTR cannot be ignored as well (Liu, 1999; Liu et al., 2007; Tan et al., 2021; Zhang et al., 2021). The contributions of these sources differ between different seasons and different locations: the groundwater contribution is 40% in Nugesha, 36% in Yangcun, 32% in Nuxia (Liu, 1999), and 27–40% in the middle reach (Tan et al., 2021). Furthermore, the distinctions of hydrochemical and isotopic composition between groundwater and precipitation are obvious in the YTR Basin (Tan et al., 2014; Liu et al., 2019). In the case of the YTR Basin, which is the largest river basin on the Tibetan Plateau, it is unclear as to the extent to which groundwater recharge and precipitation affect the spatiotemporal distribution of stable isotopes in the river water. Accordingly, this study documents the oxygen and hydrogen isotopic compositions in river water, rainfall, and groundwater in the YTR Basin. Spatially, major influences on the variability of the isotopic composition of river water along the channel are described and identified. Temporally, comparisons of the isotopic composition were conducted before and after monsoon precipitation. The anomalous spatial distribution of isotopic compositions of mainstream in the middle reach and its cause is revealed.

METHODS

Study Area

The YTR extends from the Jima Yangzong glacier above 5,200 m elevation to the Bay of Bengal and is the highest large river in the world located south of the TP (Huang et al., 2008). The YTR Basin is a long and narrow valley covering a total area of about 240,480 km^2 in a west-east direction among the Gangdise, Nyainqentanglha, and Himalaya Mountains (**Figure 1**) (Liu et al., 2007). The elevation of the basin gradually decreases from west to east. The upper reach is from the source to Saga, with the major tributaries Mayou Tsangpo, Chai Qu, and Jiada Tsangpo; the middle reach is from Saga to Qushui, with major tributaries being Dogxung Tsangpo and Nyang Qu; and the lower reach is below Qushui with major tributaries being Lhasa River, Niyang River, and Parlung Tsangpo. In general, mean annual precipitation decreases from about 1,000 mm in the east of the basin to about 200 mm at the headwaters (Ren et al., 2018). Some 65–80% of the annual precipitation occurs between June and September, with the exception of southeastern Tibet (Liu, 1999). The mean annual air temperature in this area is about 5.9°C with an average seasonal variation of 2.46 and 13.49°C (You et al., 2007). The mean annual evaporation in this area is 1,052 mm, which is higher in the west than that in the east (Huang et al., 2011). The mean annual discharge of the YTR Basin is ~1,395.4 × 108 m^3 (Liu, 1999). In the upper and middle reach, groundwater is the main source; in the lower reach, the recharge pattern is a mix of rainwater and meltwater; while into the heavy rain area below the grand canyon, the river is mainly from precipitation (Liu, 1999; Yang et al., 2011).

Geologically, TP is generally regarded as a product of the Eurasian and Indian Plates collision (Gansser, 1980). The tectonic units of the TP comprise a series of east–west-trending continental blocks, including Songpan–Ganzi, Qiangtang,

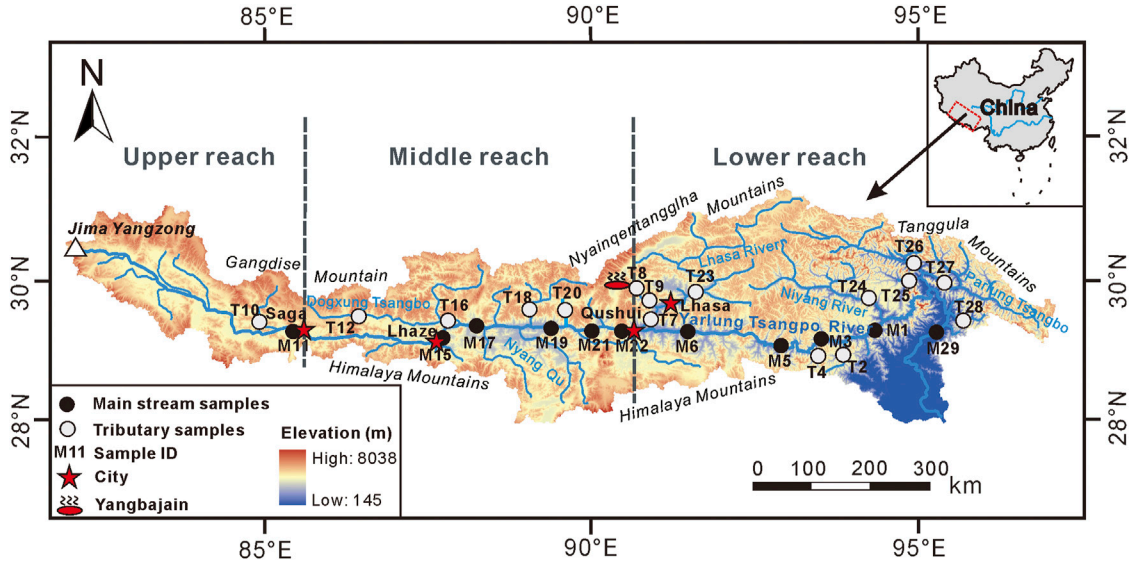

FIGURE 1 | Sampling sites in the YTR Basin (Modified from Zhang et al., 2021).

Lhasa, the Tethyan Himalayas, the high Himalaya, and the lesser Himalayas (Tapponnier et al., 2001; Zhang et al., 2004; Zhang et al., 2015). Due to the east-west extension of the TP, rifts trending approximately north–south cut across the YTR Basin (Armijo et al., 1986), From west to east, these rifts are Dingri-Nima (DN), Dingjie-Xietongmen-Shenzha (DXS), Yadong-Dangxiong-Gulu (YDG), and Gudui-Sangri (GS) rifts. Thus, the YTR Basin has widely distributed springs along the rifts (Wang et al., 2020; Tan et al., 2021). The terrane in the southern TP is dominated by Paleozoic–Mesozoic carbonate and clastic sedimentary rocks (Galy and France-Lanord, 1999). The bedrock in the basin mainly consists of igneous granite/granitic gneiss, or schist/other felsic volcanic and mafic volcanic rock. However, there are few if any carbonate rocks are in the upper and middle reaches of the catchments (Hren et al., 2007; Huang et al., 2011). Along the entire river course, ophiolites and ophiolitic mélanges are commonly found (GMRT Bureau of Geology and Mineral Resources of Xizang Tibet Autonomous Region, 1993).

Water Sampling and Isotopic Analysis

Two systematic sampling series were carried out in the YTR Basin (**Figure 1**), one in June, 2017, prior to large-scale monsoon rainfall ("BM" series) and one in September, 2017, after large-scale monsoon rainfall ("AM" series). A total of 53 river water samples were collected, comprising 22 samples from the main stream and 31 samples from the large tributaries (e.g., Jiada Tsangpo, Dogxung Tsangpo, Lhasa River, Niyang River, Parlung Tsangpo, etc.). Some of the mainstream sampling sites were located at least 1 km downstream of the confluence of major tributaries to ensure that the water from all sources was fully mixed. The other mainstream samples were evenly distributed along the whole basin. The samples of the tributaries were collected before they merged with the main stream. In addition, a hot spring sample was collected from the Yangbajain (YBJ) geothermal field, central YTR Basin. The rainwater sample was from Lhasa.

River water samples were collected at a depth of 10–15 cm on the river bank. All samples were filtered through 0.45 μM cellulose membrane and then put the filtered samples into dry, clean 15 ml HDPE bottles. To prevent sample evaporation, the bottles were completely filled and immediately sealed with parafilm. Samples were frozen in a refrigerator in the laboratory and then thawed to room temperature when required for analysis. Stable $\delta^{18}O$ and δD values of all samples were determined by Liquid Water Isotope Analyzer (IWA-35EP) in the State Key Laboratory of Environmental Geochemistry, Institute of Geochemistry, Chinese Academy of Sciences. The precision of $\delta^{18}O$ and δD measurements was better than ±0.1‰ and ±1.0‰, respectively. Results were reported as relative to the standard V-SMOW (Vienna Standard Mean Ocean Water).

RESULTS

The $\delta^{18}O$ and δD values for river water, groundwater, and rainwater in the YTR Basin are listed in **Table 1**. The $\delta^{18}O$ and δD values of river water range from −20.3 to −11.0‰ (arithmetic mean −16.1‰) and from −152 to −73‰ (arithmetic mean −121‰), similar to those of Hren et al. (2009) ($\delta^{18}O$: −20.8–9.8‰, δD: −165–59‰) and Ren et al. (2018) ($\delta^{18}O$: −18.7–11.9‰, δD: −146–86‰).

$\delta^{18}O$ and δD Values of River Water in BM and AM Series

In the BM series, the mean $\delta^{18}O$ and δD values for river water were −16.1 and −111‰, respectively. In the AM series, the mean $\delta^{18}O$ and δD values were −17.2 and −130‰, respectively. For

TABLE 1 | Sample locations and stable isotopes compositions.

Sample	Name of the river	Latitude (°)	Longitude (°)	Sample altitude (m)	BM series (sampled in the middle of June)			AM series (sampled in the middle of September)		
					$\delta^{18}O$ (‰)	δD (‰)	d-excess (‰)	$\delta^{18}O$ (‰)	δD (‰)	d-excess (‰)
Tributaries										
Upper reach										
T10	Jiada Tsangpo	29.33	85.15	4,477	−18.2	−142	4.1	−18.5	−149	−0.4
Middle reach										
T12	Dogxung Tsangpo	29.51	86.46	4,626	−17.1	−138	−1.4	−18.0	−147	−3.3
T16	Dogxung Tsangpo	29.40	87.95	3,950	−17.9	−139	3.7	−20.3	−152	10.9
T18	Xiang Qu	29.45	89.10	3,865	−16.8	−127	7.9	−17.5	−138	1.7
T20	Wuyuma Qu	29.36	89.63	3,756	−16.7	−127	6.4	−18.7	−140	9.6
Lower reach										
T8	Duilong Qu	30.05	90.59	4,140	−13.8	−97	13.7	--	--	--
T9	Duilong Qu	29.71	90.87	3,829	−14.6	−103	13.5	−16.6	−133	0.2
T7	Lhasa River	29.48	90.94	3,615	−16.1	−118	11.4	−17.8	−129	13.7
T23	Lhasa River	29.81	91.58	3,756	−15.7	−115	10.7	−16.9	−127	8.1
T4	Jindong Qu	29.00	93.32	3,003	−12.2	−82	15.7	−15.0	−104	15.8
T2	Li Longpu Qu	29.12	93.87	2,943	−11.0	−73	15.0	−14.0	−101	11.2
T24	Niyang River	29.52	94.43	2,913	−13.8	−96	14.7	−16.3	−118	12.4
T25	Layue Qu	29.99	94.88	2,362	−12.0	−80	15.7	−14.8	−100	18.6
T26	Yiong Tsangpo	30.10	95.07	2018	−12.2	−82	15.6	−15.8	−117	14.1
T27	Parlung Tsangpo	29.91	95.48	2,603	−13.7	−95	15.1	−14.3	−103	11.1
T28	Galong Qu	29.71	95.59	2,746	−11.4	−75	16.0	−15.2	−107	14.0
Mainstream										
Upper Reach										
M11	YTR	29.32	85.17	4,457	−17.3	−135	3.0	−18.0	−148	−4.1
Middle Reach										
M15	YTR	29.18	87.67	3,951	−15.5	−121	2.5	−16.6	−138	−5.6
M17	YTR	29.37	88.12	3,874	−16.1	−127	2.4	−17.1	−139	−2.8
M19	YTR	29.34	89.19	3,812	−16.5	−128	3.7	−17.5	−140	-0.2
M21	YTR	29.32	89.93	3,702	−16.6	−130	3.0	−19.2	−144	9.1
M22	YTR	29.33	90.67	3,594	−16.6	−129	3.8	−19.5	−146	9.8
Lower Reach										
M6	YTR	29.27	91.54	3,555	−16.4	−123	7.7	−19.0	−138	14.4
M5	YTR	29.07	92.93	3,059	−16.2	−123	6.5	−18.4	−137	10.6
M3	YTR	29.11	93.45	2,985	−15.9	−120	6.8	−18.1	−138	7.2
M1	YTR	29.28	94.31	2,915	−13.7	−98	10.9	−18.0	−135	8.8
M29	YTR	29.44	95.41	709	−13.5	−94	14.4	−16.7	−116	17.2
Groundwater										
YBJ	Yangbajain	30.08	90.48	4,289	−17.9	−147	-4.1	—	—	—
Precipitation										
LR	Lhasa	—	—	—	−14.9	−107	11.6	—	—	—

each sampling point, the $\delta^{18}O$ and δD of BM series were higher than those for the AM series, except for the Duilong Qu tributary (T8) sample, which was omitted in September. The results show that the river water is richer in heavy H and O isotopes before monsoon precipitation than after. The variation amplitude of stable isotopic composition in the upper and middle reach is less than that in lower reach. The sample with maximum amplitude variation of $\delta^{18}O$ and δD values between two series is from Motuo (M29) (−4.4 and −37‰, respectively); the sample with the minimum variation is from Saga (M11) (−0.7 and −13‰, respectively).

$\delta^{18}O$ and δD Values of Tributaries

Overall, $\delta^{18}O$ and δD values of tributary water ($\delta^{18}O_{tributary}$ and $\delta D_{tributary}$) increased gradually from upper to lower reach in the YTR Basin no matter in BM series or AM series (**Figure 2**). Since the YTR flows approximately from west to east, longitude was adopted as a convenient proxy for downstream distance of the main channel. The relationships between the $\delta^{18}O_{tributary}$ and the longitude are $\delta^{18}O$ (‰) = 0.65 Lon(°E)-73.89 ($R^2 = 0.79$, $p < 0.01$) before monsoon precipitation and $\delta^{18}O$ (‰) = 0.45 Lon(°E)-57.81 ($R^2 = 0.70$, $p < 0.01$) after monsoon precipitation, respectively. In addition, the relationships between the $\delta^{18}O_{tributary}$ and altitude are $\delta^{18}O$ (‰) = −0.0025 Alt(m)-5.94 ($R^2 = 0.66$, $p < 0.01$) before monsoon precipitation and $\delta^{18}O$ (‰) = −0.0018 Alt(m)-10.57 ($R^2 = 0.58$, $p < 0.01$) after monsoon precipitation.

$\delta^{18}O$ and δD Values of Main Stream

In the flow direction, $\delta^{18}O$ and δD isotopic values of mainstream waters ($\delta^{18}O_{mainstream}$ and $\delta D_{mainstream}$) increased from the upper reaches to the Lhaze (M15) section, then declined gradually from the Lhaze to Qushui (M22) section in the middle reaches, and then rose sharply again in the lower reaches (**Figure 3**). In both

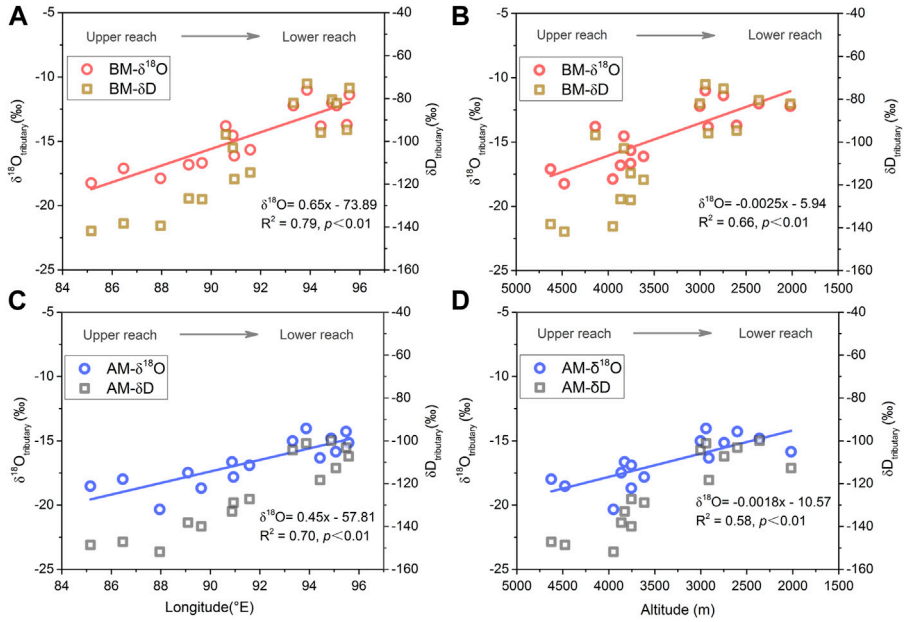

FIGURE 2 | Tributary water spatial variation of $\delta^{18}O$ and δD with longitude **(A,C)** and altitude **(B,D)**. Red circles and brown squares represent $\delta^{18}O$ and δD values before monsoon precipitation (BM) in **(A,B)**, respectively. Blue circles and gray squares represent $\delta^{18}O$ and δD values after monsoon precipitation (AM) in **(C,D)**. Red lines and blue lines show the linear fitting relationships between $\delta^{18}O$ in tributary water with longitude and altitude BM and AM, respectively.

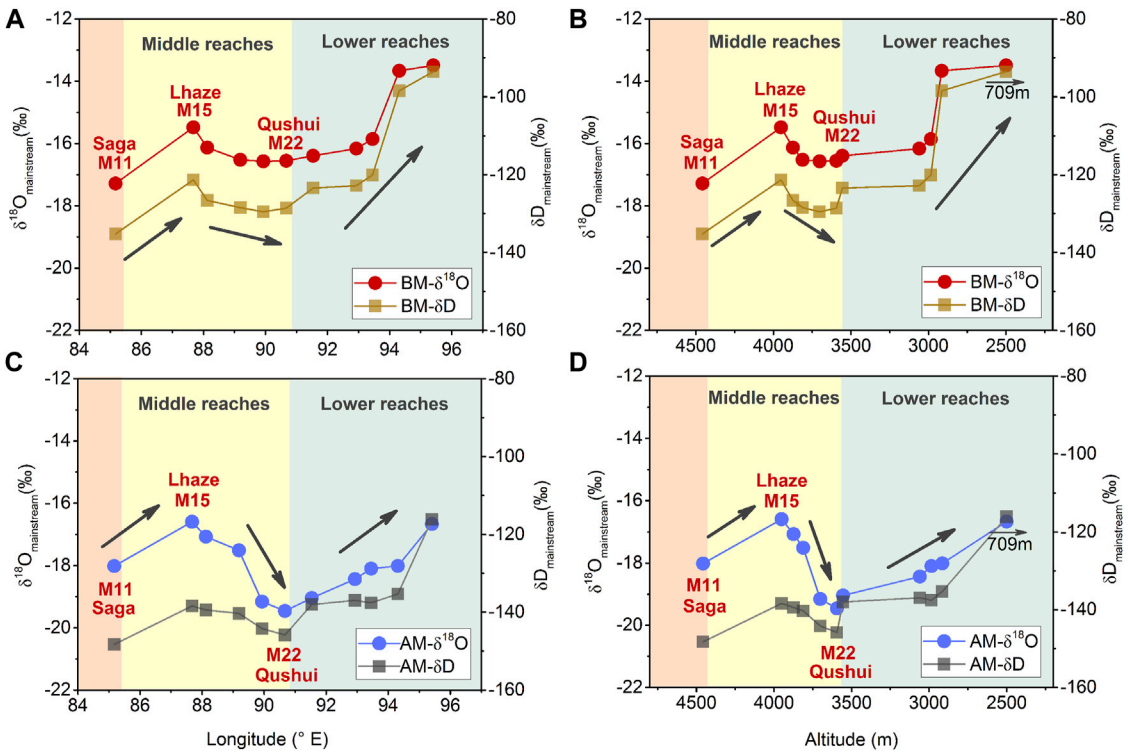

FIGURE 3 | Mainstream water spatial variation of $\delta^{18}O$ and δD values of characteristics with longitude **(A,C)** and altitude **(B,D)**. Red circles and brown squares represent $\delta^{18}O$ and δD values before monsoon precipitation (BM) in **(A,B)**, respectively. Blue circles and gray squares represent $\delta^{18}O$ and δD values of mainstream water after monsoon precipitation (BM) in **(C,D)**. In the upper part of the middle reach, $\delta^{18}O$ shows abnormally high values.

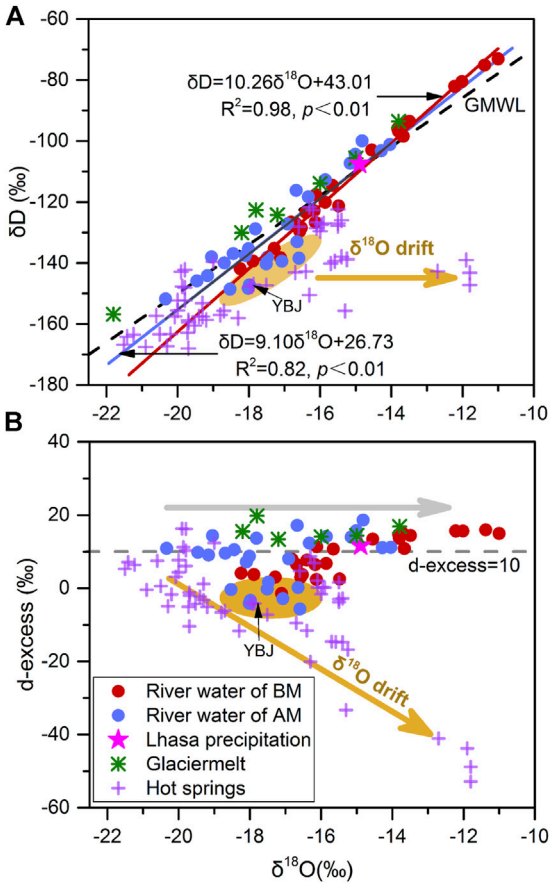

FIGURE 4 | δD vs $\delta^{18}O$ values and d-excess vs $\delta^{18}O$ values for natural water in the YTR Basin. The red dots and blue dots represent the δD vs $\delta^{18}O$ values of river water sampled before the monsoon precipitation (BM series) and after the monsoon precipitation (AM series), respectively. The red line and blue line show the linear fitting relationships between δD and $\delta^{18}O$ values of BM series and AM series river water, respectively. The black dashed line in **(A)** is the Global Meteoric Water Line (GMWL, $\delta D = 8\delta^{18}O+10$) (Craig, 1961). The gray dashed line in **(B)** is d-excess = 10‰. The brown arrow shows the downward trend of $\delta^{18}O$ drift in the groundwater; the gray arrow shows the distribution trend of global meteoric water. The δD and $\delta^{18}O$ values of glacier melt and groundwater are from Ren et al. (2017b), Tan et al. (2014), Tan et al. (2021), and Liu et al. (2019), respectively.

the BM and AM series, $\delta^{18}O_{mainstream}$ and $\delta D_{mainstream}$ showed the same spatial variation tendency. It is notable that the trends of $\delta^{18}O_{mainstream}$ and $\delta D_{mainstream}$ were significantly different from those in the tributaries, especially in the middle reach (**Figure 2**).

DISCUSSION

δD–$\delta^{18}O$ Relationship

The correlation between natural water H and O isotopic compositions is usually used to identify the recharge source, circulation paths, and mixing or exchange processes (Tan et al., 2014; Ren et al., 2018). In general, $\delta^{18}O$ and δD in meteoric water on a global scale have been found to fall close to the Global Meteoric Water Line (GMWL) of $\delta D = 8\delta^{18}O+10$ (Craig, 1961). In the YTR Basin, the Local Meteoric Water Lines (LMWLs) for several sites have been reported as $\delta D = 7.9\delta^{18}O + 4.3$ ($R^2 = 0.98$) for Bomi (Gao et al., 2011), $\delta D = 7.9\delta^{18}O + 6.3$ for Lhasa (Tian et al., 2001b), and $\delta D = 7.2\delta^{18}O–15.8$ for Xigaze (Ren et al., 2017a), but the exact LMWL for the entire basin is yet to be determined. The indicator, deuterium excess (d-excess = $\delta D–8\delta^{18}O$), was defined as a measure of non-equilibrium isotopes effects (Dansgaard, 1964) to record the difference between the actual δD and the expected equilibrium values based on measured $\delta^{18}O$. The d-excess of global meteoric water is +10‰. In the low-humidity conditions, strong kinetic fractionation in evaporation causes high d-excess value (>10‰) in precipitation. Conversely, high-humidity results in a decrease in kinetic isotope fractionation, and subsequent precipitation will have a low d-excess value (<10‰) (Gat and Matsui, 1991; Gat, 1996). For the geothermal water systems, $\delta^{18}O$ values of rocks and minerals are greater than those for water in general, and the O isotope exchange during the water-rock interaction increases $\delta^{18}O$ in water. However, since few rock minerals contain H and the δD value is low, the isotope exchange reaction has little effect on the δD of water. As a result, the isotopic composition of the groundwater is shifted horizontally to the right on the δD vs $\delta^{18}O$ diagram (**Figure 4A**) when the water residence time is long enough and the water-rock interaction is significant, a phenomenon known as "$\delta^{18}O$ drift" (Wang, 1991). As a result, the isotopic exchange reaction also reduces the d-excess value of geothermal water (Wang, 1991; Yin et al., 2001).

In this study, most of the $\delta^{18}O$ and δD values of river waters in the YTR Basin are distributed along GMWL and the line of d-excess = 10‰, which indicates that river waters should be mainly originated from precipitation. The linear regression relationships between $\delta^{18}O$ and δD values and surface water lines (SWLs) are $\delta D = 10.26\delta^{18}O + 43.01$ ($R^2 = 0.98$, $n = 27$, $p < 0.01$) before the monsoon precipitation and $\delta D = 9.10\delta^{18}O + 26.73$ ($R^2 = 0.82$, $n = 26$, $p < 0.01$) after the monsoon precipitation. Both the slopes and intercepts are larger than GMWL and LMWLs. The SWLs are approximate to previous studies of Hren et al. (2009) (slope≈10 and intercept≈38) and Ren et al. (2018) (slope 9.25 and intercept 24.1) in the basin. Evaporation is not the cause of steep slopes because that it would result in more isotopical enrichment and a lower δD-$\delta^{18}O$ slope in residual waters than GMWL (Gonfiantini 1986; Ren et al., 2018). Glacier melt is also a vital source of river water, and the points of glacier melt distributed along the GMWL inherit the isotopic composition of precipitation (**Figure 4A**). Therefore, the steep slopes of SWLs cannot be attributed to the supply of glacier melt. As shown in **Figure 4A**, there are a few samples (mainly from the upper and middle stream) fall on the lower left-hand side of the GMWL with low d-excess (**Figure 4B**), which could produce a steep δD-$\delta^{18}O$ slope. Meanwhile, the samples show greater deviation more from the GMWL, indicating that they may be supplied by another source with higher $\delta^{18}O$ and d-excess than precipitation.

In addition to precipitation and glacier melt water, groundwater may also be non-negligible sources of YTR water (Liu, 1999; Liu et al., 2007; Zhang et al., 2021). A few studies have

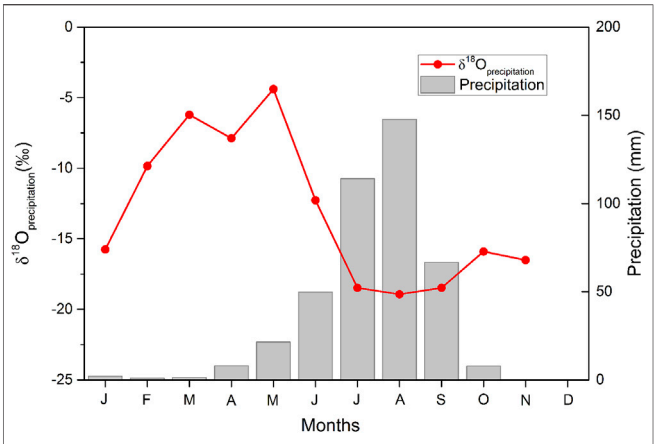

FIGURE 5 | Monthly precipitation amounts and weighted-average $\delta^{18}O$ of precipitation at Lhasa station (data are from Liu et al., 2007; Gao et al., 2011).

reported the stable isotope composition of groundwater in the YTR Basin (**Figure 4**) (Tan et al., 2014; Liu et al., 2019; Tan et al., 2021). Based on their $\delta^{18}O$ and δD values, groundwater can be roughly divided into two categories. Some dots with lower lighter-isotope composition are located in the lower left-hand corner of the δD-$\delta^{18}O$ diagram (**Figure 4A**). The research of Tan et al. (2021) suggested that the groundwater with lower values of $\delta^{18}O$ and δD in the Xietongmen to Lhasa section of the YTR Basin originated from paleo-precipitation during a cooler time. A supply of such groundwater would lower the $\delta^{18}O$ and δD values in the river water, but the slope of the SWL would not be affected; however, other groundwater samples (including YBJ) have shown a significant positive deviation of $\delta^{18}O$ from GMWL and a negative deviation of d-excess from 10‰ (**Figure 4B**). According to the study of Liu et al. (2019), some hot springs in the Semi and Daggyai geothermal fields have significant "$\delta^{18}O$ drift" due to the mixing of magmatic fluids with higher $\delta^{18}O$ values. A similar property of groundwater has been observed in other tectonic fracture zones or thermal field distribution areas (e.g., at the edge of the Guanzhong Basin, China (Ma et al., 2017), in the southeastern edge of the Eurasia (Chen et al., 2016), in Kyushu, Japan (Mizutani, 1972), and in northern Iceland (Stefánsson et al., 2019)). Consequently, from the perspective of isotopic composition characteristics, these river samples deviating from GMWL to the right and the downward trend of the d-excess = 10‰ line to the downward may be due to the recharge from a particular type of groundwater with significant $\delta^{18}O$ drift.

Temporal Patterns of δD and $\delta^{18}O$ in the Yarlung Tsangpo River Basin

As shown in **Figure 4A**, the YTR waters have high δD and $\delta^{18}O$ values before the monsoon precipitation and low values after the monsoon precipitation. As discussed in *δD–$\delta^{18}O$ Relationship*, YTR waters mainly originate from precipitation and inherit its isotopic composition of precipitation. The temporal pattern of isotopic composition in the YTR Basin river waters is dominated by precipitation.

The precipitation in the YTR Basin has a remarkable seasonal pattern. Summer precipitation contributes up to 65–80% of the annual total in this region, and it is dominated by the monsoon from the Bay of Bengal (Liu, 1999). Previous work revealed that the temporal variation of $\delta^{18}O$ in precipitation ($\delta^{18}O_{precipitation}$) was characterized by a higher value in the dry season (October to May of the following year) and lower in the monsoon season (from mid-June to September). This is known as the "amount effect" of $\delta^{18}O_{precipitation}$, as in the observational data from Lhasa station shown in **Figure 5** (Wei and Lin., 1994; Tian et al., 1997; Tian et al., 2001a; Tian et al., 2001b; Liu et al., 2007; Yu et al., 2008; Yu et al., 2016; Hren et al., 2009; Gao et al., 2011; Yang et al., 2012b; Yao et al., 2013; Ren et al., 2018). As a whole, under the influence of rainfall, the δD and $\delta^{18}O$ of the YTR Basin river waters are high before the monsoon precipitation and low afterward.

The $\delta^{18}O$ amplitude variation of sample between two series (4.4‰, the maximum) is much small than annual variation of precipitation (~14.5‰) in Lhasa. For one thing, the valley collects precipitation from an entire catchment over a period of time. For another, in addition to precipitation, the river may have other sources with stable isotopic composition, such as groundwater. So, the isotopic composition of river water is more stable than that of precipitation in different seasons. The variation amplitude of $\delta^{18}O$ in the upper reach and middle reach is less than that in the lower reach. It could be attributed that precipitation contributes more to river in the lower reach than the upper or middle reach.

Spatial Patterns of δD and $\delta^{18}O$ in the Yarlung Tsangpo River Basin

Tributaries

The δD and $\delta^{18}O$ values in tributary waters ($\delta D_{tributary}$ and $\delta^{18}O_{tributary}$) increase gradually from west to east with high to low topographical relief for both BM and AM series (**Figure 2**). The spatial distribution pattern is very similar to precipitation, which indicates that the $\delta D_{tributary}$ and $\delta^{18}O_{tributary}$ values are mainly affected by precipitation.

Spatially, the $\delta^{18}O_{precipitation}$ in the YTR Basin is influenced by the "continent effect" and "altitude effect" (Liu et al., 2007; Hren et al., 2009; Wang et al., 2000). During the summer period, moisture penetrates into the southeastern TP and is transported westward along the YTR valley, so longitude may be regarded as a convenient proxy for the transported distance of the moisture. Moreover, the terrain of the YTR valley gradually rises from east to west. As a warm and humid airmass moves westward, the moisture adiabatically cools and produces heavier monsoonal rainfall with increasing transport distance and altitude, resulting in a gradually lighter isotopic composition of precipitation (Liu et al., 2007; Hren et al., 2009). Therefore, the $\delta^{18}O$ in the precipitation decreases gradually in an upstream direction along the YTR valley. As shown in **Figure 6**, the annual weighted $\delta^{18}O_{precipitation}$ value is significantly correlated with longitude and altitude. The $\delta^{18}O_{precipitation}$ vertical lapse rate

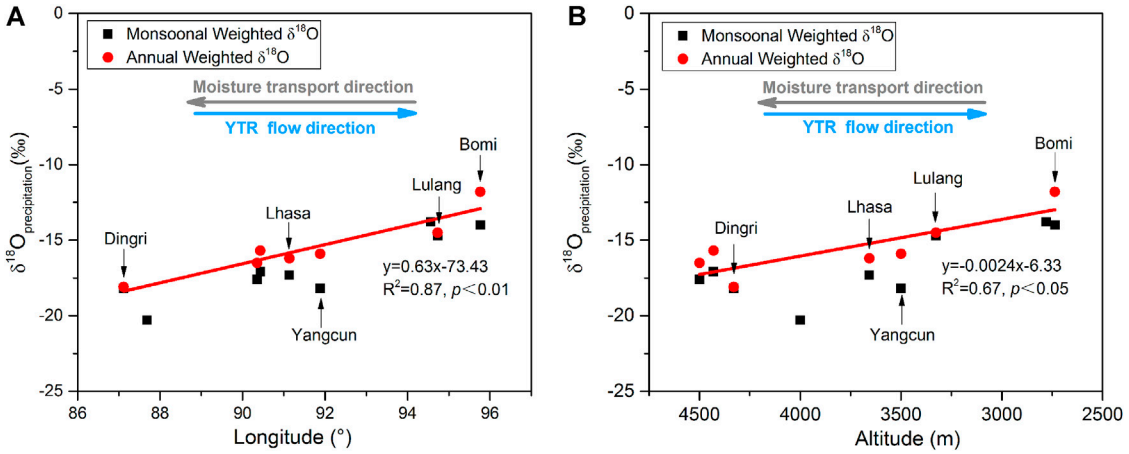

FIGURE 6 | Relationship of $\delta^{18}O$ of precipitation to **(A)** longitude and **(B)** altitude. Red dots = annual weighted $\delta^{18}O$; black squares = monsoonal weighted $\delta^{18}O$ of precipitation; red lines = linear fit of annual weighted $\delta^{18}O$ in precipitation with longitude and altitude. As moisture moves westward, altitude gradually increases and isotopic compositions of precipitation progressively decrease (data from Wang et al. (2000) and Yao et al. (2013)).

−2.4‰/km (R^2 = 0.67, p < 0.05) approximates to the global average of −2.8‰/km (Poage and Chamberlain, 2001).

The $\delta D_{tributary}$ and $\delta^{18}O_{tributary}$ show a similar spatial variation trend with precipitation (**Figures 2**, **6**). It should be noted that the change rates of $\delta^{18}O_{tributary}$ value with regard to longitude and altitude (0.65‰ per longitude degree and −2.5‰/km) before the monsoon precipitation approximate more closely to annual weighted $\delta^{18}O$ in precipitation (0.63‰ per longitude degree and −2.4‰ per 1 km) than after monsoon precipitation (0.44‰ per longitude degree and −1.8‰ per 1 km). The lower $\delta^{18}O$ vertical lapse rate after the monsoon precipitation may be related to water sources mixed from different altitudes. During the monsoon precipitation in summer, the accumulated snows from different altitudes melt and mix to recharge the river. Although the isotopic composition of melted ice and snow inherits the precipitation influenced by the altitude effect, the mixed melted waters from different elevation change $\delta^{18}O_{tributary}$ vertical lapse rate and weaken the correlation, but do not modify the spatial patterns of $\delta^{18}O_{tributary}$.

Main Stream

The spatial trends of mainstream δD and $\delta^{18}O$ values are different from those of tributaries and precipitation. As shown in **Figure 3**, $\delta^{18}O_{mainstream}$ and $\delta D_{mainstream}$ increase from the upper reach to Lhaze (M15) and then decline gradually from Lhaze to Qushui (M22) in the middle reach. Below Qushui (M22), these values rise sharply along the flow direction.

In the lower reach, the trends of $\delta^{18}O_{mainstream}$ are similar to $\delta^{18}O_{precipitation}$ and $\delta^{18}O_{tributaries}$ (**Figures 2**, **5**). Analogous patterns of evaporation and "altitude effect" on precipitation have been observed in the main flows of other large rivers globally: For example, the Ganges River in Asia (Ramesh and Sarin, 1992), the Missouri River in the United States (Winston and Criss, 2003), the Nile River in Africa (Cockerton et al., 2013), and the Yangtze River and Yellow River in China (Li et al., 2015; Fan et al., 2017). The lower reach of the YTR valley is the major transport pathway of the monsoonal moisture with more precipitation whose $\delta^{18}O$ values are relatively high, attributable to the lower altitudes and shorter transportation distance (*Tributaries*). Furthermore, rainwater is the main source of surface water downstream. Therefore, $\delta^{18}O_{tributaries}$, $\delta^{18}O_{precipitation}$, and $\delta^{18}O_{mainstream}$ have similar trends in the lower reach.

Anomalously, in the section from Saga (M11) to Qushui (M22), $\delta^{18}O_{mainstream}$ and $\delta D_{mainstream}$ firstly increase and then decrease. In particular, the decreasing tendency between Lhaze (M15) and Qushui (M22) contradicts to the expected "continent effect" and "altitude effect" on the isotopic evolution of surface water. If the local precipitation controls the isotope composition of the mainstream, the values of $\delta^{18}O_{mainstream}$ and $\delta D_{mainstream}$ would be expected to increase downstream in theory. Moreover, it is the mainstream samples from the middle reach that deviate from the GMWL line, having lower d-excess values as, shown in **Figure 4**, and weakening the correlation between stable isotopes composition with longitude and altitude (**Figure 3**). The anomalous trend in the middle reach cannot be attributed to recharge by precipitation and melt water (*δD–δ^{18}O Relationship*).

The phenomenon that main flows are isotopically enriched west of about 86°E longitude has been observed in other studies (Hren et al., 2009; Ren et al., 2016). They considered that the increasing influence of the westerlies would result in higher $\delta^{18}O$ and d-excess of surface waters, because of the upper reach being located in the transition between monsoon-dominant area and westerlies dominant area (Hren et al., 2009; Ren et al., 2016). However, this view is not supported by our results. Firstly, the $\delta^{18}O$ of the westernmost mainstream sample (M11) is lower than that of the adjacent main stream point downstream sample values (M15, M17, and M19). It is true for both two seasons, especially for BM series, where the $\delta^{18}O$ of M11 is the lowest (**Figure 3**). Secondly, the annual weighted $\delta^{18}O$ of precipitation in this section decreases from Lhasa to Dingri (**Figure 6A**). Additionally, the d-excess values of mainstream waters in this

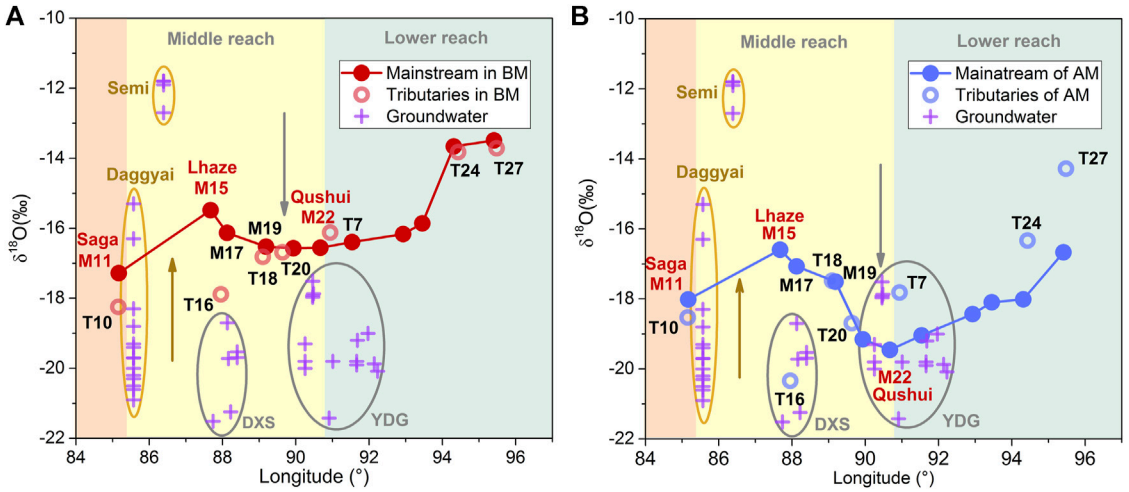

FIGURE 7 | The mainstream $\delta^{18}O$ is represented by **(A)** red dots for BM series and **(B)** blue dots for AM series, respectively. The red circles in **(A)** and blue circles in **(B)** represent the $\delta^{18}O$ of larger tributary confluences (e.g., Dogxung Tsangpo, Lhasa River, and Parlung Tsangpo) in BM and AM series. The isotopical composition values of groundwater in Semi and Daggyai geothermal field are from Liu (2018) and Liu et al. (2019). The other groundwater values for the Dingjie-Xietongmen-Shenzha (DXS) and Yadong-Dangxiong-Gulu (YDG) faults are from Tan et al. (2014) and Tan et al. (2021).

section (~3‰ for BM and ~1‰ for AM) are much lower than 10‰ (**Figure 4B**), which does not accord with the larger d-excess characteristics of westerly precipitation. Therefore, these results do not support that westerly precipitation is the main cause of the abnormal isotopic composition in the middle reach. The enhanced evaporation intensity from east to west will also lead to more positive δD and $\delta^{18}O$ values of the upstream. However, the isotopic composition of westernmost mainstream sample (M11) is not the maximum in both two seasons. Therefore, the evaporation is not the main reason for the anomaly.

The abnormal $\delta^{18}O_{mainstream}$ trend in the middle reach is most likely related to groundwater recharge. Firstly, three roughly north-south rifts (Dingri-Nima (DN), Dingjie-Xietongmen-Shenzha (DXS), and Yadong-Dangxiong-Gulu (YDG) rifts) intersect the YTR valley in the middle reach (Wang et al., 2020). The tectonic fracture zones provide the conditions for a large amount of groundwater to recharge the mainstream (Zhang et al., 2021). Additionally, the hydraulic head of over 1,000 m could drive groundwater flow over long distances (Hoke et al., 2000; Tan et al., 2014). From the hydrochemical point of view, geothermal water has been suspected as the main source of the elevated $(As)_{dissolved}$ levels in the YTR (Zhang et al., 2021). Other major ion and ^{222}Rn data have also strongly suggested a large addition of groundwater to the YTR in the middle reach (Tan et al., 2021). In addition, the $\delta^{18}O$ characteristics of groundwater show significant differences from west to east in the YTR Basin (Tan et al., 2014; Liu, 2018; Liu et al., 2019; Tan et al., 2021). The nearby groundwater in the Semi (~86.4°E) and Daggyai (~85.6°E) geothermal field near has obvious characteristics of ^{18}O drifts in the mixed recharge of meteoric waters and magmatic fluids (Liu et al., 2019). In Semi and Daggyai geothermal field, the $\delta^{18}O$ maximum values of groundwater are −11.8 and −15.3‰, respectively (Liu et al., 2019). Their locations exactly coincide with the area where $\delta^{18}O_{mainstream}$ values are abnormally high, from Saga to Lhaze (**Figure 7**). However, the groundwater sampled in the range of approximately 88–92°E has been observed to be depleted in D and ^{18}O and may have originated from paleo-precipitation during a cooler time and contributes 27–40% of the river flow (Tan et al., 2021). Near the DXS and YDG rifts, the $\delta^{18}O$ minimum values of groundwater are −21.5‰ and −21.4‰, respectively (Tan et al., 2021). Just in this section (from Lhaze to Qushui), the $\delta^{18}O$ value of mainstream is decreasing. In addition, for the tributaries, the $\delta^{18}O$ values of Jiada Tsangbo (T10), Dogxung Tsangbo (T16), and Xiang Qu (T18) before the confluence are lower than that of the main stream in the middle reach (**Figure 7**), so the inflow of the tributaries will lead to the isotopic composition declining as well. Therefore, the following conclusions can be drawn: from the Saga (M11) to Lhaze (M15) section, the recharge of D and ^{18}O enriched groundwater will result in the increase of the isotopic composition of the mainstream water; from Lhaze (M15) to Qushui (M22), the isotopic composition of the mainstream decreases due to the combined action of depleted D and ^{18}O groundwater recharge and tributaries import.

Implications

The stable isotopic characteristics of modern precipitation provide vital information to indicate moisture sources and to reconstruct paleoaltimetry. In some regions where GNIP observations are sparse, $\delta^{18}O$ values of river water have to be used to alleviate this problem (Rowley, 2007; Timsic and Patterson, 2014; Xu et al., 2014; Li and Garzione, 2017). However, the water in a large river is generally collected from two main sources: 1) recent precipitation through surface runoff or channel precipitation or by rapid flow through the shallow subsurface and 2) groundwater recharge. The relative contribution of these sources differs in each watershed (Ogrinc et al., 2008). Therefore, the stable isotopic characteristics of river

water are affected by meteorological and hydrological factors. In this study, the spatial distribution of $\delta^{18}O_{mainstream}$ in the YTR middle reach is significantly different from that of tributaries and local precipitation. Due to the groundwater recharge, $\delta^{18}O_{mainstream}$ in the section from Lhaze to Qushui is characterized by inverse isotope–elevation and isotope–moisture transport distance relationships that could produce significant misestimates of paleoaltimetry and moisture sources. Thus, when reconstructing the paleoaltimetry and tracing moisture sources using river water as a substitute for modern precipitation, it is necessary to consider that groundwater may also influence the distribution of stable isotopes in river water, especially near tectonic fracture zones where geothermal water may be characterized by remarkable high or low $\delta^{18}O$ values.

CONCLUSION

In the YTR Basin, most of the river waters originate in precipitation and inherit the δD and $\delta^{18}O$ characteristics of precipitation. Temporally, under the predominance of precipitation, the isotopic composition of river water is high before the monsoon precipitation (mid-June) and low after the monsoon precipitation (mid-September). Spatially, the δD and $\delta^{18}O$ values in tributary water increase gradually from west to east and conform to the "continent effect" and "altitude effect" of precipitation. For the mainstream, rainwater is the prime source of surface water in the lower reach, with the result that the δD and $\delta^{18}O$ variations are normally elevated. Anomalously, in the middle reach of the mainstream, the $\delta^{18}O$ and δD firstly increase and then decrease. From Saga to Lhaze, the groundwater is characterized by high $\delta^{18}O$ and low d-excess afflux causes the $\delta^{18}O_{mainstream}$ to be more positive. Then, from Lhaze to Qushui, the decrease in isotopic compositions of the mainstream is attributed to the combined action of the D and ^{18}O depleted groundwater and tributaries import. As a result, due to the recharge of groundwater with remarkable differences in isotopic composition, the mainstream no longer simply inherits the characteristics of tributaries or precipitation: therefore, when reconstructing paleoaltimetry and tracing moisture sources by using $\delta^{18}O$ of river water as a substitute for modern precipitation, it is necessary to rule out the influence of groundwater, especially near the tectonic fracture zones whose condition is conducive to groundwater drainage, and the $\delta^{18}O$ of the groundwater varies significantly.

DATA AVAILABILITY STATEMENT

The original contributions presented in the study are included in the article/Supplementary Material; further inquiries can be directed to the corresponding authors.

AUTHOR CONTRIBUTIONS

Z-QZ and J-WZ contributed to the conception of the study. Samples were collected by Z-QZ, J-WZ, G-SZ, DZ, and J-YG. JW, WZ, and Y-NY performed the isotopic analysis. Y-NY and J-WZ wrote the first draft of the manuscript. All authors contributed to article revision and approved the submitted version.

FUNDING

This work was supported jointly by the National Natural Science Foundation of China (Nos. 41661144042, 41930863, 42003007, and 42073009), the Second Tibetan Plateau Scientific Expedition and Research (2019QZKK0707), and Special Fund for Basic Scientific Research of Central Colleges, Chang'an University (No. 300102278302).

ACKNOWLEDGMENTS

The authors thank Cui Lifeng, Liu Taoze, Gao Shuang, Liu Xu, Ye Runcheng, Meng Junlun, Jia Guodong, Yang Ye, and Zhang Xiaolong for helping in the field work.

REFERENCES

Armijo, R., Tapponnier, P., Mercier, J. L., and Han, T.-L. (1986). Quaternary Extension in Southern Tibet: Field Observations and Tectonic Implications. *J. Geophys. Res.* 91, 13803–13872. doi:10.1029/jb091ib14p13803

Bershaw, J., Penny, S. M., and Garzione, C. N. (2012). Stable Isotopes of Modern Water across the Himalaya and Eastern Tibetan Plateau: Implications for Estimates of Paleoelevation and Paleoclimate. *J. Geophys. Res.* 117 (D2). doi:10.1029/2011jd016132

Chen, L., Ma, T., Du, Y., Xiao, C., Chen, X., Liu, C., et al. (2016). Hydrochemical and Isotopic (2H, 18O and 37Cl) Constraints on Evolution of Geothermal Water in Coastal plain of Southwestern Guangdong Province, China. *J. Volcanology Geothermal Res.* 318, 45–54. doi:10.1016/j.jvolgeores.2016.03.003

Cockerton, H. E., Street-Perrott, F. A., Leng, M. J., Barker, P. A., Horstwood, M. S. A., and Pashley, V. (2013). Stable-isotope (H, O, and Si) Evidence for Seasonal Variations in Hydrology and Si Cycling from Modern Waters in the Nile Basin: Implications for Interpreting the Quaternary Record. *Quat. Sci. Rev.* 66, 4–21. doi:10.1016/j.quascirev.2012.12.005

Craig, H. (1961). Isotopic Variations in Meteoric Waters. *Science* 133 (3465), 1702–1703. doi:10.1126/science.133.3465.1702

Dansgaard, W. (1964). Stable Isotopes in Precipitation. *Tellus* 16 (4), 437–463. doi:10.3402/tellusa.v16i4.8993

Ding, L., Xu, Q., Zhang, L. Y., Yang, D., Lai, Q. Z., Huang, F. X., et al. (2009). Regional Variation of River Water Oxygen Isotope and Empirical Elevation Prediction Models in Tibetan Plateau. *Quat. Sci.* 29, 1–12. doi:10.3969/j.issn.1001-7410.2009.01.01

Fan, B., Zhang, D., Tao, Z., and Zhao, Z. (2017). Compositions of Hydrogen and Oxygen Isotope Values of Yellow River Water and the Response to Climate Change. *China Environ. Sci.* 37 (5), 1906–1914. (in Chinese, with English abstract).

Fette, M., Kipfer, R., Schubert, C. J., Hoehn, E., and Wehrli, B. (2005). Assessing River-Groundwater Exchange in the Regulated Rhone River (Switzerland) Using Stable Isotopes and Geochemical Tracers. *Appl. Geochem.* 20 (4), 701–712. doi:10.1016/j.apgeochem.2004.11.006

Florea, L., Bird, B., Lau, J. K., Wang, L., Lei, Y., Yao, T., et al. (2017). Stable Isotopes of River Water and Groundwater along Altitudinal Gradients in the High Himalayas and the Eastern Nyainqentanghla Mountains. *J. Hydrol. Reg. Stud.* 14, 37–48. doi:10.1016/j.ejrh.2017.10.003

Galy, A., and France-Lanord, C. (1999). Weathering Processes in the Ganges–Brahmaputra basin and the Riverine Alkalinity Budget. *Chem. Geology.* 159 (1–4), 31–60. doi:10.1016/s0009-2541(99)00033-9

Gao, J., Masson-Delmotte, V., Risi, C., He, Y., and Yao, T. (2013). What Controls Precipitation $\delta^{18}O$ in the Southern Tibetan Plateau at Seasonal and Intra-seasonal Scales? A Case Study at Lhasa and Nyalam. *Tellus* 65 (1), 1–14. doi:10.3402/tellusb.v65i0.21043

Gao, J., Masson-Delmotte, V., Yao, T., Tian, L., Risi, C., and Hoffmann, G. (2011). Precipitation Water Stable Isotopes in the South Tibetan Plateau: Observations and Modeling*. *J. Clim.* 24 (13), 3161–3178. doi:10.1175/2010jcli3736.1

Garzione, C. N., Quade, J., DeCelles, P. G., and English, N. B. (2000). Predicting Paleoelevation of Tibet and the Himalaya from $\delta^{18}O$ vs. Altitude Gradients in Meteoric Water across the Nepal Himalaya. *Earth Planet. Sci. Lett.* (183), 219–229.

Gat, J. R., and Matsui, E. (1991). Atmospheric Water Balance in the Amazon basin: An Isotopic Evapotranspiration Model. *J. Geophys. Res.* 96, 13179–13188. doi:10.1029/91jd00054

Gat, J. R. (1996). Oxygen and Hydrogen Isotopes in the Hydrologic Cycle. *Annu. Rev. Earth Planet. Sci.* 24, 225–262. doi:10.1146/annurev.earth.24.1.225

GMRT Bureau of Geology and Mineral Resources of Xizang Tibet Autonomous Region (1993). "Regional Geology of Xizang (Tibet) Autonomous Region,". Number 31 in *People's Republic of China Ministry of Geology and Mineral Resources-Geological Memoirs, Series 1* (Beijing: Anonymous Geological Publishing House). (in Chinese with English abstract).

Gonfiantini, R. (1986). *Environmental Isotopes in Lake Studies*. B. Elsevier, 113–168. doi:10.1016/b978-0-444-42225-5.50008-5

Guo, X., Tian, L., Wang, L., Yu, W., and Qu, D. (2017). River Recharge Sources and the Partitioning of Catchment Evapotranspiration Fluxes as Revealed by Stable Isotope Signals in a Typical High-Elevation Arid Catchment. *J. Hydrol.* 549, 616–630. doi:10.1016/j.jhydrol.2017.04.037

Hoke, G. D., Liu-Zeng, J., Hren, M. T., Wissink, G. K., and Garzione, C. N. (2014). Stable Isotopes Reveal High Southeast Tibetan Plateau Margin since the Paleogene. *Earth Planet. Sci. Lett.* 394, 270–278. doi:10.1016/j.epsl.2014.03.007

Hoke, L., Lamb, S., Hilton, D. R., and Poreda, J. P. (2000). Southern Limit of Mantle Derived Geothermalhelium Emissions in Tibet: Implications for Lithospheric Structure. *Earth Planet. Sci. Lett.* 180 (3–4), 297–308. doi:10.1016/s0012-821x(00)00174-6

Hren, M. T., Bookhagen, B., Blisniuk, P. M., Booth, A. L., and Chamberlain, C. P. (2009). $\delta^{18}O$ and δD of Streamwaters across the Himalaya and Tibetan Plateau: Implications for Moisture Sources and Paleoelevation Reconstructions. *Earth Planet. Sci. Lett.* 288 (1-2), 20–32. doi:10.1016/j.epsl.2009.08.041

Hren, M. T., Chamberlain, C. P., Hilley, G. E., Blisniuk, P. M., and Bookhagen, B. (2007). Major Ion Chemistry of the Yarlung Tsangpo-Brahmaputra River: Chemical Weathering, Erosion, and CO2 Consumption in the Southern Tibetan Plateau and Eastern Syntaxis of the Himalaya. *Geochimica et Cosmochimica Acta* 71 (12), 2907–2935. doi:10.1016/j.gca.2007.03.021

Huang, X., Sillanpää, M., Duo, B., and Gjessing, E. T. (2008). Water Quality in the Tibetan Plateau: Metal Contents of Four Selected Rivers. *Environ. Pollut.* 156 (2), 270–277. doi:10.1016/j.envpol.2008.02.014

Huang, X., Sillanpää, M., Gjessing, E. T., Peräniemi, S., and Vogt, R. D. (2011). Water Quality in the Southern Tibetan Plateau: Chemical Evaluation of the Yarlung Tsangpo (Brahmaputra). *River Res. Applic.* 27 (1), 113–121. doi:10.1002/rra.1332

Kendall, C., and Coplen, T. B. (2001). Distribution of Oxygen-18 and Deuterium in River Waters across the United States. *Hydrol. Process.* 15, 1363–1393. doi:10.1002/hyp.217

Kong, Y., and Pang, Z. (2016). A Positive Altitude Gradient of Isotopes in the Precipitation over the Tianshan Mountains: Effects of Moisture Recycling and Sub-cloud Evaporation. *J. Hydrol.* 542, 222–230. doi:10.1016/j.jhydrol.2016.09.007

Li, L., and Garzione, C. N. (2017). Spatial Distribution and Controlling Factors of Stable Isotopes in Meteoric Waters on the Tibetan Plateau: Implications for Paleoelevation Reconstruction. *Earth Planet. Sci. Lett.* 460, 302–314. doi:10.1016/j.epsl.2016.11.046

Li, S.-L., Yue, F.-J., Liu, C.-Q., Ding, H., Zhao, Z.-Q., and Li, X. (2015). The O and H Isotope Characteristics of Water from Major Rivers in China. *Chin. J. Geochem.* 34 (1), 28–37. doi:10.1007/s11631-014-0015-5

Liu, J., Yao, Z., and Chen, C. (2007). Evolution Trend and Causation Analysis of the Runoff Evolution in the Yarlung Zangbo River basin. *J. Nat. Resour.* 22 (3), 471–477. doi:10.11849/zrzyxb.2007.03.017 (in Chinese with English abstract)

Liu, M. (2018). *Boron Geochemistry of the Geothermal Waters from Typical Hydrothermal Systems in Tibet Doctoral Dissertation, Ph. D. Thesis*. Wuhan: China University of Geoscience. (in Chinese with English abstract).

Liu, M., Guo, Q., Wu, G., Guo, W., She, W., and Yan, W. (2019). Boron Geochemistry of the Geothermal Waters from Two Typical Hydrothermal Systems in Southern Tibet (China): Daggyai and Quzhuomu. *Geothermics* 82, 190–202. doi:10.1016/j.geothermics.2019.06.009

Liu, T. (1999). Hydrological Characteristics of Yalungzangbo River. *Acta Geographica Sinica* 54 (Suppl. l), 157–164. (in Chinese with English abstract).

Liu, Z., Tian, L., Yao, T., Gong, T., Yin, C., and Yu, W. (2007). Temporal and Spatial Variations of δ18O in Precipitation of the Yarlung Zangbo River Basin. *J. Geogr. Sci.* 17 (3), 317–326. doi:10.1007/s11442-007-0317-1

Ma, Z., Li, X., Zheng, H., Li, J., Pei, B., Guo, S., et al. (2017). Origin and Classification of Geothermal Water from Guanzhong Basin, NW China: Geochemical and Isotopic Approach. *J. Earth Sci.* 28 (4), 719–728. doi:10.1007/s12583-016-0637-0

Mizutani, Y. (1972). Isotopic Composition and Underground Temperature of the Otake Geothermal Water, Kyushu, Japan. *Geochem. J.* 6 (2), 67–73. doi:10.2343/geochemj.6.67

Ogrinc, N., Kanduč, T., Stichler, W., and Vreča, P. (2008). Spatial and Seasonal Variations in δ18O and δD Values in the River Sava in Slovenia. *J. Hydrol.* 359 (3-4), 303–312. doi:10.1016/j.jhydrol.2008.07.010

Poage, M. A., and Chamberlain, C. P. (2001). Empirical Relationships between Elevation and the Stable Isotope Composition of Precipitation and Surface Waters: Considerations for Studies of Paleoelevation Change. *Am. J. Sci.* 301 (1), 1–15. doi:10.2475/ajs.301.1.1

Quade, J., Breecker, D. O., Daëron, M., and Eiler, J. (2011). The Paleoaltimetry of Tibet: an Isotopic Perspective. *Am. J. Sci.* 311 (2), 77–115. doi:10.2475/02.2011.01

Ramesh, R., and Sarin, M. M. (1992). Stable Isotope Study of the Ganga (Ganges) River System. *J. Hydrol.* 139 (1–4), 49–62. doi:10.1016/0022-1694(92)90194-z

Ren, W., Yao, T., Xie, S., and He, Y. (2017b). Controls on the Stable Isotopes in Precipitation and Surface Waters across the southeastern Tibetan Plateau. *J. Hydrol.* 545, 276–287. doi:10.1016/j.jhydrol.2016.12.034

Ren, W., Yao, T., and Xie, S. (2017a). Key Drivers Controlling the Stable Isotopes in Precipitation on the Leeward Side of the central Himalayas. *Atmos. Res.* 189, 134–140. doi:10.1016/j.atmosres.2017.01.020

Ren, W., Yao, T., and Xie, S. (2018). Stable Isotopic Composition Reveals the Spatial and Temporal Dynamics of Discharge in the Large River of Yarlungzangbo in the Tibetan Plateau. *Sci. Total Environ.* 625, 373–381. doi:10.1016/j.scitotenv.2017.12.310

Ren, W., Yao, T., and Xie, S. (2016). Water Stable Isotopes in the Yarlungzangbo Headwater Region and its Vicinity of the Southwestern Tibetan Plateau. *Tellus B: Chem. Phys. Meteorology* 68 (1), 30397. doi:10.3402/tellusb.v68.30397

Rowley, D. B., Pierrehumbert, R. T., and Currie, B. S. (2001). A New Approach to Stable Isotope-Based Paleoaltimetry: Implications for Paleoaltimetry and Paleohypsometry of the High Himalaya since the Late Miocene. *Earth Planet. Sci. Lett.* 188, 253–268. doi:10.1016/s0012-821x(01)00324-7

Rowley, D. B. (2007). Stable Isotope-Based Paleoaltimetry: Theory and Validation. *Rev. Mineralogy Geochem.* 66 (1), 23–52. doi:10.2138/rmg.2007.66.2

Singh, M., Kumar, S., Kumar, B., Singh, S., and Singh, I. B. (2013). Investigation on the Hydrodynamics of Ganga Alluvial Plain Using Environmental Isotopes: a Case Study of the Gomati River Basin, Northern India. *Hydrogeol J.* 21 (3), 687–700. doi:10.1007/s10040-013-0958-3

Spicer, R. A., Harris, N. B. W., Widdowson, M., Herman, A. B., Guo, S., Valdes, P. J., et al. (2003). Constant Elevation of Southern Tibet over the Past 15 Million Years. *Nature* 421 (6923), 622–624. doi:10.1038/nature01356

Stefánsson, A., Arnórsson, S., Sveinbjörnsdóttir, Á. E., Heinemaier, J., and Kristmannsdóttir, H. (2019). Isotope (δD, $\delta^{18}O$, ^{3}H, $\delta^{13}C$, ^{14}C) and Chemical (B, Cl) Constrains on Water Origin, Mixing, Water-Rock Interaction and Age of Low-Temperature Geothermal Water. *Appl. Geochem.* 108, 104380. doi:10.1016/j.apgeochem.2019.104380

Tan, H., Chen, X., Shi, D., Rao, W., Liu, J., Liu, J., et al. (2021). Base Flow in the Yarlungzangbo River, Tibet, Maintained by the Isotopically-Depleted

Precipitation and Groundwater Discharge. *Sci. Total Environ.* 759, 143510. doi:10.1016/j.scitotenv.2020.143510

Tan, H., Zhang, Y., Zhang, W., Kong, N., Zhang, Q., and Huang, J. (2014). Understanding the Circulation of Geothermal Waters in the Tibetan Plateau Using Oxygen and Hydrogen Stable Isotopes. *Appl. Geochem.* 51, 23–32. doi:10.1016/j.apgeochem.2014.09.006

Tapponnier, P., Xu, Z. Q., Roger, F., Meyer, B., Arnaud, N., Wittlinger, G., et al. (2001). Oblique Stepwise Rise and Growth of the Tibet Plateau. *Science* 294, 1671–1677. doi:10.1126/science.105978

Tian, L., Masson-Delmotte, V., Stievenard, M., Yao, T., and Jouzel, J. (2001b). Tibetan Plateau Summer Monsoon Northward Extent Revealed by Measurements of Water Stable Isotopes. *J. Geophys. Res.* 106 (D22), 28081–28088. doi:10.1029/2001jd900186

Tian, L., Yao, T., MacClune, K., White, J. W. C., Schilla, A., Vaughn, B., et al. (2007). Stable Isotopic Variations in West China: A Consideration of Moisture Sources. *J. Geophys. Res. Atmospheres* 112 (D10). doi:10.1029/2006jd007718

Tian, L., Yao, T., Numaguti, A., and Sun, W. (2001a). Stable Isotope Variations in Monsoon Precipitation on the Tibetan Plateau. *J. Meteorol. Soc. Jpn.* 79 (5), 959–966. doi:10.2151/jmsj.79.959

Tian, L., Yao, T., Pu, J., and Yang, Z. (1997). Characteristics of $\delta^{18}O$ in Summer Precipitation at Lhasa. *J. Glaciology Geocryology* 19 (4), 33–40. (in Chinese).

Tian, L., Yao, T., White, J. W. C., Yu, W., and Wang, N. (2005). Westerly Moisture Transport to the Middle of Himalayas Revealed from the High Deuterium Excess. *Chin. Sci Bull* 50 (10), 1026–1030. doi:10.1360/04wd0030

Timsic, S., and Patterson, W. P. (2014). Spatial Variability in Stable Isotope Values of Surface Waters of Eastern Canada and New England. *J. Hydrol.* 511, 594–604. doi:10.1016/j.jhydrol.2014.02.017

Wang, C., Zheng, M., Zhang, X., Xing, E., Zhang, J., Ren, J., et al. (2020). O, H, and Sr Isotope Evidence for Origin and Mixing Processes of the Gudui Geothermal System, Himalayas, China. *Geosci. Front.* 11 (4), 1175–1187. doi:10.1016/j.gsf.2019.09.013

Wang, H. (1991). *Isotope Hydrogeology Introduction*. (in Chinese).

Wang, J., Liu, T. Q., and Yin, G. (2000). Isotopic Distribution Characteristics of Atmospheric Precipitation in the Middle and Lower Reaches of the Yarlungzangbo River, Tibet. *Geogeochemistry* 28 (1), 63–67. (in Chinese with English abstract).

Wei, K., and Lin, R. (1994). Discuss on the Impact of Monsoon Climate on Isotope of Precipitation in China. *Geochemistry* 23 (1), 33–41. (in Chinese).

Wen, R., Tian, L., Weng, Y., Liu, Z., and Zhao, Z. (2012). The Altitude Effect of δ 18O in Precipitation and River Water in the Southern Himalayas. *Chin. Sci. Bull.* 57 (14), 1693–1698. doi:10.1007/s11434-012-4992-7

Winston, W., and Criss, R. (2003). Oxygen Isotope and Geochemical Variations in the Missouri River. *Env Geol.* 43 (5), 546–556. doi:10.1007/s00254-002-0679-8

Wu, H., Wu, J., Sakiev, K., Liu, J., Li, J., He, B., et al. (2019). Spatial and Temporal Variability of Stable Isotopes (δ 18 O and δ 2 H) in Surface Waters of Arid, Mountainous Central Asia. *Hydrological Process.* 33 (12), 1658–1669. doi:10.1002/hyp.13429

Xu, Q., Hoke, G. D., Liu-Zeng, J., Ding, L., Wang, W., and Yang, Y. (2014). Stable Isotopes of Surface Water across the Longmenshan Margin of the Eastern Tibetan Plateau. *Geochem. Geophys. Geosyst.* 15 (8), 3416–3429. doi:10.1002/2014gc005252

Xu, Y., Kang, S., Zhang, Y., and Zhang, Y. (2011). A Method for Estimating the Contribution of Evaporative Vapor from Nam Co to Local Atmospheric Vapor Based on Stable Isotopes of Water Bodies. *Chin. Sci. Bull.* 56 (14), 1511–1517. doi:10.1007/s11434-011-4467-2

Yang, D. D., Oyang, H., Zhou, C. P., and Chen, C. Y. (2011). Runoff Characteristics of the Nyang Qu River on the Qinghai-Tibet Plateau. *Resour. Sci.* 33 (7), 1272–1277. doi:10.5814/j.issn.1674-764x.2012.01.012 (in Chinese with English abstract).

Yang, X., Xu, B., Yang, W., and Qu, D. (2012a). The Indian Monsoonal Influence on Altitude Effect of δ 18O in Surface Water on Southeast Tibetan Plateau. *Sci. China Earth Sci.* 55 (3), 438–445. doi:10.1007/s11430-011-4342-7

Yang, X., Yao, T., Yang, W., Xu, B., He, Y., and Qu, D. (2012b). Isotopic Signal of Earlier Summer Monsoon Onset in the Bay of Bengal. *J. Clim.* 25 (7), 2509–2516. doi:10.1175/jcli-d-11-00180.1

Yao, T., Masson-Delmotte, V., Gao, J., Yu, W., Yang, X., Risi, C., et al. (2013). A Review of Climatic Controls on δ18O in Precipitation over the Tibetan Plateau: Observations and Simulations. *Rev. Geophys.* 51 (4), 525–548. doi:10.1002/rog.20023

Yin, G., Ni, S., and Zhang, Q. (2001). Deuterium Excess Parameter and Geohydrology Significance: Taking the Geohydrology Researches in Jiuzaigou and Yele, Sichuan for Example. *J. Chen GDU Univ. Technol.* 28 (3), 251–254. doi:10.1016/s1164-6756(01)00107-4

You, Q., Kang, S., Wu, Y., and Yan, Y. (2007). Climate Change over the Yarlung Zangbo River Basin during 1961-2005. *J. Geogr. Sci.* 17 (4), 409–420. doi:10.1007/s11442-007-0409-y

Yu, W., Yao, T., Tian, L., Ma, Y., Ichiyanagi, K., Wang, Y., et al. (2008). Relationships between δ18O in Precipitation and Air Temperature and Moisture Origin on a South-north Transect of the Tibetan Plateau. *Atmos. Res.* 87 (2), 158–169. doi:10.1016/j.atmosres.2007.08.004

Yu, W., Yao, T., Tian, L., Ma, Y., Wen, R., Devkota, L. P., et al. (2016). Short-term Variability in the Dates of the Indian Monsoon Onset and Retreat on the Southern and Northern Slopes of the central Himalayas as Determined by Precipitation Stable Isotopes. *Clim. Dyn.* 47 (1), 159–172. doi:10.1007/s00382-015-2829-1

Zhang, J.-W., Yan, Y.-N., Zhao, Z.-Q., Li, X.-D., Guo, J.-Y., Ding, H., et al. (2021). Spatial and Seasonal Variations of Dissolved Arsenic in the Yarlung Tsangpo River, Southern Tibetan Plateau. *Sci. Total Environ.* 760, 143416. doi:10.1016/j.scitotenv.2020.143416

Zhang, P.-Z., Shen, Z., Wang, M., Gan, W., Bürgmann, R., Molnar, P., et al. (2004). Continuous Deformation of the Tibetan Plateau from Global Positioning System Data. *Geol* 32, 809. doi:10.1130/g20554.1

Zhang, W., Tan, H., Zhang, Y., Wei, H., and Dong, T. (2015). Boron Geochemistry from Some Typical Tibetan Hydrothermal Systems: Origin and Isotopic Fractionation. *Appl. Geochem.* 63, 436–445. doi:10.1016/j.apgeochem.2015.10.006

Zhu, G. F., Li, Z. Z., Su, Y. H., Ma, J. Z., and Zhang, Y. Y. (2007). Hydrogeochemical and Isotope Evidence of Groundwater Evolution and Recharge in Minqin Basin, Northwest China. *J. Hydrol.* 333 (2-4), 239–251. doi:10.1016/j.jhydrol.2006.08.013

Conflict of Interest: The authors declare that the research was conducted in the absence of any commercial or financial relationships that could be construed as a potential conflict of interest.

Publisher's Note: All claims expressed in this article are solely those of the authors and do not necessarily represent those of their affiliated organizations, or those of the publisher, the editors, and the reviewers. Any product that may be evaluated in this article, or claim that may be made by its manufacturer, is not guaranteed or endorsed by the publisher.

frontiers in Earth Science

ORIGINAL RESEARCH
published: 18 November 2021
doi: 10.3389/feart.2021.767857

Quantifying the Seawater Sulfate Concentration in the Cambrian Ocean

Guangyou Zhu[1], Tingting Li[1], Tianzheng Huang[2], Kun Zhao[1], Wenbo Tang[3], Ruimin Wang[2], Xianguo Lang[4] and Bing Shen[2]**

[1]Research Institute of Petroleum Exploration and Development, China National Petroleum Corporation, Beijing, China, [2]Key Laboratory of Orogenic Belts and Crustal Evolution, MOE and School of Earth and Space Sciences, Peking University, Beijing, China, [3]School of Mathematical and Statistical Sciences, Arizona State University, Tempe, AZ, United States, [4]State Key Laboratory of Oil and Gas Reservoir Geology and Exploitation, Institute of Sedimentary Geology, Chengdu University of Technology, Chengdu, China*

Although the earliest animals might have evolved in certain "sweet spots" in the last 10 million years of Ediacaran (550–541 Ma), the Cambrian explosion requires sufficiently high levels of oxygen (O_2) in the atmosphere and diverse habitable niches in the substantively oxygenated seafloor. However, previous studies indicate that the marine redox landscape was temporally oscillatory and spatially heterogeneous, suggesting the decoupling of atmospheric oxygenation and oceanic oxidation. The seawater sulfate concentration is controlled by both the atmospheric O_2 level and the marine redox condition, with sulfide oxidation in continents as the major source, and sulfate reduction and pyrite burial as the major sink of seawater sulfate. It is thus important to quantify the sulfate concentration on the eve of the Cambrian explosion. In this study, we measured the pyrite contents and pyrite sulfur isotopes of black shale samples from the Yurtus Formation (Cambrian Series 2) in the Tarim Block, northwestern China. A numerical model is developed to calculate the seawater sulfate concentration using the pyrite content and pyrite sulfur isotope data. We first calibrate some key parameters based on observations from modern marine sediments. Then, the Monte Carlo simulation is applied to reduce the uncertainty raised by loosely confined parameters. Based on the geochemical data from both Tarim and Yangtze blocks, the modeling results indicate the seawater sulfate concentration of 8.9–14 mM, suggesting the seawater sulfate concentration was already 30–50% of the present level (28 mM). High seawater sulfate concentration might be attributed to the enhanced terrestrial sulfate input and widespread ocean oxygenation on the eve of the Cambrian explosion.

Keywords: sulfur isotope, pyrite, iron speciation, Tarim block, Yurtus formation

OPEN ACCESS

Edited by:
Kangjun Huang,
Northwest University, China

Reviewed by:
Xinqiang Wang,
China University of Geosciences, China
Xin-Yuan Zheng,
University of Minnesota Twin Cities, United States

****Correspondence:***
Tianzheng Huang
tzhuang@pku.edu.cn
Bing Shen
bingshen@pku.edu.cn

Specialty section:
This article was submitted to Geochemistry, a section of the journal Frontiers in Earth Science

Received: *31 August 2021*
Accepted: *15 October 2021*
Published: *18 November 2021*

Citation:
Zhu G, Li T, Huang T, Zhao K, Tang W, Wang R, Lang X and Shen B (2021) Quantifying the Seawater Sulfate Concentration in the Cambrian Ocean. Front. Earth Sci. 9:767857. doi: 10.3389/feart.2021.767857

INTRODUCTION

The seawater sulfate concentration is a critical indicator of the redox condition in the atmosphereocean system. On the one hand, the seawater sulfate concentration is controlled by both marine redox condition and atmospheric O_2 level, because oxidative weathering of sulfide in continents is one of the major sources, and sulfate reduction and pyrite burial represent one of the major sinks of seawater sulfate (Canfield, 2004; Canfield and Farquhar, 2009). On the other hand, the seawater sulfate concentration should be globally homogeneous, reflecting the overall global redox

condition of the atmosphere-ocean system. Thus, reconstruction of seawater sulfate concentration would provide a direct constraint on the global ocean redox condition and the atmospheric O_2 level.

The second rise of atmospheric O_2 level occurred in the late Neoproterozoic, coined the Neoproterozoic oxygenation event (NOE) (Shields-Zhou and Och, 2011). NOE is supported by several lines of geochemical evidence. The enrichment of redox-sensitive elements (e.g., V, U, Mo) in the early Ediacaran black shales implies the oxidation of the deep ocean immediately after the Marinoan Snowball Earth glaciation (Sahoo et al., 2012; Sahoo et al., 2016). The global occurrence of Shuram Excursion, the largest negative carbon isotope excursion in Earth's history, has been interpreted as massive oxidation of dissolved organic carbon (DOC) in the Ediacaran deep ocean (Fike et al., 2006; Kaufman et al., 2007; McFadden et al., 2008; Grotzinger et al., 2011). Furthermore, the decrease in the reactive Fe content in deep-sea deposits also indicates oxidation of the deep ocean after the Ediacaran Gaskiers glaciation (580 Ma) (Canfield et al., 2007). NOE was associated with the dramatic change in the biosphere. For example, biomarker data indicate the increase in eukaryotic primary productivity in the nonglacial interlude between the two Cryogenian (720–635 Ma) Snowball Earth glaciations, while paleontological data indicate the diversification of eukaryotes in the earliest Ediacaran and the subsequent evolution of multicellular organisms, e.g., macroscopic algae and Ediacara biota (Glaessner, 1984; Zhang, 1989; Narbonne, 2005; Yin et al., 2007; Yuan et al., 2011; Liu et al., 2014; Brocks et al., 2017).

Although the biological evolution and the atmosphereocean oxygenation were broadly coincident in the geochemical and paleontological records, more and more studies indicate inconsistent or even contradictory results drawn from different proxies. It is proposed that the redox landscape in the Ediacaran and early Cambrian ocean might be temporally dynamic and spatially heterogeneous (Li et al., 2010; Sahoo et al., 2016; Li et al., 2018), and the ocean was predominantly anoxic and was frequently punctuated by episodic or sporadic oxidation or euxinia (Sahoo et al., 2016; Zhang et al., 2018; Ding et al., 2019).

The seawater sulfate concentration would provide the key evidence to resolve the inconsistency between different proxies. However, the seawater sulfate concentration cannot be directly measured from sedimentary rocks. Based on the stratigraphic variation of sulfur isotopes of carbonate-associated sulfate (CAS, $\delta^{34}S_{CAS}$) (Kah et al., 2004), low seawater sulfate concentration of ~2 mM in the early Cambrian ocean was proposed (Loyd et al., 2012; Thompson and Kah, 2012). In contrast, the marine sulfur mass balance model indicates a higher seawater sulfate concentration of ~10 mM. In the latter scenario, it is suggested that the high seawater sulfate concentration might be attributed to the invention of bioturbation during the Cambrian explosion (Canfield and Farquhar, 2009). Such contradictory results prevent further discussion of marine-atmosphere redox coupling on the eve of the Cambrian explosion.

In this study, we develop a new method to quantify the seawater sulfate concentration by using Fe speciation and pyrite sulfur isotope data. We analyzed the black shale of the lower Cambrian Yurtus Formation in the western Tarim Block, northwestern China. Combining with geochemical data from the Yangtze Block, the seawater sulfate concentration in the early Cambrian ocean was quantified.

Geological Background

The Cambrian strata in the Arksu region, western Tarim Block, consist of, in ascending order, the Yurtus (YF), Xiaoerblak (XF), Wusongger (WF), Shayilike (SF), Awatage (AF), and Qiulitage (QF) formations. The Yurtus Formation unconformably overlies the Ediacaran Qigeblak Formation and conformably underlies the Xiaoerblak Formation (**Figure 1**) (He et al., 2010, 2018; Zhu et al., 2018). The basal Yurtus Formation is restricted to the Tommotian (equivalent to Stage 2 of Terreneuvian Series in the Geological Time Scale) by the appearances of *Asteridium-Heliosphaeridium-Comasphaeridium* acritarch assemblage (Yao et al., 2005; Dong et al., 2009). Univalve mollusk fossils (*Shabaktiella multiformis*, *Parcaconus xinjiangensis*, *Eoyochelcionella aksuensis*, etc.) discovered from the upper Yurtus Formation might be correlated with the small shelly fossils from the Qiongzhusian strata in South China or the Atdabanian Stage in the Eastern European Platform (equivalent to Stage 3 of Cambrian Series 2 in the Geological Time Scale) (Qian, 1999; Qian et al., 2000; Gradstein et al., 2012). Furthermore, the absence of trilobite suggests that the Yurtus Formation might belong to Cambrian Stage 2 and probably predate Cambrian Stage 3, i.e., between 529 and 521 Ma (Dong et al., 2009). Samples were collected from the drill core (X1). The Yurtus Formation in the X1 core is composed of, in stratigraphic order, bedded chert (~3.7 m), black shale (~23 m), intercalated mudstone and dolostone (~13 m), and dolostone (~13 m) lithological units. In this study, only the black shale samples from the lower Yurtus Formation were analyzed.

METHODS OF GEOCHEMICAL ANALYSES

Pyrite Sulfur Isotope Analysis

Pyrite sulfur isotope ratios were determined at the State Key Laboratory of Biogeology and Environmental Geology, China University of Geosciences (Wuhan). The purified Ag_2S precipitate (after chromium reduction) was mixed with an excessive amount of V_2O_5 and was wrapped in a tin cup. S isotope ratios were determined by a Thermo Instruments Delta V Plus isotope ratio mass spectrometer coupled with a Costech elemental analyzer. S isotope values are reported by delta notation as per mil (‰) deviation relative to the V-CDT (Vienna-Cañon Diablo Tribolite) international standard. Samples were calibrated by international standards: IAEA S1 (−0.3‰), IAEA S2 (22.65‰), and IAEA S3 (−32.5‰). The analytical precision is ~0.1‰ (1σ), which was determined by repeated analyses of IAEA international standards.

RESULTS

The Fe speciation and pyrite sulfur isotope data are tabulated in **Table 1**, and the Fe speciation data have been reported in Zhu

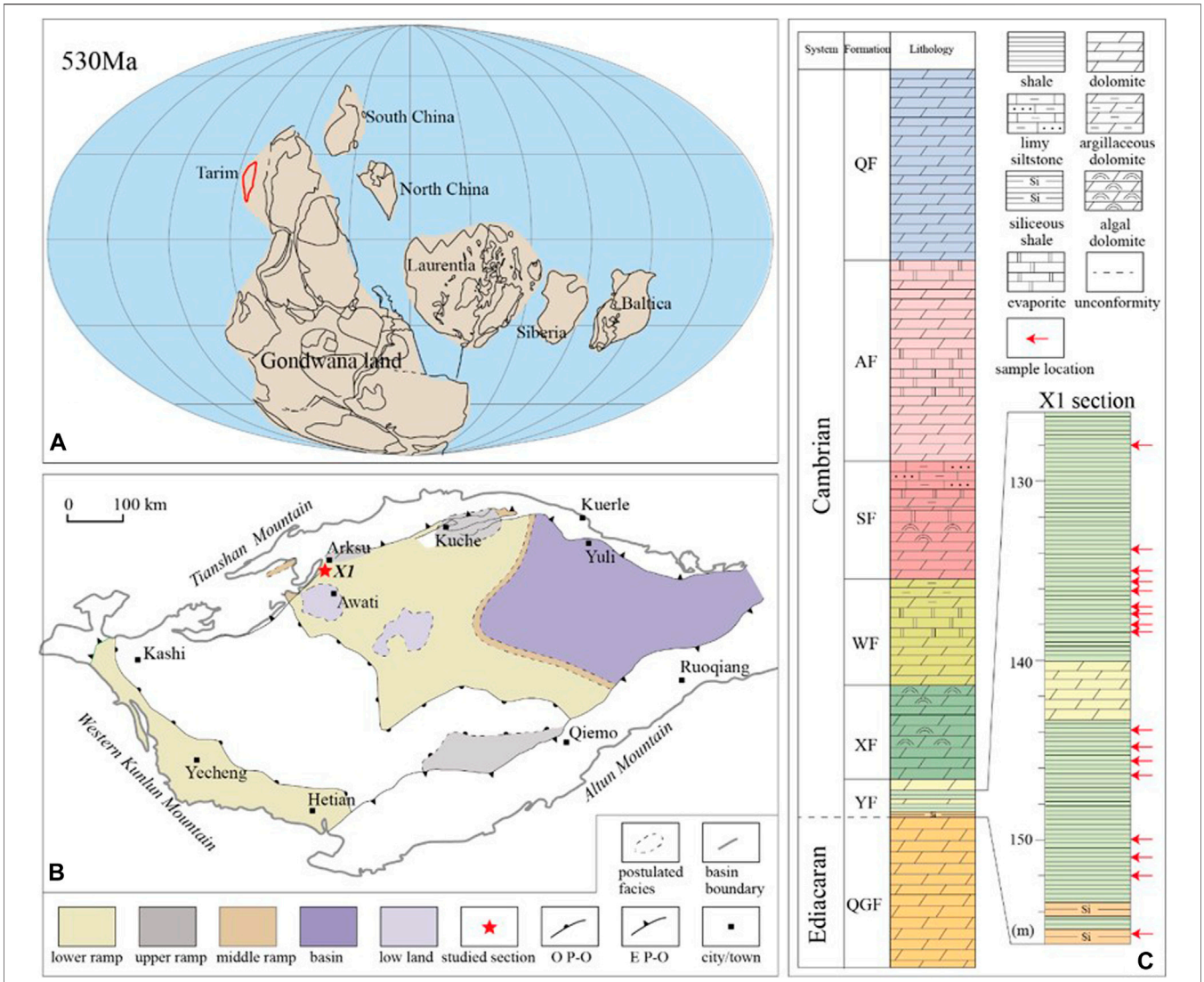

FIGURE 1 | (A) Paleogeographic map of the Tarim Block during the early Cambrian (530 Ma) [modified from Li et al. (2008)]. **(B)** Sedimentary facies map of the early Cambrian Yurtus Formation of the Tarim Block [modified from Du and Pan (2016)] and the location of drill core XK1. O P-O= Overlapping pinch-out line of the Yurtus Formation, E P-O= Erosional pinch-out line of the Cambrian strata. **(C)** Stratigraphic column of the Cambrian strata in the Tarim Block [modified from Zhu et al. (2018)] and the Yurtus Formation of XK1 drill core. Red arrows indicate the stratigraphic location of samples. QGF = Qigeblak, YF = Yurtus, XF = Xiaoerblak, WF = Wusongger, SF = Shayilike, AF = Awatage, QF = Qiulitage. The depth values are relative to the top of the drill core.

et al. (2021). The stratigraphic profiles of geochemical data are illustrated in **Figure 2**. Pyrite sulfur isotope ($\delta^{34}S_{py}$) ranges from -8.2‰ to +16.1‰ (mean = +4.2‰, n = 17), with most being higher than 5.0‰ in the lower black shale interval. The $\delta^{34}S_{CAS}$ values vary between +26.2‰ and +36.1‰ (mean = +30.4‰, n = 12). Pyrite contents range from 0.05 to 8.62% (mean = 2.26%, n = 17). These samples have wide ranges of variation of Fe_T contents, ranging from 0.49 to 4.40% (mean = 1.51%, n = 17). Fe_{HR} contents range between 0.25 and 4.48% (mean = 1.27, n = 17), with the maximum value at the uppermost black shale. Fe_{py} contents range between 0.02 and 4.02% (mean = 1.06, n = 17). The Fe_{HR}/Fe_T ratios vary between 0.20 and 1.00 (mean = 0.81, n = 17). Fe_{py}/Fe_{HR} ratios vary between 0.07 and 0.90 (mean = 0.75, n = 17).

DISCUSSION

A numerical model was developed to simulate the syndepositional pyrite formation in sediment porewater (Lang et al., 2020). The syndepositional pyrite formation involves dissimilatory sulfate reduction (DSR) in sediment porewater with sulfate supply from seawater diffusion. H_2S, the product of DSR, either converts to pyrite by reacting with reactive Fe in sediment or is oxidized back to sulfate. The modeling results indicate that both $\delta^{34}S_{py}$ and pyrite contents in sediments or sedimentary rocks are sensitive to some environmental factors, including the seawater sulfate concentration, the isotopic composition of seawater sulfate ($\delta^{34}S_{SW}$), reaction rate constant of DSR (R_{DSR}), biological S isotope fractionation in

TABLE 1 | Iron speciation data and pyrite sulfur isotopes of the early Cambrian Yurtus Formation in the Tarim Block.

Sample no.	Depth	TOC	FeT	Fepy	Fecarb	Feox	Femag	FeHR	FeHR/FeT	Fepy/FeHR	TS	CAS	Spy	δ34SCAS	δ34Spy	Δ34S	δ13Corg
–	(m)	(wt. %)	(wt%)						–	–	(wt %)	(wt. ppm)	(wt %)	(‰ VCDT)			(‰)
1	128.0	6.40	4.40	4.02	0.33	0.10	0.03	4.48	1.02	0.90	3.83	3,640.2	8.62	27.9	0.80	27.1	−28.44
2	133.8	1.59	1.51	1.24	0.08	0.06	0.01	1.39	0.92	0.90	1.85	10,179.5	2.66	33.9	−2.00	35.9	−30.45
3	135.0	2.23	2.14	0.22	0.13	0.07	0.01	0.43	0.20	0.51	2.47	8,330.8	0.48	30.3	−1.60	31.8	−34.47
4	135.6	4.78	1.04	0.67	0.16	0.04	0.01	0.87	0.84	0.77	0.81	1,355.6	1.43	26.2	−7.70	33.9	n.a[2].
5	136.1	4.13	1.08	0.68	0.13	0.03	0.01	0.85	0.79	0.80	0.88	1799.4	1.45	29.7	0.90	28.8	−32.48
6	137.0	1.44	1.98	1.33	0.16	0.06	0.01	1.55	0.79	0.85	1.88	1,090.5	2.84	26.7	−8.20	34.9	−32.22
7	137.4	1.50	2.53	1.44	0.13	0.07	0.02	1.65	0.65	0.87	1.89	4,866.3	3.09	29.8	2.90	27	−33.35
8	138.0	2.60	2.01	1.38	0.14	0.07	0.01	1.60	0.80	0.86	2.31	11,480.2	2.95	31.7	−0.10	31.8	−34.86
9	138.4	5.04	1.24	1.04	0.13	0.04	0.01	1.22	0.98	0.86	1.27	6,332.4	2.23	29.9	4.40	25.5	n.a[2].
10	143.9	4.73	0.49	0.20	0.02	0.19	0.01	0.41	0.83	0.48	0.27	1,274.5	0.42	32	12.70	19.3	−30.47
11	144.8	3.21	0.49	0.19	0.02	0.04	0.00	0.25	0.52	0.75	0.26	720.9	0.41	36.1	14.90	21.2	−29.26
12	145.6	12.24	1.39	1.19	0.25	0.05	0.01	1.50	1.08	0.79	2.87	n.a[1].	2.54	n.a.	12.40	n.c.	−34.31
13	146.4	11.57	1.27	1.23	0.23	0.06	0.01	1.53	1.20	0.80	2.74	n.a[1].	2.63	n.a.	16.10	n.c.	−36.47
14	150.0	10.93	1.17	0.96	0.12	0.00	0.00	1.08	0.92	0.89	2.51	n.a[1].	2.07	n.a.	15.50	n.c.	n.a[2].
15	151.0	6.91	1.89	1.70	0.14	0.08	0.02	1.94	1.03	0.88	2.5	n.a[1].	3.65	n.a.	5.10	n.c.	n.a[2].
16	152.0	3.92	0.52	0.45	0.03	0.05	0.01	0.53	1.03	0.83	1.66	n.a[1].	0.95	n.a.	7.50	n.c.	−33.91
17	155.5	3.83	0.59	0.02	0.03	0.24	0.01	0.30	0.50	0.07	0.04	700	0.05	30	−2.90	32.9	−34.03

n.a[1].:not applicable; n.a[2].:not available; n.c.:not calculated

DSR (Δ_{DSR}), organic matter contents in sediments (Org0), reactive Fe contents in sediments (Fe0), reaction rate constant of pyrite formation (R_{py}), and seafloor redox conditions. The latter controls the fraction of H_2S being oxidized by sulfur species with higher valence states (Lang et al., 2020). It should be noted that, for the simplicity, H_2S oxidation exclusively generates sulfate that returns to the seawater sulfate inventory, while intermediate sulfur species, such as elemental S or thiosulfate (Canfield and Thamdrup, 1994; Habicht et al., 1998), are not considered.

The purpose of Lang et al. (2020) is to display how $\delta^{34}S_{py}$ and pyrite contents are affected by the process of syndepositional pyrite formation in sediment porewater. The parameters used in the model do not represent the reactions that occurred in the natural environment. Thus, the original model only provides a theoretical framework but cannot be applied directly to quantify the marine sulfur cycle in deep time. In this study, we refine Lang's model to develop an applicable method to quantify the seawater sulfate concentration by using $\delta^{34}S_{py}$ and Fe speciation data. The differential equations that describe porewater sulfate, organic matter, reactive Fe, and H_2S profiles have been described in detail in Lang et al. (2020) and thus will not be illustrated here (for the detailed mathematics, please see **Supplementary Material**).

In this study, we made the following modifications. 1) We calibrated the key parameters, including R_{DSR} and Δ_{DSR}, based on the porewater geochemical profiles of modern marine sediments. 2) We applied the Monte Carlo simulation to eliminate uncertainties raised by other loosely constrained parameters, including sedimentation rate, initial organic matter contents in sediments, R_{py}, and redox conditions at the seafloor. The inputs from the sample measurements include $\delta^{34}S_{py}$, Fe speciation data, and $\delta^{34}S_{SW}$ (from CAS data).

Parameter Calibration

With the inputs of sedimentation rate, concentration, and isotopic composition of seawater sulfate, the initial organic carbon and reactive Fe contents in sediments, and the redox condition in seawater/seafloor, both $\delta^{34}S_{py}$ and pyrite contents in sediments/sedimentary rocks can be calculated (Lang et al., 2020). There are two key parameters that would significantly affect the modeling outputs: the reaction rate constant of DSR (R_{DSR}) and isotope fractionation in DSR (Δ_{DSR}). To apply this model to quantify the deep time seawater sulfate concentration, we need to calibrate these two parameters by porewater geochemical profiles of modern sediments in Santa Barbara Basin (Soutar and Crill, 1977; Raven et al., 2016). The porewater profile of sulfate concentration is controlled by the seawater sulfate concentration (Org0) and R_{DSR}. The former two values are already known for modern sediments. Thus, R_{DSR} can be determined by fitting the porewater sulfate concentration profile. The modeling results are illustrated in **Figure 3**, showing that D_{DSR} = 0.0033 $((mM/L)^{*}ka)^{-1}$ can simulate the porewater sulfate concentration profile.

In addition, the porewater profile of sulfur isotope composition of porewater sulfate ($\delta^{34}S_{pw}$) is controlled by Δ_{DSR}, R_{DSR}, (Org0), and seawater sulfate concentration. It is proposed that Δ_{DSR} is 46‰ if sulfate concentration is greater

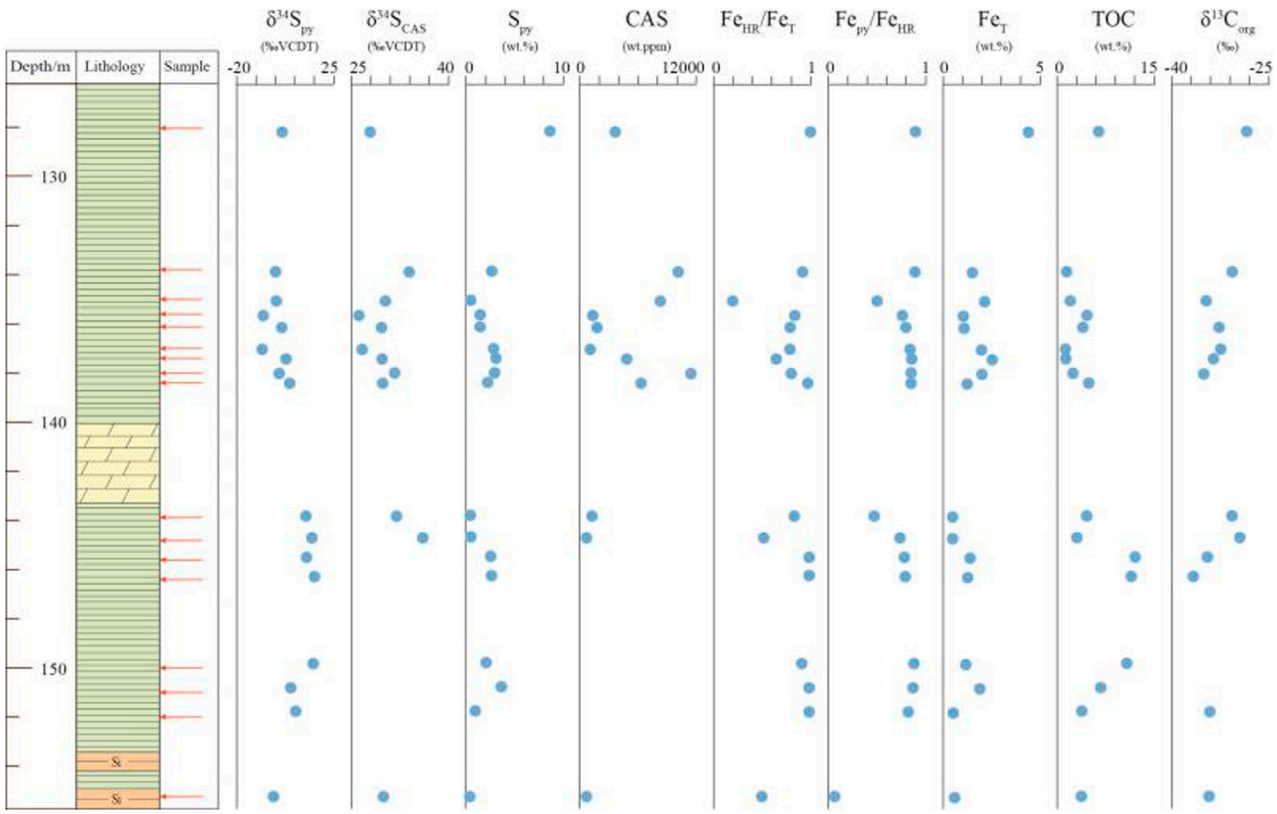

FIGURE 2 | Geochemical profiles of the early Cambrian Yurtus Formation in the Tarim Block, northwestern China. Fe speciation data have been reported in Zhu et al. (2021).

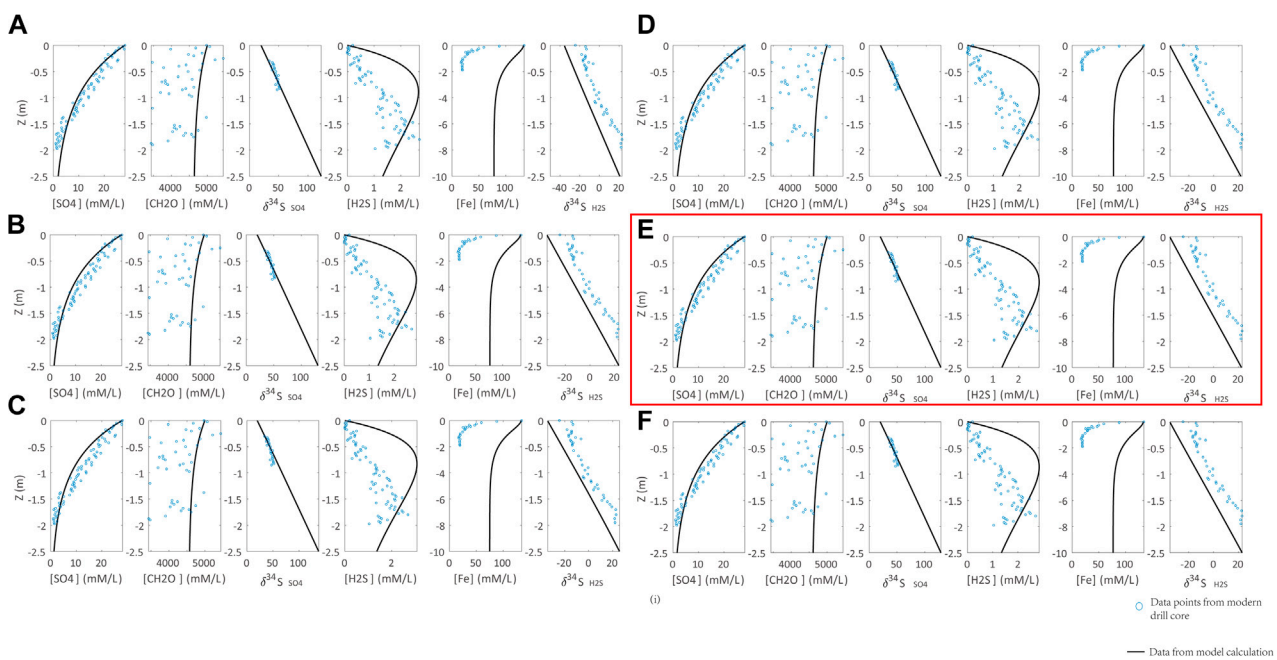

FIGURE 3 | Calibration of the DSR reaction rate constant (R_{DSR}) with observations from modern marine sediments (Soutar and Crill, 1977; Raven et al., 2016). Parameters of calculations are R_{py} = 0.3 [(mM/L)*ka]$^{-1}$, Δ_{DSR} = 70‰. R_{DSR} is set to **(A)** 0.003, **(B)** 0.0035, **(C)** 0.004, **(D)** 0.0032, **(E)** 0.0033, **(F)** 0.0034 [(mM/L)*ka]$^{-1}$. Blue points are the modern marine sediment samples. The black lines represent the modeling results. R_{DSR} = 0.0033 [(mM/L)*ka]$^{-1}$ in **(H)** can simulate the sulfate profile of modern marine sediments (highlighted by red box).

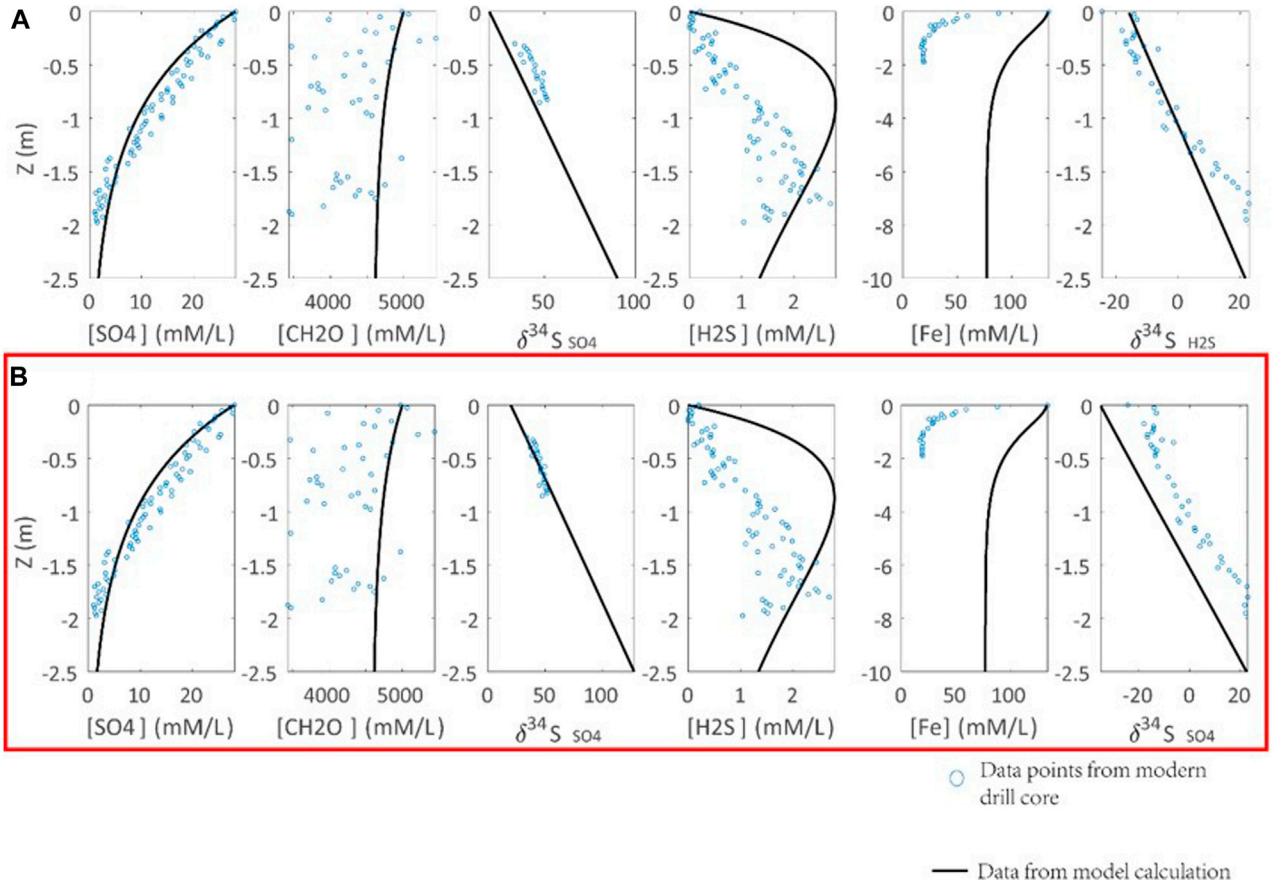

FIGURE 4 | Calibration of the S isotope fractionation in DSR (Δ_{DSR}) with observations from modern marine sediments (Soutar and Crill, 1977; Raven et al., 2016). Parameters of calculations are R_{py} = 0.3 [(mM/L)*ka]$^{-1}$, R_{DSR} = 0.0033 [(mM/L)*ka]$^{-1}$. Δ_{DSR} is set to **(A)** 46‰, **(B)** 70‰. Blue points are the modern sediment samples. The black lines are the modeling results. Δ_{DSR} = 70‰ in **(B)** can simulate the sulfate profiles in modern marine sediments (highlighted by the red box).

than 0.2 mM (Habicht and Canfield, 1997; Habicht et al., 2002). Recent studies indicate that the isotopic difference between seawater sulfate and sediment pyrite can be up to 70‰ in the past 500 ky (Pasquier et al., 2017). Thus, we allow Δ_{DSR} varying between 46 and 70‰ (**Figure 4**). The modeling results indicate that Δ_{DSR} of 70‰ can best simulate the porewater $\delta^{34}S_{pw}$ profile of modern sediments. In fact, Δ_{DSR} of 70% is consistent with the cultural DSR experiments, which indicate a similar magnitude (up to 66‰) of Δ_{DSR}, if there is no sulfur disproportionation (Sim et al., 2011).

Another key issue is the correlation between seawater/seafloor redox condition and pyrite formation reaction constant (R_{py}). R_{py} is a constant, but it is a variant in the model that is related to the seawater redox condition. Oxidation of H_2S is a complex process, involving the generation of different sulfur species of various valence states. Since we have ignored the formation of sulfur species with intermediate valence states and assumed sulfate as the only product of H_2S oxidation (Lang et al., 2020), recycling of H_2S-derived sulfate in DSR is excluded. In addition, H_2S oxidation could be further complicated by its possible connections with Fe/Mn oxidation, nitrate oxidation, and O_2 oxidation (Li et al., 2010). In order to simplify the simulation, we replace the seawater/seafloor redox condition with R_{py}. It is proposed that a larger R_{py} implies less H_2S oxidation, i.e., more reduced conditions. Furthermore, the oxidation of H_2S is simulated by the H_2S upward diffusion to seawater instead of the downward diffusion of oxidants into sediments. For these reasons, the profiles of H_2S concentration and isotope profiles can't be well simulated in our model (**Figure 5**). In the simulation, we have R_{py} = 0.3 [(mM/L)*ka]$^{-1}$ as a cutoff value for euxinic bottom water, which is closest to the actual profiles with the seafloor oxygen fugacity (f_{O2}) < 10 uM (**Figure 5**). It should be noted that the linkage between R_{py} and seafloor f_{O2} is not fixed due to the lack of modern observation.

The Monte Carlo Simulation

Because the number of parameters is much larger than the number of equations, there are multiple solutions in quantifying the seawater sulfate concentration with pyrite sulfur isotope and pyrite contents. To reduce the uncertainties raised by loosely constrained parameters, here, we apply the Monte Carlo simulation. In this method, each parameter is allowed a range of variation (**Table 2**). All possible solutions are calculated based on each assemblage

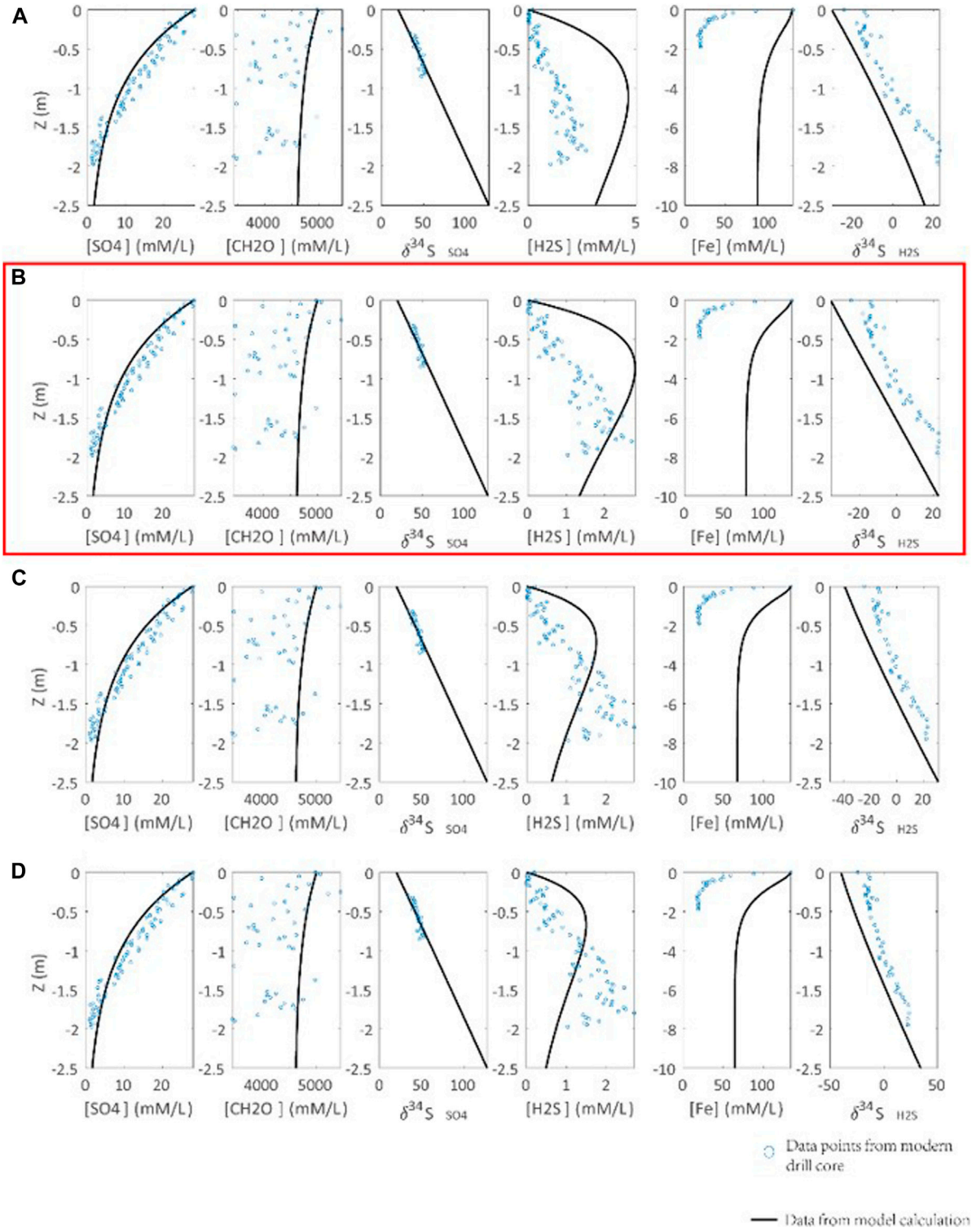

FIGURE 5 | Calibration of the seawater redox condition and pyrite formation reaction constant (R_{py}) with an observation from modern marine sediments (Soutar and Crill, 1977; Raven et al., 2016). Parameters of calculations are Δ_{DSR} = 70‰, R_{DSR} = 0.0033 [(mM/L)*ka]$^{-1}$. R_{py} is set to **(A)** 0.1, **(B)** 0.3, **(C)** 0.5, **(D)** 0.7 [(mM/L)*ka]$^{-1}$. Blue points are data points of observation from the modern drill core. Concentration and S isotope composition profile of H_2S cannot be well simulated by our model, due to simplification of oxidation mechanism of H_2S. We choose R_{py} = 0.3 [(mM/L)*ka]$^{-1}$ in **(B)** to represent seawater redox condition of O_2 < 10 uM in modern drill core (highlighted by red box).

TABLE 2 | List of parameters used in the model.

Variates	Explanation	Unit	Range
($SO4^{2-}$)	Seawater sulfate concentration	mM	28*10(n/10), *n* = −15:5
Rpy	Pyrite formation react constant, indicating redox condition of seawater	[(mM/L)*ka]-1	0.9*10(n/10), n = −10:10
(CH2O)	Initial organic carbon concentration in sediments, converted to concentration in pore water	mM	4,000*10(n/10), n = −10:10
(Fe)	Initial reactive Fe concentration in sediments, converted to concentration in pore water, data point that nearest to FeHR of sample is chosen	mM	50*n, n = 1:22
S	Sediment rate of sediments	m/ka	0.05,0.1,0.15

of parameters. If there are n parameters, each of which has m_i possible values (i ranges from 1 to n). There are $\prod_i^n m_i$ assemblages or outputs.

To save the computation resource, we take the following assumptions. 1) Sedimentation rate of similar lithology in the same section is limited to a narrow range (0.05–0.15 m/ky for our samples). This assumption is generally consistent with the estimation of sedimentation rate based on the available biostratigraphic data. In detail, the Yurtus Formation with a total thickness of ~60 m was deposited within 21 million years, including black shale of ~30 m, dolomite of 3.3 m, and carbonate dominated interval of ~27 m (Zhu et al., 2021). Considering the faster precipitation of carbonate rocks, it is estimated that the black shale was deposited between 10.5 and 21 million years. Assuming the compaction rate of 0.8, the sedimentation rate of muddy sediment (black shale) in the Yurtus Formation is between 0.075 and 0.15 m/ky. 2) Pyrite is the only major sink for reactive Fe and precipitates in sediment porewater. The second assumption allows the replacement of pyrite content by Fe_{PY}/Fe_{HR} ratio. In addition, this also implies (Fe0) equals to Fe_{HR}. For each sample, if Fe_{PY}/Fe_{HR} and $\delta^{34}S_{py}$ fall between the two nearby input points, the input points are included in the solution.

In addition, to limit the multiplicity of solution from multiple samples, we have the following assumptions. 1) The seawater sulfate concentration is invariant for samples from the same section (non-sulfidic seawater). This is likely the case given the residence time of seawater sulfate is longer than the duration of sample collections (the *Geological Background* section). 2) The seawater/seafloor redox condition was the same for all samples of the same lithology. For each set of seawater sulfate concentration and seawater/seafloor redox condition values, we calculate the frequency that the solution set of samples contains the seawater sulfate concentration range and the seawater redox condition range (**Table 3**). Because sulfate concentration is homogeneous in non-sulfidic seawater, the seawater sulfate concentration range with the frequency of 1 (indicating possible for all samples) is the plausible range of seawater sulfate concentration.

Technically, we justified the two parameters, R_{DSR} and Δ_{DSR}, based on the simulations of porewater geochemical profiles of modern marine sediments. Furthermore, to eliminate uncertainties raised by other loosely constrained or unconstrained parameters, such as sedimentation rate and redox condition, we run the Monte Carlo simulation to calculate all possible outcomes. With certain constraints from geological observations and by assuming homogeneous seawater sulfate concentration, the seawater sulfate concentration of the early Cambrian ocean can be quantified by $\delta^{34}S_{py}$ and Fe speciation data. Below, we will calculate the early Cambrian seawater sulfate concentration by this methodology.

Quantifying the Early Cambrian Seawater Sulfate Concentration

The sulfate concentration should be homogeneous in non-sulfidic seawater because the ocean mixing time is four orders of magnitude shorter than the residence time of seawater sulfate (1000s of years vs. 10s million years). Even the seawater sulfate concentration was an order of magnitude lower (Loyd et al., 2012), a homogeneous seawater sulfate concentration in the non-sulfidic seawater is still valid in a million-year time scale. In contrast, because of active DSR in sulfidic seawater, the sulfate concentration in sulfidic seawater could be different from non-sulfidic seawater (Lyons, 1997). Thus, this model can only be applied to the non-sulfidic ocean.

It is noticed that some Yurtus samples have Fe_{PY}/Fe_{HR} ratios >0.8, suggesting the deposition under sulfidic conditions (Poulton and Raiswell, 2002; Raiswell et al., 2018). However, deposition under sulfidic conditions is inconsistent with abundant fossils from the Yurtus Formation, including typical early Cambrian *Asteridium-Heliosphaeridium-Comasphaeridium* acritarch assemblage, and tubular fossil *Megathrix*, as well as small shelly fossils including *Shabaktiella multiformis*, *Parcaconus xinjiangensis*, *Eoyochelcionella aksuensis* (Qian, 1999; Qian et al., 2001; Yao et al., 2005; Dong et al., 2009), the latter of which implies the seafloor might be habitable for animals. In fact, recent studies indicate that the terrestrial input of reactive Fe is strongly affected by the intensity of continental weathering (Wei et al., 2021), implying that the Fe_{HR}/Fe_T ratio is not only affected by the redox condition of seawater. Similarly, pyrite precipitation within sediment porewater is affected by many factors, and a high fraction (high Fe_{PY}/Fe_{HR} ratio) of syndepositional pyrite could be generated in non-sulfidic conditions (Lang et al., 2020). Deposition in a non-sulfidic water column is also consistent with abundant diagenetic euhedral pyrites from the Yurtus Formation. Therefore, we argue that the above simulations can be applied to the Yurtus samples.

TABLE 3 | Frequency map on seawater sulfate concentration and redox condition. Frequency = 1 (highlight by overstriking word) indicates possible seawater sulfate concentration 8.9–14.0 mM (highlight by overstriking word) for all samples.

			Rpy [(mM/L)*ky]$^{-1}$	—	0.009	0.014	0.023	0.036	0.057	0.090	0.143	0.226	0.358	0.568	0.900	1.426	2.261	3.583	5.679	9.000	14.264	22.607	35.830	56.786
—			—	—	to	to	to	to	to	to	to	to	to	to	to	to	to	to	to	to	to	to	to	to
				0.009	0.014	0.023	0.036	0.057	0.090	0.143	0.226	0.358	0.568	0.900	1.426	2.261	3.583	5.679	9.000	14.264	22.607	35.830	56.786	90.000
($SO4^{2-}$) (mM/L)			Frequency	—	—	—	—	—	—	—	—	—	—	—	—	—	—	—	—	—	—	—	—	—
—	—	0.9	—	0.000	0.000	0.000	0.000	0.000	0.000	0.000	0.000	0.038	0.038	0.038	0.038	0.038	0.038	0.038	0.038	0.000	0.000	0.038	0.038	0.000
0.9	to	1.1		0.000	0.000	0.000	0.000	0.000	0.000	0.038	0.038	0.038	0.038	0.038	0.038	0.038	0.038	0.038	0.000	0.000	0.077	0.077	0.038	0.000
1.1	to	1.4		0.000	0.000	0.000	0.000	0.000	0.038	0.038	0.038	0.038	0.038	0.077	0.077	0.038	0.115	0.038	0.077	0.154	0.192	0.154	0.077	0.077
1.4	to	1.8		0.000	0.000	0.000	0.038	0.038	0.038	0.038	0.038	0.038	0.077	0.077	0.077	0.115	0.154	0.231	0.346	0.308	0.231	0.154	0.115	0.038
1.8	to	2.2		0.038	0.038	0.038	0.038	0.038	0.038	0.038	0.038	0.077	0.077	0.154	0.154	0.192	0.385	0.500	0.385	0.385	0.269	0.192	0.077	0.038
2.2	to	2.8		0.038	0.038	0.038	0.038	0.038	0.038	0.038	0.077	0.077	0.192	0.192	0.269	0.462	0.577	0.577	0.462	0.385	0.269	0.192	0.115	0.115
2.8	to	3.5		0.038	0.038	0.038	0.038	0.038	0.038	0.077	0.077	0.192	0.308	0.385	0.577	0.654	0.654	0.577	0.500	0.462	0.308	0.192	0.154	0.115
3.5	to	4.4		0.038	0.038	0.038	0.038	0.077	0.077	0.077	0.231	0.385	0.615	0.731	0.731	0.731	0.692	0.654	0.538	0.385	0.231	0.154	0.115	0.115
4.4	to	5.6		0.038	0.038	0.038	0.077	0.077	0.154	0.308	0.462	0.731	0.923	0.808	0.808	0.731	0.692	0.615	0.423	0.231	0.154	0.115	0.115	0.077
5.6	to	7.0		0.038	0.038	0.077	0.115	0.192	0.423	0.615	0.923	0.962	0.923	0.808	0.731	0.692	0.615	0.385	0.192	0.154	0.115	0.077	0.077	0.077
7.0	to	8.9		0.038	0.077	0.115	0.308	0.538	0.885	0.962	0.962	0.923	0.885	0.731	0.692	0.538	0.308	0.154	0.154	0.077	0.077	0.077	0.077	0.077
8.9	**to**	**11.1**		0.077	0.115	0.462	0.846	**1.000**	0.962	0.962	0.923	0.923	0.731	0.615	0.500	0.269	0.154	0.077	0.077	0.077	0.038	0.038	0.038	0.000
11.1	**to**	**14.0**		0.192	0.500	0.846	**1.000**	0.962	0.962	0.923	0.923	0.769	0.692	0.538	0.231	0.154	0.077	0.077	0.038	0.000	0.000	0.000	0.000	0.000
14.0	to	17.7		0.269	0.538	0.962	0.962	0.962	0.962	0.923	0.808	0.731	0.654	0.423	0.154	0.077	0.077	0.038	0.000	0.000	0.000	0.000	0.000	0.000
17.7	to	22.2		0.115	0.269	0.577	0.923	0.962	0.962	0.923	0.808	0.654	0.462	0.154	0.077	0.038	0.000	0.000	0.000	0.000	0.000	0.000	0.000	0.000
22.2	to	28.0		0.231	0.500	0.923	0.962	0.962	0.962	0.808	0.731	0.538	0.231	0.077	0.077	0.000	0.000	0.000	0.000	0.000	0.000	0.000	0.000	0.000
28.0	to	35.2		0.231	0.500	0.923	0.962	0.962	0.846	0.769	0.654	0.308	0.115	0.038	0.000	0.000	0.000	0.000	0.000	0.000	0.000	0.000	0.000	0.000
35.2	to	44.4		0.231	0.654	0.923	0.962	0.846	0.769	0.654	0.423	0.115	0.077	0.000	0.000	0.000	0.000	0.000	0.000	0.000	0.000	0.000	0.000	0.000
44.4	to	55.9		0.231	0.654	0.808	0.769	0.654	0.462	0.154	0.115	0.077	0.000	0.000	0.000	0.000	0.000	0.000	0.000	0.000	0.000	0.000	0.000	0.000
55.9	to	70.3		0.000	0.000	0.000	0.000	0.000	0.000	0.000	0.000	0.000	0.000	0.000	0.000	0.000	0.000	0.000	0.000	0.000	0.000	0.000	0.000	0.000
70.3	to	88.5		0.000	0.000	0.000	0.000	0.000	0.000	0.000	0.000	0.000	0.000	0.000	0.000	0.000	0.000	0.000	0.000	0.000	0.000	0.000	0.000	0.000

To validate the calculated seawater sulfate concentration from the Tarim samples, we also choose samples from the Yangtze Block, South China. The early Cambrian successions in the Yangtze Block have been extensively studied, and several sections have both $\delta^{34}S_{py}$ and Fe speciation data reported, including the Xiaotan section (Och et al., 2016), Shatan and Songtao sections (Goldberg et al., 2007), Jinsha and Weng'an sections (Jin et al., 2016), Dingtai section (Xu et al., 2012), Yangjiaping section (Feng et al., 2014), and Longbizui section (Wang et al., 2012). As discussed above, this model can only simulate syndepositional pyrite formation in non-sulfidic seawater. Although there are many samples from the Yangtze Block that might have been deposited under non-sulfidic conditions, the sampling interval from the Yangtze Block should overlap with that of the Yurtus Formation in the Tarim Block. Thus, we choose data from the Songtao section for analysis (Goldberg et al., 2007).

In the simulation, we use Fe speciation data and $\delta^{34}S_{py}$ data from the Yurtus Formation in the X1 drill core in the Tarim Block and from the Niutitang Formation (~529–515 Ma) (Jin et al., 2020; Na and Kiessling, 2015) in the Songtao section in the Yangtze Block. We also apply the calibrated R_{DSR} and Δ_{DSR} values (**Figures 3**,**4**). The early Cambrian $\delta^{34}S_{SW}$ is set to +30‰ (Fike et al., 2015). Although the validity of $\delta^{34}S_{CAS}$ has been challenged (Marenco et al., 2008; Peng et al., 2014), the assigned $\delta^{34}S_{SW}$ value is consistent with the $\delta^{34}S_{CAS}$ data from the Yurtus Formation (**Figure 2**). Other parameters are allowed a range of variation, which are listed in **Table 1**.

Based on the outputs of the simulation, the frequency map of both seawater sulfate concentration and redox condition for all samples can be created (**Table 3**). The seawater sulfate concentration is bracketed between 8.9 and 14.0 mM. These values are in agreement with a rough estimate of ~10 mM based on the marine sulfur isotope mass balance calculation (Canfield and Farquhar, 2009), but at least 4 times higher than the calculation of ~2 mM based on the stratigraphic variation of CAS sulfur isotope values (Loyd et al., 2012).

Our modeling result indicates that the seawater sulfate concentration was already high during the early Cambrian, equivalent to ~30–50% of the present level of 28 mM. The seawater sulfate concentration is controlled by both terrestrial input of sulfate and burial in the ocean. Evaporate deposition (mainly gypsum) and pyrite precipitation and burial are the two major sinks of seawater sulfate (Fike et al., 2015). It is unclear how seawater sulfate concentration could increase to 30–50% of the present level. Neither is known about when the seawater sulfate concentration increased during the EdiacaranCambrian transition. We suggest that high seawater sulfate concentration during the early Cambrian might be favored due to the following reasons. First, the terrestrial sulfate input might have dramatically increased due to extensive evaporate dissolution during the formation of "Great Unconformity" (Peters and Gaines, 2012; Shields et al., 2019). Second, although the redox landscape in the early Cambrian ocean might be highly heterogeneous with the possible development of sulfidic wedge in continental margins (Jin et al., 2014; Jin et al., 2016; Li et al., 2018), the proportion of sulfidic seafloor might be smaller than that of early Neoproterozoic and Mesoproterozoic (Lyons et al., 2014). Limited seafloor euxinia also indicates less efficient pyrite burial, reducing the pyrite sink of the seawater sulfate. This argument is consistent with high Mo content in the lower Cambrian black shales (Sahoo et al., 2012; Reinhard et al., 2013; Sahoo et al., 2016).

Finally, our model provides a new approach to quantify the seawater sulfate concentration in paleoceans. In addition to justifying some key parameters based on the modern sediment observation, the Monte Carlo simulation could reduce the uncertainties raised by loosed constrained parameters. It should be noted that the assumption of the Monte Carlo simulation is invariant seawater sulfate concentration during the interval of simulation. Thus, high-resolution sampling from non-sulfidic deposits is required. If samples were collected from multiple sections, the chrono- and/or biostratigraphic framework is required to justify the coeval deposition.

CONCLUSION

In this study, we justified the key parameters (reaction rate constant of DSR and sulfur isotopic fractionation in DSR) of the syndepositional pyrite formation model. We also develop the Monte Carlo simulation approach to avoid uncertainties raised by loosely constrained parameters, such as sedimentation rate and the initial organic matter content in sediment. The new model allows the quantification of seawater sulfate concentration in deep time by using pyrite sulfur isotope and Fe speciation data. Based on the study of the lower Cambrian Yurtus Formation in the Tarim Block, combining with the data of the coeval Niutitang Formation in the Yangtze Block, the early Cambrian seawater sulfate concentration is bracketed between 8.9 and 14.0 mM, approaching to 30–50% of the present level. The relatively high seawater sulfate concentration might be attributed to enhanced terrestrial sulfate input in the context of "the Great Unconformity" and the reduced sulfidic seafloor in the second rise of atmospheric O_2 level. Our model provides a new approach to quantify the seawater sulfate concentration in paleoceans.

DATA AVAILABILITY STATEMENT

The raw data supporting the conclusion of this article will be made available by the authors, without undue reservation.

AUTHOR CONTRIBUTIONS

BS, TH and XL contributed to conception and design of the study. GZ, TL and KZ collected and analysed samples. TH, BS, XL, WT, and RW contributed to modeling and data analyzing. TH and BS wrote sections of the manuscript. All authors contributed to manuscript revision, read, and approved the submitted version.

FUNDING

This project was funded by the Scientific Research and Technology Development Project of China National Petroleum Corporation (CNPC) (Grant Nos: 2019B-04 and 2018A-0102).

ACKNOWLEDGMENTS

We acknowledge generous funding from China National Petroleum Corporation. We would like to thank Li Chao from China University of Geosciences (Wuhan) for Fe-speciation and sulfur isotope measurements and Bian Lizeng from Nanjing University for discussion about the depositional age of the Yurtus Formation.

SUPPLEMENTARY MATERIAL

The Supplementary Material for this article can be found online at: https://www.frontiersin.org/articles/10.3389/feart.2021.767857/full#supplementary-material

REFERENCES

Brocks, J. J., Jarrett, A. J. M., Sirantoine, E., Hallmann, C., Hoshino, Y., and Liyanage, T. (2017). The Rise of Algae in Cryogenian Oceans and the Emergence of Animals. *Nature* 548, 578–581. doi:10.1038/nature23457

Canfield, D. E., and Farquhar, J. (2009). Animal Evolution, Bioturbation, and the Sulfate Concentration of the Oceans. *Proc. Natl. Acad. Sci.* 106, 8123–8127. doi:10.1073/pnas.0902037106

Canfield, D. E., Poulton, S. W., and Narbonne, G. M. (2007). Late-Neoproterozoic Deep-Ocean Oxygenation and the Rise of Animal Life. *Science* 315, 92–95. doi:10.1126/science.1135013

Canfield, D. E. (2004). The Evolution of the Earth Surface Sulfur Reservoir. *Am. J. Sci.* 304, 839–861. doi:10.2475/ajs.304.10.839

Canfield, D., and Thamdrup, B. (1994). The Production of 34S-Depleted Sulfide during Bacterial Disproportionation of Elemental Sulfur. *Science* 266, 1973–1975. doi:10.1126/science.11540246

Ding, W., Dong, L., Sun, Y., Ma, H., Xu, Y., Yang, R., et al. (2019). Early Animal Evolution and Highly Oxygenated Seafloor Niches Hosted by Microbial Mats. *Sci. Rep.* 9, 13628. doi:10.1038/s41598-019-49993-2

Dong, L., Xiao, S., Shen, B., Zhou, C., Li, G., and Yao, J. (2009). Basal Cambrian Microfossils from the Yangtze Gorges Area (South China) and the Aksu Area (Tarim Block, Northwestern China). *J. Paleontol.* 83, 30–44. doi:10.1666/07-147r.1

Du, J., and Pan, W. (2016). Accumulation Conditions and Play Targets of Oil and Gas in the Cambrian Subsalt dolomite,Tarim Basin, NW China. *Pet. Exploration Dev.* 43, 327–339. doi:10.1016/s1876-3804(16)30043-x

Feng, L., Li, C., Huang, J., Chang, H., and Chu, X. (2014). A Sulfate Control on marine Mid-depth Euxinia on the Early Cambrian (Ca. 529-521Ma) Yangtze Platform, South China. *Precambrian Res.* 246, 123–133. doi:10.1016/j.precamres.2014.03.002

Fike, D. A., Bradley, A. S., and Rose, C. V. (2015). Rethinking the Ancient Sulfur Cycle. *Annu. Rev. Earth Planet. Sci.* 43, 593–622. doi:10.1146/annurev-earth-060313-054802

Fike, D. A., Grotzinger, J. P., Pratt, L. M., and Summons, R. E. (2006). Oxidation of the Ediacaran Ocean. *Nature* 444, 744–747. doi:10.1038/nature05345

Glaessner, M. F. (1984). *The Dawn of Animal Life: A Biohistorical Study*. Cambridge, UK: Cambridge Univ. Press.

Goldberg, T., Strauss, H., Guo, Q., and Liu, C. (2007). Reconstructing marine Redox Conditions for the Early Cambrian Yangtze Platform: Evidence from Biogenic sulphur and Organic Carbon Isotopes. *Palaeogeogr. Palaeoclimatol. Palaeoecol.* 254, 175–193. doi:10.1016/j.palaeo.2007.03.015

Gradstein, F. M. (2012). *The Geological Time Scale 2012*. Amsterdam, Netherlands ; Boston, MA: Elsevier.

Grotzinger, J. P., Fike, D. A., and Fischer, W. W. (2011). Enigmatic Origin of the Largest-Known Carbon Isotope Excursion in Earth's History. *Nat. Geosci* 4, 285–292. doi:10.1038/ngeo1138

Habicht, K. S., Canfield, D. E., and Rethmeier, J. (1998). Sulfur Isotope Fractionation during Bacterial Reduction and Disproportionation of Thiosulfate and Sulfite. *Geochimica et Cosmochimica Acta* 62, 2585–2595. doi:10.1016/s0016-7037(98)00167-7

Habicht, K. S., and Canfield, D. E. (1997). Sulfur Isotope Fractionation during Bacterial Sulfate Reduction in Organic-Rich Sediments. *Geochimica et Cosmochimica Acta* 61, 5351–5361. doi:10.1016/s0016-7037(97)00311-6

Habicht, K. S., Gade, M., Thamdrup, B., Berg, P., and Canfield, D. E. (2002). Calibration of Sulfate Levels in the Archean Ocean. *Science* 298, 2372–2374. doi:10.1126/science.1078265

He, J., Qing, H., and Xu, B. (2018). The Unconformity-Related Palaeokarst in the Uppermost Ediacaran Carbonate Rocks in the Northwestern Tarim Block, NW China: Implication for Sedimentary Evolution During the Ediacaran-Cambrian Transition. *Int. Geol. Rev.* 61, 839–852. doi:10.1080/00206814.2018.1474498

He, J., Wu, G., Xu, B., Qu, T., Li, H., and Cao, Y. (2010). Characteristics and Petroleum Exploration Significance of Unconformity between Sinian and Cambrian in Tarim Basin. *Dizhi kexue* 45, 698–706. doi:10.3969/j.issn.0563-5020.2010.03.006

Jin, C., Li, C., Algeo, T. J., Planavsky, N. J., Cui, H., Yang, X., et al. (2016). A Highly Redox-Heterogeneous Ocean in South China during the Early Cambrian (~529-514 Ma): Implications for Biota-Environment Co-evolution. *Earth Planet. Sci. Lett.* 441, 38–51. doi:10.1016/j.epsl.2016.02.019

Jin, C., Li, C., Algeo, T. J., Wu, S., Cheng, M., Zhang, Z., et al. (2020). Controls on Organic Matter Accumulation on the Early-Cambrian Western Yangtze Platform, South China. *Mar. Pet. Geology.* 111, 75–87. doi:10.1016/j.marpetgeo.2019.08.005

Jin, C., Li, C., Peng, X., Cui, H., Shi, W., Zhang, Z., et al. (2014). Spatiotemporal Variability of Ocean Chemistry in the Early Cambrian, South China. *Sci. China Earth Sci.* 57, 579–591. doi:10.1007/s11430-013-4779-y

Kah, L. C., Lyons, T. W., and Frank, T. D. (2004). Low marine Sulphate and Protracted Oxygenation of the Proterozoic Biosphere. *Nature* 431, 834–838. doi:10.1038/nature02974

Kaufman, A. J., Corsetti, F. A., and Varni, M. A. (2007). The Effect of Rising Atmospheric Oxygen on Carbon and Sulfur Isotope Anomalies in the Neoproterozoic Johnnie Formation, Death Valley, USA. *Chem. Geology.* 237, 47–63. doi:10.1016/j.chemgeo.2006.06.023

Lang, X., Tang, W., Ma, H., and Shen, B. (2020). Local Environmental Variation Obscures the Interpretation of Pyrite Sulfur Isotope Records. *Earth Planet. Sci. Lett.* 533, 116056. doi:10.1016/j.epsl.2019.116056

Li, C., Cheng, M., Zhu, M., and Lyons, T. W. (2018). Heterogeneous and Dynamic Marine Shelf Oxygenation and Coupled Early Animal Evolution. *Emerging Top. Life Sci.* 2, 279–288. doi:10.1042/etls20170157

Li, C., Love, G. D., Lyons, T. W., Fike, D. A., Sessions, A. L., and Chu, X. (2010). A Stratified Redox Model for the Ediacaran Ocean. *Science* 328, 80–83. doi:10.1126/science.1182369

Li, Z. X., Bogdanova, S. V., Collins, A. S., Davidson, A., De Waele, B., Ernst, R. E., et al. (2008). Assembly, Configuration, and Break-Up History of Rodinia: A Synthesis. *Precambrian Res.* 160, 179–210. doi:10.1016/j.precamres.2007.04.021

Liu, P., Xiao, S., Yin, C., Chen, S., Zhou, C., and Li, M. (2014). Ediacaran Acanthomorphic Acritarchs and Other Microfossils from Chert Nodules of the Upper Doushantuo Formation in the Yangtze Gorges Area, South China. *J. Paleontol.* 88, 1–139. doi:10.1666/13-009

Loyd, S. J., Marenco, P. J., Hagadorn, J. W., Lyons, T. W., Kaufman, A. J., Sour-Tovar, F., et al. (2012). Sustained Low marine Sulfate Concentrations from the Neoproterozoic to the Cambrian: Insights from Carbonates of Northwestern Mexico and Eastern California. *Earth Planet. Sci. Lett.* 339-340, 79–94. doi:10.1016/j.epsl.2012.05.032

Lyons, T. W., Reinhard, C. T., and Planavsky, N. J. (2014). The Rise of Oxygen in Earth's Early Ocean and Atmosphere. *Nature* 506, 307–315. doi:10.1038/nature13068

Lyons, T. W. (1997). Sulfur Isotopic Trends and Pathways of Iron Sulfide Formation in Upper Holocene Sediments of the Anoxic Black Sea.

Geochimica et Cosmochimica Acta 61, 3367–3382. doi:10.1016/s0016-7037(97)00174-9

Marenco, P. J., Corsetti, F. A., Hammond, D. E., Kaufman, A. J., and Bottjer, D. J. (2008). Oxidation of Pyrite during Extraction of Carbonate Associated Sulfate. *Chem. Geology*. 247, 124–132. doi:10.1016/j.chemgeo.2007.10.006

McFadden, K. A., Huang, J., Chu, X., Jiang, G., Kaufman, A. J., Zhou, C., et al. (2008). Pulsed Oxidation and Biological Evolution in the Ediacaran Doushantuo Formation. *Proc. Natl. Acad. Sci.* 105, 3197–3202. doi:10.1073/pnas.0708336105

Na, L., and Kiessling, W. (2015). Diversity Partitioning during the Cambrian Radiation. *Proc. Natl. Acad. Sci. USA* 112, 4702–4706. doi:10.1073/pnas.1424985112

Narbonne, G. M. (2005). The Ediacara Biota: Neoproterozoic Origin of Animals and Their Ecosystems. *Annu. Rev. Earth Planet. Sci.* 33, 421–442. doi:10.1146/annurev.earth.33.092203.122519

Och, L. M., Cremonese, L., Shields-Zhou, G. A., Poulton, S. W., Struck, U., Ling, H., et al. (2016). Palaeoceanographic Controls on Spatial Redox Distribution over the Yangtze Platform during the Ediacaran-Cambrian Transition. *Sedimentology* 63, 378–410. doi:10.1111/sed.12220

Pasquier, V., Sansjofre, P., Rabineau, M., Revillon, S., Houghton, J., and Fike, D. A. (2017). Pyrite Sulfur Isotopes Reveal Glacial–interglacial Environmental Changes. *Proc. Natl. Acad. Sci. USA* 114, 5941–5945. doi:10.1073/pnas.1618245114

Peng, Y., Bao, H., Pratt, L. M., Kaufman, A. J., Jiang, G., Boyd, D., et al. (2014). Widespread Contamination of Carbonate-Associated Sulfate by Present-Day Secondary Atmospheric Sulfate: Evidence from Triple Oxygen Isotopes. *Geology* 42, 815–818. doi:10.1130/g35852.1

Peters, S. E., and Gaines, R. R. (2012). Formation of the 'Great Unconformity' as a Trigger for the Cambrian Explosion. *Nature* 484, 363–366. doi:10.1038/nature10969

Poulton, S. W., and Raiswell, R. (2002). The Low-Temperature Geochemical Cycle of Iron: From continental Fluxes to marine Sediment Deposition. *Am. J. Sci.* 302, 774–805. doi:10.2475/ajs.302.9.774

Qian, M., Yuan, X., Xiao, S., Li, J., and Wang, Y. (2000). Neoproterozoic Glaciations and Their Triggers in the Yangtze Platform. *Jiangsu Geology*. 24, 135–139. doi:10.1080/00206814.2018.1474498

Qian, Y., Li, G., and Zhu, M. (2001). The Meishucunian Stage and its Small Shelly Fossil Sequence in China. *Acta Palaeontologica Sinica* 40 (Suppl. ment), 54–62.

Qian, Y. (1999). *Taxonomy and Biostratigraphy of Small Shelly Fossils in China*. Beijing: Science Press.

Raiswell, R., Hardisty, D. S., Lyons, T. W., Canfield, D. E., Owens, J. D., Planavsky, N. J., et al. (2018). The Iron Paleoredox Proxies: A Guide to the Pitfalls, Problems and Proper Practice. *Am. J. Sci.* 318, 491–526. doi:10.2475/05.2018.03

Raven, M. R., Sessions, A. L., Fischer, W. W., and Adkins, J. F. (2016). Sedimentary Pyrite δ34S Differs from Porewater Sulfide in Santa Barbara Basin: Proposed Role of Organic Sulfur. *Geochimica et Cosmochimica Acta* 186, 120–134. doi:10.1016/j.gca.2016.04.037

Reinhard, C. T., Planavsky, N. J., Robbins, L. J., Partin, C. A., Gill, B. C., Lalonde, S. V., et al. (2013). Proterozoic Ocean Redox and Biogeochemical Stasis. *Proc. Natl. Acad. Sci.* 110, 5357–5362. doi:10.1073/pnas.1208622110

Sahoo, S. K., Planavsky, N. J., Jiang, G., Kendall, B., Owens, J. D., Wang, X., et al. (2016). Oceanic Oxygenation Events in the Anoxic Ediacaran Ocean. *Geobiology* 14, 457–468. doi:10.1111/gbi.12182

Sahoo, S. K., Planavsky, N. J., Kendall, B., Wang, X., Shi, X., Scott, C., et al. (2012). Ocean Oxygenation in the Wake of the Marinoan Glaciation. *Nature* 489, 546–549. doi:10.1038/nature11445

Shields, G. A., Mills, B. J. W., Zhu, M., Raub, T. D., Daines, S. J., and Lenton, T. M. (2019). Unique Neoproterozoic Carbon Isotope Excursions Sustained by Coupled Evaporite Dissolution and Pyrite Burial. *Nat. Geosci.* 12, 823–827. doi:10.1038/s41561-019-0434-3

Shields-Zhou, G., and Och, L. (2011). The Case for a Neoproterozoic Oxygenation Event: Geochemical Evidence and Biological Consequences. *Gsat* 21, 4–11. doi:10.1130/gsatg102a.1

Sim, M. S., Bosak, T., and Ono, S. (2011). Large Sulfur Isotope Fractionation Does Not Require Disproportionation. *Science* 333, 74–77. doi:10.1126/science.1205103

Soutar, A., and Crill, P. A. (1977). Sedimentation and Climatic Patterns in the Santa Barbara Basin during the 19th and 20th Centuries. *Geol. Soc. America Bull.* 88, 1161–1172. doi:10.1130/0016-7606(1977)88<1161:sacpit>2.0.co;2

Thompson, C. K., and Kah, L. C. (2012). Sulfur Isotope Evidence for Widespread Euxinia and a Fluctuating Oxycline in Early to Middle Ordovician Greenhouse Oceans. *Palaeogeogr. Palaeoclimatol. Palaeoecol.* 313-314, 189–214. doi:10.1016/j.palaeo.2011.10.020

Wang, J., Chen, D., Yan, D., Wei, H., and Xiang, L. (2012). Evolution from an Anoxic to Oxic Deep Ocean during the Ediacaran-Cambrian Transition and Implications for Bioradiation. *Chem. Geology*. 306-307, 129–138. doi:10.1016/j.chemgeo.2012.03.005

Wei, G.-Y., Chen, T., Poulton, S. W., Lin, Y.-B., He, T., Shi, X., et al. (2021). A Chemical Weathering Control on the Delivery of Particulate Iron to the continental Shelf. *Geochimica et Cosmochimica Acta* 308, 204–216. doi:10.1016/j.gca.2021.05.058

Xu, L., Lehmann, B., Mao, J., Nägler, T. F., Neubert, N., Böttcher, M. E., et al. (2012). Mo Isotope and Trace Element Patterns of Lower Cambrian Black Shales in South China: Multi-Proxy Constraints on the Paleoenvironment. *Chem. Geology*. 318-319, 45–59. doi:10.1016/j.chemgeo.2012.05.016

Yao, J., Xiao, S., Yin, L., Li, G., and Yuan, X. (2005). Basal Cambrian Microfossils from the Yurtus and Xishanblaq Formations (Tarim, North-west China): Systematic Revision and Biostratigraphic Correlation of Micrhystridium-like Acritarchs. *Palaeontology* 48, 687–708. doi:10.1111/j.1475-4983.2005.00484.x

Yin, L., Zhu, M., Knoll, A. H., Yuan, X., Zhang, J., and Hu, J. (2007). Doushantuo Embryos Preserved inside Diapause Egg Cysts. *Nature* 446, 661–663. doi:10.1038/nature05682

Yuan, X., Chen, Z., Xiao, S., Zhou, C., and Hua, H. (2011). An Early Ediacaran Assemblage of Macroscopic and Morphologically Differentiated Eukaryotes. *Nature* 470, 390–393. doi:10.1038/nature09810

Zhang, F., Xiao, S., Kendall, B., Romaniello, S. J., Cui, H., Meyer, M., et al. (2018). Extensive marine Anoxia during the Terminal Ediacaran Period. *Sci. Adv.* 4, eaan8983. doi:10.1126/sciadv.aan8983

Zhang, Y. (1989). Multicellular Thallophytes with Differentiated Tissues from Late Proterozoic Phosphate Rocks of South China. *Lethaia* 22, 113–132. doi:10.1111/j.1502-3931.1989.tb01164.x

Zhu, G., Chen, F., Wang, M., Zhang, Z., Ren, R., and Wu, L. (2018). Discovery of the Lower Cambrian High-Quality Source Rocks and Deep Oil and Gas Exploration Potential in the Tarim Basin, China. *Bulletin* 102, 2123–2151. doi:10.1306/03141817183

Zhu, G., Li, T., Zhao, K., Li, C., Cheng, M., Chen, W., et al. (2021). *Mo Isotope Records from Lower Cambrian Black Shales, Northwestern Tarim Basin (China): Implications for the Early Cambrian Ocean*. Geological Society of America bulletin. doi:10.1130/B35726.1

Conflict of Interest: GZ and TL were employed by the company China National Petroleum Corporation.

The remaining authors declare that the research was conducted in the absence of any commercial or financial relationships that could be construed as a potential conflict of interest.

The handling Editor declared a past co-authorship/collaboration with the authors (TH, XL and BS).

Publisher's Note: All claims expressed in this article are solely those of the authors and do not necessarily represent those of their affiliated organizations, or those of the publisher, the editors and the reviewers. Any product that may be evaluated in this article, or claim that may be made by its manufacturer, is not guaranteed or endorsed by the publisher.

frontiers in Earth Science

ORIGINAL RESEARCH
published: 01 December 2021
doi: 10.3389/feart.2021.779954

Effects of Ice Freeze-Thaw Processes on U Isotope Compositions in Saline Lakes and Their Potential Environmental Implications

Pu Zhang[1,2], Chenyang Cao[2], Xiangzhong Li[3]*, Xuezheng Pei[2], Chi Chen[1], Lihua Liang[2], Youfeng Ning[1], Liangcheng Tan[4] and R. Lawrence Edwards[5]*

[1]Institute of Global Environmental Change, Xi'an Jiao Tong University, Xi'an, China, [2]College of Urban and Environmental Sciences, Northwest University, Xi'an, China, [3]Research Center for Earth System Science, Yunnan University, Kunming, China, [4]State Key Lab of Loess and Quaternary Geology, Institute of Earth Environment, Chinese Academy of Sciences, Xi'an, China, [5]Department of Earth and Environmental Sciences, University of Minnesota, Minneapolis, MN, United States

OPEN ACCESS

Edited by:
Heng Chen,
Columbia University, United States

Reviewed by:
Xinming Chen,
Florida State University, United States
Aiguo Dong,
China University of Geosciences, China

***Correspondence:**
Pu Zhang
zhangpu357@xjtu.edu.cn
Xiangzhong Li
xzhli04@163.com

Specialty section:
This article was submitted to Geochemistry, a section of the journal Frontiers in Earth Science

Received: 20 September 2021
Accepted: 08 November 2021
Published: 01 December 2021

Citation:
Zhang P, Cao C, Li X, Pei X, Chen C, Liang L, Ning Y, Tan L and Edwards RL (2021) Effects of Ice Freeze-Thaw Processes on U Isotope Compositions in Saline Lakes and Their Potential Environmental Implications. Front. Earth Sci. 9:779954. doi: 10.3389/feart.2021.779954

The dissolved uranium (U) content in the water column of saline lakes varies little between ice-free seasons throughout the whole water column. Such uniformity allows for the potential absolute dating and/or paleohydrologic interpretations of lake sediments and biogenic shell materials using U isotopes. Before using these methods in cold regions, however, it is necessary to evaluate the effects that ice freeze-thaw processes have on the distribution of U isotopes in saline lake waters, and to determine the amount of variation in U isotopic values when such processes occur. In this paper, we collected ice and dissolved water samples from six lakes with variable salinity in February 2021. Five groundwater and three water samples from rivers into Qinghai Lake were sampled in November 2020. The sampled water was analyzed for dissolved concentrations of ^{238}U and the activity ratio of $^{234}U/^{238}U$ ($[^{234}U/^{238}U]_{AR}$). The results show that the ^{238}U concentration of ice samples was less than that of the underlying water. The $[^{234}U/^{238}U]_{AR}$ of ice in the five saline lakes was similar to that of the underlying water with less than a 10‰ variation, suggesting no observable fractionation between ice and dissolved water. Thus, the ice freeze-thaw processes have almost no effect on the uranium content and $[^{234}U/^{238}U]_{AR}$ of the sampled saline lakes, which were characterized by a limited recharge volume from surface runoff, groundwater, and ice volume, namely the close saline lake in arid alpine background. The results from the indoor freeze-thaw experiments also showed that the U isotopic composition of Qinghai Lake waters and ice were similar with the ^{238}U concentration of the ice was about 40% of that of the dissolved lake water, supporting the data obtained from natural saline lakes. The above results provide important insights into whether it is feasible to use U isotopes for absolute dating and/or paleohydrologic analysis of lake sediments or biogenic shell materials. In addition, the results are important for evaluating the $[^{234}U/^{238}U]_{AR}$ and uranium concentrations in seawater when there exists a process of melting polar ice, and for determining the initial delta ^{234}U variations needed for dating of coral and other fossil materials.

Keywords: U isotopes, saline lakes, freeze-thaw processes, Qinghai region, Qaidam basin

INTRODUCTION

Studies of the distribution of dissolved uranium (U) isotopes in water have mainly focused on problems of glacial sedimentation at the two poles and oceanic circulation (Sarin and Church, 1994; Moran et al., 1997). Existing research results show that the U concentration of seawater is relatively consistent, and exhibits a linear relationship with salinity (Rengarajan et al., 2003; Schmidt, 2006). Changes observed in the atmosphere, hydrosphere, cryosphere, and biosphere indicate that the Earth has warmed (Desbruyères et al., 2016; Francis et al., 2017; Lavergne et al., 2019). During the preceding decades, key indicators of the climate system are changing at unprecedented rates during at least the last two centuries, which are at levels that have not been observed in hundreds to thousands of years (Hansen et al., 2010; Tierney et al., 2020; Trewin et al., 2020). During the past 10 years (2011–2020), temperature exceeded the warmest centennial-scale range that was reconstructed for the Holocene during about the past 6,500 years [0.2–1°C relative to 1850–1900] (Gulev et al., 2021). The total loss of land ice (including both glaciers and ice sheets) was the largest contributor to global mean sea level rise, which was estimated to occur at a rate of about 3.7 [3.2–4.2] mm/year between 2006 and 2018 (Cazenave et al., 2018; Velicogna et al., 2020). The above processes will result in a change in U content and the activity ratio of $^{234}U/^{238}U$ ($[^{234}U/^{238}U]_{AR}$) of sea water. This change may provide insights into the nature of the change in sea level as well as various oceanographic circulation patterns and processes. Changes in U isotopic abundances are also needed to establish the initial delta ^{234}U variations in corals, which are often used for dating. Thus, it is necessary and of significance to understand the effects of ice freeze-thaw processes on the U isotope distribution of sea water including the ^{238}U concentration and the $[^{234}U/^{238}U]_{AR}$. Further, limited hydrological studies on saline lake systems have been conducted to date, and research methods required for their hydrological analysis have yet to be systematically developed. In fact, very few studies have explored the ^{238}U concentration and $[^{234}U/^{238}U]_{AR}$ of saline lakes, or the effects of ice freeze-thaw processes on U isotope distribution in lake waters.

Hydrologically closed saline lakes located in the Qinghai region and the Qaidam Basin of China provide the potential to precisely evaluate the effects of ice freeze-thaw processes on U isotope distribution in both saline and fresh lake waters of variable salinity. These lakes are also easily accessible allowing for efficient sample collection. In this study, we selected several lakes with different salinities in the Qinghai-Tibet Plateau and sampled ice and the underlying water for a complete U isotope analysis to gain insights into the effects of ice freeze-thaw processes on the U isotope distribution of the lake waters. We also conducted inhouse (laboratory) freezing experiments on three batches of lake water samples collected between 2018 and 2021 from Qinghai Lake to evaluate the effects of ice freeze-thaw processes on the U isotope distribution of lake water. By combining the U isotope distribution results from both the inhouse freezing experiments and natural lake water samples, we obtained a better understanding of the changes in U distribution in lake waters that occur during the ice freeze-thaw process, which helps in exploring the potential for using U isotopes as environmental indicators and/or the dating of corals and other fossil materials.

MATERIALS AND METHODS

Sampling Locations

There are many lakes in the Qinghai region and Qaidam Basin. Most of these lakes are classified as saline lakes, in that they possess a salinity with the variation from 8.86 to 72.36‰. The water samples used in this study were collected from six lakes with different salinities. Four of the sampled lakes were located in the northeastern part of the Qaidam Basin, including Gahai Lake (GH), Keluke Lake (KLK), Tuosu Lake (TS), and Xiligou Lake (XLG) (**Figure 1**). These four lakes can be divided into three categories based on the basis of salinity: freshwater lakes (including KLK), saline lakes (TS, XLG) and salt lakes (GH). The study area is characterized by a typical alpine continental climate in which large temperature differences occur between day and night. Precipitation in the region is low, while evaporation throughout the year is relatively high. The main vegetation types include alpine meadows and alpine step communities. The overall elevation of the area is about 3,000 m masl. Han et al. (2019) determined, using data from the National Meteorological Station of Delhi City, that the mean annual precipitation over the period of 1961–2017 was 185.1 mm, and the mean annual evaporation ranged between 2,242.8 and 2,439.4 mm. Precipitation is unevenly distributed during the year, showing a unimodal distribution. Maximum precipitation occurs in June to July, while the minimum precipitation occurs in December. The total area of GH is about 37 km^2; it possesses a mean water depth of 8 m and a maximum water depth of 15 m. The lake basin has no perennial surface rivers. Recharge relies on atmospheric precipitation and subsurface runoff. TS has a total area of about 180 km^2 and a maximum water depth of 25.7 m. The main source of the water in TS originates from drainage, atmospheric precipitation, and groundwater (Zheng and Zhang, 2002; Huang and Han, 2007).

In addition to the four lakes sampled in the Qaidam Basin, water and ice samples were collected from two lakes with varied salinities in the Qinghai region: Qinghai Lake (QHH) and Qinghai Gahai (QHGH) (**Figure 1**). The surface area of Lake Qinghai (36°15′–38°20′N, 97°50′–101°20′E) is approximately 4,400 km^2. The area of the lake is approximately 29,660 km^2. The geological and geographical environment and current climate of this area have been examined in detail by Colman et al. (2007) and Jin et al. (2010).

Lake Qinghai is the largest inland close lake in China by surface area. The lake is developed within a basin surrounded by three mountain ranges including the Datong Mountains to the north, the Riyue Mountains to the east, and the Qinghai Nanshan Mountains to the south (Bian et al., 2000). The lake is divided into two nearly equal sub-basins by a NNW-trending horst, from which an island (Mt Haixin) emerges. Several minor fault scarps also can be found in the lake basin. The lake bed is generally flat and the lake is hydrologically closed and evaporative (Zhang et al.,

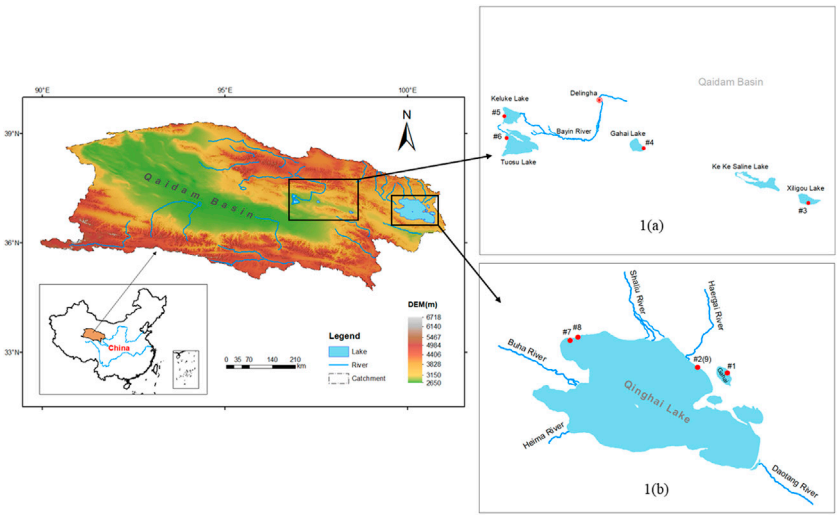

FIGURE 1 | Map showing the locations of the sampled lakes in the northeast part of the Qaidam Basin and Qinghai region.

TABLE 1 | Sampling site information for the ice and water samples.

Location	Group	Sample no	Sample type	Sample depth (m)	Latitude (°N)	Longitude (°E)	Altitude (m)	Date
Qinghai Gahai lake	1	QHGH-1-F QHGH-2-F	Ice Water	0.1 0.2	37°01′19″	100°35′40″	3,200	February 26, 2021
Qinghai Lake	2	QHH-3-F QHH-4-F	Ice Water	0.1 0.2	37°02′54″	100°26′52″	3,200	February 26, 2021
Xiligou Lake	3	XLGH-5-F XLGH-6-F	Ice Water	0.05 0.2	36°49′05″	98°27′21″	2,940	February 27, 2021
Gahai Lake	4	GH-7-F GH-8-F	Ice Water	0.05 0.2	37°06′53″	97°36′07″	2,980	February 27, 2021
Keluke Lake	5	KLK-9-F KLK-10-F	Ice Water	0.3 0.5	37°17′03″	96°51′42″	2,820	February 27, 2021
Tuosu Lake	6	TS-11-F TS-12-F	Ice Water	0.1 0.2	37°10′09″	96°51′42″	2,790	February 27, 2021

1994). The six largest rivers that form the Lake Qinghai catchment are, in order of their discharge, the Buha, Shaliu, Hargai, Quanji, Daotang and Heima rivers. Hydrologically, these rivers are greatly impacted by the area's monsoonal climate, and they supply over 87% of the water, dissolved load, and sediment discharge to the lake. Over half of these rivers come from the Buha River (Jin et al., 2009). Meltwater from surrounding mountain glaciers accounts for only 0.3% of the total runoff (Colman et al., 2007).

Qinghai Gahai Lake (36°57′–37°3′N, 100°31′–100°36′E) is located along the northeast bank of Qinghai Lake at an altitude of 3,196.6 m. As one of the three sub-lakes of Qinghai Lake, Qinghai Gahai is now hydrologically closed without river inputs. The lake is 12 km long from northwest to southeast, and 6 km wide from southwest to northeast. It possesses a surface area of 47.5 km^2. Qinghai Gahai Lake is generally 8–9.5 m deep and slightly alkaline with a pH of 9.25. The salt content of the lake water is about 31.73 g/L. The lake is recharged by shallow groundwater. The center of the lake is located about 400 m from the coast, and there is deep groundwater recharge at the bottom of the lake.

Sampling Design and Methods

All ice and water samples were collected in February 2021 (see **Table 1** for details). To determine the effect of collecting samples in different years on U content in lake water, four samples were collected in Qinghai Lake from 2017 to 2019. In addition, river water and groundwater samples were collected from the rivers recharging Qinghai Lake to verify whether surface runoff would affect lake U concentrations and $[^{234}U/^{238}U]_{AR}$. Previous studies showed that the U concentration and $[^{234}U/^{238}U]_{AR}$ of waters from the same lake in the Qaidam Basin varied little aerially or vertically within the water column or seasonally through time (Zhang et al., 2019; Zhao et al., 2020). Thus, we believe that the samples from one location of each lake are sufficient to represent the U content and the $[^{234}U/^{238}U]_{AR}$ distribution characteristics

TABLE 2 | Sampling site information for water samples from Qinghai Lake.

Location	Group	Sample no	Sample type	Depth (m)	Latitude (°N)	Longitude (°E)	Altitude (m)	Date
Qinghai lake	7	QHH-1-1 WATER-ice-F QHH-1-1 WATER-water-F	WATER-ice WATER-water	0.2	37°11′52″	99°48′34″	3,200	June 18, 2018
	8	QHH-2-1 WATER-ice-F QHH-2-1 WATER-water-F	WATER-ice WATER-water	0.2	37°12′24″	99°50′16″	3,190	July 23, 2019
	9	QHH-4 WATER-ice-F QHH-4 WATER-water-F	WATER-ice WATER-water	0.2	37°02′54″	100°26′52″	3,200	February 26, 2021

Note: In sample type, WATER-ice, indicate the overlying ice when water was frozen in refrigerator; WATER-water means the underlying water when water was frozen in refrigerator.

of these sampled lakes, and that the U data of surface water can represent the entire water column of the lake. Sampling periods were selected that possessed large quantities of lake ice in the northeastern part of the Qaidam Basin and the Qinghai region; during the other seasons, the lakes are nearly ice free. Thus, the sampled ice and lake waters should show the typical U distribution within the ice and the underlying water. By comparing the U composition of the sampled lake water in summer with the maximum water input published in Zhao et al. (2020), we expected to gain a deeper understanding of effects of ice freeze-thaw processes on U isotope distribution in saline lake waters and the potential environmental implications on the observed U data.

To further evaluate the effects of ice freeze-thaw processes on the U isotope distribution of lake water, three water samples were collected from QHH in September 2018, July 2019 and February 2021 (**Table 2**). We preformed inhouse freezing experiments on these three QHH water samples in the laboratory to further verify the results of the data obtained from the "natural" ice and water samples collected in the field.

Samples of surface ice and the underlying water were collected dozens of meters offshore in high density polyethylene (HDPE) plastic bottles (Nalgene 2002-0032) by hand wearing Derma Free Vinyl Gloves. After collection, about 1,000 ml of each water sample was filtered through a mixed cellulose filter membrane (0.8-μm pore size, Millipore AAWP04700) with a manual vacuum filter system (Nalgene, 300-4100; Nalgene, 6133-0010). The filtrates were stored for later analysis.

After collection, ice samples were placed at room temperature to melt. The melted ice water was also filtered through a mixed cellulose filter membrane (0.8-μm pore size, Millipore AAWP04700) using a manual vacuum filter system (Nalgene, 300-4100; Nalgene, 6133-0010), and stored for later analysis. The research of Ku et al. (1977) showed that there is no evident difference on the $[^{234}U/^{238}U]_{AR}$ on the filtered Atlantic seawater and the unfiltered seawater, but has little effect on U concentration. Therefore, we believe that U concentration filtered by 0.8 μm filters could represent the content of dissolved U in saline lake water to a certain extent.

QHH water samples were collected in three batches over various sampling periods for in-house freezing experiments. The experiment mimicked natural sample freezing conditions in the field, during which the three previously filtered QHH water samples were frozen at −18°C in a freezer for 5–6 h to form half water and half ice. Then the ice and water were separated, and stored for later analysis.

Analytical Methods

The samples were analyzed for selected water chemistry parameters (e.g., anions, cations, salinity, total dissolved solids (TDS), and pH at the Key Laboratory of Surface System and Environmental Carrying Capacity of Shaanxi Province, Northwest University. Anion and cation concentrations of the samples were determined using two Dionex AQUION ICs (Chen et al., 2007; Scientific, 2016). Conductivity (ms/cm), TDS (g/L), salinity (‰), and pH were determined using a Mettler-Toledo Five Easy Plus pH meter. Uranium isotopes in the samples were measured at the Xi'an Jiaotong University Isotope Laboratory. The analysis of U isotope abundances included a two-step process, including chemical separation and instrumental analysis. Chemical separation involved sample digestion, centrifugal coprecipitation, ion exchange resin separation, uranium isotope collection, and purification. More specifically, to analyze the U isotopic compositions of the water, the acidified aliquots of each sample (~25 ml) were spiked with ^{233}U–^{236}U–^{229}Th, preconcentrated and digested with HNO_3 and $HClO_4$, and then co-precipitated with Fe oxyhydroxide. The Fe precipitate was moved to a centrifuge tube for centrifugation and rinsed with deionized H_2O (>18 MΩ) to eliminate water-soluble seawater cations. The precipitate was then dissolved in 14 N HNO_3 (1 N = 1 M) and moved to a Teflon beaker, before being dried and dissolved in 7 N HNO_3 for anion-exchange chromatography with an AG1-X8, 100–200 mesh size resin and a polyethylene frit. Separation was performed in Teflon columns with a 0.25 ml column volume (CV). The first separation was performed in Teflon columns with 0.5 ml 7 N HNO_3, 0.25 ml of 8 N HCl (to get rid of Fe and Th fraction), and 0.5 ml of deionized H_2O (to gather the U fraction). The U fractions were then dried with two drops of $HClO_4$ and brought to volume with 7 N HNO_3. The final U fractions were then dried with two drops of $HClO_4$ and dissolved in weak nitric acid for analysis on the mass spectrometer. The concentrations of ^{234}U, ^{235}U, and ^{238}U were calculated by isotope dilution using the

TABLE 3 | Data information of samples and duplicate samples during chemical analysis.

Sample	Sample type	Latitude (°N)	Longitude (°E)	^{238}U (μg/L)	Error (2s)	[^{234}U/^{238}U]$_{AR}$	Error (2s)	Date
QHGH-1-F	Ice	37°01′19″	100°35′40″	2.2	0.01	1.909	0.003	2021/
duplicate sample				2.2	0.01	1.909	0.003	2/26
QHH-4 WATER-water-F	Water-water	37°02′54″	100°26′52″	3.8	0.00	1.878	0.002	2021/ 2/26
duplicate sample				3.8	0.00	1.880	0.002	

TABLE 4 | Geochemistry data for ice and the overlying water samples from the six lakes.

Location	Sample no	Sample type	TDS (g/L)	Salinity (‰)	pH	^{238}U (μg/L)	Error (2s)	[^{234}U/^{238}U]$_{AR}$	Error (2s)
Qinghai Gahai lake	QHGH-1-F	Ice	19.84	25.18	8.78	2.2	0.01	1.909	0.003
	QHGH-2-F	Water				15.5	0.04	1.924	0.003
Qinghai lake	QHH-3-F	Ice	8.7	10.21	8.86	2.1	0.00	1.886	0.002
	QHH-4-F	Water				2.7	0.00	1.878	0.002
Xiligou lake	XLGH-5-F	Ice	7.2	8.67	8.51	1.0	0.00	1.531	0.002
	XLGH-6-F	Water				23.8	0.07	1.543	0.002
Gahai lake	GH-7-F	Ice	39.31	72.36	7.84	2.5	0.01	1.906	0.002
	GH-8-F	Water				15.4	0.04	1.917	0.002
Keluke lake	KLK-9-F	Ice	0.545	0.54	7.73	0.1	0.00	1.389	0.003
	KLK-10-F	Water				2.5	0.00	1.504	0.002
Tuosu lake	TS-11-F	Ice	16.54	20.91	8.83	7.4	0.03	1.466	0.003
	TS-12-F	Water				19.5	0.05	1.472	0.002

nuclide ratios determined on a Thermo-Finnigan Neptune mass spectrometer. All measurements were performed using a peak-jumping routine in ion counting mode on the discreet dynode multiplier behind the retarding potential quadrupole. Each sample measurement was bracketed by the measurement of an aliquot of the run solution, which was utilized to adjust for the instrument background count rates on the measured masses. For U, the measurement uncertainties involved propagated errors from the ICP-MS isotope ratio measurements, spike concentrations, and blank corrections. The procedural blanks for chemical and mass spectrometric analyses at the Laboratory of Isotope Geochemistry in Xi'an Jiao Tong University are approximately 50 ag ($1.3 \times e^5$ atoms) for ^{234}U; 3 fg ($7.7 \times e^6$ atoms) for ^{235}U; and 150 fg ($3.8 \times e^8$ atoms) for ^{238}U.

The experimental analysis methods can be divided into two parts: chemical separation and MC-ICP-MS mass spectrometry. For chemical separation, we used duplicate samples in each batch to ensure the reliability of the data. The experimental results showed that the repeatability of the duplicate samples in the chemical analysis process was excellent (**Table 3**), and the yield of all samples was about 93%. For instrument analysis process, NBL-112A (New Brunswick Laboratory) U isotope standard solution was used for external calibration during the analysis by MC-ICP-MS mass spectrometer. The experimental results showed that the average of NBL-112A standard solution was −38.23 ± 1.21‰(2σ), and the measurement precision of dissolved ^{238}U content and [^{234}U/^{238}U]$_{AR}$ in lake water samples was 0.89–1.35‰ (2σ). The methods used herein have been fully described by Cheng et al. (2000, 2013) and Shen et al. (2002, 2012).

RESULTS

Distribution of Uranium Isotopes in Lake Ice and Waters in the Qinghai Region and the Northeastern Part of Qaidam Basin

The water chemistry results of each sampled lake are presented in **Table 4**, including the aqueous ^{238}U concentration and the [^{234}U/^{238}U]$_{AR}$. Aqueous ^{238}U concentrations of the freshwater lakes in the northeastern part of the Qaidam Basin were generally low, which is consistent with the results of previous analyses of lake water samples collected in June, July and the beginning of December without ice coverage (Zhao et al., 2020). The ^{238}U concentration of ice from the five sampled lakes were less than that of water under the ice, except for samples from QHH. The ^{238}U concentrations of the ice from the five lakes with varying salinity ranged from approximately three to forty percent of the U content of the underlying water. The lower the salinity of lake water, the lower U content in the forming overlying ice. The ^{238}U concentration of ice in QHH was slightly less than that of water under the ice. The reason for this is not clear at this time and will be the topic of future studies.

The [^{234}U/^{238}U]$_{AR}$ values were similar between the ice and water from the six lakes of varying salinity; the [^{234}U/^{238}U]$_{AR}$ exhibited very limited variation. In fact, the variation in [^{234}U/^{238}U]$_{AR}$ ratios between the ice and water in the five saline lakes and the salt lake were all within 2%. The variation in [^{234}U/^{238}U]$_{AR}$ between ice and water in the freshwater lake reached up to 23%.

In conclusion, during the icing process, the U content was significantly different between the ice and water; it was lower in ice than in water. In contrast, the [^{234}U/^{238}U]$_{AR}$ did not change

TABLE 5 | Results of inhouse freezing experiments on three batches of Qinghai Lake water samples collected during different seasons.

Location	Sample no	Sample type	^{238}U (μg/L)	Error (2s)	$[^{234}U/^{238}U]_{AR}$	Error (2s)	Date
Qinghai lake	QHH-1-1 WATER-ice-F	WATER-ice	8.6	0.02	1.890	0.003	June 18, 2018
	QHH-1-1 WATER-water-F	WATER-water	21.3	0.04	1.900	0.002	
	QHH-2-1 WATER-ice-F	WATER-ice	7.5	0.02	1.893	0.003	July 23, 2019
	QHH-2-1 WATER-water-F	WATER-water	17.3	0.03	1.897	0.002	
	QHH-4 WATER-ice-F	WATER-ice	1.3	0.00	1.877	0.002	February 26, 2021
	QHH-4 WATER-water-F	WATER-water	3.8	0.00	1.878	0.002	

Note: In sample type, WATER-ice, indicate the overlying ice when water was frozen in refrigerator; WATER-water means the underlying water when water was frozen in refrigerator.

TABLE 6 | U isotope data from recharge rivers and groundwater recharging in Qinghai Lake.

Location	Sample	Sample type	Latitude (°N)	Longitude (°E)	^{238}U (μg/L)	Error (2s)	$[^{234}U/^{238}U]_{AR}$	Error (2s)	Date
Daotang River	DT-1-R-F	River water	36°23′56″	100°58′28″	2.1	0.00	2.01	0.002	2020/11/18
	DT-3-R-F	Groundwater	36°23′58″	100°58′07″	14.4	0.03	1.442	0.002	2020/11/18
Haergai River	HEG-7	River water	37°13′11″	100°28′39″	2.6	0.00	2.297	0.002	2020/11/18
	HEG-6	Groundwater	37°06′22″	100°31′22″	4.3	0.01	1.742	0.002	2020/11/18
Shaliu River	SL-9	River water	37°19′92″	100°07′29″	2.6	0.00	2.325	0.002	2020/11/18
	SL-11	Groundwater	37°16′55″	100°03′40″	4.5	0.01	2.077	0.002	2020/11/19
Buha River	BH-12-R	Groundwater	37°03′10″	99°47′49″	9.7	0.02	2.562	0.003	2020/11/19
Heima River	HM-13	Groundwater	36°43′54″	99°46′22″	3.8	0.00	1.731	0.002	2020/11/19

significantly between the saline lakes; differences in the values were within 2% and slightly lower in ice than the underlying water.

Distribution of Uranium Isotopes in Ice and Water From QHH as Determined by Inhouse Freezing Experiments

Laboratory studies were carried out to 1) further determine the fidelity of the isotopic changes observed during the freezing and transformation of "natural" lake water to ice, and 2) assess the anomalies in the results of ice and water in Qinghai Lake during the ice-on (covered) season. The indoor freeze-thaw experiments were conducted on three batches of QHH water samples collected in different seasons, including periods when the lake was and was not covered in ice. The samples from QHH were obtained in September 2018, July 2019 and February 2021.

The results of the inhouse freezing experiments were similar to that observed for the natural lake samples (**Table 5**). The ^{238}U concentration of the ice was slightly less than that of the water in all three batches of samples. The ^{238}U concentration of the ice was about 40% of that in the water. In addition, we noticed that the ^{238}U concentrations of the water collected in February were lower than those of the water obtained in July and September. The $[^{234}U/^{238}U]_{AR}$ resulting from the inhouse freezing experiments also supports those of the nature samples. The activity ratios did not change significantly during the phase transition from water to ice in the three batches of collected samples; differences between the samples were within 0.5%.

Distribution of Uranium Isotope in Recharge Rivers and Groundwater Recharging in Qinghai Lake

In November 2020, five groundwater samples in recharge rivers and three water samples from recharging rivers into Qinghai Lake. The water chemistry results of each sampled river are presented in **Table 6**, including the aqueous ^{238}U concentration and the $[^{234}U/^{238}U]_{AR}$. Aqueous ^{238}U concentrations of the recharge rivers of Qinghai Lake is 2.1–2.6 μg/L, and $[^{234}U/^{238}U]_{AR}$ is 2.010–2.325, with a limited variation. The ^{238}U concentrations and $[^{234}U/^{238}U]_{AR}$ of the groundwater in Qinghai Lake region ranged from 3.8 to 14.4 μg/L and 1.442 to 2.562 respectively. The U concentration of recharge rivers and groundwater is lower than that of Qinghai Lake, while $[^{234}U/^{238}U]_{AR}$ is higher than that of Qinghai Lake.

DISCUSSION

U Isotopes Variations and the Controlling Factors in the Ocean and Saline Lake System

U Isotopes Variations and the Controlling Factors in the Ocean

Seawater $[^{234}U/^{238}U]_{AR}$ is higher than secular equilibrium (Chen et al., 1986). This reflects the process of α-recoil during decay of

^{238}U which leads to high $[^{234}U/^{238}U]_{AR}$ in river waters (Chabaux et al., 2008) and to a flux of ^{234}U into the oceans from marine sediment pore-waters (Klinkhammer and Palmer, 1991). These inputs keep the seawater $[^{234}U/^{238}U]_{AR}$ high and counteract the decay of excess ^{234}U in the oceans, which constantly attempts to return it to a secular equilibrium value of 1. Uranium concentrations and $[^{234}U/^{238}U]_{AR}$ have been determined in 63 seawater samples from the Atlantic, the Pacific, the Arctic, and the Antarctic oceans. These analyses show that: 1) the uranium concentration of seawater with a salinity of 35‰ was 3.35 ± 0.2 μgl^{-1}; and 2) the $[^{234}U/^{238}U]_{AR}$ was 1.14 ± 0.03. Current estimates of the average world river uranium concentration (0.3–0.6 μgl^{-1}) and $[^{234}U/^{238}U]_{AR}$ (1.2–1.3) and of the diffusional ^{234}U influx from sediments (0.3 dpm cm^{-2} 10^{-3} yr^{-1}) are essentially consistent with a model that depicts a steady state distribution of uranium in the ocean. However, the 0.3–0.6 μgl^{-1} values for river uranium may be an upper limit estimate. The ratios reported for global rivers ($[^{234}U/^{238}U]_{AR}$ = 1.171; Chabaux et al., 2008), and the ratios measured for four rivers discharging into Lake Qinghai located in an arid alpine climate.

$[^{234}U/^{238}U]_{AR}$ varied between 1.984 and 2.506 (Zhang et al., 2019). New Zealand rivers located in an Alpine high latitude area exhibited a wide range of $[^{234}U/^{238}U]_{AR}$, varying from 1.09 to 4.61 (Robinson et al., 2004). This range spans that previously measured in rivers from elsewhere.

Uranium is removed from the oceans by diffusion across the sediment-water interface of organic-rich sediments. This pathway is the largest single sink in the global uranium budget of this element (Klinkhammer and Palmer, 1991). Dissolved uranium is drawn into suboxic sediments along a concentration gradient established by the precipitation of an insoluble phase which forms when U(VI) is reduced to U(IV) (Ku et al., 1977). This transformation occurs relatively late in the diagenetic sequence, after the microbially mediated dissolution of manganese and iron oxides, and may be induced by the onset of sulfate reduction. Metallo-organics play an important role in the diagenetic behavior of this element as some uranium is released into solution when labile organics are consumed at the sediment-water interface (Francke et al., 2020). In contrast, the diagenesis of authigenic iron and manganese oxides exerts a negligible influence on the uranium diagenetic cycle (Klinkhammer and Palmer, 1991). Variations in the uranium concentration of sediment with time are controlled directly by the uranium content of the source material settling from the water column, and indirectly, by the organic content of this material and the sedimentation rate. Since diffusion from seawater dramatically influences the short-term burial rate of uranium, down-core distributions of dissolved and solid uranium can provide an estimate of recent sedimentation rates in rapidly accumulating sediments. The research from Cowart (1980) determined the concentration of dissolved uranium and $[^{234}U/^{238}U]_{AR}$ were determined in water samples from 23 locations in the Edwards carbonate aquifer of south central Texas. The $[^{234}U/^{238}U]_{AR}$ was about 1.20 in an oxidized aquifer and above 2.0 in a reduced aquifer.

U Isotope Variations and the Controlling Factors in the Saline Lake System

Limited studies on hydrological systems in saline lakes have been conducted and research methods have been systematically developed. The research dates back to Osmond et al. (1974) who established a two-end mixing model based on the relationship between $[^{234}U/^{238}U]_{AR}$, 1/U, and U/TDS (total dissolved solids) in the water of Sambhar lake. They found that one end of the lake had a low uranium content and low salinity, while the other end had the opposite. The U content measured by Zhao et al. (2020) in several saline lakes and our unpublished salt lakes shows the ^{238}U concentration varied with the range of 12.6–200 μg/L. Other studies have also shown that the U content of lakes water varies directly with TDS (salinity) and pH, the latter of which is partially controlled by evaporation and/or other secondary concentration pathways (Osmond et al., 1974; Borole et al., 1982; Yadav and Sarin, 2009; Zhang et al., 2019; Chen et al., 2020; Zhao et al., 2020). Moreover, the U concentration indicate that the length of these processes, which are controlled by the duration of water-rock interaction, is probably an important factor to consider when accounting for the variation in lake salinities within a similar geographical area. In addition, research has shown that biogeochemical process have an impact on the mobility of uranium species. These biogeochmical processes include the behavior of colloids suspended phase and colloids, the sorption and complexation processes on inorganic soil constituents such as clay minerals, oxides, Mn (III/IV) oxides, and organic matter, biological fixation and transformation processes, and competition with a certain number of OM and/or cations (such as Ca^{2+} and Mg^{2+}) (Andersson et al., 2001; Koch-Steindl and PröHl, 2001; Fredrickson et al., 2002; Dong and Brooks, 2006; Belli et al., 2015; Strakhovenko and Gas'kovaet, 2018; Chen et al., 2020; Francke et al., 2020). The $[^{234}U/^{238}U]_{AR}$ in saline lakes is closely related to the input of water to the lake, evaporation or other secondary concentration pathways, water–rock interactions involving sediments, the influx of atmosphere dust, and the system's organic matter, content, among other factors as well as the evolution, degree of metamorphous, and hydrochemistry and biogeochemistry of the saline lakes (Koch-Steindl and PröHl, 2001; Strakhovenko and Gas'kovaet, 2018; Zhang et al., 2019; Chen et al., 2020; Francke et al., 2020; Zhao et al., 2020).

Applications to Paleoceanography

Global greenhouse gas warming controlled erosion processes are predicted to affect 61% of the ice-free landmasses during the 21st century, a number that increases to 80% when land use is considered (Ostberg et al., 2018). These processes have the potential to induce large variability in the weathering of the continents and the composition of chemical fluxes to the ocean. Seawater $[^{234}U/^{238}U]_{AR}$ provide global-scale information about continental weathering and are vital for marine uranium-series geochronology. Existing research suggests that the Atlantic $[^{234}U/^{238}U]_{AR}$ started to increase before major sea-level rise and overshot the modern value by 3‰ during early deglaciation. In addition $[^{234}U/^{238}U]_{AR}$ during deglacial times in the Pacific

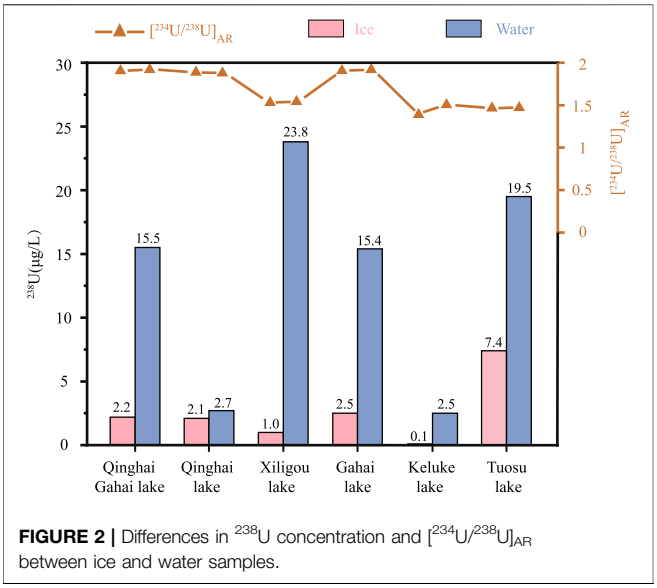

FIGURE 2 | Differences in ^{238}U concentration and $[^{234}U/^{238}U]_{AR}$ between ice and water samples.

Ocean converged with that in the Atlantic after the abrupt resumption of Atlantic meridional overturning circulation. This led Chen et al. (2016) to suggest that ocean mixing and early deglaciation released excess ^{234}U through the enhanced subglacial melting of the Northern Hemisphere ice sheets, and the change in ^{234}U has driven the observed evolution in $[^{234}U/^{238}U]_{AR}$. To assess the reliability of this hypothesis, it is necessary to evaluate the migration and transformation of ^{238}U concentration and the $[^{234}U/^{238}U]_{AR}$ during the transformation between ice and seawater of a given salinity and set of hydrochemical conditions. Therefore, we conducted this study to explore whether the freezing and thawing process of ice affects the U concentration and $[^{234}U/^{238}U]_{AR}$ in lake waters, which were easier to sample than waters in polar regions.

As shown in **Figure 2**, the ^{238}U concentration of the ice from the five lakes with varying salinity was approximately three to forty percent of the U content of the overlying water. Moreover, the lower the salinity, the lower the ratio of U in ice to the underlying water. The $[^{234}U/^{238}U]_{AR}$ between ice and water in the six lakes with varying salinity were similar and varied within a narrow range of about 2%. All exhibited lower $[^{234}U/^{238}U]_{AR}$ in ice than in the underlying water. In addition, the $[^{234}U/^{238}U]_{AR}$ observed during the inhouse freezing experiments of water from QHH supported the observations of the nature lake samples; differences in the ratios between ice and water in the three batches of samples did not change significantly as they were within the measurement error (**Figure 3**). In conclusion, the ^{238}U concentration and the $[^{234}U/^{238}U]_{AR}$ resulting from the indoor freeze-thaw experiments support the results of the field observations of the natural saline lake samples. The concentration of ^{238}U of seawater consistently varies by about 3.2 ppb between the Pacific and Atlantic Oceans (Chen et al., 1986). The ^{238}U concentration of ice possessed a lower concentration than that of water, and thus did not result in an observable change in the ^{238}U concentration of seawater.

These data show that the freezing and thawing process of ice does not cause $[^{234}U/^{238}U]_{AR}$ to change in the remaining water. Chen et al. (2016) did mention that other factors other than ice melting could be responsible for the increase $[^{234}U/^{238}U]_{AR}$. However, their main point was that the early deglacial release of excess ^{234}U drove the observed evolution in $[^{234}U/^{238}U]_{AR}$. If the increase of $[^{234}U/^{238}U]_{AR}$ was dependent on factors other than ice melting (e.g. the leaching of continental matter into the water), then the Pacific and Atlantic oceans at lower latitudes would have warmed faster, melted faster, and responded faster to the $[^{234}U/^{238}U]_{AR}$ change, which is not that the case.

To try to understand the cause of the above phenomenon, we first explored whether the freeze-thaw process of ice leads to an increase in the activity ratio of the water column using natural samples and inhouse freeze-thaw experiments. The preliminary results showed that the freezing and thawing process of ice does not cause $[^{234}U/^{238}U]_{AR}$ increase of the remaining water. Second, we explored whether the input of the river could increase the $[^{234}U/^{238}U]_{AR}$ of the remaining water. Current estimations of the average world river uranium concentration (0.3–0.6 μgl^{-1}) and $[^{234}U/^{238}U]_{AR}$ (1.2–1.3), combined with the diffusional ^{234}U influx from sediments (0.3 dpm cm^{-2} $10^{-3}yr^{-1}$), are essentially consistent with a model that depicts a steady state distribution of uranium in the ocean. However, the 0.3–0.6 μgl^{-1} values for river uranium may be an upper limit estimate (Ku et al., 1977). The ratios reported for global rivers ($[^{234}U/^{238}U]_{AR}$ = 1.171) (Chabaux et al., 2008) and the ratios of four rivers discharging into the Lake Qinghai catchment located in an arid alpine climate possessed $[^{234}U/^{238}U]_{AR}$ varying from 1.984 to 2.506 (Zhang et al., 2019). New Zealand rivers located in alpine high latitude regions exhibit a very wide range of $[^{234}U/^{238}U]_{AR}$, varying between 1.09 and 4.61 (Robinson et al., 2004). This

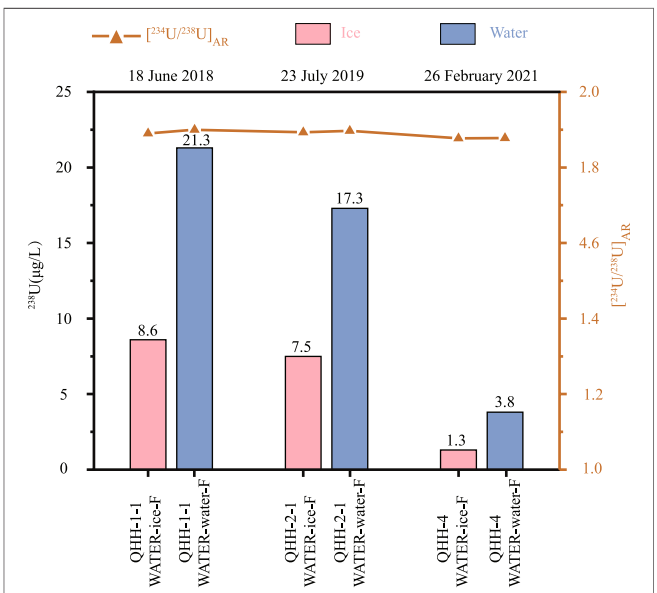

FIGURE 3 | Differences in ^{238}U concentration and $[^{234}U/^{238}U]_{AR}$ between ice and water obtained during the inhouse freezing experiments conducted on three batches of Qinghai Lake water samples.

range spans that previously measured in rivers from other locations. Based on the above $[^{234}U/^{238}U]_{AR}$ in river waters from low latitudes, and the ratios reported for global rivers ($[^{234}U/^{238}U]_{AR}$ = 1.171) (Chabaux et al., 2008), it would be difficult for low latitude riverine inputs to result in a 3 per mil increase in the $[^{234}U/^{238}U]_{AR}$ of sea water in the Pacific and Atlantic because of a higher $[^{234}U/^{238}U]_{AR}$ input of river. Thus, we speculate that the North Atlantic Ocean, which is also located at low latitudes, responds faster than the Pacific Ocean, most likely because the Arctic Ocean, located at high latitudes, carries inputs from five recharging rivers characterized by sandy and clay particle debris, then when the early deglaciation occurs. The inputs from rivers with high $[^{234}U/^{238}U]_{AR}$ leads to an increase in the $[^{234}U/^{238}U]_{AR}$ in the Arctic Ocean, which in turn affects the North Atlantic waters at low latitudes first and then affects the Pacific Ocean by way of the oceanic conveyor belt. Third, uranium is removed from the oceans by diffusion across the sediment-water interface of organic-rich sediments. This pathway is the largest single sink in the global budget of this element (Klinkhammer and Palmer, 1991). Dissolved uranium is drawn into suboxic sediments along a concentration gradient established by the precipitation of an insoluble phase which forms when U(VI) is reduced to U(IV) (Ku et al., 1977). Cowart (1980) measured the concentration of dissolved uranium and $[^{234}U/^{238}U]_{AR}$ were determined in water samples from 23 locations in the Edwards carbonate aquifer of south central Texas, and found that the $[^{234}U/^{238}U]_{AR}$ was about 1.20 in an oxidized aquifer, and above 2.0 in reduced aquifer. Thus, during deglaciation, there exists one possibility, the reduced seawater below the ice is mixed into the overlying seawater.

In summary, we suggest when early deglaciation occurs, the mixing of reduced seawater and/or the inputs from rivers with high $[^{234}U/^{238}U]_{AR}$ leads to an increase in the $[^{234}U/^{238}U]_{AR}$ in the Arctic Ocean, which in turn affects the North Atlantic waters at low latitudes first before influencing the Pacific Ocean by way of the oceanic conveyor belt. The specific reasons for this phenomenon need to be explored in future studies.

Based on the results of the in-house freezing experiments, there were differences in $[^{234}U/^{238}U]_{AR}$ in the ice and water sampled in February (winter) and July/September (summer); lower $[^{234}U/^{238}U]_{AR}$ values were measured in winter than in summer. However, there were no differences in $[^{234}U/^{238}U]_{AR}$ between the ice and water samples obtained in February (winter) (**Table 5**; **Figure 3**). Similar results were observed for the natural lake samples collected in winter and summer (**Table 4**, **Table 5**).

These results, combined with the limited ice volume in the Arctic, provide insights into the observed change in $[^{234}U/^{238}U]_{AR}$ in the Atlantic, which started to increase before major sea-level rise and overshot the modern value by 3‰ during early deglaciation. We speculate that the phenomenon may be due to a change in the redox conditions to a more oxidized state at the bottom of the water column during the early stages of deglaciation and/or from the inputs of river waters from high altitude regions that usually possess a higher activity ratio. Because at pH values and CO_2 concentrations typical of oxic seawater, the predominant uranium species, U(VI), is highly soluble and occurs as a stable carbonate ion complex, Ca/Mg-$UO^{2-}(CO_3)$ complexes (Djogić et al., 1986; Dong and Brooks, 2006; Chen et al., 2020). In contrast, in oxygen-depleted waters, rapid removal of U by the sediment depends on reduction of U(VI) to U(IV) (Tribovillard et al., 2006; Algco and Tribovillard, 2009). In addition, a large quantity of uranium in depositional archives is mostly bound to organic matter as demonstrated by weak to strong positive correlations between naturally occurring uranium and OM contents (Min et al., 2000; Regenspurg et al., 2010; Francke et al., 2020). Uranium can be mineralized in the presence of OM forming strong UO_2-OM bonds (Lenhart et al., 2000; Li et al., 2014). If the uranium bound to residual OM controls $[^{234}U/^{238}U]_{AR}$, then non-detrital uranium is usually characterized by values above 1. Thus, when polar ice melting is combined with the oxidation of the sea floor, the minerogenic U-OM bounds and/or U-carboxyl groups should be preferentially oxidized and released with higher $[^{234}U/^{238}U]_{AR}$. This hypothesis needs to be tested by further work.

The accurate evaluation of excess ^{234}U is important for marine uranium-series geochronology; thus, it is also necessary to investigate the causes of the variation in the $[^{234}U/^{238}U]_{AR}$ of seawater. For example, if the ^{234}U concentration of coral during glacial periods is about 3.2 ppm, and the initial $[^{234}U/^{238}U]_{AR}$ differs by 3‰, then the determined age will differ by thousands of years (Esat and Yokoyama, 2006).

Applications to Ancient Lakes

Previous studies of ^{238}U concentration and the $[^{234}U/^{238}U]_{AR}$ showed that there was no significant change between sampling sites in the same saline lake based on our published paper (Zhang et al., 2019; Zhao et al., 2020). There is also no evident difference between samples that were collected from a specific lake on different dates during the summer without ice coverage. Lake water samples collected during periods of maximum and minimum discharge have also been used to evaluate the seasonal variations in aqueous ^{238}U. We found that ^{238}U concentration did not change with the seasons in these saline lakes. If the ^{238}U concentration and the $[^{234}U/^{238}U]_{AR}$ remain consistent through time, then sediment ages and/or sedimentation rates can be determined from lake sediment and/or biogenic carbonate in the future, thus allowing for the accurate reconstruction of paleoclimatic and paleoenvironmental conditions.

Since the saline lakes in the Qaidam Basin and Qinghai region have a freezing period of about 3–4 months per year, it is necessary to determine whether the ^{238}U concentration and the $[^{234}U/^{238}U]_{AR}$ remain consistent. The results obtained herein show that differences in ^{238}U concentration existed between the ice and the underlying water in all sampled saline lakes and in fresh water. Significant differences in ^{238}U concentration occurred between winter ice and summer lake waters (without ice) that are significantly recharged by exogenous rivers, including TS, KLK, and QHH. Conversely, there was no significant differences in ^{238}U concentration between winter ice and summer waters (without ice) in saline lakes receiving less exogenous riverine inputs, including QHGH, XLG and GH [lake water data in summer were published in Zhang et al. (2019) and Zhao et al. (2020)]. Therefore, in the arid

Qaidam Basin and Qinghai region, the freeze-thaw process of ice does not appear to affect the concentration of ^{238}U in saline lakes, but the proportion of exogenously recharged water may affect its concentration. In addition, when ice exists with limited oxygen exchange with atmospheric, with the increase of water column, changes in the redox environment at the sediment-water interface may also affect the concentration of ^{238}U in the water column. Based on our results, the ^{238}U concentration in lacustrine sedimentary secondary carbonate minerals and the interannual resolution of biogenic carbonate shells are expected to provide useful insights into lake paleohydrological changes. The ^{238}U concentration of biogenic carbonate shells may possess a seasonal resolution that could reveal the redox environment at the water-sediment interface in QHH.

There were no significant differences in the $[^{234}U/^{238}U]_{AR}$ of the five saline lakes between ice and the underlying water when both were collected at the same time. The differences in the $[^{234}U/^{238}U]_{AR}$ were all within 2%, with lower $[^{234}U/^{238}U]_{AR}$ in ice. Except for QHGH, there were no significant differences (i.e., exceeding measurement error) in the $[^{234}U/^{238}U]_{AR}$ between winter ice and summer waters on various sampling dates. By contrast, there were significant differences in the $[^{234}U/^{238}U]_{AR}$ of lake waters between winter ice and summer waters in QHH, XLG, GH, TS and KLK (see Zhang et al. 2019; Zhao et al., 2020). The differences in U concentration and $[^{234}U/^{238}U]_{AR}$ in lake water between freezing and non-freezing seasons may be due to the influences of several factors such as surface runoff, groundwater and ice volume.

The study area of this paper is in an arid area of high altitude. Most of the lakes studied are closed saline lakes, and the area of surface runoff and underground recharge of these lakes are very limited. Taking Qinghai Lake as an example (which has the largest proportion of replenishment in the study area), the average water level is 3,193.2 m, the lake surface area is 4,260 km^2, and the lake water reserve is 71.593 billion m^3 (Liu, 2004). Using changes in calculated water volume from 1959 to 2000, the average annual surface water inflow to Qinghai Lake was 1.526 billion m^3. Precipitation on the lake surface contributed about 1.561 billion m^3 to the lake, and groundwater replenished 603 million m^3 of water to the lake (Liu, 2004). The ratio of precipitation over the lake surface to recharge for Qinghai Lake is the highest of the lakes studied. Zhu and Xie (2018) summarized the annual and seasonal precipitation of Qinghai Lake in different years during the past 50 years. The annual precipitation of Qinghai Lake was concentrated in summer and autumn, and the precipitation was the lowest in winter (Zhu and Xie, 2018). In the previous study, we selected samples collected in Qinghai Lake in different years with different precipitation patterns, and the experimental results showed that precipitation and surface runoff in Qinghai Lake had almost no effect on U content and $[^{234}U/^{238}U]_{AR}$ of the lake (**Table 7**). In 2020, we collected water from a river that recharged Qinghai Lake and groundwater near the recharge river and measured its U content and $[^{234}U/^{238}U]_{AR}$ (**Table 6**). The results showed that the effects of atmospheric precipitation, surface runoff and groundwater on U concentration and $[^{234}U/^{238}U]_{AR}$ of Qinghai Lake water were negligible. In addition, the samples studied in this paper were collected at the end of February, when the water in Qinghai Lake exhibited its maximum degree of ice cover. The average depth of Qinghai Lake is about 21m, and the average thickness of the ice sheet is about 29.4 cm. Only ~2% (by volume) of the surface water was frozen. Consequently, the limited volume of ice will not affect U concentration and $[^{234}U/^{238}U]_{AR}$ of the sampled saline lakes.

The ice freeze-thaw processes have almost no effect on the uranium content and $[^{234}U/^{238}U]_{AR}$ of the sampled saline lakes, which were characterized by a limited recharge volume from surface runoff, groundwater, and ice volume, namely the close saline lake in arid alpine background. An exception was U content in Qinghai Lake. We speculate that the low U concentration in the water column of Qinghai Lake during winter freezing is due to the 30 cm thick ice layer that prevents the infiltration of atmospheric oxygen, with the increase of depth of water column (~21 m). The ice-water interface resembles a redox interface, resulting in a low U content of the water column under the ice.

In summary, the freeze-thaw processes of the lake will not result in significant changes in $[^{234}U/^{238}U]_{AR}$ in excess of 2% in the water column of saline lakes. The $[^{234}U/^{238}U]_{AR}$ in these saline and freshwater lakes are closely related to the characteristics of the input water and the associated water–rock interactions involving sediments, atmospheric dust and organic material, among other factors during the evolution stage, metamorphous degree, and hydrochemistry of the saline lakes. Based on these results, we suggest that there is a potential to maintain relatively consistent levels of $[^{234}U/^{238}U]_{AR}$ in saline lakes characterized by a closed lake basin and which have a limited input of exogenous recharge water and limited organic matter. Usually, the $[^{234}U/^{238}U]_{AR}$ of dissolved water will increase when organic matter is present (Francke et al., 2020). The $[^{234}U/^{238}U]_{AR}$ of dissolved water from exogenously recharged water is usually above 1, increasing with an increase in latitude and altitude (Chabaux et al., 2008,2011; Zhang et al., 2019; Zhao et al., 2020). In such lake environments, lacustrine sedimentary secondary carbonate minerals and interannual biogenic carbonate shells are expected to provide data valuable for reconstructing lake chronologies.

CONCLUSION

Samples of ice and the underlying water from six lakes of differing salinity were collected for U composition analysis. These data were combined with the U composition determined for ice and water during inhouse freezing experiments conducted on three batches of water samples from QHH. The results show that there were no significant differences in the $[^{234}U/^{238}U]_{AR}$ of the five saline lakes between ice and the overlying water. The observed variations in $[^{234}U/^{238}U]_{AR}$ were all within 2%, with lower $[^{234}U/^{238}U]_{AR}$ in ice. The inhouse freezing experiments conducted on the three batches of QHH samples support the $[^{234}U/^{238}U]_{AR}$ results obtained from the natural samples. These preliminary data do not support the hypothesis presented in earlier publications that the deglacial release of excess ^{234}U from enhanced subglacial melting of the Northern Hemisphere ice sheets caused the

TABLE 7 | U isotope data from samples collected from Qinghai Lake in different years.

Location	Sample	Latitude (°N)	Longitude (°E)	^{238}U (μg/L)	Error (2s)	$[^{234}U/^{238}U]_{AR}$	Error (2s)	Date
Qinghai Lake	QHH-9-0	36°59′35″	100°05′22″	13.6	0.03	1.883	0.002	2017/9/10
	QHH-21-0	36°39′59″	100°37′18″	13.6	0.01	1.885	0.002	2017/9/17
	QHH-1-2-R	37°11′52″	99°48′34″	13.3	0.02	1.895	0.002	2018/6/18
	QHH-2-1	37°12′24″	99°50′16″	12.9	0.02	1.894	0.002	2019/7/23

observed increase in $^{234}U/^{238}U$ values by 3‰. We speculate that the phenomenon may be due to changes in redox water mixing during the onset of deglaciation and/or to the input of recharge waters from rivers located at high altitudes that usually possess a higher activity ratio. By comparing the data obtained herein with published $[^{234}U/^{238}U]_{AR}$ data from saline lakes sampled during the summer without ice coverage, we can speculate that there is a potential to maintain relatively consistent levels of $[^{234}U/^{238}U]_{AR}$ in saline lakes within closed lake basins, particularly those that possess limited organic material, and that are characterized by a limited influx of exogenous recharge water (e.g., GH). In such lake environments, lacustrine sediments containing secondary carbonate minerals and interannual biogenic carbonate shells are expected to be useful for reconstructing a lake chronology.

In addition, there was no significant difference in ^{238}U concentrations between winter ice and summer water in saline lakes with less exogenous river recharge and limited groundwater, including QHGH, XLG and GH. Thus, the ^{238}U concentration of lacustrine secondary carbonate minerals and interannual biogenic carbonate shells are expected to reveal lake paleohydrological changes in such parameters as the redox environment at the water-sediment interface.

DATA AVAILABILITY STATEMENT

The original contributions presented in the study are included in the article/supplementary material, further inquiries can be directed to the corresponding authors.

AUTHOR CONTRIBUTIONS

The research was supervised by PZ and XL with guidance provided by RE. Samples were collected by PZ, XP, CC, and XL. Experiment method was instructed by PZ, CC. The paper written by PZ with revised provided by LT, XL, YN, and RE. All authors have read and agreed to the published version of the manuscript.

FUNDING

This study was supported by the National Natural Science Foundation of China (No. 41873013, No. 41888101) and U.S. NSF (No. 1702816).

REFERENCES

Algeo, T. J., and Tribovillard, N. (2009). Environmental Analysis of Paleoceanographic Systems Based on Molybdenum–Uranium Covariation. *Chem. Geology.* 268 (3), 211–225. doi:10.1016/j.chemgeo.2009.09.001

Andersson, P. S., Porcelli, D., Gustafsson, Ö., Ingri, J., and Wasserburg, G. J. (2001). The Importance of Colloids for the Behavior of Uranium Isotopes in the Low-Salinity Zone of a Stable Estuary. *Geochimica Et Cosmochimica Acta* 65 (1), 13–25. doi:10.1016/s0016-7037(00)00514-7

Belli, K. M., DiChristina, T. J., Van Cappellen, P., and Taillefert, M. (2015). Effects of Aqueous Uranyl Speciation on the Kinetics of Microbial Uranium Reduction. *Geochimica et Cosmochimica Acta* 157 (15), 109–124. doi:10.1016/j.gca.2015.02.006

Bian, Q., Liu, J., Luo, X., Xiao, J., and Levshin, A. (2000). Geotectonic Setting, Formation and Evolution of the Qinghai Lake. *Seismology Geology.* 22 (1), 20–26.

Borole, D. V., Krishnaswami, S., and Somayajulu, B. L. K. (1982). Uranium Isotopes in Rivers, Estuaries and Adjacent Coastal Sediments of Western India: Their Weathering, Transport and Oceanic Budget. *Geochimica Et Cosmochimica Acta* 46 (2), 125–137. doi:10.1016/0016-7037(82)90240-x

Cazenave, A., Meyssignac, B., Ablain, M., Balmaseda, M., Bamber, J., Barletta, V., et al. (2018). Global Sea-Level Budget 1993-present. *Earth Syst. Sci. Data* 10 (3), 1551–1590. doi:10.5194/ESSD-10-1551-2018

Chabaux, F., Bourdon, B., and Riotte, J. (2008). Chapter 3 U-Series Geochemistry in Weathering Profiles, River Waters and Lakes. *J. Environ. radioactivity* 13, 49–104. doi:10.1016/S1569-4860(07)00003-4

Chabaux, F., Granet, M., Larqué, P., Riotte, J., Skliarov, E. V., Skliarova, O., et al. (2011). Geochemical and Isotopic (Sr, U) Variations of lake Waters in the Ol'khon Region, Siberia, Russia: Origin and Paleoenvironmental Implications. *Comptes Rendus Geosci.* 343, 462–470. doi:10.1016/j.crte.2011.07.004

Chen, J. H., Edwards, R. L., and Wasserburg, G. J. (1986). ^{238}U, ^{234}U and ^{232}Th in Seawater. *Earth Planet. Sci. Lett.* 80 (3-4), 241–251. doi:10.1016/0012-821x(86)90108-1

Chen, T., Robinson, L. F., Beasley, M. P., Claxton, L. M., Andersen, M. B., Gregoire, L. J., et al. (2016). Ocean Mixing and Ice-Sheet Control of Seawater 234U/238U during the Last Deglaciation. *Science* 354 (6312), 626–629. doi:10.1126/science.aag1015

Chen, X., Zheng, W., and Anbar, A. D. (2020). Uranium Isotope Fractionation (238U/235U) during U(VI) Uptake by Freshwater Plankton. *Environ. Sci. Technol.* 54, 2744–2752. doi:10.1021/acs.est.9b06421

Chen, Z. L., Mallavarapu, M., and Naidu, R. (2007). Determination of Bromate and Bromide in Seawater by Ion Chromatography, with an Ammonium Salt Solution as mobile Phase, and Inductively Coupled Plasma Mass Spectrometry. *Chromatographia* 65 (1-2), 115–118. doi:10.1365/s10337-006-0128-z

Cheng, H., Edwards, R. L., Hoff, J., Gallup, C. D., Richards, D. A., and Asmerom, Y. (2000). The Half-Lives of Uranium-234 and Thorium-230. *Chem. Geology.* 169 (1-2), 17–33. doi:10.1016/s0009-2541(99)00157-6

Cheng, H., Lawrence Edwards, R., Shen, C.-C., Polyak, V. J., Asmerom, Y., Woodhead, J., et al. (20132013). Improvements in 230Th Dating, 230Th and 234U Half-Life Values, and U-Th Isotopic Measurements by Multi-Collector Inductively Coupled Plasma Mass Spectrometry. *Earth Planet. Sci. Lett.* 371-372, 82–91. doi:10.1016/j.epsl.2013.04.006

Colman, S. M., Yu, S. Y., An, Z., Shen, J., and Henderson, A. C. G. (2007). Late Cenozoic Climate Changes in China's Western interior: A Review of Research on Lake Qinghai and Comparison with Other Records. *Quat. Sci. Rev.* 26 (2007), 2281–2300. doi:10.1016/j.quascirev.2007.05.002

Cowart, J. B. (1980). The Relationship of Uranium Isotopes to Oxidation/reduction in the Edwards Carbonate Aquifer of Texas. *Earth Planet. Sci. Lett.* 48, 277–283. doi:10.1016/0012-821x(80)90191-0

Desbruyères, D. G., Purkey, S. G., Mcdonagh, E. L., Johnson, G. C., and King, B. A. (2016). Deep and Abyssal Ocean Warming from 35years of Repeat Hydrography. *Geophys. Res. Lett.* 43 (19), 10,356–10,365. doi:10.1002/2016gl070413

Djogić, R., Sipos, L., and Branica, M. (1986). Characterization of Uranium(VI) in Seawater1. *Limnol. Oceanogr.* 31 (5), 1122–1131. doi:10.4319/lo.1986.31.5.1122

Dong, W., and Brooks, S. C. (2006). Determination of the Formation Constants of Ternary Complexes of Uranyl and Carbonate with Alkaline Earth Metals (Mg2+, Ca2+, Sr2+, and Ba2+) Using Anion Exchange Method. *Environ. Sci. Technol.* 40 (15), 4689–4695. doi:10.1021/es0606327

Esat, T. M., and Yokoyama, Y. (2006). Variability in the Uranium Isotopic Composition of the Oceans over Glacial-Interglacial Timescales. *Geochimica et Cosmochimica Acta* 70 (16), 4140–4150. doi:10.1016/j.gca.2006.06.013

Francis, J. A., Vavrus, S. J., and Cohen, J. (2017). Amplified Arctic Warming and Mid-latitude Weather: New Perspectives on Emerging Connections. *Wiley Interdiscip. Rev. Clim. Change* 8 (5), e474. doi:10.1002/wcc.474

Francke, A., Dosseto, A., Just, J., Wagner, B., and Jones, B. G. (2020). Assessment of the Controls on (234U/238U) Activity Ratios Recorded in Detrital Lacustrine Sediments. *Chem. Geology.* 550, 119698. doi:10.1016/j.chemgeo.2020.119698

Fredrickson, J. K., Zachara, J. M., Kennedy, D. W., Liu, C., Duff, M. C., Hunter, D. B., et al. (2002). Influence of Mn Oxides on the Reduction of Uranium(VI) by the Metal-Reducing Bacterium Shewanella Putrefaciens. *Geochimica et Cosmochimica Acta* 66 (18), 3247–3262. doi:10.1016/s0016-7037(02)00928-6

Gulev, S., Thorne, P., Ahn, J., Dentener, F., Domingues, C., Gerland, S., et al. (2021). *Climate Change 2021: The Physical Science Basis. Contribution of Working Group I to the Sixth Assessment Report of the Intergovernmental Panel on Climate Change*. UK: Cambridge University Press.

Han, T. F., Qi, D. L., Chen, H. S., Xiang, S. G., Shi, X. Y., Liu, C. F., et al. (2019). Temporal and Spatial Distribution Characteristics of Precipitation in Qaidam Basin. *Desert and Oasis Meteorology* 013 (002), 69–75. (in Chinese).

Hansen, J., Ruedy, R., Sato, M., and Lo, K. (2010). Global Surface Temperature Change. *Rev. Geophys.* 48 (4), RG4004. doi:10.1029/2010RG000345

Huang, Q., and Han, F. Q. (2007). *Salt Lake Evolution and Paleoclimate Fluctuations in Qaidam Basin*. Beijing: Science Press. (in Chinese).

Jin, Z., You, C.-F., Yu, T.-L., and Wang, B.-S. (2010). Sources and Flux of Trace Elements in River Water Collected from the Lake Qinghai Catchment, NE Tibetan Plateau. *Appl. Geochem.* 25 (10), 1536–1546. doi:10.1016/j.apgeochem.2010.08.004

Jin, Z., Yu, J., Wang, S., Zhang, F., Shi, Y., and You, C.-F. (2009). Constraints on Water Chemistry by Chemical Weathering in the Lake Qinghai Catchment, Northeastern Tibetan Plateau (China): Clues from Sr and its Isotopic Geochemistry. *Hydrogeol J.* 17 (8), 2037–2048. doi:10.1007/s10040-009-0480-9

Klinkhammer, G. P., and Palmer, M. R. (1991). Uranium in the Oceans: Where it Goes and Why. *Geochimica et Cosmochimica Acta* 55, 1799–1806. doi:10.1016/0016-7037(91)90024-y

Koch-Steindl, H., and Pröhl, G. (2001). Considerations on the Behaviour of Long-Lived Radionuclides in the Soil. *Radiat. Environ. Biophys.* 40 (2), 93–104. doi:10.1007/s004110100098

Ku, T.-L., Mathieu, G. G., and Knauss, K. G. (1977). Uranium in Open Ocean: Concentration and Isotopic Composition. *Deep Sea Res.* 24 (11), 1005–1017. doi:10.1016/0146-6291(77)90571-9

Lavergne, T., Sørensen, A. M., Kern, S., Tonboe, R., Notz, D., Aaboe, S., et al. (2019). Version 2 of the EUMETSAT OSI SAF and ESA CCI Sea-Ice Concentration Climate Data Records. *The Cryosphere* 13 (1), 49–78. doi:10.5194/tc-13-49-2019

Lenhart, J. J., Cabaniss, S. E., MacCarthy, P., and Honeyman, B. D. (2000). Uranium(VI) Complexation with Citric, Humic and Fulvic Acids. *Radiochimica Acta* 88 (6), 345–354. doi:10.1524/ract.2000.88.6.345

Li, P., Xu, Z. Q., Wang, Y., and Wang, P. C. (2014). The Relationships between Uranium Mineralization and Organic Matter in 373 Uranium deposit. *Amr* 962-965, 203–207. doi:10.4028/www.scientific.net/amr.962-965.203

Liu, X. Y. (2004). Hydrological Characteristics of Qinghai Lake Basin. *J. China Hydrol.* 24 (002), 60–61. (in Chinese).

Min, M.-Z., Meng, Z.-W., Sheng, G.-Y., Min, Y.-S., and Liu, X. (2000). Organic Geochemistry of Paleokarst-Hosted Uranium Deposits, South China. *J. Geochemical Exploration* 68 (3), 211–229. doi:10.1016/s0375-6742(99)00085-0

Moran, S. B., Ellis, K. M., and Smith, J. N. (1997). 234Th/238U Disequilibrium in the central Arctic Ocean: Implications for Particulate Organic Carbon export. *Deep Sea Res. Part Topical Stud. Oceanography* 44 (8), 1593–1606. doi:10.1016/s0967-0645(97)00049-0

Osmond, J. K., Kaufman, M. I., and Cowart, J. B. (1974). Mixing Volume Calculations, Sources and Aging Trends of Floridan Aquifer Water by Uranium Isotopic Methods. *Geochimica Et Cosmochimica Acta* 38 (7), 1083–1100. doi:10.1016/0016-7037(74)90006-4

Ostberg, S., Boysen, L., Schaphoff, S., Lucht, W., and Gerten, D. (2018). The Biosphere under Potential Paris Outcomes. *Earth's Future* 6 (4), 23–39. doi:10.1002/2017ef000628

Regenspurg, S., Margot-Roquier, C., Harfouche, M., Froidevaux, P., Steinmann, P., Junier, P., et al. (2010). Speciation of Naturally-Accumulated Uranium in an Organic-Rich Soil of an alpine Region (Switzerland). *Geochimica et Cosmochimica Acta* 74 (7), 2082–2098. doi:10.1016/j.gca.2010.01.007

Rengarajan, R., Sarin, M. M., and Krishnaswami, S. (2003). Uranium in the Arabian Sea: Role of Denitrification in Controlling its Distribution. *Oceanologica Acta* 26 (5-6), 687–693. doi:10.1016/j.oceact.2003.05.001

Robinson, L. F., Henderson, G. M., Hall, L., and Matthews, I. (2004). Climatic Control of Riverine and Seawater Uranium-Isotope Ratios. *Science* 305 (5685), 851–854. doi:10.1126/science.1099673

Sarin, M. M., and Church, T. M. (1994). Behaviour of Uranium during Mixing in the Delaware and Chesapeake Estuaries. *Estuarine, Coastal Shelf Sci.* 39 (6), 619–631. doi:10.1016/s0272-7714(06)80013-2

Schmidt, S. (2006). Impact of the Mediterranean Outflow Water on Particle Dynamics in Intermediate Waters of the Northeast Atlantic, as Revealed by ^{234}Th and ^{228}Th. *Mar. Chem.* 100 (4), 289–298. doi:10.1016/j.marchem.2005.10.017

Scientific, T. (2016). *Dionex Aquion Ion Chromatography System Installation Instructions*. Waltham, MA, USA: Thermo Scientific Press.

Shen, C.-C., Wu, C.-C., Cheng, H., Lawrence Edwards, R., Hsieh, Y.-T., Gallet, S., et al. (2012). High-precision and High-Resolution Carbonate 230Th Dating by MC-ICP-MS with SEM Protocols. *Geochimica et Cosmochimica Acta* 99, 71–86. doi:10.1016/j.gca.2012.09.018

Shen, C. C., Edwards, R. L., Cheng, H., Dorale, J. A., Thomas, R. B., Moran, S. B., et al. (2002). Uranium and Thorium Isotopic and Concentration Measurements by Magnetic Sector Inductively Coupled Plasma Mass Spectrometry. *Chem. Geology.* 185 (3), 165–178. doi:10.1016/s0009-2541(01)00404-1

Strakhovenko, V. D., and Gas'kova, O. L. (2018). Thermodynamic Model of Formation of Carbonates and Uranium mineral Phases in Lakes Namshi-Nur and Tsagan-Tyrm (Cisbaikalia). *Russ. Geology. Geophys.* 59, 374–385. doi:10.1016/j.rgg.2017.05.002

Tierney, J. E., Poulsen, C. J., Montañez, I. P., Bhattacharya, T., Feng, R., Ford, H. L., et al. (2020). Past Climates Inform Our Future. *Science* 370 (6517). doi:10.1126/science.aay3701

Trewin, B., Cazenave, A., Howell, S. E. L., Huss, M., Isensee, K., Palmer, M. D., et al. (2020). Headline Indicators for Global Climate Monitoring. *Bull. Am. Meteorol. Soc. preprint* 102 (1), E20–E37. doi:10.1175/bams-d-19-0196.1

Tribovillard, N., Algeo, T. J., Lyons, T., and Riboulleau, A. (2006). Trace Metals as Paleoredox and Paleoproductivity Proxies: An Update. *Chem. Geology.* 232 (1-2), 12–32. doi:10.1016/j.chemgeo.2006.02.012

Velicogna, I., Mohajerani, Y., Geruo, A., Landerer, F., Mouginot, J., Noel, B., et al. (2020). Continuity of Ice Sheet Mass Loss in Greenland and Antarctica from the GRACE and GRACE Follow-On Missions. *Geophys. Res. Lett.* 47 (8), e2020GL087291. doi:10.1029/2020gl087291

Yadav, D. N., and Sarin, M. M. (2009). Geo-chemical Behavior of Uranium in the Sambhar Salt Lake, Rajasthan (India): Implications to "Source" of Salt and Uranium "Sink". *Aquat. Geochem.* 15 (4), 529–545. doi:10.1007/s10498-009-9066-3

Zhang, P., Cheng, H., Liu, W. G., Mo, L. T., Li, X. Z., Ning, Y. F., et al. (2019). Geochemical and Isotopic (U, Th) Variations in lake Waters in the Qinghai Lake Basin, Northeast Qinghai-Tibet Plateau, China: Origin and Paleoenvironmental Implications. *Arabian J. Geosciences* 12 (3). doi:10.1007/s12517-019-4255-x

Zhang, P. X., Zhang, B. Z., Qian, G. M., Li, H. J., and Xu, L. M. (1994). The Study of Paleoclimatic Parameter of Qinghai Lake since Holocene. *Quat. Sci.* 14 (3), 225–238.

Zhao, C., Zhang, P., Li, X., Ning, Y., Tan, L., Edwards, R. L., et al. (2020). Distribution Characteristics and Influencing Factors of Uranium Isotopes in saline Lake Waters in the Northeast of Qaidam Basin. *Minerals* 10 (1), 74. doi:10.3390/min10010074

Zheng, X. Y., and Zhang, M. G. (2002). *China Salt Lake*. Beijing: Science Press.

Zhu, B. W., and Xie, Q. Y. (2018). Characteristics of Precipitation Changes in the Area Around Qinghai Lake in the Past 50 Years. *Sci. Technology Qinghai Agric. For.* 47(4), 5, 2018 . (in Chinese).

Conflict of Interest: The authors declare that the research was conducted in the absence of any commercial or financial relationships that could be construed as a potential conflict of interest.

Publisher's Note: All claims expressed in this article are solely those of the authors and do not necessarily represent those of their affiliated organizations, or those of the publisher, the editors, and the reviewers. Any product that may be evaluated in this article, or claim that may be made by its manufacturer, is not guaranteed or endorsed by the publisher.

frontiers | Frontiers in Earth Science

ORIGINAL RESEARCH
published: 11 April 2022
doi: 10.3389/feart.2022.866314

A Novel Tracer Technique to Quantify the Lithogenic Input Flux of Trace Elements to Qinghai Lake

Pu Zhang[1,2], Xuezheng Pei[2], Chenyang Cao[2], Chi Chen[1], Ziqin Gong[1], Xuerou Li[1], Jingya Pang[1], Lihua Liang[2], Xiangzhong Li[3]*, Youfeng Ning[1] and R.Lawrence Edwards[4]*

[1]Institute of Global Environmental Change, Xi'an Jiao Tong University, Xi'an, China, [2]College of Urban and Environmental Sciences, Northwest University, Xi'an, China, [3]Yunnan Key Laboratory of Earth System Science, Yunnan University, Kunming, China, [4]Department of Earth and Environmental Sciences, University of Minnesota, Minneapolis, MN, United States

OPEN ACCESS

Edited by:
Mao-Yong He,
Institute of Earth Environment (CAS), China

Reviewed by:
Yibo Yang,
Institute of Tibetan Plateau Research (CAS), China
Dejun Wan,
Nantong University, China
Junsheng Nie,
Lanzhou University, China

***Correspondence:**
Pu Zhang
zhangpu357@xjtu.edu.cn
Xiangzhong Li
xzhli04@163.com

Specialty section:
This article was submitted to Geochemistry, a section of the journal Frontiers in Earth Science

Received: 31 January 2022
Accepted: 15 March 2022
Published: 11 April 2022

Citation:
Zhang P, Pei X, Cao C, Chen C, Gong Z, Li X, Pang J, Liang L, Li X, Ning Y and Edwards RL (2022) A Novel Tracer Technique to Quantify the Lithogenic Input Flux of Trace Elements to Qinghai Lake. Front. Earth Sci. 10:866314. doi: 10.3389/feart.2022.866314

Thorium (Th) isotopes were applied to quantify the contributions of lithogenic inputs to the Qinghai Lake (QHH). Concentrations of dissolved ^{232}Th and ^{230}Th were measured in 59 water samples collected from Qinghai Lake and its exogenous recharge rivers. There are significant differences in the concentration of ^{232}Th of the sampled water in QHH that confirm the input of variable lithogenic material sources. The ^{230}Th concentrations were used to calculate a scavenging residence time for Th, which was then applied to calculate the flux of dissolved ^{232}Th by matching the measured concentrations of dissolved ^{232}Th. Then the ^{232}Th content of lithogenic material was used with the solubility of Th from the preliminary particle data from the Qinghai–Qaidam district. When using a Th solubility from particles of 1%, the fluxes of lithogenic material range from 0.03 to 25.25 g/m^2/yr in the surface water, consistent with the flux results of settled particles from the previous study. When a large number of exogenous recharge rivers are mixed into the northwest basin of Qinghai Lake, the ^{232}Th content and lithogenic flux of the lake water are mainly influenced by the type and content of the particles in the Buha and Shaliu rivers. Conversely, in south basin with limited recharging rivers, the ^{232}Th content of the lake water away from the estuary is mainly influenced by atmospheric dust. Furthermore, based on the ^{230}Th normalization method (combining with ^{232}Th and τ_{Th}), the Buha and Shaliu rivers located in the northwest basin contribute about 90% of the detrital flux to the lake. The lithogenic flux in the southeast lake is dominated by dust flux with a value of ~0.109 g/m^2/yr, while the higher lithogenic flux at the bottom of the lake was likely generated by accumulated sinking particulate matter and resuspension of bottom sediments in September. This study confirms the utility of long-lived Th isotopes to quantify lithogenic inputs based on the Th content of the dissolved lake water and also supply deposition resolution information for QHH sediment records with some certainty.

Keywords: ^{232}Th content, ^{230}Th normalization technique, lithogenic flux, dust flux, Qinghai Lake

INTRODUCTION

As an important component of atmospheric aerosols, dust has a significant impact on the Earth's climate system, biogeochemical cycle, water cycle, and human health. Dust plays a role in different components of the climate by influencing the radiative balance and thus the energy balance of the Earth's system. Dust can also act as cloud condensation nuclei, altering the hydrological cycle by changing cloud cover and microphysics (Jickells et al., 2005; Ding et al., 2009). The dust cycle is an important component of the Earth system, and the arid and semi-arid zones of Central Asia are one of the key regions for global change research due to their vast area and the huge amount of dust they provide (800 Tg of dust is delivered to the atmosphere each year in northwest China alone; Zhang et al., 1997). In addition, dust can also act as an exogenous source of nutrients to marine and remote terrestrial ecosystems, participating in carbon cycle processes (Martin and Fitzwater, 1988; Jickells et al., 2005). In recent years, the mechanisms of dust release and transport have become a hot topic of interest for both modern climatology and paleoclimatology. In this regard, changes in dust fluxes not only depend on regional climate changes but also can influence them in various ways, thus making dust fluxes one of the key elements in the exploration of regional climate environments (Cruz et al., 2021).

The traditional approach to calculating lake burial fluxes relies on determining the average mass accumulation rates based on age model tie points, intervening sediment thickness, and average sediment dry bulk density (Lyle and Dymond, 1976; DeMaster, 1981; Curry and Lohmann, 1986; Lyle et al., 1988; Rea and Leinen, 1988; Sarnthein et al., 1988; Mortlock et al., 1991). The temporal resolution of this approach is limited by the robustness of the age model, including the number of chronological tie points and their associated errors (Francois et al., 2004). Furthermore, this approach can easily be biased by sediment redistribution on the edge of the lake with river input, where sediment transport from the river can exceed the vertical rain of particles from the water column. As a result, constant flux proxies such as the ^{230}Th normalization technique have the potential to be developed, providing more robust estimates of mass accumulation in the lake sediment. Constant flux proxies are geochemical parameters with well-constrained and stable source functions, such as ^{230}Th (Bacon, 1984; Francois et al., 2004) and ^{3}He (Marcantonio et al., 1996; Winckler et al., 2004; McGee and Mukhopadhyay, 2013). The U concentration of saline lakes in the alpine arid background is stable (Zhang et al., 2019; Zhao et al., 2020; Zhang et al., 2021). Furthermore, ^{230}Th is produced by the steady decay of uranium dissolved in lake water, after which it is rapidly eliminated by sinking particles and buried by the lake sediment (Francois et al., 2004; Zhang et al., 2019). Because the ^{230}Th production rate is relatively uniform in space and time, variability in ^{230}Th concentrations in the sediment can be theoretically attributed to variable dilution by changes in sediment mass flux over time. This technique, ^{230}Th normalization, allows both high-resolution sediment mass flux reconstructions independent of age model tie points and isolation of only the vertical component of sedimentation, regardless of the amount of lateral sediment transport from rivers.

The different isotopes of Th provide important information about the various processes occurring in the ocean. In seawater, Th has a stable IV oxidation state, which makes it highly particle reactive (Santschi et al., 2006); readily transports from the water column to particulate matter; and is buried in the underlying sediments as the particulate matter settles (Bourdon et al., 2003). Th isotopes have a very limited source in the lake environment, in which ^{232}Th accounts for about 99.98% of all natural Th isotopes, and it is obtained almost exclusively through dissolution of river, wind, and lake sediments (Krishnaswami and Cochran, 2016), while ^{234}Th, ^{230}Th, and ^{228}Th are derived from the α radioactive decay of ^{238}U, ^{234}U, and ^{228}Ra in the ocean, respectively (Ojovan and Lee, 2014). The production rates of ^{234}Th and ^{230}Th have remained essentially stable since the reserves of U nuclides and their isotopic compositions in the saline have remained essentially stable over years (Zhang et al., 2019). The combination of particle reactivity and constrained sources makes Th isotopes one of the most versatile tools for studying particle fluxes in the ocean and sedimentary record (Costa and McManus, 2017). Under stable conditions, the residence time of Th was obtained based on the production rate of ^{232}Th in the water column. The residence time combined with the storage of ^{230}Th obtained the flux of ^{232}Th (e.g., the ^{230}Th normalization technique), which in turn was extrapolated to the flux of terrestrial or atmospheric deposition (Hayes et al., 2013).

The Qinghai–Tibet Plateau in the midlatitudes is the largest plateau in the world with the highest average altitude and is sensitive to global climate change due to the interplay of westerly winds and Asian summer winds, as well as feedbacks to atmospheric circulation and hydrological processes in the surrounding areas. Therefore, it has received much attention from researchers, and its concept as the "third pole of the earth" has been widely accepted. There are many lakes on the Qinghai–Tibet Plateau, and many of them record rich information on environmental changes at different spatial and temporal scales and are windows for research on past environmental changes. The Qinghai Lake basin is located at the confluence of the eastern monsoon region of China, the northwest arid region, and the alpine region of the Qinghai–Tibet Plateau, with distinct regional climatic characteristics, and is one of the most sensitive areas to global climate change, playing a crucial role in maintaining the regional hydrological cycle. With the expansion and in-depth study of the sedimentary environment of Qinghai Lake, more and more discussions have been made on the depositional flux or rate. However, due to the different methods or sampling points, the deposition fluxes obtained by different researchers vary greatly (Jin et al., 2009a; Xu et al., 2010; Wan et al., 2012). Little attempt has been made to define the chemical budget and mass balance of the $CaCO_3$-rich sediments in Lake Qinghai, which are the basis of paleoenvironmental and paleoclimatic reconstructions using lake sediments. The results from the Lake Qinghai River system in the northeastern Tibetan Plateau suggest that atmospheric dust contributes 36–57% of the total dissolved cations to the river waters and further into Qinghai Lake (Zhang et al., 2009).

Previous studies have confirmed that the contribution of atmospheric dust input to the elemental reservoir of Lake Qinghai water is up to about 65% based on the suspended particulate matter of the Buha River (Jin et al., 2009a). The soluble element content of lake waters is controlled by the variation of the elemental content of exogenously recharged river waters (Jin et al., 2009b). For studying the input–output budget characteristics, Qinghai Lake is uniquely positioned geographically to quantify the flux of Th and explore its potential to respond to environmental changes, thus providing more basic research information for subsequent evaluation of whether the U-series disequilibrium characteristics of lake sediments can provide the basin's paleo-weathering history.

In view of this, the study first attempts to obtain the water residence time of Qinghai Lake by assessing the ^{230}Th–^{234}U disequilibrium; second, by investigating the surface distribution characteristics of ^{232}Th concentration in the lake water column of Qinghai Lake and the recharging river and water column of the entire lake transect, we try to explore the source of ^{232}Th and the variation of lithogenic flux in the water column of Qinghai Lake, and understand its potential to the response of the environmental changes. To a certain extent, this will fill the gap in the revenue and expenditure characteristics of ^{230}Th and ^{232}Th and their geochemical significance in the lake domain and also be an important reference for understanding the ^{230}Th-indicated paleo-oceanic processes in marine sediments.

MATERIALS AND METHODS

Sampling Locations

Qinghai Lake (36°32′–37°15′N; 99°36′–100°47′E) is located in the northeastern part of the Qinghai–Tibet Plateau, with a length of about 109 km from east to west and a width of about 39.8 km from north to south, and an average water depth of 18.3 m. It is the largest inland saline lake in China. The geological and geographical environment and the current climate of this area have been examined in detail by Colman et al. (2007) and Jin et al. (2010). Qinghai Lake is developed within a basin surrounded by three mountain ranges, including Datong Mountain to the north, Riyue Mountain to the east, and the Qinghai Nanshan Mountains to the south (Bian et al., 2000). The lake is divided into two nearly equal sub-basins by an NNW-trending horst, from which an island (Mt. Haixin) emerges. Several minor fault scarps can also be found in the lake basin. The lake bed is generally flat, and the lake is hydrologically closed and evaporative (Zhang et al., 1994). The six largest rivers on the order of discharge inside the Lake Qinghai catchment are Buha, Shaliu, Hargai, Quanji, Daotang, and Heima rivers. These rivers are greatly impacted by the hydrological cycle linked to the area's monsoonal climate, and they supply over 87% of the water (Li et al., 2007), ~67% of the dissolved load (Jin et al., 2009a), and sediment discharge to the lake. Over half of these rivers start from the Buha River, whose water chemistry is affected by the underlain marine limestone and sandstones, which constrain carbonate-dominated compositions of the lake water (Jin et al., 2009b). Meltwater from surrounding mountain glaciers accounts for only 0.3% of the total runoff (Colman et al., 2007).

Qinghai Lake is a typically closed saline lake, and there is no output of surface water from the lake. The lake's recharge water is mainly the recharging rivers, followed by natural precipitation and groundwater. There are more than 70 rivers of various sizes flowing into the lake, with an obvious asymmetrical distribution, the northwestern part being relatively large and having a high runoff volume, while the southeastern part is sparse and mostly seasonal. The runoff of the rivers is unevenly distributed within the year, with July to September having the highest runoff, accounting for 60%–80% of the total annual runoff, and January to February has the lowest runoff, accounting for only about 1% of the total annual runoff. Qinghai Lake receives its annual runoff recharge mainly from seven rivers, including the Buha, Shaliu, Hargai, Quanji, Ganzi, Daotang, and Heima rivers. The total annual runoff is about 2.5 billion m^3, and the main rivers have a total annual runoff of about 2.2 billion m^3, accounting for 90% of the total runoff in the basin.

The Buha River is the largest exogenous recharge river in the Qinghai Lake basin, with a total length of 286 km, a basin area of 14,387 km^2, an average multi-year runoff of 7.85×10^8 m^3, and a contribution of 46.9% of the runoff into the lake. The Shaliu River is the second largest recharge river in the Qinghai Lake basin, with a total length of about 106 km and a basin area of 1, 500 km^2, with an average annual runoff of 2.46×10^8 m^3, accounting for 14.5% of the total runoff into the lake. The third largest recharge river in the basin is the Hargai River. The Buha River, Shaliu River, and Hargai River account for more than 75% of the total runoff into the lake. Apart from these, the rest of the recharge rivers are relatively small in terms of basin area and average annual runoff and are mostly seasonal rivers that dry up seasonally (the Quanji River is 65 km long and has a basin area of 567 km^2, the Daotang River is 60 km long and has a basin area of 727 km^2, the Heima River is 17.2 km long and has a basin area of 107 km^2, and the Ganzi River does not directly drain into Qinghai Lake but is surface runoff, which is submerged underground and then partly fed into the lake as groundwater). It is worth noting that the Daotang River is the only river in the Qinghai Lake basin that flows in a southeast to northwest direction.

Sampling Design and Methods

The water samples collected include Qinghai Lake and its exogenous recharge rivers. Among the recharge rivers, the Buha River, Shaliu River, Hargai River, and Daotang River were selected as the main study areas in view of the influence of various factors, such as the contribution rate of runoff from exogenous recharge rivers, the lithology control of the basins, and the seasonal differences of rivers. Due to the lack of seasonal water during the sampling period, no samples were collected from the Quanji River or the Heima River.

A sampling of the water samples required for the study continued from 2017 to 2020 and can be divided into four batches. In the first sampling batch, water samples were collected from Qinghai Lake in September 2017. The subsequent batches mainly sampled the duplicate samples from Qinghai Lake and the water samples from the exogenous

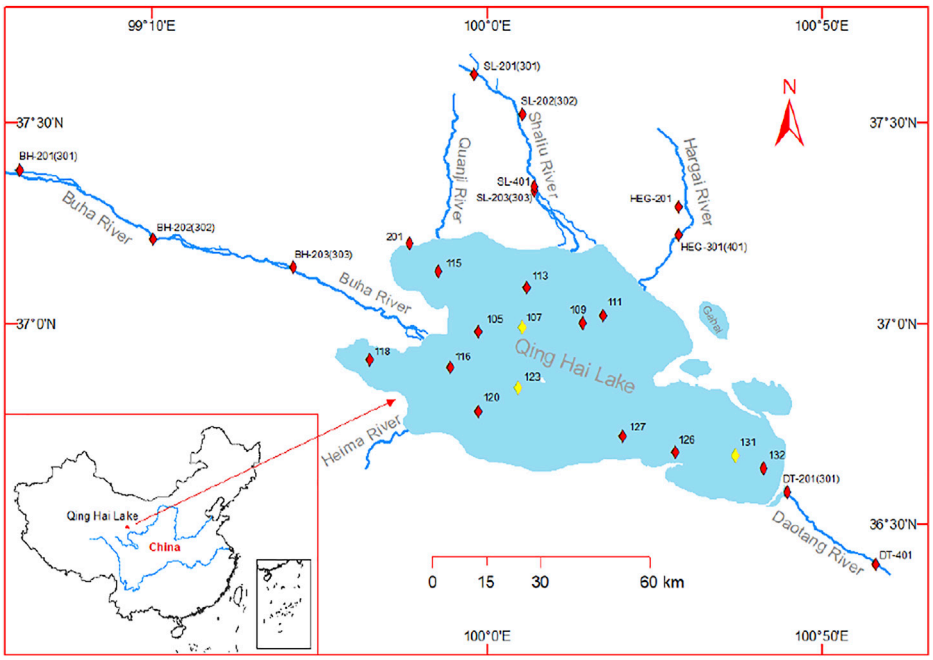

FIGURE 1 | Map showing the locations of the sampled lakes and rivers in the Qinghai region. (Red diamonds represent surface sites and yellow diamonds represent depth profiles).

recharge rivers of Qinghai Lake in June 2018, August 2019, and November 2020.

In the first batch, a total of 14 sampling sites were set up to sample the waters of Qinghai Lake, with a sampling range of 36°38′25″~37°07′52″N, 99°42′48″~100°41′23″E. Among them, three sampling sites took water samples from the surface layer (~0.2 m) to the bottom layer of the lake at 3-m intervals, while the remaining nine sampling sites collected water samples from the surface layer of the lake only. One surface water sample was also taken during the second batch of sampling, and a total of 40 samples were collected from Qinghai Lake. The second, third, and fourth batches of water samples were collected from the exogenous recharge rivers of Qinghai Lake, including 13 samples from the upper, middle, and lower reaches of the Buha River and Shaliu River (6 from the Buha River and 7 from the Shaliu River), while six samples were collected from the Hargai River and Daotang River (3 from the Hargai River and 3 from the Daotang River), which are near the entrance of the rivers. A total of 19 samples were collected from the recharge rivers. The distribution of the sampling sites is shown in **Figure 1**.

Surface water samples from Qinghai Lake and its exogenous recharge rivers were collected directly in high-density polyethylene (HDPE) plastic bottles, while other water samples at different depths were collected in HDPE plastic bottles using a Plexiglas (PPMA) water collector. The first batch of 39 water samples collected from Qinghai Lake in September 2017 were transferred to a 50 ml centrifuge tube and centrifuged three times (7 min) at 3,500 rpm to remove insoluble impurities such as insoluble particles. After centrifugation, the supernatant of each sample was taken and stored in a new HDPE plastic bottle to analyze the follow-up chemistry procedure. Samples collected from the other batches were filtered within 24 h of collection using a Nalgene manual vacuum filtration system (Nalgene 300–4,100; 6,133–0,010) with a 0.8-μm pore size mixed cellulose membrane (Millipore AAWP04700). After pretreatment, the water samples were stored in HDPE plastic bottles and sent to the laboratory for testing. The details of sampling information are shown in **Table 1**.

In order to verify whether centrifugation and filtration methods to separate particles affect the experimental results, three samples were centrifuged and filtered through 41-, 0.8-, and 0.45-μm filters, respectively, to assess the proportion of particulate matter of different sizes in the total particulate matter. The results show that the particle sizes in the centrifuged samples were less than 41 μm. In addition, we compared ^{232}Th concentrations filtered by 41-μm filters and 0.8-μm filters in four lakes from the Qaidam Basin (**Table 2**). The results show that the size of thorium-enriched particles is mostly between 0.8 and 41 μm, and the proportion of particles less than 0.8 μm is limited. Thus, the lake fluxes involved in this study are calculated from the ^{232}Th concentration in a particulate matter less than 41 μm, and the ^{232}Th concentration in river waters is in a particulate matter less than 0.8 μm. Therefore, we believe that Th concentration filtered by 0.8-μm filters and centrifugation three times could represent the content of dissolved Th in saline lake water to a certain extent.

The method of Th isotope analysis of water samples can be broadly divided into two stages: chemical separation and mass spectrometry, where the chemical separation stage consists of co-precipitation, low-speed centrifugation, ion-exchange resin

TABLE 1 | Sampling site information for the water samples.

Location	Sample no.	Depth (m)	Station	Latitude (°N) and longitude (°E)	Date	Batch
Qinghai Lake	QHH-9-0	0.2	107	36°59′35″, 100°05′22″	10 September 2017	1
	QHH-9-3	3				
	QHH-9-6	6				
	QHH-9-9	9				
	QHH-9-12	12				
	QHH-9-15	15				
	QHH-9-18	18				
	QHH-9-21	21				
	QHH-9-24	24				
	QHH-9-27	27				
	QHH-15-0	0.2	123	36°50′12″, 100°04′59″	11 September 2017	1
	QHH-15-3	3				
	QHH-15-6	6				
	QHH-15-9	9				
	QHH-15-12	12				
	QHH-15-18	18				
	QHH-15-21	21				
	QHH-15-27	27				
	QHH-21-0	0.2	131	36°39′59″, 100°37′18″	17 September 2017	1
	QHH-21-3	3				
	QHH-21-6	6				
	QHH-21-9	9				
	QHH-21-12	12				
	QHH-21-15	15				
	QHH-21-18	18				
	QHH-21-21	21				
	QHH-21-24	24				
	QHH-21-26	26				
	QHH-105-S	0.2	105	36°59′05″, 99°58′41″	10 September 2017	1
	QHH-109-S	0.2	109	36°54′45″, 100°14′06″	10 September 2017	1
	QHH-111-S	0.2	111	37°00′56″, 100°17′19″	10 September 2017	1
	QHH-113-S	0.2	113	37°05′12″, 100°05′56″	10 September 2017	1
	QHH-115-S	0.2	115	37°07′52″, 99°53′03″	10 September 2017	1
	QHH-116-S	0.2	116	36°53′15″, 99°54′46″	11 September 2017	1
	QHH-118-S	0.2	118	36°54′23″, 99°42′48″	11 September 2017	1
	QHH-120-S	0.2	120	36°46′34″, 99°59′02″	11 September 2017	1
	QHH-126-S	0.2	126	36°40′41″, 100°28′09″	17 September 2017	1
	QHH-127-S	0.2	127	36°43′19″, 100°20′18″	17 September 2017	1
	QHH-132-S	0.2	132	36°38′25″, 100°41′32″	17 September 2017	1
	QHH-201-S	0.2	201	37°11′52″, 99°48′34″	18 June 2018	2
Buha River	BH-201	0.2	201	37°22′35″, 98°50′34″	17 June 2018	2
	BH-202	0.2	202	37°12′53″, 99°09′54″	17 June 2018	2
	BH-203	0.2	203	37°08′06″, 99°30′59″	17 June 2018	2
	BH-301	0.2	301	37°22′35″, 98°50′34″	23 July 2019	3
	BH-302	0.2	302	37°12′53″, 99°09′54″	23 July 2019	3
	BH-303	0.2	303	37°08′06″, 99°30′59″	23 July 2019	3
Shaliu River	SL-201	0.2	201	37°37′18″, 99°58′17″	18 June 2018	2
	SL-202	0.2	202	37°31′09″, 100°05′11″	18 June 2018	2
	SL-203	0.2	203	37°19′43″, 100°07′28″	18 June 2018	2
	SL-301	0.2	301	37°37′18″, 99°58′17″	23 July 2019	3
	SL-302	0.2	302	37°31′09″, 100°05′11″	23 July 2019	3
	SL-303	0.2	303	37°19′43″, 100°07′28″	23 July 2019	3
	SL-401	0.2	401	37°19′92″, 100°07′29″	18 November 2020	4
Hargai River	HEG-201	0.2	201	37°17′11″, 100°28′38″	18 June 2018	2
	HEG-301	0.2	301	37°13′11″, 100°28′37″	23 July 2019	3
	HEG-401	0.2	401	37°13′11″, 100°28′39″	18 November 2020	4
Daotang River	DT-201	0.2	201	36°34′30″, 100°44′49″	19 June 2018	2
	DT-301	0.2	301	36°34′30″, 100°44′49″	24 July 2019	3
	DT-401	0.2	401	36°23′56″, 100°58′28″	18 November 2020	4

TABLE 2 | ^{232}Th concentration of samples filtered by 41-μm and 0.8-μm filters from several lakes in the Qaidam Basin.

Location	Sample	Latitude (°N) and longitude (°E)	^{232}Th (pmol/kg)	Error (2s)	Filter (μm)	Date
Qinghai Lake	QHH-4	37°02′54″,100°26′52″	326.553	5.39	41	2021/2/26
	QHH-4-F		2.046	0.01	0.8	
Qinghaigahai Lake	QHGH-2	37°01′19″,100°35′40″	41.792	0.26	41	2021/2/26
	QHGH-2-F		3.094	0.02	0.8	
Xiligou Lake	XLGH-6	36°49′05″,98°27′21″	65.287	0.52	41	2021/2/26
	XLGH-6-F		3.239	0.04	0.8	
Gahai Lake	GH-8	37°06′53″,97°36′07″	263.454	4.03	41	2021/2/26
	GH-8-F		0.340	0.00	0.8	

separation, collection, and purification. The specific steps involved are as follows:

1) Co-precipitation separation: A certain amount of water sample was weighed in a pre-prepared HDPE plastic bottle, a certain amount of 14N HNO_3 (1 N = 1 M), and 1–2 drops of $HClO_4$ and tracer (^{233}U–^{236}U–^{229}Th) were added to the water sample, heated and dried, and 2N HCl was used to dissolve the dried sample. Then, three to five drops of Fe solution was added to the sample, use $NH_3{\cdot}H_2O$ to reconcile the pH of the sample to 8 to 9, and mixed well and left for some time until a yellow precipitate appears at the bottom of the bottle.
2) Low-speed centrifugation: The water sample was transferred into a centrifuge tube and centrifuged at a low speed. After skimming off the upper clear layer, the resulting iron salt precipitate was rinsed with ultrapure water (>18 MΩ). The centrifugation process can be repeated 2–3 times to avoid other metal ions and soluble impurities from affecting the results. The resulting iron salt precipitate was dissolved by 14N HNO_3, transferred to a Teflon beaker, and then heated and dried for the next treatment.
3) Ion-exchange resin separation: The precipitate was completely dissolved using 7N HNO_3 and then transferred to a pre-prepared AG1-X8 anion resin exchange column, followed by the addition of 3CV 7N HNO_3 to remove Fe (CV: column volume), 3CV 6N HCl to achieve the Th isotope separation process.
4) Collection and purification: For this, 1 to 2 drops of $HClO_4$ was added to the separated Th isotope solution, heated and dried, and then dissolved with 14N HNO_3. The procedure was repeated 2–3 times, then fixed using a dilute acid (2% HNO_3 + 0.01% HF), and transferred to a small plastic vial for subsequent mass spectrometric analysis.

The mass spectrometry procedure was relatively straightforward. The nuclide ratio of samples was determined by Thermo Fisher's Neptune Plus MC-ICP-MS, and the concentrations of ^{230}Th and ^{232}Th in samples were calculated by isotope dilution. All measurements were carried out using the peak jump program in ion counting mode at the retarding potential quadruple. For Th, the measurement uncertainties involved propagated errors from ICP-MS isotope ratio measurements, spike concentrations, and blank corrections. The procedural blanks for chemical and mass spectrometric analyses at the Laboratory of Isotope Geochemistry in Xi'an Jiao Tong University are approximately 205 fg (5.3 e^6 atoms) for ^{232}Th, and 37 ag (1.0 e^5 atoms) for ^{230}Th. The methods used herein have been fully described by Cheng et al. (2000), Cheng et al. (2013) and Shen et al. (2002), Shen et al. (2012).

The measured ^{230}Th concentrations were corrected for in-growth due to decay of ^{234}U throughout the time the specimen was retained. To utilize ^{230}Th-^{234}U disequilibrium to obtain a Th residence time, ^{230}Thxs concentrations must also be corrected for the proportion of ^{230}Th liberated by the dissolution of lithogenic substances. This adjustment is made with concurrent measurements of ^{232}Th, with a lithogenic ratio of ^{230}Th/^{232}Th = 4.0×10^{-6} mol/mol (Roy-Barman et al., 2009).

Theory

The particle-reactive isotopes in the U and Th decay series are helpful tracers of particulate flux in water. The geochemistry of ^{230}Th in sediments is also important with respect to spatial and temporal variations in particulate flux (Ankney et al., 2017). Previous studies have shown that ^{230}Th is produced by the decay of ^{234}U at a constant rate. In natural waters, ^{230}Th is adsorbed by particulate matter in the water and eliminated from the water as it sinks. This process takes much less time than its radioactive decay rate (half-life of ^{232}Th = 14.1×10^9 years; half-life of ^{230}Th = 75.6×10^3 years) (Edmonds et al., 2004). The scavenging rate of Th is equal to the reciprocal of its corresponding residence time, and the hydraulic residence time of Th (τ_{Th}) in the lake water column can be obtained by measuring the concentration of ^{230}Thxs in water (**Eq. 1**) (Hayes et al., 2013).

$$\tau Th(z) = \frac{\int_0^z dissolved^{230}Thxs dz}{\int_0^z activity^{234}U \times \lambda_{230} dz} \quad (1)$$

where the multiplication of ^{234}U activity and λ_{230} is considered as the increment of ^{230}Th, $\lambda_{230} = 9.1705 \times 10^{-6}$ (Cheng et al., 2013).

In the following, the ^{232}Th fluxes will be calculated, and their contributions will be assessed in relation to the ^{232}Th distribution characteristics of the lake water column, respectively. The formula for calculating the ^{232}Th fluxes in lake water is given in **Equation 2** (Hayes et al., 2013).

$$dissolved^{232}Thflux(z) = \frac{\int_0^z d^{232}Thdz \times \int_0^z (\lambda_{230}^{234}U)dz}{\int_0^z d^{230}Thxsdz} = \frac{\int_0^z d^{232}Thdz}{\tau Th} \quad (2)$$

The dissolved ^{232}Th flux was then used to estimate a particulate lithogenic flux considering the content of ^{232}Th in the basaltic lithogenic material around the QHH region (10.5 μg/g; Wang et al., 2016) and the fractional solubility of ^{232}Th in lithogenic material (S_{Th}; from our preliminary Th result of particles from QHH and Qaidam Basin) as shown in **Equation 3** (Hayes et al., 2013).

$$Lithogenic\ flux(z) = \frac{Dissloved^{232}Th\ flux\ (z)}{[Th]_{QHH} \times S_{Th}} \quad (3)$$

To obtain an estimation of the flux of lithogenic material using dissolved Th-isotopes, it is first necessary to convert ^{232}Th concentrations into a dissolved flux using the residence time calculated. For this, dissolved ^{232}Th was integrated from the surface to an integration depth and divided by the corresponding ^{230}Th residence time (**Eq. (1)**).

RESULTS

The Spatial Distribution of Th Isotope Concentration in Surface Lake Water

Based on the surface water samples obtained from 15 different sampling locations in Qinghai Lake, the spatial distribution of Th isotope concentration data in the lake water is shown in Zhang et al. (2019). The details are shown in **Supplementary Table S1**. There are differences in the distribution of ^{232}Th concentrations between different sampling sites at the same depth, ranging from 0.265 to 3.356 pmol/kg, with a mean value of 1.247 pmol/kg, with the maximum value occurring at 107 and the minimum value at 131. The details are shown in the supplementary material file as **Supplementary Figure S1**. The total dissolved ^{230}Th concentration varied from 0.27 to 19.03 μBq/kg, with a mean value of 7.76 μBq/kg, with the maximum value occurring at site 127 and the minimum value at site 123, which fluctuated considerably. In the lake surface water, the ^{230}Thxs content of the 14 sites ranges from 0.2 to 18.2 μBq/kg with an average value of 7.39 μBq/kg, except for site 123, where no excess ^{230}Th occurred in the surface water. The maximum value appeared at site 127 and the minimum value appeared at site 201, with a large fluctuation and an average value of 7.39 μBq/kg.

In summary, there are significant differences in the concentrations of ^{232}Th, ^{230}Th, and ^{230}Thxs in the surface water of Qinghai Lake. The concentration of ^{232}Th at sites 107, 115, 116, 118, and 201, located at the edge of the northwest lake area, had significantly higher levels than other areas of the lake, with a mean value of 2.513 pmol/kg at the five sites, which was higher than the other samples. In contrast, the average content of ^{230}Thxs in sites 131, 126, 127, and 132 in the south lake area was 11.98 μBq/kg, far higher than the average value of surface water.

The Vertical Distribution of Th Isotope Concentrations in Lake Water

Lake water was sampled at varying depths at three sites (107, 123, and 131) in Qinghai Lake, and the results are shown in Zhang et al. (2019). The details are shown in **Supplementary Table S2**, **Supplementary Figure S2**, and **Supplementary Figure S3**. Site 107 is located in the northern lake area. The concentration of ^{232}Th varied from 3.356 to 14.995 pmol/kg, with an average value of 6.273 pmol/kg. From the surface to the bottom of the lake, the concentration of ^{232}Th exhibited a gradual and limited downward increase before decreasing at the bottom of the profile. Total dissolved ^{230}Th ranges from 7.08 to 21.59 μBq/kg, with an average value of 12.63 μBq/kg, with a maximum value at 21 m and a minimum value at 9 m. The concentration of ^{230}Thxs ranges from 5.3 to 12.5 μBq/kg, with a mean value of 8.24 μBq/kg, maximum values at 15 m and 27 m, and a minimum value at 9 m. The total dissolved ^{230}Th and ^{230}Thxs increased with depth before decreasing at a depth of 24 m.

At site 123, the concentration of ^{232}Th varied from 0.439 to 1.791 pmol/kg, with an average value of 1.005 pmol/kg. From the top to the bottom of the sampling profile, the concentration of ^{232}Th increased slightly with depth before decreasing at 21 m. The total dissolved ^{230}Th content ranges from 0.07 to 3.44 μBq/kg, with an average value of 1.35 μBq/kg, a maximum value at 21 m, and a minimum value at 3 m. The concentration of ^{230}Thxs content ranges from 0.5 to 2.2 μBq/kg, with a mean value of 1.16 μBq/kg. The maximum value occurs at 21 m and the minimum at 26 m.

At site 131, which is located in the southern lake area, the concentration of ^{232}Th ranged from 0.265 to 4.563 pmol/kg, which increased with the sampling depth, peaked at 21 m and then decreased, with an average value of 0.872 pmol/kg, lower than that of sites 123 and 107. The concentration of total dissolved ^{230}Th ranges from 7.34 to 18.61 μBq/kg, with an average value of 12.52 μBq/kg. The concentration of ^{230}Thxs ranges from 6.9 to 18.5 μBq/kg, with a mean value of 11.9 μBq/kg. The maximum and minimum values of total dissolved ^{230}Th and ^{230}Thxs occurred at 18m and 3m, respectively. Unlike sites 107 and 123, the concentration of total dissolved ^{230}Th and ^{230}Thxs in site 131 fluctuated widely and showed an overall decreasing trend with increasing depth.

Characteristics of Th Isotope Concentration Distribution in Exogenous Recharged River Waters

Overall, 19 surface water samples were sampled from the Buha River, Shaliu River, Hargai River, and Daotang River. The characteristics of the distribution of Th isotope concentration in these recharged river waters are shown in **Table 3**.

In the Buha River, the concentration of ^{232}Th ranges from 1.531 to 2.874 pmol/kg, with a mean value of 2.583 pmol/kg,

TABLE 3 | Distribution of Th isotope concentrations in exogenous recharge river water.

Sample no.	Depth (m)	$d^{234}U^*$ (Measured)	$d^{232}Th$ (pmol/kg)	$d^{230}Th$ (pmol/kg)	$d^{230}Th$ (μBq/kg)	$d^{230}Thxs$ (μBq/kg)
BH-201	0.2	902.1	3.354	1.81E-05	3.16	0.8
BH-202		934.2	2.861	2.06E-05	3.60	1.6
BH-203		1,194.8	2.36	1.90E-05	3.32	1.7
BH-301		1,017	1.531	4.13E-06	0.72	—
BH-302		1,031.8	2.874	1.06E-05	1.85	—
BH-303		1,066.2	2.518	9.23E-06	1.61	—
SL-201	0.2	1,087.7	7.976	5.30E-05	9.26	3.7
SL-202		1,148.6	7.904	5.27E-05	9.21	3.7
SL-203		1,203.3	7.530	4.96E-05	8.67	3.4
SL-301		1,279.0	4.488	2.16E-05	3.77	0.6
SL-302		898.6	7.773	3.82E-05	6.67	1.2
SL-303		1,213.0	3.800	1.80E-05	3.15	0.5
SL-401		1,325.1	46.913	2.28E-04	39.84	7.1
HEG-201	0.2	1,506.2	2.321	1.65E-05	2.88	1.3
HEG-301		1,295.2	3.132	1.50E-05	2.62	0.4
HEG-401		1,297.3	0.433	5.06E-04	88.41	88.1
DT-201	0.2	983.7	2.350	5.80E-04	101.34	99.7
DT-301		926.9	9.306	5.74E-05	10.03	3.5
DT-401		1,009.8	61.941	2.86E-04	49.97	6.7

showing a decreasing trend from the northwest (upstream) to southeast (downstream) regions. The concentration of total dissolved ^{230}Th ranges from 0.72 to 3.60 μBq/kg, with an average value of 2.38 μBq/kg. The concentration of ^{230}Thxs ranges from 0.8 to 1.7 μBq/kg, with a mean value of 1.37 μBq/kg, except for three sampling sites where no excess ^{230}Thxs was observed.

In the Shaliu River, the concentration of ^{232}Th ranges from 4.488 to 46.913 pmol/kg, with an average of 12.341 pmol/kg, which is higher than that in the Buha River and the Hargai River. The total dissolved ^{230}Th concentration ranges from 3.15 to 39.84 μBq/kg, with an average value of 11.51 μBq/kg. The concentration of ^{230}Thxs ranges from 0.5 to 7.1 μBq/kg with a mean value of 2.89 μBq/kg. The concentrations of ^{232}Th and total dissolved ^{230}Th and ^{230}Thxs of SL-401 are much higher than those in other samples, which may be related to the sampling season. The sample SL-401 was sampled in winter, while other samples were sampled in summer.

In the Hargai River, the concentration of ^{232}Th ranges from 0.433 to 3.132 pmol/kg, with an average value of 1.962 pmol/kg and little variation between sampling sites. The concentration of total dissolved ^{230}Th ranges from 2.62 to 88.41 μBq/kg, with an average value of 31.30 μBq/kg. ^{230}Thxs ranges from 0.4 to 88.1 μBq/kg, with a mean value of 29.93 μBq/kg. HEG-401, which was sampled in winter, had much lower ^{232}Th concentrations than the other two samples. However, the concentration of total dissolved ^{230}Th and ^{230}Thxs of HEG-401 is approximately 40 times and 80 times more than that of the other two samples, respectively.

In the Daotang River, the ^{232}Th concentration ranges from 2.350 to 61.941 pmol/kg, with a mean value of 24.532 pmol/kg. The concentration of total dissolved ^{230}Th ranges from 10.03 to 101.34 μBq/kg, with an average value of 53.78 μBq/kg. The concentration of ^{230}Thxs ranges from 3.5 to 99.7 μBq/kg, with a mean value of 36.6 μBq/kg. There were significant differences in the horizontal distribution of ^{232}Th, total dissolved ^{230}Th, and ^{230}Thxs in the three samples from the Daotang River. The ^{232}Th concentration of DT-401, which was sampled in winter 2020, was 7 times higher than the other samples.

DISCUSSION

Th Scavenging Residence Time in Lake Water

Th Scavenging Residence Time in Surface Lake Water

According to **Equation 1**, we measured the concentration of ^{230}Th at the surface water of Qinghai Lake, determined the ^{230}Th increment generated from ^{234}U decay, and obtained the ^{230}Th residence time (τ_{Th}) in the water column. The details are shown in **Table 4**. The ^{230}Th residence time of surface water samples has a limited variation, ranging from 0.1 to 6.2 years, with an average value of 2.3 years. The concentration of ^{230}Thxs in the southeast lake area is significantly higher than that in the northwest lake area. Thus, the ^{230}Th residence time in the southeast basin is higher than that in the northwest basin, indicating that the particle scavenging rate in the northwest basin is faster than that in the southeast basin, for instance, a slower sedimentation rate in the southeast lake area with ~7-year resolution of deposition recording core in the southeast lake area.

Th Scavenging Residence Time in Depth Profiles of Lake Water

The ^{230}Th concentration differs between stations since the short scavenging residence time of ^{230}Th makes it sensitive to variations in particulate flux (**Figure 2**). The ^{230}Th data show that the residence time of Th in the water column at different depths at 107, which is located in the north of Qinghai Lake, ranges from 1.6 to 4.3 years, with a mean value of 2.8 years and little variation in the vertical profile, indicating that there was

TABLE 4 | Dissolved ^{232}Th concentration, τ_{Th}, dissolved ^{232}Th flux and lithogenic flux of Qinghai Lake.

Sample no,	Depth (m)	Station	Density (kg/M^3)	d^{232}Th (pmol/kg)	τ_{Th} (year)	d^{232}Th Flux (nmol/M^2/yr)	Th-Litho.flux S_{Th} = 1% (g/M^2/yr)	Th-Litho.flux S_{Th} = 10% (g/M^2/yr)
QHH-9-0	0.2	107	1,200	3.356	2.5	0.318	0.70	0.070
QHH-9-3	3			3.097	2.3	4.745	10.48	1.048
QHH-9-6	6			3.815	2.2	12.547	27.72	2.772
QHH-9-9	9			3.381	1.6	22.555	49.84	4.984
QHH-9-12	12			4.885	2.5	28.625	63.25	6.325
QHH-9-15	15			4.046	4.3	17.000	37.56	3.756
QHH-9-18	18			8.978	1.8	106.033	234.28	23.428
QHH-9-21	21			13.229	4.2	78.792	174.09	17.409
QHH-9-24	24			14.995	2.5	171.366	378.64	37.864
QHH-9-27	27			2.941	4.3	22.376	49.44	4.944
QHH-15–0	0.2	123	1,200	0.439	—	—	—	—
QHH-15–3	3			0.544	—	—	—	—
QHH-15–6	6			0.670	—	—	—	—
QHH-15–9	9			0.990	0.3	34.289	75.76	7.576
QHH-15–12	12			0.911	0.5	25.027	55.30	5.530
QHH-15–18	18			1.624	0.2	155.014	342.51	34.251
QHH-15–21	21			1.791	0.7	60.487	133.65	13.365
QHH-15–27	27			1.071	0.2	185.652	410.20	41.020
QHH-21–0	0.2	131	1,200	0.265	4.7	0.013	0.03	0.003
QHH-21–3	3			0.319	6.3	0.182	0.40	0.040
QHH-21–6	6			0.379	3.6	0.766	1.69	0.169
QHH-21–9	9			0.330	4.8	0.736	1.63	0.163
QHH-21–12	12			0.376	4.3	1.256	2.78	0.278
QHH-21–15	15			0.410	2.7	2.690	5.94	0.594
QHH-21–18	18			0.632	2.3	5.811	12.84	1.284
QHH-21–21	21			4.563	4.3	26.840	59.30	5.930
QHH-21–24	24			0.868	3.0	8.341	18.43	1.843
QHH-21–26	26			0.578	4.5	3.969	8.77	0.877
QHH-105-S	0.2	105	1,200	0.560	0.1	1.493	3.30	0.330
QHH-109-S	0.2	109		0.555	3.3	0.040	0.09	0.009
QHH-111-S	0.2	111		0.803	1.9	0.099	0.22	0.022
QHH-113-S	0.2	113		0.500	2.1	0.057	0.13	0.013
QHH-115-S	0.2	115		1.951	3.2	0.146	0.32	0.032
QHH-116-S	0.2	116		3.067	1.1	0.672	1.48	0.148
QHH-118-S	0.2	118		1.735	2.7	0.155	0.34	0.034
QHH-120-S	0.2	120		0.353	1.9	0.043	0.10	0.010
QHH-126-S	0.2	126		0.704	2.1	0.082	0.18	0.018
QHH-127-S	0.2	127		1.195	6.2	0.046	0.10	0.010
QHH-132-S	0.2	132		0.769	3.4	0.055	0.12	0.012
QHH-201-S	0.2	201		2.465	0.1	11.427	25.25	2.525

*The unit of the ^{232}Th residence time obtained in **Eq. 1** is day. This table converts the unit to year for the convenience of discussion.*

no significant difference in the scavenging rate of Th at different depths of the water column in the same area. This likely suggests limited varying particulate matter size and with ~4-year resolution of deposition recording in site 107, which means that it takes ~4 years for particulate matter to be removed from the water column into the sediment. The residence time of Th in site 123 is 0.2–0.7 years, with a mean of 0.4 years, which is lower than that in the other two sites. The ^{230}Th residence time is short and therefore it can be transferred more rapidly from the water column to sinking particulate matter through vertical fluxes, meaning that the scavenging rate is the fastest in the western lake area of Qinghai Lake. This likely suggests a larger particulate matter size with faster removal rates and with ~0.7-year resolution of deposition record in site 123. Site 131 in the southern area of the lake has the longest ^{230}Th residence time varying from 2.3 to 6.3 years, with a mean value of 4.1 years, indicating the slowest scavenging rate in this area. The top depth of site 131 shows a longer residence time, suggesting that there exists another source of older water mixture in the top 10 m and finer particulate size. The relationship between the scavenging rates of the three depth profiles is 123 > 107>131. The variable disequilibrium between the western, northern, and southern regions of the lake area indicates variable and often large particle fluxes and/or changes in particle size from the western lake region rather than the other regions of the lake, which probably indicate more particle matter flux and/or larger particle size from the Buha river mixing into the lake water with hydraulic sorting effect (Tao et al., 2021). Thus, those differences are probably controlled by variations in the river water influx and its corresponding differences in particle flux and/or particle

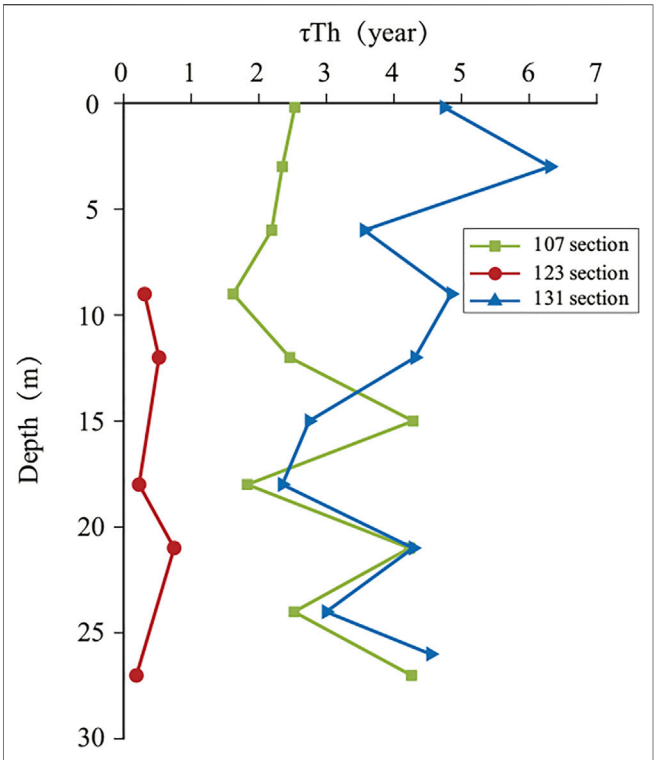

FIGURE 2 | Distribution characteristic of ^{230}Th residence time (τ_{Th}) in depth profiles of Qinghai Lake.

composition in the northern basin and western basin. However, a lower ^{232}Th content in site 131 and a longer residence time indicate a limited effect of the river in the southern basin.

Seasonal Changes in ^{232}Th Content in the Exogenous Rivers of Qinghai Lake

Due to the concentration of ^{232}Th having seasonal differences in lake water, eight samples in different months were selected from four exogenous rivers of Qinghai Lake for analysis and comparison. As shown in **Table 5**, there are visible seasonal changes in the ^{232}Th content of the rivers. The samples from November have higher ^{232}Th concentrations than the June and July samples, except for the Hargai River, where more wetlands and swamps decrease the amount of dust in Hargai during November. Therefore, in the dry season with little wet atmospheric precipitation from October to May, the ^{232}Th content of rivers in the Qinghai region was higher than that in the rainy season from June to September, which was influenced by sand and dust particles from the northwest wind into the lake water.

Thorium-Derived Dissolved ^{232}Th flux and Lithogenic Flux to the Qinghai Lake

Qinghai Lake is a typically closed saline lake, and the lake's recharge water is mainly from exogenous recharge rivers, followed by natural precipitation and groundwater. Previous studies have suggested that the ^{232}Th concentrations in surface water appear to be linked to the water column scavenging rate (Cochran et al., 1995; Edmonds et al., 1998; Edmonds et al., 2004). ^{232}Th is non-radiogenic, so most of the ^{232}Th in the lake water comes from the lake margins (bank erosion), rivers, or aeolian detrital particulate material. Th is insoluble in water and is rapidly eliminated from solution via scavenging on particulate material (Moore and Sackett, 1964). Therefore, if there were no contributions from other sources, the variation of ^{232}Th concentrations in water should decrease with depth and show the highest values in surface water. Therefore, depth profiles can be used to assess the lithogenic fluxes in lake water. More specifically, the ^{232}Th fluxes in deep water indicate a deep source of dissolved ^{232}Th, possibly as a result of boundary scavenging. The sampling profiles indicate that the ^{232}Th concentrations in Qinghai Lake increase slowly with depth, with higher bottom water concentrations in all three profiles. These trends suggest that an additional ^{232}Th enters the water column at the bottom of the lake, possibly from the contribution of the bottom sediments. The ^{232}Th concentrations at the lake surface (**Supplementary Table S1** and **Supplementary Figure S1** in the supplementary material file) suggest that the dissolved ^{232}Th flux is primarily derived from the input of aerosol (dust) in shallow waters. Furthermore, the fluxes near the entrance of the recharging river appear to be derived from the ^{232}Th contributed to the lake by the river. The ^{232}Th in the lake is therefore thought to be due to the dissolution of dust aerosols in combination with inflow from the recharging rivers (Zhang et al., 2019). The characteristics of the horizontal and vertical distribution of ^{232}Th in the lake water of Qinghai Lake suggest that there is an exogenous source contribution, of ^{232}Th to its lake water, and that different areas of the lake do not receive exactly the same proportion of the exogenous source contribution which is from hydraulic sorting of grain size and types. Because several major recharge rivers flow through stratigraphic source rocks that are different, including felsic rocks, carbonate, metamorphic rocks, and clastic rocks. In view of this, it is reasonable to assume that the main sources of ^{232}Th in the lake water column of Qinghai Lake include atmospheric deposition dust, exogenous recharge

TABLE 5 | Seasonal changes of ^{232}Th content in the exogenous rivers of Qinghai Lake.

Sample no.	Latitude (°N) and longitude (°E)	Date	d^{232}Th (pmol/kg)
BH-201	37°22′35″, 98°50′34″	17 June 2018	3.354
BH-301		23 July 2019	1.531
SL-201	37°37′18″, 99°58′17″	18 June 2018	7.976
SL-301		23 July 2019	4.488
SL-401	37°19′92″, 100°07′29″	18 November 2020	46.913
HEG-201	37°17′11″, 100°28′38″	18 June 2018	2.321
HEG-301	37°13′11″, 100°28′37″	23 July 2019	3.132
HEG-401		18 November 2020	0.433
DT-201	36°34′30″, 100°44′49″	19 June 2018	2.35
DT-301		24 July 2019	9.306
DT-401	36°23′56″, 100°58′28″	18 November 2020	61.941

river, and the mix from the interface of water-rock with the water depth increase. Selecting an integration depth at which the lithogenic inputs can be effectively quantified has been a subject of discussion with varying particle types. Due to the sampling method and evaluation method of this study being different from Jin's (Jin et al., 2009a), the lithogenic flux in this study is different from the flux in Jin's. Jin et al. estimated the dust flux based on the suspended particulate matter supplied by the Buha River to Qinghai Lake, and the lithogenic flux of Qinghai Lake in our study includes two sources, atmospheric deposition and river recharge. The dust flux in this study refers to the particulate matter caused by atmospheric dry deposition.

The dissolved ^{232}Th fluxes can be converted to lithogenic-material fluxes with knowledge about the composition of the material and its Th fractional solubility (**Eq. (3)**). In other words, this flux of lithogenic material is required to sustain the calculated dissolved ^{232}Th and therefore the measured concentration of ^{232}Th. The lithogenic material from the Qinghai region has a ^{232}Th content varying from 10.5 to 11.7 μg/g (Wang et al., 2016). Therefore, we use this value for the calculations of the lithogenic flux in our area of study.

The largest source of uncertainty in the calculation of lithogenic fluxes is the solubility of ^{232}Th from particles, which is a highly unconstrained parameter. From the few studies that report ^{232}Th solubility in marine particles, highly variable values were found, ranging from 1% to 23%, depending on the particle size and depth (Arraes-Mescoff et al., 2001; Roy-Barman et al., 2002). There is no report about ^{232}Th solubility in lake particles. According to our preliminary results from lake particles from the Qaidam Basin, ranging from 1 to 10%, depending on the particle size and types (unpublished data).

The Spatial Trends of Dissolved ^{232}Th Flux and Lithogenic Flux in Lake Water

The climatic characteristics of Qinghai Lake do not vary greatly within the region, and the contribution of ^{232}Th atmospheric dust in lake surface water is generally consistent when other exogenous factors are ignored, so the distribution of ^{232}Th concentrations in lake surface water of Qinghai Lake should generally remain consistent under ideal conditions. However, the concentration of ^{232}Th in the surface lake shows that the spatial distribution characteristics of ^{232}Th concentrations in Qinghai Lake vary (0.265–3.356 pmol/kg), with a mean value of 1.24 pmol/kg. Sites 107, 115, 116, 118, and 201, located at the edge of the northwestern lake area, had significantly higher values of ^{232}Th than those in other areas of the lake, with a mean value of 2.513 pmol/kg. The spatial distribution of ^{232}Th concentration in the surface water of Qinghai Lake near the Buha River is significantly higher than that in other areas. The ^{230}Thxs content is significantly higher in the southeast basin than in the northwest basin. The mean value of ^{230}Thxs content at sites 131, 126, 127, and 132 in the south lake is 12.0 μBq/kg, which is much higher than the mean value of surface water, and therefore, exogenous detritus contributes less Th to the south lake area than the other areas.

The results of the dissolved ^{232}Th flux and lithogenic flux in surface lake water were calculated by **equations 2** and **3**. As a study suggested in the Nansen Basin, the Arctic Ocean (Cochran et al. (1995)), elevated particle concentrations near the basin margin, if coupled with greater particle fluxes, could produce enhanced removal of reactive radionuclides from the water column. The dissolved ^{232}Th flux in surface lake water ranges from 0.013 to 26.840 nmol/m^2/yr, with an average value of 5.060 nmol/m^2/yr (**Table 4**; **Figure 3**). The dissolved ^{232}Th flux in the northwest basin has significantly higher values than that in the southeast basin, especially near the entrances of the Buha River and Shaliu River. The results show that in addition to the ^{232}Th contributed by atmospheric deposition, the exogenous recharge rivers contributed a certain amount of ^{232}Th to Qinghai Lake. Sites 105 and 201, located at the northwestern edge of Qinghai Lake, have much shorter Th residence times than average and much higher dissolved ^{232}Th fluxes than other areas, suggesting that the faster rate of particulate matter production in the lake edge area more effectively removes radionuclides, and thus the ^{230}Thxs showed minimal values here.

For lithogenic flux, when using a Th solubility from particles of 1%, we obtain fluxes of lithogenic material ranging from 0.03 to 25.25 g/m^2/yr in the surface water, while the values range from 0.003 to 2.525 g/m^2/yr when using a Th solubility from particles of 10% (**Table 4**; **Figure 4**). It is worth noting that the dissolved ^{232}Th flux and lithogenic flux at site 201 are tens to hundreds of times higher than those of the other sites, which may be due to the sampling location near the lake shore and the source of flux is the dissolution of continental material. Since the lithogenic fluxes in the southeast basin are lower than those in the northwest basin, we believe that the contribution of exogenous detrital materials by river input to lake water in the southern basin is limited. The dust flux in September from atmospheric deposition can thus be confirmed. In general, when other exogenous factors are ignored, the dust flux from Qinghai Lake in September is basically stable with a value of 0.109 g/m^2/yr.

The Depth Trends of Dissolved ^{232}Th Flux and Lithogenic Flux in Lake Water

The mixing of runoff from exogenous recharge rivers with the original water of Qinghai Lake may affect the variation of ^{232}Th flux and lithogenic flux in the lake water column and eventually affect the vertical distribution of ^{232}Th concentration in the lake water. The distribution characteristics of ^{232}Th concentration in the lake water column with vertical gradient and the residence time of Th in the water column combined with **Eq. 2** and **Eq. 3** calculated the vertical gradient profile flux. The calculation results are shown in **Table 4**. Dissolved ^{232}Th flux and lithogenic flux in all three depth profiles of Qinghai Lake showed an increasing trend with depth (**Figure 5**, **Figure 6**). Site 107, located northwest of the lake, has the highest dissolved ^{232}Th flux and a higher mean particulate flux. This site has the largest increase in dissolved ^{232}Th flux, which ranges from 0.318 to 171.366 nmol/m^2/yr from the lake surface to the bottom, with a mean value of 46.436 nmol/m^2/yr. The lithogenic flux of site 107 varied from 0.7 to 378.64 g/m^2/yr, with an average value of 102.60 g/m^2/yr. The dissolved ^{232}Th flux and lithogenic flux at site 123 near the center of the lake also increased with depth, peaking at the highest mean values of 57.56 nmol/m^2/yr and 127.18 g/m^2/yr, respectively. Site 131,

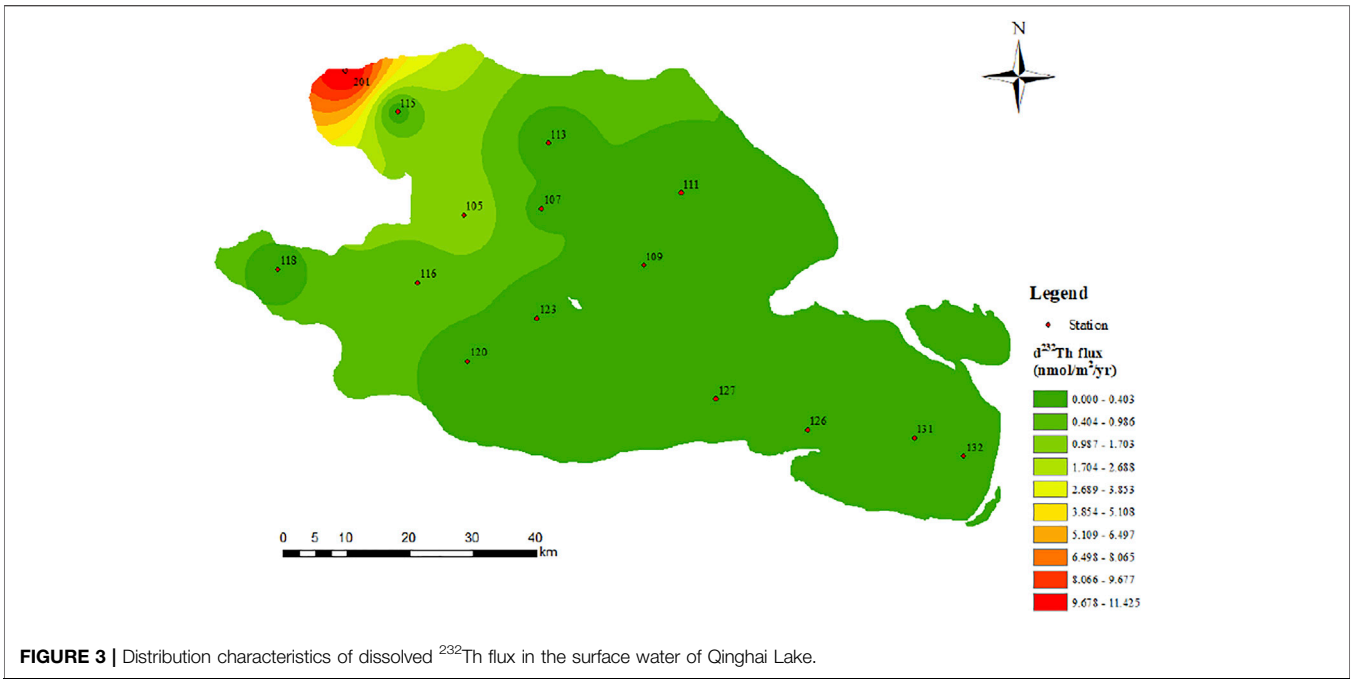

FIGURE 3 | Distribution characteristics of dissolved ^{232}Th flux in the surface water of Qinghai Lake.

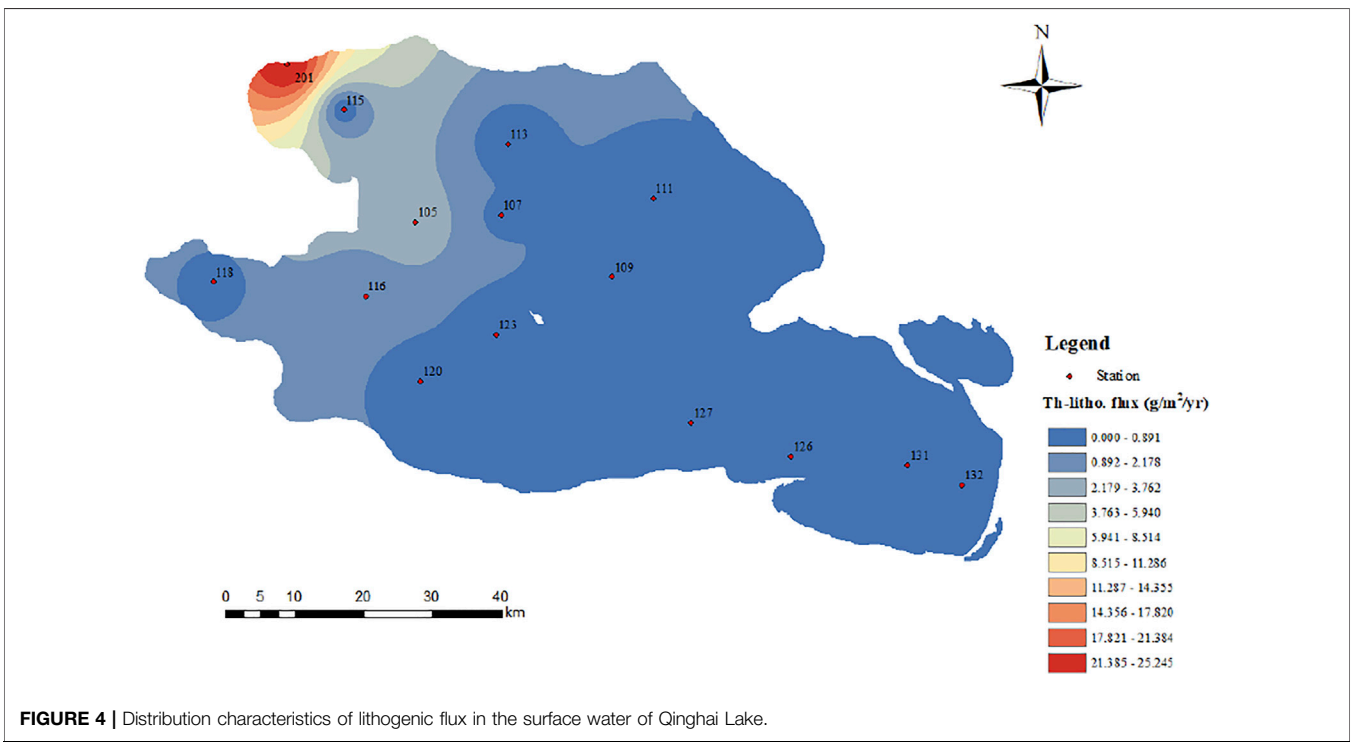

FIGURE 4 | Distribution characteristics of lithogenic flux in the surface water of Qinghai Lake.

located in the south area of Qinghai Lake, has the least dissolved ^{232}Th flux and lithogenic flux. The dissolved ^{232}Th flux ranges from 0.013 to 26.840 nmol/m^2/yr, with an average value of 5.060 nmol/m^2/yr. The lithogenic flux of site 131 ranges from 0.03 to 59.30 g/m^2/yr, with an average value of 11.18 g/m^2/yr. The data from three depth profiles in Qinghai Lake show that dissolved ^{232}Th flux and lithogenic flux increase with depth, and the average dissolved ^{232}Th flux and lithogenic flux in the northwest basin is significantly higher than that in the southeast basin, which has a great relationship with the input of the exogenous recharge river and hydraulic sorting.

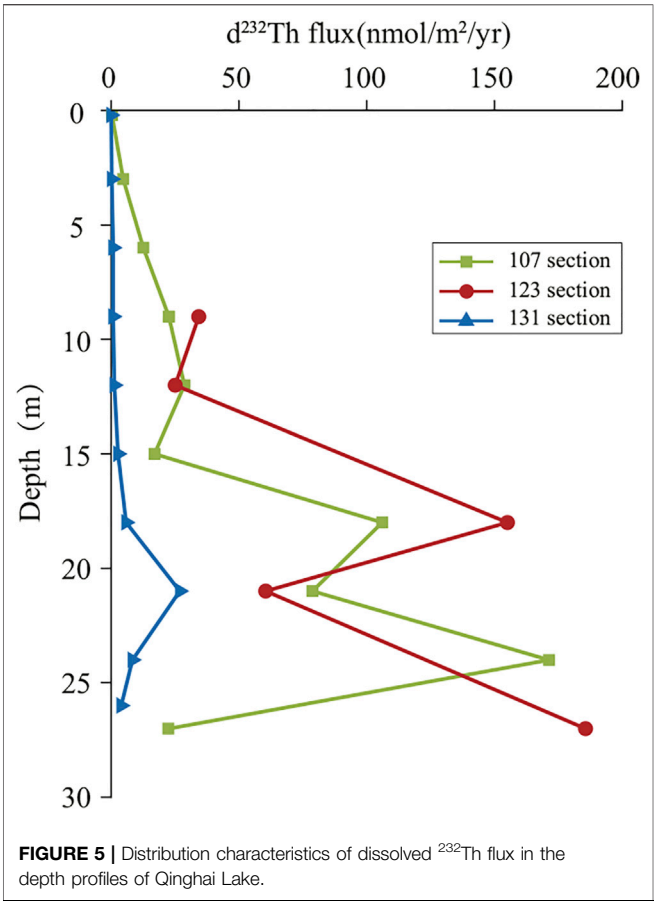

FIGURE 5 | Distribution characteristics of dissolved ^{232}Th flux in the depth profiles of Qinghai Lake.

In the three depth profiles of Qinghai Lake, sites 107, 123, and 131, total dissolved ^{230}Th and ^{230}Thxs showed an increasing trend only at sites 107 and 123, which is similar to the trend of positive correlation of ^{230}Th with water depth in marine water (Cochran et al., 1995). In contrast, ^{230}Thxs shows a decreasing trend at site 131, in complete contradiction to the linear increase in ^{230}Th content in marine water with water depth, which is probably from the mixing of other older water sources. The ^{230}Thxs values are higher than those in the northwest lake area. When the parent nuclide of ^{230}Th, ^{234}U, is approximately homogeneous in the lake water, combined with the lower contribution of ^{232}Th and ^{230}Th from exogenous particulate matter, it can be assumed that the scavenging rate at site 131 was slower. In addition, it has been shown that the nature of the particulate matter plays a role in the removal effect of ^{230}Th in the lake (Clegg and Whitfield, 1991). The mean particulate matter flux at depth profile 131 is approximately ten times lower than that at the other two sites, and the mean ^{232}Th concentration is the lowest of the three sites. Since site 131 is away from the Daotang River, which first flows into Erhai, then flows into Qinghai Lake through a limited channel, the recharge water from Erhai is characterized by low fluxes and higher Th concentrations. It can be inferred that the Daotang River and Erhai contribute very limited exogenous particulate matter to the south of Qinghai Lake and that the source of particulate matter in the southeastern lake area of Qinghai Lake is mainly the dissolution of atmospheric dust with low content ^{232}Th contribution to the lake surface water. Since there is a bird island in the center of the lake, and combined with the fact that the lithologic fluxes based on ^{232} Th decrease sequentially from northwest to southeast in the surface layer, the surface fluxes located at the south of the bird island do not show a decreasing gradient in contrast to the north, we believe that there exists a limited possibility of river transpolar to the southeast.

Quantification of Lithogenic Fluxes to the Qinghai Lake Based on the Mixing of River in Lake Water

As the two largest recharge rivers to Qinghai Lake, both the Buha River and the Shaliu River have higher mean values of ^{232}Th concentrations than those in the surface water of Qinghai Lake (mean value of 1.247 pmol/kg). The high values of ^{232}Th combined with the low values of ^{230}Thxs indicate that these two rivers carry more exogenous debris material and contribute a certain amount of particulate matter to the lake. Thus, the high values of ^{232}Th at sites near the northwestern edge of Qinghai Lake (107, 115, 116, 118, and 201) suggest that the inputs from the Buha River and the Shaliu River may be responsible for this phenomenon. The low values of ^{232}Th near the river entrances of the Hargai and Daotang Rivers show that these two rivers contribute limited flux to the lake.

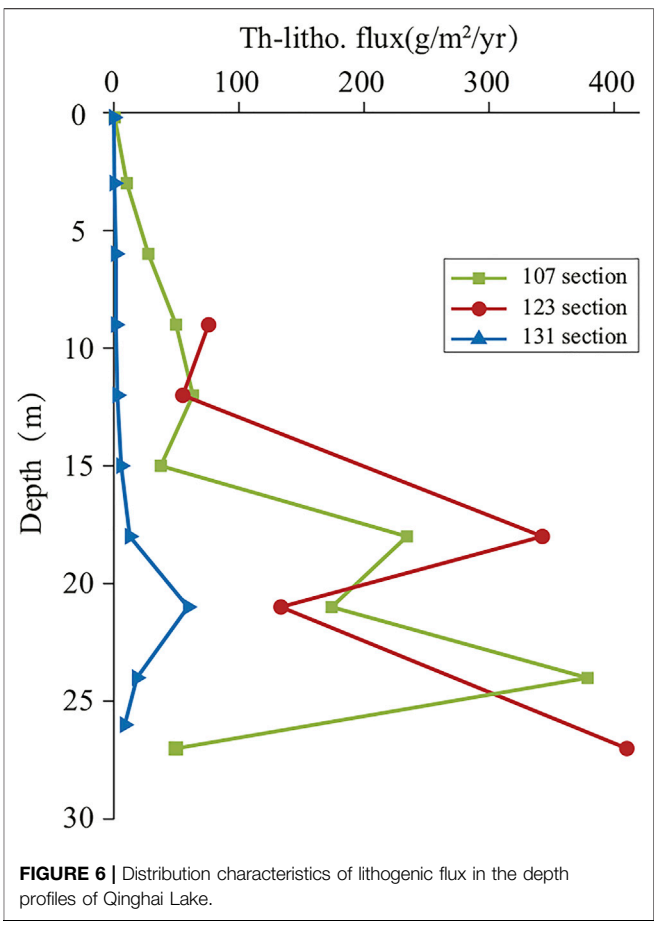

FIGURE 6 | Distribution characteristics of lithogenic flux in the depth profiles of Qinghai Lake.

TABLE 6 | Comparison of lithogenic flux in the present study with the results of sediments from the study of Jin et al. (2013).

Area of study		Th-Litho.flux S_{Th} = 1% (g/M^2/yr)	Th-Litho.flux S_{Th} = 10% (g/M^2/yr)	Fluxes of settled particles (g/M^2/yr)	
				2010.7–2010.12	2011.1–2011.10
Northwest basin of Qinghai Lake	Surface water	0.09–25.25	0.009–2.525	—	—
	Depth profiles	0.70–410.20	0.070–4.102	—	—
Southeast basin of Qinghai Lake	Surface water	0.03–1.48	0.003–0.148	-—	—
	Depth profiles	0.03–59.30	0.003–5.930	—	—
Qinghai Lake*	Rainy season	—	—	13.25–723.54	12.59–99.57
	Dry season	—	—	6.57–387.81	1.02–13.18

**Fluxes of settled particles data of Qinghai Lake is from Jin et al. (2013).*

Previous studies have shown that the uranium content in Qinghai Lake shows a uniform distribution, indicating that its activity is generally consistent, which implies that there is always a consistent and steady-state source of ^{230}Thxs in the lake water (Zhang et al., 2019). However, the determination of thorium isotopes at each station in Qinghai Lake revealed that the content varies greatly from station to station, which is very different from the distribution of uranium isotopes in the lake water. Due to the pro-particulate properties of thorium (Kretschmer et al., 2010), thorium is easily eliminated by the migration and removal of particulate materials. Therefore, the horizontal river and the amount of particulate material have a huge influence on it.

We compared the lithogenic flux of surface water and depth profiles of Qinghai Lake with the results of Qinghai Lake sediments in the study of Jin et al. (2013), and the results were consistent (**Table 6**). Thus, the lithogenic material flux calculation using thorium isotopes for the QHH region seems to be promising, and once the Th solubility in the QHH lake is better constrained, the uncertainties will be reduced. The long-lived Th isotopes offer a unique and powerful tool to evaluate the supply of lithogenic flux. However, there are a number of sources of uncertainty that must be addressed in future studies to further refine our estimates of lithogenic fluxes. These include seasonal effects of Th input and removal in the lake away from the edge of QHH, the chemical speciation and size partitioning of ^{232}Th and ^{230}Th in lake water.

In conclusion, when a large number of exogenous recharge rivers are mixed into the northwest basin of Qinghai Lake, the ^{232}Th content and lithogenic flux of the lake water are mainly influenced by the type and content of the particles in the Buha and Shaliu rivers. Conversely, when the contribution of recharge rivers is limited, the ^{232}Th content of the lake water is mainly influenced by atmospheric dust. For example, based on the ^{230}Th normalization method (combining with ^{232}Th and τ_{Th}), the dust flux in September can be evaluated. Based on the safety of sampling on the lake, the samples were collected at a time when there was no wind and no rain. Thus, the atmospheric dust could be evaluated. And based on the retention time of particulate matter in the water column, the depth profile results can reflect the lithogenic fluxes on a seasonal to annual scale with some certainty.

Contribution of Recharging Rivers of Qinghai Lake and Atmospheric Dust to ^{232}Th Fluxes in Lake Water Column

According to previous studies (Edmonds et al., 1998; Edmonds et al., 2004; Hayes et al., 2017), since most of the dissolved ^{232}Th in seawater originates from atmospheric dust which dissolves into the ocean after settling to the sea surface, the ^{232}Th concentration in marine waters decreases with depth and reaches its highest value at the sea surface. This is in contrast to the phenomenon we observed in the lake. All three depth profiles of Qinghai Lake showed a positive correlation between ^{232}Th concentration and depth, and the high ^{232}Th values in surface waters near site 107 suggested that this may be due to the input from exogenous recharge rivers. The advection of particulate matter from the nearshore shelf can increase regional scavenging rates and fluxes. The recharge rivers carried more exogenous detrital material into the lake and mixed it with the lake water, causing the particulate flux to increase with depth and reaching a maximum in the bottom water of the lake.

Based on Th isotope data and flux information of surface water in Qinghai Lake, the dust flux of lithologic material in September contributed by atmospheric dry deposition to the lake can be calculated, which is approximately 0.109 g/m^2/yr. The lithogenic fluxes delivered to the lake by rivers can be quantified based on the data from stations located near the recharging rivers. The fluxes of lithologic material from the recharge rivers input into the lake are 120.55 g/m^2/yr in the northwest basin and 12.42 g/m^2/yr in the southeast basin, which are calculated by the mean value of lithogenic fluxes at depth profiles of 107 and 123 sites and the mean value at depth profile site 131, respectively. Sites 126, 127, 131, and 132 are located in the southeast of Qinghai Lake, far away from the estuary, and the ^{232}Th of surface water is mainly derived from atmospheric dust. The mean lithogenic flux of the surface water at these four sites is 0.109 g/m^2/yr. Sites 105, 107, 113, 115, 116, and 118 are located in the northwest and southwest of Qinghai Lake near the estuary. Their lithogenic fluxes mainly come from fluvial suspended particles and atmospheric dust. The mean lithogenic flux of the surface water at these six sites is 1.046 g/m^2/yr. The contribution of atmospheric dust and river input to the lithogenic flux of Qinghai Lake can be assessed by these two mean values. For instance, the Buha River and Shaliu River contribute ~90% of the lithogenic flux to the northwest

basin of the lake, while the atmospheric dry dust deposition contributes only 10% of the flux. Therefore, unlike the northwest region, the source of particle material flux in the southeast basin of the lake is dominated by atmospheric deposition, and the contribution of the recharging river to the lake's water flux is less than that of the atmospheric dissolution of dust at the lake surface. In jin et al. (2009a), the dust input represents 65% of the total input of dissolved and particulate forms, which is estimated based on the suspended particulate matter supplied by the Buha River to Qinghai Lake. Among the four recharge rivers of Qinghai Lake, from our result, the Buha and Shaliu Rivers have higher lithogenic fluxes, including dust input into the river and ^{232}Th concentrations, contributing a large amount of particulate matter to the northwestern area of Qinghai Lake with a ratio of ~90% of the detrital flux to the lake in September, which is actually not contradictory to Jin's result with ~65% of the dust input origin of the total input of dissolved and particulate forms in the Buha River and recharge into Qinghai Lake. This study supplies several rivers' loads into the lake by a novel ^{230}Th normalization method, which is further complementary to the detrital flux into Qinghai Lake with several major incharge rivers.

Hayes et al. (2013) suggest that there are two sources of Th in the ocean: one shallow due to dust dissolution and one deep associated with sediment dissolution/resuspension; and one removal mechanism, scavenging throughout the water column. Therefore, another reason for the higher concentration of ^{232}Th in the deep water than in the surface water in the saline lakes may be due to the redissolution of ^{232}Th in the sediment at the bottom of the lake. The other possibility is from accumulated sinking flux due to the slow deposition rate. In the future, we expect to use Th isotope information in lake sediments, combined with Th concentration data of depth profile particles' composition and size, to further quantify the contribution of ^{232}Th to lake sediments.

Overall, in September, the Buha and Shaliu rivers in the northwest basin contribute about 90% of the detrital ^{232}Th flux to the lake. The lithogenic flux in the southeast lake is dominated by dust flux with a value of ~0.109 g/m^2/yr, while the higher lithogenic flux at the bottom of the lake was likely generated by accumulated sinking particulate matter and resuspension of bottom sediments in September.

CONCLUSION

The ^{232}Th concentrations on the horizontal spatial scale at the surface of Qinghai Lake are unevenly distributed, being significantly higher around the river entrance of the northwest basin than in other lake areas, with more ^{230}Th from exogenous material in the total dissolved water. When a large number of exogenous recharge rivers are mixed into the lake water in the northwest basin, the ^{232}Th content and the corresponding dust flux of the lake water are mainly influenced by the type and content of the recharging river particles. Conversely, when the recharge river contribution is limited in the southeast basin, the ^{232}Th content of the lake water away from the estuary is mainly influenced by the atmospheric dust. Furthermore, based on the ^{230}Th normalization method (combining with ^{232}Th and τ_{Th}), the dust flux of Qinghai Lake in September can be evaluated with an average of ~0.109 g/m^2/yr. When using a Th solubility from particles of 1%, the fluxes of lithogenic material range from 0.03 to 25.25 g/m^2/yr in the surface water, consistent with the flux results of settled particles from the previous study. Deposition record resolutions of 7, 4, and 0.7 years are present in the southeast, northwest, and southwest of Qinghai Lake, respectively.

Among the four recharge rivers of Qinghai Lake, the Buha and Shaliu rivers have higher ^{232}Th concentrations, contributing a large amount of particulate matter to the northwestern area of Qinghai Lake, with a ratio of ~90% of the detrital flux to the lake in September. The lithogenic flux in the southeast lake is dominated by dust flux with a value of ~0.109 g/m^2/yr, while the higher lithogenic flux at the bottom of the lake was likely generated by accumulated sinking particulate matter and resuspension of bottom sediments in September. This study confirms the utility of long-lived Th isotopes to quantify lithogenic inputs based on the Th content of the dissolved lake water and also supply deposition resolution information for QHH sediment records with some certainty.

DATA AVAILABILITY STATEMENT

The original contributions presented in the study are included in the article/**Supplementary Material**; further inquiries can be directed to the corresponding authors.

AUTHOR CONTRIBUTIONS

The research was supervised by PZ and XL, with guidance provided by RE. Samples were collected by PZ, XP, CC, JP, LL, and XL. The experiment method was instructed by PZ, CC, ZG, XL, and YN. The manuscript was written by PZ with revisions provided by LT, XL, and RE. All authors have read and agreed to the published version of the manuscript.

FUNDING

This study was supported by the National Natural Science Foundation of China (Nos. 41873013 and 41888101) and the U.S. NSF (No. 1702816).

SUPPLEMENTARY MATERIAL

The Supplementary Material for this article can be found online at: https://www.frontiersin.org/articles/10.3389/feart.2022.866314/full#supplementary-material

REFERENCES

Ankney, M., Bacon, C., Valley, J., Beard, B., and Johnson, C. (2017). Oxygen and U-Th Isotopes and the Timescales of Hydrothermal Exchange and Melting in Granitoid wall Rocks at Mount Mazama, Crater Lake, Oregon. *Geochimica et Cosmochimica Acta* 213, 137–154. doi:10.1016/j.gca.2017.04.043

Arraes-Mescoff, R., Roy-Barman, M., Coppola, L., Souhaut, M., Tachikawa, K., Jeandel, C., et al. (2001). The Behavior of Al, Mn, Ba, Sr, REE and Th Isotopes during *In Vitro* Degradation of Large marine Particles. *Mar. Chem.* 73 (1), 1–19. doi:10.1016/s0304-4203(00)00065-7

Bacon, M. P. (1984). Glacial to Interglacial Changes in Carbonate and clay Sedimentation in the Atlantic Ocean Estimated from 230Th Measurements. *Chem. Geology*. 46 (2), 97–111. doi:10.1016/0009-2541(84)90183-9

Bian, Q., Liu, J., Luo, X., Xiao, J., Ritzwoller, M., and Levshin, A. (2000). Geotectonic Setting, Formation and Evolution of the Qinghai Lake. *Ssmology Geology*. 22 (1), 20–26. (in Chinese). doi:10.3969/j.issn.0253-4967.2000.01.003

Bourdon, B., Turner, S., and Dosseto, A. (2003). Dehydration and Partial Melting in Subduction Zones: Constraints from U-Series Disequilibria. *J. Geophys. Res.* 108 (B6), 2291. doi:10.1029/2002jb001839

Cheng, H., Edwards, R.L., Hoff, J., Gallup, C.D., Richards, D. A., and Asmerom, Y. (2000). The Half-Lives of Uranium-234 and Thorium-230. *Chem. Geology*. 169 (1-2), 17–33. doi:10.1016/s0009-2541(99)00157-6

Cheng, H., Lawrence Edwards, R., Shen, C.-C., Polyak, V. J., Asmerom, Y., Woodhead, J., et al. (2013). Improvements in 230Th Dating, 230Th and 234U Half-Life Values, and U-Th Isotopic Measurements by Multi-Collector Inductively Coupled Plasma Mass Spectrometry. *Earth Planet. Sci. Lett.* 371-372, 82–91. doi:10.1016/j.epsl.2013.04.006

Clegg, S. L., and Whitfield, M. (1991). A Generalized Model for the Scavenging of Trace Metals in the Open Ocean-II. Thorium Scavenging. *Deep Sea Res. A. Oceanographic Res. Pap.* 38 (1), 91–120. doi:10.1016/0198-0149(91)90056-l

Cochran, J. K., Hirschberg, D. J., Livingston, H. D., Buesseler, K. O., and Robert, M. K. (1995). Natural and Anthropogenic Radionuclide Distributions in the Nansen Basin, Artic Ocean: Scavenging Rates and Circulation Timescales. *Topical Stud. Oceanography* 42 (95), 1495–1517. doi:10.1016/0967-0645(95)00051-8

Colman, S. M., Yu, S. Y., An, Z., Shen, J., and Henderson, A. C. G. (2007). Late Cenozoic Climate Changes in China's Western interior: A Review of Research on lake Qinghai and Comparison with Other Records. *Quat. Sci. Rev.* 26 (2007), 2281–2300. doi:10.1016/j.quascirev.2007.05.002

Costa, K., and McManus, J. (2017). Efficacy of 230Th normalization in sediments from the Juan de Fuca Ridge, northeast Pacific Ocean. *Geochimica et Cosmochimica Acta* 197, 215–225. doi:10.1016/j.gca.2016.10.034

Cruz, J. A., McDermott, F., Turrero, M. J., Edwards, R. L., and Martin-Chivelet, J. (2021). Strong Links between Saharan Dust Fluxes, Monsoon Strength, and North Atlantic Climate during the Last 5000 Years. *Sci. Adv.* 7 (26), eabe6102. doi:10.1126/sciadv.abe6102

Curry, W. B., and Lohmann, G. P. (1986). Late Quaternary Carbonate Sedimentation at the Sierra Leone Rise (Eastern Equatorial Atlantic Ocean). *Mar. Geology*. 70, 223–250. doi:10.1016/0025-3227(86)90004-6

DeMaster, D. J. (1981). The Supply and Accumulation of Silica in the marine Environment. *Geochimica et Cosmochimica Acta* 45 (10), 1715–1732. doi:10.1016/0016-7037(81)90006-5

Ding, Y. H., Li, Q. P., Liu, Y. J., Zhang, L., Song, Y. F., and Zhang, J. (2009). Air Pollution and Climate Change. *Meteorology* 035 (003), 3–14. (in Chinese).

Edmonds, H. N., Moran, S. B., Hai, C., and Edwards, R. L. (2004). ^{230}Th and 231Pa in the Arctic Ocean: Implications for Particle Fluxes and basin-scale Th/Pa Fractionation. *Earth Planet. Sci. Lett.* 227 (1-2), 155–167. doi:10.1016/j.epsl.2004.08.008

Edmonds, H. N., Moran, S. B., Smith, J. A. J. N., and Edwards, R. L. (1998). Protactinium-231 and Thorium-230 Abundances and High Scavenging Rates in the Western Arctic Ocean. *Science* 280 (5362), 405–407. doi:10.1126/science.280.5362.405

Francois, R., Frank, M., Loeff, M. R., and Bacon, M. (2004). ^{230}Th Normalization: An Essential Tool for Interpreting Sedimentary Fluxes during the Late Quaternary. *Paleoceanography* 19, 1018. doi:10.1029/2003pa000939

Hayes, C. T., Anderson, R. F., Fleisher, M. Q., Serno, S., Winckler, G., and Gersonde, R. (2013). Quantifying Lithogenic Inputs to the North Pacific Ocean Using the Long-Lived Thorium Isotopes. *Earth Planet. Sci. Lett.* 383 (383), 16–25. doi:10.1016/j.epsl.2013.09.025

Hayes, C. T., Rosen, J., Mcgee, D., and Boyle, E. A. (2017). Thorium Distributions in High- and Low-dust Regions and the Significance for Iron Supply. *Glob. Biogeochem. Cycles* 31 (2), 328–347. doi:10.1002/2016gb005511

Jickells, T. D., An, Z. S., Andersen, K. K., Baker, A. R., Bergametti, G., Brooks, N., et al. (2005). Global Iron Connections between Desert Dust, Ocean Biogeochemistry, and Climate. *Science* 308 (5718), 67–71. doi:10.1126/science.1105959

Jin, Z. D., Zhang, F., Li, F. C., Chen, L. M., Xiao, J., and He, M. Y. (2013). Seasonal and Interannual Variations of the lake Water Parameters and Particle Flux in Lake Qinghai: A Time-Series Sediment Trap Study. *J. Earth Environ.* 4 (3), 8. (in Chinese).

Jin, Z., You, C.-F., and Yu, J. (2009a). Toward a Geochemical Mass Balance of Major Elements in Lake Qinghai, NE Tibetan Plateau: A Significant Role of Atmospheric Deposition. *Appl. Geochem.* 24 (10), 1901–1907. doi:10.1016/j.apgeochem.2009.07.003

Jin, Z., You, C.-F., Yu, T.-L., and Wang, B.-S. (2010). Sources and Flux of Trace Elements in River Water Collected from the Lake Qinghai Catchment, NE Tibetan Plateau. *Appl. Geochem.* 25 (10), 1536–1546. doi:10.1016/j.apgeochem.2010.08.004

Jin, Z., Yu, J., Wang, S., Zhang, F., Shi, Y., and You, C.-F. (2009b). Constraints on Water Chemistry by Chemical Weathering in the Lake Qinghai Catchment, Northeastern Tibetan Plateau (China): Clues from Sr and its Isotopic Geochemistry. *Hydrogeol J.* 17 (8), 2037–2048. doi:10.1007/s10040-009-0480-9

Kretschmer, S., Geibert, W., Loeff, M., and Mollenhauer, G. (2010). Grain Size Effects on ^{230}Thxs Inventories in Opal-Rich and Carbonate-Rich marine Sediments. *Earth Planet. Sci. Lett.* 294 (1-2), 131–142. doi:10.1016/j.epsl.2010.03.021

Krishnaswami, S., and Cochran, J. K. (2016). Uranium-Thorium Radionuclides in Ocean Profiles. *Encyclopedia Ocean Sci.* 1, 377–391. doi:10.1016/b978-0-12-409548-9.09760-8

Li, X.-Y., Xu, H.-Y., Sun, Y.-L., Zhang, D.-S., and Yang, Z.-P. (2007). Lake-level Change and Water Balance Analysis at Lake Qinghai, West China during Recent Decades. *Water Resour. Manage.* 21 (9), 1505–1516. doi:10.1007/s11269-006-9096-1

Lyle, M., Murray, D. W., Finney, B. P., Dymond, J., Robbins, J. M., and Brooksforce, K. (1988). The Record of Late Pleistocene Biogenic Sedimentation in the Eastern Tropical Pacific Ocean. *Paleoceanography* 3 (1), 39–59. doi:10.1029/pa003i001p00039

Lyle, M. W., and Dymond, J. (1976). Metal Accumulation Rates in the Southeast pacific - Errors Introduced from Assumed Bulk Densities. *Earth Planet. Sci. Lett.* 30 (2), 164–168. doi:10.1016/0012-821x(76)90242-9

Marcantonio, F., Anderson, R. F., Stute, M., Kumar, N., Schlosser, P., and Mix, A. (1996). Extraterrestrial 3He as a Tracer of marine Sediment Transport and Accumulation. *Nature* 383 (6602), 705–707. doi:10.1038/383705a0

Martin, J. H., and Fitzwater, S. E. (1988). Iron Deficiency Limits Phytoplankton Growth in the north-east Pacific Subarctic. *Nature* 331 (6154), 341–343. doi:10.1038/331341a0

McGee, D., and Mukhopadhyay, S. (2013). Extraterrestrial He in Sediments: From Recorder of Asteroid Collisions to Timekeeper of Global Environmental Changes. *The Noble Gases Geochem. Trac.*, 155–176. doi:10.1007/978-3-642-28836-4_7

Moore, W. S., and Sackett, W. M. (1964). Uranium and Thorium Series Inequilibrium in Sea Water. *J. Geophys. Res.* 69 (24). doi:10.1029/jz069i024p05401

Mortlock, R. A., Charles, C. D., Froelich, P. N., Zibello, M. A., Saltzman, J., Hays, J. D., et al. (1991). Evidence for Lower Productivity in the Antarctic Ocean during the Last Glaciation. *Nature* 351, 220–223. doi:10.1038/351220a0

Ojovan, M. I., and Lee, W. E. (2014). "Naturally Occurring Radionuclides," in *An Introduction to Nuclear Waste Immobilisation*. (Oxford: Elsevier), 31–39. doi:10.1016/b978-0-08-099392-8.00004-8

Rea, D. K., and Leinen, M. (1988). Asian Aridity and the Zonal Westerlies: Late Pleistocene and Holocene Record of Eolian Deposition in the Northwest Pacific

Ocean. *Palaeogeogr. Palaeoclimatol. Palaeoecol.* 66, 1–8. doi:10.1016/0031-0182(88)90076-4

Roy-Barman, M., Coppola, L., and Souhaut, M. (2002). Thorium Isotopes in the Western Mediterranean Sea: an Insight into the marine Particle Dynamics. *Earth Planet. Sci. Lett.* 196 (3-4), 161–174. doi:10.1016/s0012-821x(01)00606-9

Roy-Barman, M., LemaïTre, C., Ayrault, S., Jeandel, C., Souhaut, M., and Miquel, J. C. (2009). The Influence of Particle Composition on Thorium Scavenging in the Mediterranean Sea. *Earth Planet. Sci. Lett.* 286 (3-4), 526–534. doi:10.1016/j.epsl.2009.07.018

Santschi, P. H., Murray, J. W., Baskaran, M., Benitez-Nelson, C. R., Guo, L. D., Hung, C.-C., et al. (2006). Thorium Speciation in Seawater. *Mar. Chem.* 100, 250–268. doi:10.1016/j.marchem.2005.10.024

Sarnthein, M., Winn, K., Duplessy, J.-C., and Fontugne, M. R. (1988). Global Variations of Surface Ocean Productivity in Low and Mid Latitudes: Influence on CO2reservoirs of the Deep Ocean and Atmosphere during the Last 21,000 Years. *Paleoceanography* 3, 361–399. doi:10.1029/pa003i003p00361

Shen, C.-C., Wu, C.-C., Cheng, H., Lawrence Edwards, R., Hsieh, Y.-T., Gallet, S., et al. (2012). High-precision and High-Resolution Carbonate 230Th Dating by MC-ICP-MS with SEM Protocols. *Geochimica et Cosmochimica Acta* 99, 71–86. doi:10.1016/j.gca.2012.09.018

Shen, C. C., Edwards, R. L., Cheng, H., Dorale, J. A., Thomas, R. B., Moran, S. B., et al. (2002). Uranium and Thorium Isotopic and Concentration Measurements by Magnetic Sector Inductively Coupled Plasma Mass Spectrometry. *Chem. Geology.* 185 (3), 165–178. doi:10.1016/s0009-2541(01)00404-1

Tao, H., Hao, L., Li, S., Wu, T., Qin, Z., and Qiu, J. (2021). Geochemistry and Petrography of the Sediments from the Marginal Areas of Qinghai Lake, Northern Tibet Plateau, China: Implications for Weathering and Provenance. *Front. Earth Sci.* 9. doi:10.3389/feart.2021.725553

Wan, D., Jin, Z., and Wang, Y. (2012). Geochemistry of Eolian Dust and its Elemental Contribution to Lake Qinghai Sediment. *Appl. Geochem.* 27 (8), 1546–1555. doi:10.1016/j.apgeochem.2012.03.009

Wang, X. Q., Zhou, J., Xu, S. F., Chi, Q. H., Nie, L. S., Zhang, B. M., et al. (2016). China Soil Geochemical Baselines Networks: Data Characteristics. *Geology. China* 43 (5), 12. (in Chinese). doi:10.12029/gc20160501

Winckler, G., Anderson, R. F., Stute, M., and Schlosser, P. (2004). Does Interplanetary Dust Control 100 Kyr Glacial Cycles? *Quat. Sci. Rev.* 23 (18-19), 1873–1878. doi:10.1016/j.quascirev.2004.05.007

Xu, H., Liu, X., An, Z., Hou, Z., Dong, J., and Liu, B. (2010). Spatial Pattern of Modern Sedimentation Rate of Qinghai Lake and a Preliminary Estimate of the Sediment Flux. *Chin. Sci. Bull.* 55, 621–627. doi:10.1007/s11434-009-0580-x

Zhang, F., Jin, Z., Hu, G., Li, F., and Shi, Y. (2009). Seasonally Chemical Weathering and CO2 Consumption Flux of Lake Qinghai River System in the Northeastern Tibetan Plateau. *Environ. Earth Sci.* 59 (2), 297–313. doi:10.1007/s12665-009-0027-3

Zhang, P., Cao, C. Y., Li, X. Z., Pei, X. Z., Chen, C., Liang, L. H., et al. (2021). Effects of Ice Freeze-Thaw Processes on U Isotope Compositions in saline Lakes and Their Potential Environmental Implications. *Front. Earth Sci.* 9, 1143. doi:10.3389/feart.2021.779954

Zhang, P., Cheng, H., Liu, W. G., Mo, L. T., Li, X. Z., Ning, Y. F., et al. (2019). Geochemical and Isotopic (U, Th) Variations in lake Waters in the Qinghai Lake Basin, Northeast Qinghai-Tibet Plateau, China: Origin and Paleoenvironmental Implications. *Arabian J. Geosciences* 12 (92). doi:10.1007/s12517-019-4255-x

Zhang, P. X., Zhang, B. Z., Qian, G. M., Li, H. J., and Xu, L. M. (1994). The Study of Paleoclimatic Parameter of Qinghai Lake since Holocene. *Quat. Sci.* 14 (3), 225–238.

Zhang, X. Y., Arimoto, R., and An, Z. S. (1997). Dust Emission from Chinese Desert Sources Linked to Variations in Atmospheric Circulation. *J. Geophys. Res.* 102 (D23), 28041–28047. doi:10.1029/97jd02300

Zhao, C., Zhang, P., Li, X., Ning, Y., Tan, L., Edwards, R. L., et al. (2020). Distribution Characteristics and Influencing Factors of Uranium Isotopes in saline lake Waters in the Northeast of Qaidam Basin. *Minerals* 10 (1), 74. doi:10.3390/min10010074

Conflict of Interest: The authors declare that the research was conducted in the absence of any commercial or financial relationships that could be construed as a potential conflict of interest.

Publisher's Note: All claims expressed in this article are solely those of the authors and do not necessarily represent those of their affiliated organizations, or those of the publisher, the editors, and the reviewers. Any product that may be evaluated in this article, or claim that may be made by its manufacturer, is not guaranteed or endorsed by the publisher.

frontiers | Frontiers in Earth Science

ORIGINAL RESEARCH
published: 25 April 2022
doi: 10.3389/feart.2022.838867

Seasonal River Chemistry and Lithium Isotopes in the Min Jiang at Eastern Tibetan Plateau: Roles of Silicate Weathering and Hydrology

Baiyang Liu-Lu[1,2], Zhangdong Jin[1,3], Long-Fei Gou[1,4], Fei Zhang[1,4], Mao-Yong He[1,4] and Yang Xu[1,2]*

[1]SKLLQG, Institute of Earth Environment, Chinese Academy of Sciences, Xi'an, China, [2]University of Chinese Academy of Sciences, Beijing, China, [3]Institute of Global Environmental Change, Xi'an Jiaotong University, Xi'an, China, [4]School of Land Engineering, Chang'an University, Xi'an, China

Riverine lithium (Li) isotopes have been considered as a robust tracer for silicate weathering, but processes controlling riverine δ^7Li ratios remain controversial. To address the impacts of weathering and hydrology on riverine δ^7Li, the seasonal variation of water chemistry in the Min Jiang at the eastern Tibetan Plateau was investigated over December of 2009 to the end of 2010. The results showed distinct seasonal variations in ionic chemistry and δ^7Li. Increased river discharge in the monsoon season diluted dissolved ions, and monsoonal hydrological changes caused frequent δ^7Li fluctuations. High discharge caused by monsoonal rainfall reduced Li isotope fractionation by shortened rock–fluid interaction time, resulting in lower δ^7Li, whereas the input of high δ^7Li groundwater and landslide seepage elevated riverine δ^7Li, together with lengthened rock–fluid interaction time in less rain intervals. Based on the high-resolution sampling strategy and dataset over one hydrological year, this study highlights that changes of hydrological conditions can have a significant impact on weathering processes and water sources, and therefore on riverine δ^7Li variation.

Keywords: lithium isotopes, seasonality, hydrological change, silicate weathering, eastern Tibetan Plateau

OPEN ACCESS

Edited by:
Philippe Claeys,
Vrije Universiteit Brussel, Belgium

Reviewed by:
Santosh Kumar Rai,
Wadia Institute of Himalayan Geology, India
Sambuddha Misra,
Indian Institute of Science (IISc), India

****Correspondence:***
Zhangdong Jin
zhdjin@ieecas.cn

Specialty section:
This article was submitted to Geochemistry, a section of the journal Frontiers in Earth Science

Received: *18 December 2021*
Accepted: *16 March 2022*
Published: *25 April 2022*

Citation:
Liu-Lu B, Jin Z, Gou L-F, Zhang F, He M-Y and Xu Y (2022) Seasonal River Chemistry and Lithium Isotopes in the Min Jiang at Eastern Tibetan Plateau: Roles of Silicate Weathering and Hydrology. Front. Earth Sci. 10:838867. doi: 10.3389/feart.2022.838867

1 INTRODUCTION

Silicate weathering is thought to be a major sink of atmospheric CO_2, which regulates the carbon cycle and climate on geological time scales (e.g., Walker et al., 1981; Bickle et al., 2015; Penman et al., 2020); thus, it is in turn an important control on global climate. It has been argued that tectonic uplift and exposure of fresh rocks has a strong influence on the weathering rate (Edmond et al., 1995). The uplift of the Himalayas and the Tibetan Plateau had strengthened silicate weathering and atmospheric CO_2 consumption as a proposed trigger of global cooling since ~50 Ma (e.g., Raymo and Ruddiman, 1992; Clift et al., 2008). Since materials in rivers have been used to trace weathering, that is, particulate sediments corresponding to the physical denudation rate and dissolved loads to the chemical weathering rate, respectively (Li and Zhang, 2002), the rivers draining the southern Himalayas and the eastern Tibetan Plateau are widely explored on the relationship between the tectonics and climate with weathering rates (e.g., Qin et al., 2000; Bickle et al., 2005; Wu et al., 2011; Bickle et al., 2015). For example, recent studies have shown that in the Himalayas and Qinghai, from where main Chinese rivers originate, the long-term CO_2 consumption

by silicate weathering occupies 3.8% of global silicate weathering (Wu et al., 2008), implying the role of the tectonics in enhancing silicate weathering. Similarly, Bickle et al. (2015) demonstrated that Himalayan rivers are dominated by silicate inputs, up to 60% riverine Sr in the catchment on the High Himalayan Crystalline Series from silicates, after they reviewed geochemical analyses of river waters from the headwaters and their tributaries of the Himalayan rivers. More recently, seismically enhanced ionic fluxes after the 2008 Wenchuan earthquake resulted in a 4.3 ± 0.4 time increase in CO_2 consumption flux *via* silicate-derived alkalinity and a 0.000644 ± 0.000146 increase in $^{87}Sr/^{86}Sr$ isotopic ratios (Jin et al., 2016). At the millennial scale, silicate weathering was mainly related with runoff and physical erosion, while temperature played a secondary role (Dosseto et al., 2015). However, the relationships among silicate weathering, the carbon cycle, and climate at various time scales remain elusive. One of the key reasons is the lack of a robust tracer for silicate weathering.

So far, a number of isotopic tracers have been served for evaluating the silicate weathering rate and intensity, such as Sr, Mg, Si, and Os isotopes. However, none of them would be able to trace silicate weathering reliably, owing to the effects of other processes and/or unconstrained sources, such as biological processes for Mg and Si isotopes (Li et al., 2014; Mavromatis et al., 2016; Pogge von Strandmann et al., 2016), meta-carbonate-sourced radiogenic Sr (Edmond, 1992; Galy and France-Lanord, 1999; Bickle et al., 2005; Beck et al., 2013), and black shale-derived Os (Ravizza and Esser, 1993). Lithium (Li) is one of the most promising tracers for tracing silicate weathering. This is due to the fact that Li is hosted broadly in silicates, with significant fractionation during weathering (Huh et al., 1998; Huh et al., 2001). Li is soluble, with two stable isotopes (^6Li and ^7Li) that fractionate during low-temperature rock–fluid exchange reactions. Meanwhile, Li isotope variations are not significantly affected by biological processes (Lemarchand et al., 2010; Pogge von Strandmann et al., 2016). Thus, Li isotopes can record weathering and transportation information.

Due to the analytical technique development, research on Li isotope tracing silicate weathering has been blossoming in the last decade. Previous studies have mainly focused on the spatial variation of the riverine dissolved δ^7Li, factors that control riverine Li isotopic fractionation, and how to use riverine δ^7Li as a tracer of silicate weathering at various scales (Huh et al., 1998; Huh et al., 2001; Pogge von Strandmann et al., 2006; Vigier et al., 2008; Liu and Rudnick, 2011; Dellinger et al., 2014; Wang et al., 2015). However, the dominant processes controlling riverine δ^7Li ratios remain debatable (Misra and Froelich, 2012; Dellinger et al., 2015). To address this issue, time–series change of riverine δ^7Li ratios may provide helpful clues, because its sources and end-members can be well constrained or easily defined. Researchers found that there was a ~10% difference of δ^7Li at the same site in different seasons, and δ^7Li of samples showed seasonal variations (Kısakürek et al., 2005; Liu et al., 2015), but the resolution of time–series of previous studies was not high enough to decipher the role of climate (Gou et al., 2019). In addition, there were only

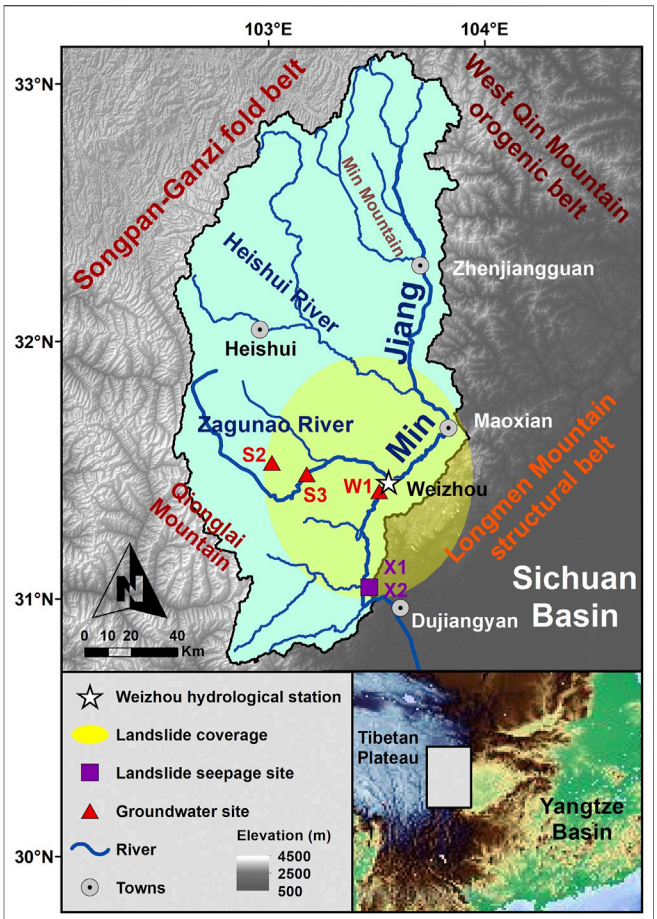

FIGURE 1 | Map of the Min Jiang catchment, including sampling sites of river water at the Weizhou hydrological station, groundwater, and landslide seepage.

a few studies that mentioned about the hydrological impacts on riverine δ^7Li (e.g., Lemarchand et al., 2010; Fries et al., 2019; Xu et al., 2021): how the hydrology (such as monsoon rain and groundwater) affecting riverine Li isotope behaviors is poorly constrained. Therefore, we set a high-resolution time–series research in order to explore the weathering processes in detail by seasonal riverine δ^7Li variation at the eastern Tibetan Plateau.

The earth surface processes on the Tibetan Plateau is sensitive to climate, and climate regulation by silicate weathering is strongest at such high elevations (West et al., 2002; Maher and Chamberlain, 2014; Caves et al., 2016; Ma et al., 2020). The Min Jiang is one of the primary tributaries of the Yangtze River, draining the eastern edge of the Tibetan Plateau (**Figure 1**). As a tectonically active and fast-eroding region, the weathering within the Min Jiang catchment would be significantly influenced by climate and hydrology, making it as an ideal setting for exploring the controlling factors of riverine δ^7Li ratios and its relationship with silicate weathering. In this study, we investigated water chemistry and Li isotope compositions of river samples collected weekly from the Min Jiang, in order to explore the

controlling factors of riverine δ^7Li during catchment weathering and the impacts of hydrology on riverine δ^7Li on the Tibetan Plateau.

2 MATERIALS AND METHODS

2.1 Study Area

The Min Jiang ("Jiang" means "river" in Chinese) catchment (**Figure 1**) is situated at about 28°–33° N and 100°–104° E, and is limited by the Qionglai Mountains in the west and the Min Mountains in the east. The main stream catchment area is 45,500 km^2 (Liu et al., 2020). The Min Jiang, as a tributary of the upper Yangtze River, is a 1279-km-long river sourced from the eastern edge of the Tibetan Plateau at an altitude of 4,579 m, with an elevation gradient of 3,560 m (Ren and Luo, 2013). The mainstream of the Min Jiang flows toward the southern direction with a rich network of tributaries, passing through Maoxian in Longmen Mountains and entering the plain of the Sichuan Basin near Dujiangyan. A significant elevation change is observed when it meets the Sichuan Basin, an alluvial plain with an average altitude of ~500 m. After entering the plain, the Min Jiang main channel joins the Qingyi Jiang at Leshan, and finally imports to the Yangtze River at Yibin.

There are two main tributaries in the upper reaches of the Min Jiang: the Heishui and the Zagunao Rivers (**Figure 1**). Both the tributaries flow toward east and import into the Min Jiang main channel. The Heishui River is 122 km in length with an elevation gradient of 1,048 m, and its catchment area (7,240 km^2) occupies about 31% of the Min Jiang upstream catchment, with an average water discharge (Q_w) of 140 m^3/s. The Zagunao River is 158 km lengthy and has 3,092 m elevation gradient, with a catchment area of 4,629 km^2 and 9.9–122 m^3/s of Q_w. The river water sampling site, the Weizhou hydrological station, is located at 31°28′48.63″N, 103°34′57.86″E in the upper reaches of the Min Jiang, below the confluences of the Zagunao River and the main channel. The catchment area upstream from the station is 18,921 km^2 (Bureau of Hydrology, 2010).

The Min Jiang catchment is located at the junction site among the Songpan-Ganzi fold belt, the west Qin Mountain orogenic belt, and the Longmen Mountain structural belt. The catchment appears to be a parallelogram inset in the Longmen Shan and the Min Mountain tectonic zone (Zhang et al., 2006). The geology of the region is dominated by bedrocks with aluminosilicate minerals, including metamorphic argillaceous sandstone and flysch, granite and monzonitic granite, and detrital sediments, as well as limestones (Jin et al., 2016). At the west side of the Min Jiang, the Songpan-Ganzi fold belt extensively develops Mesozoic flysch sedimentary formations (5–15 km thickness), within which metamorphic sandstone and limestone are dominant lithologies, with a minority of regional developed Indosinian intrusive granites, as well as minor outcrops of sandstone and mudstone interbedded with coal seams (Yoon et al., 2008). At the Longmen Mountain structural belt, the hypo-metamorphic Paleozoic basement is dominant, including slate and phyllite with intercalated marble, carbonate with clastic rocks, or coal-bearing silicates (SLCCC, 1998). From the source of the Min Jiang to north Maoxian, the riverbed is mainly Mesozoic flysch with little lithologic variation, while from Maoxian to the Dujiangyan stretch, the river bedrock is extensively made of Paleozoic complex formed in the Longmen Mountain structural belt (Zhang et al., 2006).

The climate of the Min Jiang catchment is mainly subtropical, and its upper reaches belong to a high elevation plateau climate characterized by low average temperature and little precipitation (Qin et al., 2006; Yoon et al., 2008). The rainfall of the most Min Jiang catchment is carried by Asian and Indian summer monsoons, with 75% of annual precipitation (600–1,100 mm/year) from May to October. In 2010, the annual precipitation in the whole Min Jiang catchment ranged from 455.6 to 2,782.7 mm. The annual Q_w of the Min Jiang was 1.06×10^{10} m^3 in 2000–2011 (Jin et al., 2016). In addition, the average winter and summer temperatures are 0.5°C and 15–17°C for the upper reach region but 5.5 and 26°C for the lower reach plain area in historical records before 2008, respectively (Yoon et al., 2008).

2.2 Samples and Analyses

A total of 71 river water samples were collected weekly from 7 December 2009 to 27 December 2010 at the Weizhou hydrological station. Among them, samples were collected densely during heavy rainfalls: The samples of WZ10-25 to 27 were collected on 27 May 2010, WZ10-29 to 30 were sampled on 7 June, WZ10-36 to 40 were sampled on 17 July, and WZ10-46 to 47 were sampled on 21 August. These samples were used to catch the signature of hydrological changes in river water chemistry and δ^7Li. Also, two rainwater samples were collected in the post-monsoon season in 2010. Three groundwater samples were collected from upstream of the station in November 2020, including one well water sample (W1: 31°26′35.86″N, 103°32′28.43″E), and two spring water samples S2 (31°23′56.27″N, 103°03′8.38″E) and S3 (31°30′20.98″N, 103°12′39.58″E) that just gashed out the surface.

The middle reaches of the Min Jiang experienced moderate numbers of earthquake-triggered landslides induced by the M_w 7.9 Wenchuan earthquake on 12 May 2008. The earthquake triggered tens of thousands of landslides (Li et al., 2014) which increased suspended sediment and solute flux in the Min Jiang in the years that followed (Wang J. et al., 2015; Jin et al., 2016). In order to assess the potential impact of earthquake-triggered landslides on water chemistry, two samples of landslide seepage were collected near Yingxiu in 2018: X1 was the surface runoff on a landslide slope, and X2 was the bottom stream seeped through the landslide mass.

For each river, rain, and groundwater sample, temperature, pH, and TDS (total dissolved solids) were measured at the sampling spot synchronously during the collection. All samples were filtered *in situ* though 0.2 μm Whatman® nylon filters and then collected into two types of polyethylene bottles: one 60 ml fraction was for cation analysis, in which bottles were pre-cleaned with 6 mol/L double-distilled HNO_3 and acidified to pH < 2 by proportionally adding the same pre-cleaned HNO_3 into the samples. The other 30 ml fraction contained a filtered but unacidified sample for anion analysis. All bottles were filled

without air, wrapped with a sealing film, and stored in a 3°C depository to keep from deterioration before treatment.

For the river and rain water samples, major cations (K^+, Na^+, Ca^{2+}, and Mg^{2+}) were analyzed by the Leeman Labs Profile inductively coupled plasma atomic emission spectrometer (ICP-AES), with the relative standard deviation (RSD) less than 1%. Major anions (F^-, Cl^-, and SO_4^{2-}) were measured by ion chromatography (ICS 1200) with 2% RSD, and NO_3^- was measured by a Skalar continuous flow analyzer with 2.2% RSD. The experiments aforementioned were completed at the Nanjing Institute of Geography & Limnology, Chinese Academy of Sciences (CAS). Alkalinity (expressed as HCO_3^-) was measured by a Shimadzu Corporation total organic carbon analyzer (TOC-V_{CPH}) at the Northwest Argriculture and Forestry University, with the RSD less than 1.5%. Li concentrations of these water samples were conducted at the State Key Laboratory of Loess and Quaternary Geology (SKLLQG) in the Institute of Earth and Environment, CAS (IEECAS) using a PerkinElmer NexION 300D Inductively Coupled Plasma Mass Spectrometry (ICP-MS) with the RSD better than 5%.

Pretreatment for the purification of Li was carried out in an ultraclean lab (100 classes in operating window) following the method developed by Gou et al. (2018). Briefly, it was a one-step purification procedure for Li and then an accurate and high-precision determination of its isotopic compositions by MC-ICP-MS (multi-collector inductively coupled plasma mass spectrometer) at IEECAS. First, water samples containing 100–200 ng Li were dried and transformed into 0.5 mol/L HNO_3 solution. Then all the solute samples were purified by a single-step cation exchange chromatographic column filled up with 8 ml resin (Bio-rad AG50W X-12, 100–200 mesh), with 0.5 mol/L diluted HNO_3 as an eluent. The purified Li fraction was extracted in 2% HNO_3 for MC-ICP-MS measurement. Splits collected before and after the main Li elution peak were analyzed for Na and Li contents, to ensure full column recovery. Li recoveries were measured by PerkinElmer NexION 300D ICP-MS and yielded >99.9% recoveries for all samples. The weight Na/Li ratios in all samples were less than 1, which ensured qualified standard deviations and negligible matrix effect during Li isotopic ratio measurements (Gou et al., 2017; Gou et al., 2018; Gou et al., 2020). Li isotope compositions were measured by ThermoFisher NeptunePlus MC-ICP-MS with the standard deviation (s.d.) less than 0.25 and the total procedural blank below 0.3 ng Li. The standard-sample bracketing (SSB) method was used in the measurement with NIST LSVEC as isotopic standard. The results were normalized to LSVEC as follows:

$$\delta^7\mathrm{Li}\ (‰) = 1000 \times \left[\frac{\left(\frac{^7\mathrm{Li}}{^6\mathrm{Li}}\right)_{\mathrm{sample}}}{\left(\frac{^7\mathrm{Li}}{^6\mathrm{Li}}\right)_{\mathrm{LSVEC}}} - 1\right]. \quad (1)$$

Each sample was measured in triplicate to determine average values with RSD. Standards were run together with the samples to verify precision and reliability of the measurements, including the standard of the Isotopic Geochemical laboratory of University of Science and Technology of China (USTC-L, with δ^7Li = −19.3 ± 0.2‰), standard of SPEX CertiPrep (SPEX-Li, with δ^7Li = +12.2 ± 0.2‰), seawater standard (NASS-6, with δ^7Li = +31.1 ± 0.7‰), and Li element standard GBW(E)080547 (δ^7Li = +8.3 ± 0.2‰). The long-term external reproducibility of Li isotope testing was better than ±0.9‰ (2 s.d.), with less than 100 ng sample consumption (Gou et al., 2018), and Li isotope standards tested were in agreement with the values stated previously and from previous studies (e.g., Rudnick et al., 2004; Chetelat et al., 2008; Wang et al., 2015; Pogge von Strandmann et al., 2016), with the trueness better than 2% within 0.5‰ isotopic value errors. Similar analysis methods were operated for landslide seepage samples at Nanjing University and groundwater samples at SKLLQG, IEECAS, respectively.

3 RESULTS

3.1 Hydrology and Water Chemistry

The hydrological and chemical data of the Min Jiang water during December 2009 and December 2010 are listed in **Table 1**. The air temperature (T) increased with fluctuations from middle January to middle August, and then decreased in a similar pattern until the end of 2010 (**Figure 2**), with a minimum of 1.1°C in December and a maximum 29.5°C in August. From May to October (the monsoon season), most of the daily air T were above 15°C. The whole year river water T ranged from 4.0 to 19.5°C, with the lowest value in January and the highest in August (**Figure 2**), a similar trend as the air T but with less fluctuation. The TDS ranged from 169.6 to 435.6 mg/L, with the lowest TDS in July and the highest in November, all within the range of the source region of the Yangtze River (50–3,012 mg/L) (Liu M. et al., 2021). The 2010 annual Q_w was 328.0 m^3/s in average and had a distinct difference between monsoon and non-monsoon seasons: the Q_w ranged from 53.4 to 390.0 m^3/s in the non-monsoon season and 228.0 to 1,500.0 m^3/s in the monsoon season. The minimum Q_w in the monsoon season was about two times higher than the average of the non-monsoon seasons. The Q_w kept a stable and relatively low value from January to April, and increased abruptly under strong rain when stepping into the monsoon season in May. In the monsoon season, the Q_w responded directly to the rainfall intensity, and high Q_w reflected the frequent rainfall in the Min Jiang catchment. A stormy event in 8 June generated the maximum Q_w (1,500.0 m^3/s). After the monsoon season, the Q_w quickly returned to lower values and remained stable for the rest of the year (post-monsoon season).

The water chemistry of river dissolved loads in the Min Jiang was closely related to the monsoon climate (**Figure 3**). First, all ions had a similar variation trend through different seasons: they remained stable at relatively high values in the pre-monsoon season, dropped to a lower and stable level in the monsoon season, and run ups and downs in the post-monsoon season. Second, Q_w variations impacted ion concentrations. The ions showed both dilution and chemostatic behaviors (Koger et al., 2018). As Q_w increased from 50 to 400 m^3/s in the non-monsoon seasons, ionic concentrations decreased rapidly, showing an inverse relationship with Q_w (**Figure 4**). During the monsoon season, there was a less rain interval in middle July to middle

TABLE 1 | Ionic and lithium isotopic compositions of all water samples collected within the Min Jiang river catchment.

Sample type	Sample	Date	TDS	Temp	pH	[Li]	δ^7Li	K^+	Na^+	Ca^{2+}	Mg^{2+}	Cl^-	F^-	NO_3^-	HCO_3^-	SO_4^{2-}
		Y/M/D	mg/L	°C		μmol/L	‰	μmol/L	μmol/L	μmol/L	μmol/L	μmol/L	μmol/L	μmol/L	μmol/L	μmol/L
Pre-monsoon river water	WZ09-1	09/12/7	297.4	-	-	1.274	13.53	38.08	258.92	1,083.59	638.13	67.29	4.25	18.55	3,302.67	254.35
	WZ09-2	09/12/14	290.5	-	-	1.324	13.50	38.79	305.34	1,115.97	675.98	70.16	4.27	19.34	3,165.00	234.43
	WZ09-3	09/12/21	281.5	4.1	8.4	1.403	13.71	38.84	310.61	1,084.94	652.23	105.79	4.98	19.37	2,946.00	284.30
	WZ09-4	09/12/28	291.9	4.1	8.4	1.434	13.72	40.48	304.09	1,105.08	678.67	99.65	3.86	17.82	3,120.00	270.41
	WZ10-1	10/1/4	283.8	4.3	8.4	1.437	12.66	35.96	307.37	1,077.33	651.45	97.04	3.87	19.45	3,002.00	280.08
	WZ10-2	10/1/12	299.6	4.1	8.4	1.513	12.76	42.71	348.93	1,130.60	702.49	117.59	4.87	29.27	3,116.00	316.93
	WZ10-3	10/1/18	304.4	4.0	8.4	1.513	13.26	42.10	345.25	1,162.07	725.41	117.00	4.38	33.74	3,024.00	406.92
	WZ10-4	10/1/25	290.6	5.1	8.7	1.467	13.55	39.70	305.77	1,100.12	680.36	85.46	5.39	21.61	3,047.00	309.44
	WZ10-5	10/2/1	292.1	5.8	8.6	1.566	13.28	36.55	289.18	1,096.35	710.64	59.93	4.35	15.13	3,091.00	308.47
	WZ10-6	10/2/8	291.5	9.7	8.3	1.554	13.16	38.10	318.14	1,104.33	693.38	112.54	4.09	15.44	3,043.00	306.56
	WZ10-7	10/2/15	294.7	11.7	8.3	1.535	13.63	37.30	298.96	1,103.92	702.46	86.97	5.34	20.09	3,129.00	290.01
	WZ10-8	10/2/22	289.9	8.0	8.3	1.591	13.57	38.43	305.68	1,092.35	706.95	71.62	4.00	20.02	3,045.00	308.39
	WZ10-9	10/3/1	299.3	11.7	8.3	1.596	13.81	39.58	330.23	1,123.62	726.01	72.69	4.52	19.96	3,163.00	305.76
	WZ10-10	10/3/9	311.9	6.3	8.4	1.651	13.74	41.18	373.55	1,123.30	732.58	127.24	4.31	7.78	3,209.00	374.92
	WZ10-11	10/3/15	302.5	10.0	8.7	1.680	13.48	43.33	328.16	1,131.99	754.27	86.92	4.27	21.76	3,171.00	316.70
	WZ10-12	10/3/22	298.0	10.9	8.6	1.608	13.63	40.92	324.91	1,113.83	709.71	88.42	3.67	15.44	3,088.00	342.52
	WZ10-13	10/3/28	300.4	9.2	8.7	1.585	14.20	41.63	351.51	1,088.25	718.20	104.69	4.07	18.86	3,141.00	328.39
	WZ10-14	10/4/6	286.8	10.7	8.4	1.502	13.63	41.32	391.77	1,050.50	651.90	153.22	4.92	12.39	2,956.00	310.31
	WZ10-15	10/4/12	271.8	10.7	8.3	1.418	13.55	39.88	303.58	1,030.01	616.43	83.12	4.46	22.00	2,871.00	273.10
	WZ10-16	10/4/19	298.7	11.7	8.7	1.522	14.29	48.11	340.66	1,126.08	689.38	112.45	4.87	15.87	3,005.00	387.03
	WZ10-17	10/4/26	219.7	10.8	8.5	1.339	14.02	44.24	320.88	1,011.59	566.46	111.06	5.33	-	2,029.00	269.16
	WZ10-18	10/5/3	261.1	13.9	8.6	1.278	13.91	36.24	276.77	1,008.24	592.14	72.72	3.24	21.01	2,832.00	214.87
Monsoon season river water	WZ10-19	10/5/9	202.0	11.3	8.8	0.902	12.58	24.34	193.10	884.66	429.29	62.26	-	-	2,100.00	187.35
	WZ10-20	10/5/10	211.2	11.3	8.1	0.979	13.59	23.46	190.72	889.45	455.76	50.25	7.78	-	2,210.00	211.46
	WZ10-21	10/5/17	189.6	11.3	8.5	0.784	14.01	18.51	159.65	796.82	379.50	41.76	7.78	1.34	2,029.17	172.37
	WZ10-22	10/5/21	187.1	12.4	8.6	0.762	13.86	22.69	142.21	827.45	344.51	41.90	8.66	1.64	1,815.00	281.67
	WZ10-23	10/5/22	186.4	12.4	8.6	0.742	14.09	21.49	140.84	820.79	342.10	36.27	8.64	-	1,816.67	279.75
	WZ10-24	10/5/24	195.7	12.4	8.6	0.760	14.23	20.16	164.91	837.75	405.52	45.28	6.94	-	2,057.50	191.01
	WZ10-25	10/5/27	178.4	13.8	8.8	0.788	13.13	25.85	153.31	785.69	308.05	45.47	7.48	-	1,746.67	253.72
	WZ10-26	10/5/27	178.6	13.9	8.8	0.804	12.89	31.68	152.78	795.31	311.93	57.65	7.94	-	1,734.17	253.21
	WZ10-27	10/5/27	196.4	14.1	8.7	1.060	10.48	34.28	201.22	897.28	329.98	69.98	8.46	-	1,845.00	303.50
	WZ10-28	10/6/1	207.0	12.1	8.5	0.830	13.67	20.97	162.94	855.96	419.25	44.90	7.43	25.44	2,228.33	189.29
	WZ10-29	10/6/7	187.5	12.4	8.7	0.714	13.74	29.01	138.18	780.94	366.22	48.06	6.31	16.00	2,034.17	156.22
	WZ10-30	10/6/7	219.7	13.4	8.6	1.098	10.66	39.92	173.36	983.33	390.26	57.72	9.22	3.18	2,300.00	211.34
	WZ10-31	10/6/14	199.2	12.6	8.6	0.867	11.11	23.24	145.01	928.62	331.06	44.64	8.48	12.31	2,140.00	159.51
	WZ10-32	10/6/21	181.2	14.3	8.7	0.783	12.31	24.74	134.97	798.75	340.95	43.69	7.76	13.47	1,937.50	154.43
	WZ10-33	10/6/28	193.0	14.5	8.7	0.859	13.98	28.29	162.02	835.69	392.57	63.67	7.46	3.91	2,046.67	163.44
	WZ10-34	10/7/5	174.1	15.4	8.6	0.714	16.30	20.39	143.51	757.44	327.37	36.21	8.98	-	1,864.17	150.46
	WZ10-35	10/7/12	188.2	13.6	8.2	0.775	13.33	19.15	144.80	799.71	371.32	31.72	7.93	-	2,052.50	150.17
	WZ10-36	10/7/17	190.0	14.1	8.4	0.868	11.74	22.72	158.99	815.21	363.76	42.31	7.97	7.15	2,039.17	162.91
	WZ10-37	10/7/17	169.8	14.2	8.2	0.753	12.25	21.65	126.01	735.87	311.76	32.68	7.47	7.03	1,822.50	148.93
	WZ10-38	10/7/17	171.9	14.2	8.2	0.779	12.78	22.90	132.35	759.18	316.19	31.10	8.24	13.79	1,829.17	154.30
	WZ10-39	10/7/17	171.5	13.9	-	0.770	12.76	25.26	129.81	748.92	310.55	39.11	6.23	58.15	1,820.00	158.68
	WZ10-40	10/7/17	175.4	13.4	8.1	0.789	13.01	22.66	128.56	816.92	333.73	30.89	8.06	-	1,862.50	140.57
	WZ10-41	10/7/19	169.6	14.3	8.1	0.764	13.70	22.62	139.27	763.39	316.66	29.21	7.52	11.34	1,804.17	143.26
	WZ10-42	10/7/26	234.9	13.7	8.1	1.125	13.54	57.10	253.26	951.05	470.49	78.89	8.19	20.43	2,450.83	232.51
	WZ10-43	10/8/2	237.0	15.8	8.1	1.077	13.38	56.75	252.00	951.19	470.12	77.86	6.50	21.84	2,483.33	233.55

(Continued on following page)

TABLE 1 | (*Continued*) Ionic and lithium isotopic compositions of all water samples collected within the Min Jiang river catchment.

Sample type	Sample	Date	TDS	Temp	pH	[Li]	δ^7Li	K^+	Na^+	Ca^{2+}	Mg^{2+}	Cl^-	F^-	NO_3^-	HCO_3^-	SO_4^{2-}
		Y/M/D	mg/L	˚C		μmol/L	‰	μmol/L	μmol/L	μmol/L	μmol/L	μmol/L	μmol/L	μmol/L	μmol/L	μmol/L
	WZ10-44	10/8/9	233.5	19.5	8.2	1.115	14.16	24.15	199.30	971.24	515.55	44.41	7.72	18.92	2,404.17	267.46
	WZ10-45	10/8/16	194.7	14.7	8.2	0.891	13.18	22.29	167.50	807.10	407.40	34.22	8.85	12.97	2,061.67	190.33
	WZ10-46	10/8/21	185.1	13.5	8.5	0.813	14.50	24.03	146.22	781.26	371.29	32.19	6.85	18.68	1,935.83	195.74
	WZ10-47	10/8/21	187.7	13.1	8.4	0.791	15.24	30.58	148.16	782.94	369.25	41.92	6.72	2.00	1,965.83	196.69
	WZ10-48	10/8/23	182.6	15.6	8.1	1.274	10.60	22.44	149.54	620.29	363.32	32.47	8.31	-	2,070.00	164.67
	WZ10-49	10/8/30	228.9	16.1	8.5	1.456	12.15	26.99	212.54	952.40	468.15	59.13	8.18	27.16	2,301.67	293.05
	WZ10-50	10/9/6	210.4	14.4	8.5	1.154	12.21	22.58	170.47	900.00	423.49	42.11	7.24	15.48	2,207.50	214.76
	WZ10-51	10/9/13	219.2	16.4	8.5	1.126	12.71	23.71	190.85	929.14	453.66	51.61	7.53	19.91	2,303.33	216.57
	WZ10-52	10/9/20	243.1	12.4	8.1	1.134	14.05	25.68	220.40	983.25	499.87	64.42	8.24	16.43	2,535.83	269.78
	WZ10-53	10/9/27	220.6	13.5	8.5	1.105	13.97	38.33	199.26	920.40	471.40	74.81	7.48	16.27	2,270.00	233.53
	WZ10-54	10/10/4	224.7	13.4	8.6	1.006	15.47	23.63	202.99	920.41	471.47	63.86	6.69	23.18	2,355.83	232.33
Post-monsoon river water	WZ10-55	10/10/11	220.7	12.2	8.6	0.983	14.00	23.18	202.01	916.55	470.94	63.18	7.68	24.56	2,293.33	232.95
	WZ10-56	10/10/18	363.5	11.7	8.1	1.703	15.25	55.36	434.28	1,356.34	760.61	173.23	8.18	75.95	3,012.50	892.84
	WZ10-57	10/10/25	321.9	11.9	8.4	1.454	15.15	80.58	353.41	1,259.56	687.52	179.82	8.34	56.02	2,820.83	648.61
	WZ10-58	10/11/1	381.3	11.9	8.5	1.951	15.16	81.76	565.77	1,553.87	874.88	268.20	-	94.05	3,031.67	875.67
	WZ10-59	10/11/8	409.8	14.3	8.4	2.038	15.77	83.06	607.01	1,639.20	924.25	290.49	25.42	125.47	3,072.50	1,079.68
	WZ10-60	10/11/15	340.9	10.3	8.1	2.078	16.29	83.30	659.96	1,170.59	978.97	316.49	25.84	120.15	1,997.50	1,203.05
	WZ10-61	10/11/22	435.6	13.1	8.1	2.225	16.37	91.02	670.09	1,723.75	997.29	321.83	26.21	136.95	3,143.33	1,218.01
	WZ10-63	10/11/29	308.6	11.4	8.3	2.187	16.12	93.75	642.68	1,672.85	984.93	302.99	-	24.77	1,138.33	1,206.26
	WZ10-64	10/12/6	212.0	11.5	8.3	1.622	16.16	57.99	458.40	1,316.76	761.60	185.04	-	12.39	972.50	616.86
	WZ10-65	10/12/13	318.8	10.9	8.3	2.093	15.77	89.29	646.83	1,698.95	986.18	319.96	-	126.80	1,264.17	1,220.20
	WZ10-66	10/12/20	249.6	11.2	8.7	1.461	15.14	39.45	370.18	1,131.37	669.78	141.15	-	24.55	2,275.00	329.21
	WZ10-67	10/12/27	274.7	9.8	8.6	1.891	15.25	75.90	553.95	1,492.97	887.49	251.37	-	64.21	1,260.83	926.74
Rain water	WZ10-R1	10/03/07	-	-	-	0.248	-	26.24	43.28	176.80	35.26	24.10	13.82	27.46	444.70	101.38
	WZ10-R2	10/04/06	-	-	-	0.249	-	20.68	72.94	230.85	23.21	27.13	12.87	35.15	322.00	160.09
Groundwater	WZ-W1	20/11/25	178.0	11.5	7.6	0.232	16.82	56.05	298.83	1,038.00	661.25	186.13	11.58	53.62	2,213.33	495.98
	WZ-S2	20/11/25	103.0	10.1	7.9	0.313	20.70	60.15	121.83	813.25	143.13	15.24	7.68	25.91	1,475.83	139.43
	WZ-S3	20/11/25	72.0	6.8	7.8	0.370	19.54	33.15	94.26	487.75	102.17	6.42	2.56	13.71	985.83	65.90
Landslide seepage	WZ-X1	18/11/17	-	-	-	0.140	17.10	12.06	138.74	666.25	69.88	45.79	13.98	274.74	640.00	223.49
	WZ-X2	18/11/17	79.0	11.7	8.3	0.145	14.70	12.31	140.17	658.50	70.13	44.63	9.82	258.40	640.00	230.23

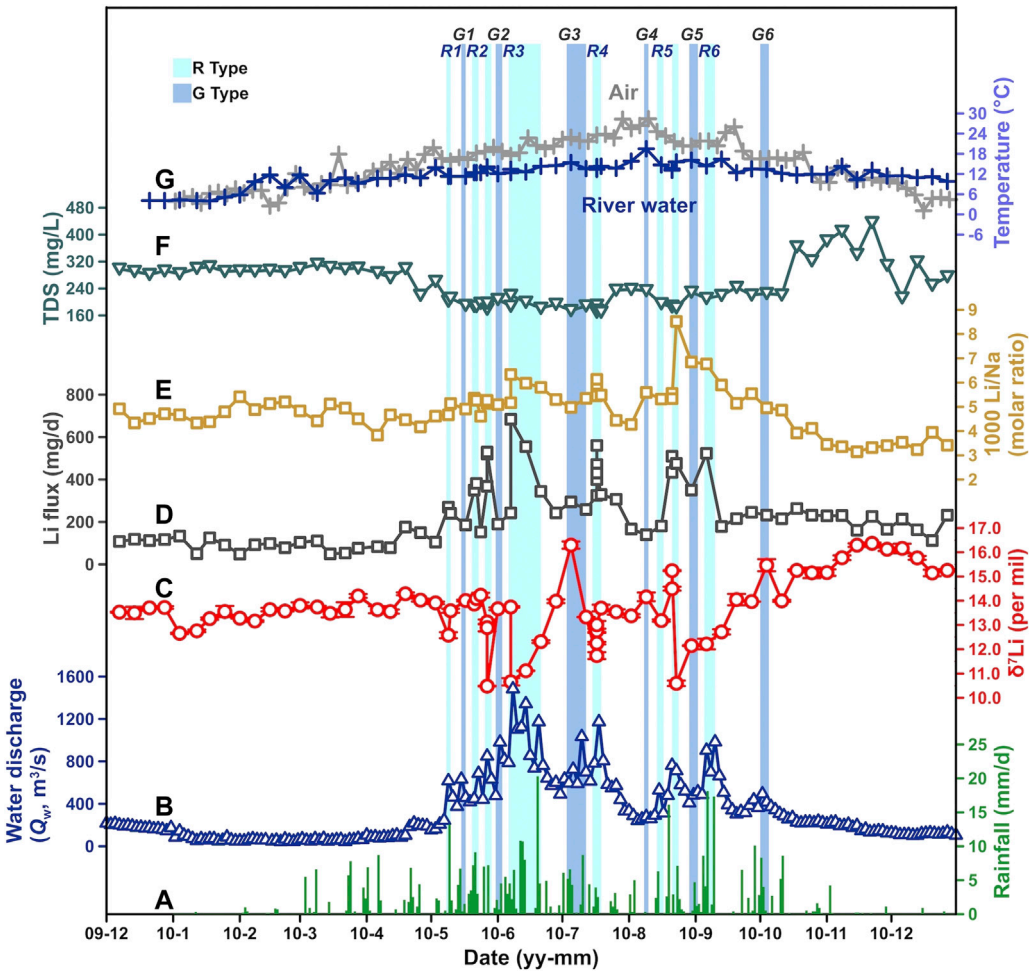

FIGURE 2 | Seasonal variations in **(A)** rainfall, **(B)** river water discharge (Q_w), **(C)** δ^7Li, **(D)** Li flux, **(E)** Li/Na, **(F)** TDS (total dissolved solid), and **(G)** water and air temperature **(T)** at the Weizhou hydrological station over 2010, all showing obvious seasonality. Light and dark blue narrow shades labeled "R" and "G" with numbers represent the R- and the G-type waters, among which R2 and R5 contain two short intervals.

August in which the ionic concentrations increased slightly (**Figure 3**). When Q_w rose continually to >400 m^3/s during the monsoon season, there was less dilution effect on ionic concentrations (**Figure 4**), suggesting an excess input under intense water flow. The ionic concentrations in the post-monsoon season were not as stable as those in other seasons. They increased with fluctuation, and dropped back with undulations to low values near the pre-monsoon season at the end of the year.

3.2 Li Concentrations and Li Isotopes

Li concentrations ([Li]) and δ^7Li values of all Min Jiang water samples are listed in **Table 1**. Over 2010, the dissolved [Li] in the Min Jiang ranged from about 0.714 μmol/L (during the monsoon season) to 2.225 μmol/L (during the non-monsoon seasons) with an average of 1.266 μmol/L, which is much higher than the world's average riverine [Li] (0.22 μmol/L) (Hu and Zhou, 2012; Liu et al., 2021). These values were generally higher than those of many rivers around the globe, such as the Amazon River with [Li] from 0.06 to 1.67 μmol/L (Dellinger et al., 2015), the Mackenzie River from 0.02 to 1.29 μmol/L (Millot et al., 2010a), and the Orinoco River from 0.01 to 0.81 μmol/L (Huh et al., 2001), but overall, they were relatively lower than those of the Yangtze River main channel, in which [Li] ranged from 0.42 to 4.57 μmol/L (Wang et al., 2015). The [Li] of groundwater in the Min Jiang catchment ranged from 0.232 to 0.370 μmol/L, within the range of the world groundwater [Li] ranging from 0.01 to 28 μmol/L depending on different settings (Su, 2012; Mayfield et al., 2021). Rainwater [Li] were generally low, reported to be 0.004–0.292 μmol/L (Millot et al., 2010b). The [Li] in the rainwater of the Min Jiang catchment were 0.248 and 0.249 μmol/L. The [Li] of landslide seepage samples were even lower, 0.140 (X1) and 0.145 μmol/L (X2) (**Table 1**).

Over the sampling period, the dissolved δ^7Li in the Min Jiang ranged from +10.48‰ in monsoon season to +16.37‰ in

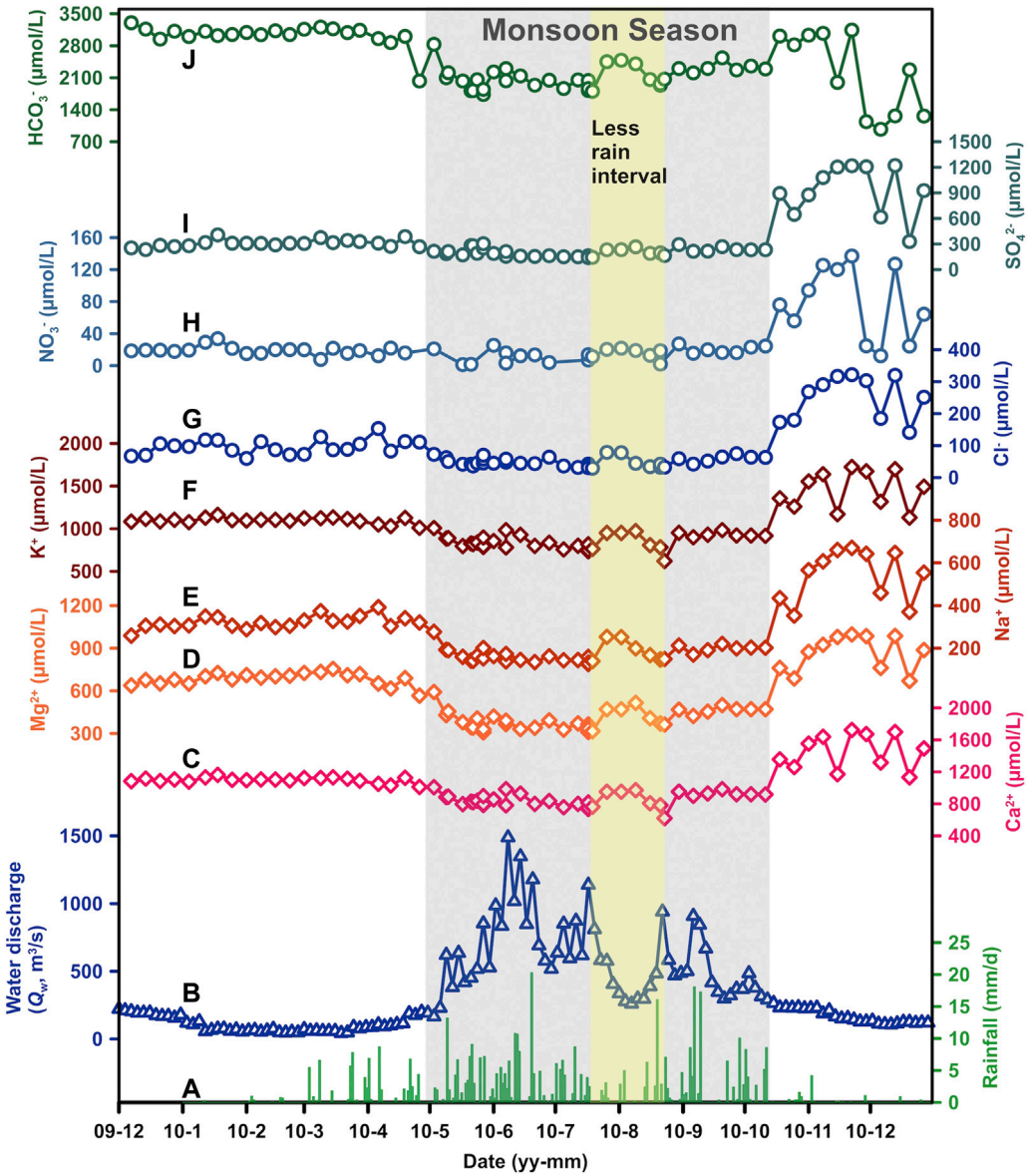

FIGURE 3 | Seasonal variation of major ions for the Min Jiang river waters, including **(C)** Ca^{2+}, **(D)** Mg^{2+}, **(E)** Na^{+}, **(F)** K^{+}, **(G)** Cl^{-}, **(H)** NO_3^{-}, **(I)** SO_4^{2-}, and **(J)** HCO_3^{-}, along with **(A)** rainfall and **(B)** water discharge (Q_w). The monsoon season is shaded by gray, with a relatively less rain interval during mid-July and mid-August shaded by faint yellow.

the non-monsoon seasons, covering a narrower range than the spatial δ^7Li variation in the Yangtze River (ranging from +7.6 to +42.1‰) (Wang et al., 2015) and other global rivers (ranging from +1.2 to +42.1‰, with an average +23.4‰) (Liu et al., 2021). The δ^7Li values of two groundwater samples in the Min Jiang catchment were +16.82 and +20.70‰, respectively, within the range of the reported global groundwater δ^7Li (+6.7 to +28.6‰) (Hu and Zhou, 2012; Su, 2012; Liu et al., 2021; Mayfield et al., 2021). Close to those of the groundwater samples, two landslide seepage samples had δ^7Li values of +17.1 and +14.7‰, respectively.

The riverine Li flux and δ^7Li also showed significant seasonal variations in response to the Q_w in the Min Jiang through time in 2010. As shown in **Figure 2**, Li flux and δ^7Li remained in invariant levels until the beginning of the monsoon season. During the monsoon season, with the increasing Q_w, Li flux increased owing to strong weathering, with large fluctuations. Along the time that the monsoon ended, Li flux returned to the level of the monsoon's beginning. Similarly, δ^7Li fluctuated dramatically with Q_w during the monsoon season, and turned to a stable level, with relatively higher values than the pre-monsoon season. One of the most interesting observations is

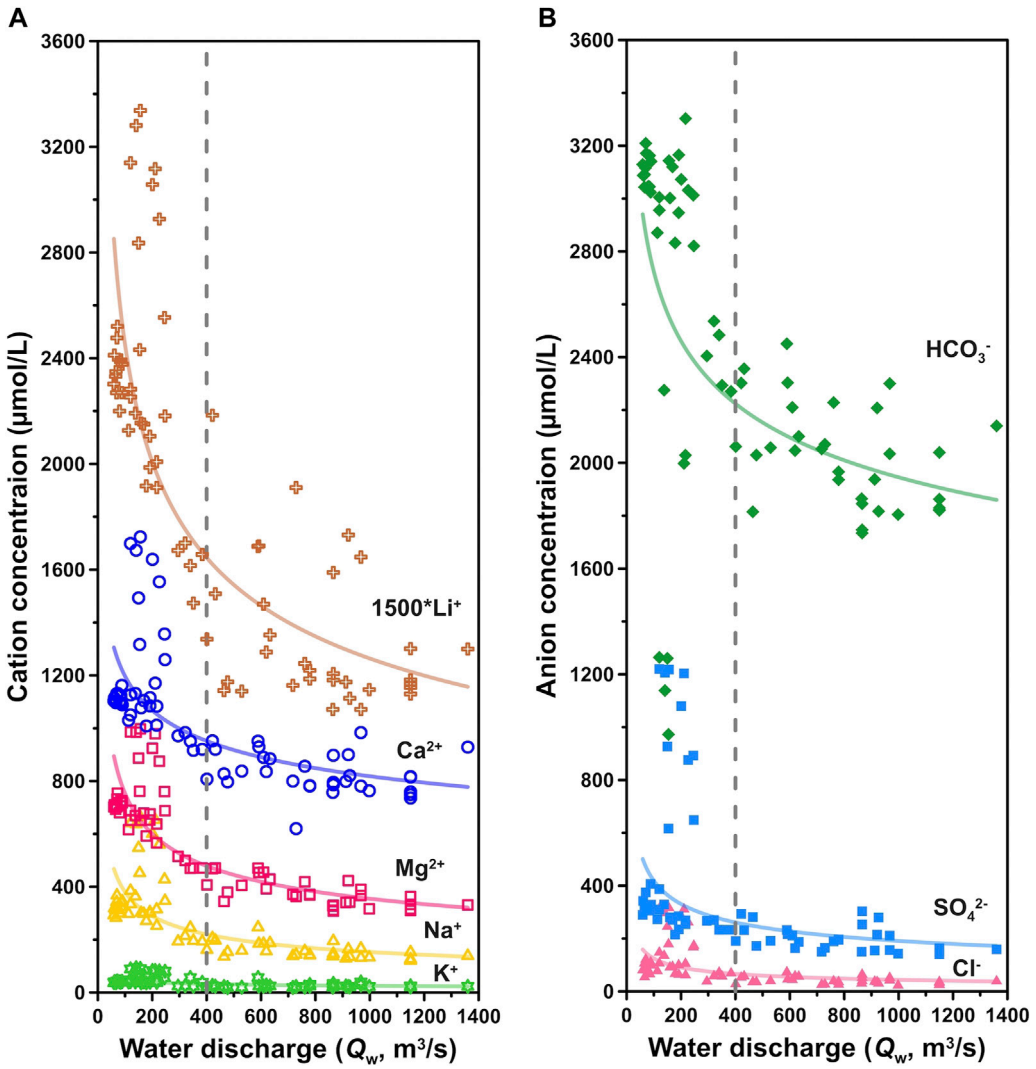

FIGURE 4 | Changes of **(A)** cation and **(B)** anion concentrations with water discharge (Q_w). Q_w at 400 m^3/s as a boundary marked gray dashed lines, where below 400 m^3/s the ionic concentrations are strongly affected by the dilution effect, whereas above 400 m^3/s the riverine ion concentrations are less affected by increasing Q_w.

that both Li flux and δ^7Li in the Min Jiang waters exhibited not only seasonal variation but also sensitive response to hydrological changes as discussed in the following text.

3.3 Riverine δ^7Li Responses to Hydrological Changes During the Monsoon Season

During the monsoon season in 2010, there were several strong rainfall intervals with high Q_w, interrupted by a less rain interval (**Figures 2**, **3**). During the strong rainfall intervals, the Min Jiang waters were characterized by decreased δ^7Li but increased Li flux relative to their neighbours (as shaded by light blue in **Figure 2**). Since these waters were associated with strong rainfall, we defined them as the "R-type" water. There were six intervals with the R-type waters, marked as R1 to R6 in **Figure 2**, in which R2 and R5 consisted of two short intervals. In each R-type water interval, when Q_w went up, riverine δ^7Li decreased abruptly. Meanwhile, its Li flux reached a high value at the moment and then quickly dropped back to a lower value. For instance, in the R4 interval, the Q_w increased from 615 to 1,190 m^3/s and δ^7Li dropped nearly 1.5‰ (from +13.33 to +11.74‰), while Li flux increased from 258.7 to 560.8 mg/day.

Between the R-type water intervals, there were another six intervals characterized by increased δ^7Li but decreased Li flux relative to their neighbours (as shaded by dark blue in **Figure 2**), in contrast to the R-type waters. In each interval, Q_w rose slightly and riverine δ^7Li increased, corresponding to lower Li flux than before and after it. Considering that the high δ^7Li may be affected by the input of groundwater and/or landslide seepage, both with higher δ^7Li, as discussed in the following text, these waters were named as the "G-type" waters, marked as G1 to G6 in **Figure 2**. Take the G4 for an example, it happened during the less rain period of the monsoon season, but its Q_w increased from 228 to 311 m^3/s with little rainfall; the riverine δ^7Li increased from +13.38 to +14.16‰, with Li flux decreasing from 166.8 to 139.6 mg/day.

TABLE 2 | Comparisons of δ^7Li, Li fluxes, and Li/Na ratios between, before, and during the intervals of the R- and G-type waters.

Type water no	Date (2010)		Water discharge Q_w (m^3/s)		δ^7Li (‰)		Li flux (mg/day)		1,000*Li/Na	
	Start date	End date	Before	During	Before	During	Before	During	Before	During
R1	05–09	05–10	301.0	633.0	+13.91	+12.58	105.10	269.50	4.62	5.14
R2-1	05–21	05–23	404.0	926.0	+14.01	+13.86	186.29	381.59	4.91	5.36
R2-2	05–27	05–28	497.0	866.0	+14.23	+10.48	152.65	529.47	4.61	5.27
R3	06–07	06–21	806.0	1,500.0	+13.67	+11.11	189.72	684.26	5.09	6.34
R4	07–16	07–19	615.0	1,190.0	+13.33	+11.74	258.66	560.79	5.35	6.14
R5-1	08–15	08–17	308.0	546.0	+14.16	+13.18	139.59	180.59	5.59	5.32
R5-2	08–22	08–24	698.0	953.0	+15.24	+10.60	433.43	476.04	5.34	8.52
R6	09–06	09–10	538.0	1,000.0	+12.15	+12.21	350.45	523.43	6.85	6.76
G1	05–16	05–17	546.0	650.0	+13.59	+14.01	240.51	186.29	5.14	4.91
G2	06–01	06–03	494.0	998.0	+10.48	+13.67	529.47	189.72	5.27	5.09
G3	07–04	07–12	564.0	1,050.0	+13.98	+16.30	294.62	258.66	5.30	4.98
G4	08–09	08–10	228.0	311.0	+13.38	+14.16	166.76	139.59	4.27	5.59
G5	08–30	09–02	426.0	562.0	+10.60	+12.15	476.04	350.45	8.52	6.85
G6	10–02	10–05	378.0	510.0	+13.97	+15.47	245.87	232.45	5.54	4.96

The value differences of Li flux, riverine δ^7Li, and Li/Na ratios before and during the intervals of the R- and the G-type waters are presented in **Table 2** and **Figure 5**. It demonstrated that riverine Li flux and δ^7Li were clearly impacted by monsoonal hydrological conditions, with two distinct responses as discussed in **Section 4.4** in the following text.

4 DISCUSSION

4.1 Control of Seasonal Variations in Min Jiang Water Chemistry

Similar to river chemistry in the Yangtze River headwaters and the Yellow River (Zhang et al., 2015; Ma et al., 2020), the summer monsoons bring abundant rainfall, resulting in dilution of the riverine ions in the Min Jiang during the monsoon season. A similar seasonal pattern was also observed elsewhere and was related to the Indian monsoon (Galy and France-Lanord, 1999; Tipper et al., 2006). However, when Q_w exceeded 400 m^3/s, the ionic concentrations seemed not to correlate with Q_w (**Figure 4**), suggesting excess input to the river water by intensified weathering and/or groundwater associated with the hydrological events (Zhang et al., 2015), as discussed in the following text. The excess input of Ca^{2+} and HCO_3^- can be further supported by the relation between Ca/Na* versus Mg/Na* ratios (where $Na^* = Na^+ - Cl^-$) at different seasons. As shown in **Figure 6**, lower Ca/Na* and Mg/Na* ratios in the river waters of the non-monsoon seasons were clearly separated from those of the monsoon season, with different slopes. The higher Ca/Na* and Mg/Na* ratios in the river waters of the monsoon season waters than those of the non-monsoon seasons reflected more contribution of carbonate dissolution relative to silicates, supported by higher Ca^{2+} and HCO_3^- in the monsoon season than those in the non-monsoon seasons (**Figure 7**). All these features can be attributed to faster dissolution kinetics of carbonates under monsoon conditions.

4.2 Sources of Major Ions and Li in the Min Jiang

In order to address the δ^7Li signatures of river waters, it is important to determine the sources of major ions and dissolved Li (Vigier et al., 2009). Major reservoirs affecting large river chemistry include dissolution of silicate, carbonate, evaporite, and human inputs (Gaillardet et al., 1999), as well as rainwater (Yoon et al., 2008). We employed the forward model to evaluate the contributions of the major reservoirs, which sequentially allocates the major ions and dissolved Li to their sources (Meybeck, 1987; Gaillardet et al., 1997; Dellinger et al., 2015; Gou et al., 2019).

For atmospheric inputs of major ions, chloride (Cl^-) was used as a reference for the rain correction:

$$X_{rain} = \left(\frac{X}{Cl}\right)_{rain} \times Cl_{ref} \quad (2)$$

where X_{rain} represents the concentration of ion X (Na^+, Mg^{2+}, Ca^{2+}, and SO_4^{2-}) derived from rainwater, $(X/Cl)_{rain}$ refers to the measured X/Cl ratio in rainwater, and Cl_{ref} was the lowest Cl^- concentration of the catchment river sample dataset (here 23.0 μmol/L of Cl^- was used from the river water sample at the upper reaches near Zhenjiangguan).

After the correction of atmospheric inputs, we attributed the remaining Cl^- and SO_4^{2-} to evaporite and sulfide (abbreviated as Cl_{eva} and $SO_{4,eva}$) dissolution. Then, the Na^+ and Ca^{2+} proportions from evaporites and sulfides were determined by **Eqs 3**, **4**.

$$Na_{eva} = Cl_{eva} = Cl_{dissolved} - Cl_{ref} \quad (3)$$

$$Ca_{eva} = SO_{4,eva} = SO_{4,dissolved} - SO_{4,rain} \quad (4)$$

For silicate dissolution, we considered that all K^+ and the residual Na^+ after the corrections of rain, evaporite, and sulfides were from silicate weathering, abbreviated as K_{sil} and Na_{sil}. Ca^{2+} and Mg^{2+} from silicate dissolution were calculated by multiplying Na_{sil} by Ca/Na (0.54) and Mg/Na (0.26) ratios of local silicate rock compositions (Qin et al., 2006; Yoon et al., 2008).

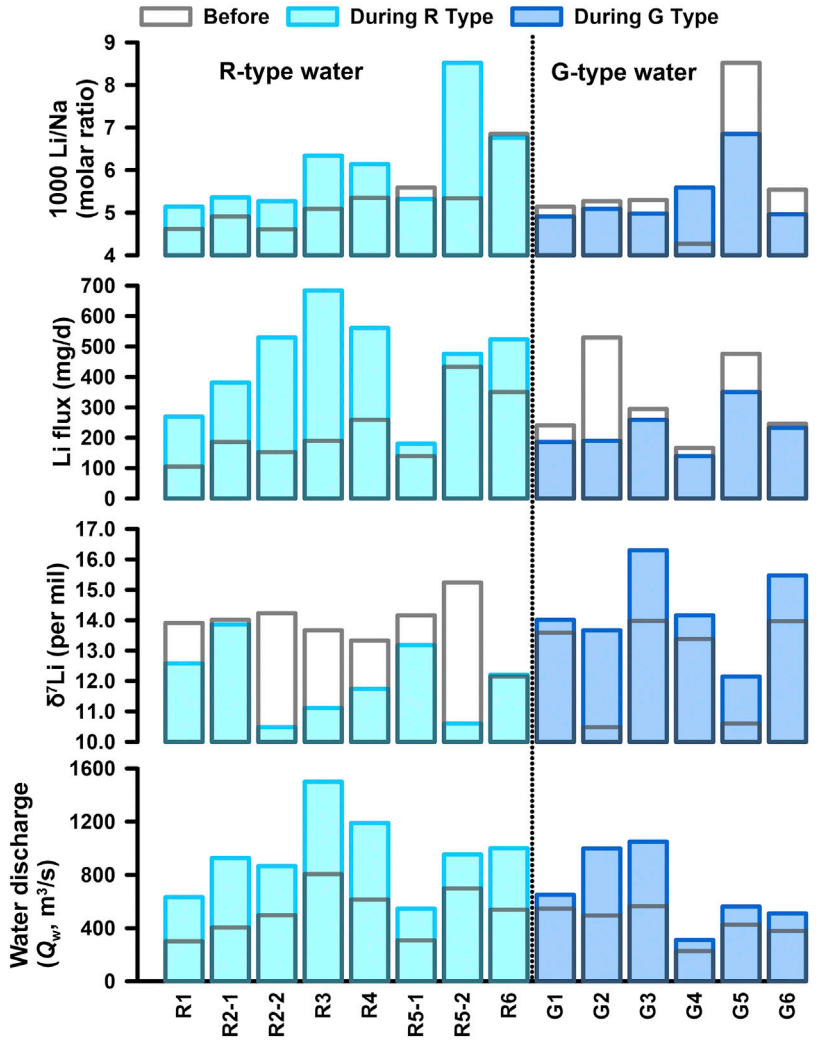

FIGURE 5 | Comparisons of δ^7Li, Li flux, and Li/Na for the R-type and G-type waters with water discharge (Q_w). The values during the intervals with the R-type and G-type waters are plotted by light and dark blue filled rectangles, and the values before the intervals by blank rectangles with gray frames, respectively.

$$\mathbf{Na_{sil} = Na_{dissolved} - Na_{eva} - Na_{rain}} \quad (5)$$

$$\mathbf{K_{sil} = K_{dissolved}} \quad (6)$$

$$\mathbf{Mg(Ca)_{sil} = Na_{sil} \times \left(\frac{Mg(Ca)}{Na}\right)_{sil}} \quad (7)$$

After the aforementioned corrections, the remaining Ca^{2+} and Mg^{2+} were thought to be from carbonate contribution by **Eqs 8** and **9**:

$$\mathbf{Ca_{carb} = Ca_{dissolved} - Ca_{sil} - Ca_{eva} - Ca_{rain}} \quad (8)$$

$$\mathbf{Mg_{carb} = Mg_{dissolved} - Mg_{sil} - Mg_{rain}} \quad (9)$$

The results showed that in the hydrological year of 2010 (four samples of 2009 are not included), the total cations from evaporites and sulfides reached 11.9 ± 6.2% in the pre-monsoon seasons, followed by 9.1 ± 8.8% in the monsoon season, and 27.9 ± 20.7% in the post-monsoon season. This indicated that dissolution of evaporites and sulfides played a more important role in the post-monsoon season than other seasons in the Min Jiang catchment. The contribution of carbonates for cations occupied 56.8 ± 8.1% in the pre-monsoon season, while 59.1 ± 14.1% in the monsoon and 41.8 ± 24.2% in the post-monsoon season. Meanwhile, the silicate contribution for cations was relatively stable through all seasons, with 18.4 ± 3.2% in the pre-monsoon season, 14.0 ± 6.0% in the monsoon season, and 17.7 ± 6.0% in the post-monsoon season.

For Li as a trace element, [Li] in rainwater is low (here 0.25 μmol/L) so that the contribution of atmospheric input to riverine Li^+ is usually assumed to be negligible (Huh et al., 2001; Wang et al., 2015). Here, we used the typical Li/Ca ratio value of ~ $(1.5 \pm 0.5) \times 10^{-5}$ in carbonates (Hathorne and James, 2006; Pogge von Strandmann et al., 2013) and a mean Li/Na value of 3×10^{-5} for evaporites (Kloppmann et al., 2001) to obtain the proportions of Li^+ derived from carbonates and evaporites by

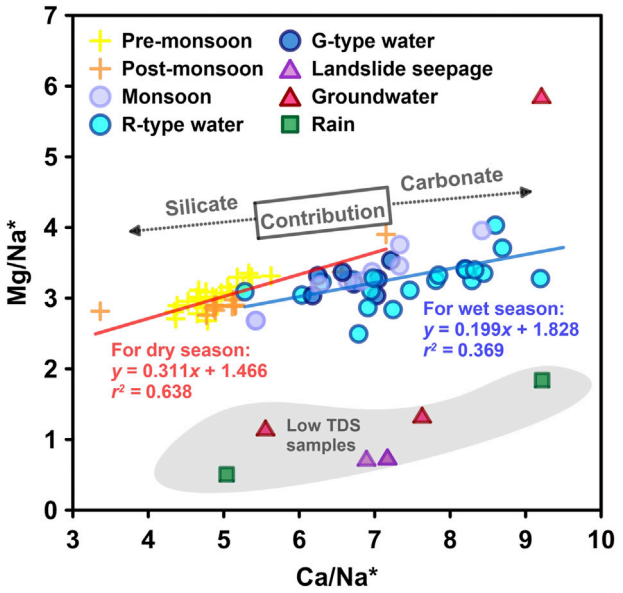

FIGURE 6 | Correlations of Mg/Na* vs. Ca/Na* ($Na^* = Na^+ - Cl^-$) for river water samples from the dry and wet seasons, respectively, also showing rainwater, groundwater, and landslide seepage with low Mg/Na* and TDS.

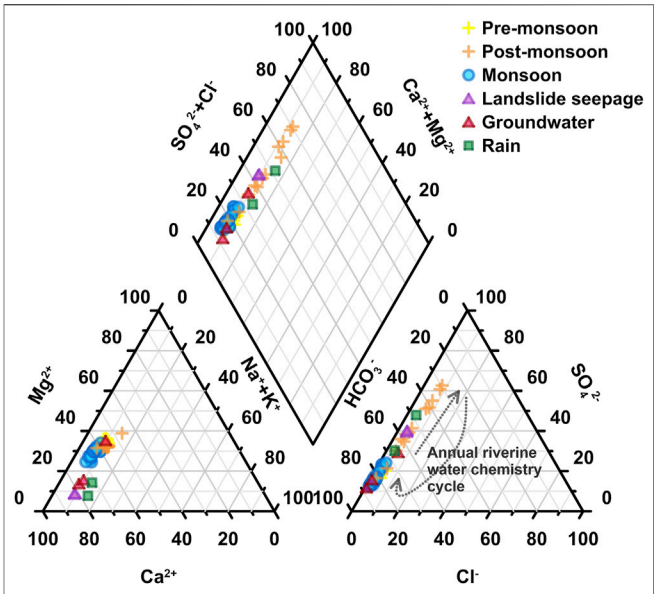

FIGURE 7 | Piper diagrams for ions of river water samples from the Min Jiang catchment. Dark gray dot curves show a surmised annual cycle of anions from pre-monsoon to post-monsoon seasons.

$$\mathbf{Li_{carb}} = \mathbf{Ca_{carb}} \times \left(\frac{\mathbf{Li}}{\mathbf{Ca}}\right)_{\mathbf{carb}} \quad (10)$$

$$\mathbf{Li_{eva}} = \mathbf{Cl_{eva}} \times \left(\frac{\mathbf{Li}}{\mathbf{Na}}\right)_{\mathbf{eva}} \quad (11)$$

The result showed that 0.9 ± 0.8% of dissolved Li^+ was sourced from carbonates and less than 0.4% of Li^+ was from evaporites. The remaining Li^+ after subtracting Li_{eva} and Li_{carb} was considered to be from silicates. The result showed 99.0 ± 0.8% Li^+ from silicates ($[Li]_{sil}$).

4.3 Weathering Rate and Its Relationship With Riverine δ^7Li

Based on the calculations aforementioned, silicate weathering dominated the source of riverine Li^+ in the Min Jiang. The rate of silicate weathering (SWR, mol/km^2/day) was calculated by silicate-derived cations multiplying daily Q_w, and then divided by the total catchment area (A) above the Weizhou hydrological station (18,921 km^2) as the following equation (Zhang et al., 2015):

$$\mathbf{SWR} = \mathbf{Cation_{sil}} \times \frac{\mathbf{Q_w}}{\mathbf{A}} \quad (12)$$

The SWR in the Min Jiang also had distinct seasonal variations. The SWR remained within 161.0 ± 62.5 mol/km^2/day in the pre-monsoon season, and then increased sharply to 523.8 ± 146.2 mol/km^2/day in the monsoon season, with fluctuations by the domination of different types of waters as discussed in the following text. In the post-monsoon season, the SWR declined to 381.2 ± 100.7 mol/km^2/day. Apparently, a higher SWR appeared during the monsoon season, also demonstrated by higher Si/Na* (**Figure 8A**), indicating that monsoon rainfall accelerated silicate weathering (**Figure 8B**). This is consistent with previous findings (Qin et al., 2006; Zhang et al., 2015). This daily SWR was generally within the range of the middle reaches of the Yellow River (~9.5–565.2 mol/km^2/day), which also showed strong weathering in the monsoon season (Zhang et al., 2015). The annual average SWR in upper Min Jiang was 129.1 × 10^3 mol/km^2/year or 3.7 t/km^2/year, within the range of the Yangtze River headwater basins (1.8 to 12 t/km^2/year) (Li S.-L. et al., 2014; Ma et al., 2020), also close to the Mackenzie (0.13–4.3 t/km^2/year) draining the Rocky Mountains in the subarctic (Millot et al., 2003), but less than the Ganga, Yamuna, and Kosi Rivers with higher annual SWR of 8.4, 10.3, and 9.3 t/km^2/year, respectively; however, their tributaries displayed lower values than main channels (Pogge von Strandmann et al., 2017). Moreover, the SWR in the Min Jiang was far less than that of the rivers draining the Andes with a mean value at 22 t/km^2/year (Moquet et al., 2011) but was 4–5 times higher than that of the Austrilian Victorian Alps region (23–31 × 10^3 mol/km^2/year) (Hagedorn and Cartwright, 2009). The CO_2 consumption yield was (186.4 ± 26.4) × 10^3 mol/km^2/year for the Min Jiang catchment area in 2010, which is higher than those of the Yellow River and the Yangtze River.

The δ^7Li of the river dissolved load was considered to be related to the intensity and regime of silicate weathering at the scale of the basin (Vigier et al., 2009; Millot et al., 2010a). Within one hydrological year in the Min Jiang catchment, the SWR was proportional to Q_w (**Figure 8B**), whereas δ^7Li and SWR exhibited a negative correlation, with relatively high δ^7Li and low SWR in the non-monsoon seasons and low δ^7Li and high SWR in the monsoon season (**Figure 8C**). This correlation was consistent with Vigier's empirical law that δ^7Li and SWR fit a negative power

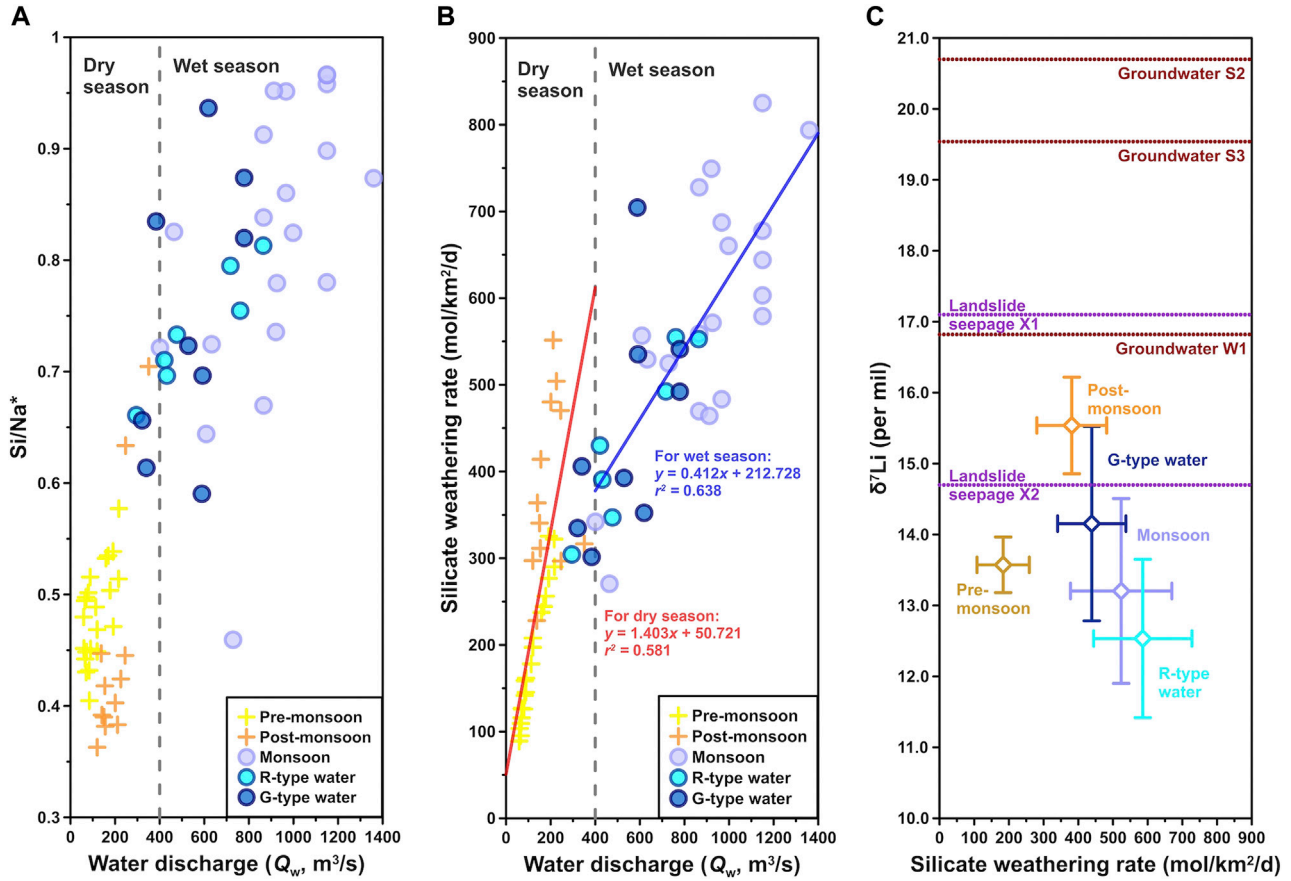

FIGURE 8 | Relations between **(A)** Si/Na* ratio (Na* = $Na^+ - Cl^-$) and **(B)** silicate weathering rate (SWR) vs. water discharge (Q_w), and **(C)** δ^7Li vs. SWR. Following the Q_w boundary in **Figure 4**, gray dashed lines divide into dry and wet seasons. In panel **(C)**, blank diamond symbols with error bars represent average δ^7Li and SWR values for each class of samples. Violet and red dot lines mark δ^7Li values of landslide seepage and groundwater samples, respectively, because they have no SWR data.

function. In fact, similar patterns had been reported by the Amazon, Ganges, Orinoco, Lena, the Yellow River, and the Qiantang River that all displayed (at their outlet) δ^7Li values higher than 21‰ for corresponding chemical erosion rates lower than 14 t/km^2/year (Huh et al., 1998; Gaillardet et al., 1999; Wu et al., 2005; Vigier et al., 2009). It was also reported that tributaries of Himalayan rivers draining silicates had lower dissolved δ^7Li values (by 2.3–4.2‰) following the monsoon when weathering was more intense due to higher runoff and elevated temperatures (Kısakürek et al., 2005).

4.4 Impacts of Hydrology on Riverine Li Isotopes

One of the most interesting observations for the seasonal δ^7Li in the Min Jiang waters is that there are two types of river waters with different responses of the δ^7Li values to hydrology during the monsoon season, as defined previously as the R- and G-type waters (as shades in **Figure 2**). Considering that Li is not involved in terrestrial biological cycles (e.g., Lemarchand et al., 2010; Pogge von Strandmann et al., 2016) and that vegetation within the upper Min Jiang catchment is sparse, $[Li]_{sil}$ should not be affected by biological processes in the Min Jiang. $[Li]_{sil}$ should be dominantly controlled by dilution/evaporation processes at the first order, and then by the balance between silicate weathering and incorporation into secondary minerals.

The R-type waters with low δ^7Li usually appeared during a major rainfall which was caused by the rapid rise of Q_w. The δ^7Li drop was accompanied by an increase in both [Li] and Li flux. The decreased riverine δ^7Li but increased Li flux can attribute to an increase in silicate dissolution during the monsoon season. As the Q_w increased, more dissolved Li^+ was flushed into the river, leading to a rise in the Li flux during the monsoon (**Figures 2**, **5**). It is further supported by increasing Si/Na* and SWR proportional to Q_w (**Figures 8A,B**). However, for the R-type waters, rapidly increased Q_w sped up water flow velocity, meaning relatively short water residence time. The decrease in riverine δ^7Li is most likely due to the increased input of silicate weathering with low δ^7Li and/or a decrease in rates of secondary mineral precipitation during the rain intervals. It means that the δ^7Li in the R-type waters should only equilibrate with the solid. Lowest average δ^7Li but highest SWR values for the R-type waters (**Figure 8C**) further support that riverine δ^7Li is a strong kinetic control (West et al., 2002). After each R-type water

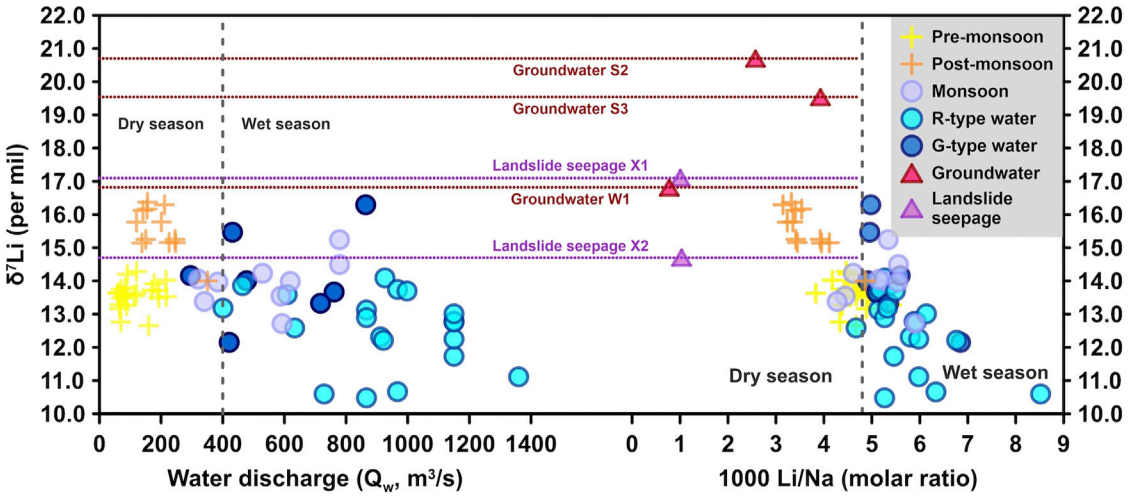

FIGURE 9 | Scatterplots for δ^7Li vs. water discharge (Q_w) and 1,000*Li/Na for river waters in the Min Jiang River. Following Q_w boundary at 400 m^3/s in **Figure 4**, the gray dashed lines divide into dry and wet seasons. As the same as **Figure 7**, violet and red dot lines mark δ^7Li values of landslide seepage and groundwater samples, respectively, because they have no Q_w data.

interval, riverine δ^7Li returned to higher values, which may result from more ^{6}Li incorporation into secondary minerals during the longer water–rock interaction when Q_w decreased (e.g., Lemarchand et al., 2010). This is also supported by laboratory water–rock interaction experiments that showed large (19‰) increases in δ^7Li in solutions over a short period of time (Pogge von Strandmann et al., 2019).

Similar changes of dissolved δ^7Li were observed both in a forested granitic catchment (Strengbach, Vosges Mountains, France) (Lemarchand et al., 2010) and in a highly weathered catchment (Quiock Creek in Guadeloupe archipelago, French West Indies) (Fries et al., 2019). Lemarchand et al. (2010) found that δ^7Li in both a spring and a stream decreased with an increasing Q_w. This was because Li isotopic fractionations occurred during the secondary phase precipitation along the water pathway through the rocks, resulting in high δ^7Li with increasing residence time of waters. Similarly, Fries et al. (2019) found that the δ^7Li values of the river dissolved load in the Quiock Creek catchment decreased by ~2% after the largest rain event and remained low afterward. The decreased δ^7Li was considered due to either input of Li from isolated pockets of soil solution with lower δ^7Li that were flushed out during the rain events, or due to a decrease in rates of secondary mineral (mostly halloysite and kaolinite) precipitation during the rain events. After a rain event, the secondary mineral phase turned unsaturated, consistent with lower rates of precipitation, in which case, either enhanced dissolution of secondary minerals or suppressed secondary mineral formation could result in lower riverine δ^7Li (Fries et al., 2019).

Between the R-type water intervals, there were six intervals with the G-type waters whose Q_w rise was not related to rainfall—sometimes, it was after rainfall (as shaded by dark blue in **Figure 2**). During the G-type water intervals, though Q_w increased, the Li fluxes became low and δ^7Li jumped to higher values relative to their neighbours. Considering that groundwater had higher δ^7Li values than river waters (**Figures 8B**, **9**), it is certainly possible that groundwater affected riverine δ^7Li in the Min Jiang. Groundwaters are typically concentrated in silicate-derived cations (such as Li^+) as a result of prolonged water–rock interaction (e.g., Tipper et al., 2006). Meanwhile, the majority (55–68%) of global groundwater discharge was from silicates in humid, low-latitude, and tectonically active regions, and groundwater derived solute fluxes occupied at least 5% of the riverine fluxes. Therefore, groundwater discharge might play an outsized role in terrestrially derived solute fluxes of silicate weathering and thus the regulation of atmospheric CO_2 (Luijendijk et al., 2020; Mayfield et al., 2021). In mountain areas, the river deeply cuts the valley and groundwater supplies river water. As a result, some rivers even have higher δ^7Li than groundwaters (e.g., Bagard et al., 2015; Liu et al., 2015; Manaka et al., 2017). Since the catchment above the Weizhou hydrological station is located at the mountain areas, discharge of such groundwater could shift river chemistry toward higher δ^7Li (**Figures 8B**, **9**). Meanwhile, seismic landslides triggered by the 2008 Wenchuan earthquakes are prevalent throughout the study region (e.g., Li et al., 2014), which can act as solute generators by producing reactive fine-grained sediment (Wang et al., 2015) and by focusing flow through this material (e.g., Jin et al., 2016). Leaching of exchangeable cations from finely grounded landslide debris could also contribute to the solute load. The landslide mass embraced large porosity in which it gave Li isotope time and physicochemical environment to fractionate, mainly by secondary minerals absorbing ^{6}Li in the pore water, making landslide seepage waters heavy Li isotope signature, but less aqueous Li remained. Indeed, two samples of landslide seepage were at relatively higher δ^7Li values compared to river waters (**Figures 8C**, **9**). On the other hand, the [Li] of both groundwater and landslide seepage were all less than that of river water within the Min Jiang catchment (**Table 1**). When such waters were delivered to the river channel, river water would increase δ^7Li but

decrease Li flux relative to their neighbours, being as a G-type water (**Figure 9**). Higher δ^7Li but lower Li/Na* ratios for the post-monsoon waters (**Figure 9**) probably indicate an excess Li supply of such waters to the Min Jiang relative to the pre-monsoon season. As the monsoon season gradually faded out, the change of strengthened evapotranspiration and oversaturation of clays probably resulted in more ^{6}Li incorporated into clays and higher δ^7Li in the residual pore water (Xu et al., 2021), which might be finally imported into the river as landslide seepage. In addition, the lengthened rock–fluid interaction times during the less rain intervals could simultaneously cause higher riverine δ^7Li (e.g., Bagard et al., 2015; Pogge von Strandmann et al., 2019) as the G-type waters.

5 CONCLUSION

In the Min Jiang catchment along the eastern Tibetan Plateau, seasonally hydrological variation caused by Asian and Indian summer monsoons influences water chemistry and riverine Li isotope compositions. Silicate weathering produced more than 98.2% of the riverine Li. Relative to distinct variation in riverine δ^7Li during the monsoon season, Li isotopic compositions were relatively stable in the pre- and post-monsoon seasons, with overall lower δ^7Li values averaged 13.6‰ in the pre-monsoon season and higher δ^7Li values averaged 15.5‰ in the post-monsoon season. Based on the distinct response of the riverine δ^7Li to increasing Q_w, two types of river waters were distinguished in the Min Jiang during the monsoon season. When the Q_w was dominated by monsoonal rainfall (the R-type waters), riverine δ^7Li decreased about 1.9‰ and Li flux increased 223.7 mg/day in average, owing to short rock–fluid interaction time by rapid water flow as a strong kinetic control of silicate weathering. In relatively less rain periods during the monsoon season and the post-monsoon season, groundwater and/or landslide seepage delivered to the river channel, with relatively longer water residence times, resulted in δ^7Li increased 1.6‰ but Li flux decreased 99.4 mg/day in average compared to their neighbors, as the G-type waters. This study highlights that both monsoon climate and hydrology could have impact on the riverine Li isotope behavior. Such impacts of hydrology on riverine δ^7Li may provide some clues for the relation between Li isotopes and hydrological conditions as proposed previously (Misra and Froelich, 2012; Dellinger et al., 2015).

DATA AVAILABILITY STATEMENT

The original contributions presented in the study are included in the article/Supplementary Material, further inquiries can be directed to the corresponding author.

AUTHOR CONTRIBUTIONS

ZJ contributed to conception and designed the study. BL-L, L-FG, and YX contributed to fieldwork and guided on research methods and calculations. M-YH and FZ provided research ideas and suggestions. BL-L did the experimental work and drafted the initial manuscript with help from all authors. All authors commented on the manuscript and approved the submitted version.

FUNDING

This work was financially supported by the second Tibetan Plateau Scientific Expedition and Research (2019QZKK0707) and the NSFC grants (41991322 and 41930864).

ACKNOWLEDGMENTS

We thank Gaojun Li at Nanjing University for providing the landslide seepage data. We are grateful to Chao Zhu at Guilin University of Technology, Yulong Li at Qinghai Institute of Salt Lakes, Chinese Academy of Sciences, Chunyao Liu at University College London, and Ningpan Chai at Institute of Earth Environment, Chinese Academy of Sciences for their kind help on graphing and laboratory work.

REFERENCES

Bagard, M.-L., West, A. J., Newman, K., and Basu, A. R. (2015). Lithium Isotope Fractionation in the Ganges-Brahmaputra Floodplain and Implications for Groundwater Impact on Seawater Isotopic Composition. *Earth Planet. Sci. Lett.* 432, 404–414. doi:10.1016/j.epsl.2015.08.036

Beck, A. J., Charette, M. A., Cochran, J. K., Gonneea, M. E., and Peucker-Ehrenbrink, B. (2013). Dissolved Strontium in the Subterranean Estuary-Implications for the marine Strontium Isotope Budget. *Geochim. Cosmochim. Atca.* 117, 33–52. doi:10.1016/j.gca.2013.03.021

Bickle, M. J., Chapman, H. J., Bunbury, J., Harris, N. B. W., Fairchild, I. J., Ahmad, T., et al. (2005). Relative Contributions of Silicate and Carbonate Rocks to Riverine Sr Fluxes in the Headwaters of the Ganges. *Geochim. Cosmochim. Atca.* 69, 2221–2240. doi:10.1016/j.gca.2004.11.019

Bickle, M. J., Tipper, E., Galy, A., Chapman, H., and Harris, N. (2015). On Discrimination between Carbonate and Silicate Inputs to Himalayan Rivers. *Am. J. Sci.* 315, 120–166. doi:10.2475/02.2015.02

Bureau of Hydrology (2010). *Hydrological Data of Changjiang River Basin*. Beijing: Annual Hydrological Report.

Caves, J. K., Jost, A. B., Lau, K. V., and Maher, K. (2016). Cenozoic Carbon Cycle Imbalances and a Variable Weathering Feedback. *Earth Planet. Sci. Lett.* 450, 152–163. doi:10.1016/j.epsl.2016.06.035

Chetelat, B., Liu, C.-Q., Zhao, Z. Q., Wang, Q. L., Li, S. L., Li, J., et al. (2008). Geochemistry of the Dissolved Load of the Changjiang Basin Rivers: Anthropogenic Impacts and Chemical Weathering. *Geochim. Cosmochim. Atca.* 72, 4254–4277. doi:10.1016/j.gca.2008.06.013

Clift, P. D., Hodges, K. V., Heslop, D., Hannigan, R., Van Long, H., and Calves, G. (2008). Correlation of Himalayan Exhumation Rates and Asian Monsoon Intensity. *Nat. Geosci.* 1, 875–880. doi:10.1038/ngeo351

Dellinger, M., Gaillardet, J., Bouchez, J., Calmels, D., Galy, V., Hilton, R. G., et al. (2014). Lithium Isotopes in Large Rivers Reveal the Cannibalistic Nature of Modern Continental Weathering and Erosion. *Earth Planet. Sci. Lett.* 401, 359–372. doi:10.1016/j.epsl.2014.05.061

Dellinger, M., Gaillardet, J., Bouchez, J., Calmels, D., Louvat, P., Dosseto, A., et al. (2015). Riverine Li Isotope Fractionation in the Amazon River Basin Controlled

by the Weathering Regimes. *Geochim. Cosmochim. Atca.* 164, 71–93. doi:10.1016/j.gca.2015.04.042

Edmond, J. M. (1992). Himalayan Tectonics, Weathering Processes, and the Strontium Isotope Record in Marine Limestones. *Science* 258, 1594–1597. doi:10.2307/288205610.1126/science.258.5088.1594

Edmond, J. M., Palmer, M. R., Measures, C. I., Grant, B., and Stallard, R. F. (1995). The Fluvial Geochemistry and Denudation Rate of the Guayana Shield in Venezuela, Colombia, and Brazil. *Geochim. Cosmochim. Atca.* 59 (16), 3301–3325. doi:10.1016/0016-7037(95)00128-m

Fries, D. M., James, R. H., Dessert, C., Bouchez, J., Beaumais, A., and Pearce, C. R. (2019). The Response of Li and Mg Isotopes to Rain Events in a Highly-Weathered Catchment. *Chem. Geol.*. 519, 68–82. doi:10.1016/j.chemgeo.2019.04.023

Gaillardet, J., Dupre, B., Allegre, C. J., and Négrel, P. (1997). Chemical and Physical Denudation in the Amazon River Basin. *Chem. Geol.* 142 (3–4), 141–173. doi:10.1016/s0009-2541(97)00074-0

Gaillardet, J., Dupré, B., Louvat, P., and Allègre, C. J. (1999). Global Silicate Weathering and CO_2 Consumption Rates Deduced from the Chemistry of Large Rivers. *Chem. Geol.* 159 (1–4), 3–30. doi:10.1016/s0009-2541(99)00031-5

Galy, A., and France-Lanord, C. (1999). Weathering Processes in the Ganges–Brahmaputra Basin and the Riverine Alkalinity Budget. *Chem. Geol.* 159 (1–4), 31–60. doi:10.1016/s0009-2541(99)00033-9

Gou, L.-F., Jin, Z., Deng, L., He, M.-Y., and Liu, C.-Y. (2018). Effects of Different Cone Combinations on Accurate and Precise Determination of Li Isotopic Composition by MC-ICP-MS. *Spectrochimica Acta B: At. Spectrosc.* 146, 1–8. doi:10.1016/j.sab.2018.04.015

Gou, L.-F., Jin, Z., Deng, L., Sun, H., Yu, H. M., and Zhang, F. (2017). Efficient Purification for Li and High-Precision and Accuracy Determination of Li Isotopic Composition by MC-ICP-MS. *Geochimica* 46 (6), 528–537 [In Chinese With English Abstract]. doi:10.3969/j.issn.0379-1726.2017.06.003

Gou, L.-F., Jin, Z., Pogge von Strandmann, P. A. E., Li, G., Qu, Y.-X., Xiao, J., et al. (2019). Li Isotopes in the Middle Yellow River: Seasonal Variability, Sources and Fractionation. *Geochim. Cosmochim. Atca.* 248, 88–108. doi:10.1016/j.gca.2019.01.007

Gou, L.-F., Liu, C. Y., Deng, L., and Jin, Z. (2020). Quantifying the Impact of Recovery during Chromatographic Purification on the Accuracy of Lithium Isotopic Determination by Multi-Collector Inductively Coupled Plasma Mass Spectrometry. *Rapid Commun. Mass. Spectrom.* 34, e8577. doi:10.1002/rcm.8577

Hagedorn, B., and Cartwright, I. (2009). Climatic and Lithologic Controls on the Temporal and Spatial Variability of CO_2 Consumption via Chemical Weathering: An Example from the Australian Victorian Alps. *Chem. Geol.*. 260, 234–253. doi:10.1016/j.chemgeo.2008.12.019

Hathorne, E., and James, R. (2006). Temporal Record of Lithium in Seawater: A Tracer for Silicate Weathering? *Earth Planet. Sci. Lett.* 246 (3–4), 393–406. doi:10.1016/j.epsl.2006.04.020

Hu, W., and Zhou, Q. (2012). Characteristics and Applications of Lithium Isotope Geochemistry. *Sci. Tech. Inform.* (5), 244 [In Chinese With English Abstract].

Huh, Y., Chan, L.-H., and Edmond, J. M. (2001). Lithium Isotopes as a Probe of Weathering Processes: Orinoco River. *Earth Planet. Sci. Lett.* 194 (1–2), 189–199. doi:10.1016/s0012-821x(01)00523-4

Huh, Y., Chan, L.-H., Zhang, L., and Edmond, J. M. (1998). Lithium and its Isotopes in Major World Rivers: Implications for Weathering and the Oceanic Budget. *Geochim. Cosmochim. Atca.* 62 (12), 2039–2051. doi:10.1016/s0016-7037(98)00126-4

Jin, Z., West, A. J., Zhang, F., An, Z., Hilton, R. G., Yu, J., et al. (2016). Seismically Enhanced Solute Fluxes in the Yangtze River Headwaters Following the A.D. 2008 Wenchuan Earthquake. *Geology* 44 (1), 47–50. doi:10.1130/g37246.1

Kısakűrek, B., James, R. H., and Harris, N. B. W. (2005). Li and δ^7Li in Himalayan Rivers: Proxies for Silicate Weathering? *Earth Planet. Sci. Lett.* 237, 387–401. doi:10.1016/j.epsl.2005.07.019

Kloppmann, W., Négrel, P., Casanova, J., Klinge, H., Schelkes, K., and Guerrot, C. (2001). Halite Dissolution Derived Brines in the Vicinity of a Permian Salt Dome (N German Basin). Evidence from Boron, Strontium, Oxygen, and Hydrogen Isotopes. *Geochim. Cosmochim. Atca.* 65 (22), 4087–4101. doi:10.1016/s0016-7037(01)00640-8

Koger, J. M., Newman, B. D., and Goering, T. J. (2018). Chemostatic Behaviour of Major Ions and Contaminants in a Semiarid Spring and Stream System Near Los Alamos, NM, USA. *Hydrological Process.* 32 (11), 1709–1716. doi:10.1002/hyp.11624

Lemarchand, E., Chabaux, F., Vigier, N., Millot, R., and Pierret, M.-C. (2010). Lithium Isotope Systematics in a Forested Granitic Catchment (Strengbach, Vosges Mountains, France). *Geochim. Cosmochim. Atca.* 74 (16), 4612–4628. doi:10.1016/j.gca.2010.04.057

Li, G., West, A. J., Densmore, A. L., Jin, Z., Parker, R. N., and Hilton, R. G. (2014). Seismic Mountain Building: Landslides Associated with the 2008 Wenchuan Earthquake in the Context of a Generalized Model for Earthquake Volume Balance. *Geochem. Geophys. Geosyst.* 15, 833–844. doi:10.1002/2013GC005067

Li, J., and Zhang, J. (2002). Weathering of Watershed Basins and Global Climate Change. *Adv. Earth Sci.* 17 (3), 411–419 [In Chinese With English Abstract]. doi:10.11867/j.issn.1001-8166.2002.03.0411

Li, S.-L., Chetelat, B., Yue, F., Zhao, Z., and Liu, C.-Q. (2014). Chemical Weathering Processes in the Yalong River Draining the Eastern Tibetan Plateau, China. *J. Asian Earth Sci.* 88, 74–84. doi:10.1016/j.jseaes.2014.03.011

Liu, F., Yin, X., and Liu, Q. (2021). Lithium Isotopes and Continental Weathering. *Acta Mineral. Sinica* 41 (2), 127–138 [In Chinese With English Abstract]. doi:10.16461/j.cnki.1000-4734.2021.41.054

Liu, M., Zhao, L. Y., Li, Q. Y., Zou, J. Y., Hu, Y., Zhang, Y. Z., et al. (2021). Hydrological Characteristics, Main Ion Sources of Main Rivers in the Souce Region of Yangtze River. *China Envion. Sci.* 41 (3), 1243–1254 [In Chinese With English Abstract]. doi:10.3969/j.issn.1000-6923.2021.03.028

Liu, X.-M., Fu, Y.-H., and Xia, R-J. (2020). Opportunities and Challenges of Watershed Ecological Comprehensive Conpensation–Taking the Min Jiang River Basin in Sichuan Province as an Example. *Environ. Ecol.* 2 (9), 25–30 [In Chinese With English Abstract].

Liu, X.-M., and Rudnick, R. L. (2011). Constraints on Continental Crustal Mass Loss via Chemical Weathering Using Lithium and its Isotopes. *Proc. Natl. Acad. Sci. U.S.A.* 108 (52), 20873–20880. doi:10.1073/pnas.1115671108

Liu, X.-M., Wanner, C., Rudnick, R. L., and McDonough, W. F. (2015). Processes Controlling δ^7Li in Rivers Illuminated by Study of Streams and Groundwaters Draining Basalts. *Earth Planet. Sci. Lett.* 409, 212–224. doi:10.1016/j.epsl.2014.10.032

Luijendijk, E., Gleeson, T., and Moosdorf, N. (2020). Fresh Groundwater Discharge Insignificant for the World's Oceans but Important for Coastal Ecosystems. *Nat. Commun.* 11, 1–12. doi:10.1038/s41467-020-15064-8

Ma, T., Weynell, M., Li, S.-L., Liu, Y., Chetelat, B., Zhong, J., et al. (2020). Lithium Isotope Compositions of the Yangtze River Headwaters: Weathering in High-Relief Catchments. *Geochim. Cosmochim. Atca.* 280, 46–65. doi:10.1016/j.gca.2020.03.029

Maher, K., and Chamberlain, C. P. (2014). Hydrologic Regulation of Chemical Weathering and the Geologic Carbon Cycle. *Science* 343 (6178), 1502–1504. doi:10.1126/science.1250770

Manaka, T., Araoka, D., Yoshimura, T., Hossain, H. M. Z., Nishio, Y., Suzuki, A., et al. (2017). Downstream and Seasonal Changes of Lithium Isotope Ratios in the Ganges-Brahmaputra River System. *Geochem. Geophys. Geosyst.* 18, 3003–3015. doi:10.1002/2016gc006738

Mavromatis, V., Rinder, T., Prokushkin, A. S., Pokrovsky, O. S., Korets, M. A., Chmeleff, J., et al. (2016). The Effect of Permafrost, Vegetation, and Lithology on Mg and Si Isotope Composition of the Yenisey River and its Tributaries at the End of the Spring Flood. *Geochim. Cosmochim. Atca.* 191, 32–46. doi:10.1016/j.gca.2016.07.003

Mayfield, K. K., Eisenhauer, A., Santiago Ramos, D. P., Higgins, J. A., Horner, T. J., Auro, M., et al. (2021). Groundwater Discharge Impacts Marine Isotope Budgets of Li, Mg, Ca, Sr, and Ba. *Nat. Commun.* 12 (1), 1–9. doi:10.1038/s41467-020-20248-3

Meybeck, M. (1987). Global Chemical Weathering of Surficial Rocks Estimated from River Dissolved Loads. *Am. J. Sci.* 287 (5), 401–428. doi:10.2475/ajs.287.5.401

Millot, R., Gaillardet, J. é., Dupré, B., and Allègre, C. J. (2003). Northern Latitude Chemical Weathering Rates: Clues from the Mackenzie River Basin, Canada. *Geochim. Cosmochim. Atca.* 67 (7), 1305–1329. doi:10.1016/S0016-7037(02)01207-3

Millot, R., Petelet-Giraud, E., Guerrot, C., and Négrel, P. (2010a). Multi-isotopic Composition (δ^7Li-Δ^{11}b-Δd-Δ^{18}o) of Rainwaters in France: Origin and Spatio-Temporal Characterization. *Appl. Geochem.* 25 (10), 1510–1524. doi:10.1016/j.apgeochem.2010.08.002

Millot, R., Vigier, N., and Gaillardet, J. (2010b). Behaviour of Lithium and its Isotopes during Weathering in the Mackenzie Basin, Canada. *Geochim. Cosmochim. Atca.* 74 (14), 3897–3912. doi:10.1016/j.gca.2010.04.025

Misra, S., and Froelich, P. N. (2012). Lithium Isotope History of Cenozoic Seawater: Changes in Silicate Weathering and Reverse Weathering. *Science* 335, 818–823. doi:10.1126/science.1214697

Moquet, J.-S., Crave, A., Viers, J., Seyler, P., Armijos, E., Bourrel, L., et al. (2011). Chemical Weathering and Atmospheric/soil CO_2 Uptake in the Andean and Foreland Amazon Basins. *Chem. Geol.*. 287, 1–26. doi:10.1016/j.chemgeo.2011.01.005

Penman, D. E., Caves Rugenstein, J. K., Ibarra, D. E., and Winnick, M. J. (2020). Silicate Weathering as a Feedback and Forcing in Earth's Climate and Carbon Cycle. *Earth-Sci. Rev.* 209, 103298. doi:10.1016/j.earscirev.2020.103298

Pogge von Strandmann, P. A. E., Burton, K. W., James, R. H., van Calsteren, P., Gíslason, S. R., and Mokadem, F. (2006). Riverine Behaviour of Uranium and Lithium Isotopes in an Actively Glaciated Basaltic Terrain. *Earth Planet. Sci. Lett.* 251 (1–2), 134–147. doi:10.1016/j.epsl.2006.09.001

Pogge von Strandmann, P. A. E., Burton, K. W., Opfergelt, S., Eiríksdóttir, E. S., Murphy, M. J., Einarsson, A., et al. (2016). The Effect of Hydrothermal Spring Weathering Processes and Primary Productivity on Lithium Isotopes: Lake Myvatn, Iceland. *Chem. Geology*. 445, 4–13. doi:10.1016/j.chemgeo.2016.02.026

Pogge von Strandmann, P. A. E., Fraser, W. T., Hammond, S. J., Tarbuck, G., Wood, I. G., Oelkers, E. H., et al. (2019). Experimental Determination of Li Isotope Behaviour during Basalt Weathering. *Chem. Geol.*. 517, 34–43. doi:10.1016/j.chemgeo.2019.04.020

Pogge von Strandmann, P. A. E., Frings, P. J., and Murphy, M. J. (2017). Lithium Isotope Behaviour during Weathering in the Ganges Alluvial Plain. *Geochim. Cosmochim. Atca.* 198, 17–31. doi:10.1016/j.gca.2016.11.017

Pogge von Strandmann, P. A. E., Jenkyns, H. C., and Woodfine, R. G. (2013). Lithium Isotope Evidence for Enhanced Weathering during Oceanic Anoxic Event 2. *Nat. Geosci.* 6 (8), 668–672. doi:10.1038/ngeo1875

Qin, J., Huh, Y., Edmond, J. M., Du, G., and Ran, J. (2006). Chemical and Physical Weathering in the Min Jiang, a Headwater Tributary of the Yangtze River. *Chem. Geol.*. 227 (1–2), 53–69. doi:10.1016/j.chemgeo.2005.09.011

Qin, J., Pan, G., and Du, G. (2000). The Effects of Cenozoic Tectonic Uplift on Earth Surface Chemical Weathering and Global Climate Change. *Earth Sci. Front.* 7 (2), 517–525. doi:10.3321/j.issn:1005-2321.2000.02.019

Ravizza, G., and Esser, B. K. (1993). A Possible Link between the Seawater Osmium Isotope Record and Weathering of Ancient Sedimentary Organic Matter. *Chem. Geol.* 107 (3–4), 255–258. doi:10.1016/0009-2541(93)90186-m

Raymo, M. E., and Ruddiman, W. F. (1992). Tectonic Forcing of Late Cenozoic Climate. *Nature* 359 (6391), 117–122. doi:10.1038/359117a0

Rudnick, R. L., Tomascak, P. B., Njo, H. B., and Gardner, L. R. (2004). Extreme Lithium Isotopic Fractionation during Continental Weathering Revealed in Saprolites from South Carolina. *Chem. Geol.*. 212 (1–2), 45–57. doi:10.1016/j.chemgeo.2004.08.008

SLCCC (Sichuan Local Chronicles Compilation Committee) (1998). *Commision on Annals of Sichuan Province (1998)*. Chengdu: Science and Technological Publishing House of Sichuan Province.

Su, Y. (2012). *Research Progress of Lithium Isotope in Underground waterNational Conference of Water Resource Allocation and Optimal Scheduling Technique*. China: Xi'an.

Tipper, E. T., Bickle, M. J., Galy, A., West, A. J., Pomiès, C., and Chapman, H. J. (2006). The Short Term Climatic Sensitivity of Carbonate and Silicate Weathering Fluxes: Insight from Seasonal Variations in River Chemistry. *Geochim. Cosmochim. Atca.* 70, 2737–2754. doi:10.1016/j.gca.2006.03.005

Vigier, N., Decarreau, A., Millot, R., Carignan, J., Petit, S., and France-Lanord, C. (2008). Quantifying Li Isotope Fractionation during Smectite Formation and Implications for the Li Cycle. *Geochim. Cosmochim. Atca.* 72 (3), 780–792. doi:10.1016/j.gca.2007.11.011

Vigier, N., Gislason, S. R., Burton, K. W., Millot, R., and Mokadem, F. (2009). The Relationship between Riverine Lithium Isotope Composition and Silicate Weathering Rates in Iceland. *Earth Planet. Sci. Lett.* 287, 434–441. doi:10.1016/j.epsl.2009.08.026

Walker, J. C. G., Hays, P. B., and Kasting, J. F. (1981). A Negative Feedback Mechanism for the Long-Term Stabilization of Earth's Surface Temperature. *J. Geophys. Res.* 86 (C10), 9776. doi:10.1029/jc086ic10p09776

Wang, J., Jin, Z., Hilton, R. G., Zhang, F., Densmore, A. L., Li, G., et al. (2015). Controls on Fluvial Evacuation of Sediment from Earthquake-Triggered Landslides. *Geology* 43, 115–118. doi:10.1130/G36157.1

Wang, Q.-L., Chetelat, B., Zhao, Z.-Q., Ding, H., Li, S.-L., Wang, B.-L., et al. (2015). Behavior of Lithium Isotopes in the Changjiang River System: Sources Effects and Response to Weathering and Erosion. *Geochim. Cosmochim. Atca.* 151, 117–132. doi:10.1016/j.gca.2014.12.015

West, A. J., Bickle, M. J., Collins, R., and Brasington, J. (2002). Small-catchment Perspective on Himalayan Weathering Fluxes. *Geology* 30 (4), 355. doi:10.1130/0091-7613(2002)030<0355:SCPOHW>2.0.CO;2

Wu, L., Huh, Y., Qin, J., Du, G., and van Der Lee, S. (2005). Chemical Weathering in the Upper Huang He (Yellow River) Draining the Eastern Qinghai-Tibet Plateau. *Geochim. Cosmochim. Atca.* 69 (22), 5279–5294. doi:10.1016/j.gca.2005.07.001

Wu, W., Xu, S., Yang, J., and Yin, H. (2008). Silicate Weathering and CO_2 Consumption Deduced from the Seven Chinese Rivers Originating in the Qinghai-Tibet Plateau. *Chem. Geol.*. 249, 307–320. doi:10.1016/j.chemgeo.2008.01.025

Wu, W., Zheng, H., Yang, J., Chao, L., and Zhou, B. (2011). Chemical Weathering of Larger River Catchments in China and the Global Carbon Cycle. *Quat. Sci.* 31 (3), 397–407 [In Chinese With English Abstract]. doi:10.3969/j.issn.1001-7410.2011.03.01

Xu, Z., Li, T., Li, G., Hedding, D. W., Wang, Y., Gou, L.-F., et al. (2021). Lithium Isotopic Composition of Soil Pore Water: Responses to Evapotranspiration. *Geology* 50, 194–198. doi:10.1130/G49366.1

Yoon, J., Huh, Y., Lee, I., Moon, S., Noh, H., and Qin, J. (2008). Weathering Processes in the Min Jiang: Major Elements, $^{87}Sr/^{86}Sr$, $\delta^{34}S_{SO4}$, and $\delta^{18}O_{SO4}$. *Aquat. Geochem.* 14, 147–170. doi:10.1007/s10498-008-9030-7

Zhang, H., Yang, N., Zhang, Y., and Meng, H. (2006). Geomorphology of the Minjiang Drainage System (Sichuan, China) and its Structural Implications. *Quat. Sci.* 26 (1), 126–135. doi:10.3321/j.issn:1001-7410.2006.01.016

Zhang, Q., Jin, Z., Zhang, F., and Xiao, J. (2015). Seasonal Variation in River Water Chemistry of the Middle Reaches of the Yellow River and its Controlling Factors. *J. Geochem. Explor.* 156, 101–113. doi:10.1016/j.gexplo.2015.05.008

Conflict of Interest: The authors declare that the research was conducted in the absence of any commercial or financial relationships that could be construed as a potential conflict of interest.

Publisher's Note: All claims expressed in this article are solely those of the authors and do not necessarily represent those of their affiliated organizations, or those of the publisher, the editors, and the reviewers. Any product that may be evaluated in this article, or claim that may be made by its manufacturer, is not guaranteed or endorsed by the publisher.

frontiers | Frontiers in Earth Science

ORIGINAL RESEARCH
published: 26 April 2022
doi: 10.3389/feart.2022.833609

Shale Heavy Metal Isotope Records of Low Environmental O_2 Between Two Archean Oxidation Events

Chadlin M. Ostrander[1,2], Brian Kendall[3], Gwyneth W. Gordon[4,5], Sune G. Nielsen[2,6], Wang Zheng[7] and Ariel D. Anbar[4,8]*

[1]Department of Marine Chemistry and Geochemistry, Woods Hole Oceanographic Institution, Woods Hole, MA, United States, [2]NIRVANA Laboratories, Woods Hole Oceanographic Institution, Woods Hole, MA, United States, [3]Department of Earth and Environmental Sciences, University of Waterloo, Waterloo, ON, Canada, [4]School of Earth and Space Exploration, Arizona State University, Tempe, AZ, United States, [5]Knowledge Enterprise, Arizona State University, Tempe, AZ, United States, [6]Department of Geology and Geophysics, Woods Hole Oceanographic Institution, Woods Hole, MA, United States, [7]Institute of Surface-Earth System Science, School of Earth System Science, Tianjin University, Tianjin, China, [8]School of Molecular Sciences, Arizona State University, Tempe, AZ, United States

Evidence of molecular oxygen (O_2) accumulation at Earth's surface during the Archean (4.0–2.5 billion years ago, or Ga) seems to increase in its abundance and compelling nature toward the end of the eon, during the runup to the Great Oxidation Event. Yet, many details of this late-Archean O_2 story remain under-constrained, such as the extent, tempo, and location of O_2 accumulation. Here, we present a detailed Fe, Tl, and U isotope study of shales from a continuous sedimentary sequence deposited between ~2.6 and ~2.5 Ga and recovered from the Pilbara Craton of Western Australia (the Wittenoom and Mt. Sylvia formations preserved in drill core ABDP9). We find a progressive decrease in bulk-shale Fe isotope compositions moving up core (as low as $\delta^{56}Fe = -0.78 \pm 0.08‰$; 2SD) accompanied by invariant authigenic Tl isotope compositions (average $\varepsilon^{205}Tl_A = -2.0 \pm 0.6$; 2SD) and bulk-shale U isotope compositions (average $\delta^{238}U = -0.30 \pm 0.05‰$; 2SD) that are both not appreciably different from crustal rocks or bulk silicate Earth. While there are multiple possible interpretations of the decreasing $\delta^{56}Fe$ values, many, to include the most compelling, invoke strictly anaerobic processes. The invariant and near-crustal $\varepsilon^{205}Tl_A$ and $\delta^{238}U$ values point even more strongly to this interpretation, requiring reducing to only mildly oxidizing conditions over ten-million-year timescales in the late-Archean. For the atmosphere, our results permit either homogenous and low O_2 partial pressures (between $10^{-6.3}$ and 10^{-6} present atmospheric level) or heterogeneous and spatially restricted O_2 accumulation nearest the sites of O_2 production. For the ocean, our results permit minimal penetration of O_2 in marine sediments over large areas of the seafloor, at most sufficient for the burial of Fe oxide minerals but insufficient for the burial of Mn oxide minerals. The persistently low background O_2 levels implied by our dataset between ~2.6 and ~2.5 Ga contrast with the timeframes immediately before and after, where strong evidence is presented for transient Archean Oxidation Events. Viewed in this broader context, our data support the emerging narrative that Earth's initial oxygenation was a dynamic process that unfolded in fits-and-starts over many hundreds-of-millions of years.

Keywords: archean, thallium, iron, uranium, isotopes, oxygen

OPEN ACCESS

Edited by:
Julia Ribeiro, Guangzhou Institute of Geochemistry (CAS), China

Reviewed by:
Ross Raymond Large, University of Tasmania, Australia
Martin Wille, University of Bern, Switzerland

****Correspondence:***
Chadlin M. Ostrander
costrander@whoi.edu

Specialty section:
This article was submitted to Geochemistry, a section of the journal Frontiers in Earth Science

Received: *11 December 2021*
Accepted: *16 March 2022*
Published: *26 April 2022*

Citation:
Ostrander CM, Kendall B, Gordon GW, Nielsen SG, Zheng W and Anbar AD (2022) Shale Heavy Metal Isotope Records of Low Environmental O_2 Between Two Archean Oxidation Events. Front. Earth Sci. 10:833609. doi: 10.3389/feart.2022.833609

INTRODUCTION

Earth's earliest O_2 history remains a topic of ongoing debate (compare Kopp et al., 2005 against Ohmoto et al., 2006 for two extreme end-member scenarios), and many important details remain unresolved. For example, evidence of O_2 production and accumulation increases in both its abundance and compelling nature in the immediate runup to the Great Oxidation Event (GOE), during the final few hundred million years of the Archean Eon (4.0–2.5 Ga; summarized in Ostrander et al., 2021). Two Archean Oxidation Events (AOEs), each of probably single-million-years duration, have been identified during the late-Archean and verified by multiple lines of independent evidence: one at ~2.65 Ga (Koehler et al., 2018; Olson et al., 2019; Ostrander et al., 2020) and another at ~2.50 Ga (Anbar et al., 2007; Kaufman et al., 2007; Wille et al., 2007; Garvin et al., 2009; Godfrey and Falkowski 2009; Reinhard et al., 2009; Duan et al., 2010; Kendall et al., 2010, 2013, 2015a; Gregory et al., 2015; Kurzweil et al., 2015; Stüeken et al., 2015; Ostrander et al., 2019, 2020; Meixnerová et al., 2021). Evidence is also presented for non-zero and fluctuating O_2 levels during the much longer intervening timeframe (e.g., Eigenbrode and Freeman 2006, Stüeken et al., 2012, Gregory et al., 2015, Eroglu et al., 2015; 2017); however, this evidence is at times not as compelling, and follow-up studies of the same and coeval samples oftentimes arrive at different conclusions. For example, progressively heavier Mo isotope compositions are found in sedimentary rocks formed between about 2.6 and 2.5 Ga and inferred as evidence of a progressive rise in atmospheric and oceanic O_2 levels (Wille et al., 2007; Kurzweil et al., 2015). Yet, in some of these same rocks, generally invariant C (Fischer et al., 2009) and U (Brüske et al., 2020) isotope compositions are inferred as evidence of little to no change to Earth's surface O_2 levels. To summarize, emerging evidence clearly identifies brief, single-million-year O_2 accumulation events on the eve of the GOE, but no clear consensus yet exists for the O_2 levels that persisted over much longer, tens-of-million-year timeframes.

What is missing up to this point, and provided here, is a detailed, multi-pronged geochemical investigation of a continuous sedimentary sequence deposited during the late-Archean. We generated Fe, Tl, and U isotope records from shales of the Wittenoom and Mt. Sylvia formations (Western Australia) deposited between about 2.6 and 2.5 Ga and recovered from the ABDP9 drill core. Each of these heavy metal isotope "paleoredox proxies" is uniquely sensitive to a specific redox threshold; Fe isotopes are directly sensitive to Fe oxidation (Johnson et al., 2008), U isotopes are directly sensitive to U oxidation (Tissot and Dauphas 2015), and Tl isotopes are indirectly sensitive to Mn oxidation (Nielsen et al., 2017). Each of these proxies is also already proven independently valuable in reconstructing atmospheric and oceanic O_2 levels during the Archean (e.g., Fe: Rouxel et al., 2005, Czaja et al., 2012, Heard et al., 2020, U: Kendall et al., 2013, Wang et al., 2018; 2020, Brüske et al., 2020, and Tl: Ostrander et al., 2019). Our study represents the first time ever, at any time in Earth's past, all three proxies are applied in a single study to the same sedimentary archive.

HEAVY METAL ISOTOPE PROXIES

Fe Isotope Proxy

Sedimentary Fe isotope ratios have the potential to trace ancient Fe redox reactions. A large equilibrium isotope fractionation effect is imparted during Fe redox reactions that can leave the Fe(II) phase up to ~3.0‰ lighter than the Fe(III) phase (Welch et al., 2003). Sediments today and their constituent minerals are shown to capture and preserve these Fe isotopic effects, at least partially (e.g., Severmann et al., 2008; Busigny et al., 2014; Scholz et al., 2014). Likewise, and by analogy, fingerprints of Fe redox reactions in Archean oceans should be left behind in the Archean sedimentary record. Indeed, a large degree of Fe isotope variability is found in Archean sedimentary rocks and interpreted as evidence of ancient Fe redox reactions (e.g., Rouxel et al., 2005; Czaja et al., 2012; Heard et al., 2020).

There are some caveats to the Fe isotope proxy. Iron redox reactions cannot be explicitly linked to aerobic processes; oxidation of Fe(II) is observed in the absence of O_2 during interaction with UV-light (Cairns-Smith 1978) and also during photo-ferrotrophy (Widdel et al., 1993). Furthermore, there exist at least two means for driving considerable Fe isotope fractionation effects without the requirement of an Fe redox change: hydrothermal processes (by up to ~0.7‰; Lough et al., 2017) and pyrite formation (by up to ~3.0‰; Guilbaud et al., 2011). These caveats can make it extremely difficult, and at times even impossible to differentiate anaerobic from aerobic redox processes using Fe isotopes alone. Notwithstanding, useful information can still be gleaned from the proxy in deep time when it is applied in tandem with other, complementary proxies (e.g., Czaja et al., 2012; Asael et al., 2013).

U Isotope Proxy

When applied to the Archean sedimentary record, the U isotope paleoredox proxy has emerged as a useful tracer of early U(IV) oxidation. On the modern well-oxygenated Earth, U(IV) is readily oxidized to U(VI) during oxidative weathering and delivered to the ocean as the soluble uranyl carbonate complex [$UO_2(CO_3)_3^{4-}$; Langmuir 1978], where it accumulates with a residence time (~400 kyr; Ku et al., 1977) that far exceeds the ocean mixing time (~1 kyr; Sarmiento and Gruber 2006). Within the U(VI)-replete modern marine realm, U is readily exchanged between seawater and sediments, and this leads to a large range of U isotope ratios across different sediment types ($\Delta^{238}U$ = ~1.3‰; Weyer et al., 2008; Tissot and Dauphas 2015). By contrast, on a primarily anoxic Archean Earth, it would be expected that U(IV) oxidation would be negligible or non-existent, at the very least stunting and in the most extreme case preventing U(VI) accumulation in seawater. In an ocean devoid of mobile U(VI), there would be no opportunity for

isotopic fractionation between seawater and marine sediments.

Following from this logic, U isotopes have been treated essentially as a binary paleoredox proxy when applied to the Archean Eon. When free-O_2 was in low abundance or non-existent, sedimentary rocks should reveal minimal U enrichments and $\delta^{238}U$ values indistinguishable from, or very close to, average upper continental crust and the mantle (both possess $\delta^{238}U$ = −0.3‰; Partin et al., 2013; Brüske et al., 2020; Chen et al., 2021). In contrast, during episodes of appreciable O_2 accumulation, sedimentary rocks should reveal some combination of U enrichments and non-crustal $\delta^{238}U$ values (Kendall et al., 2013; Wang et al., 2018).

Tl Isotope Proxy

The Tl isotope paleoredox proxy is the youngest of the three isotope systems, having emerged relatively recently as a novel tool for tracking changes in ancient marine oxygenation indirectly through Mn oxide burial (Nielsen et al., 2011; Owens et al., 2017). The strongest isotopic lever of seawater Tl isotope mass-balance today is Mn oxide minerals that get buried in well-oxygenated marine sediments (Baker et al., 2009). Manganese oxides possess a strong preference for the heavier-mass Tl isotope ($\varepsilon^{205}Tl$ = +10 to +14; Rehkämper et al., 2002; Nielsen et al., 2013), and their widespread distribution on the well-oxygenated seafloor today leads to accumulation of the lighter-mass Tl isotope in seawater ($\varepsilon^{205}Tl$ = −6.0 ± 0.3; Nielsen et al., 2006a; Owens et al., 2017) relative to global oceanic Tl inputs ($\varepsilon^{205}Tl$ = −1.8; Nielsen et al., 2017). Because the residence time of Tl in seawater today (~19 kyr; Nielsen et al., 2017) exceeds the ocean mixing time, the seawater $\varepsilon^{205}Tl$ signature today is globally homogenous. By contrast, Fe oxide minerals are unlikely to fractionate Tl isotopes because the likely fractionation mechanism—oxidation of Tl(I) to Tl(III)—does not occur during sorption to Fe oxides (Peacock and Moon 2012). Moreover, neither of the two remaining primary marine Tl outputs today imparts a substantial isotopic fractionation effect; low-temperature oceanic crust alteration imparts only a slight negative isotope fractionation effect (average $\varepsilon^{205}Tl$ = −7.2; Nielsen et al., 2017), and no isotope fractionation is observed in Tl leached from pyrite from sediments deposited under anoxic bottom waters, presumably because of quantitative Tl transfer to pyrite in these settings (Owens et al., 2017; Fan et al., 2020; Chen et al., 2022).

Akin to U isotopes, Tl isotopes can also be treated as a binary proxy when applied to the Archean. In the absence of the Mn oxide mass-balance lever—for example, in a widely anoxic Archean ocean—the seawater $\varepsilon^{205}Tl$ value will not be significantly different from that of the bulk upper continental crust and mantle (roughly $\varepsilon^{205}Tl$ = −2.0 ± 1.0; Nielsen et al., 2005; 2006b). By analogy with modern equivalents, pyrite leached from Archean sedimentary rocks deposited under anoxic conditions should capture this near-crustal seawater $\varepsilon^{205}Tl$ value (Owens et al., 2017). In support of this logic, near-crustal $\varepsilon^{205}Tl_A$ values are found in pyrite leached from shales deposited under locally anoxic conditions at a time of inferred low Archean O_2 levels, with a deviation toward more negative $\varepsilon^{205}Tl_A$ values found exclusively during a transient 2.5 Ga AOE (compare $\varepsilon^{205}Tl_A$ between the lower and upper Mt. McRae Shale in ABDP9; Ostrander et al., 2019).

MATERIALS AND METHODS

Drill Core ABDP9

Drill core ABDP9 was recovered from the Pilbara Craton of Western Australia during the 2004 NASA Astrobiology Institute Deep Time Drilling Project (**Figure 1**). Detailed descriptions of the core are provided in previous work (Anbar et al., 2007; Kaufman et al., 2007); we offer only a brief summary here. Shales are the dominant lithology in the lowermost and middle Wittenoom Formation, with organic-rich ("black") shales becoming increasingly common in the uppermost Wittenoom and overlying Mt. Sylvia Formation. Intervals of banded iron formation (BIF) deposition are present but infrequent, appearing in the middle of the Wittenoom Formation and near the base and top of the Mt. Sylvia Formation. Intervals of BIF deposition were avoided, and care was also taken to avoid depths containing macroscopic pyrite. Sedimentary rocks in ABDP9 have experienced relatively minor metamorphism considering their age (prehnite-pumpellyite facies, < 300°C; Brocks et al., 2003).

According to available geochronological constraints, the Wittenoom and Mt. Sylvia formations were deposited between about 2.6 and 2.5 Ga (Trendall et al., 2004). Wittenoom Formation deposition initiated sometime after 2.597 ± 0.005 Ga according to a zircon U–Pb age for volcanoclastics from the underlying Marra Mamba Formation (Trendall et al., 1998). A Pb-Pb age of 2.541 ± 0.018 Ga was obtained for an impact spherule bed found in coeval carbonaceous strata at a nearby location (Woodhead et al., 1998), and it is suggested that a contemporaneous spherule bed is present in ABDP9 at 295 m core depth (Kurzweil et al., 2015). An upper age limit of 2.495 ± 0.014 Ga for the Mt. Sylvia Formation comes from a Re–Os depositional age for organic-rich shales from the overlying Mt. McRae Shale in ABDP9 (Kendall et al., 2015a).

Deposition of shales from ABDP9 is thought to have taken place below storm wave base on the outer-shelf in a marginal or open-ocean setting (Morris and Horwitz 1983). According to previously published Fe speciation, trace metal, and Mo isotope data, shales from the Wittenoom and Mt. Sylvia formations were deposited under the anoxic conditions that typified most Archean marine environments (Ostrander et al., 2020). Localized anoxia seems to have persisted throughout deposition of both units, and there is a possibility that redox conditions were especially reducing during deposition of the Mt. Sylvia Formation. In the uppermost Wittenoom Formation, above around 250 m core depth, there is an increase in the ratio of total Fe (Fe_T) to Al and in the ratio of highly reactive Fe (Fe_{HR}) to Fe_T (**Figure 2**). Although there is no comparable trend in the ratio of pyritized Fe (Fe_{Py}) to Fe_{HR}, ratios indicative of euxinic conditions are approached for the first time in the section at around this same depth. By analogy with modern analogs, each of these changes in Fe

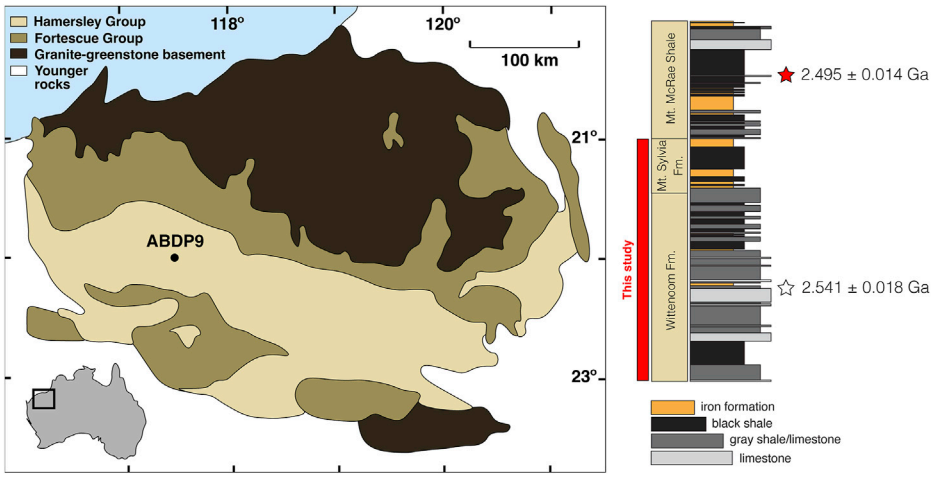

FIGURE 1 | Geological map of the Pilbara Craton and ABDP9 stratigraphy. Geological map is modified from Kurzweil et al. (2015) and stratigraphy is modified from Anbar et al. (2007) and Ostrander et al. (2020). Age constraints are from, in ascending order, Woodhead et al. (1998) and Kendall et al. (2015a).

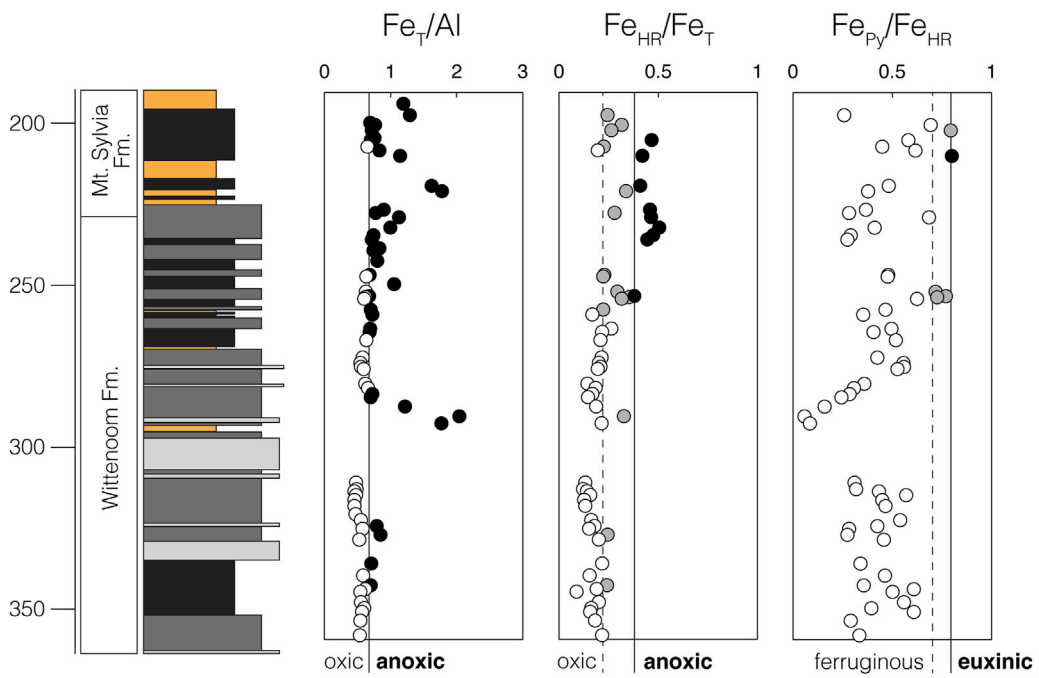

FIGURE 2 | Previously published Fe speciation data indicating persistent localized anoxia during deposition of the Wittenoom and Mt. Sylvia formations in ABDP9. Data and original interpretation are from Ostrander et al. (2020). Black datapoints exceed strict thresholds for local anoxia ($Fe_T/Al > 0.55$ or $Fe_{HR}/Fe_T > 0.38$) or euxinia ($Fe_{Py}/Fe_{HR} > 0.80$), while gray datapoints exceed relaxed thresholds for the same ($Fe_{HR}/Fe_T > 0.22$ for anoxia and $Fe_{Py}/Fe_{HR} > 0.70$ for euxinia) (summarized in Raiswell et al., 2018).

speciation would be an expected consequence of strengthened local anoxia (Raiswell et al., 2018). Previously published Mo isotopic compositions from Ostrander et al. (2020) are also heavier in the Mt. Sylvia Formation (δ^{98}Mo up to 1.43‰, and averaging 0.97‰) than in the Wittenoom Formation (δ^{98}Mo up to 1.02‰, and averaging 0.73‰) in ABDP9, which could also support more reducing local redox conditions during deposition of the former by analogy with modern equivalents (Kendall et al., 2017; but see Kurzweil et al., 2015 for an alternative interpretation that attributes these increasing δ^{98}Mo values to progressive Earth surface oxidation).

The Wittenoom and Mt. Sylvia formations were deposited in a timeframe separating two transient AOEs. Redox-sensitive trace metal enrichments are found in the ~2.65 Ga Jeerinah Formation and interpreted as evidence of oxidative sulfide weathering on land [Se up to 5 ug/g (Koehler et al., 2018) and Mo up to 10 ug/g (Olson et al., 2019)]. Heavy N isotope compositions in the same samples support coeval marine oxygenation by fingerprinting the operation of an aerobic N cycle in overlying waters (up to $\delta^{15}N$ = ~6.0‰; Koehler et al., 2018), an interpretation that gains support from heavy Se and Mo isotope compositions that imply removal of lighter-mass isotopes in shallower-water, mildly oxygenated sediments on the continental shelf (up to $\delta^{82}Se$ = 0.90‰ (Koehler et al., 2018) and up to $\delta^{98}Mo$ = 1.01‰ (Ostrander et al., 2020)). These geochemical patterns are even more pronounced in the upper member of the Mt. McRae Shale in ABDP9, indicating that an especially pronounced AOE took place at ~2.50 Ga. During this younger AOE, oxidative weathering is indicated by strong trace metals enrichments (Se up to 20 ug/g (Stüeken et al., 2015) and Mo up to 49 ug/g (Anbar et al., 2007)). Heavy N isotope values again support a local aerobic N cycle (up to $\delta^{15}N$ = 7.5‰; Garvin et al., 2009), and even heavier Se and Mo isotope compositions imply more pronounced removal of lighter-mass isotopes in mildly oxygenated settings on the continental shelf (up to $\delta^{82}Se$ = 1.43‰ (Stüeken et al., 2015) and up to $\delta^{98}Mo$ = 1.77‰ (Duan et al., 2010)). Other geochemical trends found in the upper Mt. McRae Shale also corroborate the AOE hypothesis, as do those found in coeval shales from South Africa (summarized in Ostrander et al., 2021).

Isotopic Methods

For Fe and U, sample preparation, isotope purification, and analyses were conducted at the Metals, Environment, Terrestrial Analytical Laboratory (METAL) at Arizona State University. About one-hundred milligrams of whole-rock material from each sample depth was powdered and ashed overnight in a muffle furnace at 550°C to oxidize organic material. Then, each sample was transferred to a trace metal clean lab where it was subjected to multiple rounds of concentrated acid digestion using trace metal grade hydrofluoric, hydrochloric, and nitric acids in pre-cleaned Teflon labware. Once completely dissolved, samples were transferred to trace-metal clean screw top bottles ("stock solution"), from which a small aliquot was taken and diluted in 2% nitric acid in preparation for concentration analysis on a Thermo Scientific X-series quadrupole ICP-MS following published methods (Anbar et al., 2007; Kendall et al., 2010). Isotope purification and analysis was conducted following procedures outlined in previous Fe (Beard et al., 2003; Arnold et al., 2004) and U (Weyer et al., 2008; Kendall et al., 2013) isotopic investigations. A stock solution split equivalent to 10 µg of Fe was separated from the sample matrix via ion exchange chromatography using Bio-Rad AG1X8 anion resin. To avoid isotopic fractionation associated with ion exchange purification, only samples recovering ≥95% of their original Fe contents were prepared for isotopic analysis (this was checked *via* ICP-MS). Samples that fit this criterion were dried down, brought up in 0.32 M HNO_3, and doped with a NIST 3114 Cu elemental spike to correct for instrumental mass bias during isotopic analysis. Thereafter, a separate split equivalent to 250 ng of U was taken from each stock solution and mixed with a $^{236}U/^{233}U$ double-spike solution to correct for instrumental mass bias during purification and isotopic analysis. Samples were purified using Eichrom® UTEVA resin, dried-down, and reconstituted in 0.32 M HNO_3 in preparation for isotopic analysis. Fe and U isotope ratio measurements were performed on a Thermo Neptune multi-collector ICPMS (MC-ICP-MS) in medium- and low-resolution mode, respectively, utilizing sample-standard bracketing. For Fe, IRMM-524a was used as the bracketing standard, which is shown to be isotopically indistinguishable from IRMM-014 (Craddock and Dauphas, 2011). All bulk-shale Fe isotope data are reported relative to IRMM-524a in delta notation:

$$\delta^{56}Fe\ (‰) = \left(^{56/54}Fe_{sample} \div {}^{56/54}Fe_{IRMM-524a} - 1\right) \times 1,000.$$

For U, CRM 145 was used as the bracketing standard and all bulk-shale data are reported relative to this standard in delta notation:

$$\delta^{238}U\ (‰) = \left(^{238/235}U_{sample} \div {}^{238/235}U_{CRM\,145} - 1\right) \times 1,000.$$

Sample preparation and analysis for Tl were conducted at the NIRVANA Laboratory at Woods Hole Oceanographic Institution (WHOI) and the WHOI Plasma Mass Spectrometry Facility. About one-hundred milligrams of powdered shale material from each sample depth was transferred to a Teflon reactor and treated with 2 M HNO_3 for 12–15 h at 130°C, a treatment shown to effectively "leach" authigenic Tl bound to pyrite from detrital Tl (Nielsen et al., 2011). Following this partial dissolution, samples were centrifuged, and their supernatants containing the authigenic fraction were transferred to new Teflon reactors and digested using trace metal grade concentrated HCl and HNO_3. Once dissolved, samples were reconstituted in 1 M HCl in preparation for Tl purification via the typical two-step ion-exchange chromatography procedure (using AG1X8 anion resin; Rehkämper and Halliday 1999; Nielsen et al., 2004). Thallium isotope ratio measurements were performed using previously established techniques (Rehkämper and Halliday 1999; Nielsen et al., 2004) on a Thermo Neptune MC-ICP-MS equipped with an Aridus II desolvating nebulizer sample introduction system in low-resolution mode. Sample-standard bracketing was conducted relative to NIST 997 Tl, and instrumental mass bias correction was done by external normalization to NIST SRM 981 Pb. Because each sample was doped with a known quantity of NIST SRM 981 Pb, authigenic Tl concentrations could be calculated during MC-ICPMS analysis using the measured $^{205}Tl/^{208}Pb$ ratios. We report all authigenic Tl isotope values in epsilon notation relative to NIST 997 Tl metal:

$$\varepsilon^{205}Tl_A = \left(^{205/203}Tl_{sample} \Big/ {}^{205/203}Tl_{NIST-997} - 1\right) \times 1,000.$$

USGS rock reference materials were simultaneously processed with each batch of samples and showed good reproducibility, as did various previously processed standard solutions (**Table 1**). Reported uncertainties for our samples are always in 2SD and either equal to the highest 2SD reproducibility of our standards or the individual sample's reproducibility, whichever is greater. All data are provided in the **Supplementary Material**.

TABLE 1 | Standard isotope data.

Fe isotope standards	δ^{56}Fe (2SD)	N	Previously published values (2SD)
BIR	0.07 (0.05)[a]	4	0.05 (0.02)[b]
Tag Fe	−0.86 (0.08)[a]	7	−0.99 (0.09)[c]
SDO-1	0.04 (0.07)[d]	8	−0.05 (0.12)[c]
U isotope standards	δ^{238}U (2SD)	N	Previously published values (2SD)
CRM129A	−1.72 (0.09)[a]	12	−1.71 (0.05)[e]
Ricca	−0.22 (0.11)[a]	14	−0.23 (0.06)[e]
SDO-1	−0.11 (0.09)[d]	6	−0.06 (0.04)[f]
Tl isotope standard	ε^{205}Tl (2SD)	N	Previously published values (2SD)
SCO-1	−2.9 (0.2)[d]	4	−2.6 (0.2)[g]

[a]*Previously digested and purified standard solution.*
[b]*Value reported by Craddock and Dauphas (2011).*
[c]*Value reported by Severmann et al. (2008).*
[d]*Powdered rock standard digested and purified alongside samples.*
[e]*Value reported by Zhang et al. (2018).*
[f]*value reported by Kendall et al. (2015b).*
[g]*value reported by Ostrander et al. (2017).*

RESULTS

We find a general decrease in bulk-shale δ^{56}Fe values moving up section (**Figure 3**). At and below 259.04 m, δ^{56}Fe values are generally invariant (average δ^{56}Fe = –0.01 ± 0.42‰; 2SD), with only one sample (δ^{56}Fe = +0.54 ± 0.14‰ at 292.74 m) possessing a δ^{56}Fe value vastly different from that of modern bulk upper continental crust ($\delta^{56}Fe_{BUCC} \approx 0.00$‰; Dauphas et al., 2017). At and above 253.17 m, δ^{56}Fe values become progressively lower, reaching a minimum of –0.78 ± 0.08‰ (at 228.70 m) and averaging –0.51 ± 0.36‰. Bulk-shale Fe abundances are fairly constant throughout the sedimentary sequence (averaging 5.4 wt%), with the exception of two instances of noticeable Fe enrichment near Fe-formation intervals in the middle of the Wittenoom Formation (as high as 14.2 wt% at 290.52 m) and near the base of the Mt. Sylvia Formation (as high as 10.9 wt% at 218.91 m) (**Figure 4**). These Fe enrichment trends mirror those of the Fe/Al data (**Figure 2**).

In contrast, δ^{238}U and $\varepsilon^{205}Tl_{auth}$ values are invariant and always within uncertainty of their respective modern bulk upper continental crust values. Bulk-shale δ^{238}U values average –0.30 ± 0.06‰ (2SD) in the Wittenoom Formation and –0.29 ± 0.03‰ (2SD) in the Mt. Sylvia Formation (**Figure 3**); both are identical to the estimated modern BUCC δ^{238}U value of –0.29 ± 0.03‰ (Tissot and Dauphas 2015). Authigenic ε^{205}Tl values average –1.97 ± 0.60 (2SD) in the Wittenoom Formation and –2.15 ± 0.51 (2SD) in the Mt. Sylvia Formation (**Figure 3**); both are indistinguishable from the estimated modern BUCC ε^{205}Tl value of –2.1 ± 1.3 (Nielsen et al., 2005). Bulk-shale U concentrations slightly decrease moving up section (averaging 4.3 μg/g in the Wittenoom Formation and 3.0 μg/g in the Mt. Sylvia Formation), a trend that is also preserved when normalized to Al (**Figure 4**). Authigenic Tl concentrations are slightly lower

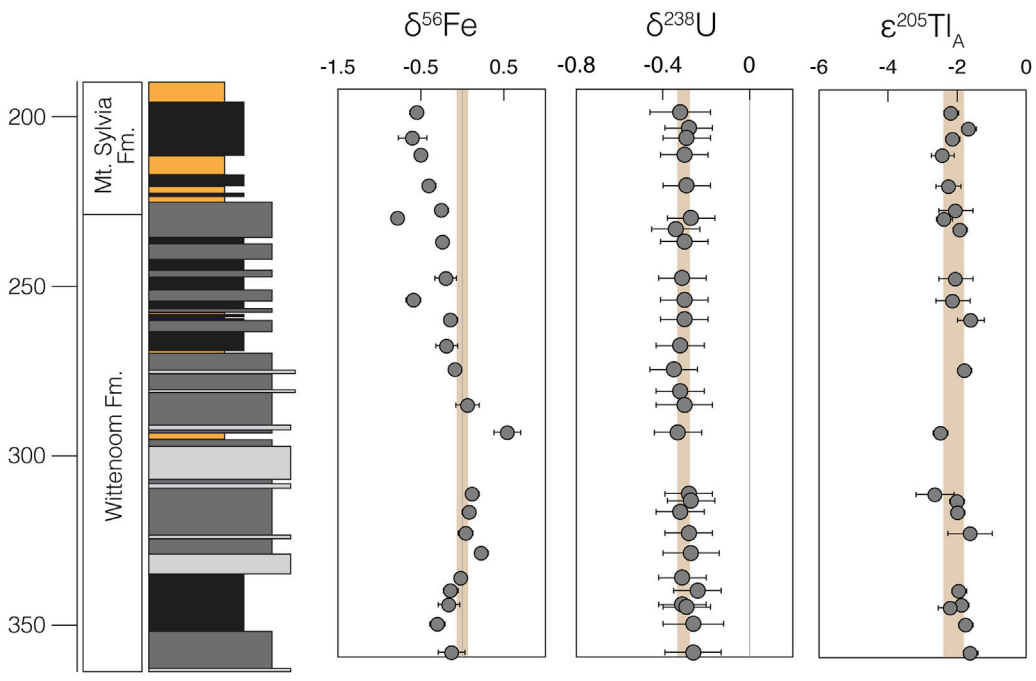

FIGURE 3 | Heavy metal isotope data generated during the current study. δ^{56}Fe and δ^{238}U values are for bulk-shale, while $\varepsilon^{205}Tl_A$ values are for leached (authigenic) fractions. The brown shaded region in each panel represents the estimated average bulk upper continental crust value for that isotope system, which is in all cases similar to the estimated mantle value. Errors are either equal to the highest 2SD reproducibility of our standards or the individual sample's reproducibility, whichever is greater.

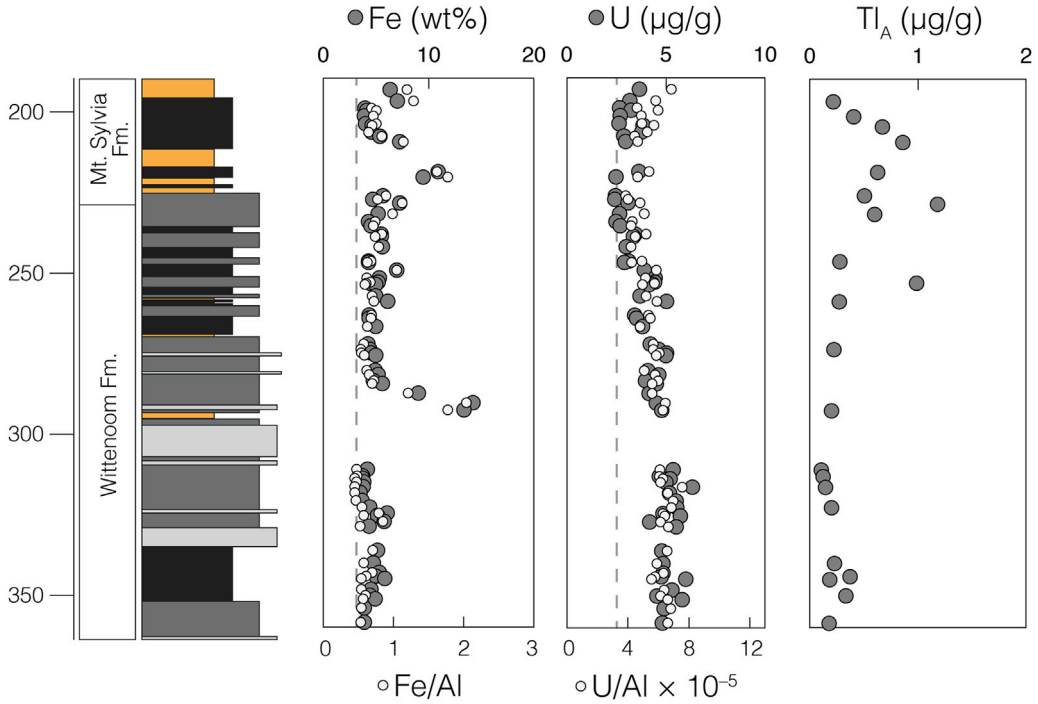

FIGURE 4 | Trace metal concentration data generated during the current study. Dark gray datapoints represent non-normalized concentrations for bulk-shale (Fe and U) and leached authigenic fractions (Tl_A). Light gray datapoints represent concentrations normalized to the non-redox sensitive element Al and gray dashed lines represent average upper continental crust values for these ratios (Rudnick and Gao 2003).

in the Wittenoom Formation (averaging 0.3 μg/g) compared to the Mt. Sylvia Formation (averaging 0.6 μg/g) (**Figure 4**).

DISCUSSION

Fe Isotope Data

As an initial step in interpreting the δ^{56}Fe data, it is important to estimate the authigenic Fe isotope contribution to each sample. The Fe in each shale sample is primarily a mixture of two components: a detrital fraction (i.e., continent-derived; f_D) and an authigenic fraction (i.e., seawater-derived; f_A). The latter is more important for tracking changes in ancient low-temperature geochemical processes. If we assume the sum of these two fractions is equal to one ($f_D + f_A = 1$), then the following equation can be used to calculate f_A:

$$f_A = 1 - (Al \times (Fe/Al)_D \div Fe).$$

where "Al" and "Fe" signify bulk shale sample concentrations, and $(Fe/Al)_D$ represents the inverted ratio of these elements in the detrital component. Because Al is not redox-sensitive, increases in shale Fe/Al ratios above the detrital background are most likely due to the preferential accumulation of authigenic Fe (e.g., Lyons and Severmann 2006). For Fe/Al_D we use 0.45, the lowest Fe/Al ratio found in our shale samples, because this value is the least likely to contain an authigenic Fe enrichment. This ratio is very similar to that estimated for the modern bulk upper continental crust (BUCC) of 0.48 (Rudnick and Gao 2003), the source of detrital material.

When calculated f_A are plotted versus their respective bulk-shale δ^{56}Fe values, a coherent relationship is revealed ($R^2 = 0.52$ when the lone sample with an especially high δ^{56}Fe value of 0.54 ± 0.16‰ is omitted; **Figure 5**). Samples with especially low f_A possess bulk-shale δ^{56}Fe values that most closely resemble modern BUCC (leftmost data in **Figure 5**). These samples are strongly affected by their high detrital Fe contributions. In contrast, samples with especially high f_A reveal continuously decreasing bulk-shale δ^{56}Fe values (rightmost data in **Figure 5**). These samples are not affected by high detrital Fe contributions, and as such are ideal for reconstructing the authigenic Fe source. Omitting one sample with an especially high bulk-shale δ^{56}Fe value, and also samples with especially high detrital Fe contributions (specifically, three samples with $f_A <$ 0.15), the remaining samples ($n = 19$) can be reconciled by two-component mixing between detrital Fe ($\delta^{56}Fe_{BUCC} \approx 0.00$‰; Dauphas et al., 2017) and an authigenic δ^{56}Fe source ($\delta^{56}Fe_A$) between −1.54‰ and −0.22‰ (**Figure 5A**).

It is possible that Fe oxide mineral formation in late-Archean marine settings led to the preferential removal of heavier-mass Fe isotopes, leaving behind an isotopically light seawater $\delta^{56}Fe_A$ component that was then transferred, at least partially, to our shale samples (e.g., Rouxel et al., 2005; Severmann et al., 2008). One hypothesis contends that partial oxidation of the seawater Fe reservoir led to a globally widespread and isotopically light seawater Fe reservoir (Rouxel et al., 2005). Another hypothesis

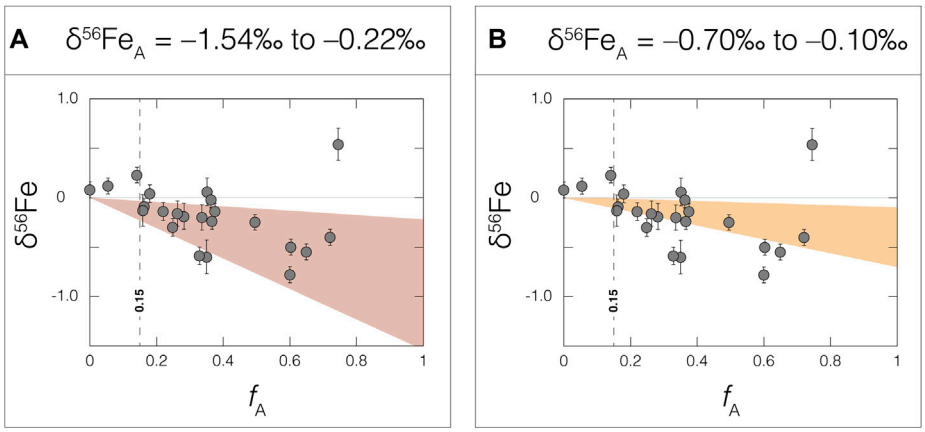

FIGURE 5 | Bulk-shale $\delta^{56}Fe$ values plotted versus calculated authigenic Fe fractions (f_A). The red field in panel **(A)** signifies an authigenic $\delta^{56}Fe$ source that can reconcile all but four datapoints ($\delta^{56}Fe$ = –1.54‰ to –0.22‰), while the orange field in panel **(B)** signifies an authigenic $\delta^{56}Fe$ source comparable to modern hydrothermal inputs ($\delta^{56}Fe_A$ = –0.70‰ to –0.10‰; Lough et al., 2017). The 0.15 vertical line in both panels represents a cut-off point, below which the Fe content present in bulk-shale samples is overwhelmingly dominated by detrital material. See the text for a description of the f_A calculation.

suggests essentially the same, just on a smaller, basinal scale (the "shuttle" hypothesis; Severmann et al., 2008). In combination with one or both Fe-oxide hypotheses, it is also suggested that local redox conditions and distance from the paleoshoreline played a strong role in how this isotopically light signal was captured in sediments, with strongly reducing and pyrite-rich euxinic conditions farther from shore being the most likely locations of capture (Ostrander et al., 2022). Interestingly, and in partial support of this idea, the appearance of lighter bulk-shale $\delta^{56}Fe$ in the Mt. Sylvia Formation coincides with the local redox transition toward more reducing conditions (see the Materials section, and also **Figure 2**). This relationship is unlikely to be coincidental. More to this point, calculated $\delta^{56}Fe_A$ values for Wittenoom Formation shales are also considerably lighter than bulk-crust (average $\delta^{56}Fe_A$ = = –0.72 ± 0.90‰; 2SD after screening out samples with positive bulk-shale $\delta^{56}Fe$ values and f_A < 0.15), indicating that an isotopically light $\delta^{56}Fe_A$ source probably persisted over longer timeframes of deposition than is evident from the bulk-shale $\delta^{56}Fe$ data alone. This light $\delta^{56}Fe_A$ source simply failed to register a strong bulk-shale $\delta^{56}Fe$ signal in some Wittenoom Formation shales because of their strong detrital Fe contents.

Alternatively, or in addition, hydrothermal Fe delivery and local pyrite formation could have helped supply an isotopically light $\delta^{56}Fe_A$ component. Of the samples with f_A > 0.15, the vast majority (74%) can be reconciled solely by a low $\delta^{56}Fe_A$ component that overlaps with modern hydrothermal fluids ($\delta^{56}Fe$ = –0.1‰ to –0.7‰; Lough et al., 2017) (**Figure 5B**). It is generally accepted that the overwhelming source of dissolved Fe(II) to Archean seawater was hydrothermal fluids (Konhauser et al., 2017). Furthermore, and again, the lowest $\delta^{56}Fe$ values are found in shales from the Mt. Sylvia Formation (**Figure 3**), perhaps coincident with a transition toward more reducing local redox conditions (see **Figure 2**). If this local redox change led to H_2S accumulation in porewaters or overlying waters, then localized pyrite formation could have led to the preferential removal of lighter-mass Fe isotopes from seawater (Guilbaud et al., 2011). The slight increase in authigenic Tl abundances observed in the Mt. Sylvia Formation (**Figure 4**) could also support enhanced local pyrite formation at this time because accumulation of Tl in sediments is often linked to pyrite (e.g., Nielsen et al., 2011). Lastly, and most convincing, shales with higher pyrite Fe contents reveal increasingly negative $\delta^{56}Fe$ values (R^2 = 0.59; **Figure 6**).

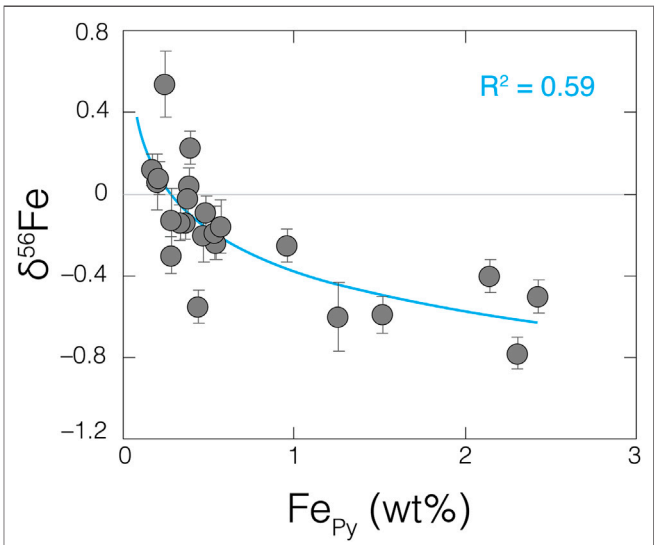

FIGURE 6 | Increasingly negative bulk-shale $\delta^{56}Fe$ values are accompanied by higher pyrite Fe contents (Fe_{Py}) in our samples, drawing a strong connection between two. Pyrite Fe data are from Ostrander et al. (2020). A logarithmic trendline through the dataset is provided in blue, along with the corresponding R^2 value.

None of the Fe isotope fractionation processes discussed above require the presence of O_2. Two anaerobic processes serve as

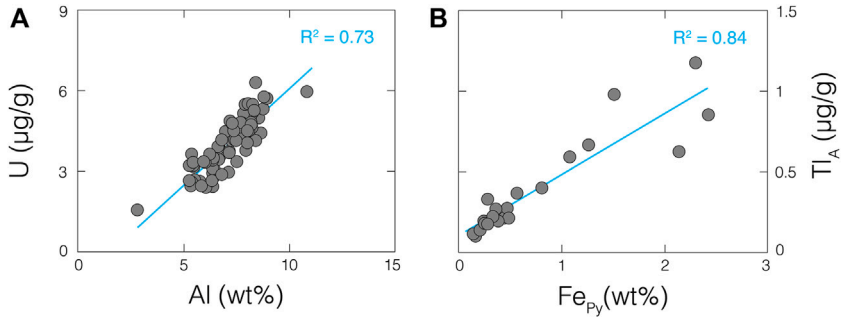

FIGURE 7 | A strong linear correlation between bulk-shale U and Al concentrations **(A)** suggests a shared detrital origin, while an even stronger linear correlation between leached Tl and pyrite Fe concentrations **(B)** suggests a strong Tl-pyrite connection. Aluminum and pyrite Fe data are from Ostrander et al. (2020). Linear trendlines are provided in blue, along with corresponding R^2 values.

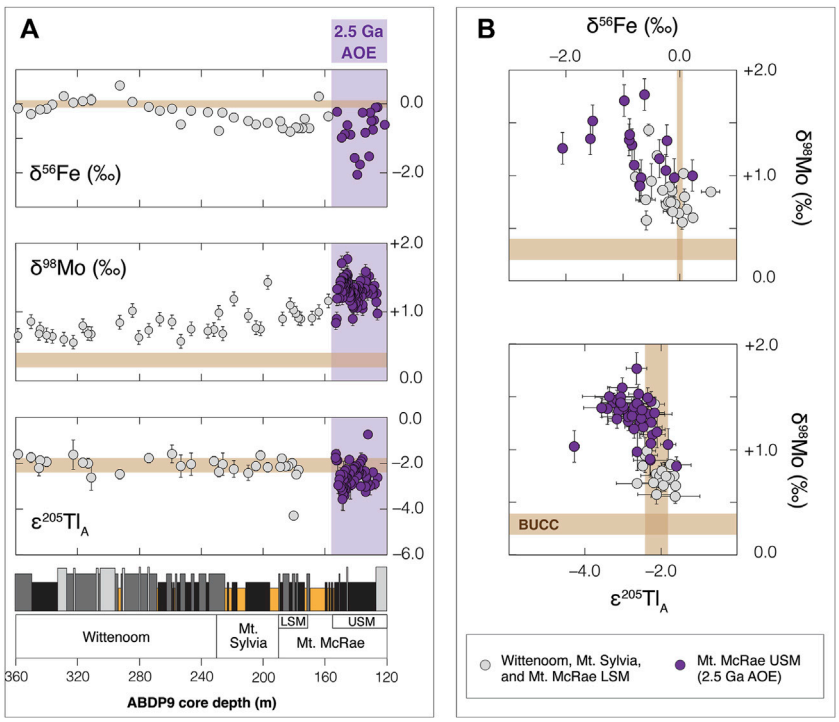

FIGURE 8 | (A) Updated Fe, Mo, and Tl isotope compilation from ABDP9 shales and **(B)** cross-plots of these same data. Brown rectangles in each panel signify bulk upper continental crust values for each isotope system (crustal δ^{98}Mo value comes from Willbold and Elliott 2017; all other crustal value references can be found in the text). Iron isotope data are from Ostrander et al. (2022) and this study. Molybdenum isotope data are from Duan et al. (2010) and Ostrander et al. (2019; 2020). Thallium isotope data are from Ostrander et al. (2019) and this study. AOE = Archean Oxidation Event, BUCC = bulk upper continental crust, LSM = lower shale member, and USM = upper shale member.

plausible Fe oxide formation pathways during the late-Archean (photo-oxidation (Cairns-Smith 1978; Braterman et al., 1983) and photo-ferrotrophy (Widdel et al., 1993; Konhauser et al., 2002)), and no Fe redox change is required during hydrothermal Fe delivery and pyrite formation.

U Isotope Data

Barring coincidence, near-crustal bulk-shale δ^{238}U values require limited isotopic fractionation of U during the late-Archean, at least in this paleo-setting and potentially beyond it. This concept is further supported by the persistently low U abundances in the Wittenoom and Mt. Sylvia formations, which imply a limited availability of dissolved U in the contemporaneous ocean. A good linear correlation is found between bulk-shale U and Al abundances (R^2 = 0.73; **Figure 7A**) that strongly suggests, like the Al, the U in these shales is of detrital origin. For some added context, the correlation between bulk-shale Fe and Al abundances is significantly weaker (R^2 < 0.01), indicating relatively minor

detrital Fe contributions (as already concluded above for most samples). As discussed in the introduction, minimal sedimentary U accumulation and U isotopic fractionation are predictable consequences of a low-O_2 late-Archean Earth (Kendall et al., 2013; Brüske et al., 2020).

Tl Isotope Data

Measured $\varepsilon^{205}Tl_A$ values are very likely representative of overlying seawater at the time of deposition. First, it is unlikely that these $\varepsilon^{205}Tl_A$ are diluted by detrital material. The dilute nitric acid partial digestion that is used to isolate Tl in shale samples from authigenic phases (namely, pyrite; Nielsen et al., 2011) is unlikely to liberate significant amounts of Tl from detrital phases. In support of this notion, we find no correlation whatsoever between $\varepsilon^{205}Tl_A$ values and Al abundances ($R^2 << 0.01$). Furthermore, invariant $\varepsilon^{205}Tl_A$ values are found in shales from both the Wittenoom and Mt. Sylvia formations despite authigenic Tl concentrations that span an order of magnitude (ranging from 0.1 to 1.2 μg/g; **Figure 4**). This wide concentration range suggests that a Tl-rich and most likely non-detrital phase was present in the shales. This Tl-rich phase was most likely pyrite—a notion that gains strong support from the correlation revealed between authigenic Tl abundances and shale pyrite Fe contents ($R^2 = 0.84$; **Figure 7B**). Second, sediments from the three anoxic settings studied thus far using Tl isotopes (Black Sea, Cariaco Basin, and Santa Barbara Basin) always capture the overlying seawater $\varepsilon^{205}Tl$ value (Owens et al., 2017; Fan et al., 2020; Chen et al., 2022). It is reasonable to assume that, by analogy, our shales deposited under comparable conditions also captured the overlying seawater $\varepsilon^{205}Tl$ value. Because the ancient depositional basin is thought to have maintained a strong connection with the open ocean (Morris and Horowitz 1983), this seawater $\varepsilon^{205}Tl$ value was at least a regional signature, and potentially global.

The most straightforward interpretation of a near-crustal seawater $\varepsilon^{205}Tl$ signature is limited Mn oxide burial over large areas of the late-Archean seafloor. In a widely anoxic ocean with limited Mn oxide burial, it would be extremely difficult to drive a change in the seawater $\varepsilon^{205}Tl$ value away from that of global oceanic inputs (discussed in the introduction). Global oceanic inputs today have an average estimated $\varepsilon^{205}Tl$ value ($\varepsilon^{205}Tl_{IN} = -1.8$; Nielsen et al., 2017) indistinguishable from the bulk upper continental crust ($\varepsilon^{205}Tl_{BUCC} = -2.1 \pm 0.3$; Nielsen et al., 2005)—and also indistinguishable from the shale $\varepsilon^{205}Tl_A$ values in the Wittenoom and Mt. Sylvia formations ($\varepsilon^{205}Tl_A = -2.0 \pm 0.6$). In order to prevent Mn oxide burial, O_2 penetration into sediment porewaters must have been minimal to non-existent over at least regions of the ancient seafloor.

Common Themes

To recap, the main findings from each isotopic dataset are:

1) There are multiple possible interpretations of the $\delta^{56}Fe$ data, but none that require strictly aerobic processes.
2) The $\delta^{238}U$ data require limited mobilization and isotopic fractionation of U, and therefore minimal U(IV) oxidation in surface environments.
3) The $\varepsilon^{205}Tl_A$ data require limited Mn oxide burial over at least regions of the seafloor, and by extension minimal O_2 penetration into marine sediment porewaters.

As a collective, the three separate isotope datasets point strongly toward a low-O_2 Earth surface between ~2.6 and ~2.5 Ga. Our sampling resolution is coarse, averaging one shale sample about every 7 m in ABDP9, and therefore an average of one shale sample about every five million-years of late-Archean time (assuming constant sedimentation rates and an age of our samples between 2.6 and 2.5 Ga). Our data therefore speak most directly to the long-term "background" redox state of Earth's oceans and atmosphere, over the many tens-of-millions of years leading up to 2.5 Ga. Given the coarse sampling resolution, our data do not preclude short-term changes in atmospheric or ocean redox, for example, those that might have occurred over hundreds-of-thousands to single-millions of years (e.g., AOEs; Ostrander et al., 2021).

Information about the background atmospheric redox state can be gleaned most directly from the U data. Multiple previous studies have leveraged the geochemical distribution of U and U-bearing minerals in the sedimentary record to reconstruct past pO_2 (e.g., Sverjensky and Lee, 2010; Johnson et al., 2014). According to the modeling results of Sverjensky and Lee, (2010), oxidation and mobilization of U from the predominant U-bearing crustal mineral, uraninite, requires more strongly oxidizing conditions compared to that required for the oxidation and mobilization of other metals hosted in sulfide minerals, such as Mo and Re. In support of this notion, evidence of mild seawater Mo accumulation and isotopic fractionation is also found in the Wittenoom and Mt. Sylvia formations in ABDP9 (Ostrander et al., 2020), and evidence of mild seawater Re accumulation is found in the coeval equivalent Nauga Formation from South Africa (Kendall et al., 2010). Yet, corresponding evidence of appreciable seawater U accumulation is not found in the Wittenoom and Mt. Sylvia formations (this study), nor is it found in the Nauga Formation (Kendall et al., 2015a; Brüske et al., 2020).

The results of a recent Mo mass-balance and weathering model suggest a pO_2 lower-limit of $10^{-6.3}$ PAL is required to explain the Neoarchean sedimentary Mo record (Johnson et al., 2021). Paired together with available MIF-S pO_2 upper limits across the same timeframe (10^{-6} PAL; Catling and Zahnle, 2020), this could suggest a narrow window of pO_2 between $10^{-6.3}$ PAL and 10^{-6} PAL is required to explain our U data, a window permitted also by pO_2 quantifications derived from the presence of rounded uraninite grains in late-Archean sandstones ($pO_2 < 10^{-3.8}$ PAL; Johnson et al., 2014). Alternatively, and perhaps more likely, atmospheric O_2 accumulation during deposition of the Wittenoom and Mt. Sylvia formations was spatially heterogenous, occurring only near the sites of O_2 production (within and near oases and benthic mats; Olson et al., 2013; Lalonde and Konhauser 2015; Sumner et al., 2015; Liu et al., 2019; Johnson et al., 2021).

Information about the background marine redox state can be gleaned from the Fe and Tl data. As discussed earlier, many scenarios requiring the formation of Fe oxide minerals elsewhere

in the ocean can explain the lower δ^{56}Fe values in the Mt. Sylvia Formation (as low as −0.78 ± 0.08‰). Trends to comparable (Eroglu et al., 2018) and even lower δ^{56}Fe values (as low as −1.47‰; Czaja et al., 2012) are found in roughly contemporaneous strata from South Africa and interpreted in a similar manner. The ubiquitous nature of banded-iron formations (BIFs) in the Neoarchean sedimentary record provides even more convincing evidence of extensive Fe oxide formation in late-Archean sediments (summarized in Konhauser et al., 2017). Yet, the Tl isotope data do not support widespread Mn oxide formation or burial in marine sediments between 2.6 and 2.5 Ga, nor are any Mn oxide BIF equivalents found in the Neoarchean record (Johnson et al., 2016). Formation and burial of Fe oxides in marine sediments occurs under less oxidizing conditions than does formation and burial of Mn oxides (Froelich et al., 1979), with a prerequisite for the latter probably being strong O_2 penetration into marine sediments (Calvert and Pederson, 1996). It therefore seems that regional, if not global marine sediments were sufficiently oxidizing between ~2.6 and ~2.5 Ga to promote long-term Fe oxide burial, but insufficiently oxidizing to promote long-term Mn oxide burial.

Interestingly, strong shale Re enrichments are found together with low-to-negligible Mo enrichments in the 2.6–2.5 Ga Nauga Formation (Kendall et al., 2010). Today, this geochemical pattern is found in marine sediments where O_2 penetration depths are relatively shallow (<~1 cm; Morford et al., 2005) and when Fe oxides are the primary electron acceptor (Morford et al., 2012), under slightly more reducing conditions than those permissive of Mn oxide formation (Froelich et al., 1979). Sedimentary environments like those identified by Kendall et al. (2010) could therefore have been commonplace during the late-Archean, proximal to sites of O_2 accumulation along ocean margins, without requiring any substantial Mn oxide burial (and thus no substantial Tl isotope fractionation effect). Further work should test this hypothesis.

It may be that only during pronounced AOEs—like that captured in the upper shale member of the overlying Mt. McRae Shale at 2.5 Ga—did Mn oxide burial become a widespread phenomenon in Archean marine sediments. This hypothesis gains support from an updated compilation of Fe, Mo, and Tl isotope data for ABDP9 shales (**Figure 8**). With minor exception, bulk-shale δ^{56}Fe and δ^{98}Mo values are lower and higher, respectively, than their crustal equivalents throughout the ABDP9 core (**Figure 8A**). It is already established that the formation of Fe oxide minerals in late-Archean oceans likely played some role in driving the light δ^{56}Fe values. Iron oxide formation can also explain the heavy δ^{98}Mo values because a strong negative isotope fractionation effect is imparted on Mo during sorption to Fe oxides (average $\Delta^{98}Mo_{oxide\text{-}solution}$ = −0.8‰ to −2.2‰; Goldberg et al., 2009). In sum, Fe oxide formation would have led to the preferential removal of heavier-mass Fe isotopes and lighter-mass Mo isotopes from seawater, driving anti-correlated seawater δ^{56}Fe and δ^{98}Mo trends that could then be transferred to sediments (apparent across all ABDP9 shale units in the upper panel of **Figure 8B**). In contrast, evidence attributable strictly to Mn oxide burial—consistently light $\varepsilon^{205}Tl_A$ values—is found only in the upper shale member of the Mt. McRae Shale, coincident with the 2.5 Ga AOE (**Figure 8A**). Especially heavy δ^{98}Mo values in the upper shale member (see the lower panel in **Figure 8B**) also support Mn oxide burial because these minerals impart an especially strong negative Mo isotope fractionation effect ($\Delta^{98}Mo_{oxide\text{-}solution}$ = −2.4‰ to −2.9‰; Wasylenki et al., 2008).

The persistently low background O_2 levels implied by our dataset are not only followed by an AOE, but also preceded by one (~2.65 Ga; Koehler et al., 2018). When viewed in this broader context, our data support the idea that Earth's initial oxygenation was no singular event, but instead a protracted process that unfolded in fits-and-starts over many hundreds-of-millions of years (summarized in Lyons et al., 2014; Ostrander et al., 2021).

CONCLUSION

The early history of O_2 on Earth is slowly coming into focus. Here, by applying three complementary heavy metal isotope systems to a rare continuous shale sequence deposited between ~2.6 and 2.5 Ga, we were able to place O_2 constraints on the eve of Earth's GOE. Negligible U accumulation and isotopic fractionation imply limited oxidative weathering of uraninite, and therefore either homogenous and low pO_2 between about $10^{-6.3}$ and 10^{-6} PAL or heterogeneous and spatially restricted O_2 accumulation nearest the sites of O_2 production. Slightly variable bulk-shale δ^{56}Fe (and δ^{98}Mo) values in the same samples, together with invariant $\varepsilon^{205}Tl_A$, imply widespread marine redox conditions sufficiently oxidizing for sedimentary Fe oxide burial (not strictly aerobic, and with weak O_2 penetration when aerobic), but insufficient for sedimentary Mn oxide burial (aerobic, with strong O_2 penetration). Given the temporal context of our shales, and our sampling resolution, these redox constraints are pertinent over ten-million-year timescales between about 2.6 and 2.5 Ga.

The low background O_2 levels implied by our dataset do not seem to be representative of the Archean as a whole. Compelling evidence has been presented for the production and mild accumulation of O_2 at Earth's surface at various times during the Archean. The most notable and pertinent examples are the many lines of independent evidence supporting transient AOEs slightly before (~2.65 Ga) and immediately after (~2.50 Ga) the timeframe studied here (summarized in Ostrander et al., 2021). As a collective, this emerging evidence points strongly toward a dynamic and protracted initial oxygenation of the Earth system.

DATA AVAILABILITY STATEMENT

The original contributions presented in the study are included in the article/**Supplementary Material**, further inquiries can be directed to the corresponding author.

AUTHOR CONTRIBUTIONS

CO, BK, GG, SN and AA developed the project idea. CO processed samples and performed Fe, Tl and U isotope analyses with contributions from WZ. CO wrote the manuscript with contributions from BK and SN.

FUNDING

This work was supported financially by the NSF Frontiers in Earth System Dynamics program award NSF EAR-1338810 (AA), a Woods Hole Oceanographic Institution Postdoctoral Scholarship (CO), a NSERC Discovery Grant (RGPIN-435930) and the Canada Research Chair program (BK), and a NASA Exobiology award 80NSSC20K0615 (SN).

SUPPLEMENTARY MATERIAL

The Supplementary Material for this article can be found online at: https://www.frontiersin.org/articles/10.3389/feart.2022.833609/full#supplementary-material

REFERENCES

Anbar, A. D., Duan, Y., Lyons, T. W., Arnold, G. L., Kendall, B., Creaser, R. A., et al. (2007). A Whiff of Oxygen before the Great Oxidation Event? *Science* 317, 1903–1906. doi:10.1126/science.1140325

Arnold, G. L., Weyer, S., and Anbar, A. D. (2004). Fe Isotope Variations in Natural Materials Measured Using High Mass Resolution Multiple Collector ICPMS. *Anal. Chem.* 76, 322–327. doi:10.1021/ac034601v

Asael, D., Tissot, F. L. H., Reinhard, C. T., Rouxel, O., Dauphas, N., Lyons, T. W., et al. (2013). Coupled Molybdenum, Iron and Uranium Stable Isotopes as Oceanic Paleoredox Proxies during the Paleoproterozoic Shunga Event. *Chem. Geology.* 362, 193–210. doi:10.1016/j.chemgeo.2013.08.003

Baker, R. G. A., Rehkämper, M., Hinkley, T. K., Nielsen, S. G., and Toutain, J. P. (2009). Investigation of Thallium Fluxes from Subaerial Volcanism-Implications for the Present and Past Mass Balance of Thallium in the Oceans. *Geochimica et Cosmochimica Acta* 73, 6340–6359. doi:10.1016/j.gca.2009.07.014

Beard, B. L., Johnson, C. M., Skulan, J. L., Nealson, K. H., Cox, L., and Sun, H. (2003). Application of Fe Isotopes to Tracing the Geochemical and Biological Cycling of Fe. *Chem. Geology*. 195, 87–117. doi:10.1016/s0009-2541(02)00390-x

Braterman, P. S., Cairns-Smith, A. G., and Sloper, R. W. (1983). Photo-oxidation of Hydrated Fe2+-Significance for Banded Iron Formations. *Nature* 303, 163–164. doi:10.1038/303163a0

Brocks, J. J., Buick, R., Logan, G. A., and Summons, R. E. (2003). Composition and Syngeneity of Molecular Fossils from the 2.78 to 2.45 Billion-Year-Old Mount Bruce Supergroup, Pilbara Craton, Western Australia. *Geochimica et Cosmochimica Acta* 67, 4289–4319. doi:10.1016/s0016-7037(03)00208-4

Brüske, A., Martin, A. N., Rammensee, P., Eroglu, S., Lazarov, M., Albut, G., et al. (2020). The Onset of Oxidative Weathering Traced by Uranium Isotopes. *Precambrian Res.* 338, 105583. doi:10.1016/j.precamres.2019.105583

Busigny, V., Planavsky, N. J., Jézéquel, D., Crowe, S., Louvat, P., Moureau, J., et al. (2014). Iron Isotopes in an Archean Ocean Analogue. *Geochimica et Cosmochimica Acta* 133, 443–462. doi:10.1016/j.gca.2014.03.004

Cairns-Smith, A. G. (1978). Precambrian Solution Photochemistry, Inverse Segregation, and Banded Iron Formations. *Nature* 276, 807–808. doi:10.1038/276807a0

Calvert, S. E., and Pedersen, T. F. (1996). Sedimentary Geochemistry of Manganese; Implications for the Environment of Formation of Manganiferous Black Shales. *Econ. Geology*. 91, 36–47. doi:10.2113/gsecongeo.91.1.36

Catling, D. C., and Zahnle, K. J. (2020). The Archean Atmosphere. *Sci. Adv.* 6, eaax1420. doi:10.1126/sciadv.aax1420

Chen, X., Li, S., Newby, S. M., Lyons, T. W., Wu, F., and Owens, J. D. (2022). Iron and Manganese Shuttle Has No Effect on Sedimentary Thallium and Vanadium Isotope Signatures in Black Sea Sediments. *Geochimica et Cosmochimica Acta* 317, 218–233. doi:10.1016/j.gca.2021.11.010

Chen, X., Tissot, F. L. H., Jansen, M. F., Bekker, A., Liu, C. X., Nie, N. X., et al. (2021). The Uranium Isotopic Record of Shales and Carbonates through Geologic Time. *Geochimica et Cosmochimica Acta* 300, 164–191. doi:10.1016/j.gca.2021.01.040

Craddock, P. R., and Dauphas, N. (2011). Iron Isotopic Compositions of Geological Reference Materials and Chondrites. *Geostandards Geoanalytical Res.* 35, 101–123. doi:10.1111/j.1751-908x.2010.00085.x

Czaja, A. D., Johnson, C. M., Roden, E. E., Beard, B. L., Voegelin, A. R., Nägler, T. F., et al. (2012). Evidence for Free Oxygen in the Neoarchean Ocean Based on Coupled Iron-Molybdenum Isotope Fractionation. *Geochimica et Cosmochimica Acta* 86, 118–137. doi:10.1016/j.gca.2012.03.007

Dauphas, N., John, S. G., and Rouxel, O. (2017). Iron Isotope Systematics. *Rev. Mineralogy Geochem.* 82, 415–510. doi:10.2138/rmg.2017.82.11

Duan, Y., Anbar, A. D., Arnold, G. L., Lyons, T. W., Gordon, G. W., and Kendall, B. (2010). Molybdenum Isotope Evidence for Mild Environmental Oxygenation before the Great Oxidation Event. *Geochimica et Cosmochimica Acta* 74, 6655–6668. doi:10.1016/j.gca.2010.08.035

Eigenbrode, J. L., and Freeman, K. H. (2006). Late Archean Rise of Aerobic Microbial Ecosystems. *Proc. Natl. Acad. Sci. U.S.A.* 103, 15759–15764. doi:10.1073/pnas.0607540103

Eroglu, S., Schoenberg, R., Pascarelli, S., Beukes, N. J., Kleinhanns, I. C., and Swanner, E. D. (2018). Open Ocean vs. Continentally-Derived Iron Cycles along the Neoarchean Campbellrand-Malmani Carbonate Platform, South Africa. *Am. J. Sci.* 318, 367–408. doi:10.2475/04.2018.01

Eroglu, S., Schoenberg, R., Wille, M., Beukes, N., and Taubald, H. (2015). Geochemical Stratigraphy, Sedimentology, and Mo Isotope Systematics of the Ca. 2.58-2.50 Ga-old Transvaal Supergroup Carbonate Platform, South Africa. *Precambrian Res.* 266, 27–46. doi:10.1016/j.precamres.2015.04.014

Eroglu, S., van Zuilen, M. A., Taubald, H., Drost, K., Wille, M., Swanner, E. D., et al. (2017). Depth-dependent δ13C Trends in Platform and Slope Settings of the Campbellrand-Malmani Carbonate Platform and Possible Implications for Early Earth Oxygenation. *Precambrian Res.* 302, 122–139. doi:10.1016/j.precamres.2017.09.018

Fan, H., Nielsen, S. G., Owens, J. D., Auro, M., Shu, Y., Hardisty, D. S., et al. (2020). Constraining Oceanic Oxygenation during the Shuram Excursion in South China Using Thallium Isotopes. *Geobiology* 18, 348–365. doi:10.1111/gbi.12379

Fischer, W. W., Schroeder, S., Lacassie, J. P., Beukes, N. J., Goldberg, T., Strauss, H., et al. (2009). Isotopic Constraints on the Late Archean Carbon Cycle from the Transvaal Supergroup along the Western Margin of the Kaapvaal Craton, South Africa. *Precambrian Res.* 169, 15–27. doi:10.1016/j.precamres.2008.10.010

Froelich, P. N., Klinkhammer, G. P., Bender, M. L., Luedtke, N. A., Heath, G. R., Cullen, D., et al. (1979). Early Oxidation of Organic Matter in Pelagic Sediments of the Eastern Equatorial Atlantic: Suboxic Diagenesis. *Geochimica et Cosmochimica Acta* 43, 1075–1090. doi:10.1016/0016-7037(79)90095-4

Garvin, J., Buick, R., Anbar, A. D., Arnold, G. L., and Kaufman, A. J. (2009). Isotopic Evidence for an Aerobic Nitrogen Cycle in the Latest Archean. *Science* 323, 1045–1048. doi:10.1126/science.1165675

Godfrey, L. V., and Falkowski, P. G. (2009). The Cycling and Redox State of Nitrogen in the Archaean Ocean. *Nat. Geosci* 2, 725–729. doi:10.1038/ngeo633

Goldberg, T., Archer, C., Vance, D., and Poulton, S. W. (2009). Mo Isotope Fractionation during Adsorption to Fe (Oxyhydr)oxides. *Geochimica et Cosmochimica Acta* 73, 6502–6516. doi:10.1016/j.gca.2009.08.004

Gregory, D. D., Large, R. R., Halpin, J. A., Steadman, J. A., Hickman, A. H., Ireland, T. R., et al. (2015). The Chemical Conditions of the Late Archean Hamersley basin Inferred from Whole Rock and Pyrite Geochemistry with Δ33S and δ34S Isotope Analyses. *Geochimica et Cosmochimica Acta* 149, 223–250. doi:10.1016/j.gca.2014.10.023

Guilbaud, R., Butler, I. B., and Ellam, R. M. (2011). Abiotic Pyrite Formation Produces a Large Fe Isotope Fractionation. *Science* 332, 1548–1551. doi:10.1126/science.1202924

Heard, A. W., Dauphas, N., Guilbaud, R., Rouxel, O. J., Butler, I. B., Nie, N. X., et al. (2020). Triple Iron Isotope Constraints on the Role of Ocean Iron Sinks in Early Atmospheric Oxygenation. *Science* 370, 446–449. doi:10.1126/science.aaz8821

Johnson, A. C., Ostrander, C. M., Romaniello, S. J., Reinhard, C. T., Greaney, A. T., Lyons, T. W., et al. (2021). Reconciling Evidence of Oxidative Weathering and Atmospheric Anoxia on Archean Earth. *Sci. Adv.* 7, eabj0108. doi:10.1126/sciadv.abj0108

Johnson, C. M., Beard, B. L., and Roden, E. E. (2008). The Iron Isotope Fingerprints of Redox and Biogeochemical Cycling in Modern and Ancient Earth. *Annu. Rev. Earth Planet. Sci.* 36, 457–493. doi:10.1146/annurev.earth.36.031207.124139

Johnson, J. E., Gerpheide, A., Lamb, M. P., and Fischer, W. W. (2014). O2constraints from Paleoproterozoic Detrital Pyrite and Uraninite. *Geol. Soc. America Bull.* 126, 813–830. doi:10.1130/b30949.1

Johnson, J. E., Webb, S. M., Ma, C., and Fischer, W. W. (2016). Manganese Mineralogy and Diagenesis in the Sedimentary Rock Record. *Geochimica et Cosmochimica Acta* 173, 210–231. doi:10.1016/j.gca.2015.10.027

Kaufman, A. J., Johnston, D. T., Farquhar, J., Masterson, A. L., Lyons, T. W., Bates, S., et al. (2007). Late Archean Biospheric Oxygenation and Atmospheric Evolution. *Science* 317, 1900–1903. doi:10.1126/science.1138700

Kendall, B., Creaser, R. A., Reinhard, C. T., Lyons, T. W., and Anbar, A. D. (2015a). Transient Episodes of Mild Environmental Oxygenation and Oxidative continental Weathering during the Late Archean. *Sci. Adv.* 1, e1500777. doi:10.1126/sciadv.1500777

Kendall, B., Brennecka, G. A., Weyer, S., and Anbar, A. D. (2013). Uranium Isotope Fractionation Suggests Oxidative Uranium Mobilization at 2.50 Ga. *Chem. Geology*. 362, 105–114. doi:10.1016/j.chemgeo.2013.08.010

Kendall, B., Dahl, T. W., and Anbar, A. D. (2017). The Stable Isotope Geochemistry of Molybdenum. *Rev. Mineralogy Geochem.* 82, 683–732. doi:10.2138/rmg.2017.82.16

Kendall, B., Komiya, T., Lyons, T. W., Bates, S. M., Gordon, G. W., Romaniello, S. J., et al. (2015b). Uranium and Molybdenum Isotope Evidence for an Episode of Widespread Ocean Oxygenation during the Late Ediacaran Period. *Geochimica et Cosmochimica Acta* 156, 173–193. doi:10.1016/j.gca.2015.02.025

Kendall, B., Reinhard, C. T., Lyons, T. W., Kaufman, A. J., Poulton, S. W., and Anbar, A. D. (2010). Pervasive Oxygenation along Late Archaean Ocean Margins. *Nat. Geosci* 3, 647–652. doi:10.1038/ngeo942

Koehler, M. C., Buick, R., Kipp, M. A., Stüeken, E. E., and Zaloumis, J. (2018). Transient Surface Ocean Oxygenation Recorded in the ~2.66-Ga Jeerinah Formation, Australia. *Proc. Natl. Acad. Sci. U.S.A.* 115, 7711–7716. doi:10.1073/pnas.1720820115

Konhauser, K. O., Hamade, T., Raiswell, R., Morris, R. C., Grant Ferris, F., Southam, G., et al. (2002). Could Bacteria Have Formed the Precambrian Banded Iron Formations? *Geol* 30, 1079–1082. doi:10.1130/0091-7613(2002)030<1079:cbhftp>2.0.co;2

Konhauser, K. O., Planavsky, N. J., Hardisty, D. S., Robbins, L. J., Warchola, T. J., Haugaard, R., et al. (2017). Iron Formations: A Global Record of Neoarchaean to Palaeoproterozoic Environmental History. *Earth-Science Rev.* 172, 140–177. doi:10.1016/j.earscirev.2017.06.012

Kopp, R. E., Kirschvink, J. L., Hilburn, I. A., and Nash, C. Z. (2005). The Paleoproterozoic Snowball Earth: a Climate Disaster Triggered by the Evolution of Oxygenic Photosynthesis. *Proc. Natl. Acad. Sci. U.S.A.* 102, 11131–11136. doi:10.1073/pnas.0504878102

Ku, T.-L., Mathieu, G. G., and Knauss, K. G. (1977). Uranium in Open Ocean: Concentration and Isotopic Composition. *Deep Sea Res.* 24, 1005–1017. doi:10.1016/0146-6291(77)90571-9

Kurzweil, F., Wille, M., Schoenberg, R., Taubald, H., and Van Kranendonk, M. J. (2015). Continuously Increasing δ 98 Mo Values in Neoarchean Black Shales and Iron Formations from the Hamersley Basin. *Geochimica et Cosmochimica Acta* 164, 523–542. doi:10.1016/j.gca.2015.05.009

Lalonde, S. V., and Konhauser, K. O. (2015). Benthic Perspective on Earth's Oldest Evidence for Oxygenic Photosynthesis. *Proc. Natl. Acad. Sci. U.S.A.* 112, 995–1000. doi:10.1073/pnas.1415718112

Langmuir, D. (1978). Uranium Solution-mineral Equilibria at Low Temperatures with Applications to Sedimentary Ore Deposits. *Geochimica et Cosmochimica Acta* 42, 547–569. doi:10.1016/0016-7037(78)90001-7

Liu, P., Harman, C. E., Kasting, J. F., Hu, Y., and Wang, J. (2019). Can Organic Haze and O2 Plumes Explain Patterns of Sulfur Mass-independent Fractionation during the Archean? *Earth Planet. Sci. Lett.* 526, 115767. doi:10.1016/j.epsl.2019.115767

Lough, A. J. M., Klar, J. K., Homoky, W. B., Comer-Warner, S. A., Milton, J. A., Connelly, D. P., et al. (2017). Opposing Authigenic Controls on the Isotopic Signature of Dissolved Iron in Hydrothermal Plumes. *Geochimica et Cosmochimica Acta* 202, 1–20. doi:10.1016/j.gca.2016.12.022

Lyons, T. W., Reinhard, C. T., and Planavsky, N. J. (2014). The Rise of Oxygen in Earth's Early Ocean and Atmosphere. *Nature* 506, 307–315. doi:10.1038/nature13068

Lyons, T. W., and Severmann, S. (2006). A Critical Look at Iron Paleoredox Proxies: New Insights from Modern Euxinic marine Basins. *Geochimica et Cosmochimica Acta* 70, 5698–5722. doi:10.1016/j.gca.2006.08.021

Meixnerová, J., Blum, J. D., Johnson, M. W., Stüeken, E. E., Kipp, M. A., Anbar, A. D., et al. (2021). Mercury Abundance and Isotopic Composition Indicate Subaerial Volcanism Prior to the End-Archean "Whiff" of Oxygen. *Proc. Natl. Acad. Sci.* 118, e2107511118. doi:10.1073/pnas.2107511118

Morford, J. L., Emerson, S. R., Breckel, E. J., and Kim, S. H. (2005). Diagenesis of Oxyanions (V, U, Re, and Mo) in Pore Waters and Sediments from a continental Margin. *Geochimica et Cosmochimica Acta* 69, 5021–5032. doi:10.1016/j.gca.2005.05.015

Morford, J. L., Martin, W. R., and Carney, C. M. (2012). Rhenium Geochemical Cycling: Insights from continental Margins. *Chem. Geology*. 324-325, 73–86. doi:10.1016/j.chemgeo.2011.12.014

Morris, R. C., and Horwitz, R. C. (1983). The Origin of the Iron-Formation-Rich Hamersley Group of Western Australia - Deposition on a Platform. *Precambrian Res.* 21, 273–297. doi:10.1016/0301-9268(83)90044-x

Nielsen, S. G., Goff, M., Hesselbo, S. P., Jenkyns, H. C., LaRowe, D. E., and Lee, C.-T. A. (2011). Thallium Isotopes in Early Diagenetic Pyrite - A Paleoredox Proxy? *Geochimica et Cosmochimica Acta* 75, 6690–6704. doi:10.1016/j.gca.2011.07.047

Nielsen, S. G., Rehkämper, M., Baker, J., and Halliday, A. N. (2004). The Precise and Accurate Determination of Thallium Isotope Compositions and Concentrations for Water Samples by MC-ICPMS. *Chem. Geology*. 204, 109–124. doi:10.1016/j.chemgeo.2003.11.006

Nielsen, S. G., Rehkämper, M., Norman, M. D., Halliday, A. N., and Harrison, D. (2006b). Thallium Isotopic Evidence for Ferromanganese Sediments in the Mantle Source of Hawaiian Basalts. *Nature* 439, 314–317. doi:10.1038/nature04450

Nielsen, S. G., Rehkämper, M., Porcelli, D., Andersson, P., Halliday, A. N., Swarzenski, P. W., et al. (2005). Thallium Isotope Composition of the Upper continental Crust and Rivers-An Investigation of the continental Sources of Dissolved marine Thallium. *Geochimica et Cosmochimica Acta* 69, 2007–2019. doi:10.1016/j.gca.2004.10.025

Nielsen, S. G., Rehkämper, M., and Prytulak, J. (2017). Investigation and Application of Thallium Isotope Fractionation. *Rev. Mineralogy Geochem.* 82, 759–798. doi:10.2138/rmg.2017.82.18

Nielsen, S. G., Rehkämper, M., Teagle, D. A. H., Butterfield, D. A., Alt, J. C., and Halliday, A. N. (2006a). Hydrothermal Fluid Fluxes Calculated from the Isotopic Mass Balance of Thallium in the Ocean Crust. *Earth Planet. Sci. Lett.* 251, 120–133. doi:10.1016/j.epsl.2006.09.002

Nielsen, S. G., Wasylenki, L. E., Rehkämper, M., Peacock, C. L., Xue, Z., and Moon, E. M. (2013). Towards an Understanding of Thallium Isotope Fractionation during Adsorption to Manganese Oxides. *Geochimica et Cosmochimica Acta* 117, 252–265. doi:10.1016/j.gca.2013.05.004

Ohmoto, H., Watanabe, Y., Ikemi, H., Poulson, S. R., and Taylor, B. E. (2006). Sulphur Isotope Evidence for an Oxic Archaean Atmosphere. *Nature* 442, 908–911. doi:10.1038/nature05044

Olson, S. L., Kump, L. R., and Kasting, J. F. (2013). Quantifying the Areal Extent and Dissolved Oxygen Concentrations of Archean Oxygen Oases. *Chem. Geology*. 362, 35–43. doi:10.1016/j.chemgeo.2013.08.012

Olson, S. L., Ostrander, C. M., Gregory, D. D., Roy, M., Anbar, A. D., and Lyons, T. W. (2019). Volcanically Modulated Pyrite Burial and Ocean-Atmosphere Oxidation. *Earth Planet. Sci. Lett.* 506, 417–427. doi:10.1016/j.epsl.2018.11.015

Ostrander, C. M., Owens, J. D., and Nielsen, S. G. (2017). Constraining the Rate of Oceanic Deoxygenation Leading up to a Cretaceous Oceanic Anoxic Event (OAE-2: ~94 Ma). *Sci. Adv.* 3, e1701020. doi:10.1126/sciadv.1701020

Ostrander, C. M., Johnson, A. C., and Anbar, A. D. (2021). Earth's First Redox Revolution. *Annu. Rev. Earth Planet. Sci.* 49, 337–366. doi:10.1146/annurev-earth-072020-055249

Ostrander, C. M., Kendall, B., Olson, S. L., Lyons, T. W., Gordon, G. W., Romaniello, S. J., et al. (2020). An Expanded Shale δ98Mo Record Permits Recurrent Shallow marine Oxygenation during the Neoarchean. *Chem. Geology*. 532, 119391. doi:10.1016/j.chemgeo.2019.119391

Ostrander, C. M., Nielsen, S. G., Owens, J. D., Kendall, B., Gordon, G. W., Romaniello, S. J., et al. (2019). Fully Oxygenated Water Columns over continental Shelves before the Great Oxidation Event. *Nat. Geosci.* 12, 186–191. doi:10.1038/s41561-019-0309-7

Ostrander, C. M., Severmann, S., Gordon, G. W., Kendall, B., Lyons, T. W., Zheng, W., et al. (2022). Significance of 56Fe Depletions in Late-Archean Shales and Pyrite. *Geochimica et Cosmochimica Acta* 316, 87–104. doi:10.1016/j.gca.2021.10.013

Owens, J. D., Nielsen, S. G., Horner, T. J., Ostrander, C. M., and Peterson, L. C. (2017). Thallium-isotopic Compositions of Euxinic Sediments as a Proxy for Global Manganese-Oxide Burial. *Geochimica et Cosmochimica Acta* 213, 291–307. doi:10.1016/j.gca.2017.06.041

Partin, C. A., Bekker, A., Planavsky, N. J., Scott, C. T., Gill, B. C., Li, C., et al. (2013). Large-scale Fluctuations in Precambrian Atmospheric and Oceanic Oxygen Levels from the Record of U in Shales. *Earth Planet. Sci. Lett.* 369-370, 284–293. doi:10.1016/j.epsl.2013.03.031

Peacock, C. L., and Moon, E. M. (2012). Oxidative Scavenging of Thallium by Birnessite: Explanation for Thallium Enrichment and Stable Isotope Fractionation in marine Ferromanganese Precipitates. *Geochimica et Cosmochimica Acta* 84, 297–313. doi:10.1016/j.gca.2012.01.036

Raiswell, R., Hardisty, D. S., Lyons, T. W., Canfield, D. E., Owens, J. D., Planavsky, N. J., et al. (2018). The Iron Paleoredox Proxies: A Guide to the Pitfalls, Problems and Proper Practice. *Am. J. Sci.* 318, 491–526. doi:10.2475/05.2018.03

Rehkämper, M., Frank, M., Hein, J. R., Porcelli, D., Halliday, A., Ingri, J., et al. (2002). Thallium Isotope Variations in Seawater and Hydrogenetic, Diagenetic, and Hydrothermal Ferromanganese Deposits. *Earth Planet. Sci. Lett.* 197, 65–81. doi:10.1016/S0012-821X(02)00462-4

Rehkämper, M., and Halliday, A. N. (1999). The Precise Measurement of Tl Isotopic Compositions by MC-ICPMS: Applications to the Analysis of Geological Materials and Meteorites. *Geochimica et Cosmochimica Acta* 63, 935–944. doi:10.1016/S0016-7037(98)00312-3

Reinhard, C. T., Raiswell, R., Scott, C., Anbar, A. D., and Lyons, T. W. (2009). A Late Archean Sulfidic Sea Stimulated by Early Oxidative Weathering of the Continents. *Science* 326, 713–716. doi:10.1126/science.1176711

Rouxel, O. J., Bekker, A., and Edwards, K. J. (2005). Iron Isotope Constraints on the Archean and Paleoproterozoic Ocean Redox State. *Science* 307, 1088–1091. doi:10.1126/science.1105692

Rudnick, R. L., and Gao, S. (2003). "Composition of the continental Crust,".in *The Crust*. Editor R. L. Rudnick (Elsevier), 3, 1–64. doi:10.1016/b0-08-043751-6/03016-4

Sarmiento, J. L., and Gruber, N. (2006). *Ocean Biogeochemical Dynamics*. Princeton, NJ, USA: Princeton University Press.

Scholz, F., Severmann, S., McManus, J., and Hensen, C. (2014). Beyond the Black Sea Paradigm: The Sedimentary Fingerprint of an Open-marine Iron Shuttle. *Geochimica et Cosmochimica Acta* 127, 368–380. doi:10.1016/j.gca.2013.11.041

Severmann, S., Lyons, T. W., Anbar, A., McManus, J., and Gordon, G. (2008). Modern Iron Isotope Perspective on the Benthic Iron Shuttle and the Redox Evolution of Ancient Oceans. *Geol* 36, 487–490. doi:10.1130/g24670a.1

Stüeken, E. E., Buick, R., and Anbar, A. D. (2015). Selenium Isotopes Support Free O_2 in the Latest Archean. *Geology* 43, 259–262. doi:10.1130/G36218.1

Stüeken, E. E., Catling, D. C., and Buick, R. (2012). Contributions to Late Archaean sulphur Cycling by Life on Land. *Nat. Geosci.* 5, 722–725. doi:10.1038/ngeo1585

Sumner, D. Y., Hawes, I., Mackey, T. J., Jungblut, A. D., and Doran, P. T. (2015). Antarctic Microbial Mats: a Modern Analog for Archean Lacustrine Oxygen Oases. *Geology* 43, 887–890. doi:10.1130/g36966.1

Sverjensky, D. A., and Lee, N. (2010). The Great Oxidation Event and mineral Diversification. *Elements* 6, 31–36. doi:10.2113/gselements.6.1.31

Tissot, F. L. H., and Dauphas, N. (2015). Uranium Isotopic Compositions of the Crust and Ocean: Age Corrections, U Budget and Global Extent of Modern Anoxia. *Geochimica et Cosmochimica Acta* 167, 113–143. doi:10.1016/j.gca.2015.06.034

Trendall, A. F., Compston, W., Nelson, D. R., De Laeter, J. R., and Bennett, V. C. (2004). SHRIMP Zircon Ages Constraining the Depositional Chronology of the Hamersley Group, Western Australia*. *Aust. J. Earth Sci.* 51, 621–644. doi:10.1111/j.1400-0952.2004.01082.x

Trendall, A. F., Nelson, D. R., De Laeter, J. R., and Hassler, S. W. (1998). Precise Zircon U-Pb Ages from the Marra Mamba Iron Formation and Wittenoom Formation, Hamersley Group, Western Australia. *Aust. J. Earth Sci.* 45, 137–142. doi:10.1080/08120099808728374

Wang, X., Ossa Ossa, F., Hofmann, A., Agangi, A., Paprika, D., and Planavsky, N. J. (2020). Uranium Isotope Evidence for Mesoarchean Biological Oxygen Production in Shallow marine and continental Settings. *Earth Planet. Sci. Lett.* 551, 116583. doi:10.1016/j.epsl.2020.116583

Wang, X., Planavsky, N. J., Hofmann, A., Saupe, E. E., De Corte, B. P., Philippot, P., et al. (2018). A Mesoarchean Shift in Uranium Isotope Systematics. *Geochimica et Cosmochimica Acta* 238, 438–452. doi:10.1016/j.gca.2018.07.024

Wasylenki, L. E., Rolfe, B. A., Weeks, C. L., Spiro, T. G., and Anbar, A. D. (2008). Experimental Investigation of the Effects of Temperature and Ionic Strength on Mo Isotope Fractionation during Adsorption to Manganese Oxides. *Geochimica et Cosmochimica Acta* 72, 5997–6005. doi:10.1016/j.gca.2008.08.027

Welch, S. A., Beard, B. L., Johnson, C. M., and Braterman, P. S. (2003). Kinetic and Equilibrium Fe Isotope Fractionation between Aqueous Fe(II) and Fe(III). *Geochimica et Cosmochimica Acta* 67, 4231–4250. doi:10.1016/s0016-7037(03)00266-7

Weyer, S., Anbar, A. D., Gerdes, A., Gordon, G. W., Algeo, T. J., and Boyle, E. A. (2008). Natural Fractionation of 238U/235U. *Geochimica et Cosmochimica Acta* 72, 345–359. doi:10.1016/j.gca.2007.11.012

Widdel, F., Schnell, S., Heising, S., Ehrenreich, A., Assmus, B., and Schink, B. (1993). Ferrous Iron Oxidation by Anoxygenic Phototrophic Bacteria. *Nature* 362, 834–836. doi:10.1038/362834a0

Willbold, M., and Elliott, T. (2017). Molybdenum Isotope Variations in Magmatic Rocks. *Chem. Geology*. 449, 253–268. doi:10.1016/j.chemgeo.2016.12.011

Wille, M., Kramers, J. D., Nägler, T. F., Beukes, N. J., Schröder, S., Meisel, T., et al. (2007). Evidence for a Gradual Rise of Oxygen between 2.6 and 2.5Ga from Mo Isotopes and Re-PGE Signatures in Shales. *Geochimica et Cosmochimica Acta* 71, 2417–2435. doi:10.1016/j.gca.2007.02.019

Woodhead, J. D., Hergt, J. M., and Simonson, B. M. (1998). Isotopic Dating of an Archean Bolide Impact Horizon, Hamersley Basin, Western Australia. *Geol* 26, 47–50. doi:10.1130/0091-7613(1998)026<0047:idoaab>2.3.co;2

Zhang, F., Xiao, S., Kendall, B., Romaniello, S. J., Cui, H., Meyer, M., et al. (2018). Extensive marine Anoxia during the Terminal Ediacaran Period. *Sci. Adv.* 4, eaan8983. doi:10.1126/sciadv.aan8983

Conflict of Interest: The authors declare that the research was conducted in the absence of any commercial or financial relationships that could be construed as a potential conflict of interest.

Publisher's Note: All claims expressed in this article are solely those of the authors and do not necessarily represent those of their affiliated organizations, or those of the publisher, the editors, and the reviewers. Any product that may be evaluated in this article, or any claim that may be made by its manufacturer, is not guaranteed or endorsed by the publisher.

frontiers | Frontiers in Earth Science

ORIGINAL RESEARCH
published: 06 July 2022
doi: 10.3389/feart.2022.909900

Oxidation of Dissolved Tetravalent Selenium by Birnessite: Se Isotope Fractionation and the Effects of pH and Birnessite Structure

Pranjal Dwivedi[1], Kathrin Schilling[2], Naomi Wasserman[3], Thomas M. Johnson[3] and Celine Pallud[4]*

[1]Department of Environmental Science, Policy and Management, University of California, Berkeley, Berkeley, CA, United States, [2]Department of Environmental Health Sciences, Columbia University Mailman School of Public Health, New York, NY, United States, [3]Department of Geology, University of Illinois at Urbana-Champaign, Champaign, IL, United States, [4]Department of Environmental Science, Policy and Management, College of Natural Resources, University of California, Berkeley, Berkeley, CA, United States

Redox reactions control the mobility and bioavailability of selenium (Se) in biogeochemical systems, both modern and ancient. Se isotope ratio measurements (e.g., $^{82}Se/^{76}Se$) have been developed to enhance understanding of biogeochemical transformations and transport of Se. Stable isotope ratios of many elements are known to be powerful indicators of redox reactions, and shifts in $^{82}Se/^{76}Se$ have been observed for Se reduction reactions. However, Se isotope shifts caused by naturally relevant oxidation reactions have not been published. Here, we report Se isotope fractionation factors for oxidation of Se(IV) by birnessite. Experiments were conducted at pH = 4.0 and 5.5, with two types of birnessite of contrasting composition at two concentrations of suspended birnessite. The results are consistent with a single $^{82}Se/^{76}Se$ fractionation factor, for all times during all experiments, of 0.99767 (±0.0035 2 s.d.). Expressed as ε, the fractionation is 2.33‰ (±0.08‰).

Keywords: isotope geochemistry, manganese oxides, Rayleigh fractionation, selenium oxidation, paleoredox

OPEN ACCESS

Edited by:
Wang Zheng,
Tianjin University, China

Reviewed by:
Xinming Chen,
Shanghai Jiao Tong University, China
Eva Stüeken,
University of St Andrews, United Kingdom

****Correspondence:***
Pranjal Dwivedi
pranjal_dwivedi@berkeley.edu

Specialty section:
This article was submitted to Geochemistry, a section of the journal Frontiers in Earth Science

Received: *31 March 2022*
Accepted: *30 May 2022*
Published: *06 July 2022*

Citation:
Dwivedi P, Schilling K, Wasserman N, Johnson TM and Pallud C (2022) Oxidation of Dissolved Tetravalent Selenium by Birnessite: Se Isotope Fractionation and the Effects of pH and Birnessite Structure. Front. Earth Sci. 10:909900. doi: 10.3389/feart.2022.909900

INTRODUCTION

Selenium (Se) is a redox-sensitive element and plays a dual role in the modern environment as an essential micronutrient (Huawei, 2009) and a contaminant detrimental to aquatic wildlife (Ohlendorf et al., 1990; Schuler et al., 1990). It also serves as a paleoredox proxy (Schirmer et al., 2014; Kipp et al., 2020; Stüeken and Kipp, 2020). In nature, it exists in four oxidation states (+6, +4, 0, −2), each displaying different solubility and sorption characteristics. Under oxic and mildly reducing conditions, Se occurs as soluble oxyanions, Se(VI) (as selenate; SeO_4^{-2}) and Se(IV) (as SeO_3^{-2} and $HSeO_3^-$). Under reducing conditions elemental Se (Se(0)) and selenide (-II) are thermodynamically stable species which are sparingly soluble in typical soil and groundwater systems. Adsorption of Se(IV) onto metal oxide surfaces is much stronger than that of Se(VI); Se(IV) forms strong inner-sphere complexes (Catalano et al., 2006) while Se(VI) is bonded *via* weaker outer-sphere complexes and some inner-sphere complexes under some conditions (Peak and Sparks, 2002).

In the global Se cycle, oxidation plays a central role in the dissolution of Se(-II)-bearing minerals and elemental Se as well as in the release of soluble Se oxyanions that are transferred from continental

to marine reservoirs (Nriagu, 1989; Haygarth, 1994; White and Dubrovsky, 1994; Fernández-Martínez and Charlet, 2009). Although oxidation has been a major Se mobilizing process throughout geologic time (Masscheleyn et al., 1990; Plant et al., 2005) and is an important process controlling fluxes in modern environments, there are gaps in our understanding of reaction rates and mechanisms with environmentally relevant mineral oxides.

The fate of Se is strongly influenced by surface reactive mineral phases (Scott and Morgan, 1996). Mn oxides play important roles in soils and sediments due to their ubiquity, with concentrations in the range of 0.02–10 g/kg (Essington, 2003), and narrow Eh-pH stability field (Tournassat et al., 2002). Birnessite (δ-MnO_2) is an important redox-sensitive Mn oxide (Scott and Morgan, 1996) commonly found in soils and sediments (Banerjee and Nesbitt, 2000). Birnessite has been shown to adsorb and oxidize cobalt(II) (Crowther, Dillard, & Murray, 1983), chromium(III) (Fendorf, 1995), and arsenic(III) (Scott & Morgan, 1995) and is also a known oxidant and adsorbent for Se(IV) (Scott and Morgan, 1996). To date, limited research has explored interactions between Se and birnessite in environmentally relevant settings. Scott and Morgan (1996) showed that Se(IV) oxidation on δ-MnO_2 surfaces was directly facilitated by electron transfer from Se(IV) to Mn(IV). The chemical reaction between Se(IV) and birnessite leads to the reductive dissolution of the mineral surface and subsequent production of Mn(II) following the reaction: (**Eq. 1**)

$$MnO_2\,(s) + HSeO_3^- + H^+ = Mn^{2+} + SeO_4^{2-} + H_2O \qquad (1)$$

Measurements of stable Se isotope ratios (e.g., $^{82}Se/^{76}Se$; other ratios have also been used) have been developed as a means to improve understanding of Se biogeochemical transformations that control the mobility and bioavailability of Se in modern environments (Clark and Johnson, 2010; Zhu et al., 2014; Schilling et al., 2015), and a means to extract information about ancient redox conditions from rocks (e.g.,Mitchell et al., 2012; Mitchell et al., 2016; Kipp et al., 2017; Kipp et al., 2020). Laboratory studies have investigated Se isotope fractionation induced by reduction, volatilization, and adsorption of Se, and it has been observed in both theoretical and empirical studies that Se isotopes are highly sensitive to redox reactions (Herbel et al., 2000; Johnson and Bullen, 2004; Li and Lui, 2011; Schilling et al., 2011; Mitchell et al., 2012; Schilling et al., 2020; Xu et al., 2020; Xu et al., 2021). Reduction reactions, which tend to immobilize aqueous Se, have been relatively well studied (Herbel et al., 2000; Johnson and Bullen, 2004; Mitchell et al., 2016; Shrimpton et al., 2015; Schilling et al., 2020). However, Se isotopic fractionation induced during oxidation is almost completely unexplored (Johnson et al., 1999; Wasserman et al., 2021), and this limits our ability to interpret Se isotope data for natural settings.

Here, we investigate the reaction of Se(IV) with birnessite and the effect of surface properties including morphology and crystallinity. We conducted a series of batch experiments *1*) with birnessite synthesized by different methods *2*) varying amount of birnessite, and *3*) at two different pH conditions. We measured aqueous Se(IV), Se(VI), Mn(II) concentrations, and $^{82}Se/^{76}Se$ produced *via* reaction of Se(IV) with birnessite at pH 4 and 5.5, birnessite concentrations of 0.24 and 0.48 g L^{-1} (**Table 1**). We varied pH conditions, birnessite type, and birnessite concentrations because these parameters have previously been shown to influence reaction kinetics (Scott and Morgan, 1996; Wang and Giammar, 2015) due to the difference between the point of zero charge (pzc) of the mineral surface and sorption affinity pH of the solution, which directly influences the sorption of ionic species involved in the reaction. All tested parameters are relevant when interpreting the fate of Se oxyanions in aquatic systems, where mixed reactive Mn oxides are abundant (Post, 1999; Tebo et al., 2004). The experiments were designed to yield Se isotope fractionation factors for Se(IV) oxidation by birnessite, in order to improve the interpretation of Se isotope data from systems with fluctuating redox conditions (e.g., shallow aquifers or seasonal fluctuations of the water table) or spatial redox contrasts (e.g., oxidative terrestrial weathering combined with reductive marine deposition). We are aware of the narrow pH range represented by our experiments, however Scott and Morgan (1996) did not observe significant oxidation and adsorption at pH 7, therefore our experiments are representative of low pH conditions which are environmentally relevant for Se(IV) adsorption and oxidation.

METHODS

Birnessite Synthesis and Characterization

The specific surface area (SSA) of the particular mineral has been shown to play a major role in determining the kinetics of oxidative reactions (Villalobos et al., 2014). Additionally, the internal structure and the Mn^{+3}/Mn^{+4} ratio, both of which determine the overall charge of the interlayer and its reactivity, vary across mineral morphologies (Feng et al., 1999). The morphologies of synthesized minerals often vary based on the synthesis method. Mn oxides synthesized by additional calcination are more crystalline (Subramanian et al., 2014; Augustin et al., 2015) than oxides prepared from other methods, such as precipitation and sol-gel/solvothermal syntheses (Handel et al., 2013). Most studies have used acid-synthesized birnessite for their experiments with low SSA between 19 and 33 m^2/g (Scott and Morgan, 1996; Manning et al., 2002; Power et al., 2005; Villalobos et al., 2014). Only a study by Lafferty et al. (2010) reported high SSA of 274 m^2/g for acid-synthesized birnessite. In order to compare birnessites with different specific surface area (SSA) and crystallinity, we synthesized birnessite using two different methods (Mckenzie, 1971; Ching et al., 1995; Scott and Morgan, 1996; Handel et al., 2013). The first method, referred to as the acid-reduction (AR) method (McKenzie, 1971; Scott and Morgan, 1996), involves the reduction of potassium permanganate ($KMnO_4$) using hydrochloric acid (HCl). More specifically, 50 ml of 2 M HCl was added slowly over 3 h to 500 ml of aqueous 1 M $KmnO_4$. The solution was constantly stirred while the temperature was maintained at 60°C. Formed birnessite, visible as brown

precipitate, was then collected and centrifuged at 1670 rcf for 15 min and washed with 18.2 MΩ Milli-Q water until the conductivity of the supernatant was less than 10 µS. The precipitate was then dried at 35°C for 48 h before calcination at 400°C for 60 h in a ceramic crucible inside a muffle furnace. The residue was then centrifuged, washed and dried as described above, to obtain the final AR birnessite.

The second method, referred to as sol-gel (SG) method (Händel et al., 2013), also involves $KmnO_4$ reduction, but is referred in the literature as a soft chemistry method (Ching et al., 1995). One milliliter of 50% sodium-lactate solution was added to 100 ml of 63.3 mM aqueous $KmnO_4$. This solution was stirred for 2 h at room temperature until the purple color disappeared and a precipitate formed. The precipitate was collected and centrifuge-washed at 1670 rcf for 15 min with 18.2 MΩ Milli-Q water until the conductivity of the supernatant was less than 10 µS. The precipitate was then freeze-dried for 48 h. We refer to the birnessite created *via* the sol-gel method as SG-birnessite.

Bulk solid phase mineralogy of the two types of birnessite before and after the batch experiments was determined using powder X-ray diffraction (XRD). XRD analyses were carried out using MicroSTAR-H APEX II diffractometer equipped with a Cu-Kα radiation source (40 kV, 40 mA). Spectra were determined spanning 2θ values from 3 to 80° with step sizes of 0.01° and 90 s. Crystal morphology and particle size estimates were imaged using scanning electron microscopy (SEM, Zeiss Evo-10 Variable Vacuum) with energy dispersive detector (EDS) with 3 mg of carbon-coated solids mounted on adhesive tape.

Fourier-transform infrared (FTIR) spectra were obtained using a Nicolet 6700 (Thermo Scientific) in the 4000–400 cm^{-1} range by mixing a small amount of birnessite in 18.2 MΩ Milli-Q water. The final spectra were obtained by subtracting the spectra for water from the slurry and baseline correction. The surface area of the two birnessite types was determined using BET (Brunauer, Emmett, and Teller) (Brunauer et al., 1938). The powdered samples were dried at 100°C overnight, then placed into 9 mm glass cells and outgassed under vacuum for 2–3 h at 150°C to remove any moisture or gasses adsorbed onto the mineral surfaces. The sample cell was stabilized at liquid nitrogen temperature (77.350 K) and measured for BET surface area under nitrogen atmosphere. Multiple-point BET surface area measurements (corresponding to P/Po ratios of 0.050, 0.075, 0.100, 0.150, 0.200, 0.250 and 0.300) were performed for each sample to determine its specific surface area using an Autosorb AS-1 (Quantachrome Instruments, Boynton Beach, FL, United States).

The average oxidation state of Mn in the synthesized birnessite was determined following a method by Kijima et al. (2001). Briefly, 0.1 g of birnessite was reacted with 10 ml of 1 M sulfuric acid (H_2SO_4) and 5 ml of 0.5 M sodium oxalate ($Na_2C_2O_4$) at 60°C. The excess oxalate was reduced by adding dropwise 0.02 M $KmnO_4$ until a steady pink color appeared. Then a subsample was taken and the concentration of Mn(II) was determined by Inductively Coupled Plasma Optical Emission Spectroscopy (PerkinElmer 5300 DV ICP–OES) in normal mode, with a detection limit of 0.5 µM. The average oxidation state (AOS) of Mn was calculated using the formula: (**Eq. 2**)

$$\text{Mn AOS} = 2 + \left(\text{Net reducing equivalents}\right) / \left([Mn]Tot\right) \quad (2)$$

where the net reducing equivalents per gram birnessite was determined as equivalent of oxalate used for dissolving birnessite (Murray et al., 1984). *[Mn]Tot* is the total amount of Mn per gram of birnessite.

Batch Experiments

Duplicate anoxic batch experiments, following Scott and Morgan (1996), were performed with the two types of birnessite. In acid-washed serum bottles, 0.03 or 0.06 g dry weight (±0.003 g) birnessite were added to 122.5 ml of 1 mM NaCl obtaining final birnessite of 0.24 and 0.48 g L^{-1} in solution. The solution was then degassed with N_2 gas for 3 h before the bottles were transferred into an anaerobic glove box. Then 2.5 ml of a 5.8 mM Se(IV) stock solution, prepared by dissolving 100.4 mg of Na_2SeO_3 in DDI and making up the volume to 1 L, was added and the pH adjusted to 4 or 5.5 with 1 M NaOH or 1 M HCl. Scott and Morgan (1996) carried out experiments at pHs 4, 5, and 7 and did not find considerable oxidation and adsorption at pH 7 therefore this experiment focussed on lower pHs. The initial Se(IV) concentration for all experiments was 120 µM. The solution was allowed to equilibrate for 2 h. The batch reactors were then consistently stirred during the experiment with a rotary shaker at 45 rpm and kept at constant temperature of 25°C. The pH of the batch solution was monitored throughout the experiment with Vernier electrodes and adjusted if needed by addition of 0.1 M HCl or 0.1 M NaOH to maintain a constant pH. The batch reactors were subsampled at 0, 2, 4, 6, 8, 12, and 24 h and then once per day for a total of 14 days and 20 time points. For each sampling point, two 1 ml subsamples were withdrawn and filtered through 0.22 µm nitrocellulose filters and made up to 10 ml with 2% HNO_3 for elemental analysis.

Chemical Analyses

Total Se and Mn concentrations were determined using a PerkinElmer 5300 DV ICP–OES. Total Se was determined using the ICP–OES operating in regular mode (detection limit of 0.05 µM) and Se(IV) concentrations were measured using ICP–OES coupled to a hydride-generation (HG) setup (detection limit of 0.1 µM). This setup is based on the phase separator setup described by Bosnak and Davidowski (2004) and with flow rates as used by Brooks (1991) in Manifold 2 (HG–ICP–OES). A sample injection time of 120 s before optical emission reading and a rinse time of at least 30 s with an additional 100 s following samples exceeding 1.9 mmol L^{-1} were used due to a significant memory effect. Elemental and speciation standards were prepared from certified reference stock solutions (LGC Standards, Teddington, United Kingdom) in a matching matrix to the measured samples. All Se(IV) concentrations measured in samples were corrected from trace concentrations in the input solutions [approximately 0.2 µM of Se(IV) and Se(VI)] (Kausch et al., 2012). Selenate concentrations were determined using ICP-OES after separation of Se(IV) from Se(VI) using anion exchange columns (Schilling et al., 2015). Two milliliters of sample was loaded onto a chromatography column filled with 1 ml of BioRad® AG1-X8 anion exchange resin. Se(IV)

TABLE 1 | List of experimental conditions with concentrations at t=0[1].

Exp.	Type of birnessite	Birnessite (g L^{-1})	pH	Se(IV) (μM)	Duration of exp. (days)
Exp1-A	SG	0.24	4	122.53	20
Exp1-B	SG	0.48	4	118.78	20
Exp1-C	SG	0.24	5.5	120.36	20
Exp1-D	SG	0.48	5.5	121.93	20
Exp2-A	AR	0.24	4	123.51	20
Exp2-B	AR	0.48	4	122.29	20
Exp2-C	AR	0.24	5.5	118.78	20
Exp2-D	AR	0.48	5.5	119.57	20

was eluted from the column by 0.1 M HCl while Se(VI) was retained. Se(VI) was then eluted with 5 M HCl and measured using ICP-OES in regular mode.

Se Isotope Analysis

Selenium isotope analysis was carried out on Se(VI) extracted from sample solutions. Samples for isotope analysis were filtered through 0.22 μm nitrocellulose filters and made up to volume in a 1 M HCl matrix. Aliquots were collected with a total Se mass of 50–100 ng from each sample. Then, an appropriate amount of double spike solution (*see* below) was added so that the ratio of spiked ^{77}Se to natural ^{78}Se in the sample was close to 2:1. After addition of the spike and overnight equilibration of the spike with the solution, Se(VI) was isolated from samples using the ion exchange method described above. The samples were eluted from the columns by 5 M HCl. To convert Se(VI) to Se(IV), the samples were heated in a hot block held at 120°C for 1 h. After cooling to room temperature, the solutions were diluted to 2 M HCl. Standard and blank solutions were prepared following the same procedure together with the samples.

Selenium isotope ratios were determined with a Multicollector Inductively Coupled Plasma Mass Spectrometer (MC-ICPMS) (Nu Plasma HR, Nu Instruments; Wrexham, United Kingdom). Selenium was introduced into the instrument *via* a custom-built hydride generator (Zhu et al., 2008). Sample Se was introduced into the mass spectrometer as H_2Se evolved *via* reaction with a 0.2% $NaBH_4$ solution in a continuous flow hydride generator. The double spike (^{74}Se + ^{77}Se) method was used to correct for instrumental mass bias and any isotopic fractionation occurring during sample preparation or hydride generation (Johnson et al., 1999) with mass spectrometry proceeding according to the method described by numerous studies (Zhu et al., 2008; Zhu et al., 2014; Schilling et al., 2015; Mitchell et al., 2016). The ratios of ^{74}Se/^{78}Se, ^{76}Se/^{78}Se, ^{77}Se/^{78}Se, and ^{82}Se/^{78}Se were measured simultaneously in Faraday detectors with a minimum of 30 integrations of 5s each. Isobaric interference from germanium (Ge) was determined by measurement of Ge using an ion-counting detector and calculation of ^{74}Ge and ^{76}Ge using mass bias-corrected natural Ge isotope ratios. Interferences from ArAr at masses 76 and 78 were determined by measuring mass 80 intensity, subtracting the ^{80}Se intensity to obtain the ArAr intensity and calculating the corresponding mass 76 and 78 isotopomers using mass bias-corrected natural Ar isotopes ratios. Interferences from Kr and ArCl were subtracted using on-mass zero measurements. The ^{82}Se/^{76}Se and ^{82}Se/^{78}Se of each sample or standard were extracted from the interference-corrected Se isotope ratios measured on the sample-spike mixture *via* an iterative data reduction calculation that determines and corrects mass bias, mathematically removes the spike from the mixture, and calculates the final results (Johnson et al., 1999). The external precision was ±0.2‰ (2 s.e) based on 10 pairs of duplicate samples.

All isotope data are reported using the δ notation to express ^{82}Se/^{76}Se relative to the standard NIST 3149 SRM: (**Eq. 3**)

$$\delta^{82/76}\mathrm{Se}\,(‰) = \left[\left(^{82}\mathrm{Se}/^{76}\mathrm{Se}_{\mathrm{Sample}}\right)\Big/\left(^{82}\mathrm{Se}/^{76}\mathrm{Se}_{\mathrm{NIST-3149}}\right) - 1\right]*1000‰ \quad (3)$$

Isotopic Fractionation and Rayleigh Distillation Model

The magnitude and direction of kinetic isotope effects are described by the isotope fractionation factor α (**Eq. 4**)

$$\alpha = \mathrm{R}_{\mathrm{product}}\Big/\mathrm{R}_{\mathrm{reactant}} \quad (4)$$

where $\mathrm{R}_{\mathrm{product}}$ and $\mathrm{R}_{\mathrm{reactant}}$ refer to the isotope ratio of the incremental, or instantaneous, product and the reactant, respectively. Expressing the magnitude of fractionation in per mil terms provides a more easily grasped measure of fractionation, and thus we use ε, in addition to α, to quantify isotopic fractionation: (**Eq. 5**)

$$\varepsilon\,(‰) = (\alpha - 1)*1000‰ \quad (5)$$

ε is useful because it is very close to the $\delta^{82/76}$Se difference between the reactant and the instantaneous (incremental) reaction product: (**Eq. 6**)

$$\varepsilon \approx \delta_{\mathrm{inst\,product}} - \delta_{\mathrm{reactan}} \quad (6)$$

Se isotopic compositions were measured on dissolved Se(VI) only, in order to focus analytical effort on the data that would most efficiently quantify the isotopic fractionation. The $\delta^{82/76}$Se values of dissolved Se(IV) could have been used to obtain a second, independent determination of ε in, but this would have required much longer experiments and double the analytical effort to obtain a redundant result. Fractionation factors were extracted from the $\delta^{82/76}$Se values of aqueous Se(VI) using a Rayleigh distillation model. The $\delta^{82/76}$Se values of an accumulated reaction product are given by (**Eq. 7**)

$$\delta_{acc.\,product} = (\delta_0 + 1000‰)\frac{1 - f^{\alpha}}{1 - f} - 1000‰ \quad (7)$$

where $\delta_{acc.product}$ is the $\delta^{82/76}$Se value of the measured (accumulated) Se(VI) in solution at some time after the reaction has started, δ_0 is that of the initial Se(IV) reactant pool before any reaction has occurred, and f is the fraction of the initial Se(IV) remaining at the time of sampling. **Equation 7** was then fitted to isotope data provided in **Tables 2**, **3** using a

TABLE 2 | Concentration and isotope data for experiments carried out with AR birnessite.

Time (hr)	Solid conc	pH	Se (IV) (μM)	s.e	Mn (μM)	s.e	Se (VI) (μM)	s.e	Adsorbed Se (μM)	s.e	82/76Se (‰)	2 s.e
0	0.24	4	133.25	2.99	0.00	0.00	0.00	0.00	0.00	0.00	—	—
2	0.24	4	120.18	5.40	0.00	0.00	0.54	0.02	12.66	0.38	—	—
4	0.24	4	117.33	1.69	0.00	0.00	0.92	1.23	15.13	2.09	—	—
6	0.24	4	111.16	2.33	0.00	0.00	1.07	1.41	21.14	1.27	—	—
8	0.24	4	103.95	2.78	0.00	0.00	2.34	2.01	27.09	8.23	—	—
12	0.24	4	100.42	3.93	0.00	0.00	2.76	1.72	30.20	7.79	—	—
24	0.24	4	102.36	1.15	0.00	0.00	3.16	2.49	27.85	7.34	—	—
48	0.24	4	89.97	3.55	0.00	0.00	4.86	1.20	38.55	6.65	—	—
72	0.24	4	100.26	5.29	2.64	0.09	5.14	2.36	27.98	6.08	−3.61	0.2
96	0.24	4	96.59	5.03	5.92	0.10	7.47	1.27	29.31	4.24	—	—
120	0.24	4	96.16	1.99	1.10	0.55	8.79	0.53	28.42	7.53	—	—
144	0.24	4	91.55	5.45	9.38	1.28	10.69	2.40	31.14	5.95	−3.74	0.2
168	0.24	4	87.68	2.58	11.65	2.00	13.67	1.42	32.03	6.84	—	—
192	0.24	4	91.59	6.22	11.56	1.46	14.44	1.26	27.34	3.04	—	—
216	0.24	4	86.28	6.17	9.28	2.91	16.21	2.59	30.89	3.42	−3.71	0.2
240	0.24	4	82.12	5.33	11.65	1.46	19.04	2.96	32.22	4.62	—	—
264	0.24	4	82.07	5.75	17.56	1.55	21.37	1.77	29.94	6.01	—	—
288	0.24	4	86.55	5.90	16.29	2.10	20.05	2.88	26.78	2.98	—	—
312	0.24	4	84.22	5.51	19.30	2.10	22.58	1.93	26.58	3.42	—	—
336	0.24	4	86.83	3.99	24.03	3.10	24.45	1.45	22.09	2.47	—	—
0	0.48	4	127.29	4.18	0.00	0.00	0.00	0.00	0.00	0.00	—	—
2	0.48	4	107.86	4.80	0.00	0.00	1.39	0.38	18.05	1.68	—	—
4	0.48	4	102.95	2.69	0.00	0.00	1.90	0.38	22.45	2.44	—	—
6	0.48	4	98.14	2.81	0.00	0.00	2.41	1.02	26.75	7.30	—	—
8	0.48	4	93.37	3.20	0.00	0.00	1.86	0.05	32.07	8.65	—	—
12	0.48	4	97.50	3.77	0.00	0.00	0.00	0.73	29.80	5.53	—	—
24	0.48	4	96.74	2.59	0.00	0.00	1.83	1.61	28.73	8.47	—	—
48	0.48	4	91.66	3.09	0.91	0.91	2.69	1.39	32.95	6.21	—	—
72	0.48	4	91.94	0.26	4.01	0.19	5.24	1.77	30.12	3.99	−4.07	0.2

"s.e" refers to standard error.

least-squares minimization approach and the line of best-fit is plotted alongside the datapoints in **Figure 1**.

RESULTS

Birnessite Characterization

SEM images showed distinct morphological differences between the two types of birnessite (**Figure 2**). However, both types were compositionally similar, with Mn content ranging from 55 to 67 wt%, O of 25–35 wt%, and K of 3–7 wt% (**Table 4**). These are consistent with values reported in mineral databases ("Birnessite Mineral Data, 2019" Web Mineral). The SSA for the SG birnessite was 134.32 $m^2\ g^{-1}$ (±8.27 $m^2\ g^{-1}$), which is much greater than AR birnessite with SSA of 82.5 $m^2\ g^{-1}$.

The XRD patterns for the two types of birnessite are shown in **Figure 3**. Both birnessites contain the dominant characteristic K-birnessite reflections at 2θ angles of 12.56 (1), 25.42(2), 38.82(3), and 51.25°(4), and corresponding d-spacings of 7.14 Å, 3.63 Å, 2.41 Å, 1.81 Å respectively (Post & Veblen, 1990). However, the presence of other peaks (1′-6′) points to the mixed nature of the synthesized oxides (Birkner and Navrotsky, 2017). Cheney et al. (2009) investigated the effect of Hoffmeister anions (Cl^-, SO_4^{2-}, and ClO_4^-) during the synthesis of birnessite nanostructures and found significant quantities of cryptomelane ($K(Mn^{4+},Mn^{2+})_8O_{16}$) mixed with the birnessite, and significant contractions in crystal size. This can explain the higher presence of cryptomelane phases in the AR birnessite XRD spectra compared to SG birnessite. XRD spectra of two different cryptomelane samples reveal that peaks 1′-6′ are representative of cryptomelane phases in the synthesized oxide (Post et al., 1982; Vicat et al., 1986).The software linked with MicroSTAR-H APEX II instrument identified birnessite and cryptomelane as the two major phases present in the oxide as well. There is also a significant difference in the intensities of the diffraction peaks, with SG birnessite being more reflective, presumably due to its higher crystalline nature compared to the AR birnessite (**Figure 3**).

FTIR spectra of the two types of birnessite (**Figure 4**) are consistent with those seen for K-birnessites (Potter and Rossman, 1979; Ling et al., 2017). Hydroxide ion and a less-ordered water of crystallization produces the two peaks in the 4000–1400 cm^{-1} region, whereas the absorbance in the 650–400 cm^{-1} represents Mn-O bonds (Potter and Rossman, 1979).

The average oxidation state for the AR birnessite was 3.28 ± 0.08, compared to 3.45 ± 0.05 for the SG birnessite.

Se Species Concentrations

Dissolved Se(IV) and Se(VI) concentrations are presented in **Figures 5**, **6** and **Tables 3**, **4**. For all experiments we observed

TABLE 3 | Concentration and isotope data for experiments carried out with SG birnessite.

Time	Solid conc	pH	Se (IV) (μM)	s.e	Mn (μM)	s.e	Se (VI) (μM)	s.e	Adsorbed Se (μM)	s.e	82/76Se (‰)	2 s.e
0	0.24	4	138.19	5.42	0.00	0.00	0.00	0.00	0.00	0.00	—	—
2	0.24	4	117.51	0.33	0.00	0.00	0.48	0.01	20.20	2.55	—	—
4	0.24	4	97.83	0.94	0.00	0.00	0.80	0.06	39.56	0.95	—	—
6	0.24	4	91.08	0.49	0.00	0.00	0.97	0.07	46.15	3.48	—	—
8	0.24	4	83.98	2.64	0.00	0.00	1.23	0.25	52.98	0.57	—	—
12	0.24	4	80.82	1.81	0.00	0.00	1.66	0.13	55.71	4.81	—	—
24	0.24	4	72.20	1.06	0.00	0.00	1.30	0.33	64.70	4.68	—	—
48	0.24	4	57.89	0.20	2.73	0.48	1.68	0.43	78.62	2.53	—	—
72	0.24	4	61.60	1.81	4.19	0.30	2.09	0.32	74.51	2.09	–3.46	0.2
96	0.24	4	51.93	2.47	16.93	1.73	3.78	0.57	82.48	2.34	—	—
120	0.24	4	49.72	0.73	24.02	2.55	4.53	0.63	83.94	0.89	—	—
144	0.24	4	45.62	0.51	37.31	3.65	5.66	0.64	86.91	0.82	–3.41	0.2
168	0.24	4	45.05	4.05	48.23	6.19	6.36	0.45	86.79	0.70	—	—
192	0.24	4	43.78	1.35	45.14	5.10	6.92	0.90	87.48	1.14	—	—
216	0.24	4	50.86	1.15	56.06	7.74	7.51	1.44	79.83	3.99	—	—
240	0.24	4	48.29	1.83	52.69	8.66	7.42	1.71	82.48	0.57	—	—
264	0.24	4	49.96	1.17	48.23	5.02	7.40	1.11	80.84	1.33	–3.44	0.2
288	0.24	4	63.30	1.49	43.32	4.21	7.60	1.38	67.29	0.19	—	—
312	0.24	4	62.21	1.53	50.05	5.86	7.92	1.20	68.05	0.06	—	—
336	0.24	4	67.18	1.22	51.69	4.19	7.95	1.16	63.05	0.25	—	—
0	0.48	4	132.35	###	2.49	0.44	0.00	0.00	0.00	0.00	—	—
2	0.48	4	79.61	4.54	6.68	0.16	0.00	0.00	52.74	0.13	—	—
4	0.48	4	72.94	2.13	8.62	0.15	0.00	0.00	59.41	3.61	—	—
6	0.48	4	69.00	###	10.62	0.98	0.00	0.00	63.35	5.00	—	—
8	0.48	4	51.85	8.78	15.13	2.39	0.00	0.00	80.50	2.72	—	—
12	0.48	4	41.02	1.87	14.43	1.43	0.36	0.04	90.98	9.43	—	—
24	0.48	4	35.34	2.36	17.68	1.47	0.52	0.15	96.50	11.08	—	—
48	0.48	4	31.35	2.24	27.36	5.03	1.18	0.18	99.82	12.85	—	—
72	0.48	4	27.22	3.08	46.46	5.09	1.87	0.39	103.26	12.72	–3.74	0.2
96	0.48	4	27.43	3.98	22.79	1.48	1.34	0.34	103.59	11.27	—	—
120	0.48	4	26.42	2.61	29.90	1.28	1.42	0.20	104.51	12.34	—	—
144	0.48	4	25.49	2.49	37.14	8.50	1.55	0.25	105.32	13.04	—	—
168	0.48	4	26.32	4.68	46.52	1.75	1.82	0.24	104.21	12.53	—	—
192	0.48	4	19.82	2.63	54.70	3.81	1.94	0.31	110.59	12.47	—	—
216	0.48	4	20.49	2.58	62.32	2.65	2.14	0.11	109.72	11.46	—	—
240	0.48	4	23.61	1.77	61.83	2.15	2.38	0.20	106.35	6.71	—	—
264	0.48	4	23.68	0.69	79.71	5.72	2.83	0.53	105.84	2.66	–3.4	0.2
288	0.48	4	20.54	0.56	66.99	9.15	2.94	0.38	108.88	4.81	—	—
312	0.48	4	22.48	0.17	78.57	8.84	3.38	0.69	106.48	1.77	—	—
336	0.48	4	18.23	1.59	100.66	7.49	3.67	0.60	110.45	4.87	—	—
0	0.24	6	129.90	4.94	0.00	0.00	0.00	0.00	0.00	0.00	—	—
2	0.24	6	112.11	2.01	0.00	0.00	0.31	0.02	17.48	2.91	—	—
4	0.24	6	111.65	5.14	0.00	0.00	0.33	0.05	17.92	0.32	—	—
6	0.24	6	101.11	2.01	0.00	0.00	1.00	0.36	27.79	2.85	—	—
8	0.24	6	100.30	0.47	0.00	0.00	0.99	0.20	28.62	4.43	—	—
12	0.24	6	97.00	1.93	0.00	0.00	1.50	0.24	31.40	2.91	—	—
24	0.24	6	94.01	1.18	0.00	0.00	1.82	0.24	34.06	3.67	—	—
48	0.24	6	90.01	1.34	0.00	0.00	2.73	0.32	37.16	3.48	—	—
72	0.24	6	91.76	4.19	0.00	0.00	2.81	0.12	35.33	4.30	—	—
96	0.24	6	90.03	6.06	0.00	0.00	2.58	0.11	37.29	3.61	–3.61	0.2
120	0.24	6	90.24	6.76	0.00	0.00	2.62	0.35	37.04	6.01	—	—
144	0.24	6	77.26	4.71	0.00	0.00	2.32	0.34	50.33	0.06	—	—
168	0.24	6	79.77	4.91	0.00	0.00	2.40	0.35	47.73	0.25	–3.88	0.2
192	0.24	6	78.02	6.32	0.00	0.00	2.57	0.37	49.31	2.85	—	—
216	0.24	6	81.48	4.38	0.00	0.00	2.72	0.33	45.71	0.25	—	—
240	0.24	6	82.25	4.10	0.00	0.00	2.26	0.23	45.39	0.44	—	—
264	0.24	6	82.88	4.59	0.00	0.00	2.26	0.22	44.76	0.06	—	—
288	0.24	6	88.60	4.70	0.00	0.00	1.99	0.28	39.32	4.87	—	—
312	0.24	6	89.36	3.22	0.00	0.00	2.24	0.18	38.30	2.09	—	—
336	0.24	6	91.41	3.41	0.00	0.00	1.90	0.26	36.60	1.65	—	—
0	0.48	6	102.25	5.36	0.04	0.02	0.14	0.05	0.00	0.00	—	—
2	0.48	6	94.55	5.64	1.20	0.08	0.28	0.06	7.56	12.91	—	—

(Continued on following page)

TABLE 3 | (*Continued*) Concentration and isotope data for experiments carried out with SG birnessite.

Time	Solid conc	pH	Se (IV) (μM)	s.e	Mn (μM)	s.e	Se (VI) (μM)	s.e	Adsorbed Se (μM)	s.e	82/76Se (‰)	2 s.e
4	0.48	6	88.29	2.92	0.62	0.10	0.43	0.11	13.66	12.15	—	—
6	0.48	6	81.64	5.74	0.29	0.14	0.54	0.07	20.21	9.68	—	—
8	0.48	6	75.99	4.30	0.30	0.17	0.64	0.11	25.76	9.68	—	—
12	0.48	6	74.26	4.75	0.29	0.14	0.93	0.16	27.19	6.77	—	—
24	0.48	6	70.15	6.31	0.10	0.02	1.01	0.12	31.23	4.62	—	—
48	0.48	6	64.31	9.20	0.30	0.20	1.25	0.10	36.82	0.89	—	—
72	0.48	6	61.72	7.88	0.95	0.82	1.18	0.19	39.49	5.44	—	—
96	0.48	6	59.87	6.44	0.15	0.05	1.28	0.17	41.24	5.00	—	—
120	0.48	6	51.88	4.98	0.65	0.03	1.09	0.21	49.42	13.04	—	—
144	0.48	6	51.01	3.12	0.15	0.02	1.16	0.12	50.23	11.84	—	—
168	0.48	6	50.50	2.16	0.28	0.09	1.36	0.17	50.53	11.27	–3.71	0.2
192	0.48	6	41.37	3.95	0.16	0.04	1.58	0.02	59.44	16.01	—	—
216	0.48	6	35.17	6.44	0.23	0.08	1.76	0.18	65.45	12.91	—	—
240	0.48	6	46.52	3.28	0.24	0.05	1.86	0.16	54.02	13.29	—	—
264	0.48	6	39.84	3.34	0.32	0.10	2.16	0.22	60.39	9.62	–3.6	0.2
288	0.48	6	41.82	3.47	0.51	0.13	2.05	0.10	58.52	13.61	—	—
312	0.48	6	41.78	2.47	0.46	0.12	2.23	0.27	58.37	16.96	—	—
336	0.48	6	40.42	1.33	0.55	0.10	2.08	0.01	59.90	20.70	—	—

"s.e" refers to standard error.

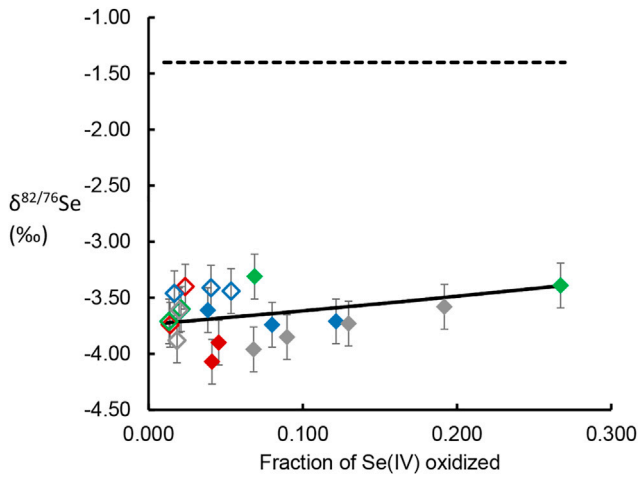

FIGURE 1 | $\delta^{82/76}$Se values of dissolved Se(VI) generated by oxidation of Se(IV) by birnessite, plotted versus the fraction of the initial Se(IV) oxidized and released into solution. Data point colors follow the scheme used in **Figures 4**, **5**, with red dots representing experimental conditions represented by orange. Closed symbols represent AR birnessite experiments; open symbol represent SG birnessite experiments. Dotted line gives the $\delta^{82/76}$Se value of the Se(IV) reactant stock solution. Solid line gives the line for a Rayleigh distillation model fit to the data across all experimental conditions.

removal of dissolved Se(IV). A sharp decrease in Se(IV) concentrations by 30–85% occurred within the first 12 h for all experiments (**Figure 6**). The decrease was generally stronger in the experiments containing the SG birnessite. After 12 h, in most experiments, Se(IV) concentration in solution continued to decrease, but at a slower rate. In the SG birnessite experiments with lower masses of birnessite, slight increases in dissolved Se(IV) occurred after 200 h. Se(IV) concentrations varied by about a factor of two for experiments with SG birnessite at different solid concentrations for the same pH after the first 48 h, compared to 1.2 for experiments with AR birnessite. It was also notable that experiments with birnessite concentration of 0.48 g L^1 at pH 5.5 had similar concentration profiles to experiments carried out with a birnessite concentration of 0.24 g L^{-1} at pH 4.

The temporal evolution in Se(IV) concentrations was similar to total Se, with an initial fast decrease followed by a stabilization or slow decrease in concentrations. A sharper decline in Se(IV) concentrations was observed for the SG birnessite compared to the AR birnessite (**Figure 6**). Se(IV) depletion rates for the SG birnessite ranged from 11.9 μM h^{-1} at pH 4 and 0.48 g L^{-1} solids to 2.1 μM h^{-1} at pH 5.5 and 0.24 g L^{-1}. For experiments with AR birnessite, the rates ranged from 5.6 μM h^{-1} to 0.87 μM h^{-1}.

Selenate concentrations did not exceed 35 μM across all experiments (**Figure 5**) which is about 30% of the initial Se(IV) concentration. We observed a faster initial production of Se(VI) in the first 48 h of the experiments, after which concentrations oscillated and stabilized for experiments with SG birnessite whereas they continued to increase linearly for AR birnessite. Higher Se(VI) concentrations of 30–35 μM were observed for experiments at pH 5.5 for AR birnessite, whereas concentrations reached 25 μM for experiments at pH 4 and a higher solid concentration. For SG birnessite, Se(VI) stabilized around 3 μM at pH 5.5 across both solid concentrations, whereas concentrations peaked and stabilized around 10 μM at pH 4. Given that there is an initial decrease in Se(IV) concentrations (**Figure 6**) without a corresponding increase in Se(VI) concentrations, adsorption seems to dominate in the first 24 h with oxidation being dominant after that.

Figure 7 shows that Mn(II) was only detected for experiments carried out at pH 4, with no Mn detected at

TABLE 4 | Elemental composition of the two birnessite types (AR= acid-reduction, SG= sol-gel) and the solid particles collected after the experiments have elapsed.[2]

Analyte	wt% Mn	wt% O	wt% K	wt% Se
AR birnessite	57.4 (±4.8)	24.9 (±1.7)	3.8 (±0.17)	0
SG birnessite	65.1 (±5.7)	35.2 (±2.3)	6.7 (±1.3)	0
AR solids, post-reaction	53.2 (±3.1)	25.2 (±2.5)	3.5 (±0.12)	1.38 (±0.13)
SG solids, post-reaction	60.7 (±2.8)	34.3 (±4.1)	7.2 (±0.5)	1.29 (±0.17)

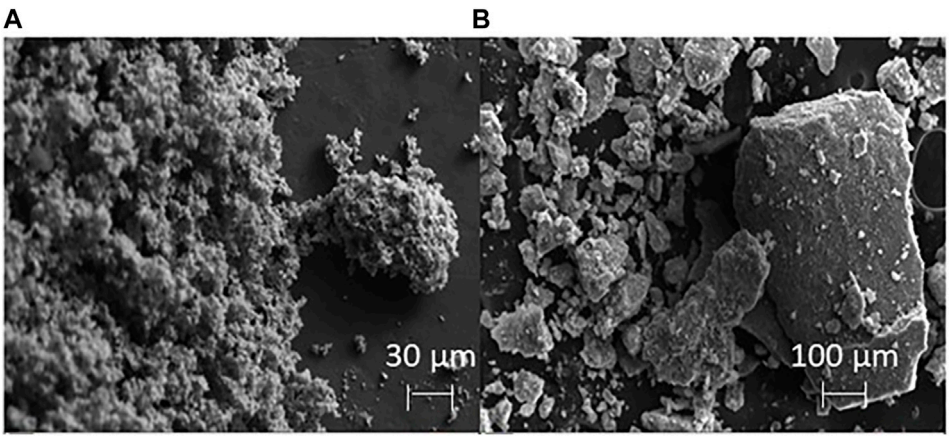

FIGURE 2 | SEM images of the synthesized birnessite using the AR method (A, scale bar is 30 µm), and the SG method (B, scale bar is 100 µm).

pH 5.5. Despite the initial rapid decrease in Se(IV) concentrations, we observed no corresponding increase in aqueous Mn(II). For pH 4 experiments with 0.48 g L^{-1} birnessite, aqueous Mn(II) reached maximum concentrations of 42 and 103 µM for AR and SG birnessite, respectively. In comparison, in experiments with 0.24 g L^{-1} birnessite, aqueous Mn(II) ranged between 24 and 48 µM.

Incorporation of Se Into Solids

Figures 8, **9** shows an SEM image of Se associated with the birnessite surface collected at the end of batch experiments with acid-reduction birnessite and associated EDS spectrum. The precipitate was washed with de-ionized water to remove the residue from the fluid from the batch experiments. The light spot corresponds to adsorbed Se, which is based on the principle that heavier atoms with larger radii reflect more electrons on excitation, leading to more backscatter and lighter colors. These spots were observed at multiple points on the mineral surface. At the end of the experiments, the collected precipitates contained 1.76 ± 0.23 wt% Se at pH 4 and 1.12 ± 0.15 wt% Se at pH 5.5. At low solid concentration experiments (0.24 g L^{-1}), AR birnessite had 0.75 ± 0.13 wt% Se, compared to 1.06 ± 0.27 wt% Se at pH 5.5 and 1.54 ± 0.36 wt% Se at pH 4.0 for SG synthesized birnessite. These values agree with Se(IV) profiles for reaction conditions with higher solid concentrations where a greater decrease in Se(IV) concentrations is observed. Based on the EDS measurements, adsorbed Se concentrations range between 0.72 and 0.4 µmol Se, and these values correspond well with the decrease in Se(IV) concentrations observed across reaction conditions with starting concentrations ranging from 1.3 to 1.1 µmol Se (**Figure 6**).

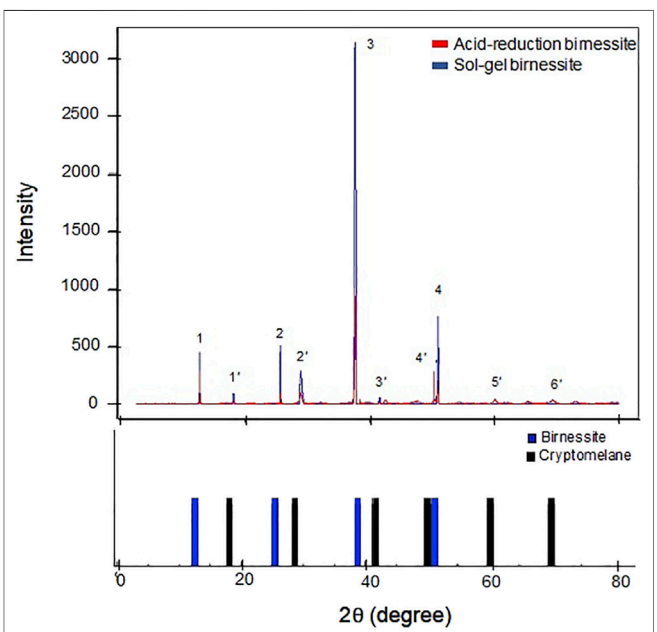

FIGURE 3 | XRD spectra for the two birnessite types used in the experiment (upper panel). Lower panel represents the characteristic peaks of birnessite (blue) and cryptomelane (black) from the American Mineralogist crystal structure database (Downs and Hall-Wallace, 2003).

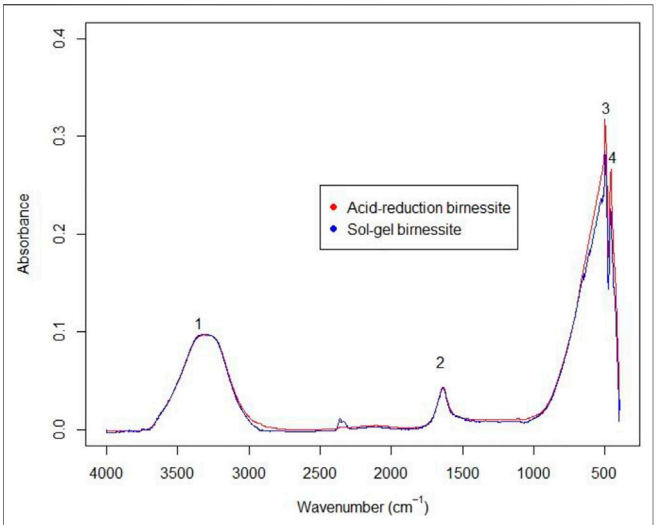

FIGURE 4 | FTIR spectra for the two birnessites used in the experiment.

Se Isotope Results

The measured $\delta^{82/76}$Se values in the dissolved Se(VI) are presented in **Tables 2**, **3** and **Figure 1**. The produced Se(VI) was always enriched in the lighter isotope (isotopically "light") relative to the Se(IV) used to make up the initial solution, with the difference ranging from −1.91‰ to −2.56‰. This indicates that Se(IV) oxidation involves mass-dependent isotopic fractionation; the reaction proceeds faster for lighter isotopes. Precise quantification of this fractionation, obtained by fitting isotope data to the Rayleigh distillation model equation using a minimization of squared residuals (**Eq. 7**), revealed fractionation factors (α; **Eq. 4**) of 0.99757 (±0.005, 2 s.d.) for the AR birnessite experiments and 0.99781 (±0.0063, 2 s.d.) for the SG birnessite experiments (**Figure 1**). Significant overlap of the uncertainty envelopes of these values indicate that they are not significantly different. When results from all experiments are fit to a single Rayleigh model, the resulting fractionation factor is 0.99767 (±0.0035 2 s.d.). Expressed as ε, the fractionation is 2.33‰.

The magnitude of isotopic fractionation is not sensitive to pH or the mass loading of birnessite in the experiments: Deviations of $\delta^{82/76}$Se measurements from the best-fit Rayleigh model show no significant correlation with either of these variables.

DISCUSSION

Aqueous Concentrations and Reaction Mechanisms

The experiments conducted with AR birnessite were modelled after those of Scott and Morgan (1996), and the changes in Se(IV) and Se(VI) concentrations (**Figures 5**, **6**) were roughly similar. The fraction of Se(IV) adsorbed in the early stages of the experiments and the rate of Se(VI) production roughly matched those observed in Scott and Morgan (1996). The SG birnessite generally exhibited somewhat greater adsorption than the AR birnessite, as would be expected given the 60% greater BET surface area of the SG birnessite. The much slower Se(VI) production observed with the SG birnessite, and the slowing of the rate during the experiments, likely results from differences in its oxidation state. AR-birnessite is known to be a stronger and faster oxidant due to higher concentrations of active Mn(III) present in its structure (Qiu et al., 2011). The difference in oxidation rate, and possible difference in kinetic mechanism between the AR and SG birnessite are helpful in our study: We expect that the structure of birnessite varies in nature, and therefore, determining the effects of some of this variation on the Se isotopic fractionation increases the applicability of the results.

The strong adsorption of Se(IV) in the first hours of all our experiments is consistent with the literature on Se(IV) adsorption (Balistrieri and Chao, 1990; Peak and Sparks, 2002; Catalano et al., 2006). Differences in Se(IV) adsorption between the two forms of birnessite can be explained by differences in average oxidation state (Wang et al., 2012); sorption is expected to be greater for SG birnessite with a higher AOS (3.45). Wang et al. (2012) found that a decrease in AOS indicated the presence of Mn(III) in inter-layer sites, which limits the sorption sites available for Se(IV) to only edge sites.

Adsorption of Se(VI) cannot be determined directly from our data. However, adsorption of Se(VI) onto oxide surfaces is known to be much weaker than that of Se(IV), and Balistrieri and Chao (1990) found no detectable adsorption of Se(VI) in an experiment at pH 5.0 with 0.3 g/L vernadite ($(Mn^{4+},Fe^{3+},Ca,Na)(O,OH)_2 \cdot nH_2O$) , and at pH = 4.2 with 0.03 g/L vernadite, in 0.1 M KCl solutions. They attributed this to the negative surface charge of vernadite. The results should apply to birnessite, which is nearly identical in its structure and characteristics. However, the lower chloride concentration (1 mM) in our experiments could allow for more Se(VI) adsorption owing to the lesser competition for surface sites. Also, the presence of a small amount of cryptomelane, which is positively charged at pH 4 and 5.5 (Lu et al., 2007), could have caused some adsorption of selenate in our experiments. Assuming selenate adsorption onto cryptomelane is similar to that onto iron oxides and hydroxides (Peak and Sparks, 2002), the adsorption would be stronger at pH 4 than at pH 5.5. Overall, we assume that some adsorption of selenate occurred in our experiments, but Se(VI) adsorption was much weaker than that of Se(IV) and thus most of the Se(VI) generated by oxidation was released quickly into solution.

The increasing Mn concentrations in the pH 4 experiments probably reflects production of soluble Mn(II) by reduction of Mn(III, IV) as it oxidized Se(IV), combined with some degree of proton-induced dissolution that would be confirmed by blank experiments with no Se(IV). Assuming the dissolved Mn is truly Mn(II) which was originally present as Mn(IV), one Mn(II) should be produced for each Se(VI) produced. In the pH 4 experiments, aqueous Mn concentrations were greater than or equal to the aqueous Se(VI) concentrations. In the pH 4 SG birnessite experiments, aqueous Mn/aqueous Se(VI) ratios in the later stages of the lower and higher birnessite mass experiments, were roughly 6 and 25 respectively. Higher Mn(II) concentrations at pH 4 could be explained by the slow dissolution of birnessite due to the protonation of the metal oxide surface (pKsp = 15.62) (Banerjee & Nesbitt, 2000; Nordstrom & Kirk, 2001). Mn(III), produced by the dissolution of birnessite in solution, disproportionates to form

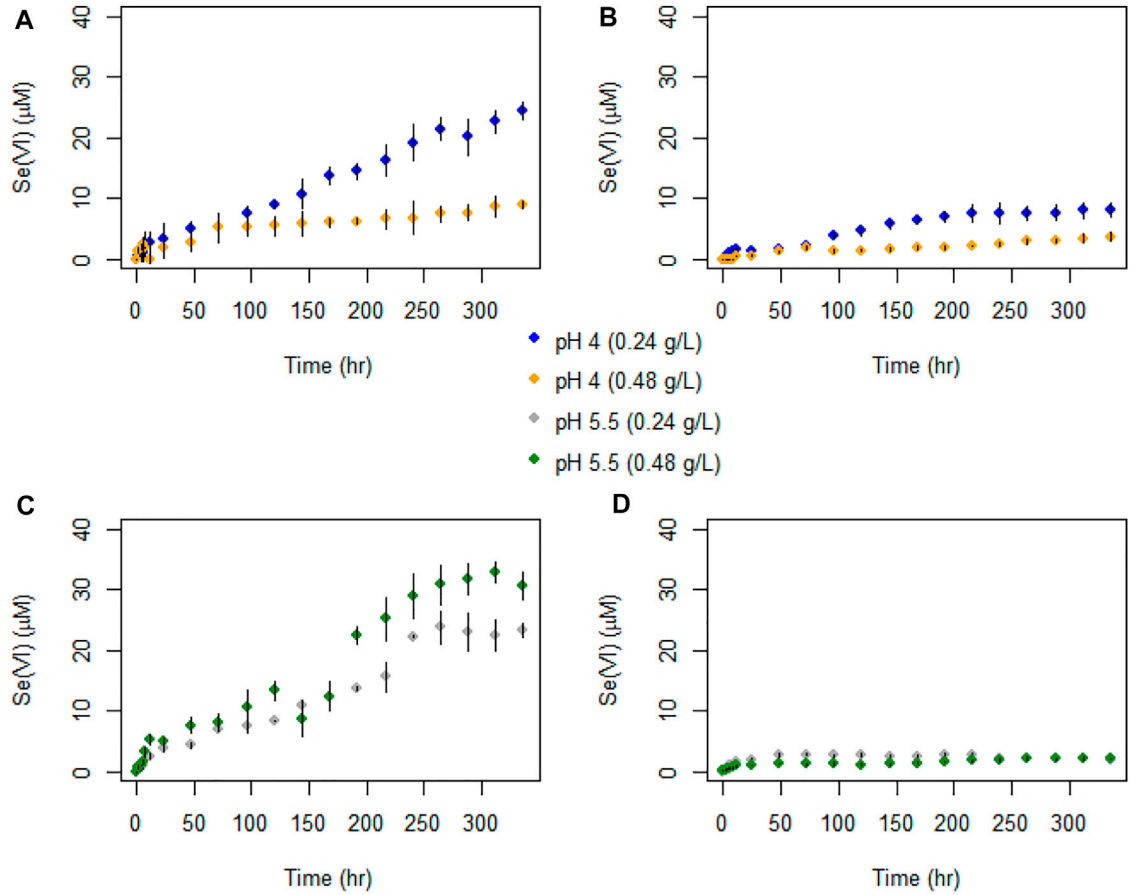

FIGURE 5 | Temporal evolution of Se(VI) concentrations in batch experiments with **(A)** AR birnessite at pH 4, **(B)** SG birnessite at pH 4, **(C)** AR birnessite at pH 5.5, and **(D)** SG birnessite at pH 5.5. All experiments were performed at 25°C with an initial Se(IV) of 120 μM. Error bars represent standard deviations for concentrations measured in duplicates.

Mn(II) and Mn(IV) (insoluble), which could explain the apparent presence of Mn(II) in excess of the amount needed to generate the observed Se(VI) concentrations. For AR-birnessite experiments, the aqueous Mn concentrations indicate that approximately 1% of the birnessite, by mass, dissolved, whereas for SG experiments it was 2%. However, it is clear that Se(IV) oxidation occurred and the experiments yield a clear and consistent quantification of Se isotope fractionation.

In the pH 5.5 experiments, aqueous Mn concentrations remained very low (<1 μM) at all times. This stark difference is probably caused by adsorption of Mn(II). Birnessite has a low point zero charge (pzc), which ranges from 1 to 2 (Tripathy et al., 2001). As pH of the solution increases, the surface negative charge on the oxide surface increases and this would cause Mn(II) to be adsorbed more strongly at pH 5.5 than pH 4.0.

Isotopic Fractionation

The Se isotopic fractionation observed in our experiments results from mass-dependent kinetic isotope effects caused by changes in the local bonding environment of Se as it is transformed from Se(IV) to Se(VI). Tan et al. (2020) have established that Se isotope exchange between aqueous Se(IV) and Se(VI) is extremely slow; isotopic equilibrium is achieved only after 1000s of years. This fact, combined with the fact that our experiments do not approach chemical equilibrium, requires that the observed Se isotope fractionation is rationalized using a kinetic framework. In the simplest case, kinetic isotope effects arise from the fact that bonds involving lighter isotopes have higher zero-point energies than those involving heavier isotopes (Schauble, 2004). Consequently, bonds involving lighter isotopes are more easily broken, and in a single-step reaction with no back reaction, lighter isotopes react at a faster rate.

However, Se(IV) oxidation by birnessite is not a simple, single-step reaction. The overall chemical reaction consists of a chain of multiple steps, with ephemeral intermediate products and potential back-reaction across some steps. According to Scott and Morgan (1996), the first step involves the formation of a surface complex between the Se(IV) and Mn(IV) on the oxide surface. The rate limiting step is the transfer of electrons from Se(IV) to Mn(IV), resulting in the formation of Mn(II) and Se(VI), followed by desorption of the surface-bound oxidized anion and reduced metal ion. According to kinetic isotopic fractionation theory, the fractionation produced by the overall reaction depends not only on the fractionation induced by each

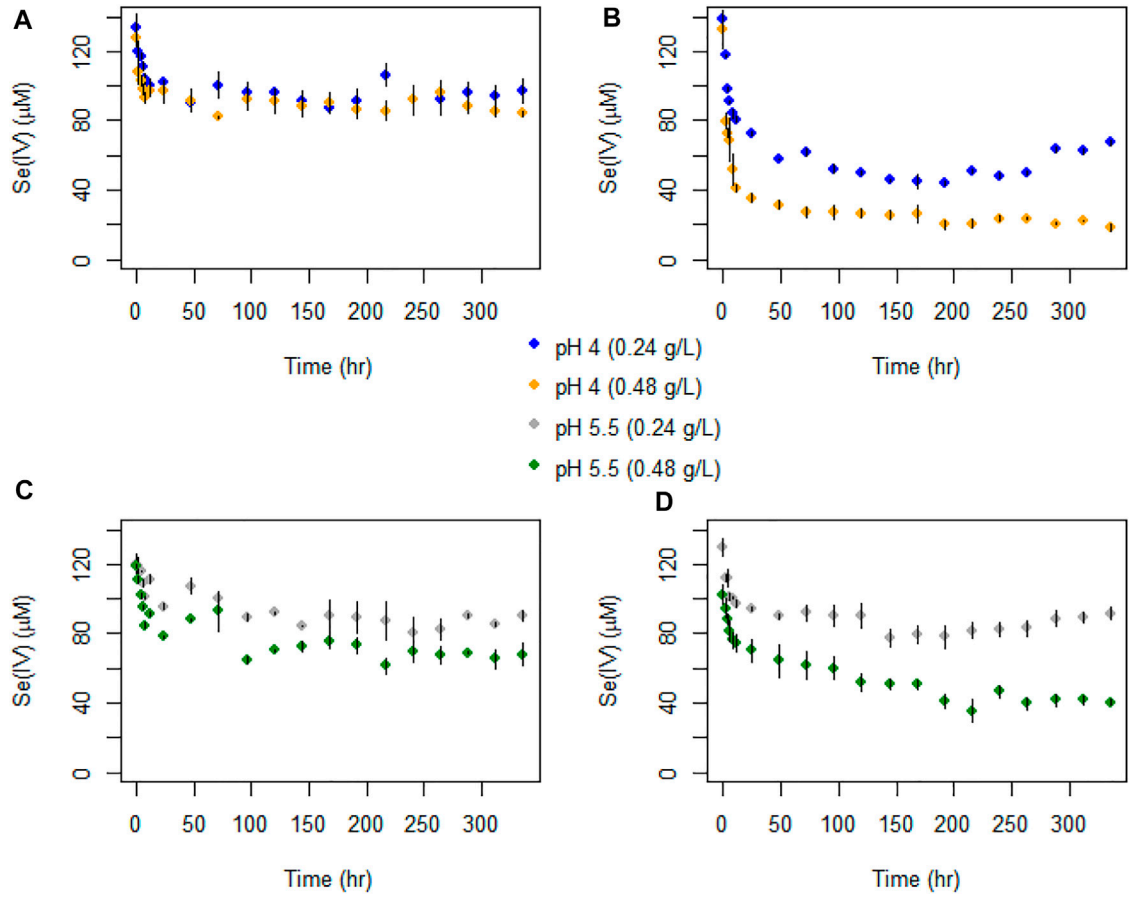

FIGURE 6 | Temporal evolution of Se(IV) concentrations in batch experiments with **(A)** AR birnessite at pH 4, **(B)** SG birnessite at pH 4, **(C)** AR birnessite at pH 5.5, and **(D)** SG birnessite at pH 5.5. All experiments were performed at 25°C with an initial Se(IV) concentration of 120 μM. Error bars represent SDs for concentrations measured in duplicates.

reaction step, but also on the kinetic characteristics of that step and the others in the chain (Rees, 1973; Schauble, 2004). Despite the net forward direction of the reaction, rapid back-reaction at one or more individual steps may occur. This promotes an approach to isotopic equilibrium between the product and reactant of any such step. Accordingly, each step may impart a characteristic kinetic isotope effect if it is a dominantly forward-reacting step or, at the other extreme, equilibrium isotope fractionation between the reactant and product.

The concept of a "rate-limiting step" from kinetic theory (Atkins.and de Paula, 2008) is crucial here: the step with the least favorable kinetics (i.e., the greatest activation energy) is the reaction "bottleneck," and Se atoms that progress beyond this step have very little chance of back-reacting across it. As a result, isotopic fractionation occurring in subsequent steps can have no effect on the isotopic fractionation of the overall reaction; this is because all the Se reaching those steps proceeds to the end of the reaction chain. This leads to a general rule: the isotopic fractionation of the complete reaction is the sum of the fractionations for each step up to, and including, the rate limiting step, with later steps not contributing to the overall isotopic fractionation even if they induce large kinetic isotope effects. This rule and more complex models of reaction chains have been applied to S and C isotope fractionation for many years (Rees, 1973; Canfield, 2001; Hayes, 2001; Brunner and Bernasconi, 2005; Johnston et al., 2007; Bradley et al., 2016).

In the specific case of Se(IV) oxidation by birnessite, steps involving electron transfers and coordination changes have the potential to fractionate Se isotopes strongly, due to the large changes in the chemical bonds. In these steps, the products involve Se in a higher valence and/or with shorter, stiffer bonds. If the steps are close to equilibrium, or have rapid back-reaction, then their products will tend to be enriched in heavier isotopes relative to their reactants. On the other hand, it is also possible that simple kinetic isotope effects, with lighter isotopes reacting faster than heavier ones, may be generated by one or more reactions steps in the chain. Thus, kinetic fractionation theory allows the product for the overall reaction to be either isotopically lighter or heavy.

The negative $\delta^{82/76}$Se shift observed in our experiments suggests that the major bonding changes involved in the oxidation reaction do not dominate the kinetic isotope

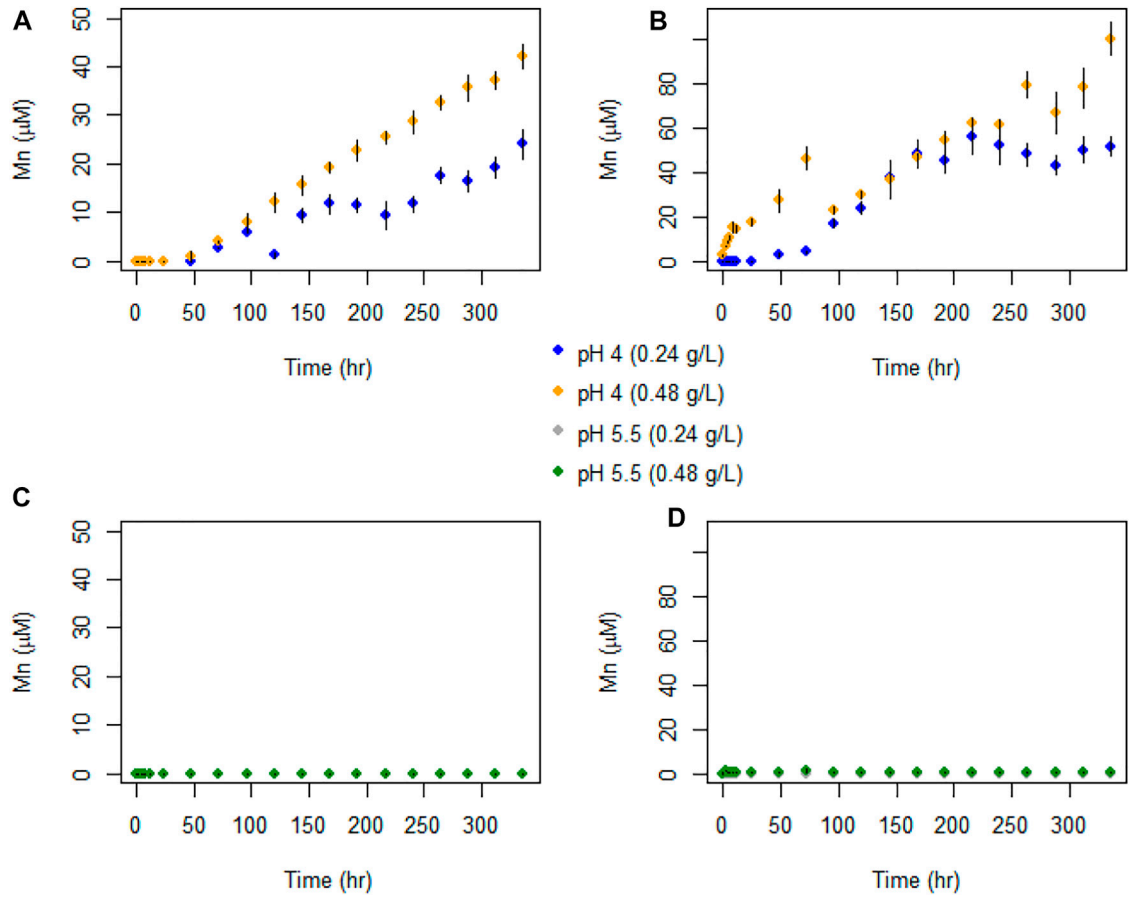

FIGURE 7 | Temporal evolution of Mn(II) concentrations in batch experiments with **(A)** AR birnessite at pH 4, **(B)** SG birnessite at pH 4), **(C)** AR birnessite at pH 5.5, and **(D)** SG birnessite at pH 5.5. All experiments were performed at 25°C with an initial Se(IV) of 120 μM. Error bars represent SDs for concentrations measured in duplicates.

fractionation of the overall reaction. Se(VI)-Se(IV) redox reactions have the potential to induce $\delta^{82/76}$Se shifts of several per mil (Johnson and Bullen, 2004; Li and Liu, 2011). The

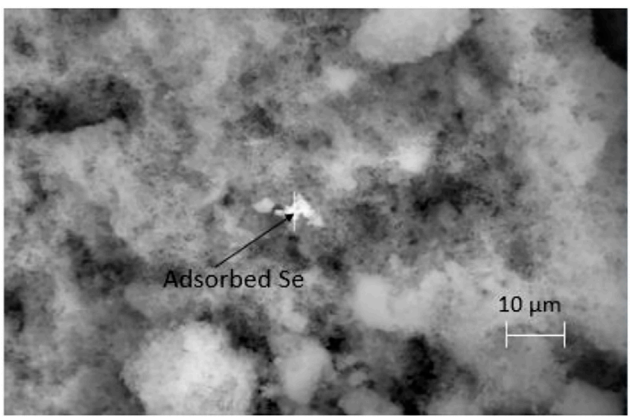

FIGURE 8 | SEM image of the precipitate collected at the end of the experiment carried out at pH 4 with 0.24 g L^{-1} AR birnessite. Adsorbed Se is identified in a single bright spot here, however lighter spots in the vicinity were also shown to have significant but lower amounts of Se by weight.

electron transfer and coordination change steps may induce large fractionations when their effects are manifested, but for an oxidation reaction, the product should be isotopically heavy. In the present study, the product was isotopically light and the magnitude was relatively small, suggesting that the rate-limiting step was prior to the electron transfer and coordination change steps. One possible contributor to the observed fractionation is the Se(IV) adsorption step. Xu et al. (2020) reported that, at pH 5, adsorption of Se(IV) onto Fe oxides and β-MnO_2 (pyrolusite) resulted in an equilibrium fractionation of −0.9 to −1.2‰ (adsorbed Se(IV) was enriched in lighter isotopes) that was approached within several hours. In our experiments, the time scale for Se(IV) oxidation was long, and thus adsorbed Se(IV) was likely close to isotopic equilibrium with aqueous Se(IV) and may have been shifted toward lower $\delta^{82/76}$Se. This step could have provided some of the $\delta^{82/76}$Se shift observed for the overall Se(IV) oxidation reaction. The Xu et al. (2020) results do not apply directly to our experiments, as β-MnO_2 differs from birnessite, but the Se(IV) adsorption step is likely a partial driver of the observed $\delta^{82/76}$Se shift.

As is common in studies of kinetic isotope effects, we lack detailed knowledge regarding the reaction mechanism and the rate-limiting step; it is therefore difficult to rationalize fully the

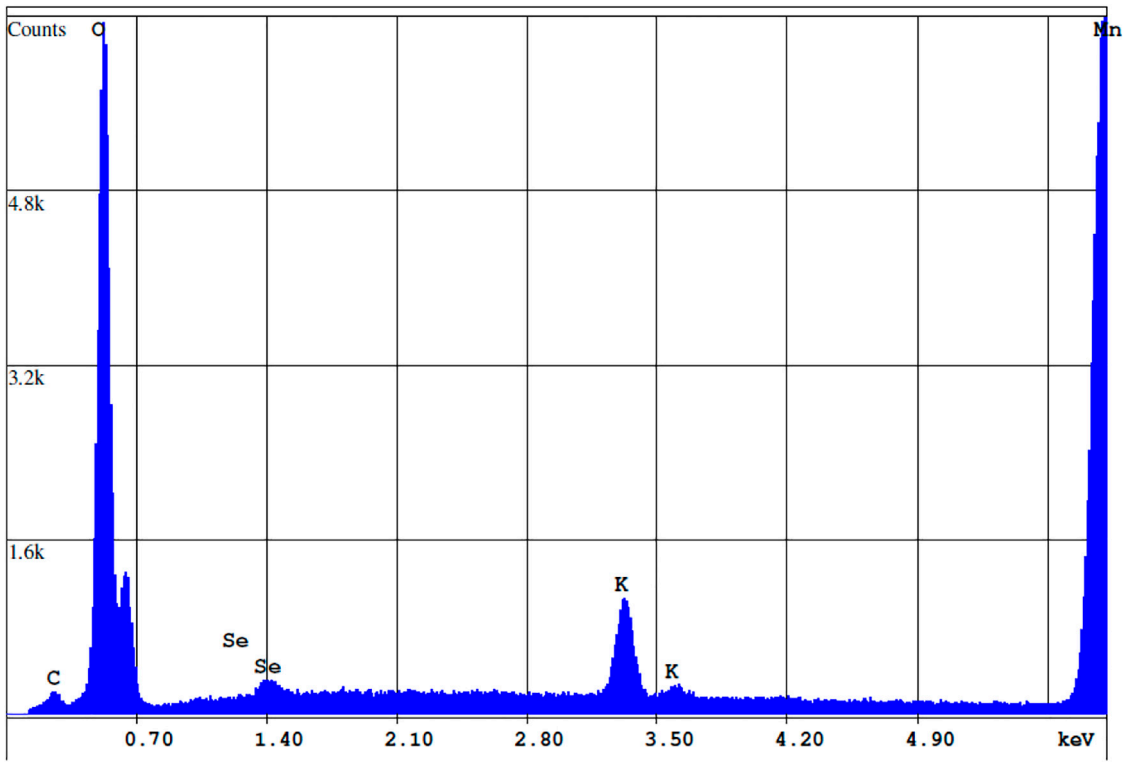

FIGURE 9 | EDS spectrum of the precipitate cross-section highlighted in **Figure 8**. Concentrations of Mn, Se, O, and K are 66.22, 1.2, 29.38, and 3.21% by weight respectively.

direction and magnitude of the observed Se isotope fractionation. Furthermore, it is difficult to predict how much the Se isotope fractionation may vary across the range of conditions under which we may wish to apply these results. It is possible that the conditions in some natural settings (e.g., pH, aqueous matrix, and characteristics of the birnessite) could change the rate-limiting step of the reaction or otherwise alter the kinetics in a way that would change the isotopic fractionation significantly. Further experiments over a wider range of solution compositions, birnessite composition and structure, and pH would be helpful in this regard. Experiments with birnessite-bearing natural soils and field-collected waters might also be helpful. However, the fact that our results did not differ between two forms of birnessite with strongly contrasting Se(IV) oxidation kinetics, and also did not differ from pH 4 to pH 5.5, suggests that the Se isotopic fractionation is controlled by some invariant reaction characteristics that may apply to a wide range of conditions.

A previous study determined the Se isotope fractionation induced by a different Se(IV) oxidation mechanism. Johnson and, Bullen, (2004) oxidized Se(IV) with H_2O_2 in a 0.8 M NaOH solution and found no detectable Se isotope fractionation at the 0.2‰ level. This reaction is clearly not relevant in natural settings, and it is not surprising that the isotopic fractionation differed from that observed in our experiments, given the very different chemical reaction involved.

Environmental Implications

Selenium isotope fractionation induced by reduction of Se(VI) to Se(IV) has been studied well, as it is helpful to develop Se isotopes as indicators of Se immobilization *via* reduction. However, in many Se-contaminated settings, modern weathering settings, or in ancient settings relevant to paleoredox studies, Se(IV) oxidation may be the dominant process, or both oxidation and reduction may occur in a single setting. At weathering conditions, oxidation of solid, Se-bearing phases such as sulphide minerals and organic matter, without any back-reduction, should tend to produce Se that is isotopically similar to the solid phases. This is because of fundamental mass-balance considerations related to the fact that weathering reactions can only access Se atoms available on surfaces, and each successive layer of solid must be removed before the next layer can be exposed (Wang et al., 2015). According to the results of the present study, the released Se(IV) could be partially oxidized to produce isotopically light Se(VI). Since Se(VI) is highly mobile, whereas Se(IV) is likely to adsorb onto solid surfaces, Se mobilized by weathering may be isotopically light. However, if partial reduction of aqueous Se(VI) or Se(IV) occurred, it would tend to drive those species toward isotopically heavy compositions (Wasserman et al., 2021). Overall, the isotopic fractionation observed in this study provides an improved understanding of Se isotope dynamics in weathering systems.

In some systems, redox cycling of Se may occur in response to seasonal changes (e.g., wet season anoxia in soils and/or aquifers) or the presence of both oxidizing and reducing zones. Schilling et al. (2015) generated $\delta^{82/76}$Se data for soils, sequential extracts of soils, and irrigation water in a Se-contaminated field site in the Punjab, India. A clear pattern was observed, whereby deeper soils had lower $\delta^{82/76}$Se values relative to those of the top 10 cm. This suggests that mobile Se(VI) transported downward from the Se-rich upper soils was isotopically light, which in turn could occur only as a result of some process involving Se isotope fractionation as immobile Se was oxidized to form Se(VI). The authors suggested that Se(IV) oxidation was a likely driver of this pattern. The results of the present study support this interpretation.

More broadly, we assert that our improved knowledge of Se isotope shifts expected in the many groundwater and soil systems that contain coexisting Se(IV) and birnessite aids in the use of $\delta^{82/76}$Se data as a powerful complement to the more commonly used Se concentration data. Redox cycling of Se is complex and it is often difficult to untangle coupled redox and transport processes. $\delta^{82/76}$Se measurements provide more direct indicators of redox reaction, as compared to concentration data, and improve insights into these complex systems. The present study provides an important parameter need to interpret those data, in modern systems as well as in rocks used to infer redox conditions in ancient environments.

DATA AVAILABILITY STATEMENT

The original contributions presented in the study are included in the article/Supplementary Material, further inquiries can be directed to the corresponding author.

AUTHOR CONTRIBUTIONS

PD, KS, NW, TJ, and CP contributed equally to the final version of the manuscript.

ACKNOWLEDGMENTS

This material is based upon work supported by the National Science Foundation (NSF) under EAR 15-29830. The authors thank Tim Teague at the Department of Earth and Planetary Science (UC Berkeley) for use of the Zeiss EVO-10 Variable Vacuum SEM.

REFERENCES

Atkins, P. W., and de Paula, J. (2008). Physical Chemistry. *Encycl. Earth Sci. Ser.* 555, 10642. doi:10.5005/jp/books/10642_2

Balistrieri, L. S., and Chao, T. T. (1990). Adsorption of Selenium by Amorphous Iron Oxyhydroxide and Manganese Dioxide. *Geochimica Cosmochimica Acta* 54 (3), 739–751. doi:10.1016/0016-7037(90)90369-V

Birkner, N., and Navrotsky, A. (2017). Thermodynamics of Manganese Oxides: Sodium, Potassium, and Calcium Birnessite and Cryptomelane. *Proc. Natl. Acad. Sci. U.S.A.* 114 (7), E1046–E1053. doi:10.1073/pnas.1620427114

Birnessite Mineral Data (2019). Available at: http://www.webmineral.com/data/Birnessite.shtml#.XeB3t-hKi00 (Accessed at September 5, 2021)

Bradley, A. S., Leavitt, W. D., Schmidt, M., Knoll, A. H., Girguis, P. R., and Johnston, D. T. (2016). Patterns of Sulfur Isotope Fractionation during Microbial Sulfate Reduction. *Geobiology* 14 (1), 91–101. doi:10.1111/gbi.12149

Brunauer, S., Emmett, P. H., and Teller, E. (1938). Adsorption of Gases in Multimolecular Layers. *J. Am. Chem. Soc.* 60 (2), 309–319. doi:10.1021/ja01269a023

Brunner, B., and Bernasconi, S. M. (2005). A Revised Isotope Fractionation Model for Dissimilatory Sulfate Reduction in Sulfate Reducing Bacteria. *Geochimica Cosmochimica Acta* 69 (20), 4759–4771. doi:10.1016/j.gca.2005.04.015

Canfield, D. E. (2001). Biogeochemistry of Sulfur Isotopes. *Rev. Mineralogy Geochem.* 43 (1), 607–636. doi:10.2138/gsrmg.43.1.607

Catalano, J. G., Zhang, Z., Fenter, P., and Bedzyk, M. J. (2006). Inner-sphere Adsorption Geometry of Se(IV) at the Hematite (100)-water Interface. *J. Colloid Interface Sci.* 297 (2), 665–671. doi:10.1016/j.jcis.2005.11.026

Cheney, M. A., Jose, R., Banerjee, A., Bhowmik, P. K., Qian, S., and Okoh, J. M. (2009). Synthesis and Characterization of Birnessite and Cryptomelane Nanostructures in Presence of Hoffmeister Anions. *J. Nanomater.* 2009, 1–8. doi:10.1155/2009/940462

Ching, S., Landrigan, J. A., Jorgensen, M. L., Duan, N., Suib, S. L., and O'Young, C. L. (1995). Sol-gel Synthesis of Birnessite from KMnO4 and Simple Sugars. *Chem. Mat.* 7 (9), 1604–1606. doi:10.1021/cm00057a003

Clark, S. K., and Johnson, T. M. (2010). Selenium Stable Isotope Investigation into Selenium Biogeochemical Cycling in a Lacustrine Environment: Sweitzer Lake, Colorado. *J. Environ. Qual.* 39 (6), 2200–2210. doi:10.2134/JEQ2009.0380

Crowther, D. L., Dillard, J. G., and Murray, J. W. (1983). The Mechanisms of Co(II) Oxidation on Synthetic Birnessite. *Geochimica Cosmochimica Acta* 47 (8), 1399–1403. doi:10.1016/0016-7037(83)90298-3

Downs, R. T., and Hall-Wallace, M. (2006). American Mineralogist Crystal Structure Database. *Choice Rev. Online* 43, 43Sup–0302. doi:10.5860/choice.43sup-0302

Essington, M. E. (2003). *Soil and Water Chemistry*. Boca Raton, Florida, United States: CRC Press. doi:10.1201/b12397

Fendorf, S. E. (1995). Surface Reactions of Chromium in Soils and Waters. *Geoderma* 67 (1–2), 55–71. doi:10.1016/0016-7061(94)00062-F

Feng, Q., Kanoh, H., and Ooi, K. (1999). Manganese Oxide Porous Crystals. *J. Mat. Chem.* 9, 319–333. doi:10.1039/a805369c

Fernández-Martínez, A., and Charlet, L. (2009). Selenium Environmental Cycling and Bioavailability: A Structural Chemist Point of View. *Rev. Environ. Sci. Biotechnol.* 8, 81–110. doi:10.1007/s11157-009-9145-3

Händel, M., Rennert, T., and Totsche, K. U. (2013). A Simple Method to Synthesize Birnessite at Ambient Pressure and Temperature. *Geoderma* 193-194, 117–121. doi:10.1016/j.geoderma.2012.09.002

Hayes, J. M. (2001). Fractionation of Carbon and Hydrogen Isotopes in Biosynthetic Processes. *Rev. Mineralogy Geochem.* 43 (1), 225–277. doi:10.2138/gsrmg.43.1.225

Johnson, T. M., and Bullen, T. D. (2004). Mass-dependent Fractionation of Selenium and Chromium Isotopes in Low-Temperature Environments. *Rev. Mineralogy Geochem.* 55 (1), 289–317. doi:10.2138/gsrmg.55.1.289

Johnson, T. M., Herbel, M. J., Bullen, T. D., and Zawislanski, P. T. (1999). Selenium Isotope Ratios as Indicators of Selenium Sources and Oxyanion Reduction. *Geochimica Cosmochimica Acta* 63 (18), 2775–2783. doi:10.1016/S0016-7037(99)00279-3

Johnston, D. T., Farquhar, J., and Canfield, D. E. (2007). Sulfur Isotope Insights into Microbial Sulfate Reduction: When Microbes Meet Models. *Geochimica Cosmochimica Acta* 71 (16), 3929–3947. doi:10.1016/j.gca.2007.05.008

Kausch, M., Ng, P., Ha, J., and Pallud, C. (2012). Soil-Aggregate-Scale Heterogeneity in Microbial Selenium Reduction. *Vadose Zone J.* 11 (2), 101–112. doi:10.2136/vzj2011.0101

Kipp, M. A., Algeo, T. J., Stüeken, E. E., and Buick, R. (2020). Basinal Hydrographic and Redox Controls on Selenium Enrichment and Isotopic Composition in Paleozoic Black Shales. *Geochimica Cosmochimica Acta* 287, 229–250. doi:10.1016/j.gca.2019.12.016

Kipp, M. A., Stüeken, E. E., Bekker, A., and Buick, R. (2017).Selenium Isotopes Record Extensive Marine Suboxia during the Great Oxidation Event. *Proc. Natl. Acad. Sci. U.S.A.*, 114 (5), 875–880. doi:10.1073/PNAS.1615867114/SUPPL_FILE/PNAS.1615867114.SD01

Lafferty, B. J., Ginder-Vogel, M., and Sparks, D. L. (2010). Arsenite Oxidation by a Poorly Crystalline Manganese-Oxide 1. Stirred-Flow Experiments. *Environ. Sci. Technol.* 44 (22), 8460–8466. doi:10.1021/es102013p

Li, X., and Liu, Y. (2011). Equilibrium Se Isotope Fractionation Parameters: A First-Principles Study. *Earth Planet. Sci. Lett.* 304 (1–2), 113–120. doi:10.1016/j.epsl.2011.01.022

Ling, F. T., Post, J. E., Heaney, P. J., Kubicki, J. D., and Santelli, C. M. (2017). Fourier-transform Infrared Spectroscopy (FTIR) Analysis of Triclinic and Hexagonal Birnessites. *Spectrochimica Acta Part A Mol. Biomol. Spectrosc.* 178, 32–46. doi:10.1016/j.saa.2017.01.032

Lu, A., Gao, X., Wang, C., Gao, Y., Zheng, D., Chen, T., et al. (2007). Natural Cryptomelane and its Potential Application in the Adsorption of Heavy Metal Cadmium. *J. Mineralogical Petrological Sci.* 102 (4), 217–225. doi:10.2465/jmps.060412

Manning, B. A., Fendorf, S. E., Bostick, B., and Suarez, D. L. (2002). Arsenic(III) Oxidation and Arsenic(V) Adsorption Reactions on Synthetic Birnessite. *Environ. Sci. Technol.* 36 (5), 976–981. doi:10.1021/es0110170

McKenzie, R. M. (1971). The Synthesis of Birnessite, Cryptomelane, and Some Other Oxides and Hydroxides of Manganese. *Mineral. Mag.* 38, 493–502. doi:10.1180/minmag.1971.038.296.12

Mitchell, K., Mansoor, S. Z., Mason, P. R. D., Johnson, T. M., and Van Cappellen, P. (2016). Geological Evolution of the Marine Selenium Cycle: Insights from the Bulk Shale $\delta^{82/76}$Se Record and Isotope Mass Balance Modeling. *Earth Planet. Sci. Lett.* 441, 178–187. doi:10.1016/J.EPSL.2016.02.030

Mitchell, K., Mason, P. R. D., Van Cappellen, P., Johnson, T. M., Gill, B. C., Owens, J. D., et al. (2012). Selenium as Paleo-Oceanographic Proxy: A First Assessment. *Geochimica Cosmochimica Acta* 89, 302–317. doi:10.1016/J.GCA.2012.03.038

Murray, J.W., Balistrieri, L.S., and Paul, B. (1984). The oxidation state of manganese in marine sediments and ferromanganese nodules. *Geochimica et Cosmochimica Acta.* 48, 1237–1247.

Ohlendorf, H. M., Hothem, R. L., Bunck, C. M., and Marois, K. C. (1990). Bioaccumulation of Selenium in Birds at Kesterson Reservoir, California. *Arch. Environ. Contam. Toxicol.* 19, 495–507. doi:10.1007/BF01059067

Peak, D., and Sparks, D. L. (2002). Mechanisms of Selenate Adsorption on Iron Oxides and Hydroxides. *Environ. Sci. Technol.* 36 (7), 1460–1466. doi:10.1021/es0156643

Post, J. E., and Veblen, D. R. (1990). Crystal Structure Determinations of Synthetic Sodium, Magnesium, and Potassium Birnessite Using TEM and the Rietveld Method. *Am. Mineralogist* 75, 477

Post, J. E. (1999). Manganese Oxide Minerals: Crystal Structures and Economic and Environmental Significance. *Proc. Natl. Acad. Sci. U.S.A.* 96 (7), 3447–3454. doi:10.1073/pnas.96.7.3447

Post, J. E., Von Dreele, R. B., and Buseck, P. R. (1982). Symmetry and Cation Displacements in Hollandites: Structure Refinements of Hollandite, Cryptomelane and Priderite. *Acta Crystallogr. Sect. B* 38 (4), 1056–1065. doi:10.1107/s0567740882004968

Potter, R. M., and Rossman, G. R. (1979). The Tetravalent Manganese Oxides: Identification, Hydration, and Structural Relationships by Infrared Spectroscopy. *Am. Mineralogist* 64, 1199

Power, L. E., Arai, Y., and Sparks, D. L. (2005). Zinc Adsorption Effects on Arsenite Oxidation Kinetics at the Birnessite–Water Interface. *Environ. Sci. Technol.* 39 (1), 181–187. doi:10.1021/es049922i

Qiu, G., Li, Q., Yu, Y., Feng, X., Tan, W., and Liu, F. (2011). Oxidation Behavior and Kinetics of Sulfide by Synthesized Manganese Oxide Minerals. *J. Soils Sediments* 11 (8), 1323–1333. doi:10.1007/s11368-011-0381-0

Rees, C. E. (1973). A Steady-State Model for Sulphur Isotope Fractionation in Bacterial Reduction Processes. *Geochimica Cosmochimica Acta* 37 (5), 1141–1162. doi:10.1016/0016-7037(73)90052-5

Schauble, E. A. (2004). Applying Stable Isotope Fractionation Theory to New Systems. *Rev. Mineralogy Geochem.* 55 (1), 65–111. doi:10.2138/GSRMG.55.1.65

Schilling, K., Basu, A., Wanner, C., Sanford, R. A., Pallud, C., Johnson, T. M., et al. (2020). Mass-dependent Selenium Isotopic Fractionation during Microbial Reduction of Seleno-Oxyanions by Phylogenetically Diverse Bacteria. *Geochimica Cosmochimica Acta* 276, 274–288. doi:10.1016/j.gca.2020.02.036

Schilling, K., Johnson, T. M., Dhillon, K. S., and Mason, P. R. D. (2015). Fate of Selenium in Soils at a Seleniferous Site Recorded by High Precision Se Isotope Measurements. *Environ. Sci. Technol.* 49 (16), 9690–9698. doi:10.1021/ACS.EST.5B00477/SUPPL_FILE/ES5B00477_SI_001.PDF

Schilling, K., Johnson, T. M., and Wilcke, W. (2011). Isotope Fractionation of Selenium during Fungal Biomethylation by Alternaria Alternata. *Environ. Sci. Technol.* 45 (7), 2670–2676. doi:10.1021/es102926p

Schirmer, T., Koschinsky, A., and Bau, M. (2014). The Ratio of Tellurium and Selenium in Geological Material as a Possible Paleo-Redox Proxy. *Chem. Geol.* 376, 44–51. doi:10.1016/j.chemgeo.2014.03.005

Schuler, C. A., Anthony, R. G., and Ohlendorf, H. M. (1990). Selenium in Wetlands and Waterfowl Foods at Kesterson Reservoir, California, 1984. *Arch. Environ. Contam. Toxicol.* 19 (6), 845–853. doi:10.1007/BF01055049

Scott, M. J., and Morgan, J. J. (1995). Reactions at Oxide Surfaces. 1. Oxidation of As(III) by Synthetic Birnessite. *Environ. Sci. Technol.* 29 (8), 1898–1905. doi:10.1021/es00008a006

Scott, M. J., and Morgan, J. J. (1996). Reactions at Oxide Surfaces. 2. Oxidation of Se(IV) by Synthetic Birnessite. *Environ. Sci. Technol.* 30 (6), 1990–1996. doi:10.1021/es950741d

Shrimpton, H. K., Blowes, D. W., and Ptacek, C. J. (2015).Fractionation of Selenium during Selenate Reduction by Granular Zerovalent Iron. *Environ. Sci. Technol.*, 49(19), 11688–11696. doi:10.1021/ACS.EST.5B01074/SUPPL_FILE/ES5B01074_SI_001

Stüeken, E. E., and Kipp, M. A. (2020). *Selenium Isotope Paleobiogeochemistry*. United Kingdom: Cambridge. doi:10.1017/9781108782203

Tebo, B. M., Bargar, J. R., Clement, B. G., Dick, G. J., Murray, K. J., Parker, D., et al. (2004). Biogenic Manganese Oxides: Properties and Mechanisms of Formation. *Annu. Rev. Earth Planet. Sci.* 32 (1), 287–328. doi:10.1146/annurev.earth.32.101802.120213

Tripathy, S. S., Kanungo, S. B., and Mishra, S. K. (2001). The Electrical Double Layer at Hydrous Manganese Dioxide/Electrolyte Interface. *J. Colloid Interface Sci.* 241 (1), 112–119. doi:10.1006/JCIS.2001.7722

Vicat, J., Fanchon, E., Strobel, P., and Tran Qui, D. (1986). The Structure of $K_{1.33}Mn_8O_{16}$ and Cation Ordering in Hollandite-type Structures. *Acta Crystallogr. Sect. B* 42 (2), 162–167. doi:10.1107/S0108768186098415

Villalobos, M., Escobar-Quiroz, I. N., and Salazar-Camacho, C. (2014). The Influence of Particle Size and Structure on the Sorption and Oxidation Behavior of Birnessite: I. Adsorption of As(V) and Oxidation of As(III). *Geochimica Cosmochimica Acta* 125, 564–581. doi:10.1016/j.gca.2013.10.029

Wang, X., Johnson, T. M., and Lundstrom, C. C. (2015). Low Temperature Equilibrium Isotope Fractionation and Isotope Exchange Kinetics between U(IV) and U(VI). *Geochimica Cosmochimica Acta* 158, 262–275. doi:10.1016/J.GCA.2015.03.006

Wang, Y., Feng, X., Villalobos, M., Tan, W., and Liu, F. (2012). Sorption Behavior of Heavy Metals on Birnessite: Relationship with its Mn Average Oxidation State and Implications for Types of Sorption Sites. *Chem. Geol.* 292-293, 25–34. doi:10.1016/j.chemgeo.2011.11.001

Wang, Z., and Giammar, D. E. (2015). Metal Contaminant Oxidation Mediated by Manganese Redox Cycling in Subsurface Environment. *ACS Symp. Ser.* 1197, 29–50. doi:10.1021/bk-2015-1197.ch002

Wasserman, N. L., Schilling, K., Johnson, T. M., and Pallud, C. (2021). Selenium Isotope Shifts during the Oxidation of Selenide-Bearing Minerals. *ACS Earth Space Chem.* 5 (5), 1140–1149. doi:10.1021/ACSEARTHSPACECHEM.1C00036/SUPPL_FILE/SP1C00036_SI_001.PDF

Xu, W., Qin, H.-B., Zhu, J.-M., Johnson, T. M., Tan, D., Liu, C., et al. (2021). Selenium Isotope Fractionation during Adsorption onto Montmorillonite and Kaolinite. *Appl. Clay Sci.* 211, 106189. doi:10.1016/J.CLAY.2021.106189

Xu, W., Zhu, J.-M., Johnson, T. M., Wang, X., Lin, Z.-Q., Tan, D., et al. (2020). Selenium Isotope Fractionation during Adsorption by Fe, Mn and Al Oxides. *Geochimica Cosmochimica Acta* 272, 121–136. doi:10.1016/j.gca.2020.01.001

Zeng, H. (2009). Selenium as an Essential Micronutrient: Roles in Cell Cycle and Apoptosis. *Molecules* 14 (3), 1263–1278. doi:10.3390/molecules14031263

Zhu, J.-M., Johnson, T. M., Clark, S. K., and Zhu, X.-K. (2008). High Precision Measurement of Selenium Isotopic Composition by Hydride Generation Multiple Collector Inductively Coupled Plasma Mass Spectrometry with a 74Se-77Se Double Spike. *Chin. J. Anal. Chem.* 36 (10), 1385–1390. doi:10.1016/S1872-2040(08)60075-4

Zhu, J.-M., Johnson, T. M., Clark, S. K., Zhu, X.-K., and Wang, X.-L. (2014). Selenium Redox Cycling during Weathering of Se-Rich Shales: A Selenium Isotope Study. *Geochimica Cosmochimica Acta* 126, 228–249. doi:10.1016/J.GCA.2013.11.004

Conflict of Interest: The authors declare that the research was conducted in the absence of any commercial or financial relationships that could be construed as a potential conflict of interest.

Publisher's Note: All claims expressed in this article are solely those of the authors and do not necessarily represent those of their affiliated organizations, or those of the publisher, the editors and the reviewers. Any product that may be evaluated in this article, or claim that may be made by its manufacturer, is not guaranteed or endorsed by the publisher.

frontiers | Frontiers in Earth Science

ORIGINAL RESEARCH
published: 22 July 2022
doi: 10.3389/feart.2022.913687

Lithium Isotope Geochemistry in the Barton Peninsula, King George Island, Antarctica

Jong-Sik Ryu[1], Hyoun Soo Lim[2], Hye-Bin Choi[3], Ji-Hoon Kim[4], Ok-Sun Kim[5] and Nathalie Vigier[6]*

[1]Department of Earth and Environmental Sciences, Pukyong National University, Busan, South Korea, [2]Department of Geological Sciences, Pusan National University, Busan, South Korea, [3]Research Center for Geochronology and Isotope Analysis, Korea Basic Science Institute, Cheongju-si, South Korea, [4]Petroleum and Marine Research Division, Korea Institute of Geoscience and Mineral Resources, Daejeon, South Korea, [5]Division of Polar Life Sciences, Korea Polar Research Institute, Incheon, South Korea, [6]LOV, CNRS, UPMC, UMR 7093, Villefranche-Sur-Mer, France

Lithium (Li) has two stable isotopes, ^{6}Li and ^{7}Li, whose large relative mass difference is responsible for significant isotopic fractionation during physico-chemical processes, allowing Li isotopes to be a good tracer of continental chemical weathering. Although physical erosion is dominant in the Polar regions due to glaciers, increasing global surface temperature may enhance chemical weathering, with possible consequences on carbon biogeochemical cycle and nutriment flux to the ocean. Here, we examined elemental and Li isotope geochemistry of meltwaters, suspended sediments, soils, and bedrocks in the Barton Peninsula, King George Island, Antarctica. Li concentrations range from 8.7 nM to 23.3 μM in waters, from 0.01 to 1.43 ppm in suspended sediments, from 9.56 to 36.9 ppm in soils, and from 0.42 to 28.3 ppm in bedrocks. δ^{7}Li values are also variable, ranging from +16.4 to +41.1‰ in waters, from −0.4 to +13.4‰ in suspended sediments, from −2.5 to +6.9‰ in soils, and from −1.8 to +11.7‰ in bedrocks. Elemental and Li isotope geochemistry reveals that secondary phase formation during chemical weathering mainly control dissolved δ^{7}Li values, rather than a mixing with sea salt inputs from atmosphere or ice melting. Likewise, δ^{7}Li values of suspended sediments and soils lower than those of bedrocks indicate modern chemical weathering with mineral neoformation. This study suggests that increasing global surface temperature enhances modern chemical weathering in Antarctica, continuing to lower δ^{7}Li values in meltwater with intense water-rock interactions.

Keywords: Li isotopes, chemical weathering, meltwater, mineral neoformation, Antarctica

OPEN ACCESS

Edited by:
Kang-Jun Huang,
Northwest University, China

Reviewed by:
Zhangdong Jin,
Institute of Earth Environment (CAS), China
Shijun Jiang,
Hohai University, China

****Correspondence:***
Jong-Sik Ryu
jongsikryu@pknu.ac.kr

Specialty section:
This article was submitted to Geochemistry, a section of the journal Frontiers in Earth Science

Received: *06 April 2022*
Accepted: *21 June 2022*
Published: *22 July 2022*

Citation:
Ryu J-S, Lim HS, Choi H-B, Kim J-H, Kim O-S and Vigier N (2022) Lithium Isotope Geochemistry in the Barton Peninsula, King George Island, Antarctica. Front. Earth Sci. 10:913687. doi: 10.3389/feart.2022.913687

1 INTRODUCTION

Chemical weathering of silicate rocks consumes atmospheric CO_2, releases solutes to ocean *via* river, and controls temporal variations in seawater chemistry. Therefore, understanding of silicate weathering has been highlighted to elucidate the global carbon cycle on a geological timescale (Walker et al., 1981; Berner, 2003). Lithium (Li) has two stable isotopes, ^{6}Li and ^{7}Li, whose large relative mass difference is responsible for significant isotopic fractionation during physico-chemical processes. The formation of secondary phases, especially clay minerals, preferentially takes up light isotope (i.e., ^{6}Li), driving residual waters isotopically heavy (Pistiner and Henderson, 2003; Vigier

et al., 2008; Pogge von Strandmann et al., 2010; Wimpenny et al., 2010a), while mineral dissolution is associated with little isotope fractionation (Pistiner and Henderson, 2003; Wimpenny et al., 2010b; Verney-Carron et al., 2011). In this context, Li isotopes have proved to be the most useful proxy for tracing the type and intensity of silicate weathering because Li is little in carbonates and Li isotopes are not affected by biological processes (Huh et al., 1998; Huh et al., 2001; Rudnick et al., 2004; Teng et al., 2004; Pogge von Strandmann et al., 2006; Lemarchand et al., 2010; Millot et al., 2010a; Liu et al., 2015). Ryu et al. (2014) assessed various factors controlling Li isotopes in soils developed along a 4 million year humid-environment chronosequence in the Hawaiian Islands, in which basalt weathering and secondary mineral formation mainly controls Li isotopes in these soil profiles.

Increasing global surface temperatures due to rising greenhouse gas levels for the Polar regions will enhances glacial melting, sea ice reduction, and organic matter decomposition in thawed permafrost as well as weathering of rocks (Kling et al., 1991; Oechel et al., 1993; Freeman et al., 2001; Jacobson and Blum, 2003; Serreze and Francis, 2006; Zimov et al., 2006; Schuur et al., 2008; Serreze et al., 2009; Ryu and Jacobson, 2012). Increased river runoff during glacial melting can promote chemical weathering and therefore negative feedbacks occur because chemical weathering of rocks regulates global carbon cycle on both human—and geological-timescales (Sharp et al., 1995). Many previous studies have long emphasized the impact of physical components of the Earth system, such as albedo, sea level, and possibly, ocean circulation (ACIA, 2005; IPCC, 2007). Recently, studies focusing on geochemical aspect have emphasized on the Arctic (Anderson et al., 2000; Tranter, 2003; Lee et al., 2004; Fortner et al., 2005; Bhatia et al., 2010; Wimpenny et al., 2010a; Wimpenny et al., 2011; Ryu and Jacobson, 2012). For example, the geochemistry of Greenland rivers has been examined to characterize dissolved organic matter associated with the ice sheet (Bhatia et al., 2010), to address the behaviors of Mg and Li isotopes during glacial weathering (Wimpenny et al., 2010a; Wimpenny et al., 2011), and to identify carbon cycle feedbacks in the present and future (Ryu and Jacobson, 2012). However, a few studies have been conducted in Antarctica (Lyons et al., 1999; Lyons et al., 2005; Harris et al., 2007; Welch et al., 2010; Witherow et al., 2010). The Barton Peninsula of King George Island, which is the focus of this study, is located in the marginal area of West Antarctica, where climate is warmer and more humid than in other parts of Antarctica (e.g., Campbell and Claridge, 1987), and will be much more sensitive to increasing global surface temperatures. Although previous studies have suggested little chemical weathering occurs in the Barton Peninsula (Lee et al., 2004; Santos et al., 2007), recent studies have indicated that chemical weathering may affect to some extent the water chemistry and soil formation (Lim et al., 2014; Lopes et al., 2019; Lopes et al., 2021).

This study focuses on Li isotopes for various types of samples (i.e., meltwater, lake, seawater, suspended sediment, soil, and bedrock) collected in the Barton Peninsula, in order to identify the various factors affecting water chemistry and then to examine if, how, and to what extent chemical weathering may occur in this area. Results will be compared with Li isotope data previously reported in the Polar regions.

2 MATERIALS AND METHODS

2.1 Study Area

Detailed descriptions of the study area are given in previous studies (e.g., Lee et al., 2004; Lim et al., 2014; Choi et al., 2022). In short, its surface area is approximately 1,310 km^2 and its 92% is covered with glaciers with a maximum thickness of 395 m. The snow cover depth ranges from 2 to 73 cm, and mainly melts in summer (November–March; Jiahong et al., 1998). Ice-free area is exposed only along the shorelines in restricted area but has expanded with an increase of surface temperature (Park et al., 1998), in which relatively various vegetation such as flowering plant, bryophytes and lichens grow (Kim et al., 2007). According to climatic data collected at the King Sejong Station in the Barton Peninsula from 1988 to 1996, the climate is warmer and more humid than other Antarctic areas with an average annual temperature of −1.8°C, relative humidity of 89%, precipitation of 437.6 mm and wind velocity of 7.9 m/s from the northwest and southwest (Lim et al., 2009).

The Barton Peninsula consists mainly of lavas, pyroclastics, and Paleocene to Eocene hypabyssal and plutonic rocks. The Sejong Formation, existing at the lowestmost part, consists of mostly volcaniclastic sediments, which is distributed along the southern and southwestern coastal area of the Barton Peninsula. Most volcanic rocks over the Sejong Formation are widely distributed in the Barton Peninsula, ranging from basalt to andesite. Granodiorite is exposed in the southwestern region of Noel Hill and hydrothermal alteration is observed at the boundary between the volcanic rock and the granodiorite in the central part of the Barton Peninsula (Lim et al., 2014 and references therein).

2.2 Samples Collection and Field Measurements

A total of 36 water and 34 suspended sediment samples were collected in January 2015 at the Barton Peninsula, which are supraglacial streams, adjacent lakes, and seawater. A total of 29 surface soil samples were collected from the uppermost 10 cm of the active layer in the soil on the Barton Peninsula, avoiding soils on altered bedrocks (**Figure 1**). All sample locations were documented with a Garmin GPSMAP 60CSx handheld GPS meter. Temperature, pH, and electrical conductivity (EC) were measured *in-situ* using an ORION 5-STAR meter equipped with an ORION Combination epoxy pH electrode and DuraProbe 4-Electrode conductivity cells. Total alkalinity was measured using a Mettler Toledo T50A titrator with 0.01 M HCl acidmetric titration to an endpoint of pH = 4.5. Samples for dissolved cations, and Sr and Li isotopes were passed through 0.2 μm filter, collected in I-CHEM LDPE bottles, and acidified to pH = 2 using ultrapure HNO_3. Samples for dissolved anions were passed through 0.2 μm filter and collected in acid-cleaned Nalgene LDPE bottles. About 500 ml of water sample was filtered in the laboratory using pre-weighed 0.2 μm filter, which were later dried at T = 60°C and reweighed in order to calculate the amount of suspended sediment (SS) per liter of meltwater.

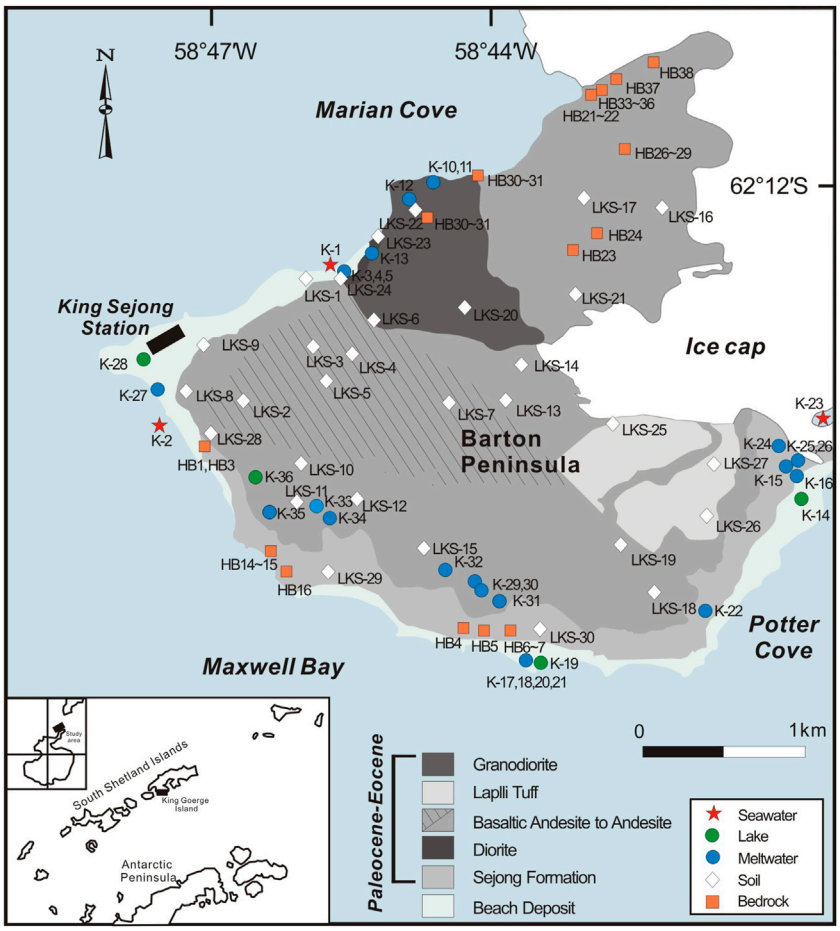

FIGURE 1 | Map showing sampling locations on Barton Peninsula, King George Island, West Antarctica. The sampling locations for suspended sediment are the same as those for water sample.

2.3 Preparation of Soil, Rock, and Suspended Sediment Samples

A total of 32 rock samples were the residual splits of bulk rock powders collected at the Barton Peninsula (**Figure 1**; Hur et al., 2001). About 0.1 g of soil and rock samples was completely digested in a 5:3 mixture of HF and HNO_3. The samples were dried, refluxed several times in 6.0 M HCl to remove fluorides, and re-dissolved in 5% HNO_3. Also, suspended sediment samples were processed in the same way as rock and soil samples.

2.4 Chemical and Isotopic Analyses

Cation and trace element concentrations were measured using a Thermo Scientific iCAP™ Q ICP–MS and a Perkin Elmer Optima 8300 ICP–AES at the Korea Basic Science Institute (KBSI). Anion concentrations were measured using a Dionex ICS–1100 ion chromatograph at the KBSI.

For water samples, strontium isotope ratios ($^{87}Sr/^{86}Sr$) were measured using a Neptune MC–ICP–MS upgraded with a large dry interface pump at the KBSI. Before the measurements, samples were dried in Teflon vessels, re-dissolved in 8 M HNO_3, and separated from matrix elements using an Eichrom Sr resin. The $^{87}Sr/^{86}Sr$ ratios were normalized to $^{86}Sr/^{88}Sr$ = 0.1194, and the mean $^{87}Sr/^{86}Sr$ ratio of the NBS987 standard during analysis was 0.710248 ± 0.000053 (2σ, n = 32).

Lithium was separated from matrix elements using an AG 50W–X8 resin (200–400 mesh), dried, and re-dissolved in 5% HNO_3 (~40 ppb Li). Lithium isotope ratios were also measured using a Neptune MC–ICP–MS at the KBSI. Samples were analyzed using a blank-standard-blank-sample-blank-standard-blank external bracketing method, in which sample intensities were matched to within 10% of the intensity of the standard. The sensitivity was ~90 V/ppm on mass 7 at a typical uptake rate of 100 μl/min, and blank values were low (~30 mV for ^{7}Li; 0.8%). Prior to the Li isotope measurement, each sample was checked for yield, which were greater than 99%. The Li isotopic composition is reported in delta notation (‰) relative to L-SVEC, where $\delta^{7}Li = [(^{7}Li/^{6}Li)_{sample}/(^{7}Li/^{6}Li)_{L\text{-}SVEC} - 1] \times 1000$. The accuracy and reproducibility of the whole method was validated using the USGS rock reference materials (BCR-2 and BHVO-2) and seawater standard (IAPSO). BCR-2 yielded + 3.2 ± 0.6‰ (2σ, n = 10), BHVO-2 yielded +4.5 ± 0.0‰ (2σ, n = 2), and IAPSO

TABLE 1 | Physicochemical and isotopic compositions for water samples.

Sample	Location		T	pH	EC	Ca	Mg	K	Na	Cl	SO_4	HCO_3[a]	Sr	Li	CBE[b]	δ^7Li	$^{87}Sr/^{86}Sr$	2SE[c]
	Latititude (N)	Longitude (W)	(°C)		(μS/cm)				(mM)				(μM)		(%)	(‰)		
Seawater																		
K-1	62.220	58.770	1.0	7.2	51230	9.49	44.9	8.28	405	502	24.9	2.24	79.8	23.3	−3	31.0	0.709136	0.000018
K-2	62.228	58.789	3.3	7.9	53090	8.64	42.7	7.96	386	468	23.5	1.84	76.6	21.8	−2	31.5	0.709025	0.000023
K-23	62.229	58.711	0.7	8.7	34280	3.56	13.8	2.94	139	162	8.03	0.97	27.4	5.36	−1	30.6	0.709397	0.000030
Lake water																		
K-12	62.216	58.760	8.0	6.4	61.5	0.05	0.03	0.01	0.31	0.33	0.06	0.03	0.19	0.02	2	33.4	0.706274	0.000022
K-14	62.233	58.713	2.2	8.2	2209	0.72	3.05	0.68	25.8	30.4	1.61	0.76	6.20	1.63	−1	30.7	0.709006	0.000024
K-19	62.241	58.747	2.3	7.2	210	0.24	0.12	0.02	0.97	1.08	0.18	0.36	0.40	0.05	−3	24.2	0.706525	0.000017
K-28	62.225	58.793	4.3	7.1	4944	0.91	3.88	0.78	32.6	39.3	2.34	0.25	7.49	2.38	−1	30.8	0.708969	0.000018
K-36	62.232	58.779	1.4	5.7	63.9	0.01	0.04	0.01	0.37	0.42	0.02	0.01	0.16	0.01	1	33.6	0.708337	0.000036
Meltwater																		
K-3	62.220	58.768	0.9	6.7	129	0.06	0.09	0.02	0.67	0.80	0.06	0.15	0.21	0.010	−3	41.1	0.706624	0.000018
K-4	62.220	58.769	0.6	6.4	248	0.15	0.19	0.03	1.24	1.65	0.11	0.14	0.44	0.019	−1	40.4	0.706482	0.000016
K-5	62.220	58.769	0.2	6.2	249	0.15	0.19	0.03	1.21	1.53	0.12	0.20	0.44	0.023	−2	39.2	0.706419	0.000021
K-6	62.220	58.775	3.6	4.4	232	0.32	0.15	0.05	0.74	0.80	0.50	0.18	0.81	0.100	−7	25.1	0.705032	0.000019
K-7	62.221	58.775	2.3	4.4	236	0.37	0.17	0.05	0.74	0.78	0.58	0.26	0.90	0.094	−8	25.0	0.704986	0.000021
K-8	62.221	58.776	1.2	4.6	270	0.41	0.17	0.05	0.73	0.76	0.64	0.18	0.95	0.101	−6	22.1	0.704870	0.000021
K-9	62.221	58.775	0.4	4.3	251	0.31	0.13	0.04	0.74	0.79	0.51	0.15	0.94	0.176	−8	16.6	0.704554	0.000011
K-10	62.215	58.758	1.6	6.7	68.6	0.06	0.04	0.01	0.33	0.29	0.08	0.06	0.21	0.039	1	21.9	0.705631	0.000026
K-11	62.215	58.758	0.9	7.1	68.6	0.06	0.03	0.01	0.33	0.29	0.08	0.07	0.21	0.042	2	19.6	0.705449	0.000026
K-13	62.219	58.766	0.2	7.7	94.7	0.06	0.04	0.01	0.54	0.48	0.04	0.16	0.19	0.029	1	18.3	0.705853	0.000039
K-15	62.231	58.713	0.2	8.3	180	0.34	0.12	0.02	0.64	0.48	0.13	0.88	0.59	0.068	−2	20.8	0.704736	0.000026
K-16	62.232	58.712	1.0	8.7	238	0.41	0.16	0.03	0.91	0.60	0.20	1.10	0.66	0.106	−1	n.d	0.705001	0.000024
K-17	62.241	58.747	0.2	7.1	192	0.22	0.12	0.02	0.80	0.81	0.22	0.35	0.30	0.058	−4	16.4	0.706225	0.000017
K-18	62.241	58.747	0.4	7.2	186	0.21	0.12	0.02	0.81	0.82	0.21	0.30	0.31	0.056	−3	17.5	0.706560	0.000023
K-20	62.241	58.748	0.0	7.3	214	0.23	0.12	0.02	1.00	1.15	0.13	0.34	0.40	0.038	−1	26.7	0.705732	0.000026
K-21	62.241	58.747	0.1	7.5	214	0.24	0.12	0.02	1.03	1.16	0.12	0.40	0.41	0.037	−1	26.6	0.706079	0.000022
K-22	62.239	58.723	0.2	7.5	132	0.15	0.05	0.01	0.66	0.66	0.05	0.34	0.24	0.024	−2	24.3	0.705869	0.000023
K-24	62.230	58.713	0.1	7.5	206	0.13	0.15	0.02	1.06	1.18	0.09	0.36	0.42	0.081	−2	24.1	0.706720	0.000022
K-25	62.231	58.710	4.5	8.0	208	0.20	0.16	0.03	1.03	1.15	0.10	0.53	0.49	0.079	−3	22.0	0.706068	0.000019
K-26	62.231	58.712	2.3	7.5	202	0.14	0.16	0.02	1.06	1.17	0.09	0.31	0.43	0.079	0	24.2	0.706324	0.000020
K-27	62.226	58.791	0.3	6.2	87.0	0.04	0.05	0.01	0.44	0.46	0.08	0.03	0.14	0.037	−1	19.7	0.706445	0.000023
K-29	62.237	58.752	0.3	7.1	84.9	0.05	0.04	0.01	0.47	0.52	0.04	0.06	0.21	0.029	1	28.4	0.706597	0.000045
K-30	62.238	58.751	1.1	6.7	84.7	0.05	0.04	0.01	0.44	0.49	0.03	0.07	0.11	0.024	0	29.6	0.706659	0.000028
K-31	62.239	58.748	0.2	6.7	71.4	0.04	0.04	0.01	0.40	0.45	0.03	0.06	0.19	0.020	0	30.8	0.706784	0.000030
K-32	62.237	58.755	0.3	6.4	49.6	0.01	0.03	0.01	0.29	0.31	0.02	0.03	0.15	0.012	1	34.3	–	
K-33	62.234	58.770	0.2	6.5	48.1	0.01	0.02	0.01	0.21	0.23	0.02	0.03	0.14	0.009	1	32.5	0.707716	0.000045
K-34	62.235	58.770	1.8	6.4	60.3	0.03	0.04	0.01	0.32	0.36	0.04	0.05	0.09	0.016	−1	31.2	0.706685	0.000020
K-35	62.234	58.777	1.5	6.2	75.1	0.02	0.04	0.01	0.43	0.44	0.05	0.02	0.17	0.013	1	33.8	–	

[a]*HCO3 ≈ total alkalinity.*

[b]*CBE: a percent charge balance error* $=(TZ^+ - TZ^-)/(TZ^+ + TZ^-) \times 100$ *(%).*

[c]*two standard error* (n = *20).*

–: not measured.

TABLE 2 | Elemental and isotopic compositions for the suspended sediments.

Sample	Al	Ca	Mg	Na	Fe	K	Li	δ^7Li
			(wt%)				(mg/kg)	(‰)
K-23	0.41	0.06	0.11	0.67	0.18	0.10	1.05	6.4
K-12	0.08	0.03	0.00	0.24	0.01	0.03	0.27	11.0
K-14	0.43	0.05	0.10	0.25	0.22	0.12	0.86	2.1
K-19	0.30	0.09	0.04	0.06	0.32	0.07	0.52	−0.4
K-28	0.27	0.04	0.05	0.44	0.21	0.02	0.65	13.4
K-36	0.16	0.01	0.01	0.35	0.02	0.00	0.30	11.2
K-3	0.16	0.02	0.02	0.23	0.05	0.04	0.48	9.8
K-4	0.11	0.01	0.00	0.26	0.01	0.01	0.31	11.8
K-5	0.08	0.02	0.00	0.25	0.00	0.03	0.29	11.1
K-6	0.58	0.15	0.11	0.33	0.35	0.05	1.18	8.6
K-7	0.42	0.07	0.08	0.28	0.25	0.04	0.94	6.4
K-8	0.68	0.21	0.16	0.15	0.52	0.05	0.98	4.4
K-9	0.03	0.02	0.01	0.01	0.06	0.03	0.06	–
K-10	0.18	0.03	0.02	0.24	0.09	0.02	0.50	7.1
K-11	0.41	0.08	0.05	0.29	0.18	0.06	0.92	3.1
K-13	0.05	0.02	0.02	0.01	0.04	0.00	0.12	–
K-15	0.67	0.14	0.12	0.17	0.45	0.11	1.43	3.1
K-16	0.22	0.02	0.02	0.25	0.08	0.03	0.58	7.4
K-17	0.19	0.04	0.01	0.25	0.26	0.01	0.44	7.7
K-18	0.20	0.05	0.02	0.26	0.22	0.02	0.51	6.4
K-20	0.00	0.01	0.00	0.01	0.00	0.00	0.02	–
K-21	0.00	0.01	0.00	0.01	0.00	0.00	0.01	–
K-22	0.09	0.02	0.00	0.25	0.01	0.03	0.32	10.4
K-24	0.16	0.02	0.01	0.28	0.04	0.00	0.39	8.4
K-25	0.28	0.04	0.03	0.30	0.11	0.04	0.62	7.2
K-26	0.20	0.02	0.01	0.33	0.04	0.02	0.41	8.3
K-27	0.13	0.01	0.00	0.25	0.02	0.00	0.29	11.7
K-29	0.39	0.04	0.01	0.91	0.04	0.02	0.27	10.9
K-30	0.17	0.02	0.01	0.38	0.03	0.01	0.28	10.5
K-31	0.19	0.03	0.01	0.26	0.08	0.02	0.39	–
K-32	0.24	0.03	0.01	0.45	0.05	0.00	0.29	10.5
K-33	0.26	0.03	0.02	0.32	0.09	0.02	0.41	10.3
K-34	0.18	0.02	0.01	0.28	0.06	0.01	0.39	11.8
K-35	0.34	0.03	0.02	0.32	0.17	0.04	0.47	9.7

–: *not measured.*

yielded + 31.5 ± 0.8‰ (2σ, n = 6), which were all in good agreement with reported values (e.g., You and Chan, 1996; Moriguti and Nakamura, 1998; Tomascak et al., 1999; Nishio and Nakai, 2002; Magna et al., 2004; Huang et al., 2010; Ludwig et al., 2011; Ryu et al., 2014).

3 RESULTS

Table 1 presents physicochemical and isotopic compositions of water samples. Elemental and isotopic compositions of suspended sediment, soil and rock samples are given in **Tables 2–4**, respectively.

3.1 General and Major Element Chemistry of Water Samples

The pH of most of water samples ranges from 5.69 to 8.72 except for four meltwater samples (K–6–9), which display much low pH (~4.41). The EC of meltwaters (n=28) and lake waters (n=5) ranges from 48.1 to 269.9 μs/cm and from 61.5 to 4,944 μs/cm, respectively. On an average molar basis (**Figure 2**), major cation abundances of meltwater samples follow the order of Na^+ (74%) > Ca^{2+} (15%) > Mg^{2+} (10%) > K^+ (2%), while lake samples follow the order of Na^+ (81%) > Mg^{2+} (9%) > Ca^{2+} (8%) > K^+ (2%). Major anion abundances of meltwater samples follow the order of Cl^- (69%) > HCO_3^- (19%) > SO_4^{2-} (13%), whereas lake samples follow the order of Cl^- (85%) > SO_4^{2-} (8%) > HCO_3^- (7%). The high abundances of Na^+ and Cl^-, and the strong correlation between them (r^2 = 0.99) suggest that water chemistry is mainly controlled by marine aerosol.

3.2 Major Element Chemistry of Solid Phases

The compositions of the suspended sediment samples are, on average, different from those of rock (Hur et al., 2001) and soil samples. Based on the average wt%. (**Tables 2–4**), major cation abundances of the suspended sediment samples collected in meltwater follow the order of Na (37%) > Al (33%) > Fe (16%) > Ca (6%) > Mg (4%) = K (4%), whereas rocks and soils follow the order of Al (35%) > Fe (27%) > Ca (17%) > Na (10%) > Mg (6%) > K (5%), and Al (40%) > Fe (26%) > Ca (12%) > Na (10%) > Mg (7%) > K (5%), respectively.

3.3 Strontium and Lithium Isotopes

The $^{87}Sr/^{86}Sr$ ratios of meltwater, lake and seawater samples range from 0.704554 to 0.707716 with an average of 0.706004 (n = 26), from 0.706274 to 0.709006 with an average of 0.707822 (n = 5), and from 0.709025 to 0.709397 with an average of 0.709186 (n = 3), respectively (**Table 1**). Previous study showed that rock samples display the $^{87}Sr/^{86}Sr$ ratios, ranging from 0.703218 to 0.704620 with an average of 0.703685 (Shin et al., 2009).

The rock samples display Li concentrations ranging from 0.42 to 28.3 mg/kg (11.6 mg/kg, n=32) and δ^7Li values ranging from −1.8 to +11.7‰ (+5.2‰, n = 29). Compared to rock samples, the soil samples show higher Li concentrations ranging from 9.56 to 36.9 mg/kg (15.9 mg/kg, n = 28) but lower δ^7Li values ranging from −2.5 to +6.9‰ (+3.8‰, n = 28). The suspended sediment samples have much lower Li concentrations ranging from 0.011 to 1.4 mg/kg (0.50 mg/kg, n = 28) but higher δ^7Li values than soil and rocks, ranging from −0.4 to +13.4‰ (+8.3‰, n = 23). On the contrary, meltwater samples have the lowest Li concentrations ranging from 8.69 to 176 nM (50.6 nM, n = 28) but much higher δ^7Li values ranging from +16.4 to +41.1‰ (+26.4‰, n = 27). Lake samples display Li concentrations ranging from 13.1 nM to 2.38 μM (819 nM, n = 5) and also higher δ^7Li values ranging from +24.2 to +33.6‰ (+30.5‰, n = 5). Seawater samples have Li concentrations ranging from 5.36 to 23.3 μM (16.8 μM, n = 3) and δ^7Li values ranging from +30.6 to +31.5‰ (+31.1‰, n = 3), consistent with reported δ^7Li value for seawater (+31‰; Millot et al., 2004) (**Figure 3**).

3.4 Correction of Atmospheric Inputs

In order to constrain the controls on the dissolved Li isotope signatures, it is important to first determine the sources of dissolved Li. Because Li concentrations of meltwater samples are relatively low, it is critical to evaluate the atmospheric contribution before considering either rock or mineral inputs in waters, especially in maritime regions. Given the proximity of

TABLE 3 | Elemental and isotopic compositions for soils.

Sample	Bedrock	Al	Ca	Mg	Na	Fe	K	Ti	Sr	Li	δ^7Li
					(wt%)				(mg/kg)		(‰)
LKS1	Basaltic andesite	10.9	3.38	1.92	3.00	6.13	1.62	0.44	689	14.5	4.5
LKS2		9.36	3.79	2.29	2.46	6.44	0.80	0.65	523	13.6	5.1
LKS3		11.5	2.55	2.17	1.70	6.08	1.20	0.72	553	17.7	6.4
LKS4		1.20	0.49	0.30	0.31	0.81	0.11	0.08	67.9	14.1	5.0
LKS5		9.11	4.85	2.44	2.82	7.16	0.43	0.98	553	14.0	5.9
LKS6		10.6	1.76	1.99	2.23	6.85	1.18	0.51	506	20.5	3.5
LKS7		10.5	2.12	2.12	2.13	6.26	1.20	0.66	517	18.2	4.8
LKS8		8.46	2.88	1.31	2.66	5.44	1.31	0.46	600	10.5	4.3
LKS9		9.54	3.14	1.74	2.74	6.29	1.23	0.55	626	13.2	3.2
LKS10		10.4	4.87	2.44	2.38	7.38	0.36	0.87	679	10.8	5.2
LKS11		8.44	3.13	1.72	1.90	5.87	0.84	0.78	521	12.8	1.5
LKS12		10.1	3.04	1.78	1.85	6.59	1.11	0.82	474	12.9	3.8
LKS13		10.8	3.66	2.28	2.42	6.87	0.75	0.97	556	16.7	4.9
LKS14		10.8	3.30	1.78	2.72	6.42	1.21	0.81	613	16.8	5.9
LKS15		10.3	0.93	0.52	2.28	5.61	2.48	0.60	434	10.6	1.5
LKS16		10.9	1.46	1.97	1.53	6.82	1.72	0.78	418	13.3	3.9
LKS17		10.3	0.48	0.44	1.47	3.75	1.67	0.48	484	36.9	3.9
LKS19		10.1	2.37	1.93	2.72	6.43	1.54	0.79	518	18.5	1.7
LKS26		10.6	5.12	2.67	2.94	7.83	0.79	1.09	606	15.9	4.4
LKS28		11.1	3.36	2.26	2.56	10.3	1.06	0.83	681	15.6	5.6
LKS20	Diorite	8.93	4.04	1.99	2.93	6.48	1.12	0.78	560	15.2	5.3
LKS21		10.8	3.15	1.46	2.02	6.21	1.78	0.83	519	9.56	4.8
LKS22		8.59	2.49	1.55	2.41	4.80	1.91	0.49	470	16.4	6.9
LKS23		9.14	3.27	0.98	3.05	6.11	1.62	0.56	594	21.1	3.6
LKS24		13.4	3.81	2.72	3.25	6.79	1.19	0.57	770	17.0	4.8
LKS25	Lapilli Tuff	9.27	1.69	1.23	1.61	7.70	1.99	0.63	377	20.2	−0.7
LKS27		10.3	2.41	2.06	2.74	6.76	1.56	0.80	551	13.8	1.5
LKS29	Sejong Formation	10.5	0.93	1.39	2.48	6.84	1.98	0.61	457	14.4	0.4
LKS30		8.24	4.95	1.54	2.49	5.57	0.98	0.86	643	16.7	−2.5

the study area to the ocean, it can be assumed that atmospheric input has the same chemical composition as seawater, as shown in other regions (Millot et al., 2010a; Millot et al., 2010b). Solute concentrations in meltwaters were corrected for atmospheric input using the equation as follows:

$$[i]^{*}_{meltwater} = [i]_{meltwater} - [Cl]_{meltwater}\left(\frac{i}{Cl}\right)_{sw}, \quad (1)$$

where $[i]^{*}_{meltwater}$ is the corrected concentration of solute i in meltwater (μmol/L), $[i]_{meltwater}$ is the measured concentration of solute i in meltwater (μmol/L), $[Cl]_{meltwater}$ is the measured concentration of Cl^- in meltwater (μmol/L), and $(i/Cl)_{sw}$ is the molar concentration ratio of solute i to Cl^- in seawater, in which two seawater samples (K−1 & 2) were used. **Eq. 1** assumes that Cl^- in meltwater only originates from atmospheric input, which is reasonable because neither Cl–rich evaporates nor hot springs occur in the study area, and Cl^- behaves conservatively during transport (Feth, 1981).

4 DISCUSSION

4.1 Sources of Dissolved Lithium

4.1.1 Atmospheric Inputs

Based on major water chemistry, it is critical to evaluate the atmospheric contribution before considering the effect of either rock or mineral dissolution on meltwater chemistry. The atmospheric contribution to dissolved Li was calculated using **Eq. 1** and the average molar ratio of 1000*Li to Cl^- in two seawater samples (K−1 & 2; 0.047) as described in Section 3.4. Interestingly, corrected Li concentrations in one sample (K−36) among five lake samples, and eleven samples (K−3–5, K−20–22, K−31–35) among twenty-eight meltwater samples display negative values, highlighting a Li loss. Indeed, this result suggests that dissolved Li was preferentially sorbed into/onto secondary phases. On the contrary, corrected Li in the other samples account for 4%–79% (mean 46%, n = 17) of measured dissolved Li, indicating Li may come from other sources.

4.1.2 Rock Weathering

Several studies have suggested that both phosphatization and sulfurization enhance chemical weathering in Maritime Antarctica (Lopes et al., 2019; Lopes et al., 2021). As it can be assumed that anthropogenic effects on major dissolved ions are negligible in Maritime Antarctica, the major sources for Li corrected from atmospheric input should be related to rock weathering.

A linear correlation between (Ca^* + Mg^*) and (HCO_3^* + SO_4^*) in meltwater samples suggests that these ions are mostly derived from chemical weathering by carbonic and sulphuric acids (**Figure 4A**). Interestingly, four samples plotted on high SO_4 (K−6–9) display low pH (~4.4), indicating that the sulphuric acid produced by sulphide oxidation is a major agent. Likewise, a plot of Mg/Na and Ca/Na ratios shows that meltwater samples plot

TABLE 4 | Elemental and isotopic compositions for bedrocks.

Sample	Lithology	Al	Ca	Mg	Na	Fe	K	Sr	Li	δ^7Li	$^{87}Sr/^{86}Sr$[a]
				(wt%)				(mg/kg)		(‰)	
HB25	Less altered basaltic andesite	10.1	6.23	2.07	2.96	6.30	1.24	665	10.9	2.6	0.703546
HB26		9.85	6.63	1.93	2.81	5.98	0.48	730	5.87	2.0	0.703454
HB37		9.83	7.20	2.86	2.76	6.09	0.95	740	7.21	1.2	0.703320
HB38		9.81	7.88	2.58	2.57	6.01	0.22	653	15.3	0.6	0.703218
HB3	Altered basaltic andesite	7.86	0.37	0.41	4.12	2.03	2.78	221	3.31	9.1	0.704188
HB21		9.16	4.37	3.21	1.82	6.14	0.43	434	10.6	4.4	0.703507
HB23		8.05	2.53	0.30	4.46	3.03	0.94	409	15.7	6.1	0.703603
HB24		9.68	4.74	2.83	3.85	6.35	1.79	626	15.1	1.7	0.703567
HB27		4.13	0.67	0.02	0.70	16.1	0.10	988	0.42	10.8	0.703430
HB28		9.54	4.33	1.85	3.28	5.95	0.79	744	8.68	4.4	0.703554
HB29		11.0	0.15	0.02	0.81	7.23	0.15	916	1.17	8.8	–
HB32-2		9.90	3.16	4.68	1.98	7.32	0.61	310	28.3	3.8	0.703578
HB32-3		9.29	0.26	0.06	0.52	5.22	2.15	110	16.4	–	0.704341
HB32-4		11.7	2.06	0.10	2.91	9.78	2.54	910	5.66	7.1	0.703536
HB32-5		7.80	0.30	0.10	0.76	5.18	2.71	169	10.0	11.7	0.704620
HB32-6		11.3	2.10	1.03	1.42	5.85	1.97	442	20.4	1.5	0.703826
HB32-7		8.89	1.75	1.26	3.38	6.93	0.96	511	16.5	1.8	0.703517
HB33		9.11	2.72	0.25	2.18	4.19	0.97	760	9.15	9.1	0.703554
HB35		9.40	10.4	2.10	2.47	7.58	0.14	789	6.52	6.4	0.703447
HB36		2.95	6.26	1.01	0.84	3.03	0.13	189	8.30	–	0.703419
HB4	Quartz-veined volcaniclastic rock	1.05	1.26	0.23	0.45	0.89	0.29	28	9.45	11.2	0.704035
HB5		4.56	4.66	0.47	1.53	5.61	0.99	89	12.2	9.2	0.704227
HB6		8.47	4.17	1.89	2.67	7.06	1.03	232	23.3	5.1	0.703711
HB7		5.60	2.59	0.73	2.46	8.54	0.44	252	12.8	8.1	0.703791
HB16A		7.97	4.46	1.00	3.19	9.86	0.96	502	12.4	2.3	0.703541
HB16B		9.07	15.5	1.06	0.55	5.74	0.38	1110	11.9	6.3	0.703491
HB1	Altered dyke	10.1	7.99	2.63	2.11	4.26	0.14	758	5.81	-1.8	0.703554
HB14		7.95	2.07	0.72	2.67	7.34	2.79	341	7.67	3.2	0.703835
HB15		6.47	4.04	1.29	1.55	12.4	1.38	408	14.4	1.0	0.703598
HB30	Granodiorite	8.77	3.79	2.08	3.36	5.50	2.32	450	19.3	–	0.703709
HB31		8.00	3.85	2.04	3.19	5.55	2.19	401	15.2	8.5	0.703682
HB32-1		8.46	2.87	1.32	3.32	4.35	2.74	375	10.4	5.2	0.703850

[a]*data from Shin et al. (2009).*

–: not measured.

near the silicate end member (**Figure 4B**), likely indicating that silicate weathering is dominant with a little carbonate weathering.

It has been shown that Li is correlated to Mg in world river waters due to similar ionic radii between Li^+ (0.78Å) and Mg^{2+} (0.72Å), allowing Li to substitute for Mg in silicate minerals (Huh et al., 1998). Corrected Li concentrations in meltwater are in general proportional to Mg/Na ratios but poorly correlated with K/Na ratios even though K comes from silicate weathering (not shown). This suggests the tendency of Li to be preferentially retained in secondary phases, substituting for Mg^{2+} or occupying the vacancy generated by Mg^{2+} substitution of Al^{3+} (Huh et al., 1998). In contrast, K preferentially remain in the dissolved phase.

4.2 Li Isotope Fractionation During Weathering

4.2.1 High δ^7Li in Meltwaters

The incorporation of Li into/onto secondary phases may results in Li isotope fractionation explaining the enrichment of ^{7}Li in the meltwater samples. However, as sea salt may also have high δ^7Li values, it is important to elucidate whether high δ^7Li values in meltwater result from isotope fractionation or source effects with high δ^7Li value.

The meltwater δ^7Li values ranging from +16.4 to +41.1‰ (26.4‰, n = 27) are significantly higher than those of suspended sediments, rocks, and soils. As described in **Section 3.3**, there is a clear difference in $^{87}Sr/^{86}Sr$ ratios among water samples. Furthermore, the negative correlation between $^{87}Sr/^{86}Sr$ ratios and Sr/Na (molar ratio) reflects that water chemistry is mainly controlled by a simple binary mixing between seawater and silicate weathering (**Figure 5A**). Likewise, it might be expected that a binary mixing affects both Li concentrations and δ^7Li values in meltwater samples because Li contents in carbonates are negligible. As shown in the correlation between $^{87}Sr/^{86}Sr$ ratios and Sr/Na, it seems that the correlation between δ^7Li and Li/Na (molar ratio) also reflect a binary mixing between seawater and silicate weathering (**Figure 5B**). However, there is a little correlation between δ^7Li and $^{87}Sr/^{86}Sr$ ratios (**Figure 5C**), indicating a simple binary mixing cannot explain Li isotopic compositions in meltwater.

If a binary mixing controls δ^7Li values in meltwater samples, one lake and eleven meltwater samples showing negative Li concentration after atmospheric input correction should have seawater δ^7Li value because all Li comes from seawater. However, their δ^7Li values range from +24.3‰ to +41.1‰ with an average of +32.9‰ (n = 12), which is higher than seawater δ^7Li value

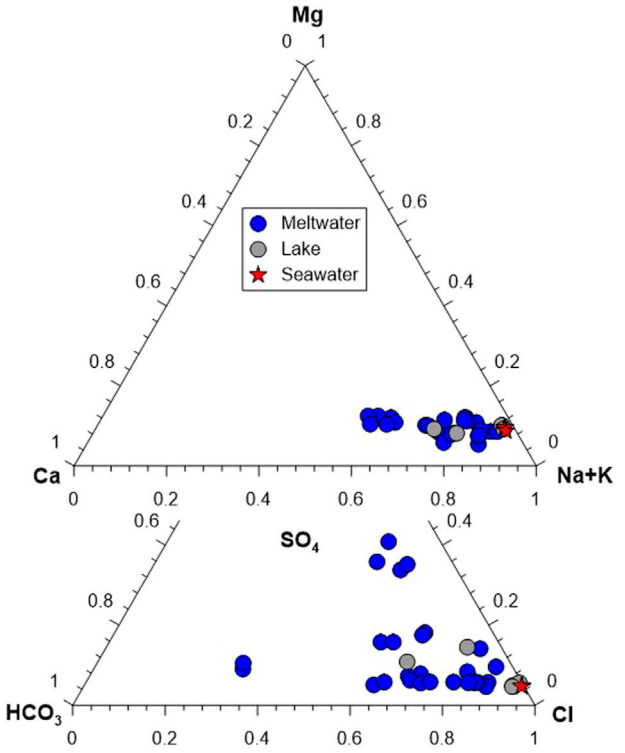

FIGURE 2 | Ternary diagrams showing the relative molar abundances of cation and anion in the water samples.

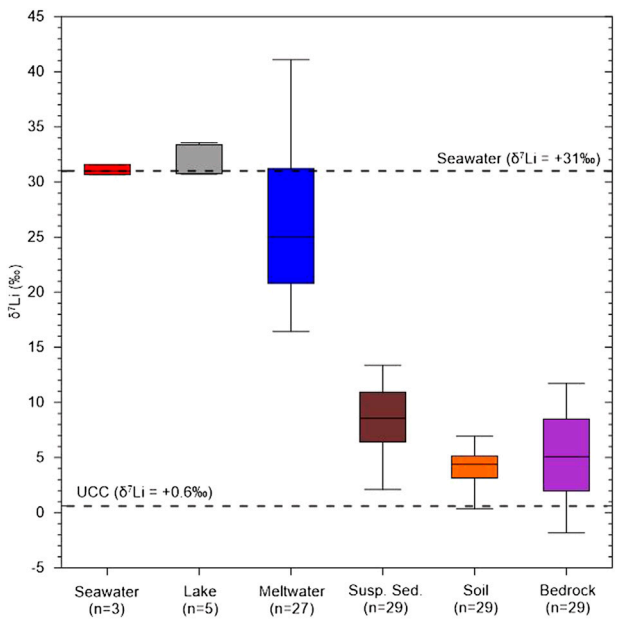

FIGURE 3 | Li isotopic compositions in different types of samples collected in this study. Seawater and UCC δ^7Li are from Millot et al. (2004) and Sauzéat et al. (2015), respectively.

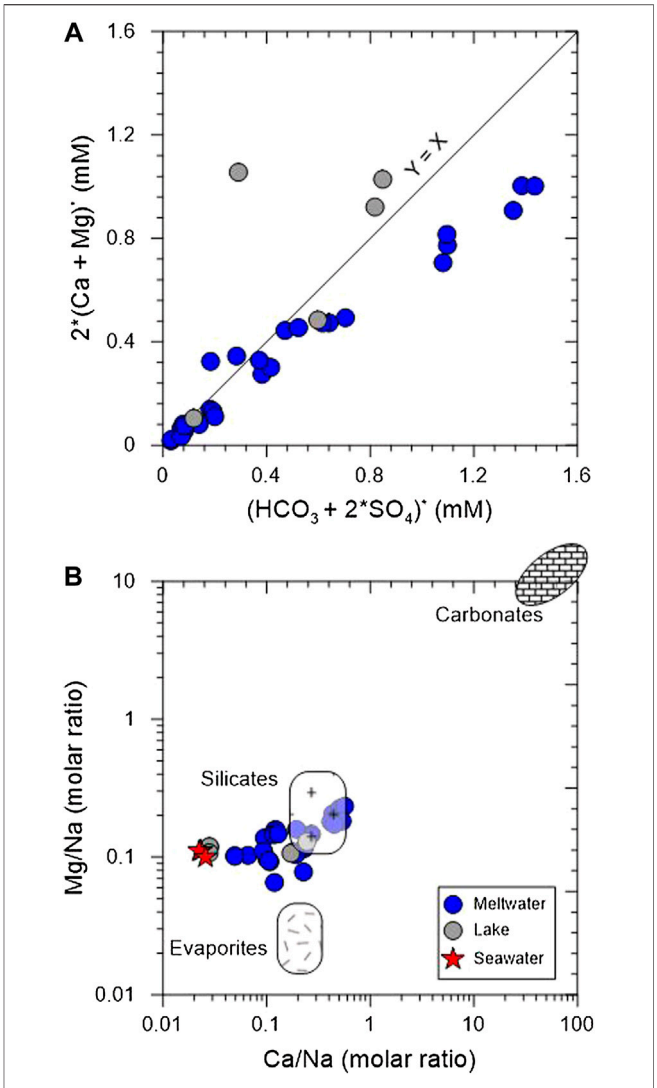

FIGURE 4 | Plots of (Ca + Mg)* and (HCO_3 + SO_4)* **(A)** and Mg/Na versus Ca/Na **(B)**. Asterisk represents the concentration corrected for atmospheric input. Bedrock endmembers are from Gaillardet et al. (1999).

(31.3‰; K–1 & 2). The other meltwater samples having excess Li after sweater correction display δ^7Li values ranging from +16.4‰ to +29.6‰ with an average of +22.0‰ (n = 16), which is much lower than seawater δ^7Li, suggesting a non-negligible contribution from silicate weathering.

As described above, we can assume that the dissolved Li is essentially explained by a binary mixing as follows:

$$\delta^7 Li_{cal} = f_{sw} \cdot \delta^7 Li_{sw} + \left(1 - f_{sw}\right) \cdot \delta^7 Li_{weathering}, \qquad (2)$$

where f_{sw} is a fraction of seawater in total Li concentration and $\delta^7 Li_{weathering}$ is an average δ^7Li value of bedrock (+5.2‰; **Table 4**). The differences in between measured and calculated δ^7Li values range from −7.0 to +10.2‰, with an average of +2.3‰ (n = 16), implying that conservative mixing is not a dominant control on δ^7Li and process-related fractionation occurs in this system. Below, multiple process-controlled fractionations are considered in more detail.

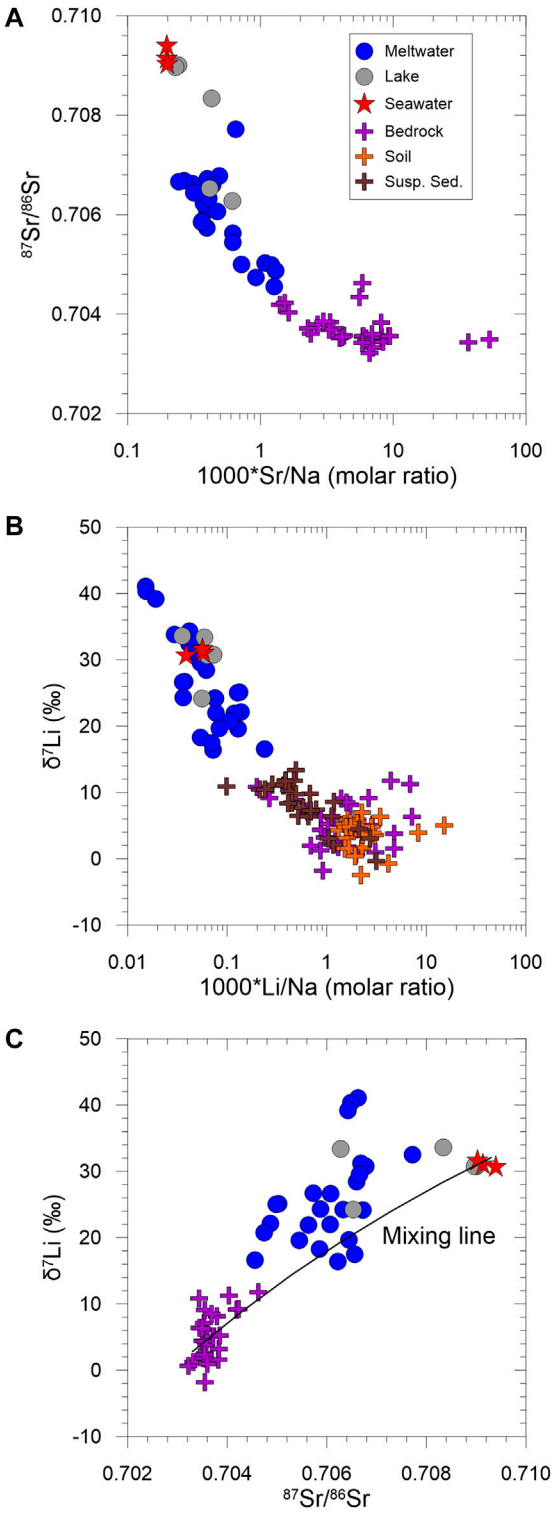

FIGURE 5 | Plots of $^{87}Sr/^{86}Sr$ ratios versus Sr/Na (molar ratio) **(A)**, δ^7Li versus Li/Na (molar ratio) **(B)** and δ^7Li versus $^{87}Sr/^{86}Sr$ ratios **(C)**. Bedrock $^{87}Sr/^{86}Sr$ ratios are from Shin et al. (2009).

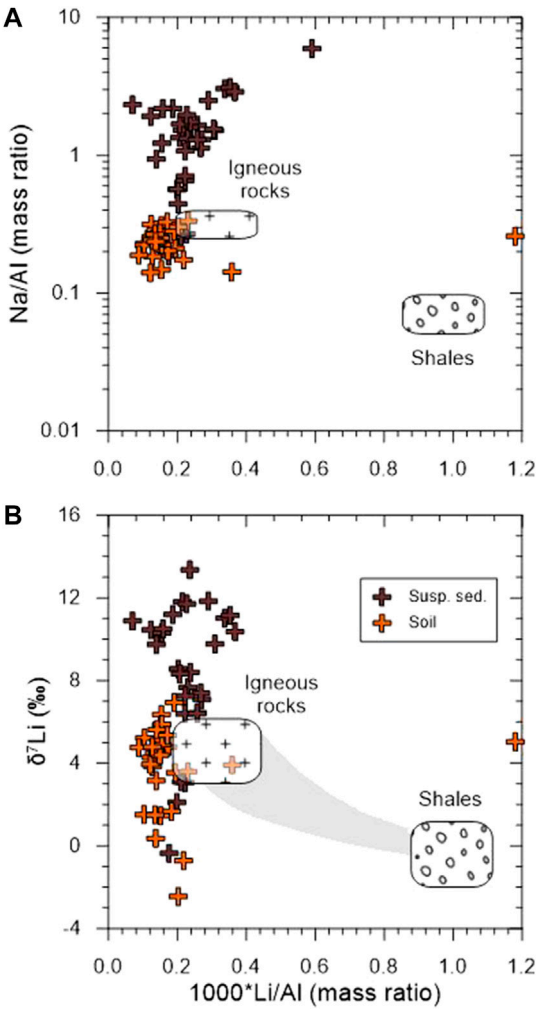

FIGURE 6 | Plots of Na/Al (mass ratio) **(A)** and δ^7Li **(B)** versus Li/Al (mass ratio) in the suspended sediment and soil samples. Bedrock endmembers are from Dellinger et al. (2014).

4.2.2 Rock Weathering and Soil Formation in This Region

Experimental studies have demonstrated that Li isotopes fractionate significantly during weathering processes, mostly during secondary phase neoformation (Vigier et al., 2008; Hindshaw et al., 2019; Zhang et al., 2021). Indeed, rock/mineral dissolution or leaching is a congruent process, not fractionating Li isotopes, except for small and temporary effects related to diffusion (e.g., Verney-Carron et al., 2011). In contrast, Li uptake by secondary phases, such as smectite, kaolinite and Fe-oxides, induce significant isotopic fractionations, resulting in ^6Li-enriched secondary phases (Maffre et al., 2020).

As reported in previous studies, if chemical weathering in Barton Peninsula is insignificant (Lee et al., 2004; Lee et al., 2019),

Li isotopic compositions of rock and soil should be consistent due to dominant physical weathering and thus little secondary phase formation. However, δ^7Li values of bedrock samples (mean +5.2‰, n = 29) are higher than those of soil samples (+3.8‰, n = 28), indicating the existence of secondary phases in soil (**Figure 3**) with lower δ^7Li values. Previous soil study in the Barton Peninsula also showed that interstratified phyllosilicates, such as smectite and vermiculite, and crystalline Fe-oxides (goethite), occur in soil profiles (Lopes et al., 2019). Recent study on soil chronosequences in Hawaii (Ryu et al., 2014) showed that the mineralogical evolution of soil profiles through time is accompanied by progressive δ^7Li decrease, resulting from sequestration of Li into ^{6}Li-rich secondary phases. Taken together, this result suggests that secondary mineral formation and sorption into/onto them are the major processes controlling isotope fractionation during soil formation even if the extent of Li isotope fractionation is different from minerals (Vigier et al., 2008).

Although soil samples plot near igneous rock endmember on a plot of Na/Al versus Li/Al (**Figure 6A**), they plot outside a weathering trend between igneous rocks and shales endmembers on a plot of δ^7Li versus Li/Al (**Figure 6B**), displaying lower δ^7Li values than igneous rocks. It clearly supports that a significant modern chemical weathering occurs with mineral neoformation in the Maritime Antarctica.

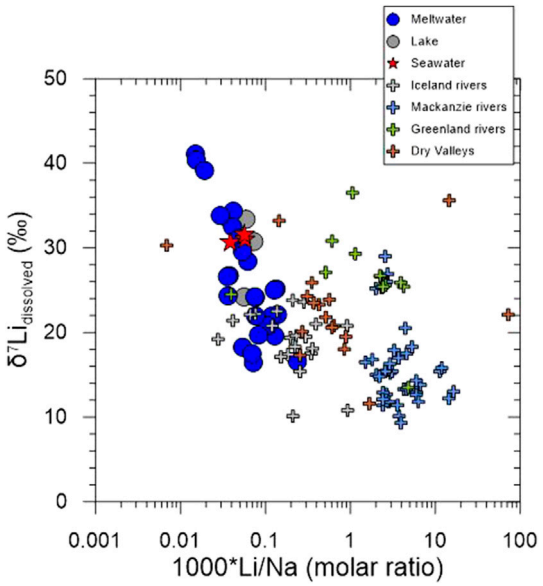

FIGURE 7 | Plot of δ^7Li versus Li/Na (molar ratio) in the water samples. Data for Iceland, Mackenzie and Greenland rivers, and the McMurdo Dry Valley are from Vigier et al. (2009), Millot et al. (2010), Wimpenny et al. (2010a), and Witherow et al. (2010), respectively.

4.2.3 Suspended Sediments

The δ^7Li values of the suspended sediment samples ranging from −0.4 to +13.4‰ (mean +8.3‰, n = 20, **Table 2**) are higher than those of bedrock (mean +5.2‰) and soil (mean +3.8‰) samples, but much lower than meltwater samples (mean +26.4‰). Due to the high solubility of Na during chemical weathering compared to immobile Al, the Na/Al ratio can be regarded as "a weathering index" (Millot et al., 2010) or an index of the leaching intensity, such as the K/Mg (Bastian et al., 2017; Bastian et al., 2021). A positive correlation between Na/Al and Li/Al ratios suggests that Al-rich phases, such as clays, mainly controls Li concentrations in the suspended sediment (**Figure 6A**), which conforms observations from the dissolved δ^7Li (see previous section). Also, a positive correlation observed in δ^7Li and Na/Li ratio shows that the low Na/Li ratios are associated with low δ^7Li values (not shown). Applying the modelling developed in previous studies (e.g., Bouchez et al., 2013; Dellinger et al., 2014; Dellinger et al., 2017), this is consistent with the fact that the particle δ^7Li values depend on the ratio of dissolution/neoformation. In this context, low δ^7Li values could be best explained by either lower dissolution rates or higher neoformation rate. However, more detailed investigations are needed to confirm it.

The fact that δ^7Li values of the suspended sediments are higher than those of bedrock and soil samples suggests additional Li input with high δ^7Li values. Interestingly, eight suspended sediment samples (mean +10.7‰; K–3–5, 22, and 32–35) collected from meltwater showing a Li loss have much higher δ^7Li values than the other samples (+7.4‰). Also, they do not show any correlation between δ^7Li and Na/Li ratio with relatively constant δ^7Li values regardless of Na/Li ratios. The differences in δ^7Li between meltwater and suspended sediment samples ($\Delta^7Li_{water\text{-}sed}$) are clearly distinct from between suspended sediments affected by high sea salt input and the others. That is, $\Delta^7Li_{water\text{-}sed}$ of the former and latter samples are +23.9‰ and +15.5‰, respectively. The results could be explained by the fact that meltwater Li entirely coming from sea salt input is sorbed onto/into secondary phases present in the glaciers, allowing the suspended sediments to be δ^7Li higher than those less affected by sea salt input as well as soils and rocks. That is, δ^7Li values in the suspended sediments are not simply controlled by incorporating light ^{6}Li that would result in lower δ^7Li than rock/soil samples. Instead, they incorporate Li from sea salt with higher δ^7Li that finally results in higher δ^7Li in the suspended sediments relative to rock/soils.

Although it is difficult to estimate the partitioning of Li transported in the dissolved and particulate load in this study because chemical weathering process is not at steady-state (Vigier et al., 2001), this study clearly suggests that both dissolved and suspended sediment samples reflect Li isotope fractionation occurring presently during chemical weathering which is operating despite icy conditions.

4.3 Comparison With Other Studies in the Polar Regions

Lithium isotope studies have been conducted in the Arctic regions (Vigier et al., 2009; Millot et al., 2010; Wimpenny et al., 2010a) although there is only one study in the Antarctica (Witherow et al., 2010). In order to understand the factors controlling Li isotope fractionation in the dissolved phases, all data plotted on a plot of δ^7Li vs. Li/Na (molar ratio) (**Figure 7**). At first glance, all δ^7Li values negatively correlate with Li/Na ratios. Interestingly, three studies (Iceland rivers, Dry Valley, and this study) are distinguished from the others (Mackenzie and Greenland rivers)

based on 1000*(Li/Na) = 1, and δ^7Li values in the Mackenzie rivers are relatively lower than other studies. This indicates that the stages of chemical weathering control dissolved Li isotopic compositions. That is, either poorly crystalline or short-range order (SRO) minerals, such as Fe-(oxyhydr)oxides, during the incipient stages of chemical weathering could cause fluids to be more ^{7}Li-enriched as shown in Greenland (Wimpenny et al., 2010a) and the Mackenzie basin (Millot et al., 2010), while crystalline secondary phases, such as clays, during relatively late stages could induce relatively low ^{7}Li-enriched fluids as shown in the low-lying plains of the Mackenzie basin (Millot et al., 2010).

Although Vigier et al. (2009) suggested that δ^7Li values in Icelandic rivers closely correlated with basalt chemical erosion rates where high δ^7Li values are associated with low chemical erosion rates but low δ^7Li values with greater chemical erosion rates, Millot et al. (2010) argued that δ^7Li values in the Mackenzie River Basin are controlled by the weathering regime where incipient weathering in the Rocky Mountains and Shield areas causes high ^{7}Li enrichment in the fluid resulting from the Li uptake by oxyhydroxide phases, whereas relatively low ^{7}Li enrichment is associated with groundwater experienced more intense water-rock interactions forming the secondary phases in the lowlands. On the contrary, δ^7Li values in Greenland rivers (both non-glacial and glacial rivers) are mainly controlled by Fe-oxyhydroxides with preferential uptake of ^{6}Li on their surface, where Fe-oxyhydroxides are formed under the ice as a product of sulphide oxidation in the glacial rivers (Wimpenny et al., 2010a). Compared to the Arctic rivers, the McMurdo Dry Valley study suggested dissolved Li isotopic compositions are affected by a mixture of different sources with different δ^7Li values (Witherow et al., 2010). Whatever processes controlling dissolved Li isotopic compositions are different in each study, it is consistent that dissolved Li isotopic compositions are enriched in ^{7}Li compared to those of suspended sediment and bedrock due to preferential ^{6}Li uptake by secondary phases. However, relatively higher δ^7Li in this study suggest that sea salt Li is sorbed into/onto secondary phases formed during incipient weathering, resulting in much higher dissolved Li isotopic compositions than seawater δ^7Li.

Overall, given that the increase in global surface temperature enhances chemical weathering in Antarctica, it is expected that the increase in temperature causes a decrease in $\Delta^7Li_{solution-solid}$ ($\delta^7Li_{solution} - \delta^7Li_{solid}$) as chemical weathering of bedrocks becomes congruent.

5 CONCLUSION

Elemental and Li isotope geochemistry of meltwaters, suspended sediments, soils and bedrocks in the Barton Peninsula, King George Island, Antarctica are investigated in order to elucidate the processes controlling Li isotopes in meltwaters. Li concentrations and isotopic compositions are quite variable in the samples, where dissolved phases display the lowest Li concentration but the highest Li isotopic composition. Correlation between elemental and Li isotope geochemistry reveals that dissolved Li isotopic compositions are mainly controlled by incongruent dissolution with secondary neoformation, rather than sea salt inputs from atmosphere or ice melting. Likewise, δ^7Li values of soils also are affected by a modern chemical weathering with mineral neoformation rather than a binary weathering between igneous rocks and shales. However, the sorption of sea salt Li into/onto the suspended sediments causes δ^7Li values higher than soils and bedrocks. Compared to other studies in polar regions, this study suggests that increasing global surface temperature enhances modern chemical weathering in Antarctica, which cause dissolved Li isotopic compositions to be as low as those in the Arctic rivers.

DATA AVAILABILITY STATEMENT

The original contributions presented in the study are included in the article/supplementary material, further inquiries can be directed to the corresponding author.

AUTHOR CONTRIBUTIONS

J-SR designed the study, analyzed the samples, interpreted the data, and wrote the manuscript. H-BC and J-HK analyzed the samples. HL and O-SK designed the study and conducted the fieldwork. NV interpreted the data, wrote and reviewed the manuscript. All authors assisted with interpretation.

FUNDING

J-SR was funded by the National Research Foundation of Korea (NRF) grants funded by the Korea government (MSIT) (No. NRF-2019R1A2C2085973), the Polar Academic Program (PAP; PD14010 and PE15020) of the Korea Polar Research Institute (KOPRI) research grant, and the Korea Basic Science Institute (National research Facilities and Equipment Center) grant funded by the Ministry of Education (No. 2021R1A6C101A415). J-HK was funded by the Korea Ministry of Oceans and Fisheries (NP 2011-040).

REFERENCES

ACIA (2005). *Impacts of a Warming Arctic: Arctic Climate Impact Assessment*. Cambridge, UK: Cambridge University Press.

Anderson, S. P., Drever, J. I., Frost, C. D., and Holden, P. (2000). Chemical Weathering in the Foreland of a Retreating Glacier. *Geochim. Cosmochim. Acta* 64, 1173–1189. doi:10.1016/s0016-7037(99)00358-0

Bastian, L., Mologni, C., Vigier, N., Bayon, G., Lamb, H., Bosch, D., et al. (2021). Co-Variations of Climate and Silicate Weathering in the Nile Basin During the Late Pleistocene. *Quat. Sci. Rev.* 264, 107012. doi:10.1016/j.quascirev.2021.107012

Bastian, L., Revel, M., Bayon, G., Dufour, A., and Vigier, N. (2017). Abrupt Response of Chemical Weathering to Late Quaternary Hydroclimate Changes in Northeast Africa. *Sci. Rep.* 7, 44231. doi:10.1038/srep44231

Berner, R. A. (2003). The Long-Term Carbon Cycle, Fossil Fuels and Atmospheric Composition. *Nature* 426, 323–326. doi:10.1038/nature02131

Bhatia, M. P., Das, S. B., Longnecker, K., Charette, M. A., and Kujawinski, E. B. (2010). Molecular Characterization of Dissolved Organic Matter Associated with the Greenland Ice Sheet. *Geochim. Cosmochim. Acta* 74, 3768–3784. doi:10.1016/j.gca.2010.03.035

Bouchez, J., Von Blanckenburg, F., and Schuessler, J. A. (2013). Modeling Novel Stable Isotope Ratios in the Weathering Zone. *Am. J. Sci.* 313, 267–308. doi:10.2475/04.2013.01

Campbell, I. B., and Claridge, G. G. C. (1987). "Antarctica: Soils, Weathering Processes and Environment," in *Developments in Soil Sciences* (Amsterdam: Elsevier), 16.

Choi, H.-B., Lim, H. S., Yoon, Y.-J., Kim, J.-H., Kim, O.-S., Yoon, H. I., et al. (2022). Impact of Anthropogenic Inputs on Pb Content of Moss *Sanionia Uncinata* (Hedw.) Loeske in King George Island, West Antarctica Revealed by Pb Isotopes. *Geosci. J.* 26, 225–234. doi:10.1007/s12303-021-0032-4

Dellinger, M., Bouchez, J., Gaillardet, J., Faure, L., and Moureau, J. (2017). Tracing Weathering Regimes Using the Lithium Isotope Composition of Detrital Sediments. *Geology* 45 (5), 411–414. doi:10.1130/g38671.1

Dellinger, M., Gaillardet, J., Bouchez, J., Calmels, D., Galy, V., Hilton, R. G., et al. (2014). Lithium Isotopes in Large Rivers Reveal the Cannibalistic Nature of Modern Continental Weathering and Erosion. *Earth Planet. Sci. Lett.* 401, 898 359–372. doi:10.1016/j.epsl.2014.05.061

Feth, J. H. (1981). *Chloride in Natural Continental Water-A Review*. Washington, D.C.: USGS Water Supply Paper, 2176.

Fortner, S. K., Tranter, M., Fountain, A., Lyons, W. B., and Welch, K. A. (2005). The Geochemistry of Supraglacial Streams of Canada Glacier, Taylor Valley (Antarctica), and Their Evolution into Proglacial Waters. *Aquat. Geochem.* 11, 391–412. doi:10.1007/s10498-004-7373-2

Freeman, C., Evans, C. D., Monteith, D. T., Reynolds, B., and Fenner, N. (2001). Export of Organic Carbon from Peat Soils: Warmer Conditions May be to Blame for the Exodus of Peatland Carbon to the Oceans. *Nature* 412, 785. doi:10.1038/35090628

Gaillardet, J., Dupré, B., Louvat, P., and Allègre, C. J. (1999). Global Silicate Weathering and CO_2 Consumption Rates Deduced from the Chemistry of Large Rivers. *Chem. Geol.* 159, 3–30. doi:10.1016/s0009-2541(99)00031-5

Harris, K. J., Carey, A. E., Lyons, W. B., Welch, K. A., and Fountain, A. G. (2007). Solute and Isotope Geochemistry of Subsurface Ice Melt Seeps in Taylor Valley, Antarctica. *Geol. Soc. Am. Bull.* 119, 548–555. doi:10.1130/b25913.1

Hindshaw, R. S., Tosca, R., Goût, T. L., Farnan, I., Tosca, N. J., and Tipper, E. T. (2019). Experimental Constraints on Li Isotope Fractionation During Clay Formation. *Geochim. Cosmochim. Acta* 250, 219–237. doi:10.1016/j.gca.2019.02.015

Huang, K.-F., You, C.-F., Liu, Y.-H., Wang, R.-M., Lin, P.-Y., and Chung, C.-H. (2010). Low-Memory, Small Sample Size, Accurate and High-Precision Determinations of Lithium Isotopic Ratios in Natural Materials by MC-ICP-MS. *J. Anal. At. Spectrom.* 25, 1019–1024. doi:10.1039/b926327f

Huh, Y., Chan, L.-H., and Edmond, J. M. (2001). Lithium Isotopes as a Probe of Weathering Processes: Orinoco River. *Earth Planet. Sci. Lett.* 194, 189–199. doi:10.1016/s0012-821x(01)00523-4

Huh, Y., Chan, L.-H., Zhang, L., and Edmond, J. M. (1998). Lithium and its Isotopes in Major World Rivers: Implications for Weathering and the Oceanic Budget. *Geochim. Cosmochim. Acta* 62, 2039–2051. doi:10.1016/s0016-7037(98)00126-4

Hur, S.-D., Lee, J.-I., Hwang, J., and Choe, M.-Y. (2001). K-Ar Age and Geochemistry of Hydrothermal Alteration in the Barton Peninsula, King George Island, Antarctica. *Ocean. Polar Res.* 23, 11–21. (In Korean with English Abstract).

Jacobson, A. D., and Blum, J. D. (2003). Relationship Between Mechanical Erosion and Atmospheric CO_2 Consumption in the New Zealand Southern Alps. *Geology* 31, 865–868. doi:10.1130/g19662.1

Jiahong, W., Jiancheng, K., Jiankang, H., Zichu, X., Leibao, L., and Dali, W. (1998). Glaciological Studies on King George Island Ice Cap, South Shetland Islands, Antarctica. *Ann. Glaciol.* 27, 105–109.

Kim, J. H., Ahn, I.-Y., Lee, K. S., Chung, H., and Choi, H.-G. (2007). Vegetation of Barton Peninsula in the Neighbourhood of King Sejong Station (King George Island, Maritime Antarctic). *Polar Biol.* 30, 903–916. doi:10.1007/s00300-006-0250-2

Kling, G. W., Kipphut, G. W., and Miller, M. C. (1991). Arctic Lakes and Streams as Gas Conduits to the Atmosphere: Implications for Tundra Carbon Budgets. *Science* 251, 298–301. doi:10.1126/science.251.4991.298

Lee, Y. I., Choi, T., and Lim, H. S. (2019). Petrological and Geochemical Compositions of Beach Sands of the Barton and Weaver Peninsulas of King George Island, West Antarctica: Implications for Provenance and Depositional History. *Episodes* 42, 149–164. doi:10.18814/epiiugs/2019/019012

Lee, Y. I., Lim, H. S., and Yoon, H. I. (2004). Geochemistry of Soils of King George Island, South Shetland Islands, West Antarctica: Implications for Pedogenesis in Cold Polar Regions. *Geochim. Cosmochim. Acta* 68, 4319–4333. doi:10.1016/j.gca.2004.01.020

Lemarchand, E., Chabaux, F., Vigier, N., Millot, R., and Pierret, M.-C. (2010). Lithium Isotope Systematics in a Forested Granitic Catchment (Strengbach, Vosges Mountains, France). *Geochim. Cosmochim. Acta* 74, 4612–4628. doi:10.1016/j.gca.2010.04.057

Lim, H. S., Han, M. J., Seo, D. C., Kim, J. H., Lee, J. I., Park, H., et al. (2009). Heavy Metal Concentrations in the Fruticose Lichen *Usnea Aurantiacoatra* from King George Island, South Shetland Islands, West Antarctica. *J. Korean Soc. Appl. Bi.* 52, 503–508. doi:10.3839/jksabc.2009.086

Lim, H. S., Park, Y., Lee, J.-Y., and Yoon, H. I. (2014). Geochemical Characteristics of Meltwater and Pondwater on Barton and Weaver Peninsulas of King George Island, West Antarctica. *Geochem. J.* 48, 409–422. doi:10.2343/geochemj.2.0316

Liu, X.-M., Wanner, C., Rudnick, R. L., and McDonough, W. F. (2015). Processes Controlling δ^7Li in Rivers Illuminated by Study of Streams and Groundwaters Draining Basalts. *Earth Planet. Sci. Lett.* 409, 212–224. doi:10.1016/j.epsl.2014.10.032

Lopes, D. D. V., Schaefer, C. E. G. R., Souza, J. J. L. L. D., Oliveira, F. S. D., Simas, F. N. B., Daher, M., et al. (2019). Concretionary Horizons, Unusual Pedogenetic Processes and Features of Sulfate Affected Soils from Antarctica. *Geoderma* 347, 13–24. doi:10.1016/j.geoderma.2019.03.024

Lopes, D. D. V., Souza, J. J. L. L. D., Simas, F. N. B., Oliveira, F. S. D., and Schaefer, C. E. G. R. (2021). Hydrogeochemistry and Chemical Weathering in a Periglacial Environment of Maritime Antarctica. *Catena* 197, 104959. doi:10.1016/j.catena.2020.104959

Ludwig, T., Marschall, H. R., Pogge von Strandmann, P. A. E., Shabaga, B. M., Fayek, M., and Hawthorne, F. C. (2011). A Secondary Ion Mass Spectrometry (SIMS) Re-Evaluation of B and Li Isotopic Compositions of Cu-Bearing Elbaite from Three Global Localities. *Mineral. Mag.* 75, 2485–2494. doi:10.1180/minmag.2011.075.4.2485

Lyons, W. B., Frape, S. K., and Welch, K. A. (1999). History of McMurdo Dry Valley Lakes, Antarctica, from Stable Chlorine Isotope Data. *Geology* 27, 527–530. doi:10.1130/0091-7613(1999)027<0527:homdvl>2.3.co;2

Lyons, W. B., Welch, K. A., Snyder, G., Olesik, J., Graham, E. Y., Marion, G. M., et al. (2005). Halogen Geochemistry of the McMurdo Dry Valleys Lakes, Antarctica: Clues to the Origin of Solutes and Lake Evolution. *Geochim. Cosmochim. Acta* 69, 305–323. doi:10.1016/j.gca.2004.06.040

Maffre, P., Goddéris, Y., Vigier, N., Moquet, J.-S., and Carretier, S. (2020). Modelling the Riverine δ^7Li Variability Throughout the Amazon Basin. *Chem. Geol.* 532, 119336. doi:10.1016/j.chemgeo.2019.119336

Magna, T., Wiechert, U. H., and Halliday, A. N. (2004). Low-Blank Isotope Ratio Measurement of Small Samples of Lithium Using Multiple-Collector ICPMS. *Int. J. Mass Spectrom.* 239, 67–76. doi:10.1016/j.ijms.2004.09.008

Millot, R., Guerrot, C., and Vigier, N. (2004). Accurate and High-Precision Measurement of Lithium Isotopes in Two Reference Materials by MC-ICP-MS. *Geostand. Geoanal. Res.* 28, 153–159. doi:10.1111/j.1751-908x.2004.tb01052.x

Millot, R., Petelet-Giraud, E., Guerrot, C., and Négrel, P. (2010b). Multi-Isotopic Composition (δ^7Li–δ^{11}B–δD–δ^{18}O) of Rainwaters in France: Origin and Spatio-Temporal Characterization. *Appl. Geochem.* 25, 1510–1524. doi:10.1016/j.apgeochem.2010.08.002

Millot, R., Vigier, N., and Gaillardet, J. (2010a). Behaviour of Lithium and its Isotopes During Weathering in the Mackenzie Basin, Canada. *Geochim. Cosmochim. Acta* 74, 3897–3912. doi:10.1016/j.gca.2010.04.025

Moriguti, T., and Nakamura, E. (1998). Across-Arc Variation of Li Isotopes in Lavas and Implications for Crust/Mantle Recycling at Subduction Zones. *Earth Planet. Sci. Lett.* 163, 167–174. doi:10.1016/s0012-821x(98)00184-8

Nishio, Y., and Nakai, S. i. (2002). Accurate and Precise Lithium Isotopic Determinations of Igneous Rock Samples Using Multi-Collector Inductively Coupled Plasma Mass Spectrometry. *Anal. Chim. Acta* 456, 271–281. doi:10.1016/s0003-2670(02)00042-9

Oechel, W. C., Hastings, S. J., Vourlrtis, G., Jenkins, M., Riechers, G., and Grulke, N. (1993). Recent Change of Arctic Tundra Ecosystems from a Net Carbon Dioxide Sink to a Source. *Nature* 361, 520–523. doi:10.1038/361520a0

Park, B.-K., Chang, S.-K., Yoon, H. I., and Chung, H. (1998). Recent Retreat of Ice Cliffs, King George Island, South Shetland Islands, Antarctic Peninsula. *Ann. Glaciol.* 27, 633–635. doi:10.3189/1998aog27-1-633-635

Pistiner, J. S., and Henderson, G. M. (2003). Lithium-Isotope Fractionation During Continental Weathering Processes. *Earth Planet. Sci. Lett.* 214, 327–339. doi:10.1016/s0012-821x(03)00348-0

Pogge von Strandmann, P. A. E., Burton, K. W., James, R. H., van Calsteren, P., and Gislason, S. R. (2010). Assessing the Role of Climate on Uranium and Lithium Isotope Behaviour in Rivers Draining a Basaltic Terrain. *Chem. Geol.* 270, 227–239. doi:10.1016/j.chemgeo.2009.12.002

Pogge von Strandmann, P. A. E., Burton, K. W., James, R. H., van Calsteren, P., Gíslason, S. R., and Mokadem, F. (2006). Riverine Behaviour of Uranium and Lithium Isotopes in an Actively Glaciated Basaltic Terrain. *Earth Planet. Sci. Lett.* 251, 134–147. doi:10.1016/j.epsl.2006.09.001

Rudnick, R. L., Tomascak, P. B., Njo, H. B., and Gardner, L. R. (2004). Extreme Lithium Isotopic Fractionation During Continental Weathering Revealed in Saprolites from South Carolina. *Chem. Geol.* 212, 45–57. doi:10.1016/j.chemgeo.2004.08.008

Ryu, J.-S., and Jacobson, A. D. (2012). CO_2 Evasion from the Greenland Ice Sheet: A New Carbon Climate Feedback. *Chem. Geol.* 320-321, 80–95. doi:10.1016/j.chemgeo.2012.05.024

Ryu, J.-S., Vigier, N., Lee, S.-W., Lee, K.-S., and Chadwick, O. A. (2014). Variation of Lithium Isotope Geochemistry During Basalt Weathering and Secondary Mineral Transformations in Hawaii. *Geochim. Cosmochim. Acta* 145, 103–115. doi:10.1016/j.gca.2014.08.030

Santos, I. R., Fávaro, D. I. T., Schaefer, C. E. G. R., and Silva-Filho, E. V. (2007). Sediment Geochemistry in Coastal Maritime Antarctica (Admiralty Bay, King George Island): Evidence from Rare Earths and Other Elements. *Mar. Chem.* 107, 464–474. doi:10.1016/j.marchem.2007.09.006

Sauzéat, L., Rudnick, R. L., Chauvel, C., Garçon, M., and Tang, M. (2015). New Perspectives on the Li Isotopic Composition of the Upper Continental Crust and its Weathering Signature. *Earth Planet. Sci. Lett.* 428, 181–192. doi:10.1016/j.epsl.2015.07.032

Schuur, E. A. G., Bockheim, J., Canadell, J. G., Euskirchen, E., Field, C. B., Goryachkin, S. V., et al. (2008). Vulnerability of Permafrost Carbon to Climate Change: Implications for the Global Carbon Cycle. *BioScience* 58, 701–714. doi:10.1641/b580807

Serreze, M. C., Barrett, A. P., Stroeve, J. C., Kindig, D. N., and Holland, M. M. (2009). The Emergence of Surface-Based Arctic Amplification. *Cryosphere* 3, 11–19. doi:10.5194/tc-3-11-2009

Serreze, M. C., and Francis, J. A. (2006). The Arctic Amplification Debate. *Clim. Chang.* 76, 241–264. doi:10.1007/s10584-005-9017-y

Sharp, M., Tranter, M., Brown, G. H., and Skidmore, M. (1995). Rates of Chemical Denudation and CO_2 Drawdown in a Glacier-Covered Alpine Catchment. *Geology* 23, 61–64. doi:10.1130/0091-7613(1995)023<0061:rocdac>2.3.co;2

Shin, D., Lee, J.-I., Hwang, J., and Hur, S.-D. (2009). Hydrothermal Alteration and Isotopic Variations of Igneous Rocks in Barton Peninsula, King George Island, Antarctica. *Geosci. J.* 13, 103–112. doi:10.1007/s12303-009-0009-1

IPCC (2007). *Climate Change 2007: The Physical Science Basis. Contribution of Working Group I to the Fourth Assessment Report of the Intergovernmental Panel on Climate Change*. Editors S. Solomon, D. Qin, M. Manning, Z. Chen, M. Marquis, K. B. Averyt, et al. (Cambridge, United Kingdom and New York, USA: Cambridge University Press).

Teng, F. Z., McDonough, W. F., Rudnick, R. L., Dalpé, C., Tomascak, P. B., Chappell, B. W., et al. (2004). Lithium Isotopic Composition and Concentration of the Upper Continental Crust. *Geochim. Cosmochim. Acta* 68, 4167–4178. doi:10.1016/j.gca.2004.03.031

Tomascak, P. B., Tera, F., Helz, R. T., and Walker, R. J. (1999). The Absence of Lithium Isotope Fractionation During Basalt Differentiation: New Measurements by Multicollector Sector ICP-MS. *Geochim. Cosmochim. Acta* 63, 907–910. doi:10.1016/s0016-7037(98)00318-4

Tranter, M. (2003). "Geochemical Weathering in Glacial and Proglacial Environments," in *Treatise on Geochemistry* (Oxford: Pergamon), 189–205. doi:10.1016/b0-08-043751-6/05078-7

Verney-Carron, A., Vigier, N., and Millot, R. (2011). Experimental Determination of the Role of Diffusion on Li Isotope Fractionation During Basaltic Glass Weathering. *Geochim. Cosmochim. Acta* 75, 3452–3468. doi:10.1016/j.gca.2011.03.019

Vigier, N., Bourdon, B., Turner, S., and Allègre, C. J. (2001). Erosion Timescales Derived from U-Decay Series Measurements in Rivers. *Earth Planet. Sci. Lett.* 193, 549–563. doi:10.1016/s0012-821x(01)00510-6

Vigier, N., Decarreau, A., Millot, R., Carignan, J., Petit, S., and France-Lanord, C. (2008). Quantifying Li Isotope Fractionation During Smectite Formation and Implications for the Li Cycle. *Geochim. Cosmochim. Acta* 72, 780–792. doi:10.1016/j.gca.2007.11.011

Vigier, N., Gislason, S. R., Burton, K. W., Millot, R., and Mokadem, F. (2009). The Relationship Between Riverine Lithium Isotope Composition and Silicate Weathering Rates in Iceland. *Earth Planet. Sci. Lett.* 287, 434–441. doi:10.1016/j.epsl.2009.08.026

Walker, J. C. G., Hays, P. B., and Kasting, J. F. (1981). A Negative Feedback Mechanism for the Long-Term Stabilization of Earth's Surface Temperature. *J. Geophys. Res.* 86, 9776–9782. doi:10.1029/jc086ic10p09776

Welch, K. A., Lyons, W. B., Whisner, C., Gardner, C. B., Gooseff, M. N., Mcknight, D. M., et al. (2010). Spatial Variations in the Geochemistry of Glacial Meltwater Streams in the Taylor Valley, Antarctica. *Antarct. Sci.* 22, 662–672. doi:10.1017/s0954102010000702

Wimpenny, J., Burton, K. W., James, R. H., Gannoun, A., Mokadem, F., and Gíslason, S. R. (2011). The Behaviour of Magnesium and its Isotopes During Glacial Weathering in an Ancient Shield Terrain in West Greenland. *Earth Planet. Sci. Lett.* 304, 260–269. doi:10.1016/j.epsl.2011.02.008

Wimpenny, J., Gíslason, S. R., James, R. H., Gannoun, A., Pogge von Strandmann, P. A. E., and Burton, K. W. (2010b). The Behaviour of Li and Mg Isotopes During Primary Phase Dissolution and Secondary Mineral Formation in Basalt. *Geochim. Cosmochim. Acta* 74, 5259–5279. doi:10.1016/j.gca.2010.06.028

Wimpenny, J., James, R. H., Burton, K. W., Gannoun, A., Mokadem, F., and Gíslason, S. R. (2010a). Glacial Effects on Weathering Processes: New Insights from the Elemental and Lithium Isotopic Composition of West Greenland Rivers. *Earth Planet. Sci. Lett.* 290, 427–437. doi:10.1016/j.epsl.2009.12.042

Witherow, R. A., Lyons, W. B., and Henderson, G. M. (2010). Lithium Isotopic Composition of the McMurdo Dry Valleys Aquatic Systems. *Chem. Geol.* 275, 139–147. doi:10.1016/j.chemgeo.2010.04.017

You, C.-F., and Chan, L.-H. (1996). Precise Determination of Lithium Isotopic Composition in Low Concentration Natural Samples. *Geochim. Cosmochim. Acta* 60, 909–915. doi:10.1016/0016-7037(96)00003-8

Zhang, X., Saldi, G. D., Schott, J., Bouchez, J., Kuessner, M., Montouillout, V., et al. (2021). Experimental Constraints on Li Isotope Fractionation During the Interaction Between Kaolinite and Seawater. *Geochim. Cosmochim. Acta* 292, 333–347. doi:10.1016/j.gca.2020.09.029

Zimov, S. A., Schuur, E. A. G., and Chapin, F. S., III (2006). Permafrost and the Global Carbon Budget. *Science* 312, 1612–1613. doi:10.1126/science.1128908

Conflict of Interest: The authors declare that the research was conducted in the absence of any commercial or financial relationships that could be construed as a potential conflict of interest.

frontiers | Frontiers in Earth Science

TYPE Original Research
PUBLISHED 23 January 2023
DOI 10.3389/feart.2022.1056881

OPEN ACCESS

EDITED BY
Xiao-Ping Xia,
Guangzhou Institute of Geochemistry (CAS), China

REVIEWED BY
Yaowu Hu,
Fudan University, China
Huimin Yu,
University of Science and Technology of China, China

*CORRESPONDENCE
Kang-Jun Huang,
hkj@nwu.edu.cn

SPECIALTY SECTION
This article was submitted to Geochemistry, a section of the journal Frontiers in Earth Science

RECEIVED 29 September 2022
ACCEPTED 31 October 2022
PUBLISHED 23 January 2023

CITATION
Gao F, Zhang P, Liu K, Ling X and Huang K-J (2023), Magnesium isotopic composition of modern human teeth enamel and its implications for dietary reconstructions.
Front. Earth Sci. 10:1056881.
doi: 10.3389/feart.2022.1056881

Magnesium isotopic composition of modern human teeth enamel and its implications for dietary reconstructions

Fan Gao[1,2,3], Pan Zhang[1], Keyu Liu[4], Xue Ling[4] and Kang-Jun Huang[1]*

[1]State Key Laboratory of Continental Dynamics and Shaanxi Key Laboratory of Early Life and Environment, Department of Geology, Northwest University, Xi'an, China, [2]State Key Laboratory of Lithospheric Evolution, Institute of Geology and Geophysics, Chinese Academy of Sciences, Beijing, China, [3]College of Earth and Planetary Sciences, University of Chinese Academy of Sciences, Beijing, China, [4]Key Laboratory of Cultural Heritage Research and Conservation (Northwest University), Ministry of Education, Xi'an, China

Metal stable isotopic composition of dental enamel is a novel proxy for reconstructing human dietary structure. Magnesium is the second most prevalent element in teeth only after calcium. Significant isotopic fractionation of Mg isotopes during biological processes implies its great advantages in reconstructing human recipes. To evaluate the potential of the Mg isotopic composition of dental enamel in learning the human dietary structure, elemental and Mg isotopic analyses were performed on the modern human teeth from regions in northern and southern China with various dietary characteristics. Our findings reveal that southern Chinese teeth enamel has higher Mg contents and heavier Mg isotopic compositions (-0.69‰ for SN and -0.66‰ for Hangzhou) than those of their northern counterparts (–1.27‰ for Weinan and –1.33‰ for Puyang). Such discrepancy cannot be attributed to the provenance heterogeneity or individual metabolic processes. Instead, the correlations between cereal-based dietary patterns and the δ^{26}Mg in dental enamel demonstrate that the structure of the staple diet is more responsible for the Mg isotopic signatures. Moreover, heavier Mg isotopic compositions have been observed in dental enamel of individuals with higher rice and lower wheat in the diet, indicating that Mg isotopes are a promising tracer for rebuilding individual or population plant-based dietary structures as well as distinguishing more specific species within C_3 plants. These findings suggest that Mg isotopes in teeth enamel have the great potential to better identify the food composition and constrain the diet structure of ancient humans.

KEYWORDS

stable isotope, magnesium, dental enamel, plant food, dietary indicator

Introduction

Diet is a fundamental approach to comprehending human culture, including productivity, economic status, and society's cultural characteristics (Lambert et al., 1984; Ling, 2010). Furthermore, it has been proposed that the evolution of early humans is accompanied by a shift in nutritional structure (Ungar et al., 2006). As a result, reconstructing the ancient human diet could provide key information about human evolution and paleoecology.

Over the past few decades, stable isotopes have been frequently employed to rebuild diet and trophic structures in ancient food webs (Kiple and Ornelas, 2000). Most proxies rely on stable isotope ratios of light elements (e.g., carbon, nitrogen, oxygen, and sulfur) preserved in fossilized teeth and bones (Schoeninger, 2010). These traditional isotope ratio studies, however, have many limitations. For example, although C isotopes can distinguish C_3 plants from C_4 plants, no additional information is available within C_3 (C_4) plant groups (Katzenberg and Waters-Rist, 2018). In addition, traditional isotope ratios analysis relies on organic matter fractions (e.g., collagen), which are difficult to be preserved in human tissues older than 10 ka due to the diagenesis, restricting the application of this method to ancient human remains.

The recent development of Multi-Collector Inductively Coupled Plasma Mass Spectrometry (MC-ICP-MS) allows the precise measurement of metal isotope ratios with low concentrations in human organs or tissues, such as Mg isotopes (Teng, 2017). Magnesium is an essential element that plays an irreplaceable role in both plants and animals. It is the center of chlorophyll in plants and vital to photosynthesis (Black et al., 2006). Due to comparable ionic radii and chemical behavior, Mg^{2+} typically substitutes Ca^{2+} into the apatite structure in the tissues of animals (bones and teeth). There is about 25 g Mg in an adult human body, which is involved in more than 600 enzymatic reactions and regulates cellular metabolic processes (Elin, 1987; Nadler and Rude, 1995; Vormann, 2003; De Baaij et al., 2015). In addition, Mg isotopes are usually significantly fractionated during plant and animal physiological activities (Black et al., 2008; Bolou-Bi et al., 2010; Teng, 2017; Wang et al., 2020; Wrobel et al., 2020). Recent research on plants manifested that different species of plants have distinguishable Mg isotopic compositions, and the light Mg isotopes are progressively enriched from the roots to the stems (Black et al., 2006; Black et al., 2007; Black et al., 2008; Bolou-Bi et al., 2010; Wang et al., 2020). Studies on terrestrial vertebrates in the same ecosystem demonstrated that the Mg isotopic compositions of animals feeding on C_3 plants were lighter than that of animals grazing on C_4 plants and that the δ^{26}Mg values of hard tissues became gradually higher as trophic levels increased (Martin et al., 2014; Martin et al., 2015b). Thus, Mg isotopes may have the potential to trace ancient human recipes.

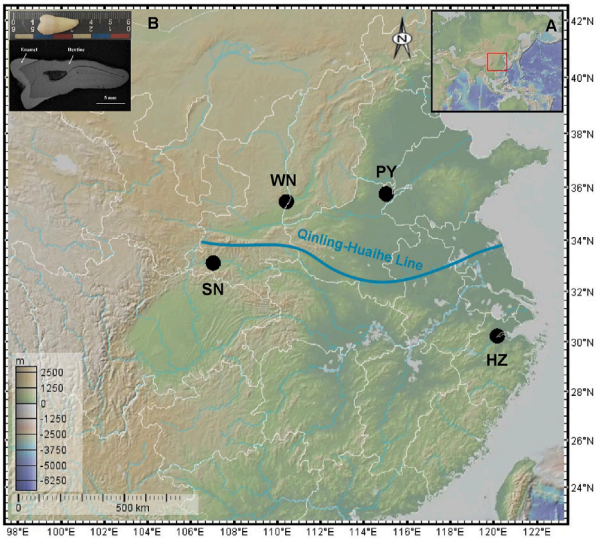

FIGURE 1
(A) Location of the sampling sites. WN-Weinan, PY-Puyang, SN-Southern Shaanxi regions, HZ-Hangzhou. **(B)** The morphology of a tooth sample and Back-scattered electron image of a tooth sample section.

To date, however, few studies have reported the Mg isotopic composition of human tissues. A recent experiment has displayed that teeth enamel is the most reliable material within all the tissues for dietary and physiological reconstruction because of its dense structure (Weber et al., 2021). Nevertheless, the relationship between the Mg isotopic composition of human teeth enamel and individual diet is still unclear, which dramatically hinders the application of the Mg isotopic system for tracing ancient human dietary structures. In this study, elemental and Mg isotopic composition of modern human dental enamel from four Chinese regions with different nutritional characteristics were measured to explore the relationship between the δ^{26}Mg in dental enamel and human dietary structure. This first database of the Mg isotopic compositions in human dental enamel provides novel information on ancient human recipes and evolution: the δ^{26}Mg in dental enamel is mainly controlled by plant-based dietary structure and the various intake proportions of rice and wheat indicate that the Mg isotopic system has the potential to trace specific plant species within the C_3 group.

Materials and methods

Geological background and samples

Based on the geographical Qinling-Huaihe Line, China can be divided into northern China and southern China (Figure 1A).

TABLE 1 Magnesium elemental contents and isotopic compositions of modern human teeth enamel from WN (Weinan), PY (Puyang), SN (Southern Shaanxi regions) and HZ (Hangzhou).

Region	Sample number	Tooth type	Mg content (wt%)	δ^{25} Mg (‰)	2SD	δ^{26} Mg (‰)	2SD
WN	WN 1	-	0.21	−0.82	0.04	−1.65	0.08
	WN 2	premolar	0.27	−0.61	0.03	−1.23	0.07
	WN 3	premolar	0.21	−0.57	0.07	−1.14	0.06
	WN 4	molar	0.28	−0.53	0.03	−1.05	0.08
PY	PY 1	molar	0.24	−0.64	0.05	−1.28	0.07
	PY 2	molar	0.23	−0.47	0.02	−0.98	0.04
SN	SN 1	incisor	0.44	−0.09	0.01	−0.22	0.02
	SN 2	premolar	0.40	−0.19	0.05	−0.41	0.03
	SN 3	incisor	0.26	−0.55	0.06	−0.93	0.10
	SN 4	premolar	0.31	−0.66	0.04	−1.25	0.01
	SN 5	molar	0.75	−0.38	0.11	−0.78	0.04
	SN 6	molar	0.28	−0.29	0.06	−0.61	0.07
	SN 7	molar	0.28	−0.31	0.01	−0.63	0.05
	SN 8	premolar	0.56	−0.35	0.08	−0.68	0.01
HZ	HZ 1	molar	0.28	−0.36	0.11	−0.69	0.05
	HZ 2	molar	0.19	−0.32	0.05	−0.69	0.04
	HZ 3	premolar	0.23	−0.48	0.00	−0.84	0.02
	HZ 4	molar	0.31	−0.28	0.04	−0.53	0.09
	HZ 5	premolar	0.34	−0.29	0.10	−0.60	0.06
	HZ 6	molar	0.28	−0.15	0.00	−0.35	0.08
	HZ 7	premolar	0.28	−0.20	0.01	−0.46	0.01
	HZ 8	canine	0.29	−0.22	0.03	−0.44	0.08
	HZ 9	molar	0.18	−0.38	0.02	−0.75	0.02
	HZ 10	molar	0.27	−0.43	0.03	−0.82	0.06
	HZ 11	molar	0.23	−0.50	0.07	−0.95	0.02
	HZ 12	molar	0.46	−0.26	0.02	−0.49	0.05
	HZ 13	molar	0.56	−0.35	0.04	−0.72	0.09
	HZ 14	molar	0.25	−0.36	0.02	−0.75	0.01
	HZ 15	molar	0.23	−0.44	0.00	−0.80	0.01
Standard	SW	N.D	N.D	−0.42	0.06	−0.83	0.12
	BCR-2	N.D	N.D	−0.13	0.02	−0.23	0.06
samples	BHVO-2	N.D	N.D	−0.14	0.05	−0.30	0.06

"-" means that the tooth is incomplete to identify the types. "N.D." means no data.
All samples were measured 3 times.

Northern China has lower precipitation and wheat and maize are the main food crops; while the wetter southern China produces rice as the main food crop. To cover various typical dietary characteristics, 29 modern human permanent teeth from were selected four regions of China (Figure 1). More specifically, four teeth were collected from Weinan (WN), central Shaanxi, which is located in the middle reaches of the Yellow River, eastern Guanzhong Plain. It belongs to the semi-humid and semi-arid monsoon climate zone, and wheat is the main crop in this area. Two teeth were collected from Puyang (PY), northeast of Henan, which seats in the lower reaches of the Yellow River in the central plains. It has a warm temperate sub-humid continental monsoon climate, while wheat and maize are the main crops here. Eight teeth were selected from southern Shaanxi regions (SN), which is located right below the Qinling-Huaihe line and bears a wet climate and mainly lives on rice. The rest 13 teeth were from Hangzhou (HZ), Zhejiang Province, located on the south side of the Yangtze River Delta in the subtropical monsoon region and mainly produces rice. In short, WN and PY are typical northern China cities, while SN and HZ represent southern cities.

Except for one fragment without morphological characteristics (WN1, Table 1), samples include 17 molars, eight premolars, two incisors, and one canine. All the samples

were collected at local clinics or hospitals. Detailed information about the samples is provided in Table 1.

Analytical methods

The tartar on the teeth surface was removed mechanically by drill firstly and then freeze-dried at -60°C for 7 days. After that, ~10 mg enamel powder closed to enamel surface of each tooth (Figure 1B) was drilled and dissolved in 1 ml double-distilled 14 N HNO_3 on an electric hot plate overnight. After completely dissolved, the sample solution was dried and re-dissolved in 0.5 ml double-distilled 14 N HNO_3. Then aliquots of solutions were extracted and diluted for elemental concentration analyses on iCAP PRO ICP-OES at the State Key Laboratory of Continental Dynamics (SKLCD), department of geology, Northwest University, China. Gravitationally prepared standard solutions were used to calibrate the concentration curve of measured elements; multi-element standard solutions were used for monitoring and the uncertainties of measured elements were better than 10%.

Then the solutions containing ~10–50 μg Mg were dried and dissolved by 12 N distilled HCl to pass through two columns for the purification of Mg. Detailed separation methods have been established in previous studies (Bao et al., 2019). Column #1, filled with 2.0 ml of Bio-Rad AG-50 W-X12 resin (200–400 mesh), was used to separate Mg from Ca. Column #2, filled with 0.5 ml of Bio-Rad AG50 W-X12 resin (200–400 mesh), was designed to separate Mg from all other matrix metals (Al, Na, Fe, *etc.*). To achieve the complete elution of matrix metals, each sample was passed through both columns twice. At least two standard references (seawater, BCR-2, BHVO-2) were passed through the columns along with samples to test the effect of separation and purification of each batch. The recovery of Mg was as much as 99% in the whole procedure, and the total blank was negligible compared to the mass of Mg in samples. After that, all purified Mg solutions were dried down on the electric hot plate and then re-dissolved in 14 N HNO_3 for the following isotopic measurement.

Magnesium isotopic ratios were measured using Nu plasma II MC-ICP-MS at the SKLCD. The pure Mg solution was introduced with 2% HNO_3 as the acid media and pure argon as the carrier gas through an autosampler, a self-priming nebulizer, and a dual-path quartz fog chamber. During the test, three Mg isotopes (24, 25, 26) were monitored simultaneously in L5, Ax, and H5 Faraday cups under low-resolution mode. The background signal for ^{24}Mg (~2×10^{-3} V) was negligible relative to the sample signal (>8 V). The standard-sample bracketing technique (SSB) was used to correct the instrumental mass bias to obtain the Mg isotopic ratios. The analysis results are expressed as the per mil deviation from the isotopic compositions of the DSM3 international standard (Dead Sea Magnesium Ltd., Israel):

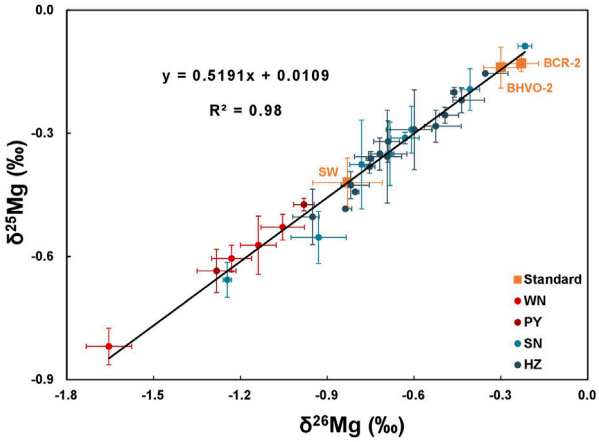

FIGURE 2
Diagram of $\delta^{26}Mg$ vs $\delta^{25}Mg$ values for human dental enamel. The solid line represents the fractionation line with a slope of 0.519. Error bars indicate the 2SD of the mean value.

$$\delta^{X}Mg = \left\{ \left[\left({}^{X}Mg/{}^{24}Mg \right)_{sample} / \left({}^{X}Mg/{}^{24}Mg \right)_{DSM3} \right] - 1 \right\} \times 1000 \quad (1)$$

where x refers to mass 25 or 26. Uncertainties for $\delta^{25}Mg$ and $\delta^{26}Mg$ of standards and samples are given as two standard deviations (2SD) based on repeated measurements. During the analytical session, data for seawater (−0.83 ± 0.12‰), BCR-2 (−0.23 ± 0.06‰), and BHVO-2 (−0.30 ± 0.06‰) obtained in this study are all identical within errors to the established values (Huang et al., 2018; Bao et al., 2019; Ma et al., 2019). In addition, the $\delta^{26}Mg$ and $\delta^{25}Mg$ values of all samples and standards in this study lie on a mass-dependent fractionation line with a slope of 0.519 (Figure 2), which is consistent with the theoretical mass-dependent fractionation law (Young et al., 2002).

Results

The Mg contents of Chinese dental enamel vary by region, ranging from 0.18 to 0.75 wt% (Table 1). Overall, human teeth enamel from southern China has higher Mg contents than those from northern China (Figure 3A). Teeth enamel from WN and PY have almost the same level of Mg content, with a mean value of 0.24 wt%. Teeth enamel from HZ has higher Mg contents (averagely 0.29 wt%). Remarkably, teeth enamel from SN has a mean Mg content of 0.41 wt%, which is the highest value among these four areas.

The $\delta^{26}Mg$ values of human dental enamel from different China regions exhibit a large variation, ranging from -1.65‰ to -0.22‰ (Figure 3B). Dental enamel from southern China has

overall heavier Mg isotopic compositions than those from northern China. It is worth noting that WN samples are highly depleted in heavy Mg isotopes with an average δ^{26}Mg value of -1.27 ± 0.27‰ (SD). Samples from PY have intermediate δ^{26}Mg values, with an average value of -1.13 ± 0.21‰ (SD). Teeth enamel in southern China has notable heavier mean δ^{26}Mg values: 0.69‰ ± 0.31‰ (SD) for SN samples and -0.66 ± 0.17‰ (SD) for HZ samples, respectively. Overall, the Mg isotopic composition of dental enamel gradually becomes heavier from northern China (WN and PY) to southern China (SN and HZ).

Discussion

Our data show distinct geographical differences in both Mg content and Mg isotopic composition of human dental enamel. Teeth enamel from southern China has overall higher Mg contents and heavier Mg isotopic compositions than those from northern China (Figure 3). Magnesium in the human body firstly involves the uptake of Mg from food and drinking water, which Mg and δ^{26}Mg features are controlled by the local context (including soil and water) through cultivating agricultural products. Furthermore, the partition and fractionation during the growth of these products may influence the Mg and δ^{26}Mg features of the food and drinking water intake. Then, the dietary preference and the digestion and migration of Mg in the human body may also produce the variations of Mg contents and δ^{26}Mg values in enamel among individuals and groups of people. Therefore, these systematic differences in Mg contents and δ^{26}Mg values in human enamel may be generated by provenance heterogeneity, physiological metabolism, dietary structure, and the associated Mg isotope signature inheritance and fractionation, which will be discussed accordingly in the followings.

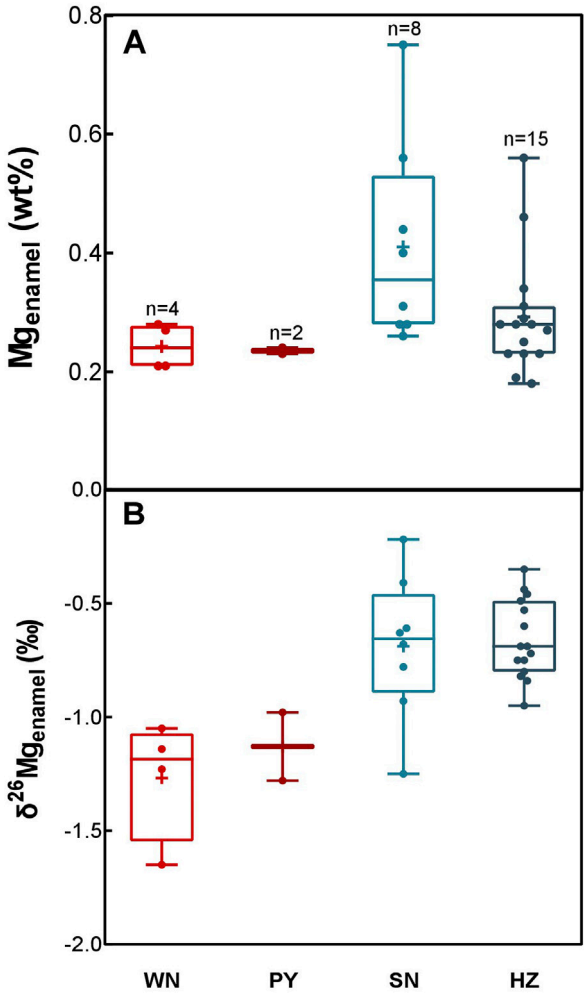

FIGURE 3
Magnesium content **(A)** and δ^{26}Mg values **(B)** in modern human teeth enamel from different regions. "+" represent the average value. The boxes range between min to max and show the median value.

The provenance effect

The regional context may inevitably affect the Mg isotopic signatures of human tissues by controlling the isotope ratios of soil and regional water. Briefly, drinking water could involve the human body by direct absorption. Soil and soil water characteristics could be transferred to the human body *via* producers into the food web. Published Mg isotopic compositions of natural waters and soils span a relatively wide range (Tipper et al., 2006; Wimpenny et al., 2014; Fan et al., 2016; Gao et al., 2018; Zhao et al., 2022), and the Mg isotopic signatures are highly controlled by several factors, such as local lithologies, seasonality, and runoff (Tipper et al., 2006; Nitzsche et al., 2019). Furthermore, the plants and animals also show large Mg isotope variability (Black et al., 2008; Bolou-Bi et al., 2012; Martin et al., 2014; Martin et al., 2015b). Some variations in plants and animals are suggested to involve the provenance (Martin et al., 2014), although the direct evidence is lacking. These contexts indicate that it is imperative to evaluate the provenance effect before further interpretation of the Mg isotopic variability in human enamel.

The precise local isotopic signatures of each region are unavailable, which are also meaningless since the exact isotopic compositions of the context may vary among each product and are impractical to be traced. Therefore, δ^{26}Mg data from the Yellow River and loess here are tentatively used to represent the Mg isotopic signatures of the water and soil in northern China, and the limited δ^{26}Mg data for the Yangtze River and southern red soils are also used for the representative of the substrate of southern China (Tipper et al., 2006; Wimpenny et al., 2014; Fan et al., 2016; Gao et al., 2018; Xu et al., 2022). Compiling

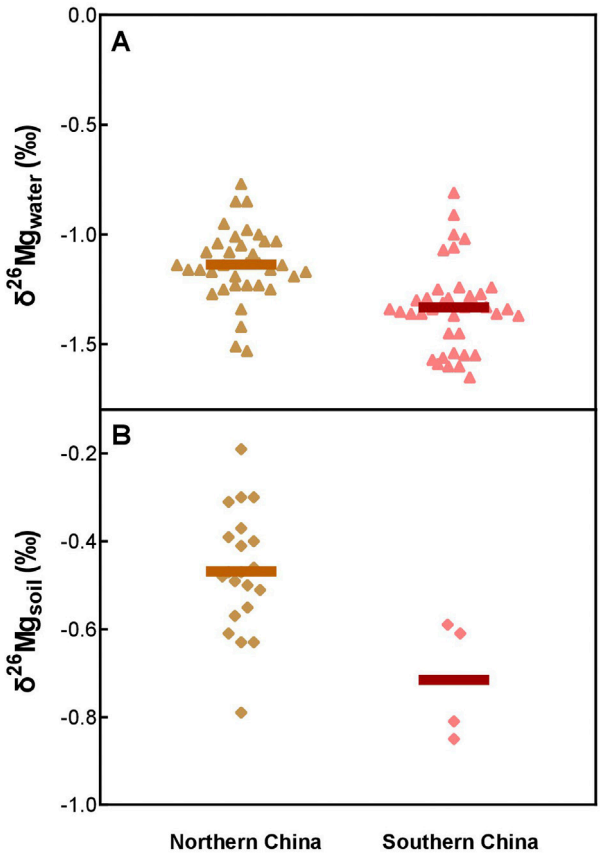

FIGURE 4
Mg isotopic compositions of soils **(A)** and regional water **(B)** in northern and southern China. Data are from Fan et al., 2016; Gao et al., 2018; Tipper et al., 2006; Wimpenny et al., 2014; Xu et al., 2022. The horizontal bars are mean values.

these data, we found that the mean δ^{26}Mg value of river water in southern China (−1.46‰) is lighter than that of northern China (−1.14‰). Similarly, the mean δ^{26}Mg value of soil in southern China (−0.72‰) is also lighter than that of northern China (−0.47‰). This compilation dataset indicates that the context δ^{26}Mg in southern China is relatively lighter than that of northern China (Figure 4), which cannot account for the relatively heavier δ^{26}Mg values of human enamel in southern China. Therefore, the provenance likely has limited effects on the distinct Mg isotopic compositions in human teeth enamel between southern and northern regions.

The physiology effect

Magnesium is indispensable for maintaining structural and biochemical homeostasis in vertebrate animals, including humans (Ryan, 1991; Brown, 1999). It assists in activating more than 600 enzymes in the body and regulating human cells (Mark and Mediawerks, 2007; Faryadi, 2012). The pervasive participation of Mg in the physiological activities of human beings reflects that the potential migration and re-distribution of Mg inside human tissues and organs may generate Mg isotope fractionations. Thus, it should be considered whether the physiology, gender, age or tooth types have an impact on the δ^{26}Mg values in human enamel.

The Han Chinese, the most widely distributed ethnic group in China, belongs to the typical East Asian ethnic group in terms of their origins and formation, with homogeneous and differentiated physical characteristics (Zhao, 2016). There should be no significant physiological differences between modern Chinese if the effects of the disease are not considered. That means the isotopic fractionation of Mg produced by human metabolism can be considered consistent among individuals. Hence, the differences in population metabolism are unlikely to generate such huge a regional discrepancy in enamel δ^{26}Mg.

Unlike iron isotopes, which behave divergently between males and females (Walczyk and Blanckenburg, 2002; Jaouen and Balter, 2014; Van Heghe et al., 2014), Mg isotopes do not show a direct discrepancy between the sexes due to their existing status and physiological activities involved (Elin, 1987; Nadler and Rude, 1995; Faryadi, 2012; De Baaij et al., 2015). Furthermore, although our teeth samples do not have specific age information due to incomplete sample collection, dental enamel normally developed completely in childhood and did not change once formed and thus records the isotopic composition of adolescence (Grupe, 1998). Therefore, it can be inferred that age could not lead to such a vast distinction in the Mg isotopic composition of enamel.

In addition to metabolism, gender, and age effects, the influence of tooth types on enamel δ^{26}Mg also should be considered. The δ^{26}Mg of different types of teeth (canine, incisor, premolar, and molar) display overlapped variations (Table 1), and the Student's *t* test for every two tooth types does not show significant differences ($p > 0.05$). It thus suggests that the influence of tooth types on the Mg isotopic difference in dental enamel between southern Chinese and northern Chinese is negligible. Overall, the metabolic effect is thought to have limited influence on Mg isotopic variation in human teeth enamel.

The dietary structure effect

Food-intaking is the main way humans derive nutrients, including Mg. Individuals have various dietary habits which contain Mg with large variability. Published studies have shown significant variations of δ^{26}Mg among plants and animals (Black et al., 2008; Bolou-Bi et al., 2012; Martin et al., 2014; Martin et al., 2015b). Moreover, animals feeding on different types of plants or different trophic levels of food

TABLE 2 The annual yield of major crops in four regions (Unit: ten thousand tons).

Major crops	Regions	WN	PY	SN	HZ
	Wheat	3.92	166.92	40.34	31.00
	Rice	0.00	18.29	7.26	590.10
C_3plants	Bean	0.09	6.37	4.77	24.20
	Peanut	0.06	9.80	30.30	4.01
	Rapeseed	0.14	0.08	30.30	25.90
C_4plant	Maize	2.52	93.35	74.16	30.10

1)Considering the output, six major crops are collected in our study, including 5 kinds of C_3 plants and 1 type C_4 plant; 2) SN includes three prefecture-level cities of Hanzhong, Ankang and Shangluo, and the values in the table are the average of the production of the three cities; 3) There is no crop production data of Hangzhou, so the crop production in Hangzhou is substituted by Zhejiang Province agricultural data; 4) Referring China Food Composition (2009), the M_{crop}, M_{wheat}, M_{rice} could be calculated. The Mg content is 5 of wheat, 12 of rice, 199 of bean, 110 of peanut, 3 of rapeseed and 32 of maize (unit: mg / 100 g).

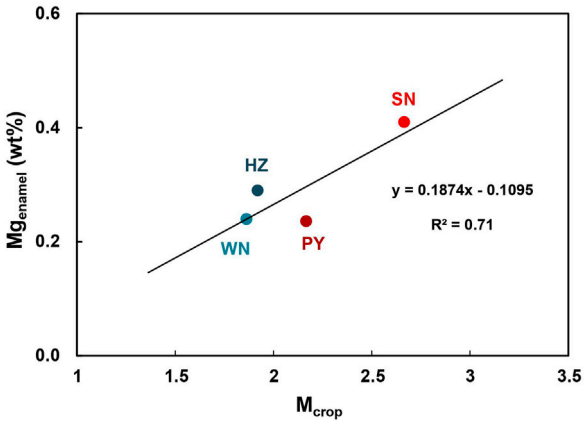

FIGURE 5
Relationship between M_{crop} and Mg_{enamel}. Regional M_{crop} is measured by the local crop yield structure. Detailed calculation is referred to Table 2.

display distinct Mg isotopic compositions and variations (Martin et al., 2014; Martin et al., 2015a), reflecting that enamel δ^{26}Mg can be significantly affected by food and dietary structure. Thus, the effect of dietary structure on the systematic Mg isotopic differences in human enamel from southern and northern China, which rely on different dietary habits, should be considered and evaluated.

The Chinese Balanced Dietary Pagoda (2016) gives the Chinese a scientifically daily dietary quantity model that an adult should take ~1600 ml water, ~350 g grain, ~400 g vegetable, ~300 g fruit, ~50 g egg, *etc.* The contributions of Mg from different dietary sources can be estimated based on this criterion and the food Mg content from The China Food Composition (Yang et al., 2019). Drinking water contributes less than 1‰ Mg to the human body, while meat and plant foods account for ~24% and ~75.7% respectively. It directly demonstrates that plant foods, including grain and vegetables, are primarily responsible for human Mg sources. Thus, the dietary diversities, especially plant-based nutritional structures may be deemed to result in the regional Mg isotopic differences in human enamel. However, it is impractical to directly calculate the Mg content and Mg isotopic compositions of meals for individuals or regional people. Here we tentatively use the output proportion of local crops to quantitively evaluate the average grain-food consumption of local humans. Assuming the people's dietary preference is in proportion to the local crops' yield, that means the southern diet is dominated by rice and the northern diet is wheat (Chen et al., 2018; Li et al., 2020). According to these, the uptake of Mg from food of people from four regions can be estimated. Then given that the enrichment coefficient of Mg in enamel is the same for all the people, the entire enamel Mg content acquired by grain food should proportionally equal to the sum of Mg content that all local crops contain. Furthermore, since wheat and rice are two dominant staple food in the regions studied, the leverage of these two crops on Mg content and Mg isotopic compositions of human teeth enamel can also be evaluated. To make a qualitative comparison of dietary structure, we give some calculations as follows:

$$M_{crop} = \Sigma_{CS}\left(Y_{crop} \times C_{crop}\right) \quad (2)$$

$$M_{wheat} = Y_{wheat} \times C_{wheat} \quad (3)$$

$$M_{rice} = Y_{rice} \times C_{rice} \quad (4)$$

where M_{crop} is the total Mg content provided by all local crops, CS is the crop species, Y_{crop} is the crop yield, C_{crop} is the crop unit Mg content, M_{wheat} is the Mg content provided by local wheat, Y_{wheat} is the wheat yield, C_{wheat} is the unit Mg content of wheat, M_{rice} is the Mg mass fraction provided by local rice, Y_{rice} is the rice yield, and C_{rice} is the unit Mg content of rice. More information is in Table 2.

The calculated M_{crop} values are positively correlated to the Mg content in local human enamel (Figure 5). This result convinces that it is plausible to use dietary structure and local crop yield to estimate the uptake of Mg from food for people from different regions. It also qualitatively explains the phenomenon that southerners have higher enamel Mg content and northerners have lower enamel Mg content (Figure 3A). Besides, there is a straightforward linear positive (negative) correlation between $\delta^{26}Mg_{enamel}$ and M_{wheat}/M_{crop} (M_{rice}/M_{crop}) (Figure 6). These trends support that staple diet composition likely controls the enamel δ^{26}Mg values differences among regions. From WN to PY to SN to HZ, people become increasingly reliant on rice and less dependent on wheat, corresponding to the sequentially heavier Mg isotopic composition in teeth enamel (Figure 6). Moreover, the opposite

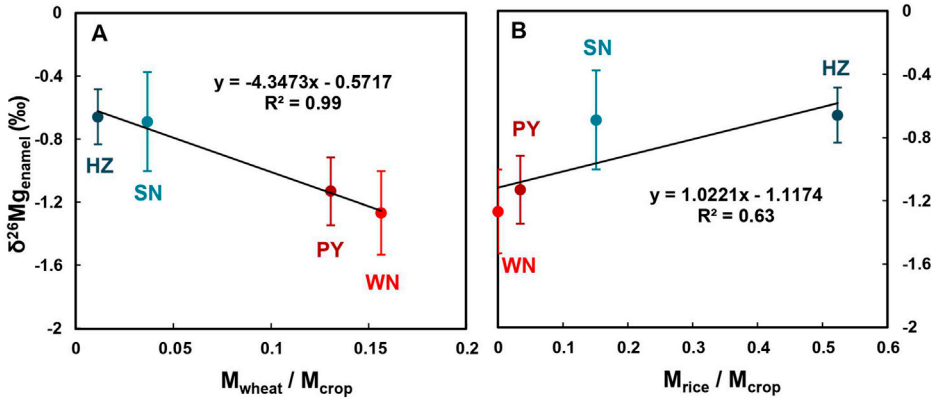

FIGURE 6
The M_{wheat}/M_{crop} **(A)** and M_{rice}/M_{crop} **(B)** in different regions and the $\delta^{26}Mg_{enamel}$ in local people (mean with 2SD, refer to Table 2 for detailed calculation method). Error bars indicate the 2SD of the mean value.

tendency of the two crops indicates that wheat provides isotopically lighter Mg while rice has heavier Mg isotopes (Figure 6). Although it is still unclear whether wheat preferentially incorporates lighter Mg isotopes into its seed compared to rice, the limited published data show isotopically lighter wheat seed compared to rice seed (δ^{26}Mg -0.8‰ ~ -1.83‰ vs -0.67‰) (Black et al., 2008; Bolou-Bi et al., 2009; Bolou-Bi et al., 2010; Bolou-Bi et al., 2012; Martin et al., 2014; Mavromatis et al., 2014; Martin et al., 2015b; Gao et al., 2018; Kimmig et al., 2018; Grigoryan et al., 2020; Wang et al., 2020; Wrobel et al., 2020). However, current research conditions on wheat and rice are not consistent and the specific mechanism is not clear. Hence, it is unavailable to compare δ^{26}Mg values directly. Moreover, the growth conditions of wheat and rice in northern and southern China need to be taken into account. Thus, published data only demonstrate the δ^{26}Mg values indeed differ between rice and wheat, which potentially supports our findings, but more research limitations on rice and wheat are needed. Furthermore, both rice and wheat are typical C_3 plants. The difference in the intake proportions of rice and wheat is reflected in the Mg isotopic composition of human enamel (Figure 6), which offers a potentially novel tool to understand human dietary structure ulteriorly. It indicates that the δ^{26}Mg value of human dental enamel is related to a cereal-based food structure. The Mg isotopic system may trace more details and potentially distinguish specific plant species within the C_3 plants. Additionally, the enamel δ^{26}Mg of people from all regions display large variations (Figure 3B), which may involve the diversity of dietary structures among individuals and the possible influence of other factors abovementioned.

To date, it is still unclear about the isotope fractionation from diet to enamel. Limited studies brought up with a biological isotopic fractionation model of Mg in mammals that there is no fractionation between bone and diet, while muscle accumulates heavier Mg isotopes and feces is the ^{26}Mg-depleted reservoir (Martin et al., 2015b). We could not elucidate the physiology of Mg isotope fractionation, but the higher Mg content and higher δ^{26}Mg values in human enamel from southern China are consistent with their rice-dependent dietary characteristic, demonstrating the dietary structure dominates enamel Mg isotopic compositions. Also, the distinct δ^{26}Mg values in human enamel of southerners and northerners relying on different C_3 staple crops indicate that Mg isotopic system potentially distinguishes crop species among the C_3 group.

Implications for tracing dietary structure

Diet reconstruction is vital for studying the paleoecology and evolution of early hominins (Ungar, 2012). Direct food remains are often absent or under-represented in the depositional record, but stable isotopes in human apatite remain greatly documented the dietary inputs of ancient humans and are well-established dietary tracers (Makarewicz and Sealy, 2015; Katzenberg and Waters-Rist, 2018). The high abundance and biological isotopic fractionation of Mg make the Mg isotopic system promising for exploring human diet information. Bone Mg concentration has proven to be a poor dietary discriminator due to the unpredictable results (Lambert et al., 1979; Francalacci, 1989; Klepingera, 1990), but the Mg isotopic signatures detected in human enamel could provide another dimensional evidence.

In this study, we found a remarkable geographical distribution pattern that dental enamel of southerners has higher Mg content and heavier Mg isotopic composition than those of northerners. The strong correlation between the enamel

δ^{26}Mg and diet structure shows that Mg isotopes in enamel are more responsible for human nutritional structure, especially cereal-based dietary structure. Briefly, the northerners who prefer wheat have lower Mg content and lighter Mg isotopic composition in teeth enamel, while the southerner is opposite. Thereinto, the specific dietary structure means the proportion of wheat and rice, which are both C_3 plants. The intake ratio of different C_3 plants is reflected in the Mg isotopic composition in enamel, indicating that the Mg isotopic system may potentially distinguish specific plant species within the C_3 plants. In addition, human hard tissues inherit all dietary sources' weighted average Mg isotopic ratio characteristics (Martin et al., 2020), the other food intake, such as meat, may potentially be measured according to Mg isotopes.

Since the limited dataset has shown the large variability of δ^{26}Mg in human enamel and the distinct characteristics among groups with different dietary structures, more work can be done to develop Mg isotopes as a promising tracer in diet and relevant areas. The large δ^{26}Mg variability in one region and δ^{26}Mg differences between food and enamel may involve associated intake preference and isotope fractionation, which cannot be addressed by the current study. Feeding experiments on mammals may reveal the physiological processes associated with Mg isotope fractionation, the dominant control among various foods, and other key factors. The Mg isotope signatures of the source of foods also require systematic investigations.

Conclusion

In this study, we present the first dataset for Mg isotopic compositions of the human apatite tissues to our knowledge. The linear correlation between the Mg isotopic compositions of human enamel and the intake proportion of cereal crops reveals the Mg isotopic composition in human enamel relative to the plant-based diet structure. The regional δ^{26}Mg diversity in human enamel resulting from diet structure helps make the Mg isotopic system promising for identifying specific species among C_3 (C_4) plants. It suggests that Mg isotopes in human enamel could serve as a promising new tracer for human dietary structure, especially cereal food structure. Furthermore, the dense structure of enamel, which can resist diagenetic contamination and preserve the dietary records during the period of enamel deposition, provides an approach to exploring the ancient human recipe. Considering that the Mg isotopic signature is a relatively novel tool for reestablishing human diet structure and only a small sample dataset is analyzed, the application of this work still needs to be explored more by subsequent research.

Data availability statement

The datasets presented in this study can be found in online repositories. The names of the repository/repositories and accession number(s) can be found in the article/supplementary material.

Ethics statement

The studies involving human participants were reviewed and approved by The Medical Ethics Committee of Northwest University. The patients/participants provided their written informed consent to participate in this study. The animal study was reviewed and approved by Northwest University Medical Ethics Committee.

Author contributions

K-JH and XL conceived this study and Huang led the overall scientific questions. FG and PZ performed the test and data analysis. KL contributed to the sample pretreatment and data discussion. FG prepared and drafted the paper with contributions from all authors.

Acknowledgments

We thank Dr. Mao-Yong He (Institute of Earth Environment, Chinese Academy of Sciences) for the help with providing SN teeth samples. We also thank Zihua Tang (Institute of Geology and Geophysics, Chinese Academy of Sciences) for stimulating discussions. This work is financially supported by the National Natural Science Foundation of China (No. 41973008), and the project of The Key Laboratory of Cultural Heritage Research and Conservation, Ministry of Education, Northwest University.

Conflict of interest

The authors declare that the research was conducted in the absence of any commercial or financial relationships that could be construed as a potential conflict of interest.

Publisher's note

References

Bao, Z., Huang, K.-J., Huang, T., Shen, B., Zong, C., Chen, K.-Y., et al. (2019). Precise magnesium isotope analyses of high-K and low-Mg rocks by MC-ICP-MS. *J. Anal. At. Spectrom.* 34, 940–953. doi:10.1039/C9JA00002J

Black, J., Epstein, E., Rains, W., Yin, Q.-Z., and Casey, W. (2008). Magnesium-isotope fractionation during plant growth. *Environ. Sci. Technol.* 42, 7831–7836. doi:10.1021/es8012722

Black, J., Yin, Q.-Z., and Casey, W. (2006). An experimental study of magnesium isotope fractionation in Chlorophyll-a Photosynthesis. *Geochim. Cosmochim. Acta* 70, 4072–4079. doi:10.1016/j.gca.2006.06.010

Black, J., Yin, Q.-Z., Rustad, J., and Casey, W. (2007). Magnesium isotopic equilibrium in chlorophylls. *J. Am. Chem. Soc.* 129, 8690–8691. doi:10.1021/ja072573i

Bolou-Bi, E. B., Poszwa, A., Leyval, C., and Vigier, N. (2010). Experimental determination of magnesium isotope fractionation during higher plant growth. *Geochim. Cosmochim. Acta* 74, 2523–2537. doi:10.1016/j.gca.2010.02.010

Bolou-Bi, E. B., Vigier, N., Brenot, A., and Poszwa, A. (2009). Magnesium isotope compositions of natural reference materials. *Geostand. Geoanal. Res.* 33, 95–109. doi:10.1111/j.1751-908X.2009.00884.x

Bolou-Bi, E. B., Vigier, N., Poszwa, A., Boudot, J.-P., and Dambrine, E. (2012). Effects of biogeochemical processes on magnesium isotope variations in a forested catchment in the Vosges Mountains (France). *Geochim. Cosmochim. Acta* 87, 341–355. doi:10.1016/j.gca.2012.04.005

Brown, R. (1999). Magnesium. *Min. Annu. Rev.*, B95–B96.

Chen, Y., Zhang, Z., and Tao, F. (2018). Impacts of climate change and climate extremes on major crops productivity in China at a global warming of 1.5 and 2.0°C. *Earth Syst. Dyn.* 9, 543–562. doi:10.5194/esd-9-543-2018

De Baaij, J., Hoenderop, J., and Bindels, R. (2015). Magnesium in man: Implications for health and disease. *Physiol. Rev.* 95, 1–46. doi:10.1152/physrev.00012.2014

Elin, R. (1987). Assessment of magnesium status. *Clin. Chem.* 33, 1965–1970. doi:10.1093/clinchem/33.11.1965

Fan, B.-L., Zhao, Z.-Q., Tao, F., Li, X., Tao, Z., Gao, S., et al. (2016). The geochemical behavior of Mg isotopes in the Huanghe basin, China. *Chem. Geol.* 426, 19–27. doi:10.1016/j.chemgeo.2016.01.005

Faryadi, Q. (2012). The magnificent effct of magnesium to human health: A critical review. *Int. J. Environ. Sci. Technol.* 2, 118–126.

Francalacci, P. (1989). Dietary reconstruction at Arene Candide Cave (Liguria, Italy) by means of trace element analysis. *J. Archaeol. Sci.* 16, 109–124. doi:10.1016/0305-4403(89)90060-5

Gao, T., Ke, S., Wang, S.-J., Li, F., Liu, C., Lei, J., et al. (2018). Contrasting Mg isotopic compositions between Fe-Mn nodules and surrounding soils: Accumulation of light Mg isotopes by Mg-depleted clay minerals and Fe oxides. *Geochim. Cosmochim. Acta* 237, 205–222. doi:10.1016/j.gca.2018.06.028

Grigoryan, R., Costas-Rodríguez, M., Vandenbroucke, R., and Vanhaecke, F. (2020). High-precision isotopic analysis of Mg and Ca in biological samples using multi-collector ICP-mass spectrometry after their sequential chromatographic isolation – application to the characterization of the body distribution of Mg and Ca isotopes in mice. *Anal. Chim. Acta X.* 1130, 137–145. doi:10.1016/j.aca.2020.07.045

Grupe, G. (1998). *Dental anthropology: Fundamentals, limits and prospects*. New York: Springer.

Huang, K.-J., Teng, F.-Z., Plank, T., Staudigel, H., Hu, Y., and Bao, Z.-Y. (2018). Magnesium isotopic composition of altered oceanic crust and the global Mg cycle. *Geochim. Cosmochim. Acta* 238, 357–373. doi:10.1016/j.gca.2018.07.011

Jaouen, K., and Balter, V. (2014). Menopause effect on blood Fe and Cu isotope compositions. *Am. J. Phys. Anthropol.* 153, 280–285. doi:10.1002/ajpa.22430

Katzenberg, M. A., and Waters-Rist, A. L. (2018). *Biological anthropology of the human skeleton*. New York: Wiley-Liss.

Kimmig, S., Holmden, C., and Bélanger, N. (2018). Biogeochemical cycling of Mg and its isotopes in a sugar maple forest in Québec. *Geochim. Cosmochim. Acta* 230, 60–82. doi:10.1016/j.gca.2018.03.020

Kiple, K. F., and Ornelas, K. C. (2000). *The Cambridge World history and food*. Cambridge: Cambridge University Press.

Klepingera, L. (1990). Magnesium ingestion and bone magnesium concentration in paleodietary reconstruction: Cautionary evidence from an animal model. *J. Archaeol. Sci.* 17, 513–517. doi:10.1016/0305-4403(90)90032-Z

Lambert, J. B., Simpson, S. V., Szpunar, C. B., and Buikstra, J. E. (1984). Ancient human diet from inorganic analysis of bone. *Acc. Chem. Res.* 17, 298–305. doi:10.1021/ar00105a001

Lambert, J. B., Szpunar, C. B., and Buikstra, J. E. (1979). Chemical analysis of excavated human bone from Middle and Late Woodland sites. *Archaeometry* 21, 115–129. doi:10.1111/j.1475-4754.1979.tb00248.x

Li, F., Zhou, M., Shao, J., Chen, Z., Wei, X., and Yang, J. (2020). Maize, wheat and rice production potential changes in China under the background of climate change. *Agric. Syst.* 182, 102853. doi:10.1016/j.agsy.2020.102853

Ling, X. (2010). "Study on dietary of ancient Qin people,". Dissertation thesis (Xi'an: Northwest University).

Ma, L., Sun, Y., Jin, Z.-D., Bao, Z., Zhang, P., Meng, Z.-K., et al. (2019). Tracing changes in monsoonal precipitation using Mg isotopes in Chinese loess deposits. *Geochim. Cosmochim. Acta* 259, 1–16. doi:10.1016/j.gca.2019.05.036

Makarewicz, C. A., and Sealy, J. (2015). Dietary reconstruction, mobility, and the analysis of ancient skeletal tissues: Expanding the prospects of stable isotope research in archaeology. *J. Archaeol. Sci.* 56, 146–158. doi:10.1016/j.jas.2015.02.035

Mark, S., and Mediawerks, P. (2007). *Transdermal Magnesium therapy*. Bloomington: iUniverse Inc.

Martin, J. E., Tacail, T., Adnet, S., Girard, C., and Balter, V. (2015a). Calcium isotopes reveal the trophic position of extant and fossil elasmobranchs. *Chem. Geol.* 415, 118–125. doi:10.1016/j.chemgeo.2015.09.011

Martin, J. E., Vance, D., and Balter, V. (2015b). Magnesium stable isotope ecology using mammal tooth enamel. *Proc. Natl. Acad. Sci. U. S. A.* 112, 430–435. doi:10.1073/pnas.1417792112

Martin, J. E., Vance, D., and Balter, V. (2014). Natural variation of magnesium isotopes in mammal bones and teeth from two South African trophic chains. *Geochim. Cosmochim. Acta* 130, 12–20. doi:10.1016/j.gca.2013.12.029

Martin, J., Tacail, T., Braga, J., Cerling, T., and Balter, V. (2020). Calcium isotopic ecology of Turkana Basin hominins. *Nat. Commun.* 11, 3587–7. doi:10.1038/s41467-020-17427-7

Mavromatis, V., Prokushkin, A. S., Pokrovsky, O. S., Viers, J., and Korets, M. A. (2014). Magnesium isotopes in permafrost-dominated Central Siberian larch forest watersheds. *Geochim. Cosmochim. Acta* 147, 76–89. doi:10.1016/j.gca.2014.10.009

Nadler, J. L., and Rude, R. K. (1995). Disorders of magnesium metabolism. *Endocrinol. Metab. Clin. North Am.* 24, 623–641. doi:10.1016/S0889-8529(18)30035-5

Nitzsche, K., Kato, Y., Shin, K.-C., and Tayasu, I. (2019). Magnesium isotopes reveal bedrock impacts on stream organisms. *Sci. Total Environ.* 688, 243–252. doi:10.1016/j.scitotenv.2019.06.209

Ryan, M. F. (1991). The role of magnesium in clinical biochemistry: An overview. *Ann. Clin. Biochem.* 28, 19–26. doi:10.1177/000456329102800103

Schoeninger, M. J. (2010). *A companion to biological anthropology*. Chichester: Wiley-Blackwell.

Teng, F.-Z. (2017). Magnesium isotope Geochemistry. *Rev. Mineral. Geochem.* 82, 219–287. doi:10.2138/rmg.2017.82.7

Tipper, E., Galy, A., Gaillardet, J., Bickle, M., Elderfield, H., and Carder, E. A. (2006). The magnesium isotope budget of the modern ocean: Constraints from riverine magnesium isotope ratios. *Earth Planet. Sci. Lett.* 250, 241–253. doi:10.1016/j.epsl.2006.07.037

Ungar, P., Grine, F., Teaford, M., and El Zaatari, S. (2006). Dental microwear and diets of African early Homo. *J. Hum. Evol.* 50, 78–95. doi:10.1016/j.jhevol.2005.08.007

Ungar, P. S. (2012). Dental evidence for the reconstruction of diet in african early Homo. *Curr. Anthropol.* 53, S318–S329. doi:10.1086/666700

Van Heghe, L., Deltombe, O., Delanghe, J., Depypere, H., and Vanhaecke, F. (2014). The influence of menstrual blood loss and age on the isotopic composition of Cu, Fe and Zn in human whole blood. *J. Anal. At. Spectrom.* 29, 478–482. doi:10.1039/C3JA50269D

Vormann, J. (2003). Magnesium: Nutrition and metabolism. *Mol. Asp. Med.* 24, 27–37. doi:10.1016/S0098-2997(02)00089-4

Walczyk, T., and Blanckenburg, F. (2002). Natural iron isotope variations in human blood. *Science* 295, 2065–2066. doi:10.1126/science.1069389

Wang, Y., Wu, B., Berns, A., Xing, Y., Kuhn, A., and Amelung, W. (2020). Magnesium isotope fractionation reflects plant response to magnesium deficiency in magnesium uptake and allocation: A greenhouse study with wheat. *Plant Soil* 455, 93–105. doi:10.1007/s11104-020-04604-2

Weber, K., Weber, M., Menneken, M., Kral, A. G., Mertz-Kraus, R., Geisler, T., et al. (2021). Diagenetic stability of non-traditional stable isotope systems (Ca, Sr, Mg, Zn) in teeth – an *in-vitro* alteration experiment of biogenic apatite in

isotopically enriched tracer solution. *Chem. Geol.* 572, 120196. doi:10.1016/j.chemgeo.2021.120196

Wimpenny, J., Yin, Q.-Z., Tollstrup, D., Xie, L., and Sun, J. (2014). Using Mg isotope ratios to trace cenozoic weathering changes: A case study from the Chinese loess plateau. *Chem. Geol.* 376, 31–43. doi:10.1016/j.chemgeo.2014.03.008

Wrobel, K., Karasiński, J., Tupys, A., Arroyo Negrete, M., Halicz, L., Wrobel, K., et al. (2020). Magnesium-isotope fractionation in chlorophyll-a extracted from two plants with different pathways of carbon fixation (C3, C4). *Molecules* 25, 1644–1655. doi:10.3390/molecules25071644

Xu, Y., Jin, Z.-D., Gou, L.-F., Galy, A., Jin, C.-Y., Chen, C., et al. (2022). Carbonate weathering dominates magnesium isotopes in large rivers: Clues from the Yangtze River. *Chem. Geol.* 588, 120677. doi:10.1016/j.chemgeo.2021.120677

Yang, Y.-X., Wang, G.-Y., and Pan, X.-C. (2019). *China food composition*. Beijing: Peking University Medical Press.

Young, E. D., Galy, A., and Nagahara, H. (2002). Kinetic and equilibrium mass-dependent isotope fractionation laws in nature and their geochemical and cosmochemical significance. *Geochim. Cosmochim. Acta* 66, 1095–1104. doi:10.1016/S0016-7037(01)00832-8

Zhao, D.-Y. (2016). *The origin and formation of the Han population —a new perspective from physical anthropology*. Dissertation thesis (Changchun: Jilin University).

Zhao, T., Liu, W.-J., and Xu, Z.-F. (2022). Magnesium isotope fractionation during silicate weathering: Constrains from riverine Mg isotopic composition in the southeastern coastal region of China. *Geochem. Geophys. Geosyst.* 23, e2021GC010100. doi:10.1029/2021GC010100

frontiers | Frontiers in Earth Science

TYPE Original Research
PUBLISHED 25 January 2023
DOI 10.3389/feart.2022.1090983

OPEN ACCESS

EDITED BY
Kang-Jun Huang,
Northwest University, China

REVIEWED BY
Hongyan Bao,
Xiamen University, China
Meng Yu,
Ocean University of China, China

*CORRESPONDENCE
Zhangdong Jin,
zhdjin@ieecas.cn
Xiaojuan Feng,
xfeng@ibcas.ac.cn

SPECIALTY SECTION
This article was submitted to Biogeoscience, a section of the journal Frontiers in Earth Science

RECEIVED 06 November 2022
ACCEPTED 01 December 2022
PUBLISHED 25 January 2023

CITATION
Wang J, Ma T, Zhang F, Hilton RG, Feng X and Jin Z (2023), The role of earthquakes and storms in the fluvial export of terrestrial organic carbon along the eastern margin of the Tibetan plateau: A biomarker perspective. *Front. Earth Sci.* 10:1090983. doi: 10.3389/feart.2022.1090983

The role of earthquakes and storms in the fluvial export of terrestrial organic carbon along the eastern margin of the Tibetan plateau: A biomarker perspective

Jin Wang[1,2,3], Tian Ma[2,4], Fei Zhang[1], Robert G. Hilton[5], Xiaojuan Feng[2]* and Zhangdong Jin[1]*

[1]State Key Laboratory of Loess and Quaternary Geology, Institute of Earth Environment, Chinese Academy of Sciences, Xi'an, China, [2]State Key Laboratory of Vegetation and Environmental Change, Institute of Botany, Chinese Academy of Sciences, Beijing, China, [3]Department of Geography and Institute of Hazard, Risk and Resilience, Durham University, Durham, United Kingdom, [4]State Key Laboratory of Grassland and Agro-ecosystems, and College of Pastoral Agriculture Science and Technology, Lanzhou University, Lanzhou, China, [5]Department of Earth Sciences, University of Oxford, Oxford, United Kingdom

Driven by earthquakes and intense rainfall, steep tectonically active mountains are hotspots of terrestrial organic carbon mobilization from soils, rocks, and vegetation by landslides into rivers. Subsequent delivery and fluvial mobilization of organic carbon from different sources can impact atmospheric CO_2 concentrations across a range of timescales. Extreme landslide triggering events can provide insight on processes and rates of carbon export. Here we used suspended sediment collected from 2005 to 2012 at the upper Min Jiang, a main tributary of the Yangtze River on the eastern margin of the Tibetan Plateau, to compare the erosion of terrestrial organic carbon before and after the 2008 Wenchuan earthquake and a storm-derived debris flow event in 2005. To constrain the source of riverine particulate organic carbon (POC), we quantified lignin phenols and *n*-alkanoic acids in the suspended sediments, catchment soils and landslide deposits. We found that riverine POC had higher inputs of less-degraded, discrete organic matter at high suspended sediment loads, while the source of POC seemed stochastic at low suspended sediment concentrations. The debris flow in 2005 mobilized a large amount of POC, resulting in an export of lignin within a single day equivalent to a normal year. In comparison, the 2008 Wenchuan earthquake increased the flux of POC and particulate lignin, albeit with limited impact on POC sources in comparison to seasonal variations. Our results highlight the important role of episodic events in the fluvial export of terrestrial carbon.

KEYWORDS

particulate organic carbon, landslide, Wenchuan earthquake, debris flow, biomarker, organic carbon source

1 Introduction

Rivers transfer 200 $^{+135}/_{-75}$ megatons of particulate organic carbon (POC) to the oceans every year (Galy et al., 2015), and play important roles in the global carbon cycle (Mayorga et al., 2005; Hilton and West, 2020). A large fraction of riverine POC is derived from terrestrial biosphere ($POC_{biosphere}$), equating to 157 $^{+74}/_{-50}$ MtC yr^{-1}, which represents photosynthesized carbon of varied residence time stored in plants and soils. The fluvial export and deposition of recently fixed $POC_{biosphere}$ (such as from litter and surface soils) in the sedimentary basins are an important mechanism of atmospheric CO_2 drawdown over millennial timescales (Berner, 1982; France-Lanord and Derry, 1997; Hilton and West, 2020). On the contrary, fluvial mobilization and subsequent oxidation of pre-aged $POC_{biosphere}$ (such as from deep soils) or even petrogenic POC from bedrocks (POC_{petro}) constitute a CO_2 source to the atmosphere (Bouchez et al., 2010; Petsch et al., 2000). Therefore, delineating the source of POC mobilized by rivers is important to understand the potential impact of fluvial transport on atmospheric CO_2 levels (Feng et al., 2013; Hilton and West, 2020). Landslides have been noted as a process of particular importance in mountainous regions, as they are able to rapidly mobilise vegetation and soil from hillslopes and deliver them into rivers (Wang et al., 2016).

Storms and earthquakes can both trigger landslides (Keefer, 1984; Lin et al., 2008), but *via* different mechanisms and locations (Marc et al., 2018; Meunier et al., 2008; Wang et al., 2020) on spatial and temporal scales (Hovius et al., 2011; Lin et al., 2008). Large earthquakes can trigger widespread and deep landslides due to strong ground motions. They may impact sediment and POC erosion over years to centuries (Howarth et al., 2012; Li et al., 2017; Wang et al., 2015). In contrast, storms are thought to mainly initiate small, shallow landslides by increasing pore fluid pressures at the soil-bedrock transition (Densmore and Hovius, 2000; Marc et al., 2018). Thus, storm-derived landslides not only increase sediment supply to rivers, but also increase runoff and enhance river transport capacity, resulting in a large export of $POC_{biosphere}$ over short periods of time (Clark et al., 2016; Hilton et al., 2008). Therefore, earthquakes and storms are likely to impact erosion and fluvial transfer of sediments and terrestrial POC in different ways. Previous studies have assessed the role of earthquakes and storms in the erosion and transport fluxes of POC in regions with different climatic and tectonic settings (Clark et al., 2016; 2022; Frith et al., 2018; Märki et al., 2021; Qu et al., 2020; Wang et al., 2016). In contrast to these flux-centric studies, the impacts of earthquake- and rainfall-triggered landslides on the source and characteristics (e.g., degradation) of POC are less clear.

One of the major difficulties in studying fluvial POC sources and characteristics related to earthquakes and storms is sampling for these sporadic and infrequent events. The Longmen Shan, located at the eastern margin of the Tibetan Plateau, is an ideal

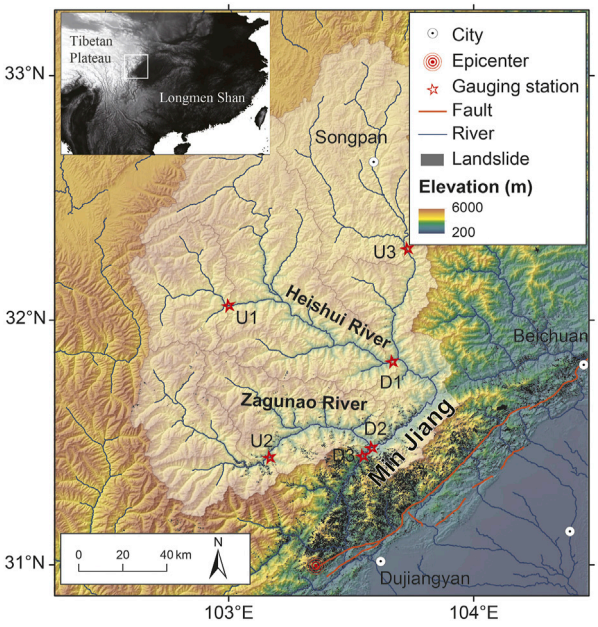

FIGURE 1
Map of sampling locations at the upper Min Jiang, showing the paired upstream (U) and downstream (D) gauging stations (red stars) and landslides (black polygons, after Li et al. (2014) triggered by the 2008 M_w 7.9 Wenchuan earthquake.

place for such sampling, because this active mountain belt is prone to earthquakes and storms under the influence of East Asian monsoon. Here, we collected suspended sediments from the upper Min Jiang before and after the 2008 M_w 7.9 Wenchuan earthquake and a large debris flow event in 2005. Using a binary mixing model, our previous study quantified $POC_{biosphere}$ and POC_{petro} flux with the analysis of bulk carbon isotopes (Wang et al., 2019). The annual POC_{petro} yields range from 0.04 ± 0.02 tC km^{-2} yr^{-1} to 1.69 ± 0.56 tC km^{-2} yr^{-1}, while $POC_{biosphere}$ yields range from 0.21 ± 0.04 tC km^{-2} yr^{-1} to 3.33 ± 0.57 tC km^{-2} yr^{-1}, which are correlated to the intense runoff events during the monsoon season (Wang et al., 2019). The export of $POC_{biosphere}$ downstream of the Zagunao River, a tributary of Min Jiang doubled after the earthquake (Wang et al., 2016). However, bulk carbon isotope ratios of soils and vegetation are similar, and as such previous work has not been able to distinguish the contribution of (pre-aged) soil vs. (modern) plant litter to total POC. Molecular compounds (or biomarkers) are useful in assessing the source and chemical characteristics of riverine $POC_{biosphere}$ (Feng et al., 2013; Tao et al., 2015). Long-chain *n*-alkanoic acid and lignin phenol are two types of biomarkers that are abundant in the higher plants and soils and are widely used to identify the source of terrestrial organic matter. In this study, we quantified *n*-alkanoic acids and lignin phenols at the upper Min Jiang, Longmen Shan, in combination with previously published bulk carbon

concentrations and stable and radioactive isotope measurements (Wang et al., 2019), to assess the source and molecular characteristics of riverine POC. We aim to 1) compare the impacts of a large earthquake versus a debris flow event on the $POC_{biosphere}$ source; 2) shed new light on POC transport dynamics in a tectonically-active monsoon mountain range.

2 Materials and methods

2.1 Study area

The Min Jiang drains the Longmen Shan area, on the eastern margin of the Tibetan Plateau (Figure 1) with two major tributaries in the upper Min Jiang—the Zagunao River and the Heishui River. We collected samples at three pairs of upstream (U) and downstream (D) gauging stations in the Heishui River (U1 = Heishui station, D1 = Shaba station), the Zagunao River (U2 = Zagunao, D2 = Sangping), and the mainstream of Min Jiang (U3 = Zhenjiangguan, D3 = Weizhou).

The climate, geology, topography and runoff of the Longmen Shan have been described in the previous study (Wang et al., 2019 and references therein). Briefly, the area features very high relief with elevation from 1400 to 4500 m along a length of 126 km. The geology of the study area is dominated by bedrock of Songpan-Ganze flysch, a moderately metamorphosed detrital sequence that was intruded by granitic plutons, and a series of green schist-facies shallow margin sediments, including detrital and carbonate deposits (China Geological Survey, 2004). The annual precipitation is approximately 800–1000 mm yr^{-1}, making the annual runoff of these stations from 300 to 800 mm yr^{-1} (Liu-Zeng et al., 2011; Wang et al., 2015). The monsoon climate of medium latitudes in combination with the high relief makes the mountain area at the erosion rate of 0.1–0.2 mm yr^{-1} (Liu-Zeng et al., 2011) and prone to debris flows (Francis et al., 2022; Huang et al., 2012; Huang and Fan, 2013).

2.2 2005 debris flow and 2008 Wenchuan earthquake

Our study captured two events that caused landslides and the removal of landslide material into the river channels. First, a debris flow event occurred in the mid-stream of the Zagunao River on 2 July 2005 (Huang et al., 2012). Multiple debris flows generated a large volume of sediment, which damaged the roads and houses, and caused 10 deaths. The riverine suspended sediment concentration reached up to 29.4 g L^{-1}, while the water discharge (Q_w) was triple of the annual average (Supplementary Table S1). Second, a M_w 7.9 earthquake occurred in the study area on 12 May 2008. The large earthquake triggered ~60,000 landslides, producing clastic sediment of ~2.8 $^{+0.9}/_{-0.7}$ km^3, with half (~$1.4^{+0.4}/_{-0.3}$ km^3) in the Min Jiang catchment (Li et al., 2014). The earthquake enhanced the annual suspended sediment by 3–7 times lasting 4 years after the earthquake (Wang et al., 2015), while most of the sediment was still on the hillslope (Francis et al., 2022). We note here that the study area suffered low to moderate co-seismic landslide impact: the drainage areas of stations U1, D1, and U3 had an aerial landslide density <0.01%, while the landslide densities of stations U2, D2 and D3 were 0.22, 0.35, and 0.18%, respectively (Li et al., 2014; Wang et al., 2015). These are high but are not as high as nearer the fault rupture at the frontal range (Li et al., 2014).

2.3 Sampling and methodology

The organic carbon content [(OC), %] and isotopic ratios of some samples used in this study have been analysed in Wang et al. (2019), which focused on quantifying $POC_{biosphere}$ and POC_{petro} flux. In this study, we added 83 more suspended sediments and 4 landslide sediment samples. Together, this study used 112 suspended sediments (including 2 large suspended load samples were wet sieved into clay and silt (<63 μm), sand (63–250 μm) fractions), 7 soils, 4 landslide- and 1 bed-material samples. Because the most landslides caused by the earthquake and the 2005 debris flow occurred at the downstream of the Zagunao River, the majority of analysis was carried out on samples from the downstream of the Zagunao River (Figure 1; station D2).

The suspended sediments from 2005 to 2009 were collected by the Chinese Bureau of Hydrology. The sampling method followed a national standard, and the details are provided in the Ministry of Water Resources of China (2007) and Wang et al. (2019). In summary, 2 or 4 L of water was passed through ~1-μm paper filters, and the sediment and filter paper were air-dried. Because these samples were initially collected for suspended sediment quantification only, they were collected on paper filters. We conducted a blank test to estimate the contribution of OC from the paper to the samples. The results showed that the blank carbon contribution was <5% (Wang et al., 2016). The suspended sediment after 2009 was collected weekly at the gauging station for geochemical analysis. For those samples, 1 L of water was passed through a 0.7-μm glass fiber (GF/F) filter, which was then dried at 60°C and stored in a Petri dish. All sediments were gently removed from the filters and homogenized using a mortar and a pestle (Wang et al., 2019). The river bed material, landslide sediment and soils were also collected to constrain the source of the POC. Seven soil samples from 4 sites were used in this study, including 4 topsoils (0–5 cm) and 3 subsoils (~10–50 cm). A river bed material sample was collected at the surface of the river bed near the river bank. Four landslide sediment sample were

collected at a landslide profile near the station D2. All samples were stored in clean sealed bags and were dried at 60°C in the oven after returning to the laboratory.

Organic carbon content and $\delta^{13}C_{org}$ were determined by a Costech CHN elemental analyser coupled by continuous flow *via* a CONFLO-III to a Thermo Delta V advantage isotope ratio mass spectrometer at Durham University. Duplicates of the samples (n = 42) returned an average relative standard deviation ±2.5% for [OC] and an average standard deviation ±0.1‰ for $\delta^{13}C_{org}$ (Wang et al., 2019). Radiocarbon activity ($F^{14}C$) were measured by an accelerator mass spectrometry (AMS) after carbonate removal and graphitization at the Keck-Carbon Cycle AMS Facility at the University of California, Irvine, United States.

A subset of samples was selected for the quantification of biomarkers following published methods (Dai et al., 2019; Wang et al., 2020) at the Institute of Botany, Chinese Academy of Sciences. The total lipids were extracted from 2 g of suspended sediment or 1 g of soil by sequential sonication (15 min) with 30 ml of dichloromethane (DCM), DCM:methanol (1:1, v:v), and methanol each. The lipid extract was first filtered through combusted glass fiber filters (Whatman GF/F) and then dried under nitrogen gas (N_2). After addition of an internal standard (non-adecanoic acid, Sigma-Aldrich), the lipid extract was saponified with 8% KOH in methanol:water (99:1) at 70°C for 1 h. The "base" fractions were liquid–liquid extracted in 2.5 ml of pure hexane three times. After pH adjustment to <2 with 5-M HCl, the 'acid' fractions were extracted with 2.5 ml hexane:DCM (4:1) three times. Alkanoic acids in the acid fraction were further methylated with 3 ml mixture of 12-M HCl and methanol (5: 95) at 70°C for 12 h. Then, 4 ml of deionized water was added to the solvent, and the methylated fatty acid methyl esters (FAMEs) were liquid–liquid extracted with hexane:DCM (4:1) three times. The *n*-alkanoic acids were identified and quantified on a Thermo TRACE 1310 gas chromatograph (GC) coupled to an ISQ mas spectrometer (MS; Thermo Fisher Scientific, United states) using a DB-5MS capillary column for separation. Quantification was achieved by comparison of the peak area of individual compounds with that of the internal standard in the total ion current by assuming a constant response factor for all compounds.

Lignin-derived phenols were isolated from solvent-extracted sediments or soils using the CuO oxidation method (Hedges and Ertel, 1982; Feng et al., 2016). In summary, the sediment or soil samples were mixed with 0.5 g CuO, 50 mg ammonium iron II) sulfate hexahydrate [$Fe(NH_4)_2(SO_4)_2 \cdot 6H_2O$], and 20 ml of N_2-purged sodium hydroxide solution (2M) in Teflon-lined vessels. The headspace of all vessels was flushed with N_2 for 10 min before capping. All vessels were heated at 170°C for 2.5 h. After cooling, an internal standard (ethyl vanillin) was added to the lignin oxidation products, which is further acidified to pH 1 with 12 M HCl, and kept in the dark for 1 h. Upon centrifugation, the lignin phenols were liquid–liquid extracted from the supernatant with ethyl acetate. Lignin phenols were derivatized with N,O-bis-(trimethylsilyl)trifluoroacetamide and pyridine (70°C, 1 h). The quantification of the lignin phenols was conducted on a Thermo TRACE 1310 GC-ISQ-MS, based on compound responses relative to the internal standard.

2.4 Biomarker indicators

The *n*-alkanoic acids C_{10} to C_{32} were identified and quantified in the soil and sediment. The concentration of individual homologues and the sum of the short-chain (C_{10}-C_{20}) and long-chain (C_{24}-C_{32}) *n*-alkanoic acids were reported after being normalized to particulate mass (μg g^{-1} sediment/soil; $\Sigma_{Cn1\text{-}Cn2}$) or organic carbon (μg g^{-1} OC; $\Lambda_{Cn1\text{-}Cn2}$).

The carbon preference index (CPI) has been widely used as a diagnostic indicator to trace the origin and degradation state of lipids in sediments and soils (Rielley et al., 1991; Wang et al., 2020). The CPI of long-chain *n*-alkanoic acid was calculated as:

$$CPI = 0.5 \times \left(\frac{C_{24}+C_{26}+\ldots+C_{32}}{C_{23}+C_{25}+\ldots+C_{31}} + \frac{C_{24}+C_{26}+\ldots+C_{32}}{C_{25}+C_{27}+\ldots+C_{33}}\right) \quad (1)$$

Where C_n is relative abundance of *n*-alkanoic acids with n number of carbon atoms. The terrestrial-to-aquatic ratio (TAR) is frequently applied in assessing the relative contribution of terrestrial and aquatic lipids, and is defined as:

$$TAR = \frac{C_{24}+C_{26}+C_{28}}{C_{12}+C_{14}+C_{16}} \quad (2)$$

Lignin phenol concentrations refer to the summed concentrations of eight lignin monomers and are reported as μg g^{-1} sediment/soil (Σ_8) or μg g^{-1} OC (Λ_8). The eight lignin monomers include three vanillyl phenols [V; vanillin (Vl), acetovanillone (Vn), vanillic acid (Vd)], three syringyl phenols [S; syringaldehyde (Sl), acetosyringone (Sn), syringic acid (Sd)], and two cinnamyl phenols (C; *p*-coumaric acid, ferulic acid), which are abundant in vascular plants (Hedges and Ertel, 1982). CuO oxidation also releases *p*-hydroxyl phenols (P; including *p*-hydroxybenzaldehyde, *p*-hydroxyacetophenone, and *p*-hydroxybenzoic acid) and 3,5-dihydroxybenzoic acid (3,5 Bd) that may derive from proteins or from the demethylation of lignin (Goñi and Hedges, 1995). The ratio of C/V indicate the relative contribution of non-woody and woody plants, whereas S/V the relative contribution of angiosperm versus gymnosperm plants (Goñi and Hedges, 1995; Goñi and Thomas, 2000). However, the two ratios also decrease with the degradation of lignin (Hedges et al., 1988; Otto and Simpson, 2006). Due to the selective loss of S and V phenols relative to the P phenols, the ratio of P/(S+V) represents the degree of demethylation (Dittmar and Lara, 2001). Additionally, the acid-to-aldehyde (Ad/Al) ratios of V and S phenols are used to indicate lignin degradation through propyl side-chain oxidation (Hedges et al., 1988; Otto and Simpson, 2006).

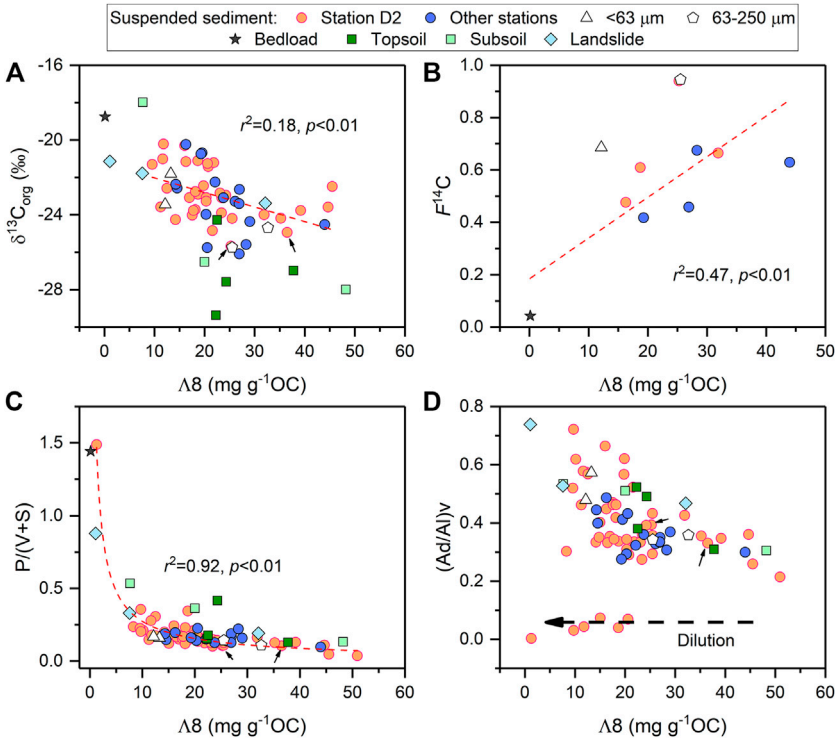

FIGURE 2
Relationships of lignin phenol concentration with organic carbon isotopes **(A,B)** and lignin degradation proxies **(C,D)**. P/(V+S) is the ratio of p-hydroxyl (P) phenols to the sum of vanillyl and syringyl phenols. (Ad/Al)v is the ratio of acid-to-aldehyde vanillyl phenols. The arrows indicate the samples influenced by the 2005 debris flow event. The dash lines are the linear regression best-fit to data of suspended sediment in panel A, and of suspended sediment and bed material in panel B. The dash line in panel C is power-law regression best-fit to the data of suspended sediment. The dash arrow in panel D shows the trend of dilution by clastic rocks.

3 Results and discussion

3.1 Sources of POC and controls by sediment supply and transport

The measured [OC] of bulk suspended sediments ranged from 0.40% to 4.02%, with a mean value of 1.34 ± 0.59% (n = 71), which was higher than the mean of the landslide samples (0.54 ± 0.17%), but lower than that of the topsoil (4.60 ± 2.82%; Supplementary Table S1). The $\delta^{13}C_{org}$ values of suspended sediments overlapped with those of soils and landslides, ranging from -26.1‰ to -20.2‰, with a mean of -23.1 ± 1.5‰ (n = 53). $\delta^{13}C_{org}$ was positively correlated with 1/[OC] (r^2 = 0.10, p = 0.59, n = 38 at station D2; r^2 = 0.51, p = 0.02, n = 10 at station U2), which was consistent with the trend generated from a larger dataset reported previously due to mixing of POC_{petro} and $POC_{biosphere}$ (Wang et al., 2019).

The contents of lignin phenols and long-chain n-alkanoic acids ranged from 0.005—1.02 mg g^{-1} sediment (Σ_8) and 0.003—0.041 mg g^{-1} sediment ($\Sigma_{C24\text{-}C32}$), or 1.28—50.95 mg g^{-1} OC (Λ_8) and 0.31—1.82 mg g^{-1} OC ($\Lambda_{C24\text{-}C32}$), respectively. In contrast to short-chain n-alkanoic acids ($\Lambda_{C10\text{-}C20}$), long-chain n-alkanoic acids ($\Lambda_{C24\text{-}C32}$) and lignin phenols (Λ_8) were not related to SSC or [OC] (Supplementary Figure S1). Their variation may be explained by the varied contribution of soils with high Λ_8 and $\Lambda_{C24\text{-}C32}$, and river bed material or landslide deposits with low Λ_8 and $\Lambda_{C24\text{-}C32}$ (Supplementary Figure S1). The Λ_8 of suspended sediments, soils and river bed materials was correlated with the bulk organic carbon isotopic ratios ($\delta^{13}C$ and $F^{14}C$) and lignin degradation indicators (P/(V+S) and (Ad/Al)v; Figure 2). These relationships further supported that the POC had a mixed source of OC with different degradation degrees and was dominated by soil-originated OC and lignin (Figure 2). However, the *in situ* production also contributed to the POC, especially during a low SSC period (Supplementary Figure S2). The analysis of n-alkanoic acids and lignin phenols on different grain sizes suggested that fine POC was characterized by ^{14}C-depletion, ^{13}C-enrichment, low CPI and high degree of degradation, while less degraded OC was transported as coarse particles (Figure 2; Wang et al., 2016). This phenomenon is observed in Tainwan rivers, where the coarse material (>500 μm) of the river suspended sediment is dominated by organic clasts (Hilton et al., 2010) and the

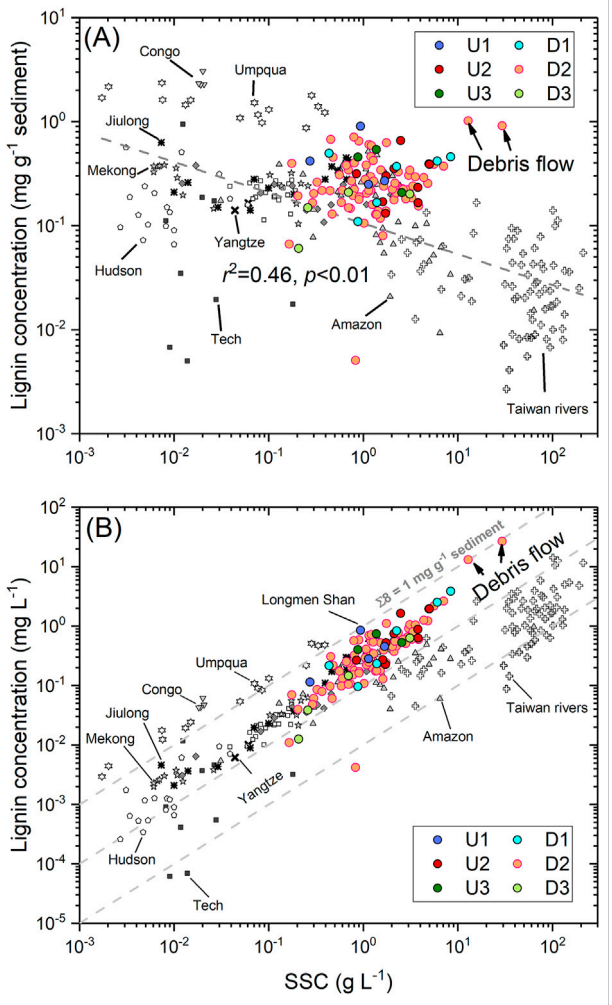

FIGURE 3
The relationship of lignin phenol concentration per unit mass **(A)** and per unit volume **(B)** with SSC of the upper Min Jiang, in the context of the world rivers modified after Bao et al. (2015) (black and grey symbols). The two highest SSC and lignin phenol concentration data in this study is immediately after the 2005 debris flow, highlighting the important role of intense rainfall in the in-land tectonic-active mountains. The dash line in panel A is the power-law regression fitted to data of global river suspended sediment using log-transformed least-squares regression. The dash lines in panel B show the range of lignin phenol concentration per unit mass.

Mackenzie River (Hilton et al., 2015). However, we note that this pattern is less clear in the Amazon rivers (Bouchez et al., 2014; Sun et al., 2017).

Erosion is the primary factor that controls riverine POC flux (Galy et al., 2015; Hilton and West, 2020) and prevenance. Globally, lignin phenol concentration Σ_8 decreased with SSC, suggesting that clastic sediment exerted a diluting effect on terrestrial OC (Figure 3A). However, such dilution effect was not observed in either POC or lignin phenol concentrations in the upper Min Jiang (Figure 3, Supplementary Figures S1; Wang et al., 2019). We suspect that a sufficient supply of biosphere OC counteracted the dilution effect, as riverine $POC_{biosphere}$ only accounts for <0.5% of net primary production in this area (Wang et al., 2019). Sources of POC varied among samples, exhibiting no explicit pattern (Figure 4), likely caused by the large scatter at low SSC. However, as erosion enhanced, Λ_8 increased with SSC when SSC was >2 g L^{-1} (Supplementary Figure S1F). Meanwhile, lignin exhibited a low degree of degradation, as shown by P/(V+S) and (Al/Ad)v, consistent with most of the topsoils and discrete OC, particularly during the debris flow event (Figure 4A).

A similar trend in export lignin was found in tropical rivers, such as the Congo River (Spencer et al., 2016) and the Jiulong River (Qiao et al., 2020), where high runoff mobilized less degraded lignin. The ratios of C/V and S/V for the high SSC samples were closer to the endmember value of the gymnosperm wood which is widely distributed in the study region (Wang et al., 2019), and the majority of the samples fell on the mixing line between the gymnosperm wood and angiosperm endmembers (Figure 4B). Thus, POC in Min Jiang was likely derived from woody parts of gymnosperms and surface soils with a low lignin degradation degree at high SSC. In contrast, the source of POC was stochastic at low SSC (Figure 4).

The SSC in rivers is not only controlled by water discharge but also impacted by the supply of sediments (Hovius et al., 2000). The relationship between catchment sediment supply and river transport capacity exerted a dual influence on the source of POC. Plots of water discharge against suspended sediment load suggested a power-law relationship between the two variables (Wang et al., 2015; Figure 5). The scatter of the plot indicated the complication between the sediment supply and river transport capacity (Hovius et al., 2000). Supply limitation occurred when the river transported a limited amount of sediments and even a rising water discharge could not effectively mobilize more sediment, e.g., the data on the lower right of the plot (Figure 5; Hovius et al., 2000). On the contrary, transport limitation occurred when a large amount of sediment/soil was available on the hillslope (during landslide or debris flow) and its rate of removal was governed by the water discharge, e.g., data on the upper left of Figure 5. We found that the river transported coarse sediment when the sediment supply was sufficient, while the suspended sediment was finer under supply-limited conditions (Figure 5A). Additionally, sediment supply also influenced lignin phenol concentrations, in that sufficient sediment supply was accompanied by high lignin phenol concentrations (Figure 5B). In other words, at a certain water discharge, lignin phenol and suspended sediment concentrations were higher when the hillslope provided more sediments, such as during earthquakes or intense rainfall-caused mass wasting (Section 3.2).

In order to investigate the control of sediment supply on the source of the riverine POC independently of variations in transport capacity, we used the parameter of unit sediment concentration, *k*, from a plot of SSC and water discharge

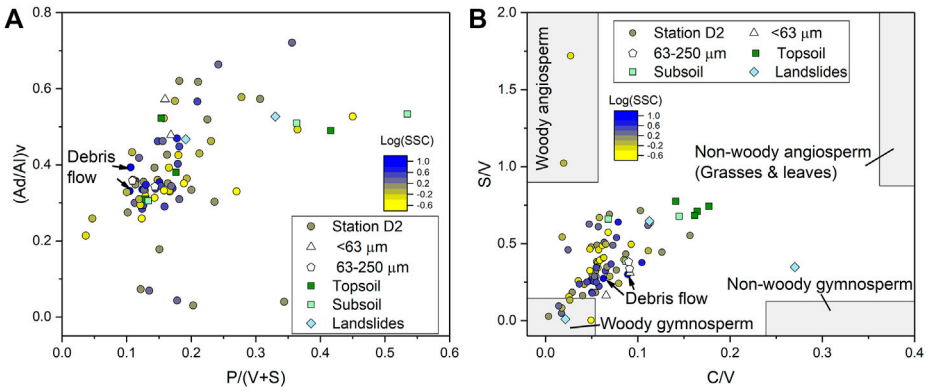

FIGURE 4
The source of the terrestrial organic carbon as shown by **(A)** P/(V+S) and (Ad/Al)v; **(B)** C/V and S/V at the station D2, the Zagunao River. The colors of bubbles represent the suspended sediment concentration (SSC). The ranges of S/V and C/V for different vegetation (squares) are from Goñi and Hedges (1995).

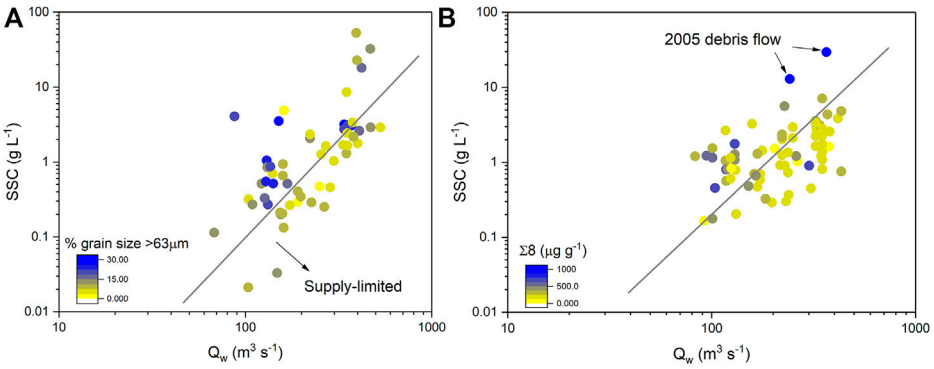

FIGURE 5
The power-law relationship between water discharge (Q_w) and suspended sediment concentration (SSC) at the Zagunao River (station D2). The colors of the circle show **(A)** the fraction of coarse sediment and **(B)** concentration of lignin phenols (Σ_8). The grey lines show the potential separation of supply-limited and transported limited scenarios. The scatter of data is due to relationship between the sediment availability (supply) and river transport capacity. For the sample in the lower right of line, the low SSC is limited by the sediment supply, while the SSC in the upper left corner is limited by the river transport capacity (Hovius et al., 2000).

(Figure 5) by fitting a function of the form SSC= $k^*Q_w^b$, which method had been applied by Dadson et al. (2013). Based on a unified parameter b, we calculated k for every sample and used it as a proxy of sediment supply. We found that sediment supply also regulated the POC source and flux. Sufficient sediment supply enhanced the input of higher plant-sourced POC with a lower degradation degree (Supplementary Figure S3).

3.2 Impacts of the earthquake and debris flow on the export of POC and lignin

Earthquakes impact river POC export by triggering widespread landslides (Frith et al., 2018; Wang et al., 2016). Our previous study showed an increase of $POC_{biosphere}$ flux lasting 4 years after the earthquake with the analysis of OC concentration and isotope ratios (Wang et al., 2016). Here, we found that the long-chain *n*-alkanoic acid and lignin phenol per unit volume (μg L^{-1}) increased 6 and 15 times from 9 May to 13 May, respectively, following the earthquake (Table S1; Figure 6). TAR also increased from 0.1 to 0.3, together suggesting an increasing input of terrestrial organic carbon into the rivers due to the co-seismic landslide. Similar to the suspended sediment and POC (Wang et al., 2015; 2016), lignin phenol concentration decreased over the following 10 days with the removal of the river-connected landslide debris (Figure 6). The values of lignin degradation indicators (Ad/Al, P/(V+S)) and long-chain *n*-alkanoic acid CPI exhibited no significant variation

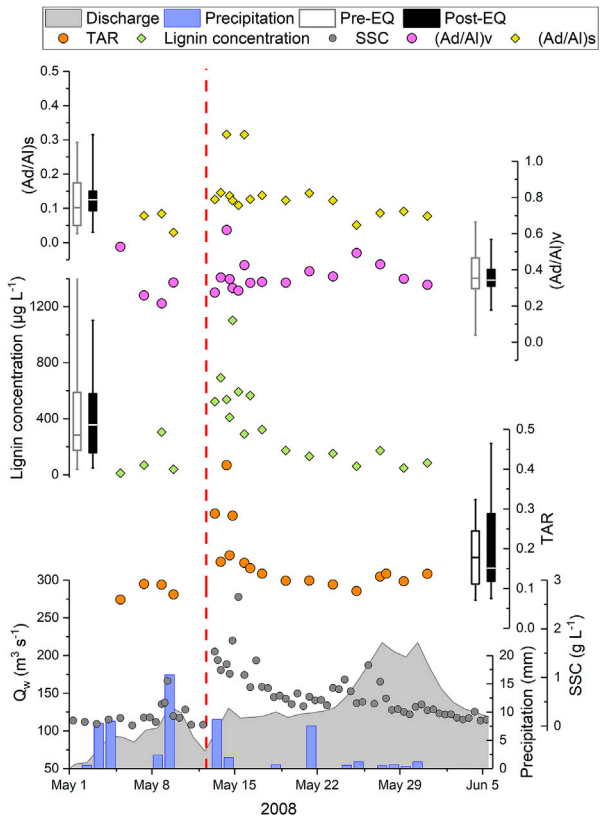

FIGURE 6
The POC source and hydrology in May 2008, before and after the earthquake. The open and filled boxes show the mean values before and after the earthquake with 25% and 75% percentile, while whiskers indicate the 5% and 95% percentile of each proxy. The red dash line represents the occurrence time of 2008 Wenchuan earthquake.

immediately after the earthquake (Figure 6). The long-term impact on the source of POC had not been observed either, which was consistent with bulk carbon isotopic measurements (Wang et al., 2016).

The response of POC to the earthquake in Longmen Shan differed from the observation of lake sediment records in the Alpine fault, New Zealand (Frith et al., 2018; Wang et al., 2020), where a large shift occurred in the carbon isotopes, long-chain *n*-alkane CPI and hydrogen isotopes after earthquakes, suggesting that the four earthquakes enhanced sediment erosion from the high elevation in the last millennium (Wang et al., 2020). There are three possible reasons for the difference. First, the landslide impact on our study area was relatively low for a catastrophic landsliding event (landslide areal density = 0.35%). Second, this area experiences frequent monsoon-triggered debris flow, which also contributed large amounts of sediment to the hillslope and fluvial system even before the earthquake. High mass wasting background masked the impacts of landslides on sediment and POC sources, which is thought to be one of the main reasons for the unchangeable carbon budget before and after the 2015 Gorkha earthquake (Märki et al., 2021). The third reason may be attributed to the large seasonal variation and stochastic source at low SSC.

Although our previous study found that the earthquake-triggered landslide impact on the POC flux lasted 4 years after the earthquake, the source of POC did not dramatically shift at the upper Min Jiang after the 2008 earthquake (Wang et al., 2016). This similar pattern also applied to lignin source, as observed in this study. We note that the lignin phenol concentration was correlated with SSC in a power-law regression and that the unit sediment concentration k slightly increased after the earthquake (Supplementary Figure S4). Using the power-law relationship, we estimated the lignin phenol flux for the date without lignin analysis using the daily SSC and Q_w data. The lignin phenol yields were 43 ± 28, 34 ± 32, 67 ± 53, 54 ± 30, and 34 ± 29 kg km^{-2} yr^{-1} at stations U1, D1, U2, D2 (2006–2011), and U3, respectively (Table 1). For station D2, the flux was 37 ± 17 kg km^{-2} yr^{-1} before the earthquake and 62 ± 34 kg km^{-2} yr^{-1} after the earthquake.

To assess the impact of the earthquake on the lignin flux independently of variations in water discharge, we applied a method used in the previous POC flux assessment (Wang et al., 2016), termed Downstream Lignin Gain. We assume that the proximity of the two nested gauging stations means that they have similar changes in runoff. We then quantified Downstream Lignin Gain by the ratio of downstream to upstream lignin phenol discharge. Erosion of lignin from hillslope soil and vegetation between the stations would result in a Downstream Lignin Gain of >1. Summing the annual fluxes to average short-term variability, we estimated that Downstream Lignin Gain before the earthquake (2006 and 2007) were ~1.0 and increased to 5.2 ± 0.9 in the first year after the earthquake, which can be explained by the increased input of lignin to river channels from earthquake-triggered landslides. Then, the Downstream Lignin Gain decreased with the removal and transport of lignin from the higher plants and soils by the earthquake-triggered landslide (Supplementary Figure S5).

In comparison to the earthquake, the impacts of debris flow on the source and flux of lignin were much more obvious (Figures 3, 4). Intense rainfall not only triggered mass wasting that enhanced the supply of sediments, soils and plant debris, but also increased runoff that effectively transported POC and lignin. The debris flow exported 309 t of lignin phenols on 3 July using <1% of the annual water discharge, which was even higher than the total average annual lignin phenol flux of 2006–2011 (Supplementary Figure S5; Table 1). Additionally, predominantly fresh $POC_{biosphere}$ and lignin from plant debris and surface soils were eroded during the debris flow (Figure 4). The different responses of POC export to earthquake and debris flow were likely explained by the relationship between sediment supply and river transport capacity. Both events could generate landslides, increasing the

TABLE 1 Characteristics of gauging stations in the upper Min Jiang and estimates of sediment, POC and lignin phenol yield at each station.

River	Heishui tributary		Zagunao tributary		Min Jiang main stream	
Gauging station	Heishui (U1)	Shaba (D1)	Zagunao (U2)	Sangping (D2)	Zhenjiangguan (U3)	Weizhou (D3)
Latitude	N 32°03′39″	N 31°49′53″	N 31°26′24″	N 31°29′42″	N 32°17′21″	N 31°26′58″
Longitude	E 102°59′52″	E 103°39′38″	E 103°10′00″	E 103°34′36″	E 103°44′00″	E 103°32′42″
Suspended sediment yield ($t\ km^{-2}\ yr^{-1}$)[a]	174 ± 17	137 ± 10	235 ± 24	208 ± 21	131 ± 13	NA
$POC_{biosphere}$ yield ($tC\ km^{-2}\ yr^{-1}$)[b]	1.51 ± 0.37	0.92 ± 0.28	1.30 ± 0.46	1.45 ± 0.37	1.28 ± 1.10	NA
POC_{petro} yield ($tC\ km^{-2}\ yr^{-1}$)[b]	0.22 ± 0.15	0.43 ± 0.06	0.86 ± 0.15	0.62 ± 0.10	0.19 ± 0.10	NA
TAR	0.09 ± 0.04 (n=4)	0.20 ± 0.10 (n=5)	0.20 ± 0.16 (n=10)	0.20 ± 0.14 (n=66)	0.63 ± 0.35 (n=3)	0.15 ± 0.15 (n=4)
$CPI_{C24-C32}$	5.11 ± 0.59 (n=4)	5.57 ± 1.79 (n=5)	6.09 ± 1.70 (n=10)	6.92 ± 2.37 (n=66)	6.61 ± 1.24 (n=3)	9.99 ± 6.08 (n=4)
Σ_8 ($mg\ g^{-1}$ sediment)	0.46 ± 0.31 (n=4)	0.34 ± 0.16 (n=6)	0.30 ± 0.15 (n=11)	0.29 ± 0.18 (n=73)	0.40 ± 0.17 (n=3)	0.15 ± 0.07 (n=4)
Λ_8 ($mg\ g^{-1}$ OC)	NA	33 ± 9 (n=6)	20 ± 4 (n=10)	21 ± 10 (n=49)	24 (n=2; 27, 21)	29 (n=1)
(Ad/Al)v	0.30 ± 0.06 (n=4)	0.31 ± 0.02 (n=6)	0.37 ± 0.07 (n=11)	0.36 ± 0.14 (n=73)	0.35 ± 0.07 (n=3)	0.42 ± 0.07 (n=4)
(Ad/Al)s	0.12 ± 0.04 (n=4)	0.12 ± 0.04 (n=6)	0.14 ± 0.07 (n=11)	0.13 ± 0.07 (n=71)	0.15 ± 0.01 (n=3)	0.08 ± 0.04 (n=4)
P/(V+S)	0.13 ± 0.02 (n=4)	0.14 ± 0.06 (n=6)	0.15 ± 0.03 (n=11)	0.19 ± 0.17 (n=73)	0.20 ± 0.02 (n=3)	030 ± 0.22 (n=4)
Lignin phenol yield ($kg\ km^{-2}\ yr^{-1}$)	43 ± 28 (2006–2012)	34 ± 32 (2006–2012)	67 ± 53 (2006–2012)	54 ± 30 (2006–2011)	34 ± 29 (2006–2012)	NA

[a]Average of suspended sediment yield of 2006–2012, except for station D2 (2006–2011). Data from Wang et al. (2015).
[b]Average of POC, yield of 2006–2012, except for station D2 (2006–2011). Data from Wang et al. (2019).

10.3389/feart.2022.1090983

sediment and OC supply. Storms were more efficient at mobilizing the landslide deposits and surface soils to the rivers due to the increasing transport capacity. In comparison, the mobilization of earthquake-triggered landslide and eroded OC was depended on the hydrological conditions (Wang et al., 2019; Zhang et al., 2019). Massive landslide-eroded OC could stay on the hillslope and influence the sediment and POC export over a longer term and a wider area. The different locations of the earthquake- and storm-triggered landslide (Wang et al., 2020) likely amplified the difference, since the connectivity of landslides to the river channels regulated the evacuation time of landslide-eroded materials (Croissant et al., 2021).

Lignin is the second most abundant biopolymer in vascular plants and thus plays a prominent role in the global carbon cycle. The riverine particulate lignin phenol concentration was broadly correlated with the annual suspended sediment concentration, which was consistent with the global trend (Figure 3B; Bao et al., 2015). We noted that the lignin phenol concentration on 3 July during the debris flow event was the highest among the reported data, even higher than that of the Taiwan rivers during a typhoon flood (Figure 3B). The comparison between the upper Min Jiang and global rivers highlighted the role of extreme events on lignin erosion in the inland active mountain belts.

Due to the abundant supply and shorter residence time of soil and biospheric OC, small mountain rivers transfer disproportionately high discharges of terrestrial organic carbon to the sedimentary deposit (Bao et al., 2015; Hilton et al., 2008). Our data suggest that the inland tectonic active mountains eroded large amounts of terrestrial OC and earthquakes drove long-term biospheric POC and lignin export. In comparison, the monsoon-triggered debris flow mobilized large amounts of less degraded OC. The high turbidity during these events could facilitate the preservation and burial of the biospheric OC in the downstream reservoirs and/or marginal sea. Under the global change, the increased frequency of intense rainfall events (Mountain Research Initiative EDW Working Group, 2015) would increase the flux of lignin and $POC_{biosphere}$ and put the monsoon-impact active mountain belts to a more important place on the global carbon cycle.

4 Conclusion

Impacted by monsoon and tectonic activities, the Longmen Shan erodes and transports a significant amount of organic carbon from soils, vegetation and sedimentary rocks. We detected the source of terrestrial OC by analysing the abundances of *n*-alkanoic acid and lignin phenol. In combination with the bulk carbon isotopes, the biomarker analysis further confirmed that POC was a mixture of OC from clastic sediment, plant debris, and soils with different degradation degrees. Fine, degraded terrestrial OC preferred to be bound to minerals with high specific surface areas, while coarse, discrete POC was removed from the soil and plant detritus and is prevalent during high SSCs, e.g., debris flows. In contrast, the source of the POC during the low SSC was stochastic.

The impacts of the 2008 Wenchuan earthquake and a debris flow event in 2005 were assessed on the source of terrestrial OC and the flux of lignin phenol. The earthquake, with moderate landslides in the study area, enhanced the supply of POC and lignin into the fluvial system, while its impact on the POC source was limited. In comparison, the monsoon-driven debris flow mobilized a large amount of POC, especially the less-degraded plant detritus and soil. Our results shed light on the role of the storm and earthquake in the carbon cycle in active mountain forests. An increased frequency of intense rainfall events in the future (Mountain Research Initiative EDW Working Group, 2015) will not only facilitate the erosion of the pre-aged POC deep in the soil (Wang et al., 2019) but also enhance the mobilization of discrete, less-degraded plant detritus and soil with a higher fraction. Yet, their fates are still not well constrained in the inland headstream. Our study calls for future work on the roles of earthquakes and extreme rainfall at different locations in the carbon cycle over different timescales.

Data availability statement

The original contributions presented in the study are included in the article/Supplementary Material, further inquiries can be directed to the corresponding authors.

Author contributions

ZJ, XF, RH, and JW conceived of the study. FZ and JW collected the samples. JW and TM carried out the sample and data analyses. JW drafted the manuscript with input from all authors.

Funding

This research was provided by NSFC (42003056) to J.W. and NSFC programs (42221003, 41991322, 41930864) to J.W. and Z.J. R.G.H. acknowledges support from NERC (NE/P013538/1).

Acknowledgments

We thank Z. Liu, Y. Wang, Y. Cai, S. Zhu, G. Dai, T. Liu and Z. Cao for assistance in the laboratory and L. Chen and Aba Hydrology Bureau for assistance with sample collection. We thank the two referees for insightful comments that improved the manuscript.

Conflict of interest

The authors declare that the research was conducted in the absence of any commercial or financial relationships that could be construed as a potential conflict of interest.

The handling editor declared a past co-authorship with the author ZJ.

Publisher's note

Supplementary material

The Supplementary Material for this article can be found online at: https://www.frontiersin.org/articles/10.3389/feart.2022.1090983/full#supplementary-material

References

Bao, H., Lee, T.-Y., Huang, J.-C., Feng, X., Dai, M., and Kao, S.-J. (2015). Importance of Oceanian small mountainous rivers (SMRs) in global land-to-ocean output of lignin and modern biospheric carbon. *Sci. Rep.* 5, 20710. doi:10.1038/srep20710

Berner, R.A. (1982). Burial of organic carbon and pyrite sulfur in the modern ocean: its geochemical and environmental significance. *Am. J. Sci.* 282, 451–473. doi:10.2475/ajs.282.4.451

Bouchez, J., Galy, V., Hilton, R. G., Gaillardet, J., Moreira-Turcq, P., Pérez, M. A., France-Lanord, C., and Maurice, L. (2014). Source, transport and fluxes of Amazon River particulate organic carbon: insights from river sediment depth-profiles. *Geochim. Cosmochim. Acta* 133, 280–298. doi:10.1016/j.gca.2014.02.032

China Geological Survey (2004). China Geological Base Map and Instructions (1: 2,500,000). Beijing: SinoMaps Press.

Clark, K.E., West, A.J., Hilton, R.G., Asner, G.P., Quesada, C.A., Silman, M.R., Saatchi, S.S., Farfan-Rios, W., Martin, R.E., Horwath, A.B., Halladay, K., New, M., and Malhi, Y. (2016). Storm-triggered landslides in the Peruvian Andes and implications for topography, carbon cycles, and biodiversity. *Earth Surf. Dynam.* 4, 47–70. doi:10.5194/esurf-4-47-2016

Clark, K.E., Stallard, R.F., Murphy, S.F., Scholl, M.A., Gonzalez, G., Plante, A.F., and McDowell, W.H. (2022). Extreme rainstorms drive exceptional organic carbon export from forested humid-tropical rivers in Puerto Rico. *Nat. Commun.* 13 (1), 2058. doi:10.1038/s41467-022-29618-5

Croissant, T., Hilton, R.G., Li, G.K., Howarth, J., Wang, J., Harvey, E.L., Steer, P., and Densmore, A.L. (2021). Pulsed carbon export from mountains by earthquake-triggered landslides explored in a reduced-complexity model. *Earth Surf. Dynam.* 9, 823–844. doi:10.5194/esurf-9-823-2021

Dadson, S.J., Hovius, N., Chen, H., Dade, W.B., Lin, J.C., Hsu, M.L., Lin, C.W., Horng, M.J., Chen, T.C., and Milliman, J. (2004). Earthquake-triggered increase in sediment delivery from an active mountain belt. *Geology* 32, 733–736. doi:10.1130/g20639.1

Dai, G., Zhu, E., Liu, Z., Wang, Y., Zhu, S., Wang, S., Ma, T., Jia, J., Wang, X., Hou, S., Fu, P., Peterse, F., and Feng, X. (2019). Compositional characteristics of fluvial particulate organic matter exported from the world's largest alpine wetland. *J. Geophys. Res. Biogeosci.* 124, 2709–2727. doi:10.1029/2019jg005231

Densmore, A.L., and Hovius, N. (2000). Topographic fingerprints of bedrock landslides. *Geology* 28, 371–374. doi:10.1130/0091-7613(2000)028<0371:tfobl>2.3.co;2

Dittmar, T., and Lara, R.J. (2001). Molecular evidence for lignin degradation in sulfate-reducing mangrove sediments (Amazônia, Brazil). *Geochim. Cosmochim. Acta* 65, 1417–1428. doi:10.1016/s0016-7037(00)00619-0

Feng, X., Feakins, S.J., Liu, Z., Ponton, C., Wang, R.Z., Karkabi, E., Galy, V., Berelson, W.M., Nottingham, A.T., Meir, P., and West, A.J. (2016). Source to sink: Evolution of lignin composition in the Madre de Dios River system with connection to the Amazon basin and offshore. *J. Geophys. Res. Biogeosci.* 121, 1316–1338. doi:10.1002/2016jg003323

Feng, X., Vonk, J.E., van Dongen, B.E., Gustafsson, O., Semiletov, I.P., Dudarev, O.V., Wang, Z., Montlucon, D.B., Wacker, L., and Eglinton, T.I. (2013). Differential mobilization of terrestrial carbon pools in Eurasian Arctic river basins. *Proc. Natl. Acad. Sci. U. S. A.* 110, 14168–14173. doi:10.1073/pnas.1307031110

France-Lanord, C., and Derry, L.A. (1997). Organic carbon burial forcing of the carbon cycle from Himalayan erosion. *Nature* 390, 65–67. doi:10.1038/36324

Francis, O., Fan, X., Hales, T., Hobley, D., Xu, Q., and Huang, R. (2022). The Fate of Sediment After a Large Earthquake. *J. Geophys. Res. Earth. Surf.* 127, e2021JF006352. doi:10.1029/2021jf006352

Frith, N.V., Hilton, R.G., Howarth, J.D., Gröcke, D.R., Fitzsimons, S.J., Croissant, T., Wang, J., McClymont, E.L., Dahl, J., and Densmore, A.L. (2018). Carbon export from mountain forests enhanced by earthquake-triggered landslides over millennia. *Nat. Geosci.* 11, 772–776. doi:10.1038/s41561-018-0216-3

Galy, V., Peucker-Ehrenbrink, B., and Eglinton, T. (2015). Global carbon export from the terrestrial biosphere controlled by erosion. *Nature* 521, 204–207. doi:10.1038/nature14400

Goñi, M.A., and Hedges, J.I. (1995). Sources and reactivities of marine-derived organic matter in coastal sediments as determined by alkaline CuO oxidation. *Geochim. Cosmochim. Acta* 59, 2965–2981. doi:10.1016/0016-7037(95)00188-3

Goñi, M.A., and Thomas, K.A. (2000). Sources and transformations of organic matter in surface soils and sediments from a tidal estuary (North Inlet, South Carolina, USA). *Estuaries* 23, 548–564. doi:10.2307/1353145

Hedges, J.I., Blanchette, R.A., Weliky, K., and Devol, A.H. (1988). Effects of fungal degradation on the CuO oxidation products of lignin: A controlled laboratory study. *Geochim. Cosmochim. Acta* 52, 2717–2726. doi:10.1016/0016-7037(88)90040-3

Hedges, J.I., and Ertel, J. R. (1982). Characterization of lignin by gas capillary chromatography of cupric oxide oxidation products. *Anal. Chem.* 54, 174–178. doi:10.1021/ac00239a007

Hilton, R.G., Galy, A., Hovius, N., Chen, M.C., Horng, M.J., and Chen, H.Y. (2008). Tropical-cyclone-driven erosion of the terrestrial biosphere from mountains. *Nat. Geosci.* 1, 759–762. doi:10.1038/ngeo333

Hilton, R.G., Galy, A., Hovius, N., Horng, M.-J., and Chen, H. (2010). The isotopic composition of particulate organic carbon in mountain rivers of Taiwan. *Geochim. Cosmochim. Acta* 74, 3164–3181. doi:10.1016/j.gca.2010.03.004

Hilton, R.G., Galy, V., Gaillardet, J., Dellinger, M., Bryant, C., O'Regan, M., Grocke, D.R., Coxall, H., Bouchez, J., and Calmels, D. (2015). Erosion of organic carbon in the Arctic as a geological carbon dioxide sink. *Nature* 524, 84–87. doi:10.1038/nature14653

Hilton, R.G., and West, A. J. (2020). Mountains, erosion and the carbon cycle. *Nat. Rev. Earth Environ* 1, 284–299. doi:10.1038/s43017-020-0058-6

Hovius, N., Meunier, P., Lin, C.-W., Chen, H., Chen, Y.-G., Dadson, S., Horng, M.-J., and Lines, M. (2011). Prolonged seismically induced erosion and the mass balance of a large earthquake. *Earth Planet. Sci. Lett.* 304, 347–355. doi:10.1016/j.epsl.2011.02.005

Hovius, N., Stark, C.P., Chu, H.T., and Lin, J.C. (2000). Supply and removal of sediment in a landslide-dominated mountain belt: Central Range, Taiwan. *J. Geol.* 108, 73–89. doi:10.1086/314387

Howarth, J.D., Fitzsimons, S.J., Norris, R.J., and Jacobsen, G.E. (2012). Lake sediments record cycles of sediment flux driven by large earthquakes on the Alpine fault, New Zealand. *Geology* 40, 1091–1094. doi:10.1130/g33486.1

Huang, H., Shi, S.-W., Xie, Z.-S., and She, T. (2012). Geomorphic features of rainstorm-induced debris flow gullies in Zagunao River basin. *Bulletin of Soil and Water Conservation* 32, 203–207. (in Chinese with English abstract).

Huang, R., and Fan, X. (2013). The landslide story. *Nat. Geosci.* 6, 325–326. doi:10.1038/ngeo1806

Keefer, D.K. (1984). Landslides caused by earthquakes. *Geol. Soc. Am. Bull.* 95, 406–421. doi:10.1130/0016-7606(1984)95<406:lcbe>2.0.co;2

Li, G., West, A.J., Densmore, A.L., Jin, Z., Parker, R.N., and Hilton, R.G. (2014). Seismic mountain building: Landslides associated with the 2008 Wenchuan earthquake in the context of a generalized model for earthquake volume balance. *Geochem. Geophys. Geosyst.* 15, 833–844. doi:10.1002/2013gc005067

Li, G., West, A.J., Densmore, A.L., Jin, Z., Zhang, F., Wang, J., Clark, M., and Hilton, R.G. (2017). Earthquakes drive focused denudation along a tectonically active mountain front. *Earth Planet. Sci. Lett.* 472, 253–265. doi:10.1016/j.epsl.2017.04.040

Lin, G.-W., Chen, H., Hovius, N., Horng, M.-J., Dadson, S., Meunier, P., and Lines, M. (2008). Effects of earthquake and cyclone sequencing on landsliding and fluvial sediment transfer in a mountain catchment. *Earth Surf. Process. Landf.* 33, 1354–1373. doi:10.1002/esp.1716

Liu-Zeng, J., Wen, L., Oskin, M., and Zeng, L. (2011). Focused modern denudation of the Longmen Shan margin, eastern Tibetan Plateau. *Geochem. Geophys. Geosyst.* 12, Q11007. doi:10.1029/2011gc003652

Marc, O., Stumpf, A., Malet, J.P., Gosset, M., Uchida, T., and Chiang, S.H. (2018). Initial insights from a global database of rainfall-induced landslide inventories: the weak influence of slope and strong influence of total storm rainfall. *Earth Surf. Dynam.* 6, 903–922. doi:10.5194/esurf-6-903-2018

Meunier, P., Hovius, N., and Haines, J.A. (2008). Topographic site effects and the location of earthquake induced landslides. *Earth Planet. Sci. Lett.* 275, 221–232. doi:10.1016/j.epsl.2008.07.020

Märki, L., Lupker, M., France-Lanord, C., Lavé, J., Gallen, S., Gajurel, A.P., Haghipour, N., Leuenberger-West, F., and Eglinton, T. (2021). An unshakable carbon budget for the Himalaya. *Nat. Geosci.* 14, 745–750. doi:10.1038/s41561-021-00815-z

Mayorga, E., Aufdenkampe, A.K., Masiello, C.A., Krusche, A.V., Hedges, J.I., Quay, P.D., Richey, J.E., and Brown, T.A. (2005). Young organic matter as a source of carbon dioxide outgassing from Amazonian rivers. *Nature* 436, 538–541. doi:10.1038/nature03880

Ministry of Water Resources of China (2007). *Code for Measurements of Suspended Sediment in Open Channels (GB50159-92)*. Beijing, China: China Planning Press. (in Chinese).

Mountain Research Initiative EDW Working Group (2015). Elevation-dependent warming in mountain regions of the world. *Nat. Clim. Change* 5, 424–430. doi:10.1038/nclimate2563

Otto, A., and Simpson, M.J. (2006). Evaluation of CuO oxidation parameters for determining the source and stage of lignin degradation in soil. *Biogeochemistry* 80, 121–142. doi:10.1007/s10533-006-9014-x

Petsch, S.T., Berner, R.A., and Eglinton, T.I. (2000). A field study of the chemical weathering of ancient sedimentary organic matter. *Org. Geochem.* 31, 475–487. doi:10.1016/s0146-6380(00)00014-0

Qiao, J., Bao, H.Y., Huang, D.K., Li, D.W., Lee, T.Y., Huang, J.C., and Kao, S.J. (2020). Runoff-driven export of terrigenous particulate organic matter from a small mountainous river: sources, fluxes and comparisons among different rivers. *Biogeochemistry* 147, 71–86. doi:10.1007/s10533-019-00629-7

Qu, Y.X., Jin, Z.D., Wang, J., Wang, Y.Q., Xiao, J., Gou, L.F., Zhang, F., Liu, C.Y., Gao, Y.L., Suarez, M.B., and Xu, X.M. (2020). The sources and seasonal fluxes of particulate organic carbon in the Yellow River. *Earth Surf. Process. Landf.* 45, 2004–2019. doi:10.1002/esp.4861

Rielley, G., Collier, R.J., Jones, D.M., and Eglinton, G. (1991). The biogeochemistry of Ellesmere Lake, U.K. —I: source correlation of leaf wax inputs to the sedimentary lipid record. *Org. Geochem.* 17, 901–912. doi:10.1016/0146-6380(91)90031-e

Spencer, R.G.M., Hernes, P.J., Dinga, B., Wabakanghanzi, J.N., Drake, T.W., and Six, J. (2016). Origins, seasonality, and fluxes of organic matter in the Congo River. *Global Biogeochem. Cycles* 30, 1105–1121. doi:10.1002/2016gb005427

Sun, S., Schefuß, E., Mulitza, S., Chiessi, C.M., Sawakuchi, A.O., Zabel, M., Baker, P.A., Hefter, J., and Mollenhauer, G. (2017). Origin and processing of terrestrial organic carbon in the Amazon system: lignin phenols in river, shelf, and fan sediments. *Biogeosciences* 14, 2495–2512. doi:10.5194/bg-14-2495-2017

Tao, S., Eglinton, T.I., Montluçon, D.B., McIntyre, C., and Zhao, M. (2015). Pre-aged soil organic carbon as a major component of the Yellow River suspended load: Regional significance and global relevance. *Earth Planet. Sci. Lett* 414, 77–86. doi:10.1016/j.epsl.2015.01.004

Wang, J., Hilton, R.G., Jin, Z., Zhang, F., Densmore, A.L., Gröcke, D.R., Xu, X., Li, G., and West, A.J. (2019). The isotopic composition and fluxes of particulate organic carbon exported from the eastern margin of the Tibetan Plateau. *Geochim. Cosmochim. Acta* 252, 1–15. doi:10.1016/j.gca.2019.02.031

Wang, J., Howarth, J.D., McClymont, E.L., Densmore, A.L., Fitzsimons, S.J., Croissant, T., Gröcke, D.R., West, M.D., Harvey, E.L., Frith, N.V., Garnett, M.H., and Hilton, R.G. (2020). Long-term patterns of hillslope erosion by earthquake-induced landslides shape mountain landscapes. *Sci. Adv.* 6, eaaz6446. doi:10.1126/sciadv.aaz6446

Wang, J., Jin, Z., Hilton, R.G., Zhang, F., Densmore, A.L., Li, G., and West, A.J. (2015). Controls on fluvial evacuation of sediment from earthquake-triggered landslides. *Geology* 43, 115–118. doi:10.1130/g36157.1

Wang, J., Jin, Z., Hilton, R.G., Zhang, F., Li, G., Densmore, A.L., Gröcke, D.R., Xu, X., and West, A.J. (2016). Earthquake-triggered increase in biospheric carbon export from a mountain belt. *Geology* 44, 471–474. doi:10.1130/g37533.1

Zhang, F., Jin, Z., West, A.J., An, Z., Hilton, R.G., Wang, J., Li, G., Densmore, A.L., Yu, J., Qiang, X., Sun, Y., Li, L., Gou, L., Xu, Y., Xu, X., Liu, X., Pan, Y., and You, C.-F. (2019). Monsoonal control on a delayed response of sedimentation to the 2008 Wenchuan earthquake. *Sci. Adv.* 5, eaav7110. doi:10.1126/sciadv.aav7110

Frontiers in Earth Science

Investigates the processes operating within the major spheres of our planet

Advances our understanding across the earth sciences, providing a theoretical background for better use of our planet's resources and equipping us to face major environmental challenges.

Discover the latest Research Topics

See more →

Frontiers

Avenue du Tribunal-Fédéral 34
1005 Lausanne, Switzerland
frontiersin.org

Contact us

+41 (0)21 510 17 00
frontiersin.org/about/contact